FUNDAMENTAL STUDY OF THE SYNTHESIS, STRUCTURAL AND ELECTROCHEMICAL CHARACTERIZATION OF NANOPARTICULATE TRANSITION METAL OXIDE AND NITRIDE BASED SUPERCAPACITOR SYSTEMS

by

Prashanth Jampani Hanumantha

B.Tech. in Chemical & Electrochemical Engineering,

Central Electrochemical Research Institute, Anna University, 2006

M. S. in Materials Science & Engineering,

Carnegie Mellon University, 2008

Submitted to the Graduate Faculty of

Swanson School of Engineering in partial fulfillment

of the requirements for the degree of

Doctor of Philosophy

University of Pittsburgh

2014

UNIVERSITY OF PITTSBURGH

SWANSON SCHOOL OF ENGINEERING

This dissertation was presented

by

Prashanth Jampani Hanumantha

It was defended on

June 24, 2014

and approved by

Robert M. Enick, Ph.D., Bayer Professor and Vice Chair for Research

Department of Chemical & Petroleum Engineering

Giannis Mpourmpakis, Ph.D., Assistant Professor

Department of Chemical & Petroleum Engineering

Spandan Maiti, Ph.D., Assistant Professor

Department of Bioengineering

Dissertation Director: Prashant N. Kumta, Ph.D., Edward. R. Weidlein Chair Professor,

Department of Chemical & Petroleum Engineering

FUNDAMENTAL STUDY OF THE SYNTHESIS, STRUCTURAL AND ELECTROCHEMICAL CHARACTERIZATION OF NANOPARTICULATE TRANSITION METAL OXIDE AND NITRIDE BASED SUPERCAPACITOR SYSTEMS

Prashanth Jampani Hanumantha, Ph.D.

University of Pittsburgh, 2014

Supercapacitors are electrochemical charge storage devices capable of delivering large bursts of charge over a very short period of time. There is a need for identification and development of alternative low-cost, high energy, high-power materials for widespread implementation of supercapacitor technologies. Nanostructured vanadium nitride (VN) coated with a thin vanadium oxide (VO_x) surface layer has previously been identified to be a very promising electrode material for supercapacitor application.

In this work, attempt was made to develop a fundamental understanding of the supercapacitor response of both the nitride and oxide nanomaterials. In order to understand the charge storage behavior of the nitride nanomaterials, both the materials and electrode properties were altered to understand the exact role of each aspect on the charge storage characteristics. Using a combination of solid state and wet-chemical methods a number of nitride materials were synthesized and via a thorough materials and electrochemical characterization, a fundamental understanding of the structure-property relationships in the nitride materials was obtained. The roles of particle size, electronic conductivity, and electrode thickness and most importantly, the surface oxide nature are also explored in this work.

The investigations conducted in the nitride systems made it clear that the prodigious amount of charge storage in nitride nanomaterials was primarily due to a surface oxide layer and that the stabilization and improvement in electronic conductivity of the surface oxide was pivotal in attaining a reversible and stable charge storage. Nanostructured oxides of vanadium (VO_x) as standalone supercapacitor materials were therefore explored. Thin films of vanadium oxide were deposited on an array of vertically aligned carbon nanotubes (VACNTs) derived using chemical vapor deposition (CVD). This study also made it very clear that the presence of a conductive support structure is imperative to achieve good charge storage response in oxides. Using dopants identified by *ab-initio* computational studies of doped vanadium oxide materials (VO_x: M), very high areal and gravimetric capacitances in doped materials coated on VACNTs was demonstrated.

Identical doping strategies were used to derive doped vanadium nitride ($M_yV_{1-y}N$) with a doped surface oxide layer ($M_yV_{1-y}O_x$). Dopants were selected on the basis of improvement in electronic conductivity without compromising the chemical stability. Improvement in charge storage properties of nanoparticulate nitride particles by systematic tailoring of the architecture was demonstrated.

TABLE OF CONTENTS

LIST OF TABLES

LIST OF FIGURES

NOMENCLATURE

Table 1. Commonly used terms and their relevance to charge storage in supercapacitors

Term	Units	Definition/Relevance	Nomenclature /calculation	Observation
Capacitance	F/g or F/cc	Measure of ability of a material to store charge	$C=\frac{\varepsilon A}{dm}=\frac{Q}{V}$	Higher capacitance implies higher energy density
Energy density	Wh/kg or Wh/l	Measure of the amount of energy that a material/device can store per unit mass/volume	$E.d.=\frac{CV^2}{2m}$	Higher energy materials/devices can run for longer time periods
Power density	W/kg or W/l	Measure of ability of a material/device to release large amount of energy in a short time	$P.d.=\frac{i(t)V(t)}{m}$	Higher power density materials/devices can supply large currents

Table 1(continued)

Rate capability	N/A	Ability of a material to retain energy density even upon increasing power		Ideal materials/devices would have minimal rate dependent fade
Cyclability	N/A	Measure of stability of a material		Ideal materials/devices would have minimal fade upon cycling
Scan Rate	mV/s		v	
Electrode active material loading	mg/cm^2	Measure of electrode thickness	l	Thicker electrodes are preferred since an indication of good capacitor response is the retention of gravimetric capacity in thick film electrodes

Table 1(continued)

Electrode Areal capacitance	mF/cm^2	Measure of ability of a material to store charge per unit electrode area	$C_{ae} = C * l$	Ideal capacitor materials would have very high areal capacity
Coating thickness	μm		t	
Electrode Volumetric capacitance	F/cc		$C_{ve} = \frac{C_{ae} * 10}{t}$	
Powder density	g/cm^3		d	
BET surface area	m^2/g		A	
Particle Areal Capacitance	mF/cm^2		$C_{ap} = \frac{C}{A * 10}$	
Particle Volumetric capacitance	F/cc		$C_{vp} = C * d$	
Radius of oxide shell	nm		r_{VO_x}	
Radius of nitride core	nm		r_{VN}	

Table 1(continued)

Mole percentage of oxide			n_{VO_x}	
Mole percentage of nitride			n_{VN}	
Molecular weight of the oxide	g/mol		M_{VO_x}	
Molecular weight of the nitride	g/mol		M_{VN}	
Density of the oxide	g/cm^3		ρ_{VO_x}	
Density of the nitride	g/cm^3		ρ_{VN}	
Lattice parameter	nm			
Molar volume	cm^3/mol			
Series resistance/ solution resistance	Ω-cm^2		R_s	
Faradaic charge-transfer resistance	Ω-cm^2		R_f or R_F	
Double-layer capacitance	F		C_{dl}	

Table 1(continued)

Pseudo-capacitance	F		C_p	
Double layer constant phase element			CPE_{dl}	
Pseudocapacitance constant phase element			CPE_p	
Electronic conductivity	S/cm		σ	
Electrical resistivity	Ω-cm		ρ	
Temperature	^oC or K			
Synthesis time	Mins/h			
Normal hydrogen reference electrode/ Standard hydrogen electrode	NHE/SHE			

Table 1(continued)

$\square_x$	Depicts vacancies of atom x in a lattice			

ACKNOWLEDGEMENTS

At the outset, I would like to thank my committee members Dr. Robert Enick, Dr. Sachin Velankar, Dr. Spandan Maiti and Dr. Giannis Mpourmpakis for their valuable suggestions and guidance at different stages of my thesis work. I would like to convey my heartfelt gratitude to my advisor Dr. Prashant Kumta without whose immense guidance and support, my appreciation for research and innovation would not be what it is today. It is his immense commitment and desire to innovate that has often proven an inspiration to me in pursuit of my research work.

I would also like to gratefully thank the Research Faculty and postdoctoral fellows who have mentored me over the years especially Dr. Moni Datta, Dr. Oleg Velikokhatnyi, Dr. Abhijit Roy, Dr. Daiwon Choi, Dr. Nicolaus Rock and Dr. Wei Wang. Their input has often been the difference between hitting a wall and resolving a challenging problem. I would like to thank my friends and colleagues Dr. Karan Kadakia, Dr. Saurabh Bhavsar, Keith Harper, Yugal Kishore Das, HHRNS for the many fruitful discussions and arguments I have had with them over the course of my graduate life. These conversations have helped shape my understanding of science and appreciation of its relationship to real life scenarios. I owe my gratitude to all my labmates and colleagues through the years. Without their encouragement, I could never have completed my graduate education. Last but not the least, I would like to thank my parents for their blessings and support through the length of my graduate career.

1.0 INTRODUCTION TO ELECTROCHEMICAL CAPACITORS

With the growing interest in alternative energy sources and the cognitive recognition of the benefits of green energy, there is clearly a pressing need for the development of sustainable and clean energy storage systems which has led to burgeoning research over the last two decades in both industry as well as academia[1-6]. Research has primarily focused on two aspects, energy generation and energy storage with some effort focused on distribution.

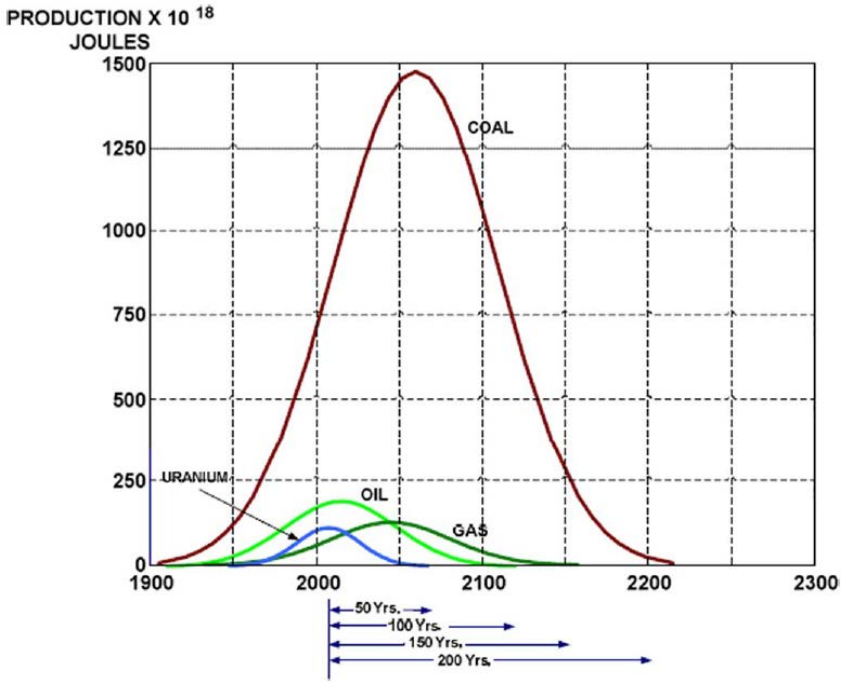

Figure 1. Plot showing estimates of production of currently used energy sources (Reproduced with permission from © 2013 IEEE [7]).

Clean renewable energy generation is quintessential for the sustainable development of the industrial world. The predominant energy sources driving today's economy (primarily carbon based fuels) are expected to run out by the year 2200 (see **Figure 1**)[7]. The need for the switch to non-carbon based renewable energy sources is hastened by the seemingly irreversible anthropogenic alteration of the earth's climate resulting in global eco-system alteration threatening the extinction of a number of species, amphibious, aerial as well as terrestrial[8, 9].

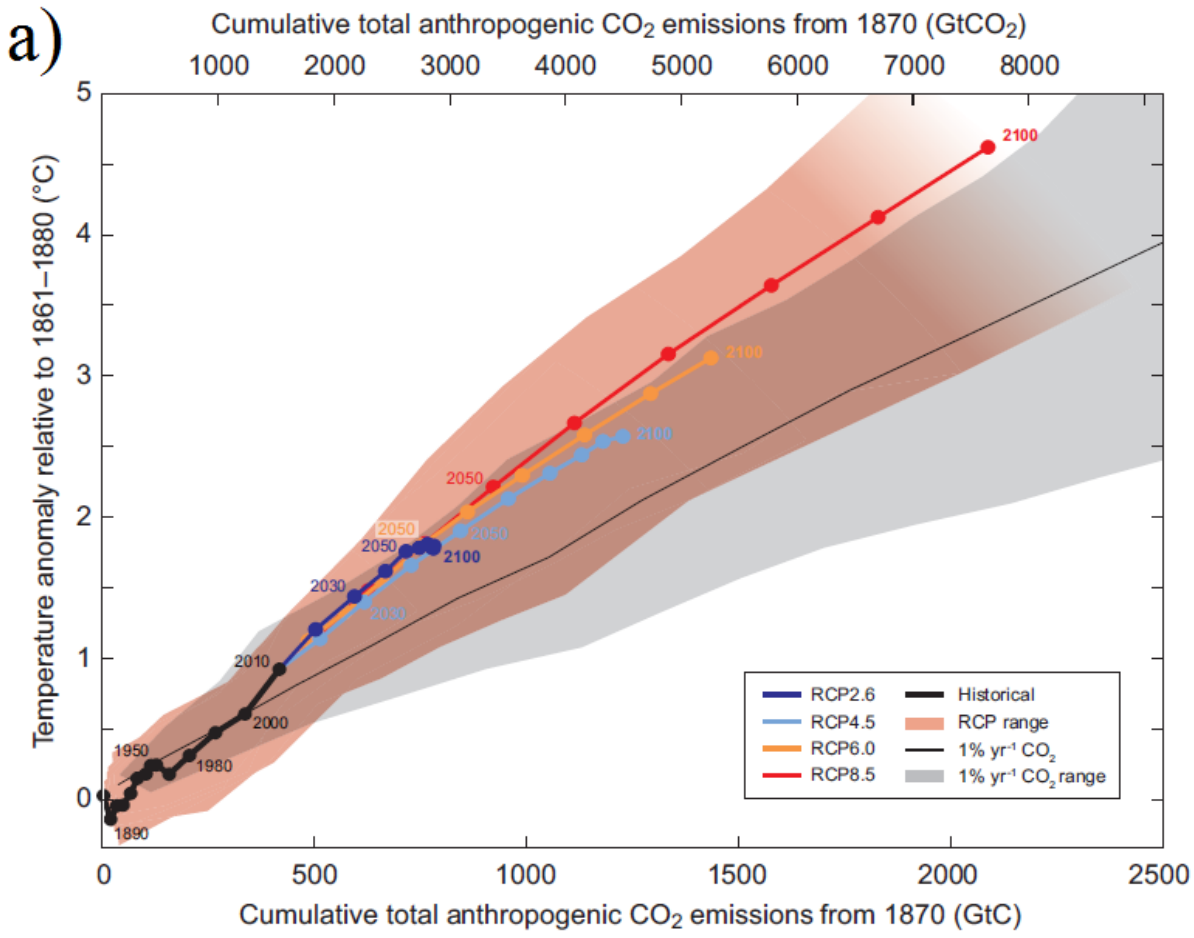

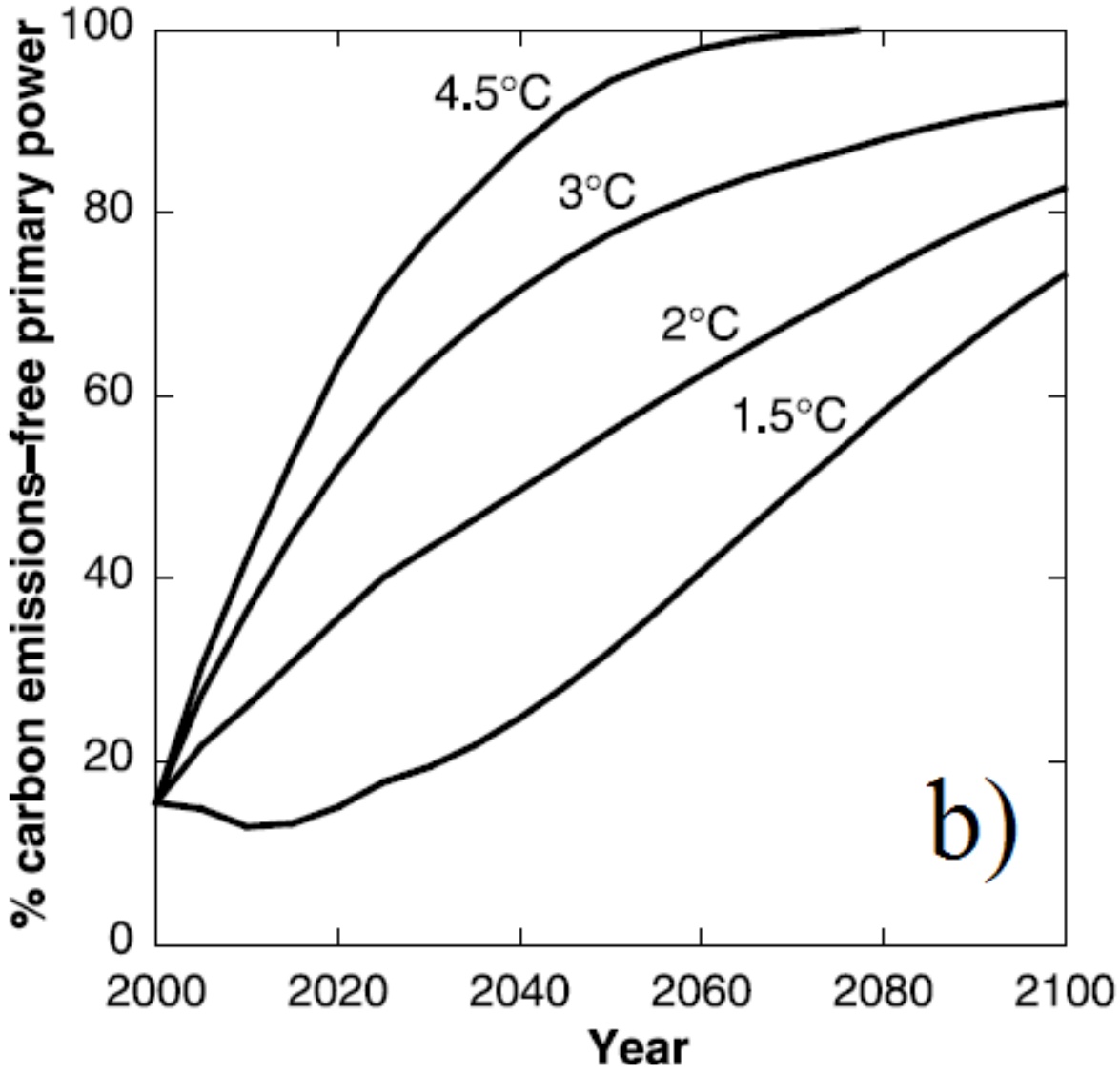

Figure 2. Plot depicting the estimates of (a) temperature rise as a result of global warming (Reproduced from © 2013 IPCC Climate Report)[8]and (b) amount of carbon-free fuel sources required to prevent temperature rise as a result of global warming (Reproduced with permission from © 2003 AAAS)[10].

Figure 2 depicts the necessity for transitioning to carbon-free sources in order to prevent large-scale global temperature change[10]. A 2^{o}C change (estimated to be a suitable target for minimal anthropogenic alteration[9]) according to WRE550[11] (the Wrigley, Richels and Edmonds

standards) economic and environmental choices dictate that we reach a 50% carbon-free source based economy by the year 2050. Carbon-capture technology, a key component in the transition to renewable energy[12-14] including CO_2 storage and utilization[15], carbon capture[16] using chemical looping combustion[17], and use of supercritical carbon dioxide in oil recovery[18] are potential solutions to the climate crisis. However, they do not offer a long-term solution to the energy (usage, generation, storage and distribution) conundrum[19, 20]. A paradigm shift in energy policy is required for achieving sustainable long-term clean energy solutions capable of meeting the needs of an ever-increasing world population and the concomitant needs for energy and power to match the meteoric rise in global development.

Two models have primarily been suggested for the same, the 'Hydrogen-economy'[21, 22] and 'The Distributed Energy Grid'[1]. The idea of a hydrogen-driven economy, given hydrogen's energy density, appears very promising but current materials limitations especially use of high cost catalysts, the lack of suitable hydrogen storage materials system and the accompanying safety issues make the use of hydrogen as an energy-medium impractical at the present time[23-25]. Studies have predicted that the electron-energy based 'distributed-grid model' is a better model economically[26]. The distributed-energy grid based on the 'electron-energy' model involves large scale energy generation from renewable energy sources such as solar and wind farms and distribution of the same in the form of electricity. Transmission of large quantities of electricity over long distances is at a technologically advanced stage to allow for the same with minimal losses[1]. Successful execution of this strategy requires local energy storage technologies of varying functionalities[27]. The aim of using energy storage on a local scale is to decouple generation and load[14]. Efficient energy generation from renewable sources needs to be coupled with the distribution and storage of energy with minimal losses.

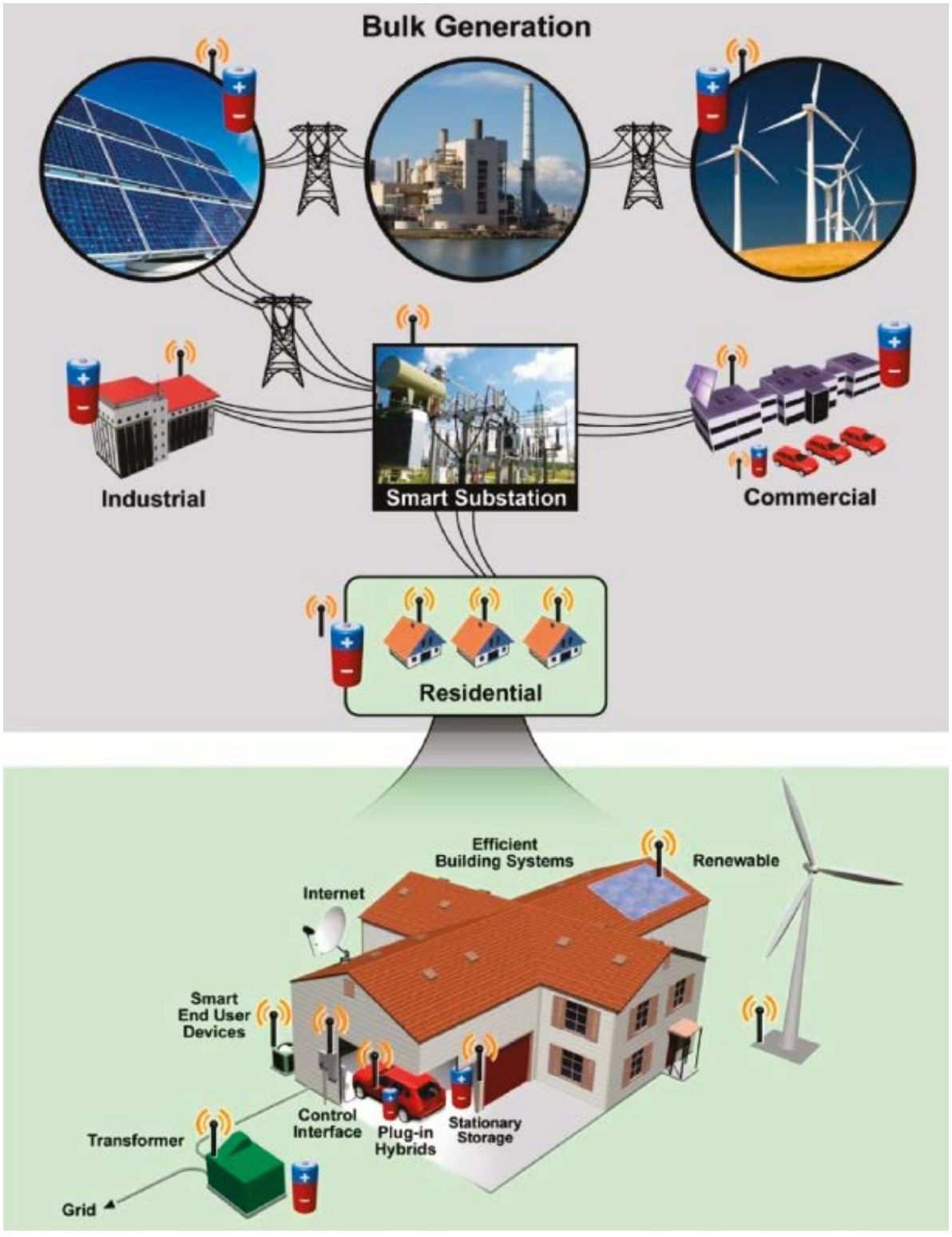

Figure 3. Figure depicting the concept of the smart grid to be used for distributed energy generation and storage. Local energy storage is coupled with large scale energy generation from renewable sources ((Reproduced with permission from © 2011 American Chemical Society[28]).

Figure 3 depicts the concept of the smart grid capable of sustaining the concept of the distributed grid[28]. As shown therein, efficient energy storage and distribution is a multi-scale problem with applications varying from small electronics such as cellular phones to very large industrial reactors. Local energy storage consists of both stationary as well as mobile devices. In addition to grid level, development of energy storage devices for mobile energy storage based smart devices such as laptops, cameras, electric cars etc. is of immediate relevance. The success of these devices and their longevity depends on the identification and development of novel chemistries and configurations to store and deliver charge in cheap, economical and convenient manner. There is therefore no one overarching solution to the energy storage problem. A number of applications require use of small amounts of energy over long periods while others need large bursts of energy in a very small time scale.

These requirements can be quantified in a very facile manner by two parameters, energy density (kWh/kg or kWh/l) and power density (W/kg or W/l). Energy density is a quantification of the total amount of energy a device can hold per either unit weight or unit volume. It is an integral term that defines the propensity of a material to store energy. On the other hand, power density is a rate term that characterizes the amount of energy that can be retrieved over unit time. Higher rates drive systems away from equilibrium resulting in irreversibility and thus loss of energy density. A trade-off is thus achieved between energy density and power density for various devices defining what kind of applications they find practical utility in. Another parameter that acts as a useful barometer for gauging performance in energy storage is cycling stability which is a convenient means for examining how long a device will be able to provide useful energy storage. **Table 1** details the parameters of relevance to charge storage, their significance and units of measurement.

Electrochemical energy storage is one of the most efficient (Theoretical~80%, achievable~50-75%) and clean means of reversibly storing energy making devices such as rechargeable batteries, flow batteries and supercapacitors relevant for local energy storage to aid the distributed grid[29, 30]. Alternative solutions also exist which include thermal energy storage using phase change materials for energy storage [31, 32] and mechanical energy storage[33]. The one outstanding advantage yielded by electrochemical charge storage devices is that they are not limited by Carnot limitations, which plague efficiencies (Theoretical~50%, achievable~25-40%) of all thermal energy storage devices[34, 35]. Based on both the energy density vs. power density ratios and the mechanism of charge storage, reversible electrochemical charge storage devices can be divided into two categories; batteries and supercapacitors. **Figure 4** shows the plot of energy density vs. power density, commonly referred to as the Ragone plot[3, 29, 36]. While batteries can store exceptionally large amounts of energy (high energy density) they are incapable (low power density) of delivering bursts of power required in applications such as automobiles or peak loads on large scale grids[3, 30, 37-45]. Supercapacitors on the other hand, complement batteries and are emerging as highly relevant devices for myriad electronic devices and systems on account of their short charging times (high power density) and seemingly infinite cyclability. Thus they find application in a number of applications such as renewable energy storage[46], grid-leveling and power conditioning[14].

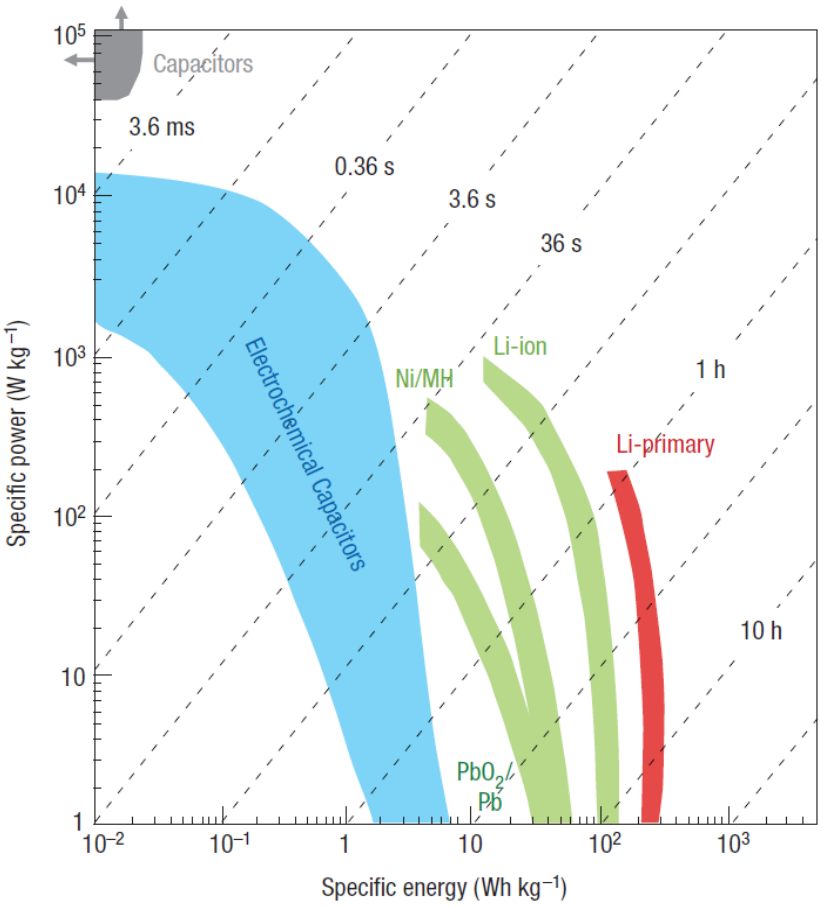

Figure 4. Ragone plot showing performance of various electrochemical energy storage devices with respect to a specific power/specific energy tradeoff (Reprinted with permission from Macmillan Publishers Ltd. [Nature Materials][3], copyright (2008)).

Electrochemical supercapacitors are emerging as devices of prime importance owing to their superior characteristics unmatched by any other charge storage device. These include: high power densities at relatively high energy densities and long cycle life. These characteristics have already been exploited in various applications such as power electronics, large scale transport systems comprising subway trains and buses, energy storage at intermittent generators including windmills, and smart grid applications. Smart grid needs will include grid stability, frequency smoothing, peak shifting, and frequency regulation. Supercapacitors bear relevance to a number

of applications. One of the primary purposes where supercapacitors are being considered is large-scale load-leveling and power quality applications. The smart grid requires a variety of energy storage devices to meet certain specific requirements and **Figure 5** details where supercapacitors could be used. Regenerative braking and energy recovery in mobile applications is a second area of great relevance to supercapacitors. Southeastern Pennsylvania Transit Authority (SEPTA), in collaboration with ABB, Viridity Energy, Saft Battery, and Maxwell Technologies have developed a regenerative braking based energy recovery system for the subway that not only recovers the energy but uses it as a means for frequency regulation of the local grid[47]. Regenerative braking is also used in hybrid cars and buses for energy recovery such as NYC Hybrid buses™, Capabus™ and Lion's City Hybrid™ buses in Paris and trams in Germany[48]. Power burst applications such as start-stop and burst power applications in heavy load applications such as cranes is also an application requiring deployment of supercapacitors. UPS (Uninterrupted Power Supply) systems of varying sizes also require the use of supercapacitors.

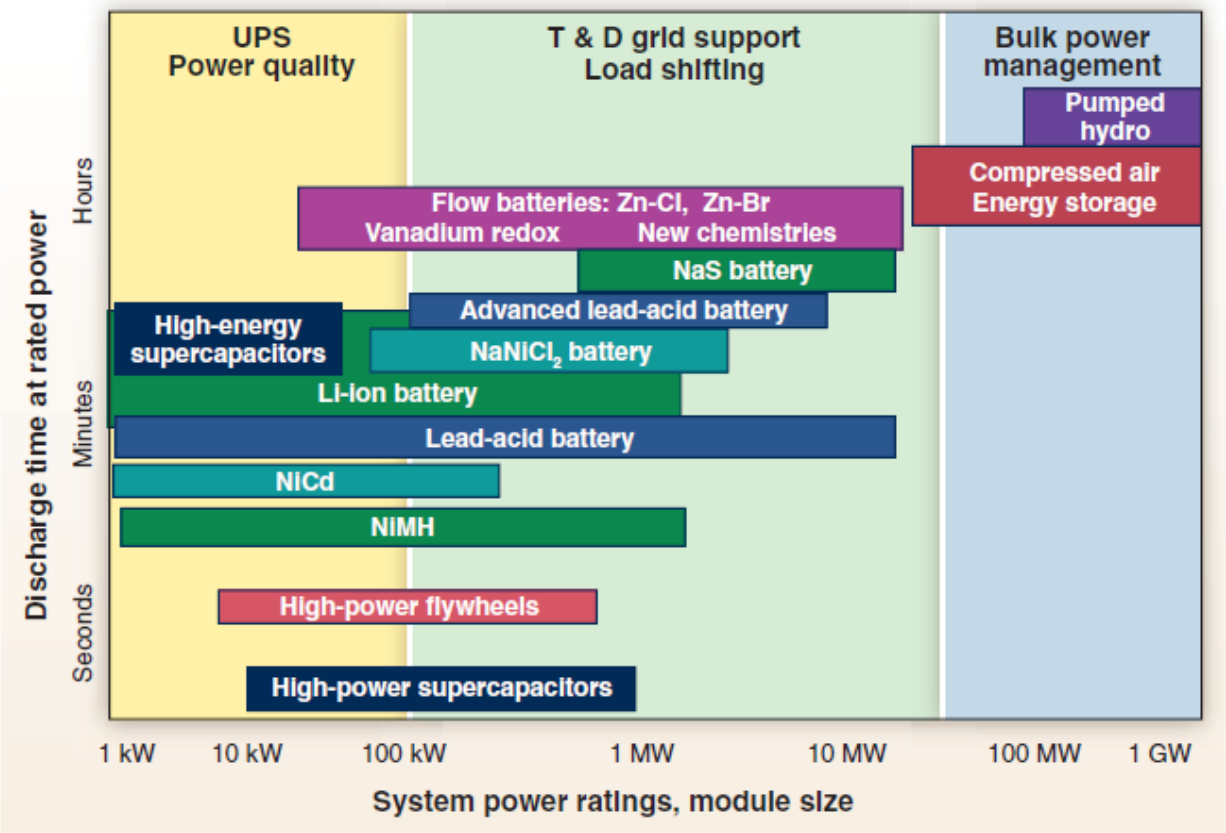

Figure 5. Applicability of supercapacitors in large-scale grid applications (Reproduced with permission from © 2011 AAAS) [14].

The nature of supercapacitor charge storage allows for rapid charge and discharge as shown in **Figure 6**. The use of supercapacitors ensures rapid charge and discharge irrespective of the rate of energy production as seen therein. This is especially relevant for grid level applications wherein primary energy sources are renewable energy production media which are intermittent, and storage is essential to make the solution economically viable in the long run[49].

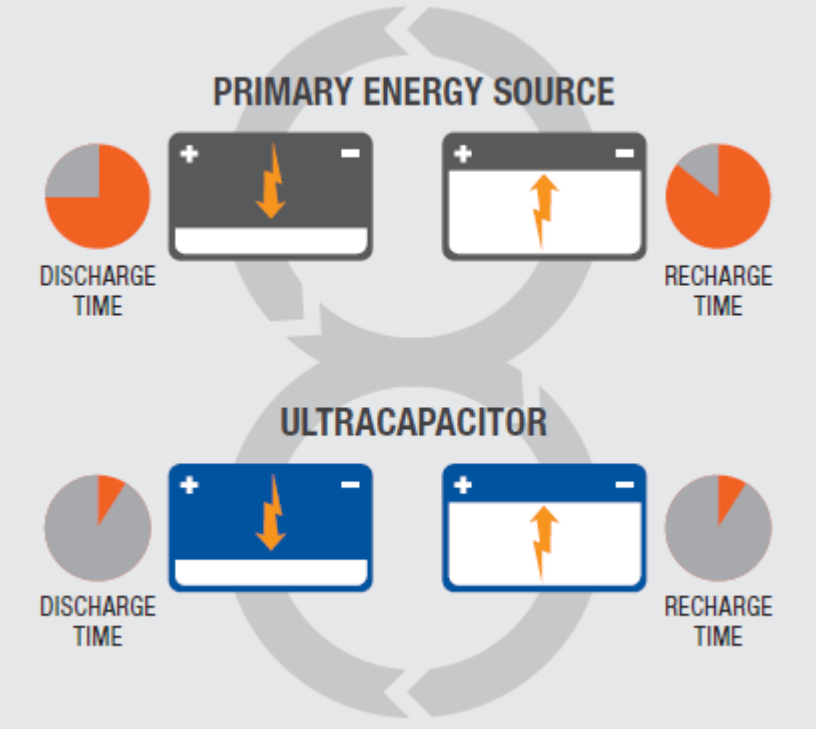

Figure 6. Relevance of supercapacitors and their nature for grid applications (Reproduced with permission from © 2014, Maxwell Technologies, Inc.)[50].

Electrochemical capacitors often referred to as ultracapacitors or supercapacitors are electrochemical devices which exploit surface charge storage properties of electrode materials, thus enabling rapid charge-discharge and making them very attractive for high rate mobile applications such as automobiles and electronic devices. Unlike conventional batteries, supercapacitors can be cycled at very high rates over millions of cycles without losing much of their charge storage capabilities. There is however a critical need to improve energy densities of supercapacitor materials to render them commercially viable for myriad small and large scale device applications[37, 51].

Table 2. Comparison between batteries and electrochemical capacitors.

Batteries	Electrochemical Capacitors
Ideally possesses single-valued free energy of individual components	Exhibits continuous variation of free energy with the degree of conversion of material or extent of charge held
The EMF is ideally constant with the degree of charge and discharge, except for non-thermodynamic extraneous effects, or phase changes occurring during discharge.	The potential is thermodynamically related to the state of charge through a log [θ/1-θ] factor varying in a continuous manner for a supercapacitor, or directly to charge, Q for a double-layer capacitor
Electrochemical response of a battery is Faradaic, not capacitive, except in a very general sense	Electrochemical response is typically capacitive (non-Faradaic)
Observance of irreversibility is normal	High degree of reversibility is common (10^4-10^6 cycles with typical capacitor materials)
Response to linear modulation of potential gives irreversible I vs. V profile with a non-constant current	Response to linear modulation of potential gives more or less constant charging current profile but with some dependence on the type of electrode and electrolyte materials
Discharge at a constant current arises at a more or less constant potential except for intercalation Li batteries	Discharge at a constant current results in primarily linear decline of potential with time, which is a characteristic of capacitors

Supercapacitors differ from batteries in the nature of their charge storage and rate capability. Materials for batteries have been studied for almost a century[52]. Though the fundamental chemistry of supercapacitor electrodes was studied in the mid-20th century, the idea of using such electrodes for large scale energy storage applications commenced in the last decade. The transition from batteries to capacitors depends on a number of factors including the facile nature of kinetics, electronic conductivity of the material, and band-gap. In addition,

electrode loading is also a characteristic which decides the time constant of electrochemical response and therefore the type of charge storage. It has previously been reported that certain battery materials behave as supercapacitors at low loadings[53]. Though the transition is less and less well-defined[54], some fundamental differences exist and have all been listed in **Table 2**.

The concept of supercapacitors originates from the fundamental discovery of static charge occurring as a result of relative motion of two or more surfaces in contact. Early demonstrations of such charge separation phenomena such as the Leyden jar[55] and glass condensers[56] gave way to conventional dielectric capacitors[57] of the 20th century[58]. Early work involving the use of such phenomena for charge storage occurred in the mid-20th century[59-61]. With the gradual realization of the importance of energy storage devices, the late 20th century witnessed significant advances in the field of supercapacitors. Seminal research by Conway et al.[44, 58, 62-65] and others[66] have led to the identification of fundamental chemistries and concepts rendering supercapacitors viable for energy storage applications. Supercapacitors can be characterized into various categories based on electrode/electrolyte and system configuration as shown in **Figure 7**. Traditionally, supercapacitors have been classified as electrochemical double layer capacitors (EDLCs) and pseudocapacitors (PC) based on the charge storage mechanisms which are described in detail below[58].

1.1.1 Electrochemical double layer capacitors

It is common knowledge in electrochemistry that an electrochemical double layer is formed at an electrode-electrolyte interface as a result difference in Fermi energy-levels of electrons in the electrode and the electrolyte[58, 67, 68]. This difference in energy acts as a barrier to electron tunneling from electrode to electrolyte or vice-versa until a certain potential is applied to the

electrode. The electrochemical interface thus acts as a nanometer sized ‘double-layer’ of separated charges resembling a conventional dielectric capacitor (**Figure 8**)[37, 44]. Charge storage devices based on this mechanism are aptly named electrochemical double layer capacitors (EDLCs).

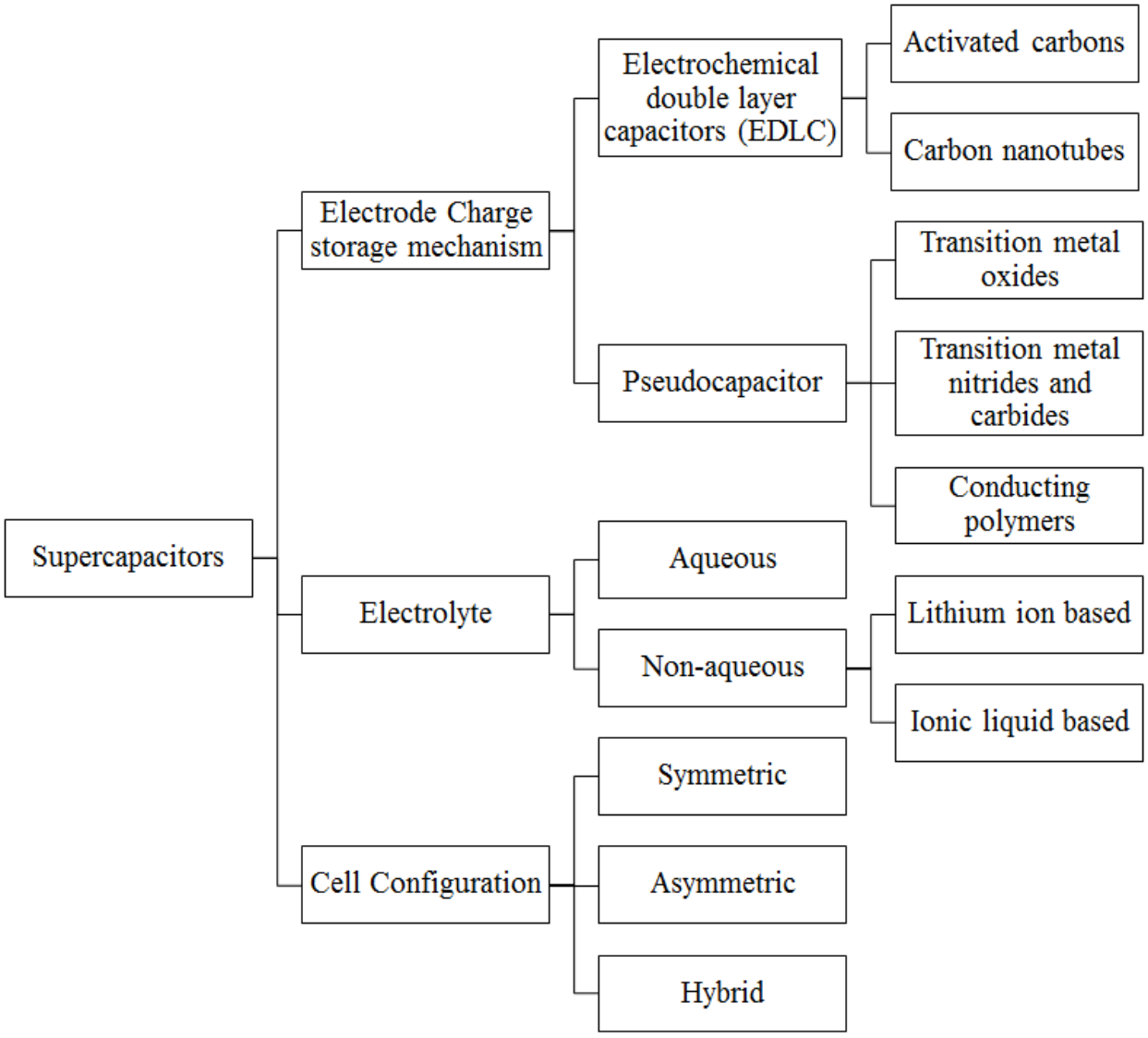

Figure 7. Classification of supercapacitors based on electrode mechanism, electrolyte and cell configuration.

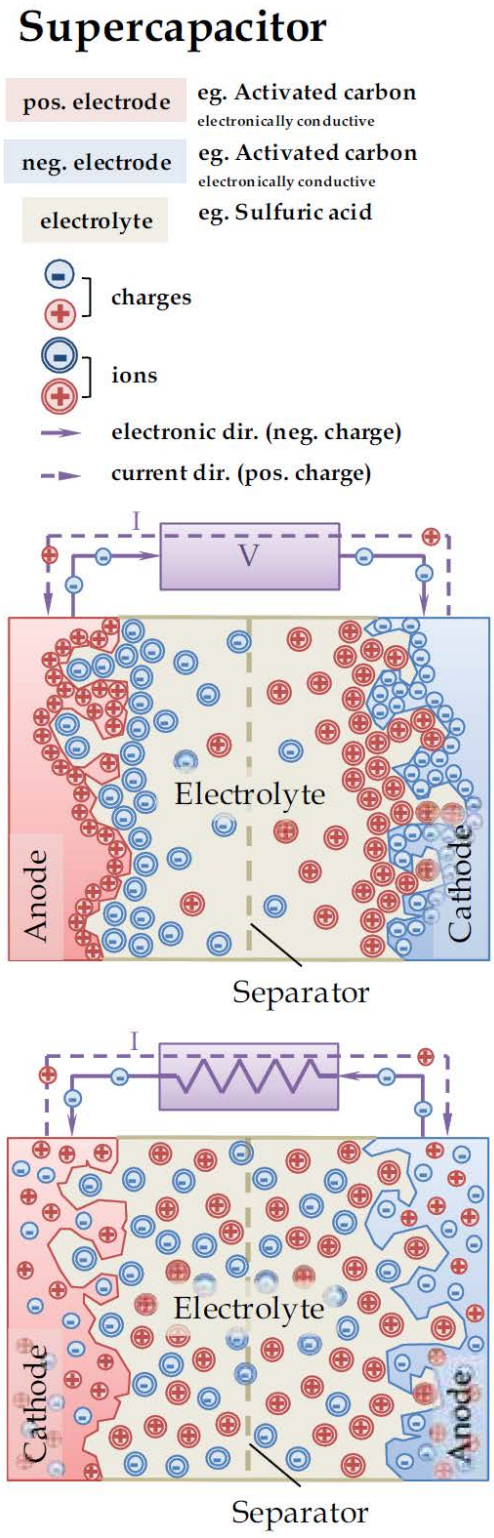

Figure 8. Schematic of an electrochemical double layer type capacitor showing charged (left) and discharged states (right).

1.1.2 Pseudocapacitors (PCs)

A second class of capacitors is termed as pseudo-capacitors (PCs) wherein charge transfer is brought about by the virtue of reversible Faradaic electrochemical redox reactions undergone by specific electrochemically active elements within a compound or compounds. The nature of the successive reversible electrochemical reactions of these compounds allows the charge storage response of the device to resemble that of a capacitor[65].

Table 3. Comparison between EDLCs and Pseudocapacitor electrode materials

Mechanism	**Double layer charge storage**	**Pseudocapacitor electrodes**
Materials	Very high surface area activated carbons (1000-3000 m^2/g), single wall and multi wall carbon nanotubes, graphene	Transition metal oxides and nitrides such as hydrous Ruthenium oxide, Manganese dioxide, Vanadium oxide, Vanadium nitride
Energy density	Capacitances between 100 and 300 F/g are usually observed on account of non-Faradaic surface charge storage leading to relatively low energy densities	Faradaic and sometimes intercalation supercapacitance are observed resulting in capacitances between 200 and 1400 F/g
Rate capability	Very fast response time on account of non-Faradaic response results in much better rate capability	Reduced rate capability on account of either poor electronic conductivity or time constant of Faradaic processes
Cyclability	Infinitely cycle-able	Charge transfer processes either result in bulk phase change or surface reorientation over time resulting in significantly higher fade

While double layer capacitors are much more reversible and represent a rapid response form of charge storage devices, pseudocapacitors have much higher energy densities while at the

same time maintaining a moderately high rate capability on account of the simplistic redox reactions occurring at the surface of the electrode.

Table 3 shows a comparison between the fundamental characteristics of EDLCs and pseudocapacitors. With regards to electronic systems providing high power and energy densities, pseudocapacitor materials fit this bill very well on account of the charge storage mechanism that tends to be a hybrid match of both the battery and supercapacitor worlds[58]. One could therefore envisage hybrid composite materials capable of both very high rate capability and high energy density.

Conventional dielectric and double layer electrochemical capacitors are generally incapable of storing such large amounts of charge. Pseudocapacitors involving a chain of successive reversible Faradaic reactions occurring at the surface thus ensure short charging times and seemingly infinite cyclability with sufficiently large capacitances[44, 58, 65]. Transition metal oxides in particular are very attractive for this genre of application on account of their ability to accept variable oxidation states. Of particular interest for pseudocapacitor applications is the ability of the surface oxide to undergo reversible hydration as in Ruthenium oxide [44, 58]. The current-voltage characteristics of the successive oxidation/reduction reactions ensuing at the surface of the electrode resemble that of a capacitor, hence the term pseudocapacitor. Hydrous Ruthenium oxide serves as a classic example of a pseudocapacitor material with the ability to maintain stable capacitances of up to 900 F/g over a large number of cycles[69]. However, the prohibitive price of noble metal based capacitors impels the search for alternative materials with similar charge storage characteristics. Other non-noble metal oxides and hydroxyl-oxides have been widely explored in this light including those of Mn, Ni and V[70-75]. However, most bulk oxide materials have limited energy densities. There is therefore an urgent need to explore novel

chemistries to identify cheap pseudocapacitor materials with high energy densities and good rate capability. Moreover, there is also a desire to merge the fundamental characteristics of EDLCs and PCs to form hybrid or composite complex systems that will provide a combination of the surface related double layer as well as the surface related Faradaic response to yield the optimally performing supercapacitor. Materials or composite systems that will provide a combination of these characteristics are very much in demand. Concomitantly identification or development of economic processes that will provide these combined responses will further aid the quest while at the same time making supercapacitors highly competitive in the complex arena of energy storage.

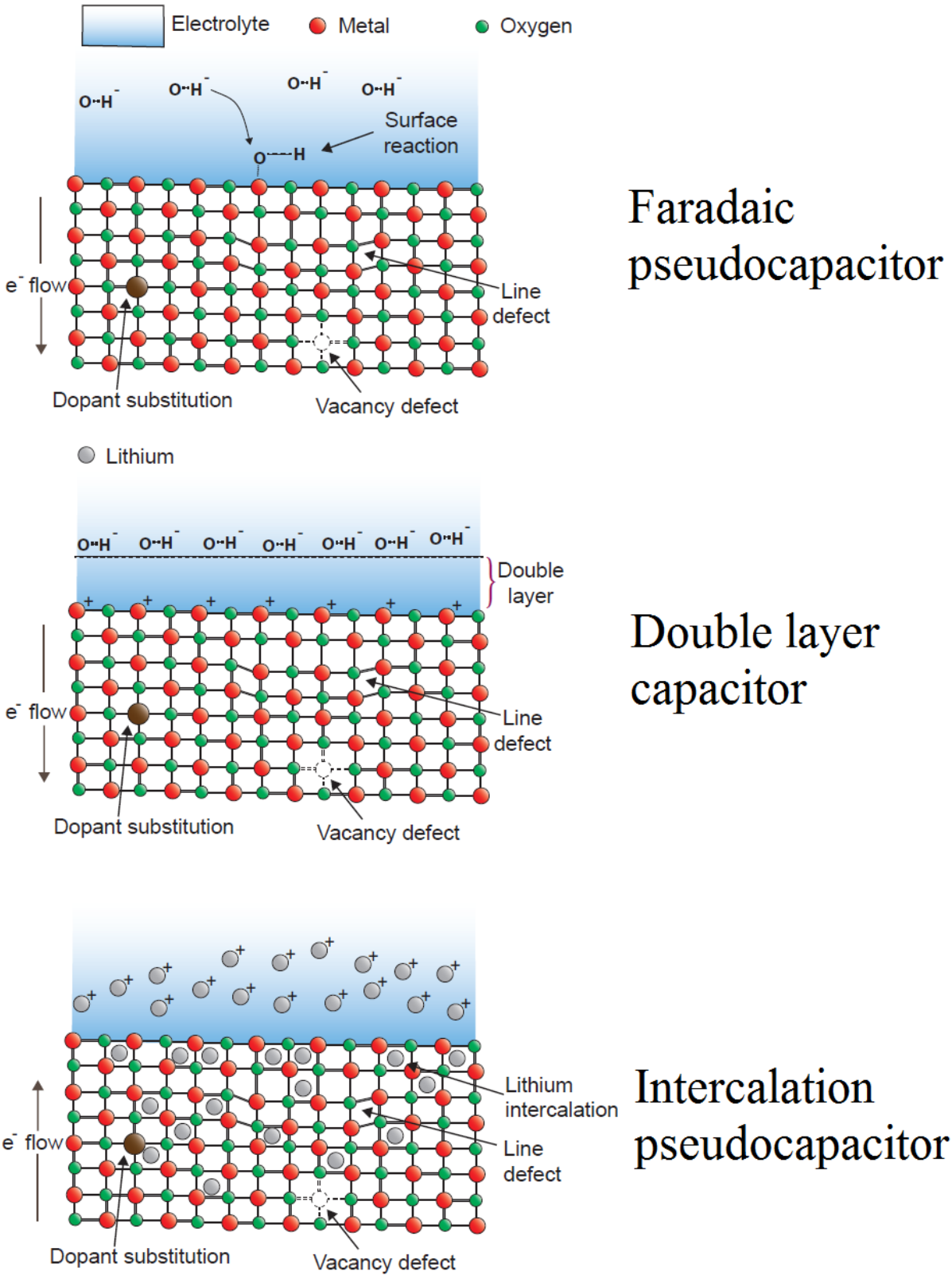

Figure 9. Mechanisms of charge storage in supercapacitor electrodes.

Table 4. Properties of different electrolyte systems used in supercapacitors.

Aqueous electrolyte	Non-aqueous electrolytes
Limited energy densities on account of low voltage window of water electrolysis (~1.2 V) Energy density = ½ CV^2.	Much larger voltage windows of upto 3 V allows for very high energy densities.
Smaller ions present lead to higher capacitances as fewer sites are occupied during adsorption pseudocapacitance.	Pseudocapacitance and other such Faradaic response are usually limited by site occupancy and de-solvation from organic moieties.
High pH and ion concentration implies good ionic conductivities.	Usually consist of large ions in organic solvents leading to lower conductivities resulting in increased solution resistances.
Very acidic or very alkaline conditions involved tend to result in corrosion of electrodes.	Faradaic intercalation supercapacitance usually seen in organic Li-ion based electrolytes is sluggish on account of diffusion within electrodes and results in reduced rate capabilities.

Supercapacitors can be further classified based on the electrolyte used there-in. **Table 4** details the properties of various electrolyte systems used in supercapacitors. In addition to conventional aqueous and non-aqueous electrolytes, a new class of 'green' electrolytes using ionic species obtained from low-melting ionic salts has been used in supercapacitor systems[76-80]. Properties of ionic-liquid electrolyte based supercapacitors are quite similar to those of non-aqueous electrolytes described in **Table 4**.

1.2 ELECTRODE MATERIALS FOR SUPERCAPACITORS

Supercapacitors complement batteries and are emerging as highly relevant devices for myriad electronic devices and systems on account of their short charging times (high power density) and seemingly infinite cyclability. Thus they find application in a number of applications such as renewable energy storage[46], grid-leveling and power conditioning[14]. The need to tailor energy storage devices to suit such applications is highlighted by the current targets established by the Department of Energy[81] for the same i.e. 7.5 Wh/kg at 625 W/kg lasting upto 15 years. One only needs to examine the classic Ragone plot (**Figure 4**) to identify devices capable of achieving the same[3]. It is clear that only lithium-ion batteries and electrochemical capacitors have the reasonable likelihood of achieving these targets, at-least as far as automotive applications are concerned. The need for high power energy storage devices for both stationary and mobile applications is being realized more and more of late[3-5]. One of the outstanding challenges in this regard is to have devices with sufficiently large amount of charge stored while at the same time being able to deliver the same at rapid rates. **Table 5** details the DOE supercapacitor targets established for various applications. There is therefore an urgent need for supercapacitor materials with large energy storage capacities. Extensive research has been undertaken to improve the supercapacitor electrodes to match the targets detailed in **Table 5**[3, 43, 64, 82-91]. A variety of carbon materials[3, 92], transition metal oxides[80, 93-95](such as those of Ru, Fe, Mn, Sn, V,Bi oxides, $BiFeO_3$, $NiFe_2O_4$)[93], MnO_2[94] and hierarchical structures using mesoporous carbon[96] have previously been studied. In addition, conducting polymers have also been explored for supercapacitor electrodes[97]. Developments in various electrode materials have been briefly detailed in **Sections 1.2.1-1.2.4**.

Table 5. Targets for supercapacitors.

Purpose	Energy density (Wh/kg)	Power density (W/kg)	Volumetric energy density (Wh/l)	Volumetric power density (W/l)	Cost ($/kWh)	Reference
Power Assist Hybrid Electric Vehicle (PAHEV)	8.25	2750	10	3438	2424	[98]
Transient Power Assist (TPA)	3	600	3.75	812.5	2167	[99]
Start-stop applications (SSA)	3	840	3.75	1050	2667	[99]
Electric vehicle power source (EVP)	350	700	750	1500	100	[100]
Mobile applications	250		300		125	[40]
Grid applications	250		300		100	[40]

1.2.1 Carbon based materials

Early investigations in supercapacitor materials for commercial devices primarily involved carbon compounds that exhibit double layer type capacitance. This is due to the simplicity of design, abundance and rapid response of carbon based materials. Prominent among these materials were activated carbons and carbon gels, which exhibited highly reversible surface adsorption/desorption of ions but were limited in energy density largely on account of the surface phenomenon (capacitances ranged between 50 and 130 F/g in aqueous electrolytes)[88]. It was therefore expected that increasing surface areas would lead to increase in gravimetric capacitance and hence energy density. This was attempted by creating porosity in the carbons through activation of the carbons or by use of templates, as well as generating the carbons from transition metal carbides or even silicon carbide by selectively etching of the electropositive metal or semiconductor in acidic environments[85, 101]. Following this approach, TiC -derived nanoporous materials have been shown to exhibit energy densities of 10.8 Wh/l (120 F/g capacitance) at a voltage of 2.7 V[102]. Carbide derived carbon (CDC) showed dependence of pore size on heat treatment temperature[101, 102]. Larger pores formed between 600 and 800^{o}C demonstrated great potential for energy storage. Capacitances of 130 F/g were demonstrated with retention for upto 10000 cycles[103]. Electrospun TiC was converted to carbon felts which exhibited capacitances of ~95 F/g at 1 V/s in 1M H_2SO_4[104]. Activation of carbon using different agents and their effect in development of porosity has also been reported[105]. 3-D Hierarchical porous graphitic carbon (HPGC) prepared by precipitation using NaOH and $NiNO_3$-phenolic resin used to coat the carbon followed by hydroxide etching to remove the template was shown to have considerable promise for capacitor charge storage[106]. Activated carbons are excellent double layer supercapacitor materials on account of their high surface area and large pore volume[92, 107].

However, they suffer from the problem of wettability, inability to sustain a uniform deposit on the pores of the carbons. In addition, high surface area carbons usually are very porous resulting in poor volumetric capacitance.

It was however observed that double layer type capacitance did not directly scale with surface area in many instances on account of the pores being too small for electrolyte to enter. Investigation into this phenomenon led to the conclusion that an optimal porosity of the size of two solvated ions was ideal to obtain maximum capacitance. An interesting twist to this understanding came from results of work by Gogotsi et. al. in which it was shown that sub-nanometer pores allowed for ion desolvation and thus increased the capacitance significantly on account of the smaller distance of charge separation[108]. It was also found that the pore size required for desolvation was solvent dependent and that this phenomenon leads to shape distortion in the cyclic voltamogramms[109, 110]. Maximum capacitance has also been realized in the case of non-aqueous electrolytes when the ion size is almost comparable and equal to the pore size (see **Figure 10**).

It has also been previously shown that large pores can be accessed more readily while the rate of access to smaller pores is more kinetically limited[111]. Various carbons with porosities varying between 9 and14 Å were electrochemically cycled in KOH and it was determined that carbons with 9Å pores exhibited relatively lower capacitances.

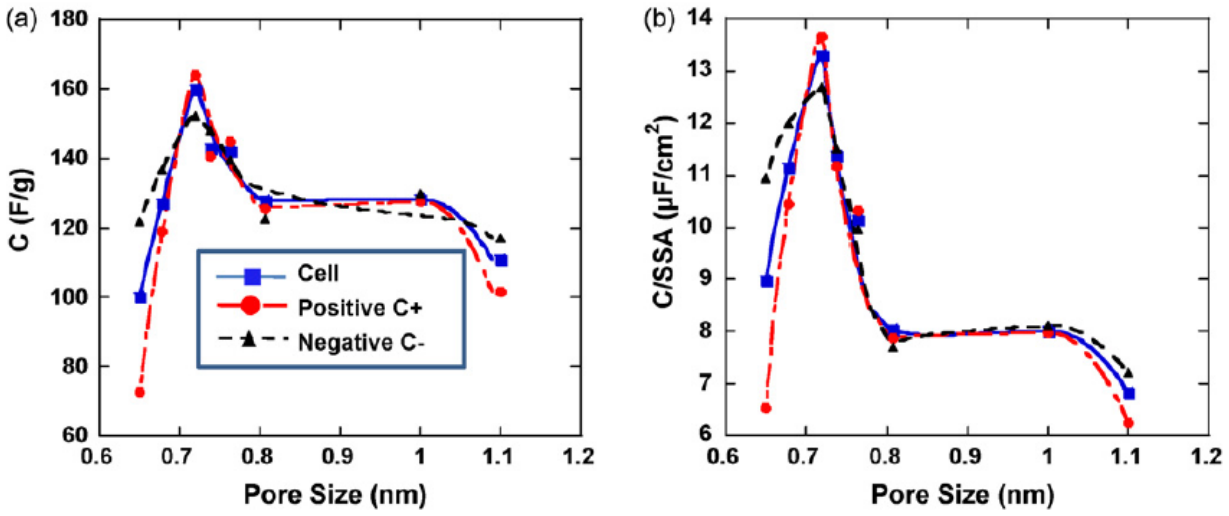

Figure 10. Figure showing effect of pore size on capacitance. Optimal capacitance is obtained when pore size and electrolyte ion size are almost equal (Reproduced with permission from © 2009 Elsevier)[112].

In addition to the relationship between surface area and capacitance in carbon, the effect of pore size is found to be of vital importance. Pore size of 0.7 nm is found to be ideal for aqueous while 0.8 nm is found to be ideal for non-aqueous electrolyte[112, 113]. Activated carbons prepared by the heat-treatment of bituminous coal at different temperatures were used for this study. Pore shape and size were also found to affect capacitance properties. It was determined that there was a difference in charge storage between exohedral vs endohedral pores[114]. Furthermore, diffuse layer and pore shape were also reported to have an effect on the capacitance in mesoporous carbon[115].

The anomalous increase of the capacitance with a decrease in the pore size of a carbon-based porous electric double-layer capacitor[85, 108, 112] was explained to be a result of the so-called 'overscreening effect' occurring as a voltage-induced first order transition between a cation(anion)-deficient phase and a cation(anion)-rich phase manifesting itself in a jump of capacitance as a function of voltage. This effect was proposed to result in super-ionic state

screening electrostatic interactions of ions within a pore called 'super-ionic' state[116]. Other significant studies relating ion size-pore size interactions and their effect on capacitance behavior were undertaken by Largeot et al.[117] and Aurbach et al.[118] among others[85, 101, 108, 112, 119]. Molecular dynamic simulations were also undertaken to understand the nature of ions within pores in carbon based capacitors. In a study using ionic liquid in carbon pores (using a model by Roy and Maroncelli[120]) the nature of the charge storage in ionic liquid based graphite electrodes was correlated with experimentally obtained data[121]. Molecular modeling was also performed by Merlet et al.[122]. A new variant of the Gouy-Chapman model was proposed for ionic liquids using correlation for the diffuse double-layer capacitor[80]. In another modeling study of supercapacitors based on ionic liquid electrolytes and carbon electrodes, electrodes were found to deviate from the conventional model of constant charge surfaces. Such a deviation was found to alter both the structure of the adsorbed fluid at the interface and the time scales over which the relaxation phenomena occur[123].

Other carbon materials being considered for supercapacitor applications are carbon nanotubes (CNTs), graphene and conducting polymers. CNTs were considered to hold a distinct advantage over activated and high surface area carbon powders in that the nature of the pores was more mesoporous rather than micropores. Combined with their good conductivity and linear current to voltage response in Lithium based electrolytes, they were thought to be ideal supercapacitor materials. Capacitance values of 4 to 135 F/g were reported on multi-wall carbon nanotubes (MWNTs)[124] in aqueous electrolytes over a 0.8V window. It has also been observed that carbon nanotube capacitance depends largely on the diameter of the tubes and accessibility of the inner channel to ions in electrolyte. Single walled carbon nanotubes (SWNTs) are also attractive on account of the high conductivity and possibly larger voltage window of stability[125].

Recent study on SWNTs in organic electrolyte (1M Et_4NBF_4/acetonitrile (AN)) has shown capacitances similar to the commercially obtained activated carbons[126]. Gravimetric capacitance has found to vary in the range of 7 and 20 F/g for SWNTs as compared to 9-32 F/g for activated carbons. Though the inherent capacitance of carbon nanotubes is small, their high electronic conductivity, mechanical strength and unique three-dimensional morphology have made them very useful templates for high power applications wherein pseudocapacitor materials such as conducting polymers or metal oxides are deposited on the carbon nanotubes and the composite is used as the functional electrode for supercapacitors. Among such composites, the CNT/ polypyrrole composite has been extensively explored[127-129]. Conducting polymers such as polypyrrole exhibit pseudocapacitance behavior through p or n type doping. Capacitances as high as 192 F/g were reported with polypyrrole composites with MWNTs synthesized using electrochemical templating[130]. Doping carbon nanotubes with nitrogen has also been shown to improve capacitance significantly[131, 132].

An often-neglected aspect when using highly conductive materials such as CNTs is the contact resistance between current collector and the material itself. For example, Shaijumon et.al[133] have shown that significant improvement in rate capability is noticed on tailoring the interface between the CNTs and the current collector including templating. CNTs using gold contacts have been synthesized using alumina templates and power densities as high as 48 kW/kg have been demonstrated.

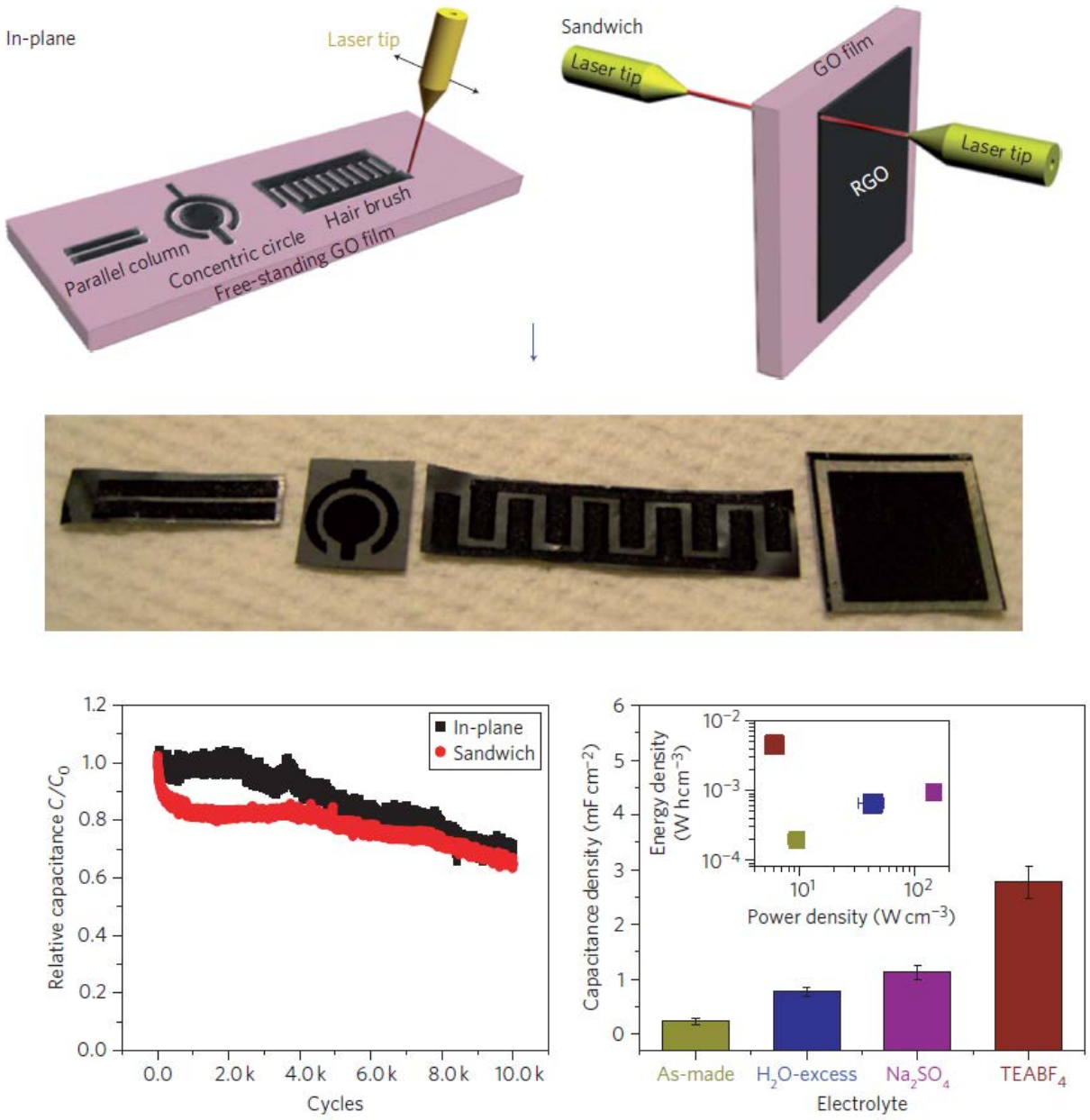

Figure 11. Micro-supercapacitor electrodes prepared by using CO_2 laser (Reproduced with permission from © 2011 Macmillan Publishers Ltd.) [134]

Another notable development is the emergence of graphene (the most recent and prodigious development in the area of carbonaceous materials) and the noticeable advances of graphene in the recent years as a possible supercapacitor material. Ruoff et al. pioneered the

research into chemically modified graphene and demonstrated the ability of the material to show capacitances of 99F/g and 135 F/g in organic and aqueous electrolytes respectively[135, 136]. Graphene, as the name suggests is a single sheet of graphite which allows for ballistic 1-D transport of electrons leading to electronic conductivities of up to 10^5 Sm^{-1} in composites made with graphene[91, 137-141]. Recently, Chen et al. have reported capacitances as high as 205 F/g with graphene synthesized by chemical reduction of graphene oxide using hydrazine[142]. Electrochemical tests were performed in an aqueous electrolyte over a 1 V window. Energy densities as high as 28.5 Wh/kg and power densities of 10 kW/kg have been demonstrated in a 2-electrode cell. Graphene's superior properties have been attributed to the higher accessible surface area (~ 2600 m^2/g on account of lack of agglomeration), very high conductivity (~ 100 S/m) and excellent chemical stability. Capacitor performance of graphene is also independent of nature of porosity on account of the 2-D structure, thus bypassing most of the complications involved with other carbon based materials. Ruoff et al. have also reported studies into activation of graphene prepared from activated microwave-exfoliated graphite oxide (a-MEGO). Activation was performed by using KOH and hence capacitances of 172 F/g were reported at 1 A/g in 1-butyl-3-methyl-imidazolium tetrafluoroborate (BMIM BF_4)/acetonitrile (AN) electrolyte over a 3.5 V window. A KOH/a-MEGO ratio of 6.5 and activation temperature of 800^oC were found to result in the optimal material with very high surface area (~3100 m^2/g)[91, 141]. Other novel techniques to produce graphene such as laser scribing have also been explored to prepare flexible sheets. Flexible graphene with good mechanical properties was prepared by coating graphene oxide onto discs and placing the discs in an optical disk drive for converting to sp^2 carbon. Capacitances of ~276 F/g were reported in1-ethyl-3-methylimidazolium tetrafluoroborate ($EMIMBF_4$) with superb rate capability. The sheets were reported to have high areal

capacitances of ~5.02 mF/cm^2 at very high power density~20 W/cm^3[143] over a 4 V window. It was found that the electronic conductivity of the sheets increased by increasing the number of repeats the scribing was performed[144].

Carbon based supercapacitors are also being considered as free-standing, flexible applications such as electronic papers and roll-up displays[145]. Graphene shows great promise here on account of its super-excellent mechanical properties. Graphene/polyaniline composites were made by electropolymerization of polyaniline onto graphene paper formed by membrane filtration of graphene suspension[146]. Capacitances of about 230 F/g were reported in sulfuric acid over a 1 V window. Higher capacitances of about 530 F/g at 200 mA/g were also reported for polyaniline-doped graphene synthesized by in-situ polymerization within graphene oxide before reduction[147]. Using CO_2 laser writing on graphene oxide electrode architectures shown in **Figure 11** were synthesized by Gao et al.[134]. Two different configurations were explored 'in-plane' and 'sandwich'. The idea exploits the poor electronic conductivity and high ionic conductivity of graphene oxide to use it as a separator resembling Nafion. Other flexible microsupercapacitors using graphene have also been reported to have very high power density[148].

Novel strategies have been pursued to increase aqueous supercapacitance in carbon-based electrodes. The idea involves the use of redox-active electrolytes in order to exploit charge storage occurring as a result of in-solution reactions. Using a well-known Bielousov-Zhabotinsky reaction with cerium-based autocatalytic redox shuttle for brominated species, capacitances between 500 and 200 F/g were reported with stable cycling for upto 5000 cycles. Electrolyte used was a mixture of 1 M $KBrO_3$ and 1 M $(NH_4)_2Ce(NO_3)_6$ in aqueous media with mesoporous carbon electrodes[149].

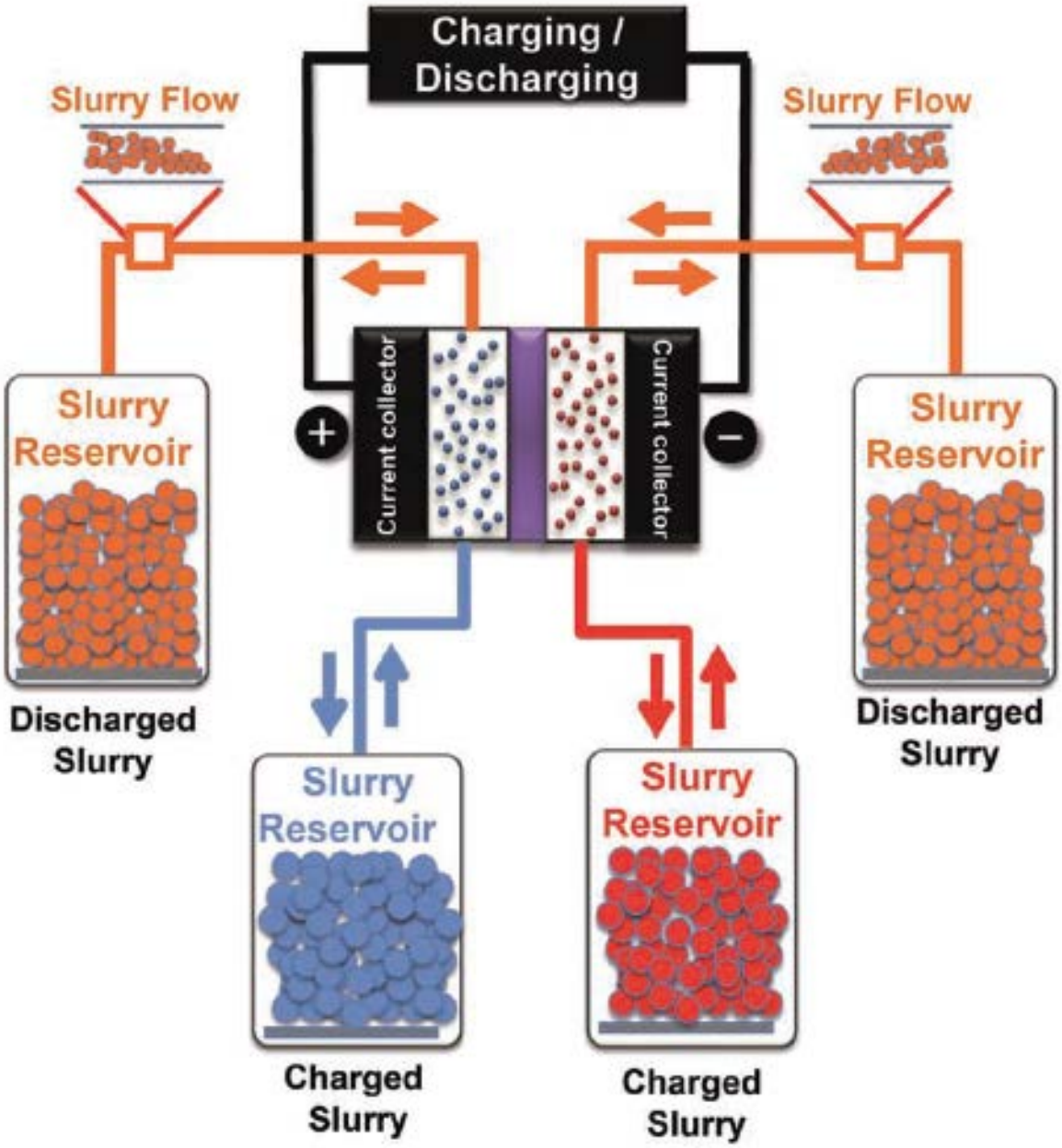

Figure 12. The flow capacitor concept demonstrated by Presser et al. showing promise for grid level energy storage applications (Reproduced with permission from © 2011 Macmillan Publishers Ltd.)[150]

Another novel concept being actively pursued for grid-scale applications involves the overlap of the flow-battery concept with supercapacitor materials aptly called the flow capacitor (**Figure 12**). Herein, thick slurries of carbon materials are charged and discharged reversibly by

maintaining them in contact with current collectors. The charge is stored within the particles in a manner similar to EDLCs. Charge separation at the double-layer occurring within individual; carbon particles is exploited herein but the energy density and power density are decoupled. Percolation networks ensure easy transport of electrons to most of the carbon suspension[151]. Effects of flow cell design on capacitance have also been reported[152]. The effectiveness of the system was improved by using a redox mediator based slurry (P-phenylenediamine (PPD) suspension carbon electrolyte)[153]. Carbon beads from phenolic resin were also reported to show good energy storage in flow cells[150].

Strategies have been developed for the synthesis of carbon materials for supercapacitor applications derived from cheap and abundant materials. Straw (prepared by carbonization of wheat straw at 420^0C for 2 h after crushing and sieving) was used to prepare the carbon- having micro- and mesoporous structure with the peak pore size of 2.1 nm and high specific surface area of 2316 m^2/g. The carbon obtained after KOH activation was reported to have capacitances of ~251.1 F/g at 2 mV/s scan rate in $MeEt_3NBF_4$ (Methyl-triethyl-ammonium Tetrafluoroborate)/AN electrolyte. The material however suffered from poor rate capability with capacitances dropping to 70 F/g at 300 mV/s. Solvent effect was also studied and acetonitrile was found to be better because of easier access to pores than the bulkier molecule containing PC (propylene carbonate) solvent[154]. Using dead neem and Ashoka tree leaves occurring in India, carbon material of 1230 m^2/g area and capacitances of ~400 F/g were reported at 0.5 A/g in 1 M H_2SO_4 [155]. No further activation was needed and the authors justify that metal and organics present in the leaves provide activation. Capacitive electrodes have also been used for alternative applications such as desalination/deionization (without using ion exchange membranes)[156, 157].

1.2.2 Transition metal oxides

Transition metal oxides have been widely explored for supercapacitor applications on account of their layered structure and ability to accept wide variety of oxidation states. Electrochemical behavior of oxides is pseudo-capacitative in nature due to either highly reversible surface chemical reactions or extremely fast and reversible lattice intercalation. Most commonly studied pseudocapacitor electrode materials to date are hydrous ruthenium oxide and manganese oxide, the former limited by the high cost and the latter restricted primarily due to the low energy density, respectively[5, 70, 71, 158]. Hydrous Ruthenium oxide has been demonstrated to have very high capacitances of about 900F/g[44, 58, 69, 159, 160]. The I-V characteristic of the successive oxidation/reduction reactions at the surface of the electrode resemble that of a capacitor, hence the term pseudocapacitor. However the prohibitive cost of Ruthenium oxide makes it impractical for commercialization. Efforts in this front are on to form composites with other oxides, conducting polymers or carbon materials to retain performance while reducing noble metal content[161]. In one such work, Ruthenium dioxide was electrodeposited into poly (3,4-ethylenedioxythiophene) and electrochemically cycled at 50mV/s in 1M H_2SO_4 over a 1 V window[162]. Energy densities of 28Wh/kg at power densities of 20 kW/kg have been reported. Manganese dioxide on the other hand is a cheap alternative to Ruthenium oxide, but has much lesser capacitance and thus efforts are on to increase capacitance and rate capability. MnO_2 has also been deposited onto CNTs and conducting polymers such as polypyrrole in order to overcome the problem of inherent low conductivity[163-165].

In a recent work, Brezesinski et. al., have shown the importance of retaining meso-porosity and crystallinity in nanoparticles to obtain maximum pseudocapacitance. Improvement in charge storage capacity has thus been shown to depend on the porosity of the external walls[166].

The mesoporosity and resulting nanoparticulate nature is important to have large surface and easy intercalation. At the same time, it is important to maintain crystallinity (**Figure 13**) to reduce grain boundaries and their resulting mass transfer effects. They have already demonstrated this using both TiO_2 and MoO_3 synthesized by template methods. Upon comparison with sol-gel derived materials, template-synthesized materials have been shown to have much better porosity and hence easy diffusion of electrolyte into inner pores, thus leading to increase in both capacitance and intercalation[167].

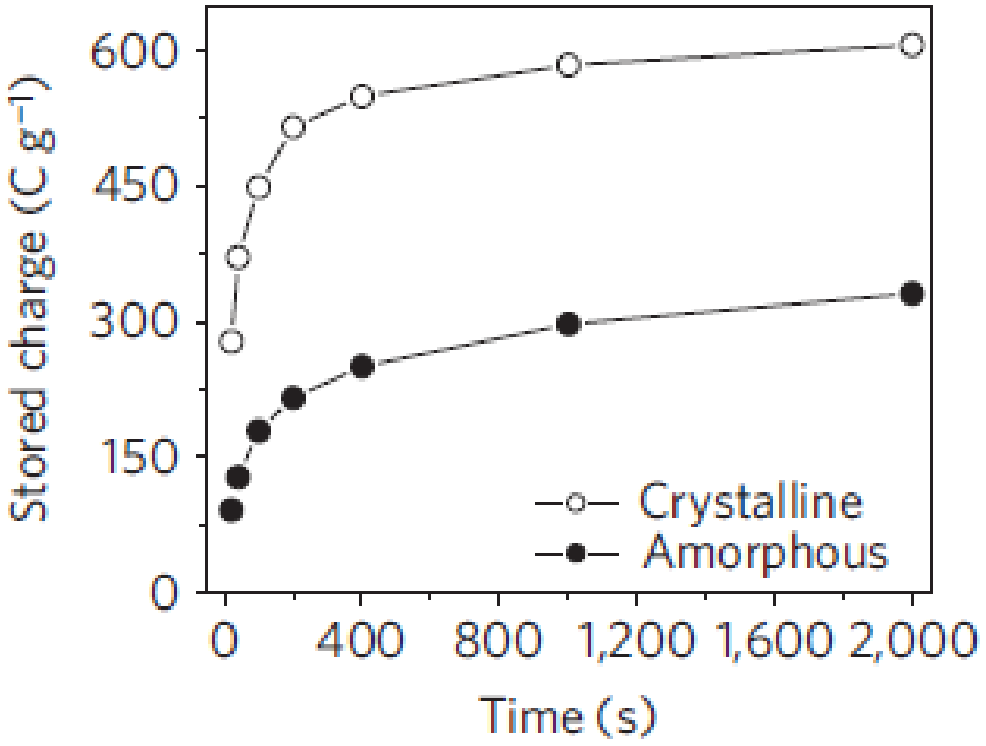

Figure 13. Charge storage in crystalline and amorphous MoO_3 showing effect of crystallinity on intercalation supercapacitance (Reproduced with permission from Macmillan Publishers Ltd.)[168].

One such oxide resembling the multiple oxidation states of the metal similar to Ru is vanadium oxide which has previously been studied as a supercapacitor material in non-aqueous electrolytes [75, 169-172]. Vanadium is an element belonging to Group 5 of the periodic table with a half empty d-shell allowing it to exhibit multiple valence states of +2 to +5. Vanadium oxide has previously been studied as a material for lithium ion battery (LIB) cathodes. Different morphologies of the oxide including nanotubes have been explored. Amorphous and hydrated vanadium oxide has also been studied widely as a viable supercapacitor electrode in lithium and sodium ion electrolytes[75, 170, 173-175]. Amorphous vanadium oxide gel/ carbon composites have demonstrated capacities ~ 360 $mAhg^{-1}$ with very high intercalation rates. Oxide nanotubes on the other hand, have been studied extensively by Nesper et al.[176, 177]as electrode materials using lithium ion electrolytes and have shown great promise. In addition, a class of so called Lithium-ion based aqueous supercapacitors have been identified by Hu et . al. demonstrating capacitances of upto 740 F/g in aqueous LiCl[178-181]. In all these studies, thin oxide films have shown to result in good electrochemical performance on account of the short diffusion lengths for lithium intercalation. The importance of loading and its influence in achieving attainable capacitance in vanadium nitride based supercapacitor has been highlighted by us in our earlier work[182]. Nanoparticulate materials such as oxides/nitrides of transition metals are very advantageous in terms of achieving desirable electrochemical performance on account of the high specific surface area (SSA) and the enhanced activity that is achievable at the nano-scale dimensions. However, the very nanoparticulate nature which is responsible for enhanced electrochemical activity results in also loss of electronic conductivity on account of the large number of grain boundaries.

Table 6 details the theoretical charge-storage characteristics of various non-noble metal oxide materials in aqueous electrolytes occurring as a result of Faradaic processes alone. The

numbers therein are representative of the total possible capacitance achievable in aqueous electrolyte assuming that all the material was to be used for obtaining Faradaic charge storage. This however seldom occurs in pseudocapacitor materials and hence the greater the surface area, typically this translates to a greater exposed surface for both double layer as well as pseudocapacitance reactions. Among these materials, vanadium oxide and manganese oxide are most promising for capacitor charge storage.

Table 6. Theoretical capacity and cost of common oxide supercapacitor materials.

Material	Molecular weight (gm/mol)*	Oxidation states accepted	Number of electrons transferred	Theoretical Capacity (C/gm)	Cost ($/kg)#
Ruthenium oxide	133.07	2-4	2	1450.36	28500
Vanadium oxide	181.88	2-5	3	3183.42	162
Iron oxide	159.69	2-3	1	604.30	87.8
Manganese oxide	86.94	2-4	2	2220.00	137
Cobalt oxide	165.86	2-3	1	581.80	770
Titanium oxide	79.87	3-4	1	1208.27	87.8

** Highest oxidation state material;# Reagent grade-Sigma Aldrich Inc. (2013)*

Nanostructured vanadium oxide has a relatively low conductivity [183-185] on the order of 10^{-6}-10^{-2} $\Omega^{-1}cm^{-1}$. Carbon based hetero-structures have demonstrated improved rate capabilities for various Li-ion and supercapacitor electrode materials including silicon, ruthenium oxide, manganese dioxide and nickel oxide[164, 186-193]. Electrodeposited amorphous hydrated vanadium oxide coatings on CNTs have shown to exhibit capacitances as high as 910 Fg^{-1} by Kim et al[170] and Balkus et al.[194] in lithium electrolyte cells. In a recent report Sathiya et al. reported energy storage behavior of oxide coated carbon nanotubes in a Swagelok type cell with a lithium electrolyte and a lithium counter electrode exhibiting capacities as high as 850 $mAhg^{-1}$ with up to 60% of the energy storage coming from a capacitive contribution[195]. Vanadium oxide/CNT composites have also been explored for capacitance behavior in aqueous electrolytes and capacitances as high as 400 Fg^{-1} have been reported[196]. A similar approach of using a 3-D conducting support to create conductive heterostructures was recently exploited by Yushin et al. wherein they demonstrated that vanadium oxide thin films on Al nanowires generated by atomic layer deposition could be used as electrode materials in a Li-ion based supercapacitor[197, 198]. Intertwined CNT-V_2O_5 fibers were shown to have high capacity in $LiClO_4$-propylene carbonate[199]. The effect of pH was studied to understand the charge-storage behavior of electrodeposited V_2O_5 in different media with coarsening of vanadium oxide occurring at higher pH (acidic going to neutral)- resulting in best stability in 1M KCl at pH~3. Coating of the films with agar gel was found to improve stability[200]. Composite electrodes using autoclave synthesized vanadium oxide prepared from isopropoxide and Pluronic-P123 and hydrazine reduced graphene oxide was shown to have capacitances of ~80 F/g[201] in LiTFSI electrolyte in acetonitrile. Vanadium oxide nanowire coated carbon cloth wrapped by LiCl/PVA polymer gel

with 5M LiCl aqueous electrolyte tested in a symmetric cell using a filter paper separator was used to demonstrate high areal capacitances of ~236 mF/cm^2 at 0.2 mA/cm^2[202].

Though manganese oxide is a very promising supercapacitor material, poor electronic conductivity is a problem in bulk manganese oxide capacitors as well[94]. Graphene oxide-MnO_2 electrodes were shown to have capacitances of ~200 F/g in 1M Na_2SO_4[203]. Gold based metal-oxide electrodes (MnO_2) –supercapacitors were shown to have capacitances between 950 and 1150 F/g in 2 M Li_2SO_4[204]. Such carbon-oxide nanostructures have been explored to improve the supercapacitor characteristics of oxide materials[96, 205]. Flexible asymmetric thin film capacitors using oxide-single wall carbon nanotubes (SWNTs) (MnO_2-NWs (nanowires)/SWNTs and In_2O_3-NWs/SWNTs) have been reported with operating voltage window of ~2V with a capacity of 184 F/g resulting in energy densities of ~25.5 Wh/kg at very high power densities of ~50.3 kW/kg[206]. Use of flexible electrodes using nanorods arrays of MnO_2 has been shown to result in capacitances of~660.7 F/g at 10 mV/s and 485.2 F/g at 3 A/g in 0.5 M Na_2SO_4[207].

Doping of oxides (Mo, Mn, W, Ti, Cu, and Ag) has been previously studied as an excellent pathway to improve the electrical resistivity and electrochemical charge storage properties[208-215]. Silver and copper doped oxides have been shown to increase the electronic conductivities by up to 2 orders of magnitude[185, 216]. Ti and W doped vanadium oxide has also been shown to lead to improvement in pseudocapacitor characteristics[217]. In a doping study using Mn_2O_3, evidence of doping altering structure and decreasing capacitance was observed in V doped Mn_2O_3[218]. On the other hand, Co doping increases Mn_2O_3 capacitance since it retains the structure (3% Co doping shows highest capacitance of 99 F/g)[219].

Other hierarchical oxides have been reported to bear great promise for supercapacitor applications. $MnMoO_4$ nanowires coated with $CoMoO_4$ nanorods were reported to have

capacitances of ~204 F/g at 0.5 A/g[220]. Pt/MCNT (mesoporous carbon nanotubes), Pt/CCNT (closed carbon nanotubes) were reported to exhibit capacities of 250 F/g and 200 F/g in 1M H_2SO_4 at 0.5 A/g[221]. Co_3O_4/NiO-core/shell nanowire arrays[222] have also been studied. Iron oxide-graphene composite electrodes have been reported with capacitances of 150 F/g (coprecipitation derived co-Fe_3O_4-RGO(reduced graphene oxide)) and 350 F/g (electrochemically derived e-Fe_3O_4-RGO(reduced graphene oxide))[223]. $Ni(OH)_2$ nanoplates grown on graphene were reported to demonstrate capacitances of upto 1335 F/g[224]. V_2O_5-TiO_2-vertically aligned nanotube array (Ti-V anodization using 18 at% V were shown to have capacitances of ~220 F/g resulting in an energy density~19.56 Wh/kg[225]. Innovative electro-chromic supercapacitor using V_2O_5 using in $LiClO_4$-propylene carbonate with capacitances of ~155 F/g were shown with a visible change in color of the electrode material based on the state of charge of the electrode[226].

Oxide supercapacitor work has also led to understanding of certain important criteria while evaluating capacitor performance. According to a work using Mn_3O_4-graphene composite electrodes, the most important criterion for choosing the highest acceptable cell voltage of asymmetric supercapacitors is the phase angle of cell capacitance[227]. Energy efficiency is also reported to be an approximate indicator of capacitor or non-capacitor like behavior. Since a number of battery materials behave almost like supercapacitors when tested as thin films, the importance of loading as a vital parameter affecting sustained response and efficient cyclability that can be obtained at higher current and voltage rates has only been realized recently and there is significant effort directed at this aspect. Loading i.e. the amount of mass per unit area and per unit volume is of utmost importance for commercialization of supercapacitor materials. Characteristics exhibited in thin films are seldom retained in thicker electrodes and the necessity

to report both gravimetric and volumetric energy densities and power densities has been identified as quintessential for a realistic evaluation of the materials performance for supercapacitor application(see **Figure 14**)[228]. Low temperature properties of capacitors have been found to be important for commercial capacitors and testing protocols and results thereof have been reported by Iwama et al.[229]. Importance of film thickness and testing methods were established in various critical review literature published[228, 230-232].

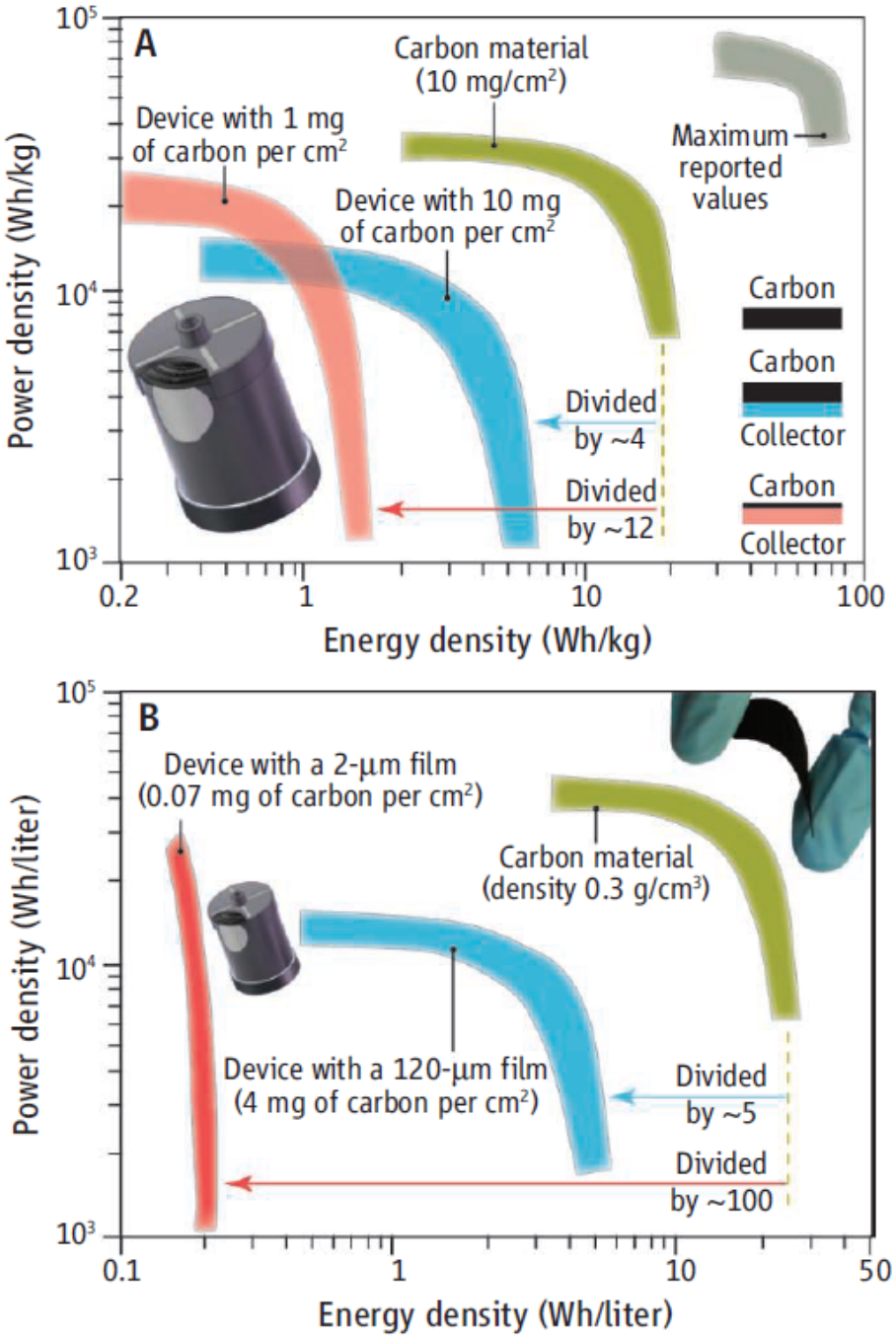

Figure 14. Ragone plots as a realistic representation of capacitor charge storage. It can be seen that observed energy densities and power densities do not scale when thick electrodes are prepared and drop further when considering the packing material and final device properties (Reproduced with permission from Macmillan Publishers Ltd.) [228]. This is found to be true both in the case of gravimetric and volumetric Ragone plots.

1.2.3 Inorganic transition metal nitrides and sulfides

Unlike oxide materials, which have been extensively studied for supercapacitors, nitrides and sulfides have received little or no attention until recently. Conventionally, some nitrides are known to have better electronic conductivity than oxides and are hence more suitable for high rate devices such as capacitors. Recent work by various groups has shown the viability of nitrides, carbides and sulfides for catalysis and energy storage applications[182, 233-259]. Transition metal nitrides were first shown to have promise as energy storage materials by various groups identifying molybdenum nitride as a suitable pseudocapacitor material[240-244]. Molybdenum nitride was first explored by Conway et. al and was shown to exhibit promising supercapacitor properties[241]. Following this, Daiwon et. al have explored various nitrides synthesized using non-aqueous approaches but tested in aqueous electrolytes and observed that these systems if tailored properly can achieve capacitances upto 1300 F/g[182, 236, 238]. Vanadium nitrides (VN) nanoparticles synthesized by a solvothermal process have been shown to exhibit these superexcellent capacitance values on account of a thin oxide layer present on the surface of the nitride (see **Figure 15**). Glushenkov et. al have also explored supercapacitor properties of VN albeit with much higher loadings than reported by Daiwon et. al and have reported capacitances between 150 and 180 F/g in different aqueous electrolytes[260]. A thorough investigation into transition metal nitride supercapacitors was then undertaken by Choi et. al and they determined them to be excellent supercapacitor materials in aqueous electrolytes [182, 235-238]. Among the various nitrides evaluated, VN was found to exhibit capacitances as high as 1350 F/g[182, 235, 238]. This exceptional performance has been attributed to a combination of both double layer type capacitance and pseudo-capacitance type response occurring on the nitride surface. Following this groundbreaking discovery, a number of studies have evaluated the capacitor properties of

VN with reported capacitances ranging between 50 and 250 F/g [246, 249-251, 260-262]. The large difference in capacitive charge storage obtained in VN explored by various methods indicates that charge storage in VN is very much dependent on the nature of the VN, i.e. crystallinity, particle size, surface area and the type of the surface oxide[246, 262]. In addition, electrode properties could have a distinct bearing on the gravimetric and areal capacitance of VN that can be achieved[228].

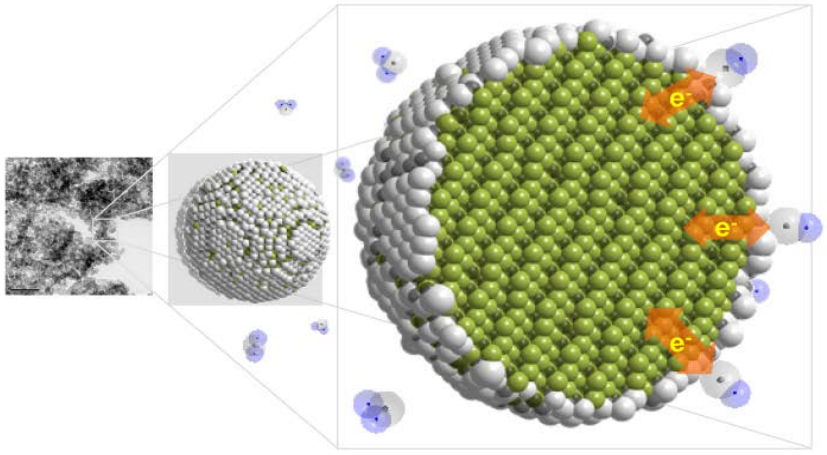

Figure 15. Scheme showing the presence of a thin oxide layer over nanoparticle VN, shown to exhibit very high capacitances of upto 1300 F/g (Reproduced with permission from Copyright © 2006 WILEY-VCH Verlag GmbH & Co. KGaA, Weinheim)[182, 263] .

Supercapacitance properties of nitrides have been found to be loading dependent indicating conductivity issues, which could be solved by tailoring various architectures as in the case of MnO_2. Though nitrides have been shown to possess very high capacitances, they suffer from stability problems limiting their cycle life, an issue that needs to be overcome for commercialization of these materials. Other than nitrides, copper and cobalt sulfide have also been explored for supercapacitors and have shown to exhibit capacitances in the range of 100-200 F/cm[2264-266].Work by Eustache et al has demonstrated high areal capacitances of ~3.5 mF/cm[2267] in vanadium nitride coated on nickel oxide in 1M KOH. In addition, the dependence of capacitance on oxygen content was also reported. High capacity tungsten oxynitride capacitors were reported in different electrolytes with highest capacitance of 85 F/g reported in 1M H_2SO_4 and best stability reported in 1M KOH[268].

Among the various nitrides evaluated, vanadium nitride consisting of a small amount of oxide/oxynitride especially as a surface layer has been shown to be the most promising material. Most nanoparticulate nitrides form surface oxide layers either spontaneously or as a result of a passivation step usually undertaken to prevent instantaneous pyrolysis upon exposure to air by virtue of the high reactivity of the nanocrystalline state. The exceptional performance of VN_xO_y has been attributed to a combination of both double layer type capacitance and pseudo-capacitance arising at the surface oxide. Vanadium is an element in Group 5 of the periodic table with a half empty d-shell thus allowing it to accept valences of +2 to +5, thereby allowing it to exhibit reversible Faradaic reactions occurring within the window of water electrolysis yielding pseudocapacitance in aqueous electrolytes[269]. Vanadium oxide has an achievable theoretical capacity of ~3183 C/g (884 mAh/g) (see **Table 6**) over a 1.3 volt window (~2400 F/g theoretical capacitance)[269].

Previous studies have demonstrated the charge storage capability of vanadium oxide with capacitances as high as 1400 F/g demonstrated in thin film vanadium oxide [170, 175, 178-181, 194-196, 270]. Bulk vanadium oxide however does not demonstrate such high capacitances since it suffers from poor electronic conductivity (~10^{-6}-10^{-2}S/cm) [183-185] making it necessary to tailor either the electronic nature or the architecture to overcome existing limitations[271]. The use of nitride particles for supercapacitor charge storage allows for the occurrence of a naturally occurring high surface area thin oxide layer circumventing the issues of low conductivity associated with thick oxide films. Most nitrides particularly those of transition metals traditionally being metallic have electronic conductivities much higher than the corresponding transition metal oxides making them ideal templates for pseudocapacitance behavior in the surface oxide[272, 273]. The existence of oxynitride phases could possibly be a contributing factor to the observed enhanced pseudocapacitance behavior of the surface oxide in nanoparticulate transition metal nitrides. Three outstanding problems have however been observed in nanoparticulate VN which includefade in capacity with increase in scan rate, loading and the cycling stablity[182, 235, 238, 246]. These characteristics are indicative of two problems, the poor electronic conductivity of nitride electrodes when coated as thick films and the poor stability of the surface oxide in highly basic media wherein the charge storage characteristics of VN are most pronounced. The nanoparticulate nature of the nitride yields large number of surface sites for the reversible faradaic reactions to occur on the nitride surface yielding very high pseudocapacitance. At the same time, the very same nanoparticulate nature leads to an increased number of grain boundaries within the nanoparticle which act as electron conduction barriers and scattering sites on account of the surface oxide causing a drop in overall conductivity of the nitride electrode. This in-turn implies that the very high capacitance associated with the nanoparticulate VN can

only be observed at low material loadings and at low scan rates which to date has been a prime limitation, a factor that has been adequately addressed in this thesis work.

Sulfide materials have lately been studied for supercapacitor applications. WS_2 nanoparticles inside carbon tubes have been reported to have capacitances of ~337 F/g at 10 A/g[274]. Similarly, MoS_2 nanocomposites inside carbon tubes have been reported to have capacitances of ~210 F/g at 1A/g with stability upto 1000 cycles[275]. Anisotropic morphologies and high-curvature surfaces of non-spherical structures have impact on supercapacitor properties. Hollow NiS hierarchical nanospheres using silica coated nickel silicate were converted to NiS using Na_2S resulting in formation of NiSOH which was found to be electroactive over a 0.7 V window in aqueous electrolyte with capacitances of ~583 F/g at 10 A/g[276]. CoS nanocages made using zeolitic imidazolate framework-67 (ZIF-67) nanocrystals as the templates (converted to CoS using cobalt nitrate hexahydrate electrochemical oxidation-reduction to CoSOH). CoSO material synthesized using this methodology were shown to have capacitances of ~1812 F/g at 5 mV/s (over a 0.8 V window)[277]. CoS 3-dimensional hetero-architectures were tested in 2M KOH with capacitances of ~555 F/g at 5 mV/s and 464 F/g at 100 mV/s[278]. CoS hollow nanosheets have been generated and when tested in 1M KOH electrolyte demonstrate excellent stability for upto 10000 cycles. Energy densities of ~13.2 Wh/kg were reported therein[279]. CoS spheres[280] using a surface redox Co^{2+}/Co^{4+} couple exhibited ~400 F/g capacitance. Cobalt sulfide derived by Tao et al. showed 475 F/g in 6M KOH[254]. CNT/CoS composite electrodes were shown to have very high capacity[281]. CNT-CuS nanoneedles supercapacitor were also derived with capacitances of 100-125 F/g[282]. Carbide materials have also been studied for supercapacitors by Pande et al.[247].

1.2.4 Other non-oxide electrodes

Conducting polymers are organic polymers such as polyaniline (PANI) which exhibit good electronic conductivity which have recently been explored extensively for supercapacitor applications[97]. Carbon nanotube-conducting polymer composite electrodes have also been widely studied[283]. CNT polymer composite electrodes using different polymers were studied in 1M H_2SO_4 and polyaniline (PANI)-CNT electrodes were found to be most stable while Polypyrrole (Ppy)-CNT were found to be the least stable[284]. Other such studies have studied stability of polymer-CNT electrodes in different electrolytes[285]. Conducting polymer hydrogel electrodes for 3-D supercapacitor applications were also reported[286]. Conducting polymer-carbon nanotube supercapacitance dependence on cell-configuration was reported by Khomenko et al.[287]. A large body of recent work on supercapacitors has focused on the use of non-aqueous electrolytes for supercapacitor applications. This is due to the squared dependence of energy density on the voltage window of the cell. Aqueous electrolytes are inherently limited on account of gas evolution at high voltages. To overcome this, commonly used lithium ion battery type electrolytes and ionic liquids have been used to test various oxides and carbon based electrode materials discussed in the previous sections[77, 78, 288-290]. Among these electrolytes, Et_4NBF_4 in acetonitrile seems most promising and has been shown to have very high energy density with materials like single wall nanotubes[126]. A more prominent direction in the supercapacitor field has been towards the use of asymmetric cells using a capacitor type electrode in conjunction with a battery type electrode. Following pioneering work by Amatucci et. al[291] using the Lithium titanate/acetonitrile/Activated carbon cell, various other materials have been similarly tested and shown to have very high energy densities. MnO_2 has also been tested in a 2.2V aqueous hybrid cell with activated carbon and shown to have energy densities as high as 21 Wh/kg. Zheng et. al

have shown that energy densities of asymmetric cells are dependent on the electro mass ratios and the ionic concentration of the electrolyte[292]. On this account, electrode matching is very important for asymmetric cells and Li et. al have proposed a theoretical model of electrode matching and verified the same using an $LiMn_2O_4$/Activated carbon system[293].

2.0 MOTIVATION

A large number of double layer and pseudocapacitor materials have been explored for supercapacitor electrodes. Amongst them, hydrous ruthenium oxide has been identified to be the preeminent supercapacitor material with the ability to maintain stable capacitances of upto 900 F/g over a large number of cycles on account of its pseudocapacitive charge storage[3, 43, 58, 63, 69, 159-161, 170, 191, 294]. However, the prohibitive price of noble metal based capacitors impels the search for alternative materials with similar charge storage characteristics. Other non-noble metal oxides and hydroxyl-oxides have been widely explored in this light including those of Mn, Ni and V[70-75]. Despite considerable research in these new systems, there is a critical need to improve the energy density of currently available materials while identifying novel and innovative cost effective approaches to generate these systems with the desired materials, chemical, physical and improved electrochemical properties to render them commercially viable. There is therefore a need to explore novel chemistries to identify cheap pseudocapacitor materials with high energy densities and good rate capability.

The development of high power energy storage devices for both stationary and mobile applications has been deemed critical for the attainment of sustainable energy storage systems to meet the global energy storage demands and the development of energy efficient global systems[3-5, 14, 295]. Supercapacitor materials as outlined in the earlier chapters are capable of rapid charge storage and distribution thus ensuring short charging times and seemingly infinite

cyclability with sufficiently large capacitances[44, 58, 65, 296-298]. There is however, a dire need for identification of materials systems and development of simple and cost effective synthesis techniques to render supercapacitor systems suitable for large-scale commercialization[37, 299, 300]. The need to tailor energy storage devices to suit such applications is highlighted by the current targets shown in **Table 5**. Identification of high energy and power density systems amenable for large-scale implementation of energy storage is clearly required to acheive upto 20% wind penetration on grid by 2030 which requires cheap and reliable energy devices at ~100$/kWh[40].

Transition metal nitrides are traditionally known for their refractory characteristics primarily due to their high melting point and chemical stability against corrosive acids and bases. Recent work by various groups has shown the viability of nitrides for catalysis and energy storage applications. Transition metal nitrides were first shown to have promise as pseudocapacitors by Thompson et al and Liu et al.[241, 255]. A thorough investigation into transition metal nitride supercapacitors was thus undertaken by the Kumta group in the early 2000s exploring a simple two step ammonolysis approach exploiting the characteristic nitridation reaction exhibited by the family of transition metal precursors containing identical halide functional groups.

The research studies by the Kumta group have shown that these nitrides exhibit excellent supercapacitor response in simple aqueous electrolytes [182, 235-238]. Among the various nitrides explored, VN was found to be the most promising, exhibiting a uniquely high capacitance of 1350 F/g albeit under low loading conditions [182, 238]. This exceptional performance at low active material loadings has been attributed to a combination of both double layer type capacitance and pseudo-capacitance response primarily attributed to the presence of a thin surface oxide layer (VO_x) that is grown over the centrally preserved core of the transition metal nitride providing the

required electronically conducting platform. Other groups have subsequently also evaluated the capacitor properties of VN and have reported capacitances of 161 F/g and 186 F/g, respectively[251, 260].

There are however, a number of outstanding issues plaguing the performance of VN as a supercapacitor material some of which was outlined in **Section 1.2.3**, that make it necessary to understand in depth the charge storage mechanisms occurring at the nitride surface, before it can be considered commercially viable[182, 235, 236, 238]. Significant among them are the poor rate capability and cycling stability. It was also observed that the achievable amount of charge that could be stored and readily available was significantly reduced when considering thick films of VN indicating an inherent limitation of the intrinsic electrical conductivity of the nanostructured system. This was corroborated by an observed fade in capacitance with increasing scan rate. A drop in capacitance with cycling was also observed indicating an inherent instability of the material in the electrolyte over the measured voltage window. Since the supercapacitance behavior of vanadium nitride was found to be very much dependent on the nature of surface oxide present on the nitride, a two pronged approach was undertaken to develop a fundamental understanding into the supercapacitor behavior of the nanoparticulate VN, i.e. independent evaluation of supercapacitance behavior in both the nitride (VN) and oxide (VO_x) nanomaterials and nitride nanomaterials. The first part of this research study thus focuses on the comparison of the structural and surface composition of VN synthesized by two disparate approaches to clearly identify the source of both the superior capacitance and the problems contributing to the fade in capacitance with scan rate and cycling.

Table 7. Synthesis conditions of VN as reported by various groups showing that VN preparation usually involves high temperature processing for extended periods of time.

Material	Synthesis Temp. (K)	Synthesis time (mins)	Reference
VNC_x	1073	155	301
$VN_{0.996}C_x$	1223	245	302
VN	1073	660	303
VNO_x	973	420	304
$VN_{1.08}O_{0.3}Cl_{0.1}$	673	1200	182, 238
VO_yN_z y=0.04-0.46 z=1.02-0.85	1273	1200	305
VN	873	1020	306

Traditionally, nitride materials are synthesized by very high temperature nitridation of the metal or oxide which is both energy inefficient and at the same time, produces crystalline VN with very low surface areas contributing to properties that are very undesirable for the above-stated stationary and mobile energy storage applications (see

Table 7). Most of the methods usually involve the use of very volatile precursors such as chlorides[182, 238, 307], cyanamides [308], dicyanamides [309, 310], C_3N_4 [311] or NH_3 [255, 302, 303]. Additionally, foam based methods commonly use carbon based surfactants leading to impurities

in the final nitride formed[301, 312]. In the work by Zhou et. al. the disadvantages of amorphous carbon, from foam-based synthesis, on supercapacitor performance are clearly outlined[251].

In light of the above, a simple, low cost, low temperature approach for bulk synthesis of VN was designed. High energy mechanical milling (HEMM) is a facile, low cost synthesis route commonly used to make ceramic, metal alloys and nanocomposites in large quantities[313, 314]. It was selected for the solid state synthesis of VN on account of low temperatures involved and the ease of the process itself thus rendering bulk synthesis simple, easy and economically viable. In addition, the intimate mixing of precursors that is enabled during the milling reaction of the solid state precursors would provide the energy required to trigger a diffusion induced chemical reaction thus resulting in the formation of the chemically inert nitride bonds, which is the primary reason for the need for high temperatures needed to generate the transition metal nitrides via most commonly used commercial approaches. The precursors used in the high energy mechano-chemical process described in this thesis involves the use of vanadium oxide and lithium nitride which are both benign and easily amenable for open air handling thus making this approach the most facile, low temperature route for the synthesis of nitride reported thus far in the open available literature. The material, structural and electrochemical properties of the VN synthesized by this technique were compared to that of nanoparticulate VN synthesized by low temperature ammonlysis of halide precursors (with very high capacitance previously reported by the Kumta group)[182, 235, 238].

As previously identified by Choi et. al., the pseudocapacitance contribution to charge storage in nitrides was largely due to a surface oxide layer[182, 235, 238]. Transition metal oxides as outlined earlier are very attractive for pseudocapacitive charge storage on account of their ability to accept variable oxidation states. Of particular interest to pseudocapacitor applications is the

ability of the surface oxide to undergo reversible electrochemical reactions as is the case in ruthenium oxide [44, 58]. The I-V characteristic of the successive oxidation/reduction reactions at the surface of the electrode resembles that of a capacitor, hence the term pseudocapacitor. Hydrous ruthenium oxide is an excellent pseudocapacitor material with the ability to maintain stable capacitances of upto 900 Fg^{-1} over a large number of cycles[69]. However, the prohibitive price of noble metal oxides impels the search for alternative oxide materials with similar charge storage characteristics. Vanadium is an element belonging to Group 5 of the periodic table with a half empty d-shell thus enabling it to exhibit multiple valence states of +2 to +5.

Vanadium oxide has previously been studied as a material for lithium ion battery (LIB) cathodes and non-aqueous supercapacitors[75, 169-172] as described in **Section 1.2.2**. In all these studies, thin oxide films have shown to result in good electrochemical performance on account of the short diffusion lengths for lithium ion intercalation. The importance of loading and its influence in achieving attainable capacitance in vanadium nitride based supercapacitor has already been highlighted by the Kumta group in earlier work[182]. Nanoparticulate materials such as oxides/nitrides of transition metals are very advantageous in terms of achieving desirable electrochemical performance on account of the high specific surface area (SSA) and the enhanced activity that is achievable at the nano-scale dimensions. However, the very nanoparticulate nature which is responsible for enhanced electrochemical activity results in loss of electronic conductivity on account of the large number of grain boundaries. Nanostructured vanadium oxide has a relatively low electronic conductivity [183-185] on the order of 10^{-6}-10^{-2} $\Omega^{-1}cm^{-1}$.

A strategy has therefore been undertaken using composite electrodes employing a combination of a double layer material and an oxide pseudocapacitor material. The oxide

material when coated on a conductive support matrix will thus exhibit minimal electronic conductivity issues resulting in high capacity and rate capability. The identification of ideal double-layer type capacitor materials to couple with doped vanadium oxide in order to form a hybrid electrode capable of high rates is relatively complex to be handled on account of the plethora of carbon based double layer materials identified by the capacitor community at large that was discussed in **Section 1.2.1**[92, 107, 124]. The material that was selected must be therefore suitable to overcome the low electronic conductivity usually observed in nanoparticulate oxides. These systems have been examined individually to identify suitable support materials for the various applications outlined earlier requiring the high rate capability i.e. very high conductivity, capacitor behavior and excellent stability in the voltage window of interest. It is also essential to maintain good carbon material loading and good carbon-oxide interface while at the same time avoiding thick oxide film formation on the carbon, making the underlying carbon material substrate effects redundant. Activated carbons are excellent double layer supercapacitor materials as described earlier on account of their high surface area and large pore volume[92, 107]. However, they suffer from the problem of wettability, inability to sustain a uniform deposit on the pores of the carbons. In addition, the high surface area carbons usually are very porous resulting in poor volumetric capacitance further compounded by the relatively low intrinsic atomic weight and density. Another excellent material described earlier studied intensely is graphene. Graphene, as the name suggests is a single sheet of graphite which allows for ballistic 1-D transport of electrons leading to electronic conductivities of up to 10^5 Sm^{-1} in composites made with graphene[91, 137-141]. However, a major problem with using graphene is that the individual graphene sheets are too thin to achieve sufficient loading of the oxide to achieve high energy densities in practical devices.

On the other hand, too thick a deposit of oxide would render the graphene sheet redundant as it would not be able to act as an electron channel to most of the oxide material. A better solution then would be to use carbon nanotubes which have very high conductivity on account of the 1-D electron transport. In addition, it is relatively easy to generate CNTs in the form of vertically aligned arrays which would ensure direct contact of each individual CNT with the current collector as well as creating a 3-D architecture which would act as an ideal substrate for oxide growth[270]. Carbon nanotubes are of two types, single wall nanotubes (SWNTs) and multi-wall nanotubes (MWNTs). SWNTs usually demonstrate slightly better electrical properties than MWNTs. However, the synthesis of pure vertically aligned SWNTs is very expensive and it renders the synthesis of the composite electrodes accordingly cost prohibitive. Alternatively, multi-wall carbon nanotubes are relatively inexpensive to synthesize and can be synthesized on a variety of substrates.

Carbon nanotube based hetero-structures have demonstrated improved rate capabilities for various Li-ion and supercapacitor electrode materials including silicon, ruthenium oxide, manganese dioxide and nickel oxide[164, 186-193]. A recent critical review by Gogotsi et. al has identified the need to understand the importance of thick films for commercial supercapacitor electrodes and the need to report volumetric capacitance along with gravimetric capacitance[228]. Nanostructured vanadium oxide has a relatively low electronic conductivity [183-185] on the order of 10^{-6}-10^{-2} Scm^{-1}. The high electronic conductivity of carbon nanotubes (CNTs) could thus be exploited to create composite 3-D architectures to minimize the oxide–oxide particle contact leading to efficient electron transport from the current collector to the surface of the vanadium oxide wherein the pseudocapacitance behavior is exhibited. In order to achieve this, architecture similar to that shown in **Figure 16** comprising vertically aligned carbon nanotubes (VACNT)

covered with electrochemically active doped-vanadium oxide would be ideal to obtain maximum capacitance while allowing for slight expansion/contraction likely as a result of the ensuing possible phase change. One of the goals of this study is to demonstrate the ability of vanadium oxide to exhibit very high charge storage when coated on an excellent electron conducting structure such as carbon nanotubes. Though some studies have tried to examine CNT-vanadium oxide structures, the effect of coating thin nanospheres on CNTs has not been used to effectively show capacitances approaching the theoretical values reported in **Table 6**.

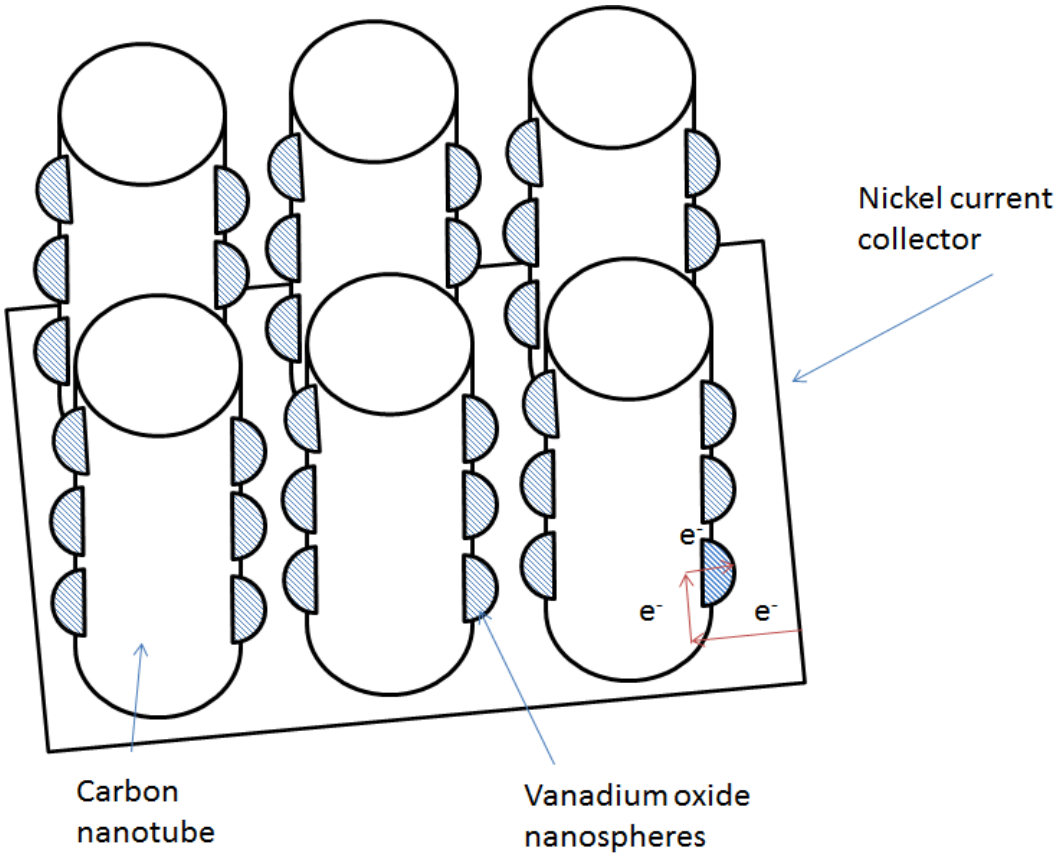

Figure 16. Schematic of VACNTs covered with vanadium oxide nanospheres which would be ideal for improved electronic transport while allowing for any expansion/contraction of the oxide occurring as a result of phase change due to Faradaic processes.

Chemical methods can be utilized to synthesize carbon nanotube-vanadium oxide composite hybrid electrode materials. However, wet chemical methods usually do not afford the freedom for tailoring the morphology of the composite electrode as the thickness of oxide film deposited on the carbon nanotubes is usually very high since the oxide usually forms a matrix around the CNTs rather than retaining nanoparticle nature. Synthesis of oxides usually involves the sol-gel method which is non-ideal for obtaining thin films on carbon nanotubes[315]. The sol-gel procedure leads to increased oxide-oxide particle contact rather than carbon-nanotube-oxide electron transport. In addition, carbon nanotubes usually need to be dispersed in an oxide sol, leading to loss in alignment of the CNTs. The very purpose of using CNTs i.e. one dimensional transport of electrons to nano-sized film of the oxide is thus lost. Chemical vapor deposition (CVD) is an ideal and versatile method to obtain uniform architectures on carbon structures[316, 317] while also tailoring the nature of the deposited film depending on the deposition conditions. Various groups have previously reported CVD as a technique for the growth of vanadium oxide thin films[186, 318-324] using both chloride and metal organic precursors. Oxide films with varying V oxidation states have been reported with ratios of oxides depending on the various deposition conditions including temperature and reagent concentrations[323].

In this work, an atmospheric pressure chemical vapor deposition (APCVD) method has been explored to deposit vanadium oxide (VO_x) on vertically aligned carbon nanotubes (VACNTs) for use as a supercapacitor electrode in aqueous media. Implementation of CVD as a synthesis method also provides the advantage of avoiding the incorporation of binders for generating the electrodes which can consume upto 50% of the total weight of the electrode in high surface area systems contributing largely to inactive dead weight[187, 317]. To demonstrate the superior performance of the CVD derived vanadium oxide-VACNT composite (VO_x-VACNT), a

thin film of vanadium oxide (VO_x) was deposited on nickel current collector and tested in conditions similar to those used to examine capacitor performance of the VO_x-VACNT. This comparison also provides a basis to identify the materials properties needed to maximize the capacitance behavior in nanoparticulate oxides. Very high capacitance values approaching the theoretical capacitance of vanadium oxide have been demonstrated in this study using the VO_x-VACNT hybrid heterostructured electrodes detailed in subsequent chapters.

Table 8. Choice of architecture for oxide-CNT composite materials to maximize areal capacitance.

Morphology	Characteristics
Nanoparticle film 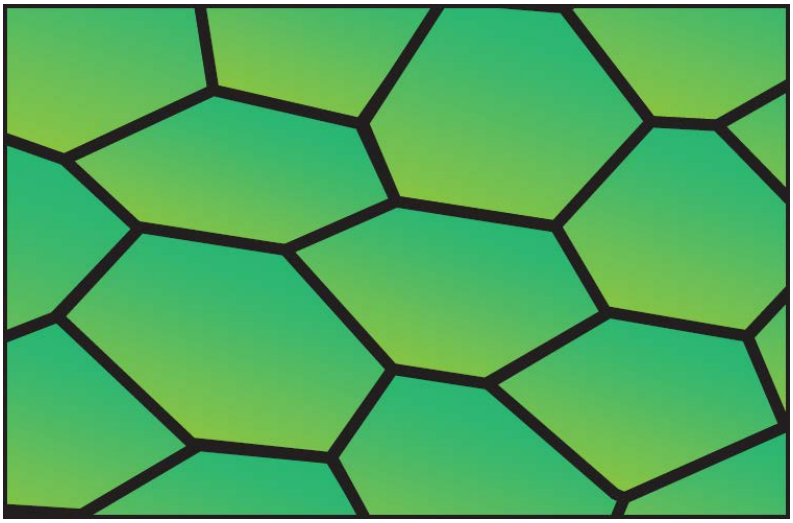	a) High surface area b) Poor electronic conductivity c) Large number of grain boundaries limiting flow d) Inherently low conductivity of oxide materials hampered further

Table 8 (continued)

Thick oxide matrix on carbon nanotubes/CNT-oxide mix film 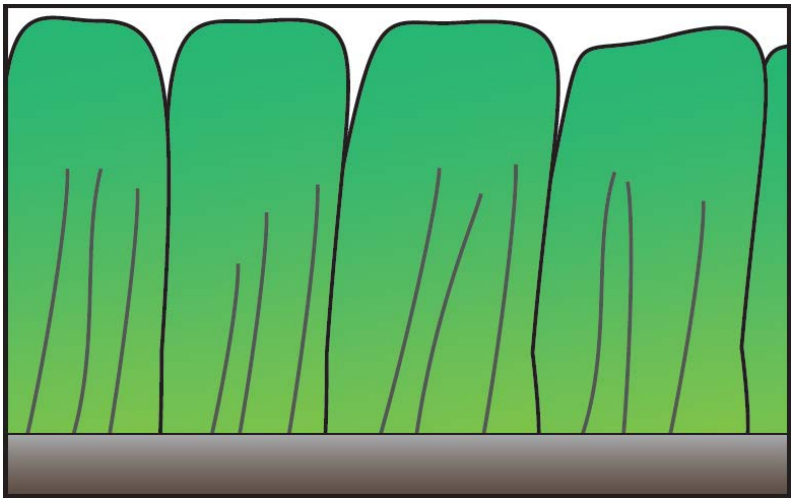	a) Carbon nanotubes ineffective in reaching all parts of the oxide resulting in large grains and number of grain boundaries b) Acts like thick film of oxide alone with little conduction of electrons to grains far from CNTs/current collector
Thin oxide coating on vertically aligned carbon nanotube matrix 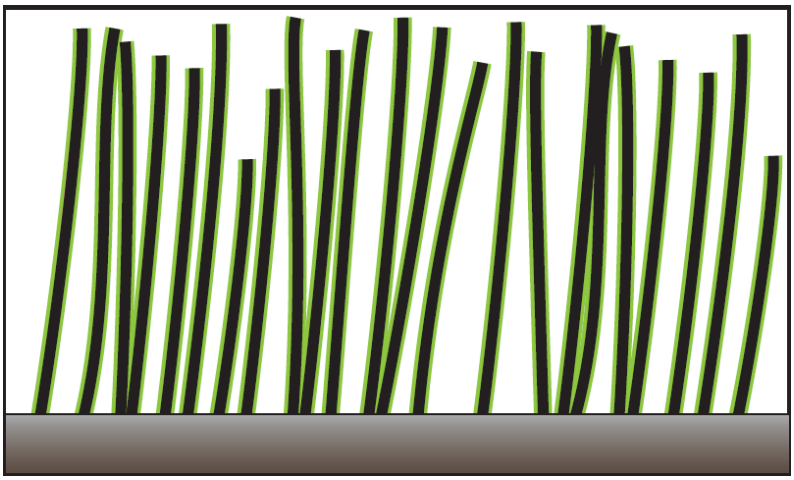	a) Very good electronic contact b) 3-D architecture ensuring ballistic electron transport to oxide film/grains c) High oxide-electrolyte contact maximizing pseudocapacitive contribution d) Low oxide/CNT weight ratio resulting in low overall capacity when CNTs do not possess significant capacitance e) Very short diffusion distances from oxide-CNT interface to oxide-electrolyte interface

Table 8 (continued)

Moderately thick doped oxide coating on vertically aligned carbon array 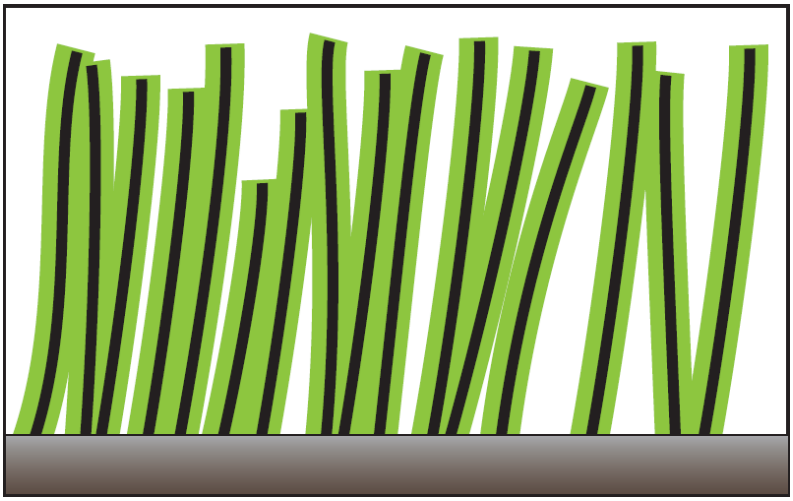	a) Very good electronic contact between carbon nanotubes and oxide particles b) 3-D architecture ensuring ballistic electron transport to oxide film/grains c) High oxide-electrolyte contact maximizing pseudocapacitive contribution d) Relatively short diffusion distances from oxide-CNT interface to oxide-electrolyte interface e) Effects of electron mobility reduction due to grains overcome to a large extent by the increased conductivity of the doped oxide f) Thicker film results in greater oxide/CNT ratio and thus high overall capacitance

Doping of oxides (Mo, Mn, W, Ti, Cu, and Ag) has been previously studied as an excellent pathway to improve electrical resistivity and electrochemical charge storage properties[208-215]. Silver and copper doped oxides have been shown to increase the electronic conductivities by up to 2 orders of magnitude[185, 216]. Ti and W doped vanadium oxide has also been shown to lead to improvement in pseudocapacitor characteristics[217]. Tungsten doping of VO_2 nanopowders and thin films has also been demonstrated and sometimes shown to result in a reduction in electrical resistivity[320, 325-328]. Pure vacancy-free vanadium pentoxide is a n-type semiconductor[329] with a forbidden energy gap between valence and conduction zones. However,

the introduction of vacancies and doping elements increases the number of charge carriers and thus the electronic conductivity to such an extent that vanadium oxide is rendered a metallic conductor[185, 216]. Though some improvement in electronic conductivity and evidence of improvement of charge storage by doping of oxides has been demonstrated, a detailed fundamental study has not been undertaken correlating supercapacitor behavior with doping in both nanoparticulate oxide and nitride materials. On the basis of the existing evidence in literature, it is to be expected that a first principles computational screening study to identify suitable dopants could be used to predict and engineer high capacity, high rate, and stable supercapacitor materials. The aim of this work is thus to use doping of oxides as an approach that allows for modifying the electronic conductivity and thus the electrochemical activity, as well as the electrochemical stability of nanoparticulate oxides and nitrides. Using a theoretical density functional theory (DFT) simulation involving d-band assessment of the structure, suitable dopants have been identified to improve the electronic conductivity and thus the supercapacitor behavior of nanostructured oxides. Using such approaches, the current study provides a unique methodology for generating thick film architectures of doped vanadium oxides grown on vertically aligned CNTs (VACNTs) resulting in capacitance values that are uniquely distinct from currently reported values in the literature. Accordingly, in this work, an atmospheric pressure chemical vapor deposition (APCVD) method has been explored to deposit titanium doped-vanadium oxide on vertically aligned carbon nanotubes for use as a supercapacitor electrode in aqueous media.

Table 8 shows the various architectures commonly used for supercapacitor applications and their accompanying problems. As seen therein the use of a moderately thick doped oxide coating on a forest of vertically aligned carbon nanotubes should allow for minimum electron

transport limitations, while maximizing active material use with considerable reduction in the inactive phase weight. This should be reflected as a significant improvement in areal capacity, a measure of more relevance than gravimetric capacity. As a result of the improved electronic conductivity of doped vanadium oxide and high conductivity of vertically aligned carbon nanotubes, it is possible to demonstrate the attainment of high gravimetric capacitances in thick electrodes resulting in high areal capacities, an aspect that has never been demonstrated clearly in the published literature to date.

It will be established as a part of this study that the nature of supercapacitor behavior in nanostructured nitrides is very much dependent on the surface oxide layer, especially as far as cycling stability is concerned. However, the poor electronic conductivity of the nanostructured nitride limits the loading which adversely affects the achievement of the high capacitor response. Doping of other transition metals either directly into the nitride lattice or into the surface oxide could thus be a suitable means to obtain a more stable high capacitance nitride material due to the possibility of significantly improving the electronic conductivity and electro-catalytic activity. The position of the d-band center is distinctly different in the doped VN when compared to the undoped VN. This is expected to alter the catalytic activity significantly. In addition, the introduction of dopants leads to a change in the density of electronic states which is a direct measure of electronic conductivity. Thus, in tandem with the doped oxides, doped nitrides will also be screened to identify a superior charge storage material.

In addition to increase in electronic conductivity of the surface oxide and inherent conductivity of the core nitride, doping could result in improvement in cycling stability by stabilizing the oxidation state of the surface oxide. Niobium nitride has previously been shown to have excellent stability in basic media over the window of interest albeit with limited charge

storage capability[234, 235]. Based on earlier studies performed as a part of work by Kumta et al. into nanoparticulate nitrides, tungsten and niobium appeared to be promising materials for doping to improve stability and capacitance of nanoparticulate VN[235]. Therefore, in the present study, it was decided to evaluate supercapacitor performance of tungsten and niobium doped vanadium nitride nanoparticles. An extensive study using various other dopants was however not undertaken due to the scale of the task. It is expected that initial understanding and experiemental data obtained as a part of this study will serve as the harbinger of new data that will be collected to be fed into a computational methodology for effective screening of dopants. Niobium was chosen particularly due to the known very stable performance of NbN in high pH of KOH previously reported by the Kumta group. Niobium doping is not expected to result in significant improvement in electronic conductivity since niobium and vanadium are isovalent although providing significant electrochemical stability. However, tungsten is expected to induce a large number of extra carriers resulting in a significant improvement in electronic conductity of VN. On the basis of this logic, doping studies were undertaken and effect of doping on charge-transfer parameters was explored in great detail. The doped powders were prepared by a simple wet-chemical method and the effect of tungsten and niobium doping on the electronic structure of vanadium nitride and surface oxide has been theoretically derived using ab-initio d-band modeling in order to obtain a fundamental understanding into the electronic characteristics affecting electrochemical capacitor behavior of the doped nitride materials.

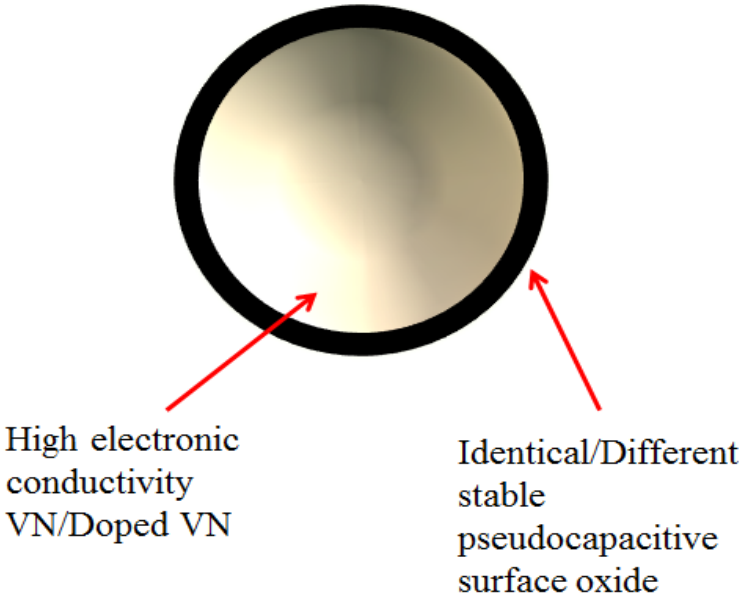

Figure 17. Core-shell type transition metal nitride/doped nitride with a stable surface oxide either of the same composition or of a suitably doped composition with excellent pseudocapacitor behavior as well as electrochemical stability.

A core-shell type composite doped nanomaterial (**Figure 17**) with superior supercapacitor characteristics was developed based on the fundamental understanding gained into the nature of charge storage behavior in transition metal oxides and nitrides. This material consists of a highly conductive transition metal nitride/doped nitride core coated with a stable shell consisting of either an oxide of the same composition or a different composition. On account of the highly conductive nature of the nitride, the material exhibits high rate capability while on the other hand it will also potentially exhibit high energy density and cyclability on account of the stable pseudocapacitive surface oxide layer. The thesis goals have been accordingly crafted to shed light into these fundamental issues affecting vanadium oxides as well as vanadium nitirides. Efforts to improve electronic conductivity as well as chemical stability have been made exploring tethered hybrid heterostructures as well as nanoparticulate

architectures. The subsequent chapters outline in detail the fundamental studies conducted to engineer these novel structures to exhibit the desired improved and sustainable electrochemical response utilizing active material loading rendering the system more amenable to industrial and commercial level implementation and use in actual device grade capacitor systems in the near future.

2.1 SPECIFIC AIMS

There is a fundamental need to understand the nature of the double layer and the pseudocapacitance arising in nanostructured transition metal nitrides and oxides. Using the understanding and first principles studies, doping of oxide and nitride materials has been performed and the charge storage properties of these materials are studied in detail. Thus, the major research goals have been divided into different categories based on the fundamental understanding of the synthesis and electrochemical analysis of undoped and doped transition metal oxides and nitrides. The objectives are discussed accordingly in the following sections.

Specific aim 1: To understand the bulk and surface structural and compositional properties leading to the origin of supercapacitor behavior in transition metal nitrides. This is achieved by a thorough materials and electrochemical characterization of VN synthesized by the two approaches i.e. mechano-chemical reduction of oxides and the chimie-douce ammonolysis reaction of transition metal halides. The two approaches result in the generation of VN nanoparticles with disparate properties allowing for a thorough mechanistic understanding of the charge storage mechanisms prevalent in the two separately synthesized nitride materials. The dependence of supercapacitor performance of VN on specific surface area, particle size, electronic conductivity and surface oxide composition has been established so far. Electrochemical impedance spectroscopy (EIS) has been utilized to gain an understanding into the fundamental charge transfer properties.

Specific aim 2: To study the nature of the capacitance behavior in nanostructured transition metal oxides. A chemical vapor deposition method is utilized to achieve oxide thin films (VO_x) and VACNT coated oxide nanocomposites(VO_x-VACNT), which are then thoroughly investigated to identify the conditions required to achieve superior charge storage

response in the same. Chemical vapor deposition approach has been used to show that vanadium oxide, though an insulator can be coated on vertically aligned carbon nanotubes to attain excellent supercapacitor charge storage.

Specific aim 3: To alter the fundamental electronic behavior of nanostructured oxides and nitrides by the incorporation of suitable dopants. Using a modified version of the chemical vapor deposition technique used to obtain VO_x-VACNTs, doped vanadium oxide-vertically aligned carbon nanotube composite heterostructures (VO_x:M-VACNT) are obtained and their performance is evaluated. Improvement in charge storage behavior is demonstrated and in-depth analysis is performed to identify the underlying mechanisms behind the same. Similarly, doped nitrides of vanadium ($V_xM_{1-x}N$) are obtained using a two-step ammonlysis reaction. Effect of dopant element and concentration on capacitance has been evaluated in an in depth manner.

Specific aim 4: The fundamental understanding obtained from the above studies will be utilized to generate a stable, high rate, high capacity hybrid nitride-oxide supercapacitor material suitable for commercial applications. A composite material with superior charge storage properties has been demonstrated using the insight into oxide and nitride charge storage obtained as a result of the previous Specific aims. The material will consist of a stable, highly conductive nitride material having a surface oxide which is both conductive as well as chemically stable in the electrolyte of interest.

3.0 EXPERIMENTAL METHODS

3.1 MATERIALS SYNTHESIS

3.1.1 Synthesis of nanoparticulate nitrides

3.1.1.1 Mechanochemical reduction

Mixtures of powders of lithium nitride (Li_3N, Alfa Aesar, 99.4%) and vanadium oxide (V_2O_3, Alfa Aesar, 99.7%) of suitable compositions were subjected to mechanical milling in a high energy shaker mill (SPEX CertiPrep 8000 M) for up to 3 hours in a stainless steel (SS) vial using 20 SS balls of 2 mm diameter (~20g) with a ball to powder weight ratio 10:1. The resultant milled powders were washed in de-ionized (DI) water at 40^{o}C to dissolve the lithium oxide formed as a by-product of the mechanochemical reaction.

3.1.1.2 Chimie-douce reaction

A two-step chemical method was used to obtain nanoparticulate vanadium nitride for comparison with the VN synthesized by mechanochemical reduction[182, 235, 238]. Vanadium nitride was synthesized using a two-step ammonlysis method. In this procedure, approximately, 3ml vanadium tetrachloride (Sigma Aldrich, Inc.,97.5-99%) was dissolved in 150 ml of anhydrous chloroform (<5 ppm H_2O, ACROS Organics) inside an inert atmosphere glove box (Vacuum Atmospheres Inc.). The dissolved chloride was then reacted with flowing anhydrous ammonia

gas (100 sccm, Valley National gas, 99.99%) to form a halide complex of the form $V(NH_2)_3Cl$. The solvent was then evaporated at 100 ^{0}C and the powder was recovered in a glove bag and introduced into a tube furnace. Subsequently, the powder was heat-treated in anhydrous ammonia (100 sccm) at 400 ^{0}C to convert the complex to vanadium nitride. The two-step ammonolysis procedure results in very fine VN crystallites which require surface passivation to avoid pyrophoric reactivity of the resulting nanostructured nitride upon exposure to air. A very low concentration of oxygen-argon (0.1% O_2-Ar) gas mixture was passed at 100 sccm for 4 hours to passivate the nitride nanoparticles resulting in a very thin surface oxide layer thus stabilizing the nitride against any exothermic oxidation of the nanoparticulate nitrides.

The reasoning behind choosing this procedure to synthesize the nitride lies in that a liquid-gas reaction enables for enhanced contact of the reactants with the ammonia and also leads to very fine controlled nanoparticles of ~ 6 nm with a thin oxide film forming on the surface of the nitride.

3.1.1.3 Mechanical milling of commercial VN

Commercially procured vanadium nitride (STREM, Goodfellow; 99.5% V) was simultaneously examined as-obtained for comparison of material properties. In addition, high energy mechanical milling was performed on the commercial VN in a high energy shaker mill (SPEX CertiPrep 8000 M) for up to 10 hours (in a stainless steel (SS) vial using 20 SS balls of 2 mm diameter (~20g) with a ball to powder weight ratio 10:1. The aim of this procedure was to characterize the change in materials properties of commercial VN and compare the same with VN derived by the two-step ammonlysis method.

The synthesis of nitride by three distinct methods with differing structural and surface properties allows us to gain an understanding into the capacitance characteristics of vanadium nitride.

3.1.2 Synthesis of nanoparticulate doped nitrides

A modification of the two-step chemical method reported by Choi et al was used to obtain nanoparticulate doped vanadium nitride[182, 234-238]. First, the premixed chloride precursors were dissolved in an organic solvent (anhydrous chloroform <5 ppm H_2O, ACROS Organics). The solution was mixed for over two hours to ensure complete dissolution of the chlorides in chloroform. Anhydrous ammonia (99.999%, Matheson TriGas Inc.) was used to convert the chlorides to an ammoniated complex of the form $V_xM_{1-x}(NH_2)_3Cl$ (M=W,Nb) following the procedure detailed by Choi et al [182, 235-238]. The ammonolyzed complex was then nitrided in anhydrous ammonia at 400^0 C for upto 10 hours to form the doped nitrides. The reasoning behind choosing this complexation method over conventional heat treatment procedures to synthesize the doped nitrides was to avoid selective precipitation and thus phase separation of the dopant from the parent nitride. In addition, a liquid-gas complexation reaction enables for enhanced contact of the reactants leading to very fine nanoparticles which when heat treated crystallize to form very fine doped nitride nanoparticles of ~ 6 nm. Different compositions of the doped nitride were synthesized using this techniques [$(V_{1-x}M_x)N$; M=W,Nb; x=0.05, 0.1, 0.2 for W and x=0.005, 0.01, 0.05, 0.1 for Nb].

3.1.3 Chemical vapor deposition of vanadium oxide-VACNT (VO_x-VACNT) composites and thin film vanadium oxide (VO_x)

A two-step CVD process was used to obtain vanadium oxide film coated CNT hetero-structures on nickel substrate disks. First, the nickel disks were properly cleaned using dilute acids and acetone, and then weighed. Vertically aligned carbon nanotubes (VACNTs) were then deposited on the Ni disks (Alfa Aesar Inc., 0.05 mm thick, annealed, 99+% (metals basis)) using a xylene-ferrocene mixture following a hot wall chemical vapor deposition procedure similar to that reported by Ajayan et al using an Ar/H_2 mixture[330, 331]. m-Xylene (ACROS organics, extra pure, >99%) was used as the carbon source with ferrocene (ACROS Organics, 98%) acting as the catalyst for CNT nucleation and growth (**Figure 18a**). The mixture was vaporized and bled into a hot-wall CVD tube maintained at 770^o C. The deposition was carried out for 30 minutes resulting in growth of a uniform forest of vertically aligned carbon nanotubes. The VACNT coated Nickel disks were then weighed and a low temperature hot-wall APCVD setup was used to deposit the VO_x directly onto the vertically aligned carbon nanotubes (VACNTs). Appropriate amount of vanadium tetrachloride (VCl_4, Sigma Aldrich) was measured in an inert atmosphere glove box (Vacuum Atmospheres Inc.) and retrieved in a sealed stainless steel evaporator bottle. Vanadium oxide nanospheres were deposited on the VACNTs using a hot wall tubular APCVD setup (**Figure 18b**) consisting of two separate nitrogen (UHP N_2, Grade 5, Valley National gas) carrier gas lines running through the evaporator vessels, one containing the chloride precursors and another containing a distilled water (Millipore QGARD, Resistivity=18.2 MΩ-cm) line driven by a syringe pump (Thermo Scientific Orion M365 Sage syringe pump). Both precursors were then evaporated and carried into a hot wall CVD reactor tube wherein the CNT coated nickel (Ni) disks were placed[217, 323, 332-334]. Deposition was carried out at 250 ^{o}C for 20 minutes. The oxide

coated disks were then weighed and characterized. Thin film vanadium oxide (VO_x) was also deposited directly on Ni substrate disks by CVD using the same precursors to compare the electrical and electrochemical properties of the thin films of the VO_x with that of the composite heterostructure of VO_x-VACNTs.

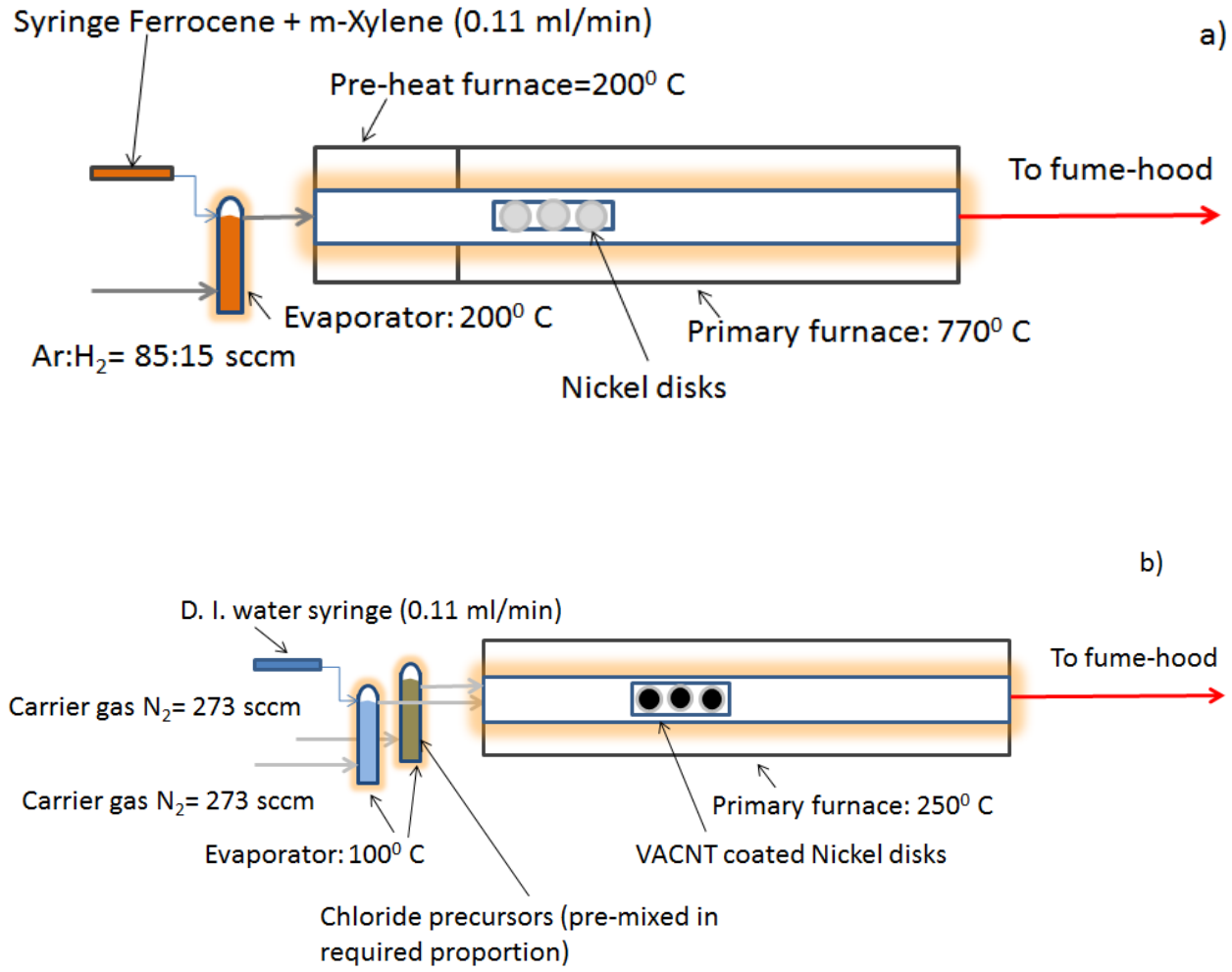

Figure 18. Chemical vapor deposition setup for deposition of (a) VACNT forest (b) VO_x-VACNT composite.

3.1.4 Chemical vapor deposition of doped vanadium oxide-VACNT (VO_x:M-VACNT) composite electrodes and thin film doped vanadium oxide (VO_x:M)

To generate the doped vanadium oxide, appropriate mixtures of vanadium tetrachloride (VCl_4, Sigma Aldrich) and metal dopant introduced as a chloride precursor, i.e. titanium tetrachloride ($TiCl_4$, Sigma Aldrich, 99.9% metals basis) were dissolved in an aprotic solvent, chloroform ($CHCl_3$, ACROS Organics, 99.9% Extra dry) in an inert atmosphere glove box (Vacuum Atmospheres Inc.: model EE-493, below 5ppm O_2 + H_2O) and recovered in a sealed stainless steel evaporator bottle. The doped vanadium oxide nanospheres were deposited on the VACNTs using a hot wall tubular APCVD setup (**Figure 18b**) consisting of two separate nitrogen (UHP N_2, Grade 5, Valley National gas) carrier gas lines running through the evaporator vessels, one containing the mixture of chloride precursors and another containing a distilled water (Millipore QGARD, Resistivity=18.2 MΩ-cm) line driven by a syringe pump (Thermo Scientific Orion M365 Sage syringe pump). Both precursors were evaporated and carried into a hot wall CVD reactor tube wherein the CNT coated nickel (Ni) disks were placed[175, 217, 323, 332-334]. Deposition was carried out at 250^oC for 20 minutes. The oxide coated disks were then weighed and characterized. Doped vanadium oxide thin film was also generated by depositing the doped oxide directly on the Ni substrate disks by CVD using the same precursors to compare the electrical and electrochemical properties of the thin films of the doped oxide with that of the composite heterostructure comprised of doped oxide coated on VACNTs.

3.2 MATERIALS CHARACTERIZATION

3.2.1 X-ray diffraction

In order to perform qualitative phase analysis, the synthesized nitride materials were characterized by X-ray diffraction (XRD) using Philips XPERT PRO system employing CuK_α (λ = 0.15406 nm) radiation with operating voltage and current set at 45kV and 40mA, respectively. The XRD peak profile was analyzed using the Pseudo-Voigt function to determine the Lorentzian and Gaussian contribution of the peaks. The integral breadth of the Lorentzian contribution, determined from peak profile analysis using single line approximation method after eliminating the instrumental broadening and lattice strain contribution, was implemented in the Scherrer formula to calculate the effective crystallite size of the VN derived by ammonolysis method, mechanochemically derived VN, the commercially procured VN and the milled samples of the commercial VN[335, 336]. The lattice parameter and molar volume of VN were calculated using the least square refinement techniques.Similar analyses were performed on the various doped compositions of VN [$(V_{1-x}M_x)N$; M=W,Nb; x=0.05, 0.1, 0.2 for W and x=0.005, 0.01, 0.05, 0.1 for Nb].

3.2.2 Electron microscopy & composition analysis

To investigate the microstructure of the various VN materials, scanning electron microscopy (SEM) and transmission electron microscopy (TEM) were conducted. Philips XL-30FEG comprised of an ultrathin beryllium window and Si (Li) detector operating at 20 kV was employed for executing the secondary electron (SE) image. The nitride powder was

homogenously spread out over a carbon background to obtain the SEM images. Quantitative elemental analysis was performed using the energy dispersive X-ray spectroscopy (EDX) analyzer integrated into the SEM machine. High resolution transmission electron microscopy (HR-TEM) analysis was conducted on the sample using JEOL JEM-2100F to investigate the particle size and morphology of the various VN materials and doped VN compositions. Samples for HRTEM were prepared from the various VN materials and doped VN compositions by dispersing the powders in in methanol followed by sonication. The dispersion was coated on 3.05 mm diameter Nickel grids (JEOL, 400 mesh nickel) containing a holey carbon film. The grids were then vacuum-dried for 24 hours and used for conventional and HRTEM characterization. In addition, the oxygen and nitrogen content in the VN and doped VN samples were independently analyzed using inert gas fusion analysis [LECO TC600 analyzer (Alternative Testing Laboratories, Inc.). The inert gas fusion technique analyzes oxygen content by allowing the oxygen to react with carbon and analyzing carbon dioxide formed using infrared spectroscopy. Nitrogen content is measured by using a thermal conductivity cell. The analysis was performed by Alternative Testing Laboratories, Inc. Finally, the specific surface area (SSA) of the VN was also measured using a Micromeritics ASAP 2020 (Accelerated surface area and porosimetry) system. Nitrogen adsorption and desorption partial pressures were measured and a BET (Brunauer Emmett Teller) type adsorption was assumed to obtain the surface area. Multi-point BET surface area is reported in this work using an adsorption-desorption isotherm over partial pressure values P/P_o going between 0.06 and 0.35.

The microstructure of the oxide thin film (VO_x), VO_x-VACNT and VO_x:M-VACNT materials was investigated using scanning electron microscopy (SEM) and high resolution transmission electron microscopy (HR-TEM). Quantitative elemental analysis was performed

using the energy dispersive X-ray spectroscopy (EDX) analyzer integrated into the SEM machine. Samples for HRTEM were prepared from the CVD synthesized samples by scraping off the VO_x-VACNTs and VO_x:M-VACNTs from the Ni substrate and dispersed on 3.05 mm diameter Nickel grids (JEOL, 400 mesh nickel) containing a holey carbon film in methanol by sonication. The grids were then vacuum-dried for 24 hours and used for conventional and HRTEM characterization.

To study the nature of the oxides coated on the CNTs and to identify any amorphous deposits other than the oxide present on the CNTs, micro-Raman spectroscopy was performed on a Reinshaw inVia Raman microscope. Raman spectra were collected in air at room temperature using a 633 nm laser. Low laser intensities were chosen to avoid beam modification of the samples and the spectra were collected by averaging multiple scans over a frequency range of 3500-100 cm^{-1}.

To analyze the surface composition, determine the valence state of V ions in the nitride before, and ascertain any changes in the oxidation state of V upon cycling, x-ray photo electron spectroscopy (XPS) was performed (Perkin-Elmer PHI-5600) before cycling and after electrochemical cycling for 200 cycles in 1M KOH. XPS on the pristine and cycled VN was conducted using a Physical Electronics (PHI) model 32-096 X-ray source control and a 22-040 power supply interfaced to a model 04-548 X-ray source with an Omni Focus III spherical capacitance analyzer (SCA). The system is routinely operated within the pressure range of 10^{-8} to 10^{-9} Torr (1.3×10^{-6} to 1.3×10^{-7} Pa). The system was calibrated in accordance with the manufacturer's procedures utilizing the photoemission lines, E_b of $Cu_{2p}^{3/2}$ - 932.7 eV, E_b of $Au_{4f}^{7/2}$ - 84 eV and E_b of $Ag_{3d}^{5/2}$ - 368.3 for a magnesium anode. All the reported intensities are in effect experimentally determined peak areas divided by the instrumental sensitivity factors.

Charge correction was obtained by referencing the adventitious C 1s peak to 284.8 eV. Similar analysis was performed on the CVD derived oxide-VACNT composite electrodes and doped oxide-VACNT composite electrodes.

3.2.3 Electronic conductivity analysis

Since the electronic conductivity of the active material is a crucial parameter affecting the supercapacitor performance, a four point probe was used to measure the electronic conductivity of the vanadium nitride derived by the various methods and doped VN materials, vanadium oxide thin films, vanadium oxide-VACNT composite electrodes and doped oxide-VACNT composite electrodes. To measure the electronic conductivity of powder nitride materials, pellets were prepared by compaction of the VN powder using a uniaxial pressure of 7000 lb in a manual press (Carver Inc.). A FPP 5000 four-probe conductivity instrument (Miller Design & Equipment, Inc.) was used for the measurements, and the sheet resistance values obtained correspondingly, were then converted to yield the respective electronic conductivity. The thickness of the pellets was measured and sheet resistance data was obtained by depressing the pellets (with an insulator backing plate) against four equally spaced probes, two of which supply current while the other two measure voltage across them. Sheet resistance data was obtained in ohm/sq and multiplied with the sample thickness to obtain the resistivity. The flatness and crack-free nature of the pellets was ensured to avoid artifacts in the measurement of resistivity. Four-probe conductivity data is usually obtained by preparing pellets from powders and supporting them on insulators while maintaining contact with four equally spaced probes, two of which supply current while the other two measure voltage across them. The measurement of resistivity of thin films on conducting metal substrates however is a difficult proposition. This is because

the flow of electrons from the two current probes would probably occur through the substrate current collector. This current flow does not however occur in the CVD derived oxide thin films, VACNT-oxide composite electrodes and doped vanadium oxide-VACNT composite electrodes as the deposit is sufficiently thick and crack free to avoid interference from the substrate. Thus the CVD derived oxides were used as synthesized to obtain electronic conductivity.

3.3 ELECTROCHEMICAL TESTING

Extensive electrochemical examination was performed on VN synthesized by ammonolysis, mechanochemically derived VN, the commercial VN and VN that was milled for various time durations upto 10 h in order to understand the nature of charge storage in VN. Similar testing was performed on the doped nitrides of VN. Cyclic voltammetry was performed on the VN materials to evaluate capacitor performance. Slurries of the various materials were prepared with a composition of 85% active nitride, 5% conductive additive (Super-P Carbon) and 10% binder poly-vinylidene flouride (PVDF) (Aldrich Chemicals) in a solution of N-methyl 2-pyrollidone (NMP) (Fisher Scientific). After sufficient stirring of the slurries to allow for uniform dispersion, they were cast onto pre-weighed nickel current collector disks (1” diameter Nickel disks). The slurry coated current collector disks were allowed to dry overnight in a vacuum oven at 100^{o}C before the final weight was recorded. The active material weight was then used to calculate the gravimetric capacitance. A three electrode half-cell configuration was used to perform cyclic voltammetry and electrochemical impedance spectroscopy (EIS) on the active material coated Ni disks to understand the electrochemical mechanisms involved and calculate the specific capacitance of the VN prepared by the various methods. The cell assembled comprised of a

platinum counter electrode, an Hg/HgO (in 1M KOH) reference electrode [0.14 V vs. NHE] and an active material coated Ni disks described above as the working electrode. An aqueous 1M KOH solution (pH~14) was used as the electrolyte in all the electrochemical tests.

A three electrode cell configuration was used to perform cyclic voltammetry and on the various electrodes fabricated as described above in order to evaluate supercapacitor performance of the active materials. The nitride materials were evaluated in 1 M KOH electrolyte solution since superior nitride performance of VN (~1400 F/g) was reported in 1M KOH of pH~14[182, 235, 238]. Cyclic voltammetry tests were performed on a Princeton Applied Research Versastat 3 potentiostat in the -1.2 V to 0 V range with respect to the reference electrode to evaluate the specific capacitance of the VN materials. Cycling was performed at different rates and the area of the cyclic voltammogram was used to calculate the gravimetric capacitance. The gravimetric, areal and volumetric capacitances were calculated from the cyclic voltammograms using previously reported procedures[175, 246]. To further characterize the electrochemical behavior and stability of the chemically derived nitride, extended cycling (200 cycles) was performed at a scan rate of 10 mV/s. The areal (mF/cm^2) and volumetric capacitance (F/cc) of the mechano-chemically synthesized VN were calculated on the basis of both the electrode basis and materials basis. To calculate areal capacitance and volumetric capacitance on the basis of electrode parameters, the area of the working electrode and volume of the material coated on the current collector were used. The areal capacitance on the basis of experimentally observed surface area and material density were also calculated. In addition, galvanostatic charge-discharge cycling was performed on mechanochemically derived VN on an Arbin BT-2000 cycler at a current density of 100 mA/g to observe the nature of the V-t characteristic and to carry out long term cycling upto 1000 cycles.

The effect of the electrode properties on capacitance of ammonolysis derived VN is not well understood. In order to understand this in depth, cyclic voltammetry was performed on electrodes of VN at different loadings. Cyclic voltammetry (CV) tests were performed on a Princeton Applied Research (PAR) Versastat-3 potentiostat at a number of scan rates varying from 2 mV/s to 200 mV/s over suitable voltage windows to evaluate gravimetric and areal capacitance and rate dependence of the same in the doped nitrides of VN. The voltage window in the aqueous electrolyte was selected on the basis of its pH(~14) which affects the electrode potential of electrolyte breakdown as detailed by the Pourbaix diagram[269, 337]. In addition to rate dependence of the capacitance, cycling stability was evaluated in the above-stated electrolytes by performing repeated CV cycling over 500 cycles.

Binder-free electrodes made by chemical vapor deposition were used as is for electrochemical evaluation of the oxide and doped oxide thin films and carbon nanotube composite electrodes. Since the gravimetric capacitance of various materials was used a barometer for performance, weights of electrodes were meticulously recorded at various stages of preparation using a high precision 6-digit balance (Denver Instruments, Inc.) The supercapacitance behavior of the oxide materials was evaluated in 1 M Na_2SO_4 using a platinum counter electrode, Ag/AgCl (in 3M KCl) reference electrode, and the active material coated Ni disks described above as the working electrode. Cyclic voltammetry tests were performed on a Princeton Applied Research Versastat 3 potentiostat in the voltage window of interest [VN: -1.2 V to 0 V (with respect to Hg/HgO (1M KOH)); VO_x: -1 to 0.8 V (with respect to Ag/AgCl (in 3M KCl))] to evaluate the specific capacitance of the active materials. Cycling was performed at different rates and the area of the cyclic voltammogram was used to calculate the capacitance. The capacitance was calculated using the formula:

Capacitance C (in F/g) = $\frac{\int I\, dV}{s*2*V*m}$ Equation (i)

where

$\int I\, dV$ = Area of the cyclic voltammogram

s= scan rate in V/s

V= voltage window

m= Mass of active material in grams

3.3.1.1 Electrochemical impedance analysis

To further evaluate the nature of the VN as a supercapacitor and compare the electrochemical performance of the various undoped and doped compositions of VN, electrochemical impedance spectroscopy (EIS) was performed in the three-electrode cell configuration reported in **Section 3.3**. Electrochemical impedance spectroscopy is a versatile technique which can be used to quantify charge transfer parameters in electrochemical systems. Electrochemical impedance spectroscopy (EIS) was also performed on the Versastat 3 over a frequency range of 0.01Hz-100KHz. A.C. amplitude of 5 mV was used and the spectra were obtained between 0 and -1.2 V at potentials where Faradaic reactions were predominant. The aim of the study of impedance spectra will be to study individual mechanisms and identify differences in mechanisms between various nitride materials. Randall circuit fitting was performed using ZView-2 (Scribner Associates, Inc.) software to derive charge transfer parameters from the EIS data. Since loading is an important characteristic affecting charge storage in chemically derived VN, the effect of loading on charge transfer parameters in chemically derived VN was also analyzed by

performing EIS. Z-View (Scribner Associates, Inc.; version 3.3) was used for Randall's equivalent circuit modeling of the impedance spectra.

Two primary mechanisms of capacitive charge storage described by Conway *et. al.* will be used to the Randall's equivalent circuit modeling[58] namely, the under-potential deposition (UPD) and the over-potential deposition (OPD). The under-potential deposition mechanism (UPD) involves charge storage by the classical double layer mechanism along with mono-layer adsorption occurring at the electrode surface. Over-potential deposition (OPD) on the other hand, involves redox reactions occurring over and above the monolayer of adsorbed ions at the surface. This process is also the precursor to gas evolution on the particular electrode, also commonly referred to as the onset potential of electrolysis in aqueous electrolyte systems.

To further evaluate the supercapacitor response of the CVD-deposited doped vanadium oxide thin films, doped vanadium oxide-VACNT heterostructures, electrochemical impedance spectroscopy was performed on the Applied Research (PAR) Versastat 3 over a frequency range of 0.1Hz-100 KHz. A 5 mV amplitude was used and the spectra were collected between -1.0 and 0.8 V at the specific voltages where Faradaic reactions were observed to be predominant. The impedance spectra were obtained on the undoped and titanium doped vanadium oxide thin film and the doped and undoped VACNT-vanadium oxide composite heterostructure hybrid electrodes to observe any noticeable changes in charge storage mechanism induced by the presence of carbon nanotubes. The ZView-2 (Scribner Associates, Inc.) software was used for theoretical modeling and fitting using the Randall's equivalent circuit models, and the charge transfer parameters corresponding to the CVD synthesized vanadium oxide-VACNT nanostructures were obtained and correspondingly compared to the oxide thin film to understand the effect of VACNTs and doping on the performance vanadium oxide.

4.0 RESULTS AND DISCUSSION

4.1 VANADIUM NITRIDE CAPACITORS

4.1.1 Materials properties

4.1.1.1 Chemically derived VN and milling of commercial VN

Figure 19 shows the X-ray diffraction patterns of VN prepared by the two-step ammonolysis. It can be observed that the X-ray pattern matches very well that of cubic vanadium nitride and that of commercially obtained vanadium nitride (STREM, Goodfellow, 99.5% V). The effect of milling the commercial VN is also seen in the diffraction patterns in **Figure 19**. It can be observed that the peak breadth increases with increasing milling time indicating a possible decrease in crystallite size. The effective crystallite size of the various samples of vanadium nitride calculated using the Scherrer formula, from the integral breadth of the Lorentzian contribution determined from the peak profile analysis using the single line approximation method after eliminating the instrumental broadening and lattice strain contribution[335, 336], are seen in **Table 9**. In addition, the lattice parameter and molar volume of the various nitride samples in **Figure 19** was calculated using the least square refinement technique and were determined to be between 0.4111-0.4127±0.0027nm and ~10.46-10.58cm^3/mol respectively. It is seen that the lattice parameter is in good agreement with the bulk lattice parameter of cubic VN

of 0.4105-0.414 nm[338, 339]. The multi-point BET surface area and four-probe electronic conductivity of the samples are also shown therein. It is observed that there is a marked change and reduction in crystallite size from 200 nm to 24 nm upon milling the commercially procured vanadium nitride. The 10 h milled sample of commercial VN has a crystallite size of ~24 nm which approaches that of the VN prepared by the two-step ammonlysis method. Further milling did not however yield any significant crystallite size reduction or surface area increase. The trends in electronic conductivity parallel those of the crystallite size and surface area (**Table 9**) which is to be expected since smaller grains would result in increased grain boundary domains thereby resulting in a decrease in electron conduction and hence increased electrical resistivities.

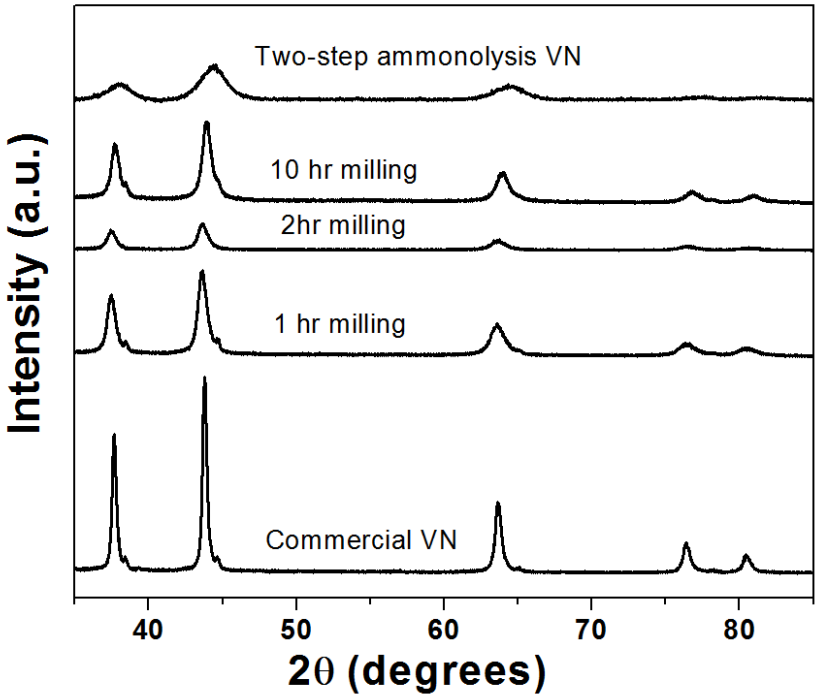

Figure 19.X-ray diffraction patterns obtained on as-procured commercial VN, commercial VN milled for varying amounts of time and chemically synthesized VN.

Table 9. Comparison of powder properties of different vanadium nitride materials.

Material	Crystallite size (nm)	BET surface area (m^2/g)	Composition	Oxide layer thickness (nm)	Electronic conductivity (S/cm)
As procured commercial VN	178.6	0.8	$VN_{0.77}O_{0.23}$	32.4	120
Commercial VN-1 h milling	40.2	4.8			
Commercial VN-2 h milling	34.1	4.5			
Commercial VN-10 h milling	23.8	7.0	$VN_{0.71}O_{0.29}$	11.5	96.2
VN: Two-step ammonolysis	4.10	28.8	$VN_{0.98}O_{0.36}$	1.2	81.8

Since the structures of vanadium nitride (VN) and vanadium monoxide (VO) are almost identical, the oxygen and nitrogen content in the VN prepared by ammonolysis, commercial VN and 10 h milled commercial VN were measured using inert gas fusion analysis (LECO analysis, Alternative Testing Laboratories, Inc.) and are shown in **Table 9**. The composition of the commercial VN is almost identical before milling and after 10 h of milling indicating that the primary change occurring as a result of the milling process is morphological rather than compositional. Both the ammonlysis based VN and the commercial VN have a small amount of oxygen (usually present at the surface in nitride and sulfide materials). The thickness of the oxide

layer calculated using Equation (ii) is also seen in **Table 9**. The amount of oxygen present in all three nitride materials is small enough to account for a thin surface layer.

$$\frac{r_{VO_x}}{r_{VN}} = \left(1 + \frac{n_{VO_x} M_{VO_x} \rho_{VN}}{n_{VN} M_{VN} \rho_{VO_x}}\right)^{1/3} - 1 \qquad \text{Equation (ii)}$$

wherein

r_{VO_x}= Radius of the oxide shell in nm

r_{VN}= Radius of the nitride core in nm

n_{VO_x}= Mole percentage of oxide

n_{VN}= Mole percentage of nitride

M_{VO_x}= Molecular weight of the oxide in g/mol

M_{VN}= Molecular weight of the nitride in g/mol

ρ_{VO_x}= Density of the oxide in g/cm^3

ρ_{VN}= Density of the nitride in g/cm^3

The morphological evolution of the commercial VN upon milling is observed in **Figure 20a-Figure 20c**. A distinct reduction in particle size is visible between the as-obtained commercial VN, 2 h milled VN and 10 h milled VN corroborating the trends in surface area and

crystallite size observed in **Table 9**. The particle size of the 10 h milled VN as mentioned above, approaches that of VN prepared by the two-step ammonlysis procedure as seen in **Table 9.**

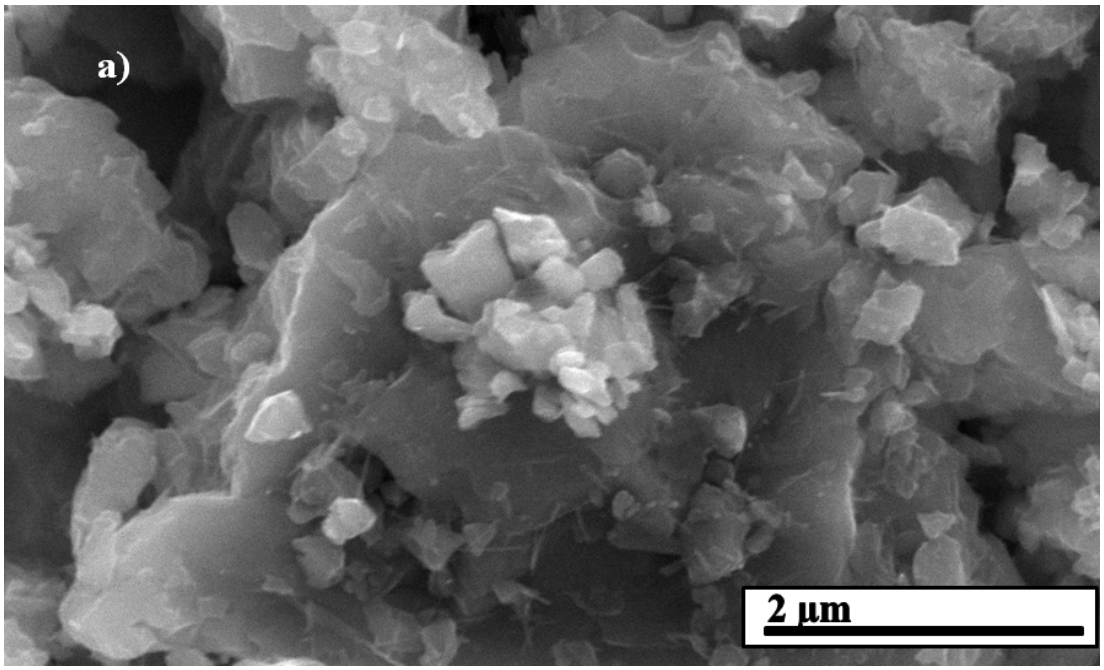

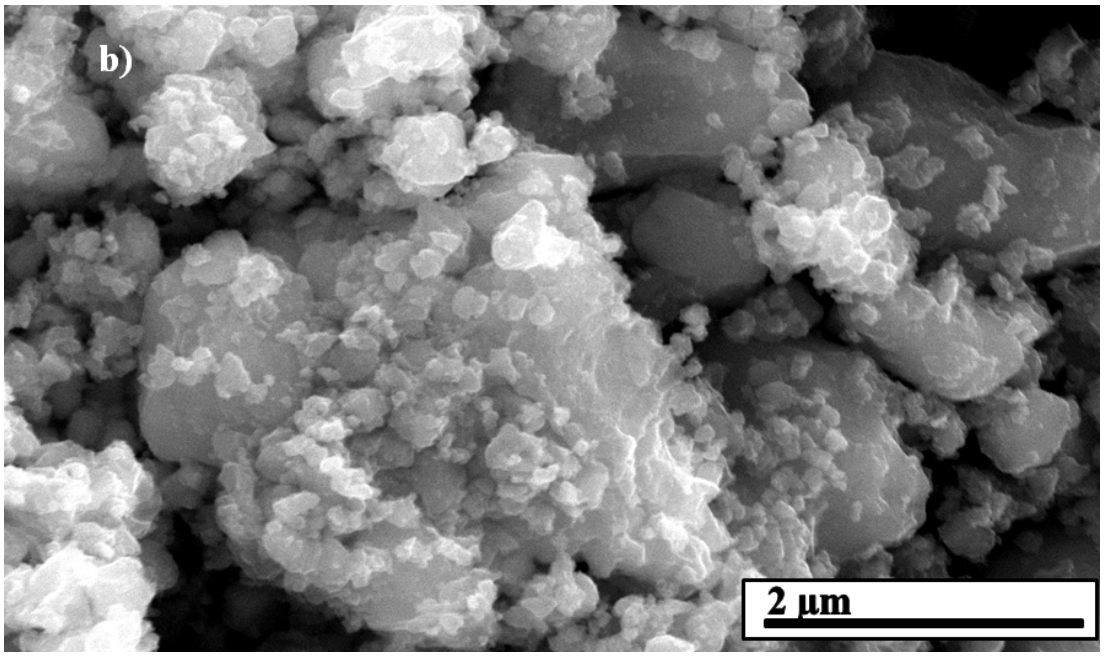

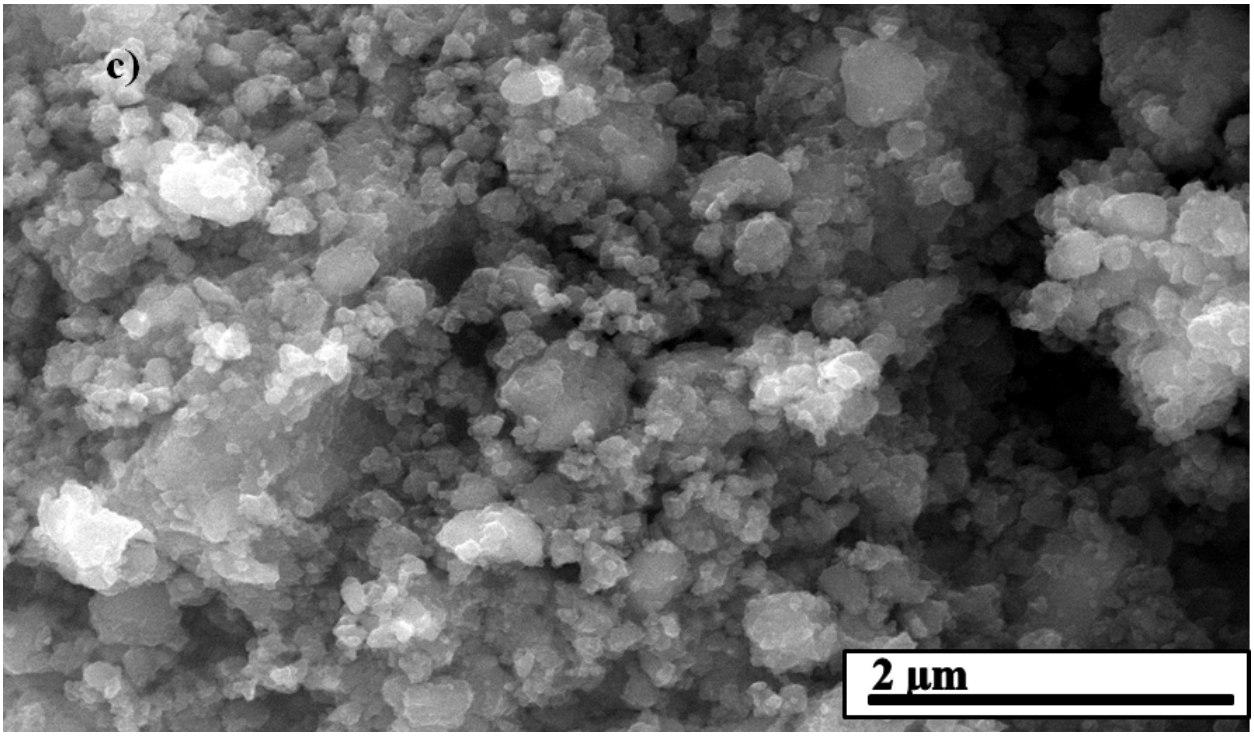

Figure 20. Scanning electron micrographs of (a) As procured commercial VN (b) Commercial VN milled for 2 h (c) Commercial VN milled for 10 h.

TEM analysis was used to draw further inferences about possible change in morphology on account of the aggregated nature of the particles which limited proper analysis based on SEM alone. The TEM bright field image of the various vanadium nitride materials is shown in **Figure 21a-Figure 21d**. Commercial VN (**Figure 21a**) consists of large nanoparticles of ~400 nm which get progressively reduced in size upon milling as expectedd (**Figure 21b** and **Figure 21c**) to form fine 40-50 nm particles after 10 h of milling. The high resolution TEM images of the three VN samples shows lattice fringes with a spacing of ~0.24 ±0.002 nm (PDF number: 00-035-0768) which corresponds to the (111) interplanar spacing of the face centered cubic VN and ~0.206±0.002 (PDF number: 00-035-0768), 0.214±0.002 (PDF number: 00-035-0136) corresponding to those of (002) planes of VN. The effect of milling upon both particle size and

crystallinity is distinctly observed. While the unmilled sample contains uniform crystalline domains, both the 2 h and 10 h milled samples contain a mixture of amorphous and crystalline domains and a distribution in particle size. This is to be expected given the mechanical milling and the resulting comminution induced by the continuous impingement and collision of the milling media with the reacting precursors due to the nature of the milling process. The amorphous domains might also correspond to the inherent oxide coating formed on the crystalline nitride material by virtue of the size reduction induced by the mechanical milling reaction. **Figure 21d** shows the fine nanoparticulate nature (~5 nm) of the VN synthesized by the two-step ammonlysis procedure resembling the morphology reported previously[182, 235, 238]. The particles aggregate into large clusters as seen in the low magnification image. The particle sizes of the various materials seen in **Figure 21a-Figure 21d** match closely to the values calculated from the X-ray diffraction data using the well known Scherrer equation (**Table 9**).

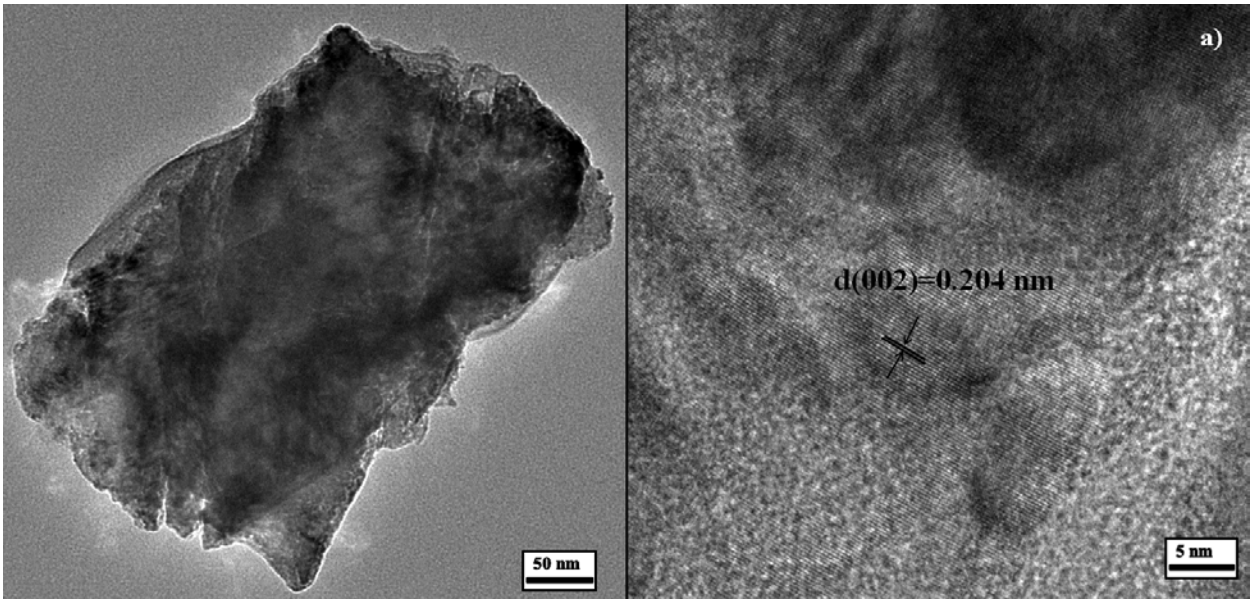

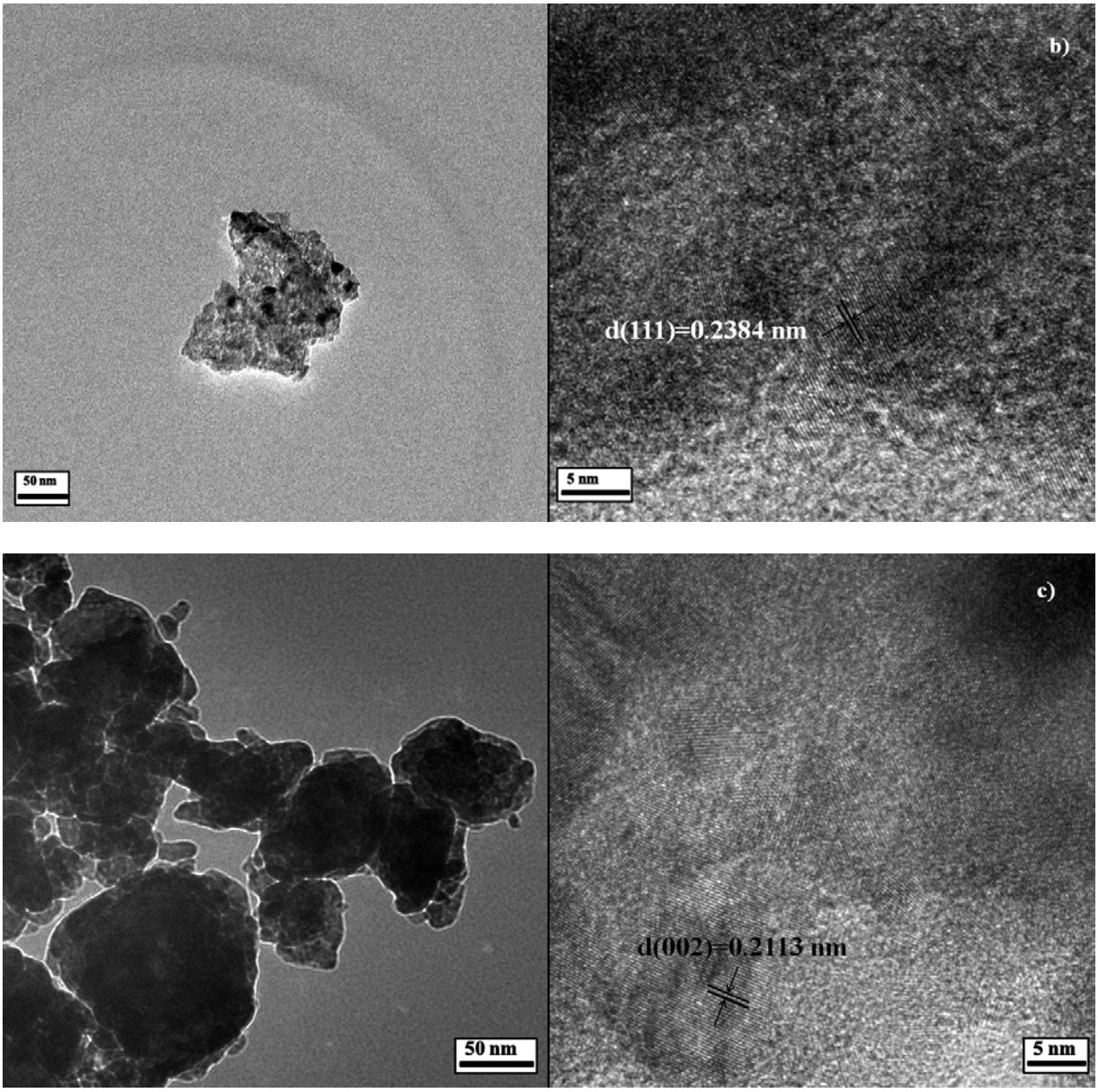
50 nm
b)
d(111)=0.2384 nm
5 nm
50 nm
c)
d(002)=0.2113 nm
5 nm

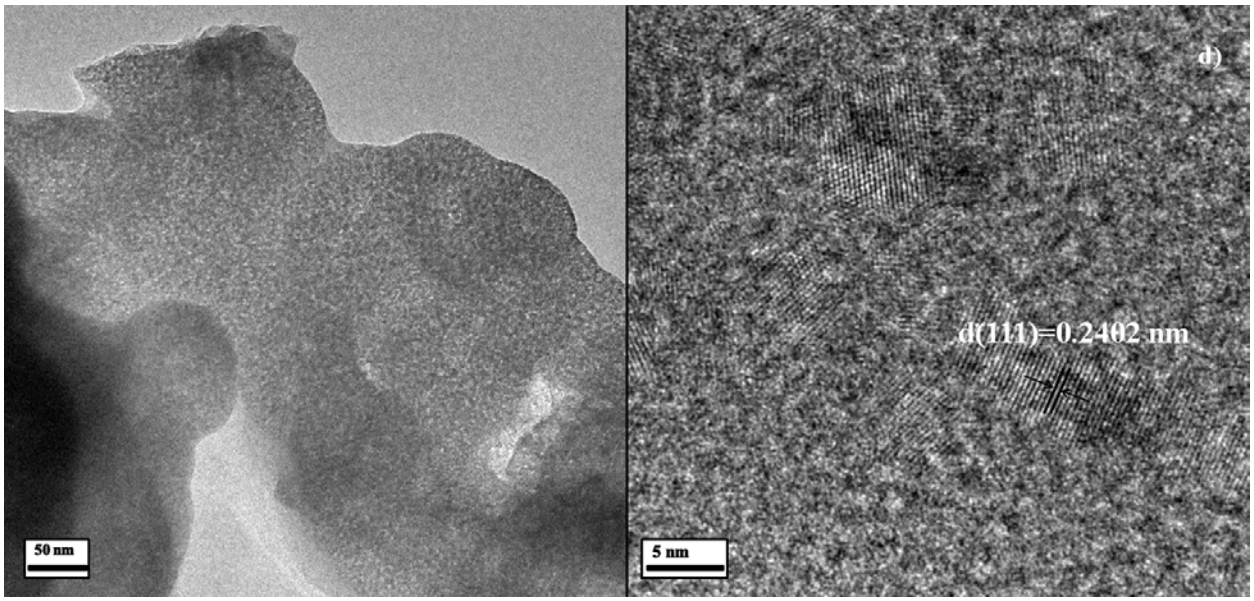

Figure 21. Transmission electron micrographs of (a) As procured commercial VN (b) Commercial VN milled for 2 h (c) Commercial VN milled for 10 h (d) VN prepared by the two-step ammonolysis method.

Figure 22a shows the cyclic voltammogram (CV) of VN prepared by the two-step ammonlysis method, the commercial VN and 10-h milled commercial VN in 1M KOH over a voltage window of -1.2 V to 0 V (50 mV/s) with respect to Hg/HgO (in 1M KOH). Both double layer and pseudocapacitor type response are exhibited in the CV of the various samples. It can be seen that the various VN materials exhibit reversible Faradaic reactions of the surface oxide corresponding to a change in oxidation state of vanadium[182, 235, 246, 337, 340-342]. The Faradaic reactions are more pronounced on the ammonlysis derived VN on account of the higher surface area resulting in increased surface oxide contact with the electrolyte. **Figure 22b** shows the cyclic voltammograms of VN derived by two-step ammonolysis at various scan rates varying from 200 mV/s to 2 mV/s (at an active material loading of 0.1 mg/cm^2). It can be seen that the behavior changes from almost square-like behavior to a more distorted parallelogram as scan rate increases. The specific capacitance of the VN synthesized using the different approaches was

calculated at various scan rates using Equation (i). One artifact that sometimes leads to overestimation of capacitance calculated from integration of cyclic voltammograms is the asymmetry of the curve with respect to the horizontal axis. The cyclic voltammograms seen in **Figure 22a** though appearing asymmetric in-fact have an almost identical area on either side of the current axis indicating that the capacitance calculated by the integration of the C-V curve is not overestimated. **Figure 22c** plots the peak current density (ip, A/g) of the CVs seen in **Figure 22b** against the scan rate(s, mV/s). For capacitor material, the slope of log (ip) exhibits a linear dependence on log(s)[54, 343]. As seen in **Figure 22c**, the VN material prepared by the two-step ammonlysis exhibits a linear relationship with a good R^2 value and slope of 0.98 indicating that the material is indeed a capacitor material.

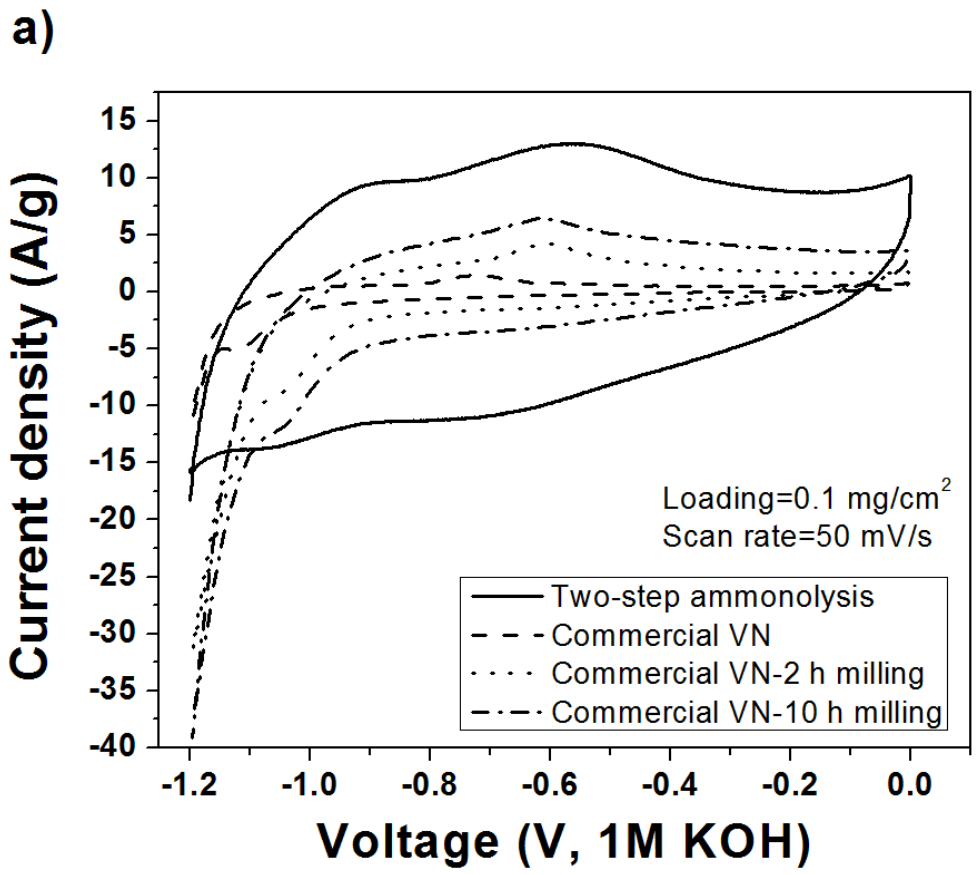

b)

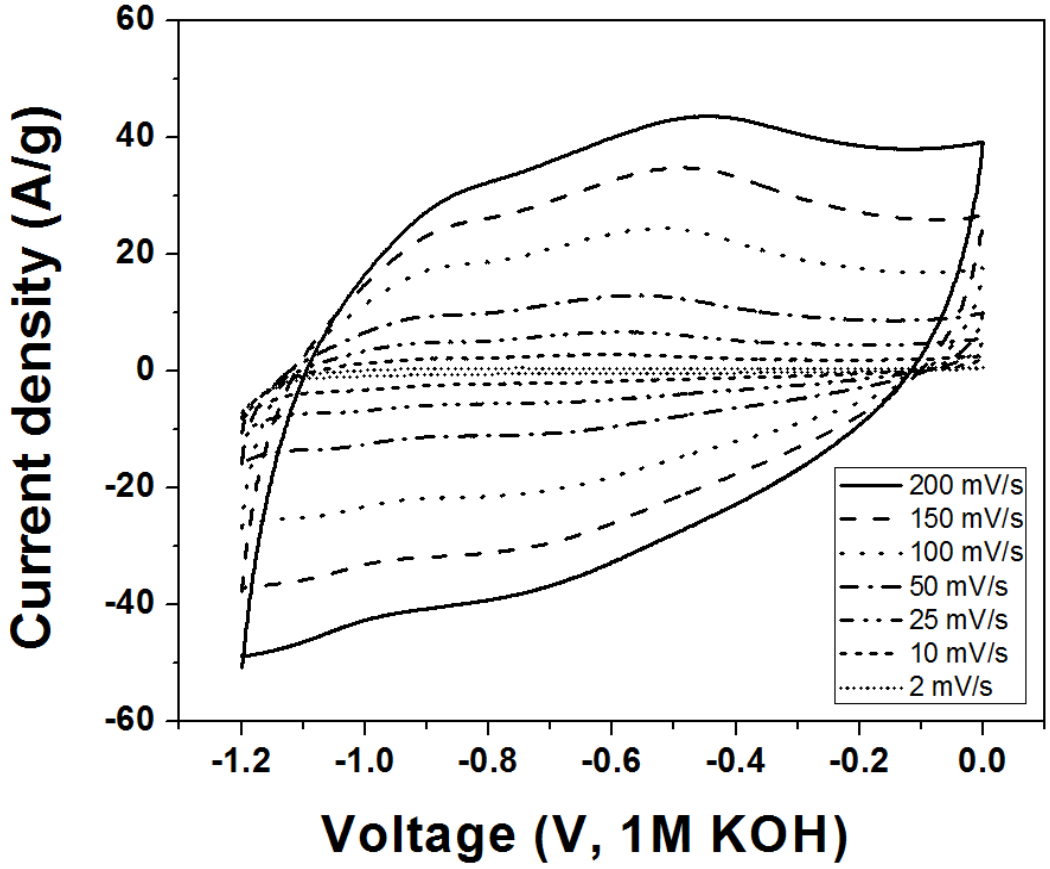
60
40
20
0
-20
-40
-60
-1.2
-1.0
-0.8
-0.6
-0.4
-0.2
0.0
Current density (A/g)
Voltage (V, 1M KOH)
200 mV/s
150 mV/s
100 mV/s
50 mV/s
25 mV/s
10 mV/s
2 mV/s

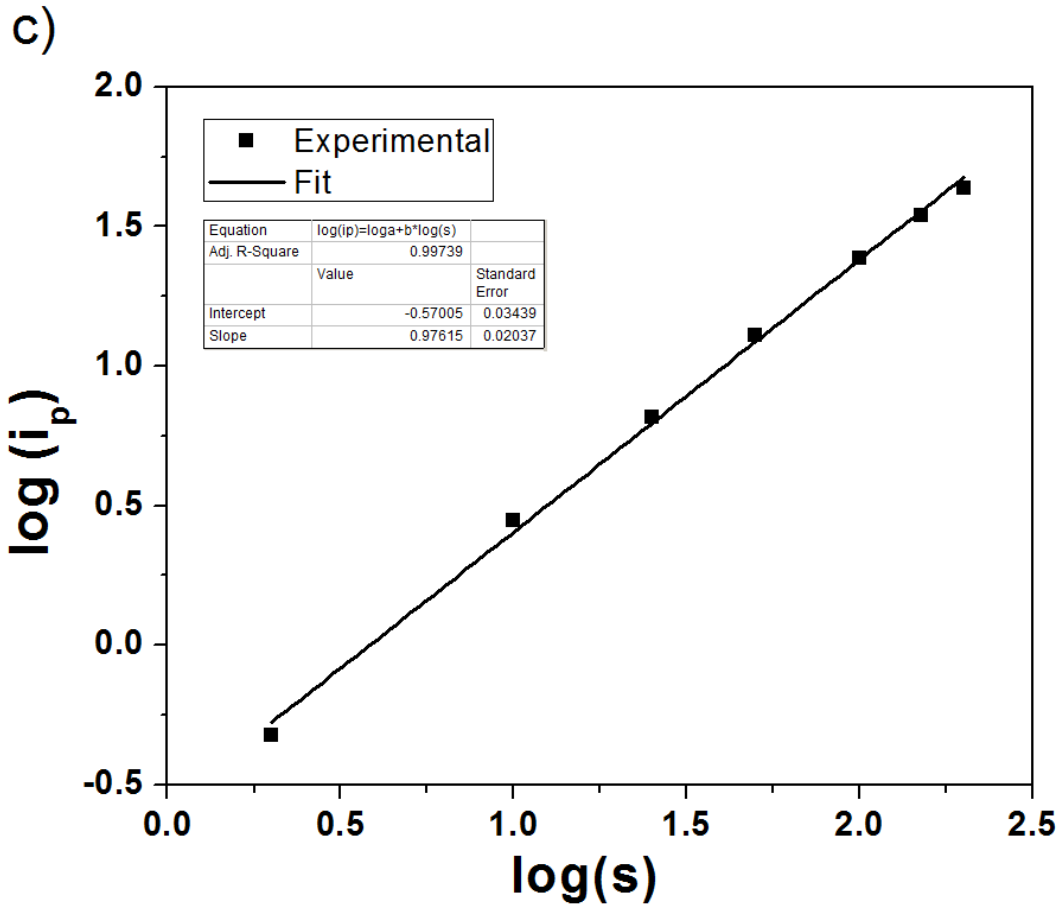

Figure 22. (a) Cyclic voltammograms of the various VN materials in 1M KOH over a voltage window of -1.2 V to 0 V with respect to Hg/HgO (in 1M KOH) (active material loading ~ 0.1 mg/cm^2; scan rate=50 mV/s) (b) Cyclic voltammogram of VN derived by two-step ammonolysis at various scan rates varying from 200 mV/s to 2 mV/s (active material loading ~ 0.1 mg/cm^2) (c) Dependence of peak current on scan rate indicating that the VN derived by two-step ammonlysis behaves like a capacitor-type charge storage material rather than a battery-type material.

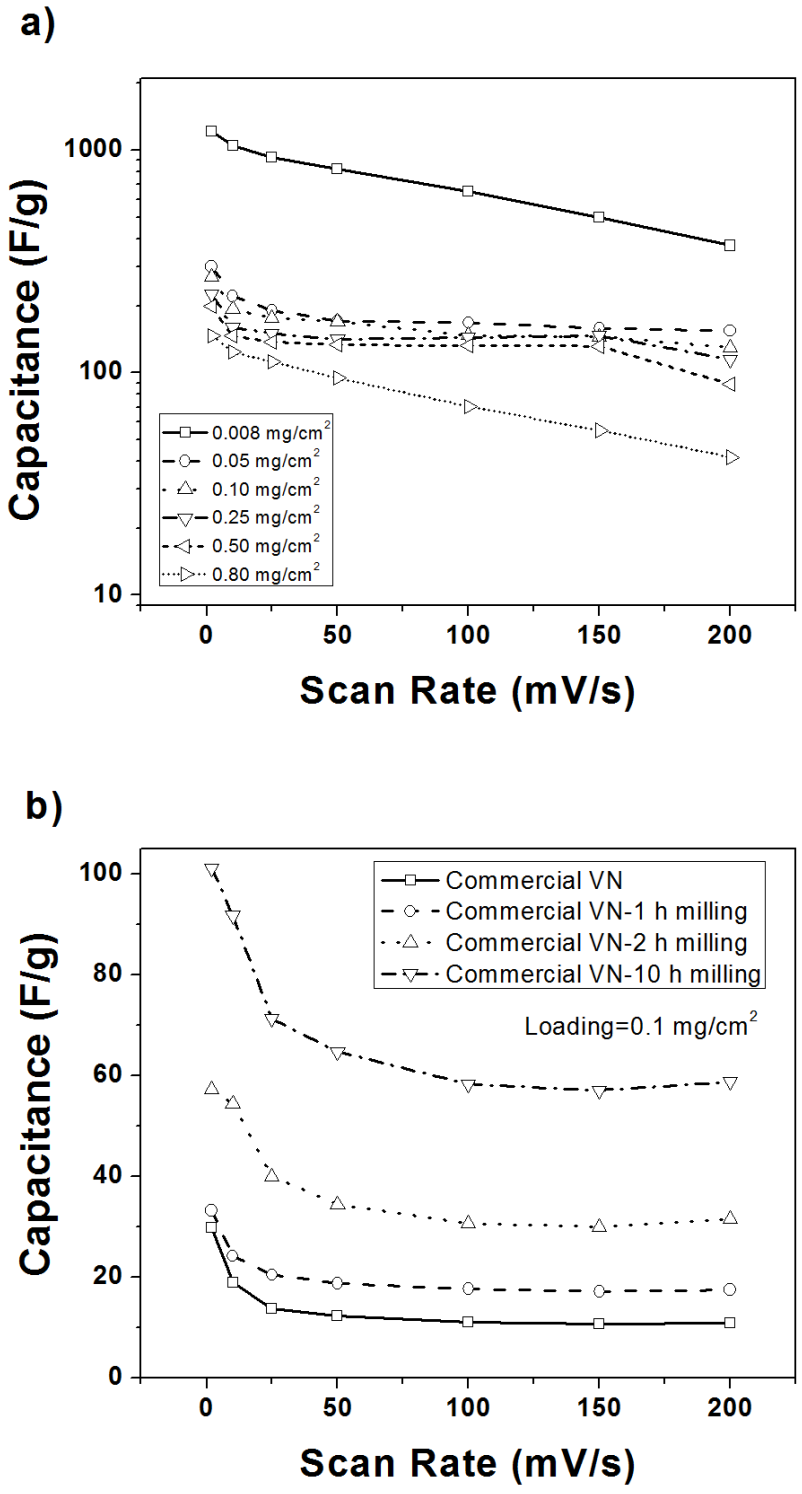

Figure 23. (a) Loading and scan rate dependence of capacitor charge storage in two-step ammonlysis derived VN (b) Effect of milling on capacitance of commercial VN (active material loading ~ 0.1 mg/cm^2).

Figure 23a shows the dependence of capacitance of the ammonlysis derived VN on both scan rate and active material loading. It can be clearly observed that the capacitance of VN decreases with increasing scan rate as a result of either the reaction kinetics of the pseudocapacitance reactions becoming rate-limited[58] or the electronic conductivity of the very fine nanoparticles acting as a barrier to increased charge storage at higher rates. The effect of the poor electronic conductivity on the charge storage behavior of the ammonlysis derived VN is also visible in the pronounced loading dependence of capacitance. It can be seen that very high capacitances of ~1200 F/g are observed at very low loadings of vanadium nitride indicating that the material is indeed capable of such high capacitive charge storage though it cannot retain the same at higher loadings on account of poor electronic conductivity of the fine nanoparticles as outlined earlier and reflected in **Table 9**. **Figure 23b** shows the effect of milling on capacitance of commercial VN at a particular loading. The rise in capacitance with increasing milling time is to be expected given the trend in surface area and crystallite size reduction tabulated in **Table 9**. Such a rise is characteristic of a surface charge storage phenomenon either as double layer charge storage or as surface oxide pseudocapacitance. It is clear from **Figure 23a** and **Figure 23b** and previous reports on vanadium nitride[246] that loading dependence of capacitance is very material specific and is dependent on the materials properties docmented in **Table 9**. In order to further understand the dependence of capacitance on loading and to understand mechanistic factors leading to the same, electrochemical impedance analysis was performed on VN electrodes (two-step ammonlysis VN) of different loadings. The dependence of charge storage on particle and electrode properties is further discussed in **Sections 4.1.3-4.1.4**.

The cycling characteristics of two-step ammonlysis derived VN is displayed in **Figure 24**. It can be observed that there is a rapid fade in capacity over 30 cycles following which the

capacity becomes stable. This fade in capacity we believe is the result of change of surface oxidation state i.e. instability of higher oxidation state vanadium in the very highly basic 1M KOH electrolyte[182, 235, 246]. These three reactions correspond to the transformation of vanadium from a +5 oxidation state to a ~+2 oxidation state. The effect of surface composition on charge storage and fade characteristics is further discussed in **Section 4.1.3**.

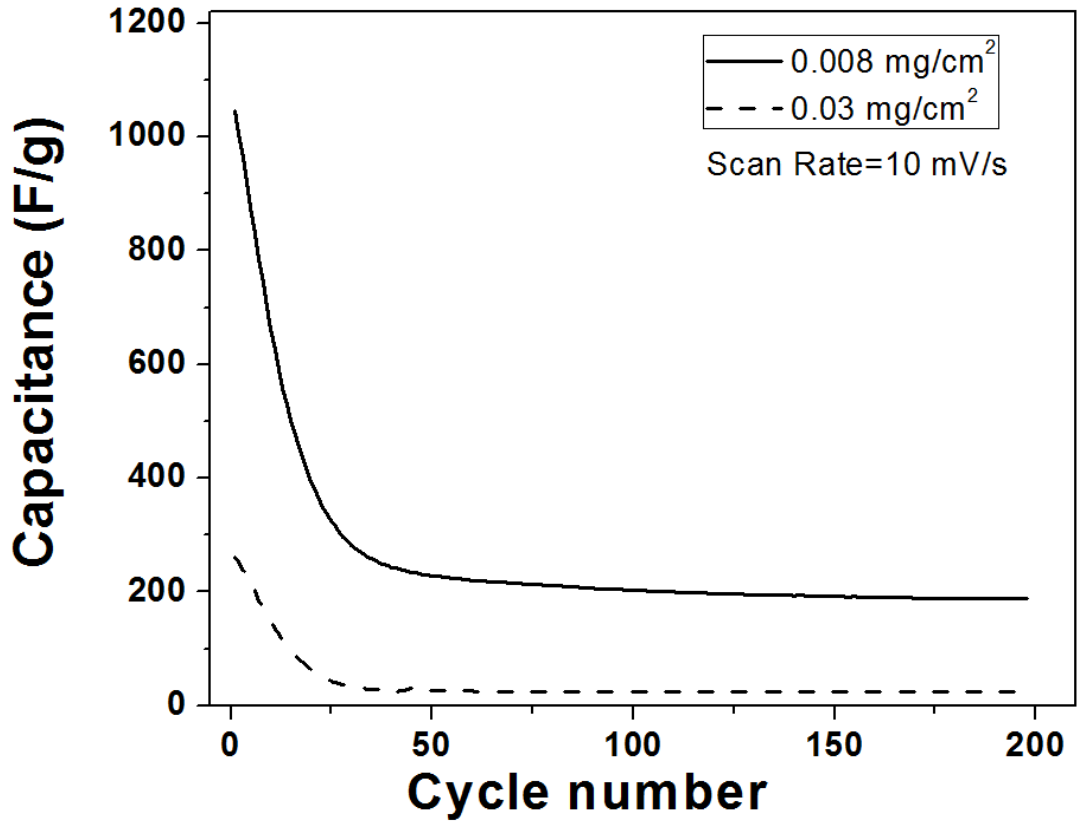

Figure 24. Cycling data for two different loadings of the chemically derived VN when the electrode is cycled between -1.2 and 0 V with respect to Hg/HgO (in 1M KOH) clearly shows rapid fade of capacity.

Figure 25 shows the area normalized capacitance of the various vanadium nitride materials on the basis of electrode area. It can be seen that both the areal capacitance of the ammonlysis derived nitride is comparable to those reported for other capacitor materials on account of the high capacity of the VN as seen in **Figure 23a**[267, 344]. Though the gravimetric capacitance of ammonlysis derived VN drops with increase in loading the areal capacitance is comparable to that of other hitherto reported state-of-the-art capacitor materials such as ruthenium oxide[344]. The nitride material however does not exhibit areal capacitances as high as highly active ruthenium oxide supercapacitors (12-30 mF/cm^2)[345, 346] but is still commercially viable on account of its relatively low cost as compared to ruthenium oxide (~4.98 $/gm as compared to ~10$/gm).

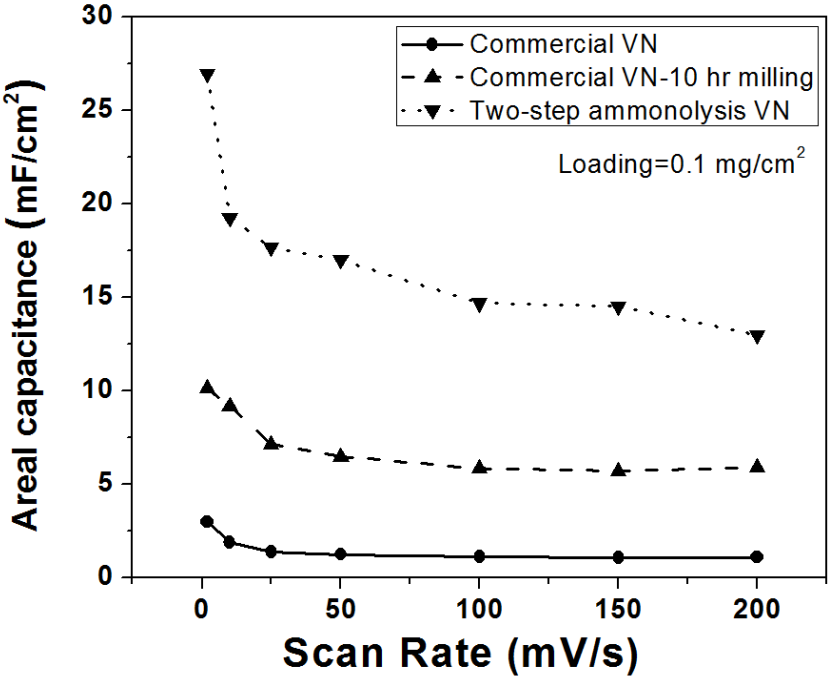

Figure 25. Area normalized capacitance of the various vanadium nitride materials.

4.1.1.2 Mechano-chemically derived VN

The XRD pattern obtained after 3h of high energy milling of Li_3N and V_2O_3 is shown in **Figure 26a**. It can be seen that the X-ray pattern consists of peaks corresponding to those of vanadium nitride, lithium oxide and an unidentified phase. Formation of VN and Li_2O as the by product has been identified which is expected to arise due to the solid state reaction between Li_3N and V_2O_3 yielding VN and Li_2O according to the following reaction,

$$2Li_3N + V_2O_3 \rightarrow 3Li_2O + 2VN \qquad \text{ii)}$$

However, in addition to the above stated peaks, a third phase is seen to occur in the X-ray which is unidentified indicating that a unknown side-reaction occurs as a result of the milling process. In order to remove the undesired by-products from the mechanically milled powder, the as-prepared powder was washed in DI water at 40^oC. The XRD pattern of the washed powder, displayed in **Figure 26b**, shows all the peaks corresponding to single phase face centered cubic (fcc) VN which suggest complete removal of Li_2O from the resulting mixture of VN+Li_2O after washing. A number of peaks in **Figure 26a** are unidentified but are water soluble and are absent in the washed sample (**Figure 26b**).

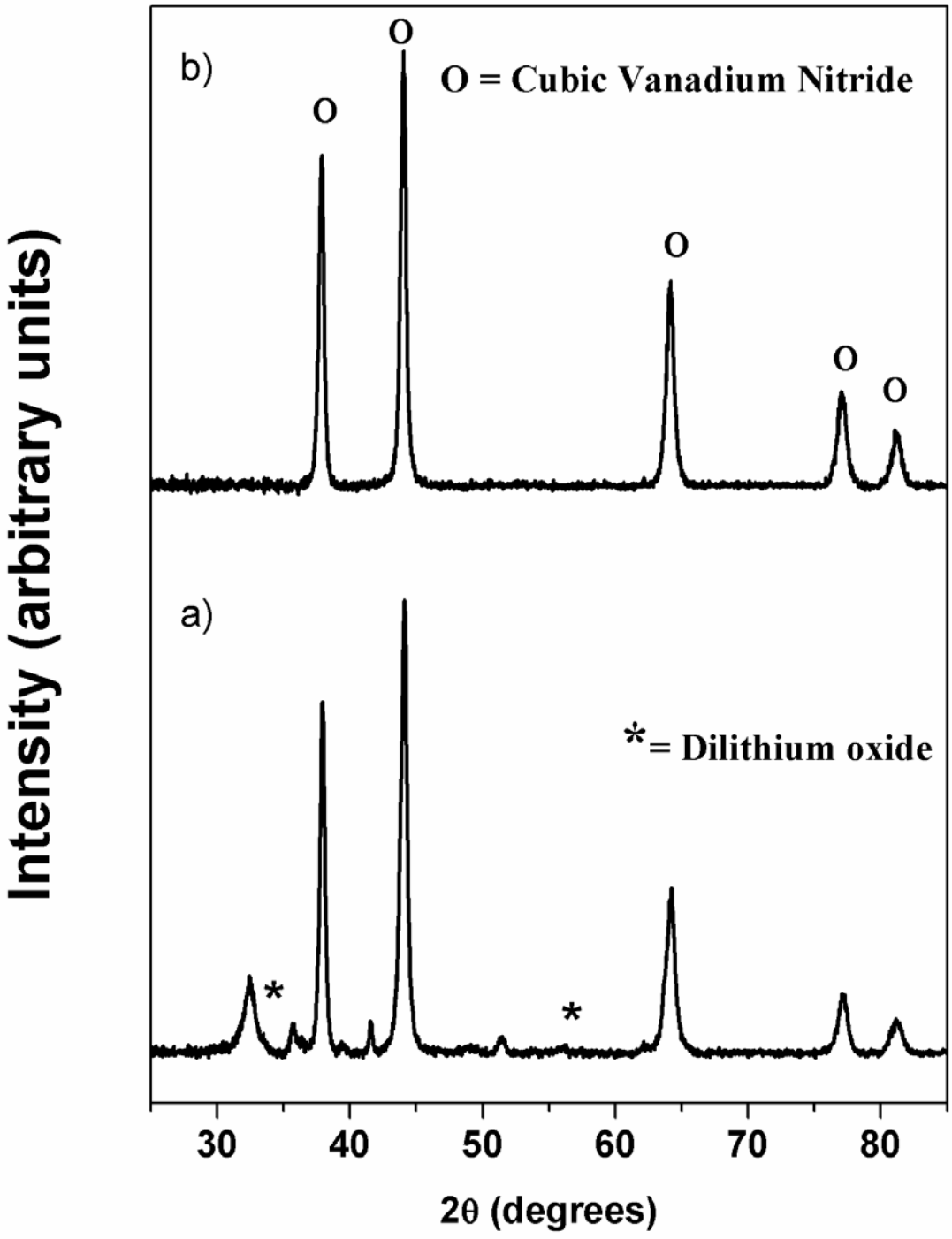
b)
O = Cubic Vanadium Nitride
O
O
O
O
O
a)
*= Dilithium oxide
*
*
Intensity (arbitrary units)
30
40
50
60
70
80
2θ (degrees)

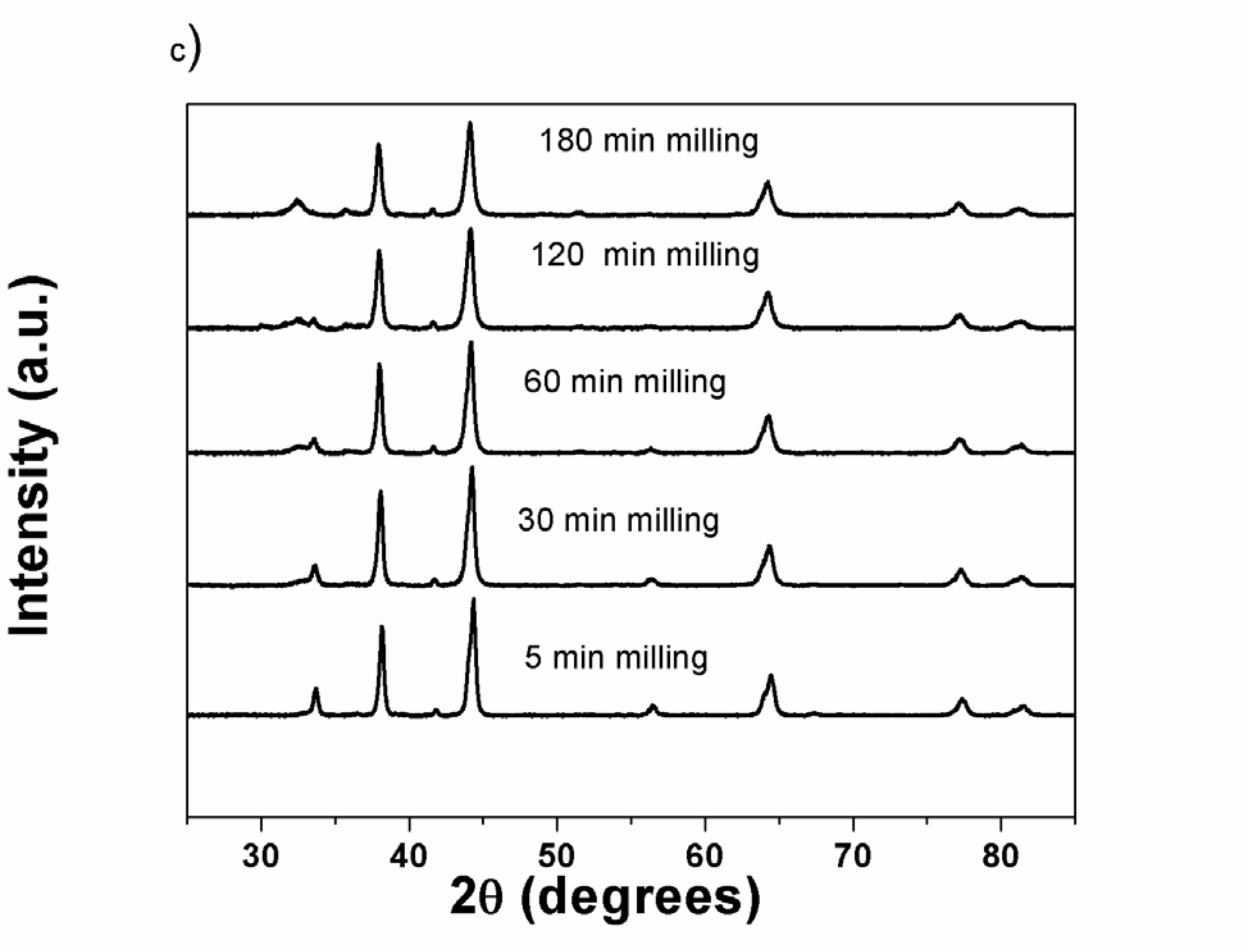

Figure 26. X Ray diffraction patterns of VN prepared by HEMM taken (a) as-prepared (b) after washing with distilled water at 40^{o}C (c) as-prepared at various milling times ranging from 5 minutes to 180 minutes.

The unidentified peaks do not match those of the initial reactants or oxide phase. A common contaminant in milling based synthesis is iron abraded from the walls of the milling vials. However, no such contaminant was observed in the case of the nitride made by this method. The reaction between the oxide and the lithium nitride was instantaneous. In fact, nitride formation occurs in 5 minutes as shown in **Figure 26c**. Even though it is possible that the phase conversion occurring from the time period of 5-180 minutes might have involved a change from VO to VN, none of the initial oxide precursors and lithium nitride are observed in the 5 min

milled sample. This indicates that the reduction reaction involving the lithium nitride occur rapidly at first and gradually subsequently as indicated by the change in peak width seen in the X-ray patterns in **Figure 26c**. Lithium nitride is a highly flammable air-sensitive material. When trying to recover the sample after milling for 5 minutes no fumes or fire was observed indicating the absence of unreacted lithium nitride. It should be pointed out here that the crystal structures of vanadium nitride (VN) and vanadium monoxide (VO) are almost identical making it difficult to identify when exactly the transition from VO to VN occurs completely. The oxygen and nitrogen content in the VN prepared by mechano-chemical reduction was thus independently analyzed using an inert gas fusion analyzer (LECO analysis, Alternative Testing Laboratories, Inc.). The oxygen content was evaluated to be ~4.83% by weight and the nitrogen content to be 17.2% by weight. The final composition of the nitride formed by mechano-chemical reduction was thus found to be $VN_{0.8}O_{0.2}$. The lattice parameter of the VN obtained after washing of the material milled for 180 minutes seen in Figure 1b, calculated using the least square refinement technique, was found to be ~0.4111±0.0002 nm with a molar volume ~10.46cm^3/mol which is in good agreement with the bulk lattice parameter of cubic VN of 0.4105-0.414 nm [338, 339]. The effective crystallite size of VN, calculated using the Scherrer formula from the integral breadth of the Lorentzian contribution determined from the peak profile analysis using the single line approximation method after eliminating the instrumental broadening and lattice strain contribution[335, 336], is in the range of ~28nm confirming the nano-crystalline nature of the resultant VN obtained following the mechano-chemical reaction. The crystallite size of VN derived by the mechano-chemical reaction is however much larger than that of the nanoparticulate VN (6.33 nm) reported previously generated by the ammonolysis chemical approach[182]. This is also reflected in the specific surface area (SSA), measured by the nitrogen

adsorption-desorption technique and fitted to a BET type isotherm, of the VN synthesized by mechano-chemical reaction (9 m^2/g) which is almost four times lower than the specific surface area (SSA) of the nano-particulate nitride (39 m^2/g) generated by the two step ammonolysis chemical approach.

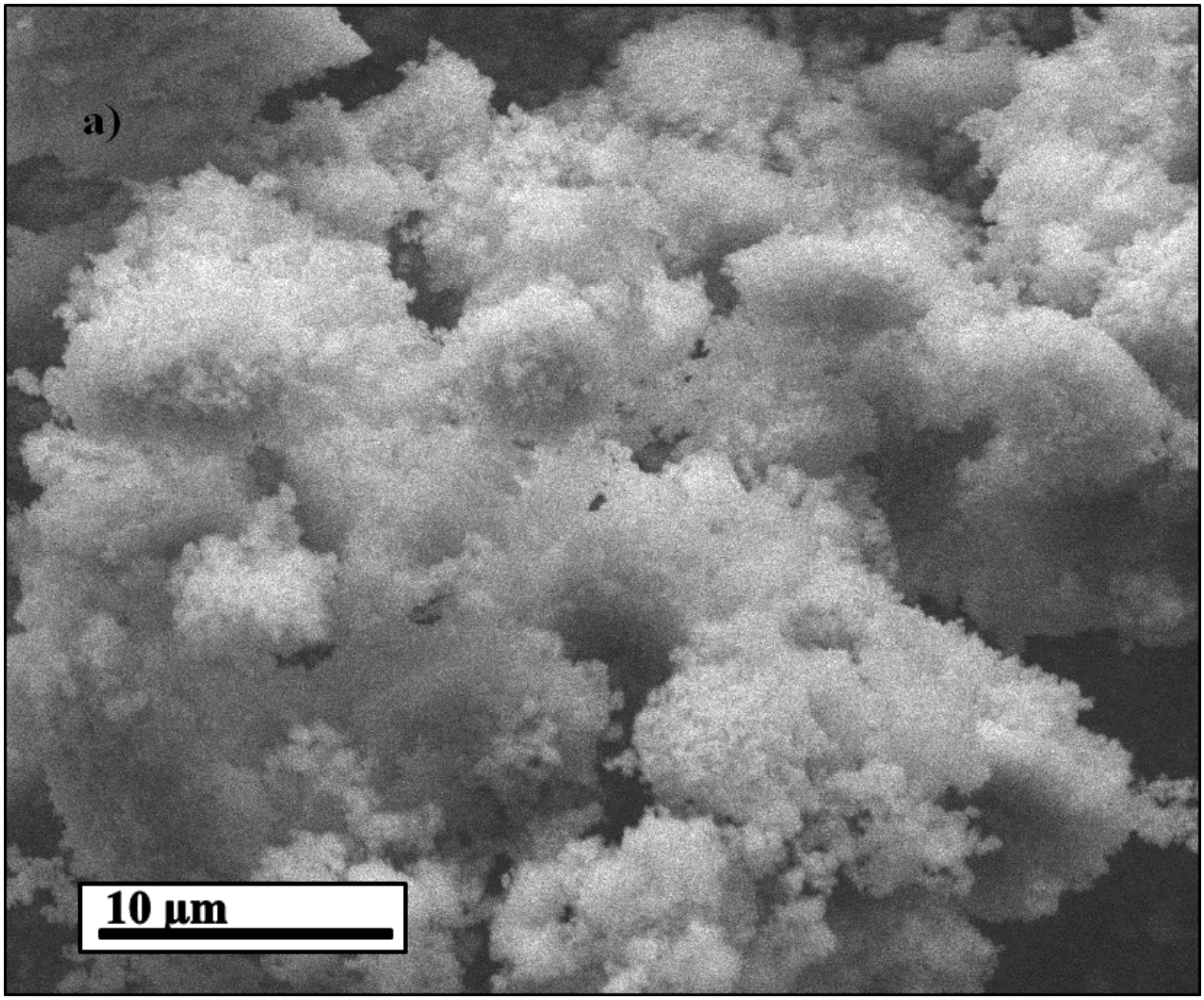

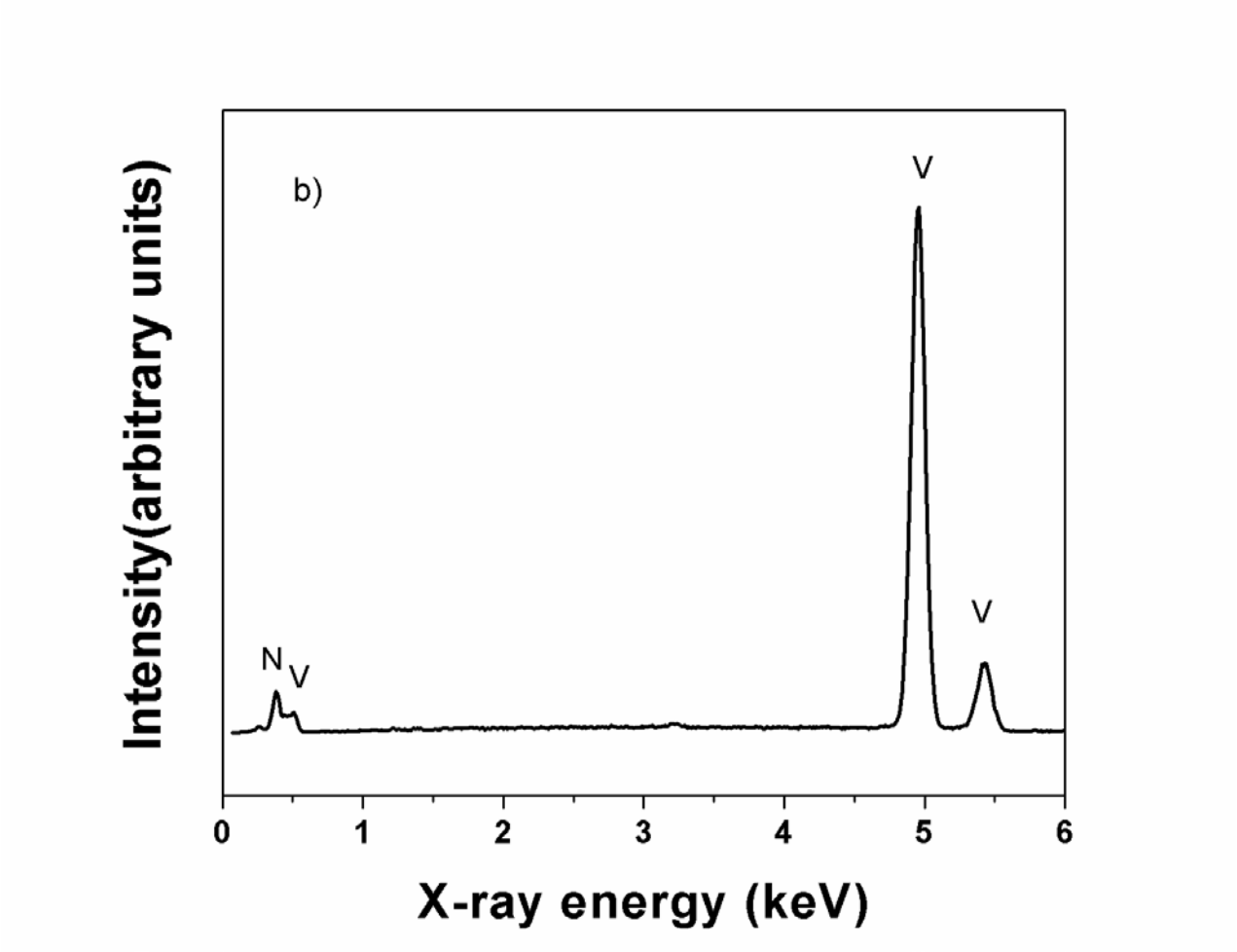

Figure 27. (a) SEM micrographs of milled VN showing flocculated spherical nature of VN particles synthesized by the mechano-chemical reaction of V_2O_3 and Li_3N (b) EDAX spectrum confirming the presence of V and N in the post-wash milled material.

The presence of elemental V and N in the VN particles has been confirmed using energy dispersive x-ray spectroscopy analysis (EDAX) configured to the SEM. The SEM image along with EDAX of VN, shown in **Figure 27a** and **Figure 27b**, respectively, indicates the presence of agglomerates of fine particles with varying morphologies. TEM bright field image and analysis (discussed below) was used to draw further inferences about the morphology on account of the

aggregated nature of the particles. The presence of oxygen in the VN could however not be ascertained by EDAX since the L-edge of vanadium coincides with the peak of K-edge of oxygen. The distinctly visible peaks seen at 386 eV (N-K, L2, L3) and 513 eV (V, L3, M4, M5) have a broad band between them as a result of peaks occurring at 447 eV (V, L3, M1) and 454 eV (V, L2, M1) making deconvolution of the oxygen peaks [525 eV (O K-L2, L3) and 532 eV (O K)] impossible. On account of this overlap, it was not possible to draw conclusions about the oxygen presence from the EDAX data. However, the presence of oxygen was confirmed from the inert gas fusion elemental analysis and X-ray photoelectron spectroscopy (discussed in **Section 4.1.3**). In addition to the conclusion about the presence of vanadium and nitrogen in the final post-wash milled product, the absence of other contaminants can be observed indicating that the washing procedure was effective in removing any other unidentified phases present in **Figure 26a** that could have been introduced during the synthesis and post processing steps. The TEM bright field image along with selected area diffraction (SAD) pattern of VN, shown in **Figure 28a**, confirms the formation of nano-sized VN particles with discrete sizes ranging between 30 and 150 nm and an average particle size of ~ 50nm. The high resolution TEM image of VN (**Figure 28b**) shows lattice fringes with a spacing of ~0.24 ±0 002 nm which corresponds to the (111) interplanar spacing of the face centered cubic VN. The spacing observed between the lattice fringes of (111) plane of VN in the HRTEM image is also in good agreement with the calculated d_{111} value (~0.237nm) from XRD patterns and the planes are well oriented. Considering the particle size to be ~50 nm as indicated by the TEM images seen in **Figure 28a** and assuming the particles to be spherical, the thickness of the oxide layer can be approximated to be ~3.15 nm. Since the lattice constant of vanadium oxide is very similar to that of vanadium nitride, it was not possible to make a distinction between the nitride and the oxide layer in the

TEM image seen in **Figure 28b**. It is also possible that the material synthesized by mechano-chemical reduction has the oxygen atoms distributed throughout the bulk nitride lattice, i.e. an oxy-nitride phase could have resulted instead of a core-shell particle as reported by Choi et al[238].

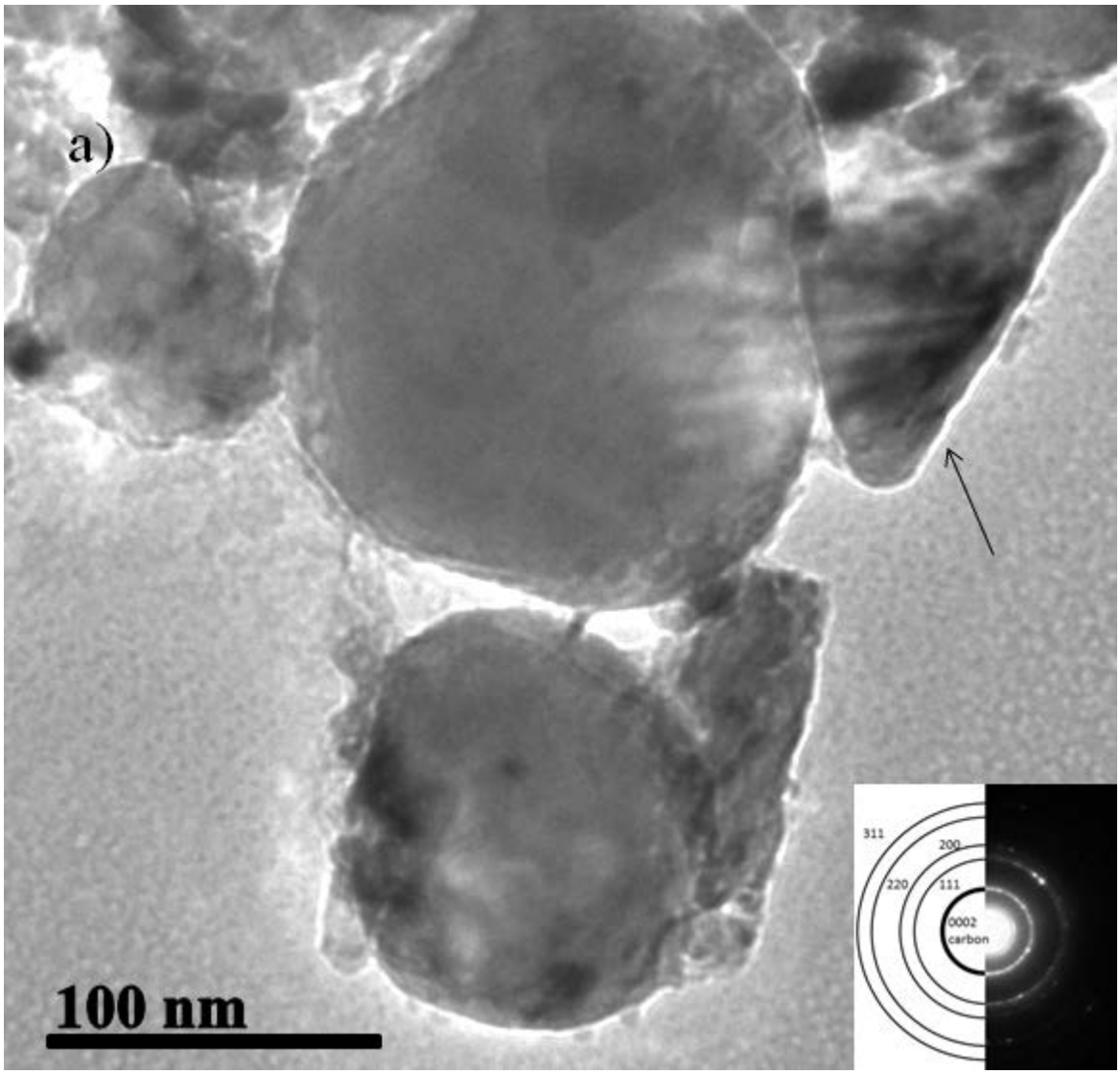

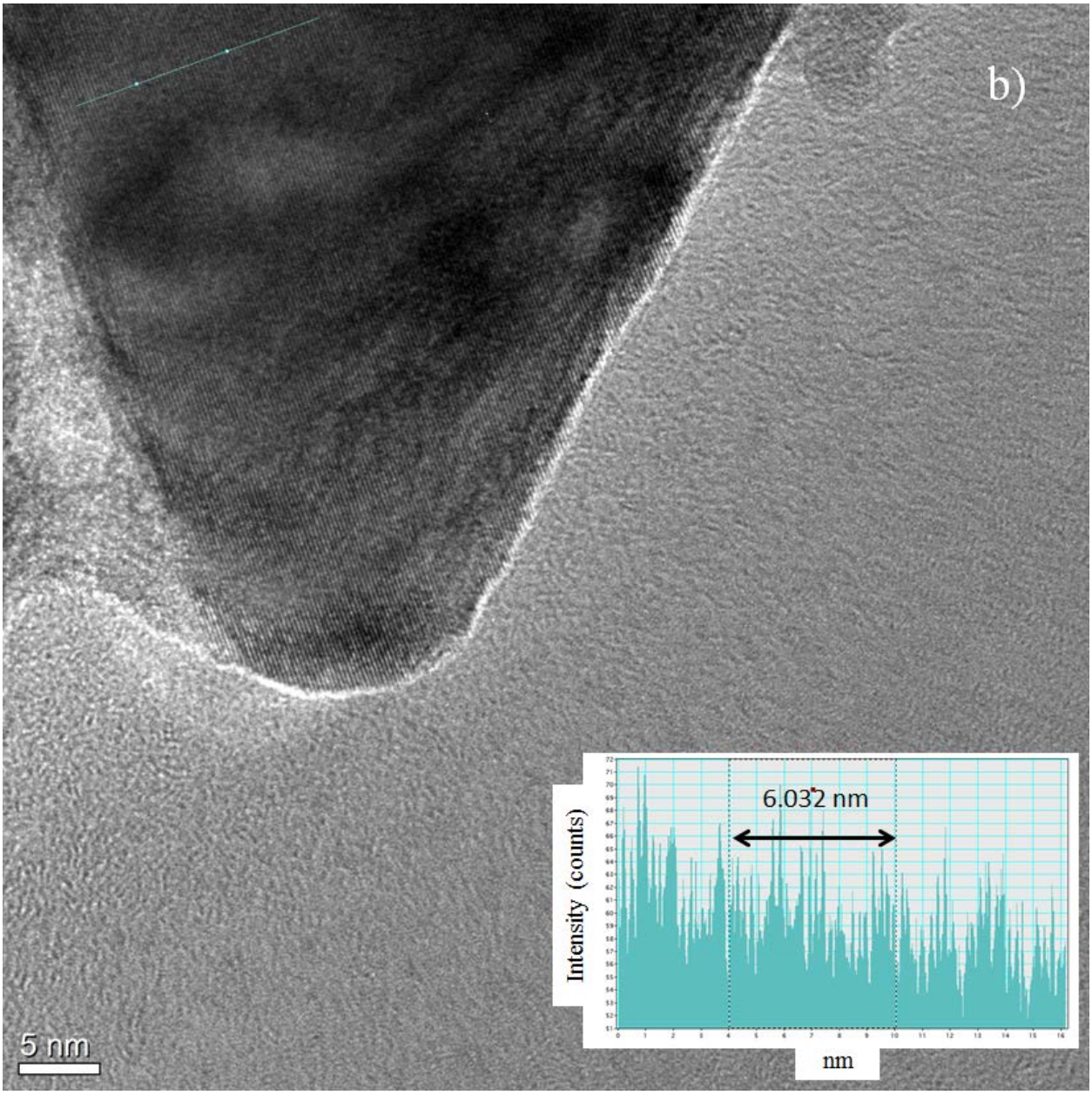

Figure 28. (a) Low magnification bright field TEM image of VN particle prepared by the mechano-chemical reaction with Selected Area Diffraction pattern of VN shown in the inset; (b) HRTEM image of milled VN with inset showing the interplanar spacing of region marked in (b) consisting of 25 planes(used to calculate d-spacing).

In order to determine the chemical oxidation states of V and N, x-ray photoelectron spectroscopy (XPS) techniques has been conducted on the nano-crystalline VN particles prepared by the mechano-chemical reaction method. The XPS spectra of V_{2p}, N_{1s} and O_{1s} peak of VN are shown in **Figure 29a**, **Figure 29b**, and **Figure 29c**, respectively. **Figure 29a** shows the vanadium and oxygen oxidation states before cycling and **Figure 29b** depicts the same after cycling the electrode at 100 mV/s for 100 cycles.

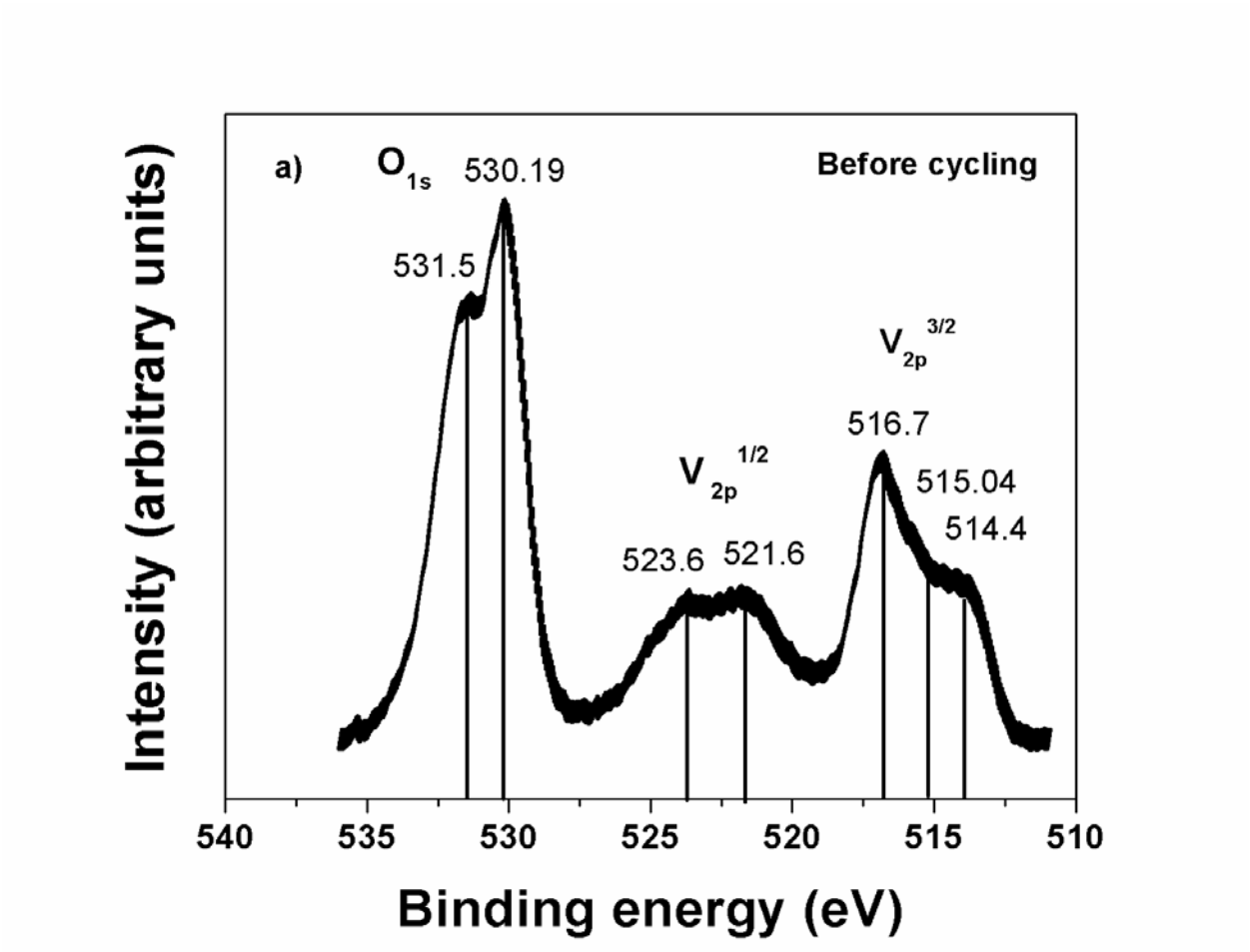

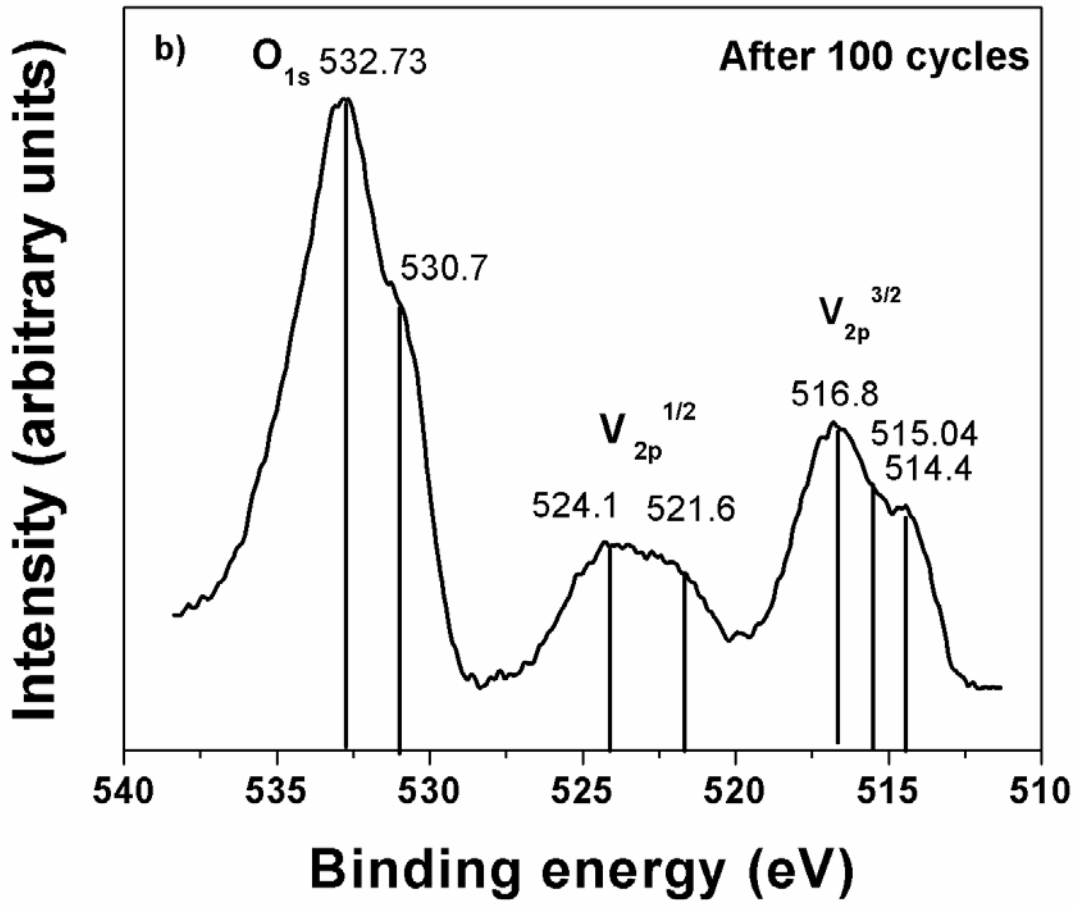
b)
O_{1s} 532.73
After 100 cycles
530.7
$V_{2p}^{3/2}$
516.8
$V_{2p}^{1/2}$
515.04
514.4
524.1
521.6
Intensity (arbitrary units)
540
535
530
525
520
515
510
Binding energy (eV)

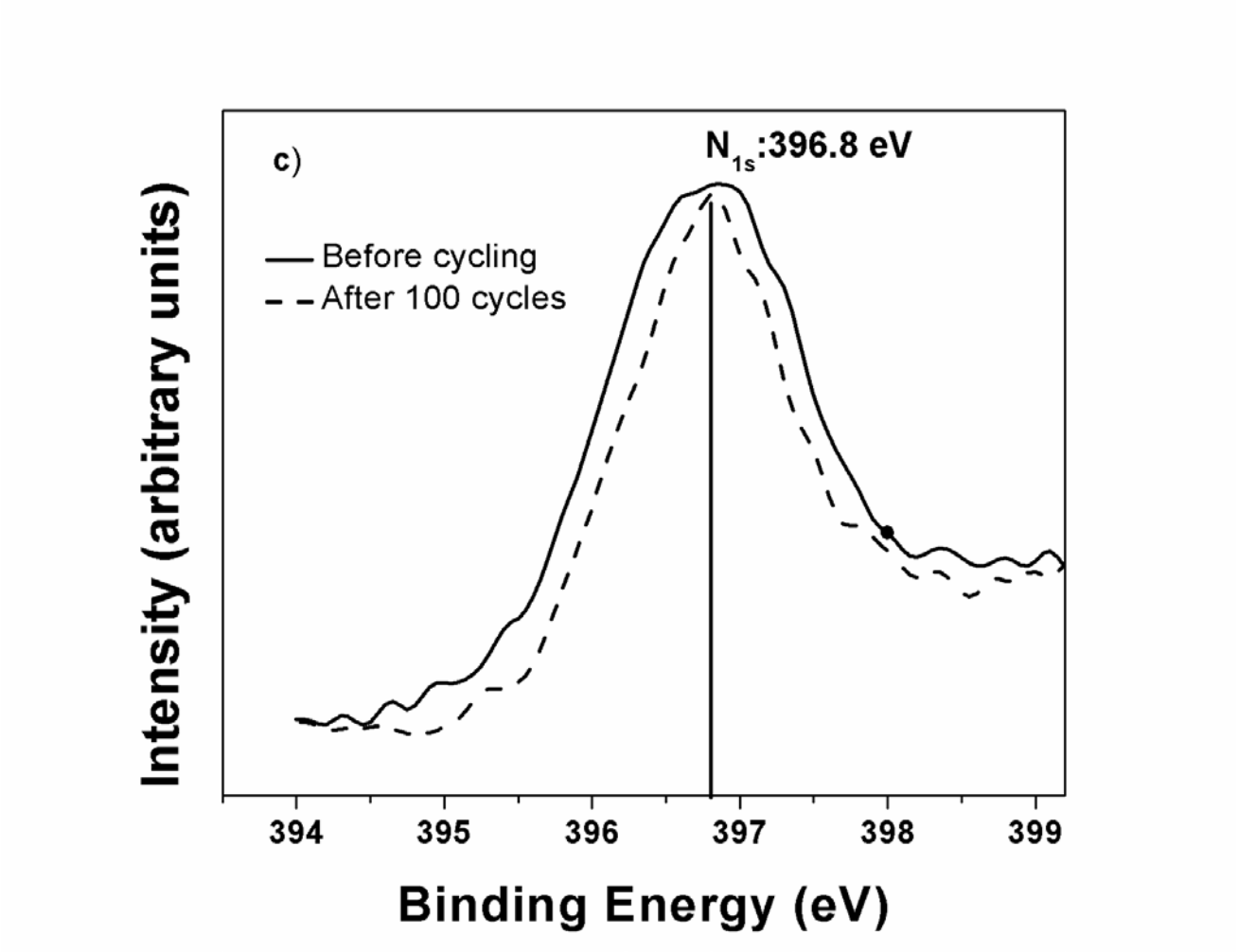

Figure 29. (a) X-ray photoelectron spectroscopy data showing Vanadium and Oxygen binding energies in the mechano-chemically synthesized VN powder in cycled VN electrodes (b) X-ray photoelectron spectroscopy data showing Vanadium and Oxygen binding energies in the mechano-chemically synthesized VN electrodes after cycling at 100 mV/s for 100 cycles (c) X-ray photoelectron spectroscopy data showing Nitrogen binding energies in the milled VN powder and in cycled VN electrodes.

Table 10 outlines in detail the binding energies of $V_{2p}^{3/2}$, $V_{2p}^{1/2}$, O_{1s} and N_{1s} peaks seen in **Figure 29a**-**Figure 29c**. The binding energy of the $V_{2p}^{3/2}$ peaks at 516.7 and 514.4 eV correspond to those of VO_2 and VN, respectively [347-350], indicating the presence of an oxide rich VN surface. O_{1s} peaks at 530.2 and 532.7 eV correspond to the presence of a mixed oxide (with a

predominant +3 oxidation state of Vanadium) of vanadium and terminal hydroxyl groups respectively[174, 351, 352]. Figure 4c shows the N_{1s} peak of VN generated by the mechano-chemical approach before and after 100 cycles with a binding energy of 398.8 eV which corresponds well with the binding energy of the nano-particulate VN previously reported[182] . This indicates that the VN formed by milling the vanadium oxide and lithium nitride also has a thin surface oxide film as is the case in nano-crystalline VN reported by Choi et al. [182]

Table 10. Binding energies obtained by de-convolution of peaks in XPS spectra seen in Figure 29a-Figure 29c.

Binding energies		Before cycling	After cycling	Reference
$V_{2p}^{3/2}$	VN	514.4	514.4	347-349
	VO_2	516.7	516.3	347, 350
	$VO_2 + V_2O_3$	515.04		347, 350
$V_{2p}^{1/2}$		521.6	521.6	
		523.6	524.1	
O_{1s}	VO_2	530.2	530.7	350
		531.5		352
			532.7	347
N_{1s}	VN	396.8	396.8	353, 354

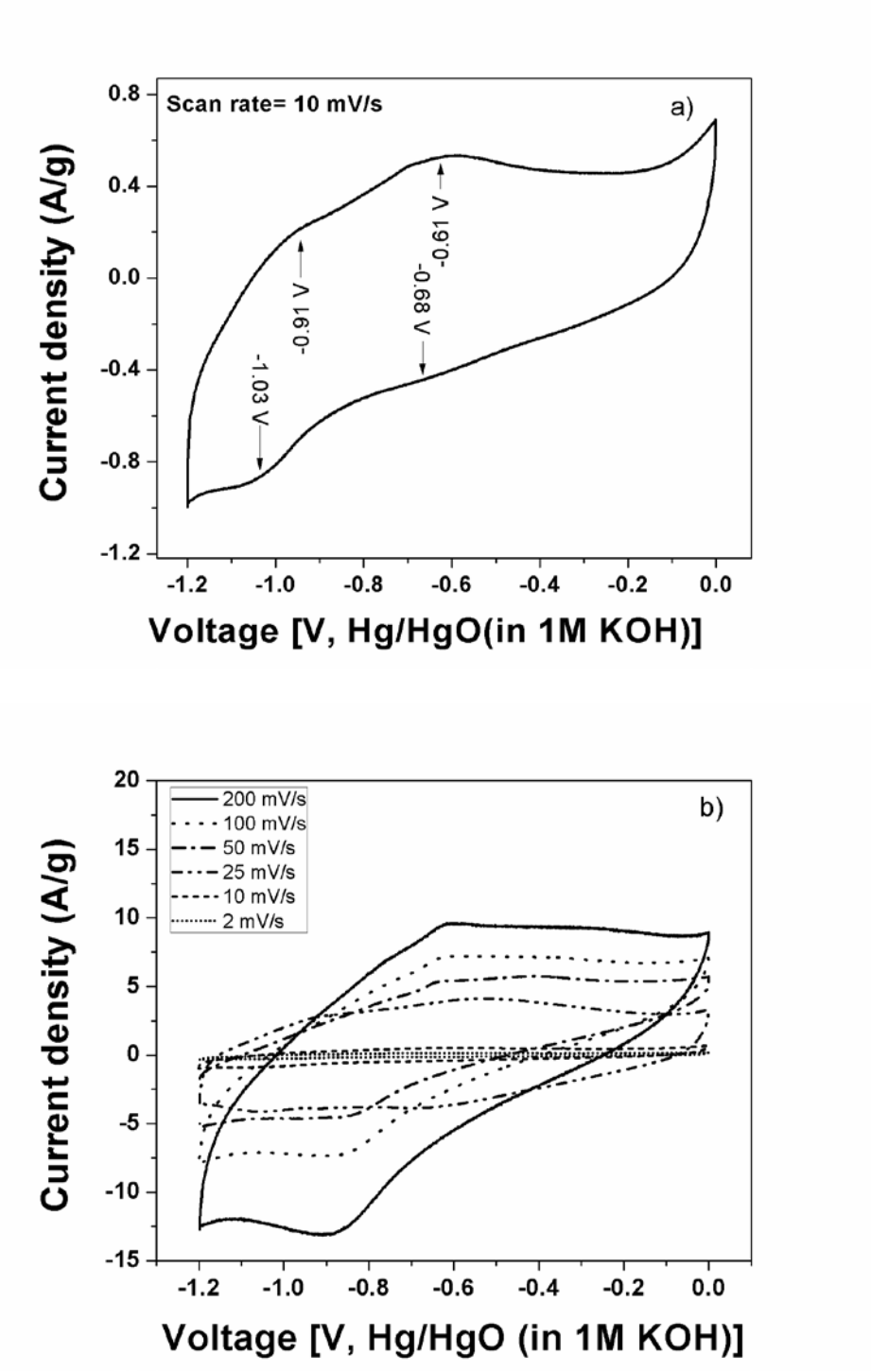

Figure 30. (a) Cyclic Voltammogram of VN synthesized by mechano-chemical reduction at a slow scan rate of 10 mV/s (active material loading=0.32 mg/cm^2) (b) Cyclic voltammograms of mechano-chemically synthesized VN at a number of scan rates from 200 mV/s to 2 mV/s (active material loading=0.36 mg/cm^2).

Figure 30a shows the cyclic voltammogram (CV) of VN prepared by mechano-chemical reaction in 1M KOH over a voltage window of -1.2 V to 0 V with respect to Hg/HgO. As can be seen, both double layer and pseudocapacitor type response is visible in the CV. It can be seen that VN from HEMM exhibits reversible Faradaic reactions much like those of the nanoparticulate VN derived by the two step ammonolysis approach. Faradaic charge storage occurs at the surface oxide layer covering the nitride. Faradaic peaks are observed at -0.91 V and -0.61 V on the anodic scan and at -0.68 V and -1.03 V on the cathodic scan. Equations (iii) to (v) describe the various reactions potentially occurring in the voltage window of interest[340-342]. It should also be noted that the standard electrode potentials reported in the references are with respect to standard hydrogen electrode. Furthermore, the electrode potentials are calculated on the basis of the Nernst equations which are pH dependent. The electrode potentials were calculated with respect to Hg/HgO (in 1M KOH) by using a standard electrode potential for Hg/HgO (1M KOH) of 0.14 V with respect to standard hydrogen electrode.

$$V_6O_{13}\,(s) + 2H^+ + 2e^- \leftrightarrow 3V_2O_4\,(s) + H_2O$$

$$V_6O_{13}\,(s) + H_2O + 2e^- \leftrightarrow 3V_2O_4\,(s) + 2OH^-$$

$$E = 0.4352 - 0.0591 \times pH \quad \text{(Volts vs. SHE)}$$

$$E = -0.5322 \text{ (Volts vs. Hg/HgO (1M KOH))} \qquad \text{Equation (iii)}$$

$$3V_2O_4\,(s) + 4H^+ + 4e^- \leftrightarrow 2V_3O_5\,(s) + 2H_2O$$

$$3V_2O_4\,(s) + 2H_2O + 4e^- \leftrightarrow 2V_3O_5\,(s) + 4OH^-$$

$$E = 0.3901 - 0.0591 \times pH \quad \text{(Volts vs. SHE)}$$

$$E = -0.5773 \text{ (Volts vs. Hg/HgO (1M KOH))} \qquad \text{Equation (iv)}$$

$$2V_3O_5\,(s) + 2H^+ + 2e^- \leftrightarrow 3V_2O_3\,(s) + H_2O$$

$$2V_3O_5\,(s) + H_2O + 2e^- \leftrightarrow 3V_2O_3\,(s) + 2OH^-$$

$$E = 0.1149 - 0.0591 \times pH \quad \text{(Volts vs. SHE)}$$

$$E = -\ 0.8525 \quad \text{(Volts vs. Hg/HgO (1M KOH))} \qquad \text{Equation (v)}$$

From the potentials observed in the cyclic voltammogram, the predominant pseudocapacitance reactions occurring in the alkaline KOH solution at pH 14 can thus be attributed to the reversible cycling of the surface oxide between V_2O_4 and V_6O_{13} and between V_2O_3 and V_3O_5 similar to those reported by Choi et al. [182, 235, 337]. It must also be noted that the electrode potentials observed in the cyclic voltammogram in **Figure 30a** however do not perfectly match the potentials reported in the above references. This can be attributed to the amorphous nature of the surface oxide which is clearly not observed in the X-ray diffraction pattern seen in **Figure 26b**. In addition, it will be seen from the XPS spectra discussed in the later section that the surface oxide is non-stoichiometric resulting in a shift in the corresponding oxidation and reduction peaks. A notable difference in the electrochemical behavior of VN made by mechano-chemical reduction as compared to chemically synthesized nanoparticulate VN reported by Choi et. al. is the complete absence of reversible oxidation-reduction peaks at -0.23 V with respect to Hg/HgO reference electrode on the anodic scan and -0.32 V on the cathodic scan [182] described by Equation (vi) below. This could possibly be attributed to the nature of the surface oxide and the oxidation state of vanadium in the VN synthesized by mechano-chemical reduction as will be identified by XPS data discussed in the section to follow.

$$3V_2O_5\,(s) + 4H^+ + 4e^- \leftrightarrow V_6O_{13}\,(s) + 2H_2O$$

$$3V_2O_5\,(s) + 2H_2O + 4e^- \leftrightarrow V_6O_{13}\,(s) + 4OH^-$$

$$E = 0.8425 - 0.0591 \times pH \quad \text{(Volts vs. SHE)}$$

$$E = -\ 0.1249 \quad \text{(Volts vs. Hg/HgO (1M KOH))} \qquad \text{Equation (vi)}$$

Figure 30b shows the cyclic voltammograms of mechano-chemically derived VN at various scan rates varying from 200 mV/s to 2 mV/s (at an active material loading of 0.36 mg/cm^2). It can be seen that the response changes from an almost square-like behavior to a more distorted parallelogram as scan rate increases. The specific capacitance of the VN synthesized using the mechano-chemical milling approach was calculated at various scan rates using Equation (i) outlined in **Section 3.3** above. One artifact that sometimes leads to an overestimation of capacitance calculated from integration of cyclic voltammograms is the asymmetry of the curve with respect to the horizontal axis. The cyclic voltammogram seen in **Figure 30a** though appearing assymetric in-fact has an almost identical area on either side of the current axis (Integrated area of 0.44VA/g above the potential axis, and an integrated area of 0.47VA/g below the potential axis indicating a Columbic efficiency of ~94%) indicating that the capacitance calculated by the integration of the C-V curve is not overestimated.

Figure 31shows the dependence of capacitance of the mechano-chemically obtained VN on both scan rate and active material loading. It can be clearly observed that the capacitance of VN as expected decreases with increasing scan rate as the reaction kinetics of the pseudocapacitance reactions become evidently rate-limited[58]. However, contrary to the trend reported by Choi et al. [182] , it was observed that the capacitance of these mechano-chemically derived nitrides are almost independent of the active material loading. This can be attributed to

the much reduced pseudocapacitance contribution, which traditionally is observed to be scan-rate limiting on account of either the inferior electrical conductivity of nano-crystalline nitrides or the combined limited conductivity as well as the chemical instability of the nanocrystalline system in the highly basic electrolyte. This is also observed by comparing the decrease in capacitance with increase in scan rate (44% drop from 2 mv/s to 25 mV/s after which it is stable) with that of the chemically derived nanocrystalline VN reported by Choi et al. The chemically derived nanocrystalline VN synthesized by the two step ammonolysis approac reported by Choi et al. has a fade in capacitance of ~ 24% from 25 mV/s to 100 mV/s as a result of the nano-crystalline nature of the VN reported therein. The capacitance drop from 2 mV/s to 25 mV/s occurs as a result of kinetics of the electrochemical reaction and can be seen in the work by Choi et al as well. Beyond that point however, there is minimal fade indicating lack of electrical conductivity limitations.

The primary aim in pointing this out is to draw contrast and point out the characteristics of the currently synthesized mechanochemcally synthesized material which is different and also to point out the result of particle size on capacitor characteristics. The capacitance values however are less than those reported in the literature for both pure vanadium nitride and oxy-nitride[182, 248, 251, 262, 267, 308]. This could be attributed to the relatively large particle size and low surface area of the mechano-chemically synthesized vanadium nitride. The result nevertheless, indicates that the nano-crystalline VN obtained by the mechano-chemical approach does not remarkably suffer from the electron transport limitations typically seen in the ~6 nm VN reported by Choi *et al.* [235]. The milled nitride thus exhibits capacitances between 25 and 55 F/g as compared to 100-850 F/g for the chemically synthesized nanoparticulate VN at similar scan rates and loadings of ~1 mg/cm[2182]. Another remarkable feature of the supercapacitor behavior of

mechano-chemically synthesized VN is that there is very good retention in capacity with increasing active material loadings, as a result of higher electronic conductivity, which is reflected in the superior areal and volumetric capacitance of the material shown in **Figure 32b**.

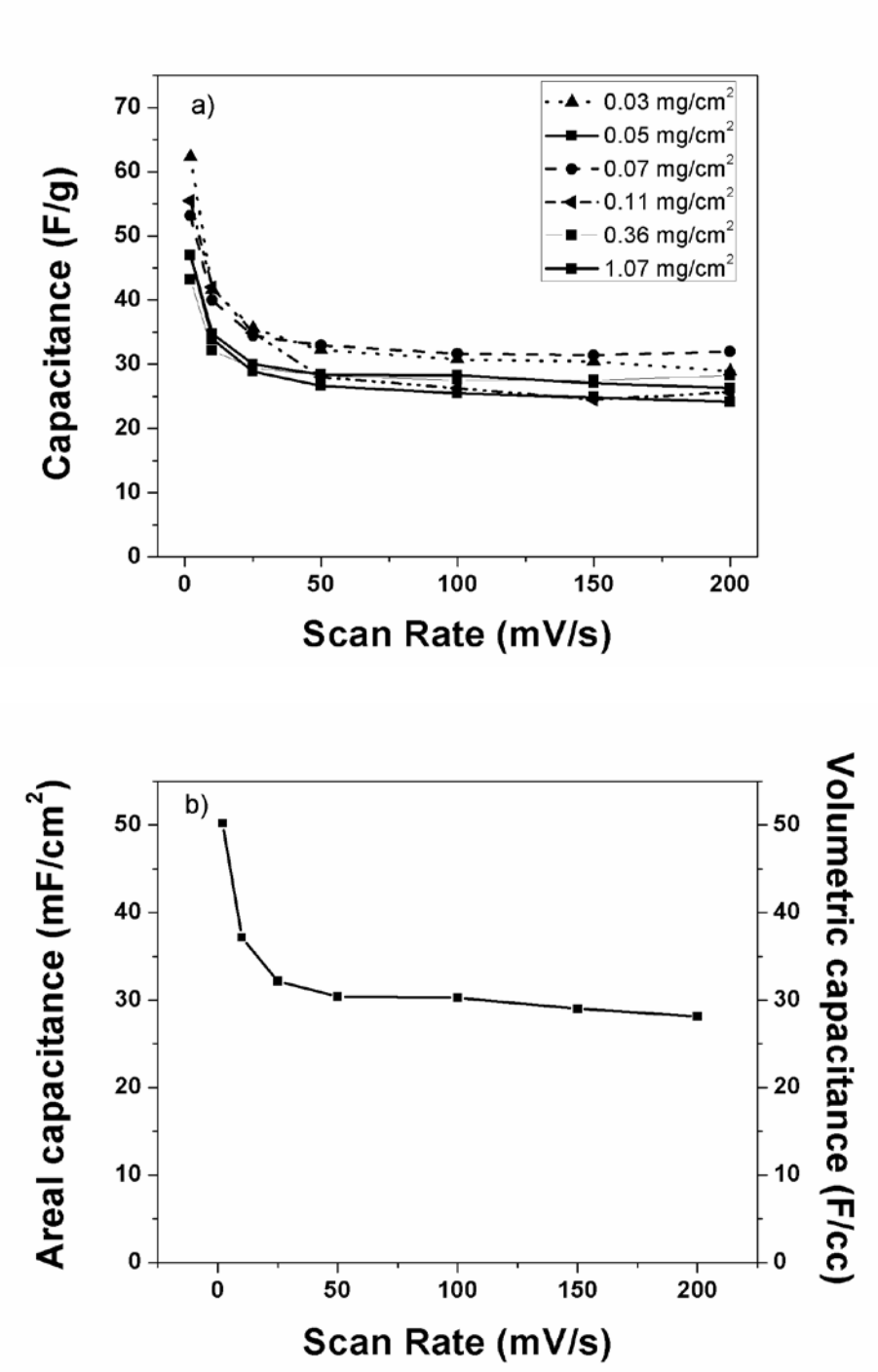

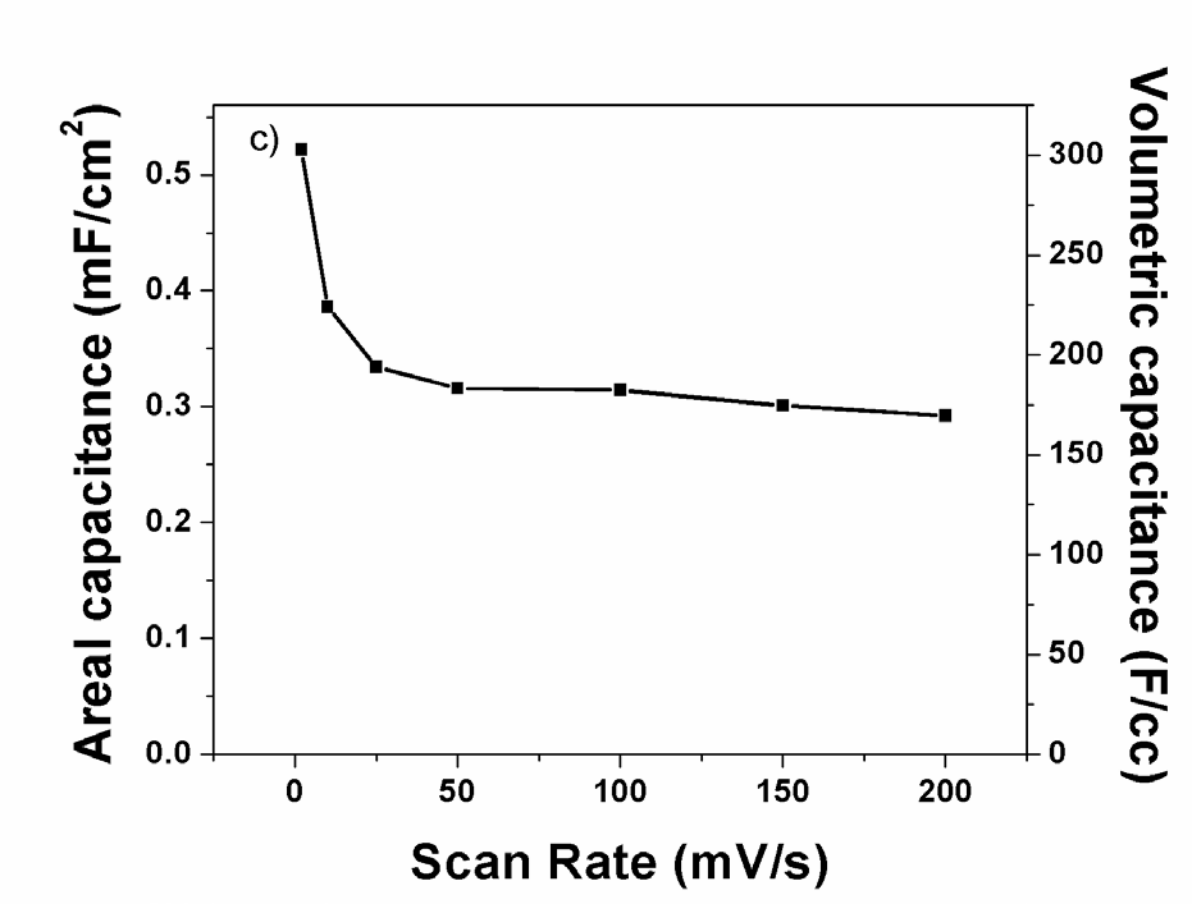

Figure 31. (a) Dependence of gravimetric capacitance of milled VN on scan rate at different active material loadings (b) Areal capacitance on the basis of electrode area and electrode volume of vanadium nitride made by mechano-chemical reduction plotted at different scan rates (c) Areal capacitance on the basis of material surface area and density of vanadium nitride made by mechano-chemical reduction plotted at different scan rates.

Figure 31b and **Figure 31c** show the area normalized and volume normalized capacitance of the mechano-chemically synthesized vanadium nitride on the basis of the electrode area and thickness (**Figure 31b**) and powder surface area and density (**Figure 31c**). The powder density was obtained using Micromeritics AccuPyc II 1340 gas pycnometer to be 6.46 g/cc which is comparable to that of commercially obtained VN. It can be seen that both the areal capacitance and volumetric capacitance of the nitride are comparable to those reported for

other capacitor materials on account of the loading independence of the capacity of the VN as seen in **Figure 31a**[267, 344]. The areal capacitance (mF/cm^2) on electrode area basis was calculated by multiplying the gravimetric capacitance (F/g) with the materials loading (mg/cm^2) for the electrode which in the present case is 1.1 mg/cm^2. This was then divided by electrode thickness (which in this case was approximately 10^{-3}cm) to obtain the volumetric capacitance (F/cc).Though the gravimetric capacitance of mechano-chemically synthesized VN is low, on account of the loading independence of capacity, the areal capacitance is however comparable to that of other capacitor materials such as ruthenium oxide(12-30 mF/cm^2)[344]. The nitride material however does not have areal capacitances as high as highly active ruthenium oxide supercapacitors[345, 346] but is still commercially viable on account of its relatively low cost as compared to ruthenium oxide (~2.38 $/gm as compared to ~10$/gm). The areal capacitance of supercapacitor materials is usually reported on the basis of electrode areas i.e. a quantitative measure of the amount of energy stored per electrode area. On the other hand, volumetric capacitance is generally reported on the basis of material volume[355]. In order to avoid confusion, the areal and volumetric capacitance have been plotted on the basis of electrode and material basis separately. The areal capacitance is superior to that of various other nitride materials and volumetric capacitance compares with that of high capacity materials such as ruthenium oxide (66-630 F/cc)[355].

Galvanostatic charge-discharge testing was performed on an Arbin BT2000 cycler using a half-cell configuration similar to that used for cyclic voltammetry experiments at a current density of 100 mA/g. The charge-discharge profile and fade in capacity with cycling over 1000 cycles have been plotted in **Figure 32a** and **Figure 32b** respectively. In charge-discharge profiles, sometimes extended plateaus occur as a result of either of two processes occurring in

aqueous electrolytes. One of them being the irreversible conversion of higher oxidation state vanadium into soluble $HV_2O_5^-$ being the root cause of the plateau occurring between -0.3 V and 0 V [wrt Hg/HgO (in 1M KOH)]. This is indeed an irreversible process seen to occur with higher oxidation state vanadium oxide containing vanadium nitride. However, this phenomenon is minimal in the VN prepared by mechano-chemical reduction due to the absence of V^{+5} state as observed in **Figure 32a** and **Figure 32b**. The other plateau occurs as a result of the onset of water electrolysis in aqueous electrolytes. Depending on the exact pH of the electrolyte, onset of oxygen evolution occurs at approximately, ~0.3 V [(wrt Hg/HgO (in 1 M KOH)) at pH 14] and the onset of hydrogen evolution occurs at ~-1 V [(wrt Hg/HgO (in 1M KOH)) at pH 14]. This is in-fact not a real charge storage process but an electrolyte breakdown. This phenomenon is observed clearly in the charge-discharge profile seen in **Figure 32a**. The discharge tails off after about -1 V wrt Hg/HgO and the Columbic efficiency drops off to ~75%. This indicates that the capacitance calculated from charge-discharge data is overestimated by an approximate 25%.

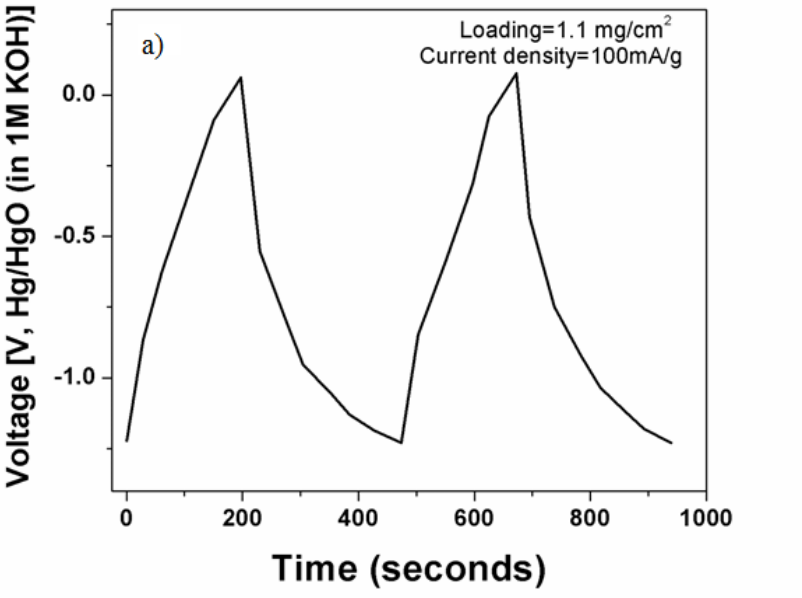

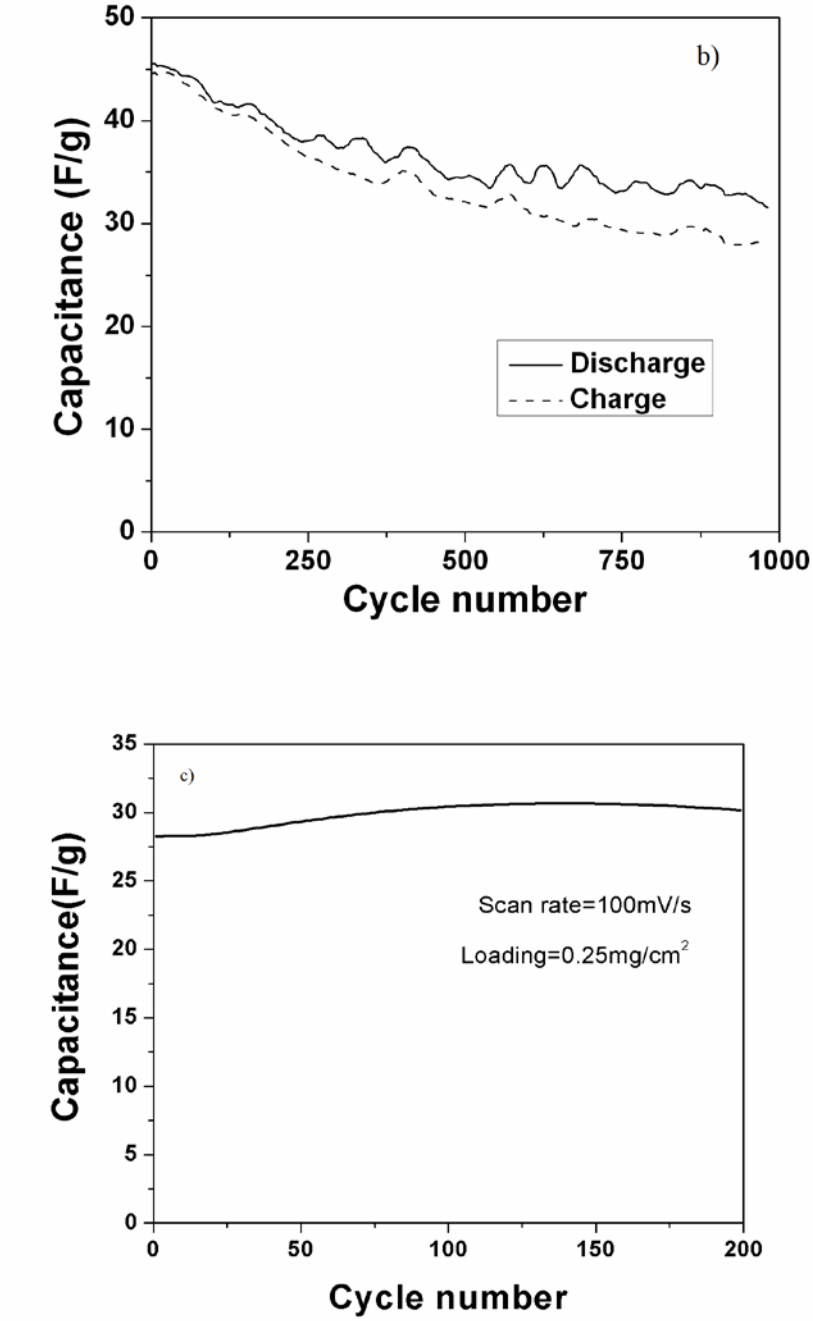

Figure 32.(a) Galvanostatic charge-discharge profile of mechano-chemically synthesized VN at a current density of 100 mA/g (Active material loading=1.1 mg/cm^2) (b) Long term charge-discharge cyclability of mechano-chemically synthesized VN (Current density= 100 mA/g; Active material loading=1.1 mg/cm^2) (c) Cycling behavior of VN synthesized by mechano-chemical milling at a scan rate of 100 mV/s (Active material loading= 0.25 mg/cm^2).

Figure 32b shows the charge-discharge capacity over 1000 cycles. There is indeed some fade over extended cycling probably occurring as a result of particle coarsening and the irreversibility discussed occurring as a result of the gas release occurring below -1V. This phenomenon is usually observed in the cyclic voltammogram as a large tail with a distinctly different slope on the I-V curve. However, no such tail is observed in the cyclic voltammograms in **Figure 30a** and **Figure 30b** indicating that the kinetics of the process are sluggish even at low scan rates. This overpotential deposition process runs in parallel with the capacitive processes (underpotential deposition). As it can be seen the capacitance is more stable with a fade rate of ~0.042 % per cycle (41% fade in 1000 cycles) as compared to that of ~0.1% per cycle (97% fade in 1000 cycles) reported by Choi et al. **Figure 32c** shows the cycling stability of VN (obtained from cyclic voltammetry) prepared by milling in 1M KOH at a relatively high scan rate of 100 mV/s for a higher loading of 0.25 mg/cm^2. The reason for using 100 mV/s as the rate of choice to evaluate the capacitance fade of VN is in order to compare the stability with that reported in the work by Choi et al. It is clearly observed that the capacitance is stable and the typical fade in capacitance previously observed in the nano-crystalline VN is totally absent. This can be attributed to the minimal pseudo-capacitance contribution associated with the VN prepared by the mechano-chemical approach as discussed above. The difference in properties between mechano-chemically derived VN and nanoparticulate VN have been discussed further in S**ections 4.1.3-4.1.4**.

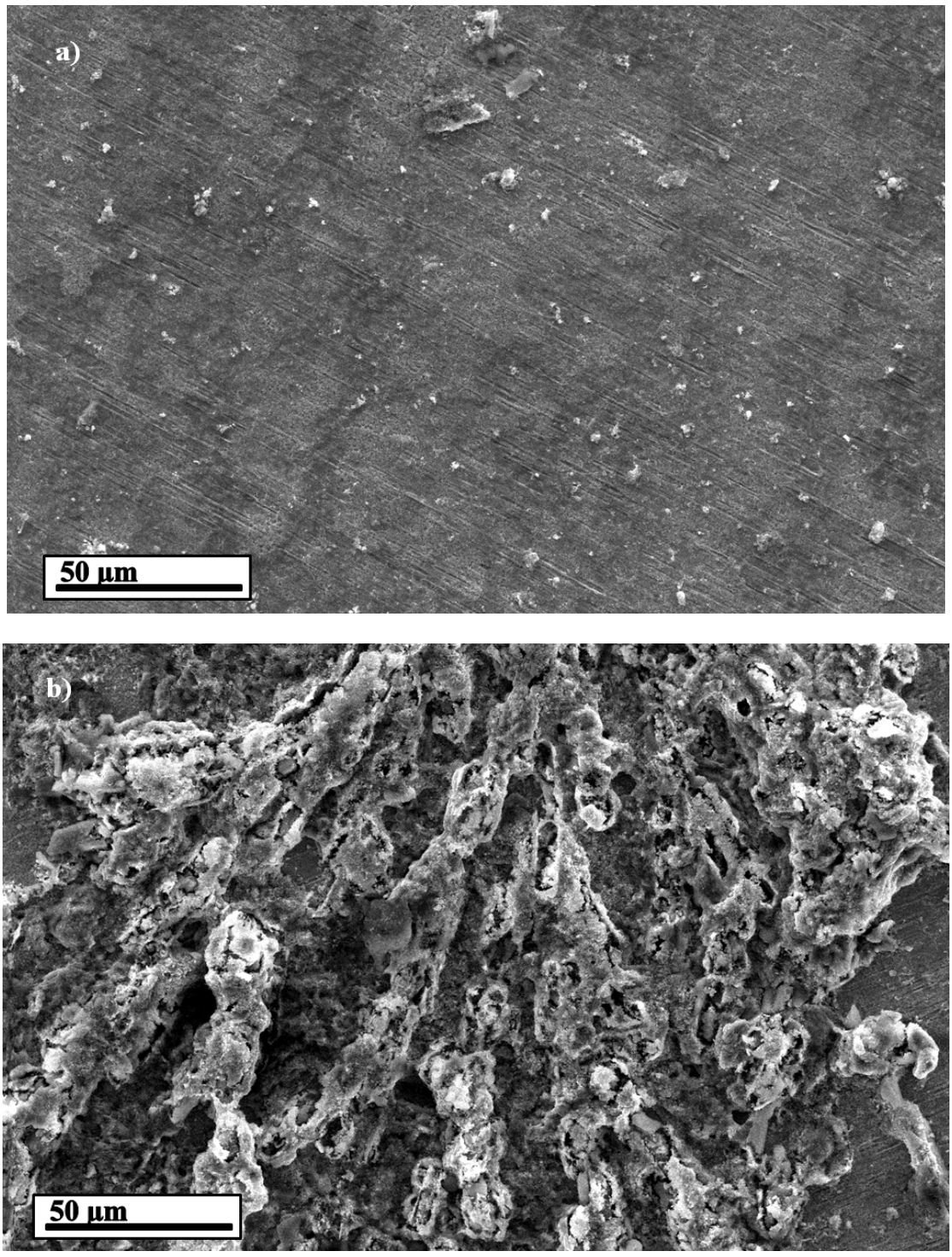

Figure 33. Scanning electron microscope image of (a) As-coated active material using mechano-chemically synthesized VN based slurry (Active material loading=1 mg/cm^2) (b) Electrochemically cycled electrode of mechano-chemically synthesized VN on Nickel substrate (1000 cycles, 100 mA/g).

Figure 33a and **Figure 33b** show the difference in electrode morphology as a result of cycling over 1000 cycles (100 mA/g; active material loading=1.1 mg/cm^2) of the VN. It can be seen that there is a change in macroscopic morphology of the material with cycling. The uncycled material exists in the form of a uniform film covering the substrate while the cycled material has a porous morphology resembling that of tubular islands. This change in morphology could be attributed to the Faradaic charge transfer reactions and gas evolution occurring as a result of electrolyte decomposition below -1V with respect to Hg/HgO in 1M KOH leading to the fade occurring in **Figure 32b**. Post-cycling solution analysis using inductively-coupled plasma (ICP) analysis was not performed since no significant fade in capacity was observed in **Figure 32b**.

4.1.2 Surface area-VN behaves like a Faradaic catalyst

It should be noted that although the VN obtained from high energy mechanical milling (HEMM) exhibits similar Faradaic and pseudocapacitor response as the nano-particulate VN prepared by ammonolysis of VCl_4, the large observed difference in the supercapacitance values between the two indicates the importance and predominance of the nano-particulate nature necessary for achieving the high capacitive response, and the absence of V^{+5} state.

Table 11 shows the materials properties deemed to be primarily responsible for achieving the good capacitor performance of the nitride. VN prepared by milling can be seen to exhibit both lower specific surface area (SSA, 9.1 m^2/g) and a much larger crystallite size (26.76 nm) in contrast to VN generated by the chemical approach (SSA 38.8 m^2/g, and crystallite size 6.33 nm) reported by the Kumta group previously[182]. It should also be noted that although the electronic conductivity of the HEMM derived nanostructured VN (473 S/cm) is much higher than that of

the chemically derived nanoparticulate VN (81.8 S/cm), which is expected of a material possessing higher crystallinity as is the case with the HEMM derived VN, the reduced surface area and the larger particle size more than compensate for the high conductivity thus resulting in a lower capacitance. The material properties of the VN obtained by the mechano-chemical approach are however very similar to those obtained by ammonolysis at 700 and 800^{o}C reported by Choi et al. [238]. At the same time, the capacitance is only a third of the capacitance reported for those materials for reasons outlined earlier.

Table 11. Comparison of the material properties of VN made by milling and nanoparticulate VN derived by chemical synthesis following published report ([182, 235, 238]).

Material	Specific Surface area (m^2/g)	Crystallite size (nm)	Electronic conductivity (Siemens/cm)
Nanoparticulate VN*	38.8	6.33	81.8
VN from HEMM	9.1	26.76	473

*Chemically synthesized VN from the two-step ammonolysis approach.

A similar phenomenon is observed in **Figure 23b**, which shows the effect of milling on capacitance of commercial VN at a particular loading. Milling of commercial vanadium nitride also results in a rise in capacitance with increasing milling time. This is to be expected given the trend in surface area and crystallite size seen in **Table 9**. Such a rise is characteristic of a surface charge storage phenomenon either as double layer charge storage or as a surface oxide pseudocapacitance.

4.1.3 Surface oxide-Fade in nanoparticulate VN capacitance with cycling

To further understand the reason contributing to this major difference in the capacitance behavior, XPS was performed on the nitride prepared by mechanical milling to compare with the previously reported data for the chemically derived nano-crystalline VN [182]. **Figure 29a** and **Figure 29b** show the XPS pattern of HEMM derived uncycled and cycled VN, respectively. The presence of vanadium nitride in both the bulk and core of the uncycled material is confirmed by the $V_{2p}^{3/2}$ peak at 514.4 eV [356]. The same peak is observed in the cycled sample as well. The $V_{2p}^{3/2}$ peak at 516.7 eV present in the uncycled milled nitride has binding energies lower than that of pure V_2O_5 which has been reported to have binding energy of 517.2 eV. The $V_{2p}^{3/2}$ peak of 516.8eV thus corresponds more closely to the V^{+4} present in VO_2 [347, 350]. The 516.7 eV peak corresponds to that of VO_2 and 515.1 eV to mixed non-V_2O_5 type oxides present in the uncycled milled VN. Similar $V_{2p}^{3/2}$ peaks are seen in the VN sample obtained after cycling indicating that both the 3+ or 4+ oxidation states of V in oxides initially present on the surface of the VN are reversibly cyclable in the alkaline KOH electrolyte at pH 14 without substantial dissolution. Furthermore there appears to be no change in the nature of the VN before and after cycling as shown by the invariance of the N1s peak at 396.8 eV before and after 100 cycles shown in **Figure 29c**. This is also corroborated by the cycling data seen in **Figure 32c** indicating no significant loss in capacitance for 200 cycles. Upon comparing the plot with that of the nanoparticulate VN generated by chemical approach and reported in the previous work of Choi et al from the Kumta group[182], the reason for the lower capacitance in the nitride derived by the mechano-chemical synthesis can be easily construed. The chemically derived nano-particulate VN has been reported to exhibit a +5 oxidation state due to the surface oxide of V_2O_5 present on the surface of the as-prepared VN prior to cycling as compared to the +4 state of VO_2 and mixed

+3 and +4 oxidation states observed on the surface of the HEMM and mechano-chemically derived VN. The attribution of vanadium peaks, in the work by Choi et al. to those of vanadium in +5 state is a result of the composition of the material identified there-in $VN_{1.08}O_{0.36}Cl_{0.1}$ [182, 235]. The presence of large halide species such as chlorine tends to result in destabilization of the lattice resulting in lower binding energies (i.e. poorer cohesion). It is believed that this is reflected in the lower binding energies for the surface oxide species seen in their work. The attribution of a binding energy of 516.3 eV to a +5 oxide is seen in other such instances previously reported [357, 358]. The reasoning behind this conclusion was the difference in average oxidation state of vanadium observed in both nitrides calculated from the experimentally determined composition (Choi et al.: 4.1; Mechano-chemical synthesis: 2.8). The higher oxidation state of the vanadium is definitely a contributing factor to the fade though further studies are on-going into the exact extent to which this affects the same. The absence of a +5 oxidation state is also reflected in the cyclic voltammogram seen in **Figure 30a**. Peaks corresponding to reduction of V_2O_5 (soluble in the form of $HV_2O_5^-$ at pH~14) previously reported for nanocrystalline VN by Choi *et al.* seen at ~-0.3 V with respect to Hg/HgO, are absent in the VN prepared by the mechano-chemical approach. It is therefore proposed that the presence of a +5 surface oxide is probably critical for obtaining the very high capacitance reported for the chemically synthesized nano-particulate VN. Another contributing factor to the disparity in the fade between the mechano-chemically synthesized nitride and the VN reported by Choi et al. is possibly the difference in particle size and surface area. The 6nm particles reported in the work by Choi et al afford large oxide-electrolyte contact not only aiding in the large pseudocapacitive charge storage but possibly also in the more rapid fade[182].

The O_{1s} peak of uncycled VN has binding energies (530.2 eV) corresponding to that of VO_2 as compared to that of cycled VN which has O_{1s} corresponding to a mixed Vanadium oxide consisting of V_2O_3 as well as other V species not corresponding to V_2O_5 (530.7 eV). These are thought to correspond to the intermediate oxides of VO_2 and V_3O_5 proposed to have been formed as a result of the pseudocapacitance reactions described in Equations (iii) to (v). The presence of hydroxyl groups seen as a peak at 532.7 eV confirms a pseudocapacitance mechanism similar to that proposed previously by us in Ref. 21 involving hydroxyl adsorption at the electrochemical interface following the scheme[347]. The contribution as explained earlier is much lower compared to the chemically synthesized nitrides reported earlier by Choi et al.[182, 235, 359].

$$VN_xO_y + OH^- \leftrightarrow VN_xO_y\text{-}OH \qquad \text{Equation (vii)}$$

To further validate this conclusion inferred from CV and XPS analyses, electrochemical impedance spectroscopy (EIS) was performed. Electrochemical Impedance Spectroscopy experiments were carried out in parallel to XPS to understand the electrochemical phenomena involved in the HEMM derived nitride both before cycling (**Figure 34a**), and after cycling (**Figure 34b**). **Figure 34a** and **Figure 34b** show the Nyquist plots of VN prepared by milling at the voltages wherein Faradaic charge transfer reactions were identified in VN made by both mechano-chemical (**Figure 30a**) and ammonolysis[182, 235, 359]. In addition, the impedance spectra obtained at the initial and final cell potential in the cyclic voltammogram have been included in the Nyquist plots. Semi-circular arcs corresponding to the double layer and pseudocapacitance reactions can clearly be seen in the zoomed in plots of **Figure 34a** and **Figure 34b** that are represented separately in **Figure 34c** and **Figure 34d** for clarity. These plots correspond to the high frequency region of the same spectra shown in **Figure 34a** and **Figure 34b** respectively. Semi-circular arcs commonly seen as a result of the double layer are clearly observed in both the

uncycled and cycled samples. In addition, it can be seen that the radius of the arcs decreases with increase in voltage (towards more negative values on the cathodic scan) which is common in the charge storage systems involving Faradaic reactions (Vanadium oxidation state transitions from +2 to +4). This usually occurs since Faradaic processes are voltage-activated and an increase in voltage usually results in a smaller barrier for electron tunneling. It can also be seen that semi-circular arcs in **Figure 34d** appear pronounced as compared to those in **Figure 34c** indicating a slight increase in charge transfer resistance upon cycling. This is however not reflected in the cycling data as the scan rate is maintained constant during cycling.

With extended cycling however, a slight fade in capacitance can be expected as a result of the incumbent loss of electronic conductivity. This loss is probably an effect of particle fragmentation also depicted in **Figure 33b** resulting in increase in grain boundaries arising from the pseudocapacitance reactions. In addition, it can clearly be seen that there is a change in the mechanism over the voltage window of interest in both cycled and uncycled VN. A second large semi-circular arc is seen at -1.2 V with respect to Hg/HgO in addition to the suppressed arcs visible at other potentials in the cycled HEMM derived nitride shown in **Figure 34b** which is indicative of an additional charge-storage/reaction phenomenon occurring at -1.2V. The secondary charge transfer process occurring between -1 and -1.2 V is the onset of water electrolysis which has a thermodynamic onset potential of ~-1.04 V with respect to Hg/HgO (in 1 M KOH)[342]. This does not however limit the application of the material for charge storage in the voltage window upto -1.2 V on account of the limited extent of water electrolysis as seen in **Figure 30a**.

In order to further understand this phenomenon, equivalent circuit modeling was performed using the Z-View software and UPD and OPD models described in **Section 3.3.1.1**

(shown in **Figure 35**). The UPD model consists of electrolyte series resistance (R_s) in series with a double layer, conventionally modeled as a resistor (R_F) in parallel with a capacitor (C_{dl}). The model also considers monolayer adsorption at the electrochemical interface resulting in pseudo-capacitance (C_p) in series to the charge transfer resistance (R_F). The OPD model adds an extra resistor (R_F') in parallel with the pre-existing capacitor corresponding to a second type of charge transfer process that is observed upon cycling at -1.2V. In porous electrodes, ideal capacitor behavior is usually not observed and the capacitors are replaced by a constant phase element [65, 360]. As seen in the inset in both **Figure 34a** and **Figure 34b**, ideal semi-circular arcs are not observed in the present EIS spectra indicating the effect of porosity and the need for use of constant phase elements in the reported impedance fits.

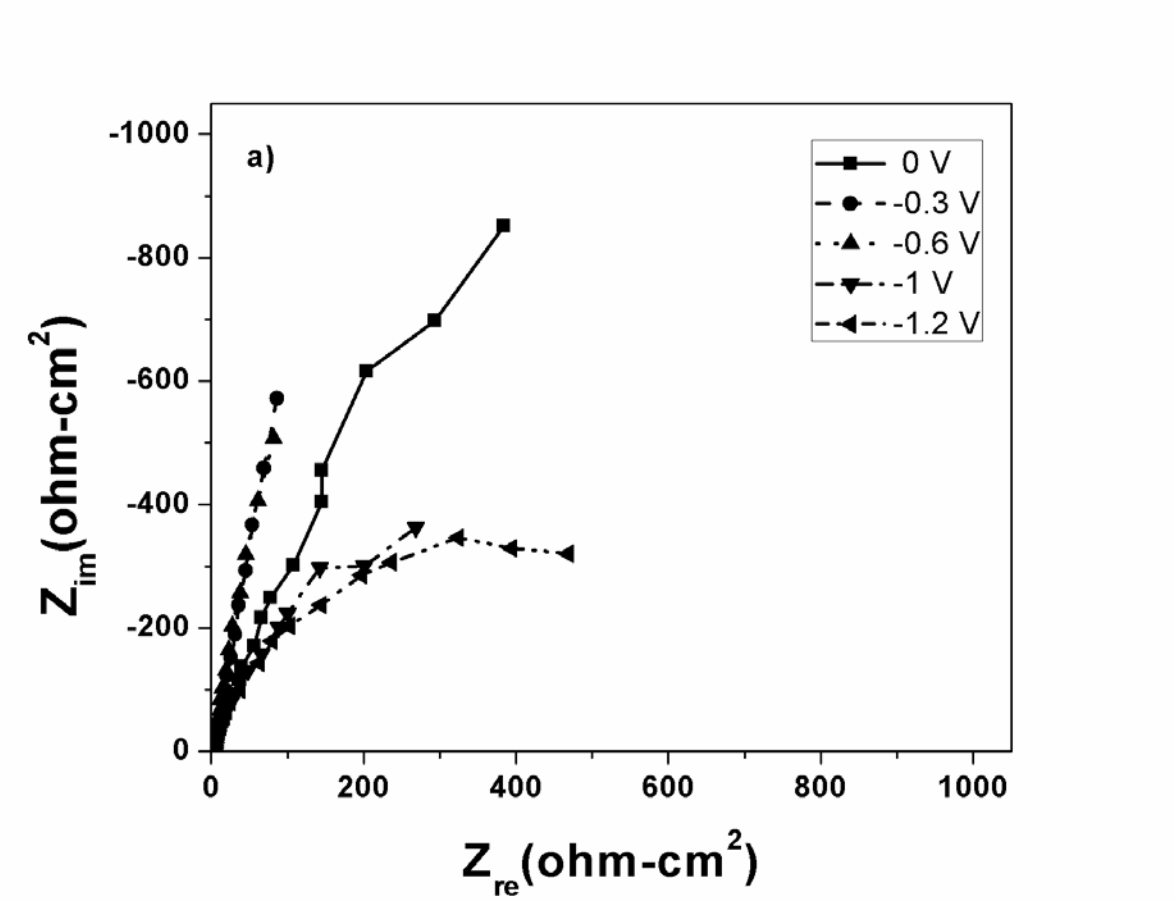

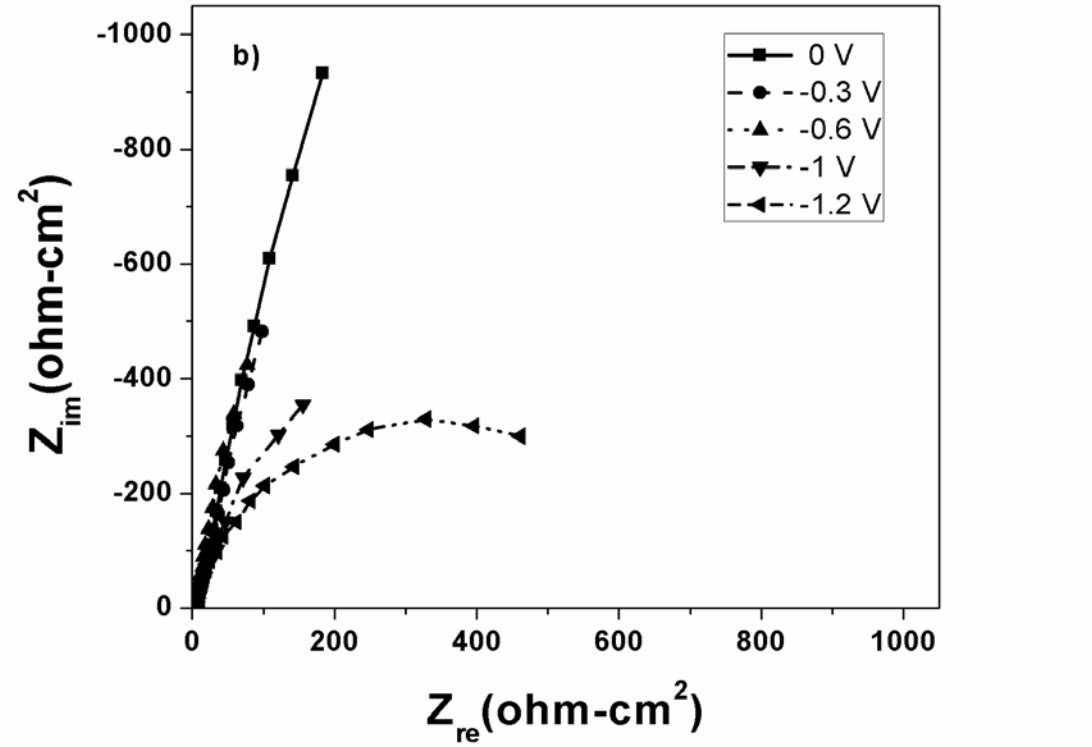
b)
0 V
-0.3 V
-0.6 V
-1 V
-1.2 V
-1000
-800
-600
-400
-200
0
0
200
400
600
800
1000
Z_im (ohm-cm^2)
Z_re (ohm-cm^2)

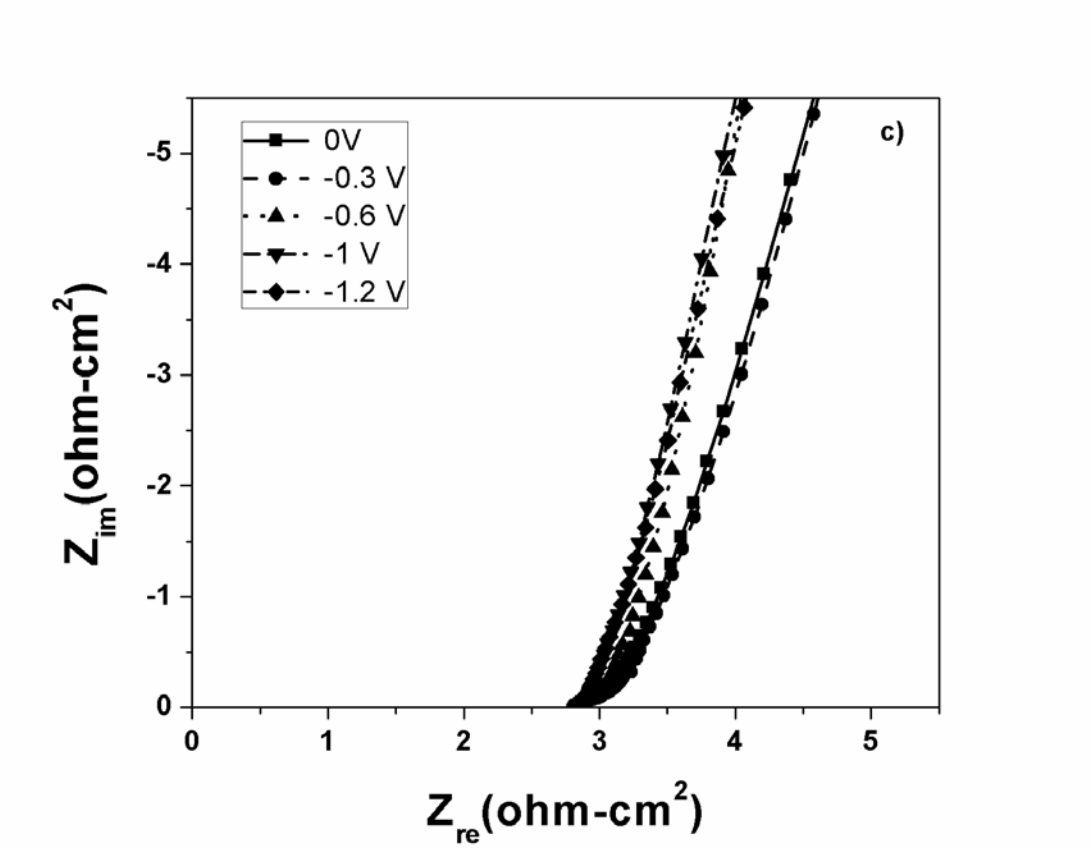
c)
0V
-0.3 V
-0.6 V
-1 V
-1.2 V
-5
-4
-3
-2
-1
0
0
1
2
3
4
5
Z_im (ohm-cm^2)
Z_re (ohm-cm^2)

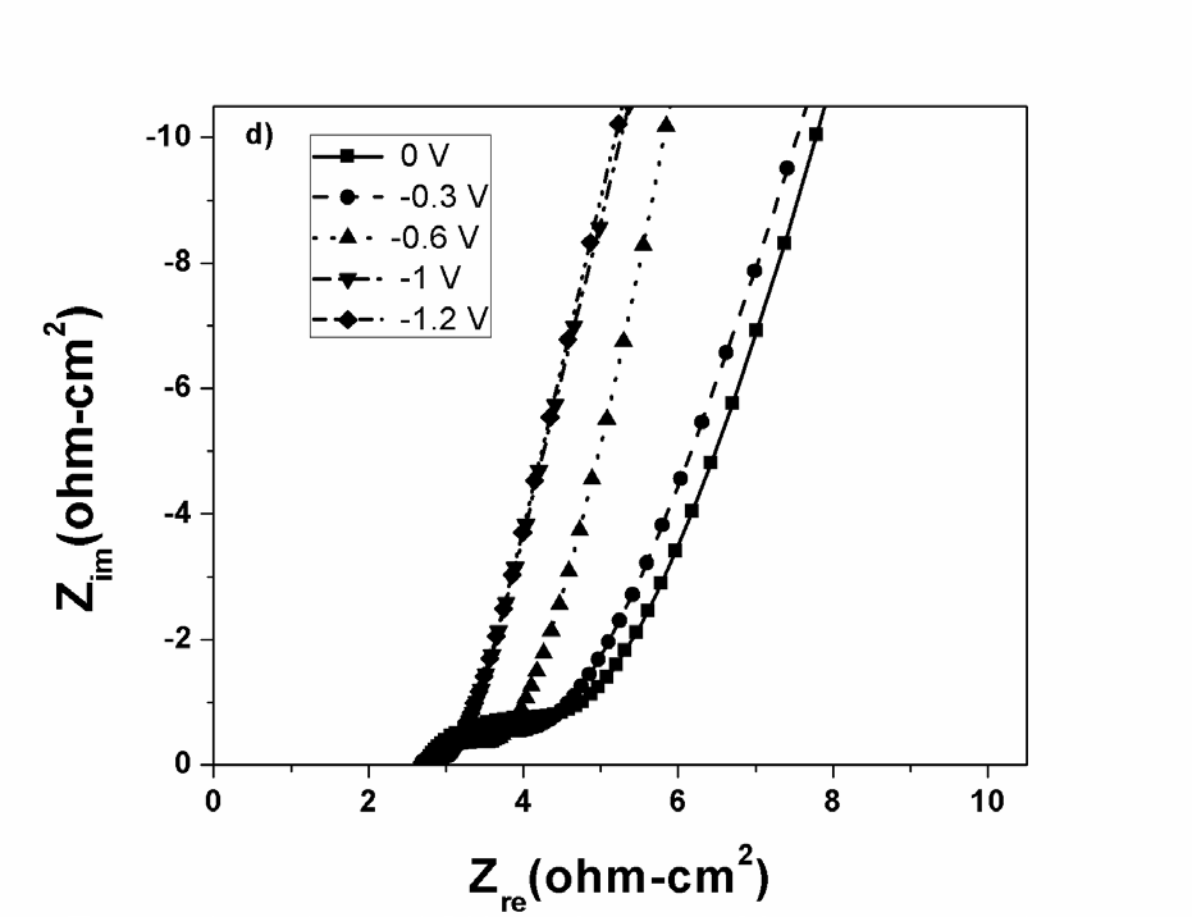

Figure 34. Nyquist plots of mechano-chemically synthesized VN electrodes (active material loading~0.25 mg/cm^2) at different potentials of interest (a) before cycling (100 kHz-0.01 Hz) (b) after 200 cycles at 100mV/s (100 kHz-0.01 Hz)(c) high frequency range before cycling (100 kHz-2.5 Hz) (d) higher frequency range after 200 cycles at 100 mV/s (100 kHz-2.5 Hz). (c) and (d) are zoomed in plots of (a) and (b) corresponding to the high frequency region.

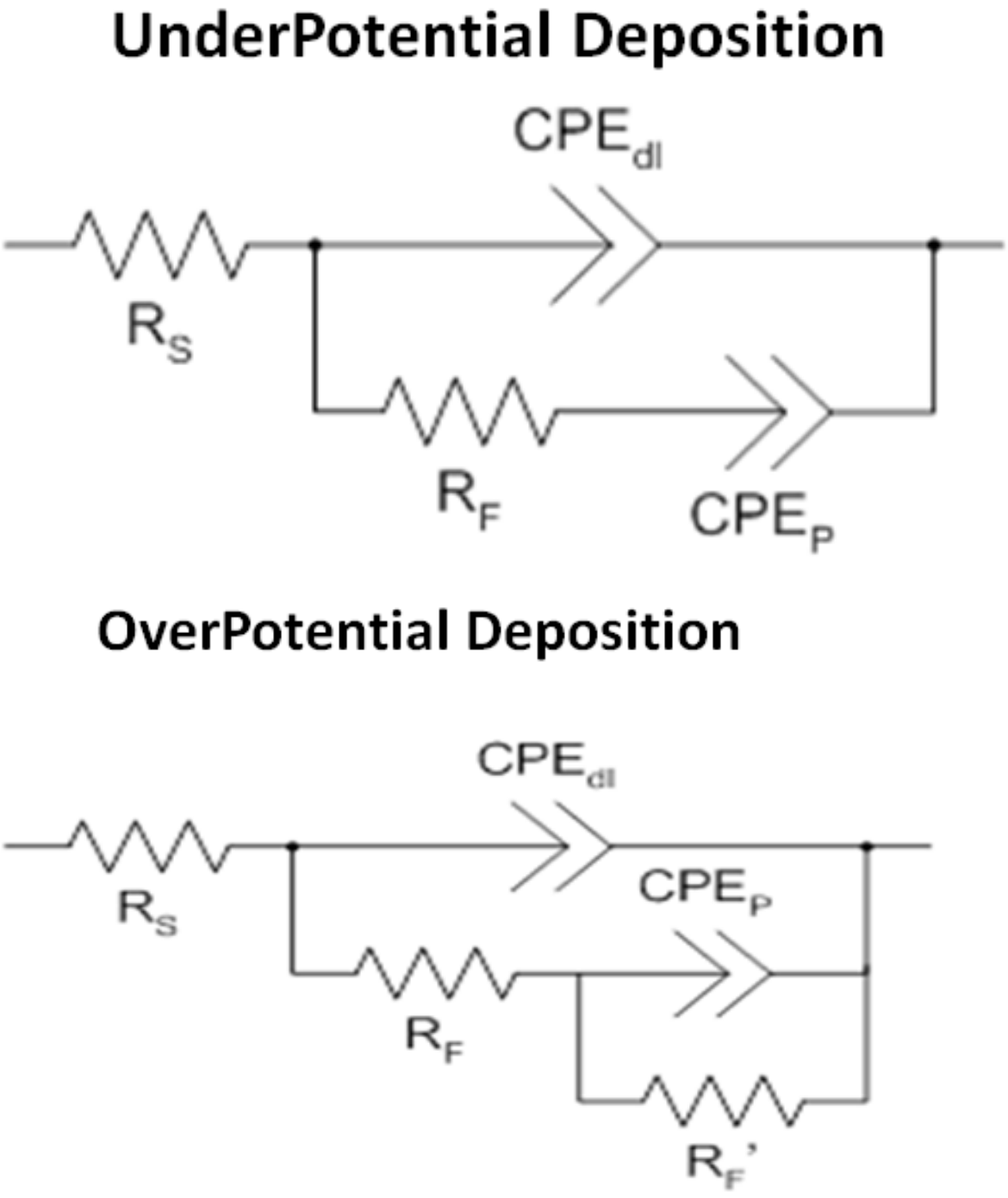

Figure 35. UPD and OPD models used for impedance analysis.

Table 12. Electrochemical impedance parameters of HEMM derived VN obtained before electrochemical cycling following fitting of the experimental data to the equivalent circuits.

Voltage (V)	R_s(Ω-cm^2)	R_F(Ω-cm^2)	R_F'(Ω-cm^2)	Relevant model	CPE-dl		CPE-p	
					T	Φ	T	φ
0	2.89	0.26		Upd	1.05E-03	0.94	1.76E-02	0.75
-0.3	2.88	0.23		Upd	1.26E-03	0.93	3.69E-02	0.72
-0.6	2.86	0.14		Upd	1.20E-03	0.99	4.66E-02	0.77
-1.0	2.83	0.14		Upd	5.21E-03	0.90	2.42E-02	0.83
-1.2	2.86	3.13	731.80	Opd	8.80E-03	0.93	5.62E-03	0.91

Table 13. Electrochemical impedance parameters of HEMM derived VN obtained after electrochemical cycling following fitting of the experimental data to the equivalent circuits.

Voltage (V)	R_s(Ω-cm^2)	R_F(Ω-cm^2)	R_F'(Ω-cm^2)	Relevant model	CPE-DL		CPE-P	
					T	Φ	T	φ
0	2.74	2.02		Upd	8.83E-04	0.78	1.85E-02	0.71
-0.3	2.71	1.60		Upd	1.29E-03	0.76	3.31E-02	0.71
-0.6	2.70	1.13		Upd	3.67E-03	0.72	3.78E-02	0.80
-1.0	2.71	0.51		Upd	5.16E-03	0.75	2.58E-02	0.85
-1.2	2.79	0.67	742.20	Opd	2.16E-03	0.91	1.19E-02	0.92

Table 12 and **Table 13** show the charge transfer parameters obtained by fitting the equivalent circuits to the experimental data in **Figure 34a** and **Figure 34b**. It can be seen that the series resistance (R_s) varies between 2.5 and 3 Ω which is close to values reported for most porous electrodes[361]. It can also be clearly observed that both double layer and pseudocapacitor type behavior are exhibited by VN prepared by the mechano-chemical reaction. The presence of Faradaic pseudocapacitance type behavior is confirmed by the observed decrease in charge transfer resistance (R_F) seen in **Table 12** and **Table 13**. Electrochemical Faradaic charge transfer processes are voltage activated as previously indicated resulting in this trend. The values of charge transfer resistance obtained however, are very small compared to that of nanocrystalline VN synthesized by ammonolysis of VCl_4 reported previously on account of the crystalline nature of the nitride formed [235]. The low values of series resistance and charge transfer resistance indicate a highly conductive material corroborated by the four probe conductivity data seen in **Table 11** as well.

The increased electronic conductivity of the HEMM derived VN results in high rate capability as observed and shown in **Figure 31a**. Though the VN made by mechano-chemical reduction is pseudocapacitative in nature as indicated by the cyclic voltammogram in **Figure 30a** and the impedance data in **Table 12** and **Table 13**, the overall capacitance is lower than that of nanoparticulate VN[182] on account of both the reduced available surface area and surface oxidation state of vanadium oxide exo-shell present on the VN. The slight increase in Faradaic charge transfer resistance observed after cycling (see **Table 12** and **Table 13**) can possibly be attributed to particle coarsening and resulting decrease in conductivity. As the change is within ~1-3 ohms-cm^2 of the uncycled sample, it can be understood that this effect is not playing a

major role in loss of capacity. This is corroborated by the evident stability in capacity seen in **Figure 32c**.

In addition to the low values of R_F, the electrochemical resistance to water electrolysis indicated by the values of R_F' are very large before and after cycling indicating that the activation of electrolysis reaction is very sluggish on this particular electrode material over the voltage window of (-1 to -1.2 V with respect to Hg/HgO). This large activation over-potential for electrolysis indicates that the material can be used for charge storage up to -1.2 V with respect to Hg/HgO even though the thermodynamic onset potential for water electrolysis at pH 14 of KOH is -1.04 V. This phenomenon results in the overestimation of capacity calculated from charge-discharge analysis (**Figure 32a**) and the fade in capacity seen in **Figure 32b**. It does not however have any adverse effect on the electrochemical stability of the material as seen in **Figure 32c**. It can thus be concluded from the electrochemical impedance analysis that the VN synthesized by the novel and simple mechano-chemical reduction reaction exhibits both Faradiac and non-Faradaic double layer charge storage mechanisms. It has also been established that the VN has relatively high conductivity which results in improved rate capability of the material as confirmed by the cycling results thus validating the efficacy of the VN generated by this simple low temperature highly scalable approach.

4.1.4 Electronic conductivity and diffusion effects-Fade in capacitance with increased scan rate/Capacitance drops in thick electrodes

It is clear from **Figure 23a** and **Figure 23b** and previous reports on vanadium nitride[246] that loading dependence of capacitance is very much material specific and is dependent on the materials properties displayed in **Table 9**. In order to further understand the dependence of

capacitance on loading and to understand the mechanistic factors leading to the same, electrochemical impedance analysis was performed on VN electrodes (two-step ammonlysis VN) for the different loadings, the results of which are displayed in **Figure 36a** and discussed below.

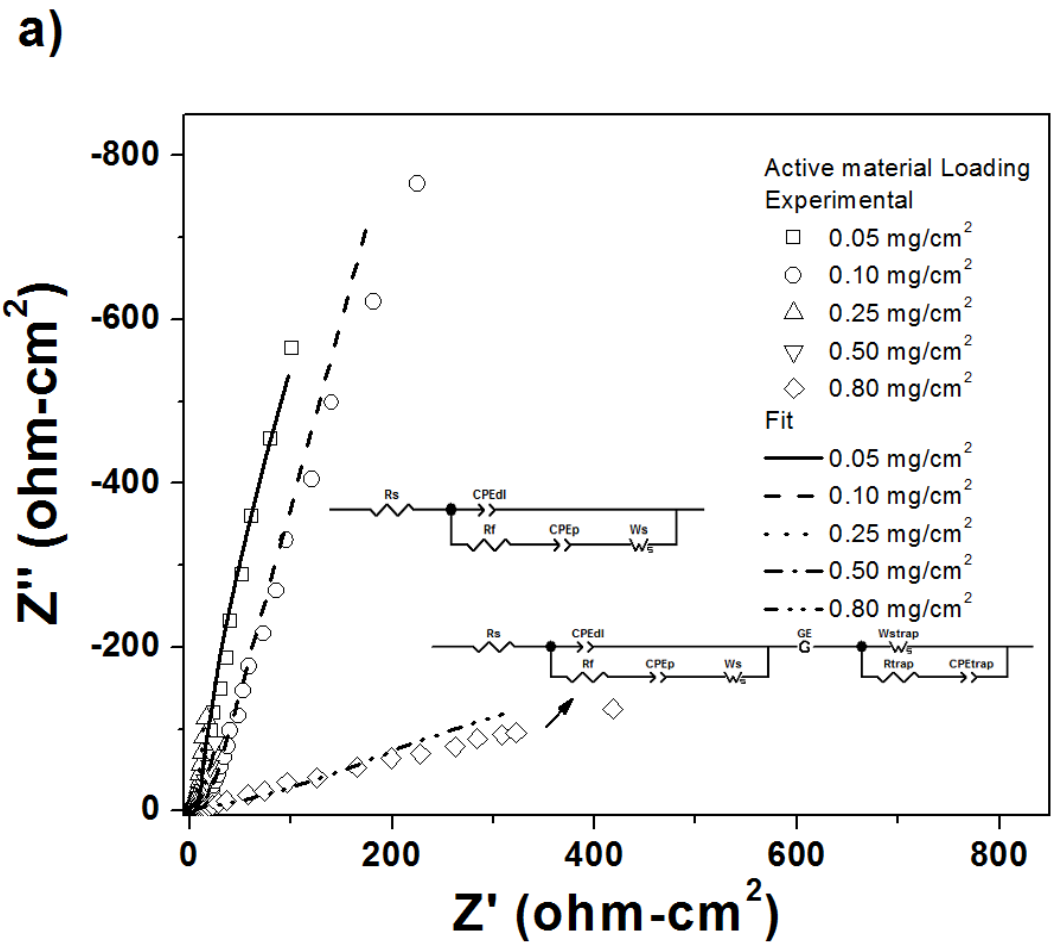

b)

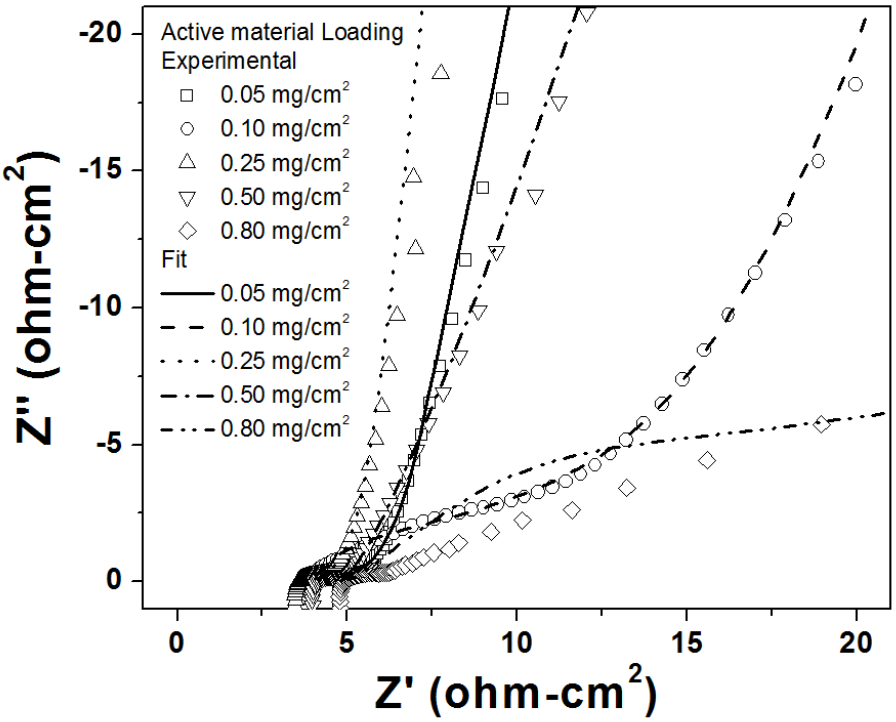
Active material Loading
Experimental
0.05 mg/cm2
0.10 mg/cm2
0.25 mg/cm2
0.50 mg/cm2
0.80 mg/cm2
Fit
0.05 mg/cm2
0.10 mg/cm2
0.25 mg/cm2
0.50 mg/cm2
0.80 mg/cm2
Z'' (ohm-cm2)
Z' (ohm-cm2)
-20
-15
-10
-5
0
0
5
10
15
20

c)

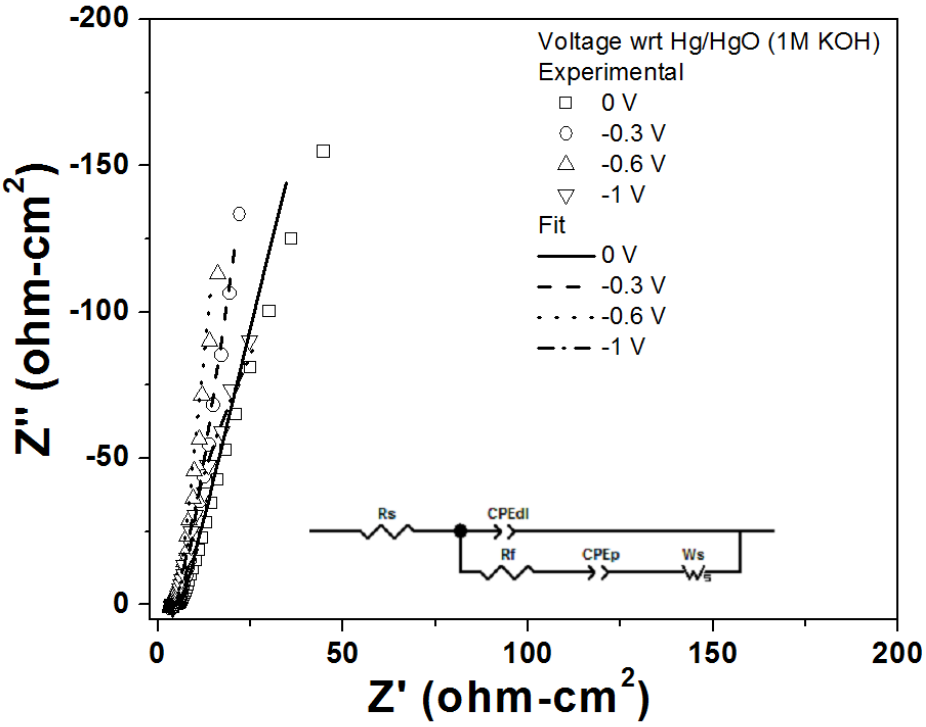
Voltage wrt Hg/HgO (1M KOH)
Experimental
0 V
-0.3 V
-0.6 V
-1 V
Fit
0 V
-0.3 V
-0.6 V
-1 V
Rs
CPEdl
Rf
CPEp
Ws
Z'' (ohm-cm2)
Z' (ohm-cm2)
-200
-150
-100
-50
0
0
50
100
150
200

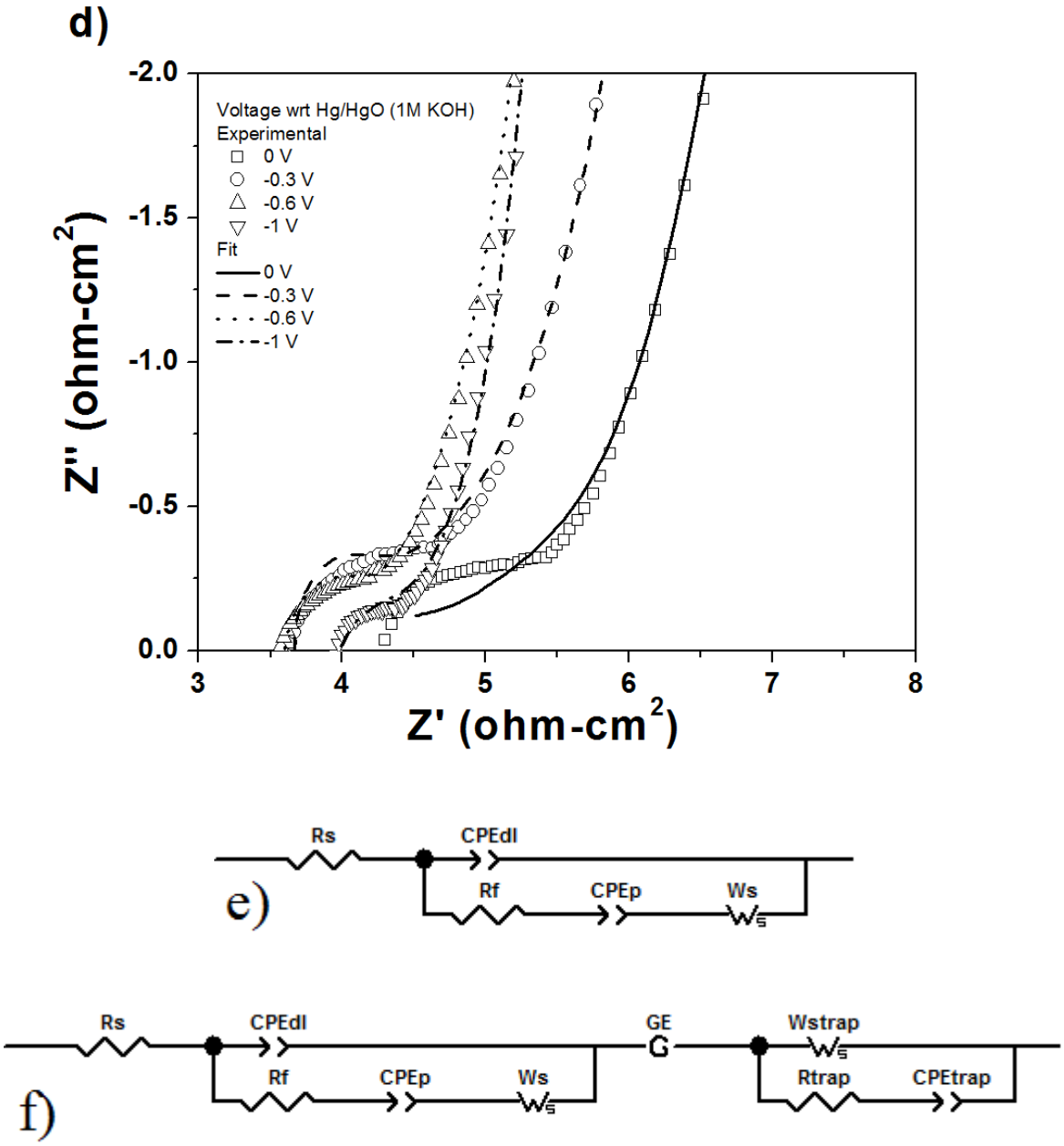

Figure 36. Nyquist plots of [(a) and (b)] ammonolysis derived VN electrodes of different loadings at a bias of -0.6 V wrt Hg/HgO (in 1M KOH) [(c) and (d)] ammonolysis derived VN at different voltages of relevance (active material loading ~ 0.25 mg/cm^2). Plots (b) and (d) are magnified versions of (a) and (c) showing the high-frequency semi-circle. (e) Modifed underpotential deposition model used for equivalent cicuit modeling of electrodes with lower active material loading (f) Trapping based model used for modeling of electrodes with high active material loadings showing mas-transfer effects and charge-trapping.

Figure 36a and Figure 36b show the EIS spectra of ammonolysis derived VN electrodes for different loadings at a bias of -0.6 V wrt Hg/HgO (in 1M KOH). The potential was chosen since it lies closest to the most significant charge transfer reaction as evidenced by **Figure 22a**. The EIS spectra are characteristic of most capacitor materials with a fairly small and constant series resistance, double layer capacitance, pseudocapacitance and charge transfer resistance. The circuit model used for equivalent circuit analysis is seen as an inset in **Figure 36a**. In addition to the elements of underpotential deposition (UPD) most commonly observed in aqueous pseudocapacitor systems[58], a Warburg element (W_s) was also used to account for the mass transfer effects. **Figure 36a** shows the impedance behavior of electrodes of varying thickness (represented as materials loading). A marked change in impedance characteristics is observed when the loading is increased. Electrodes with very low loadings (<0.1 mg/cm^2) exhibit an almost vertical capacitor type characteristic with very small charge transfer resistance. This characteristic can be attributed to the expected low resistance to electron flow and ionic species flow occurring in thin electrodes. Such a low resistance results in superior charge storage characteristics as reflected in **Figure 23a**. As the loading increases, a change in character is observed as a result of the increase in charge transfer resistance (**Table 14**). This increase in charge transfer resistance results in the decrease in over all capacitance with loading as clearly shown in **Figure 23a**. The effect is most significant in very thick electrodes (0.80 mg/cm^2) where mass transport and electrode resistance is seen to effect most predominantly, and it is no longer possible to use the simple UPD model for a phenomenological explanation of the behavior. The thick electrodes resemble an intercalation type behavior with strong diffusion effects.

Table 14. Charge transfer parameters of ammonlysis derived VN electrodes of different loadings derived by Randall circuit modeling using Z-view 2 (Scribner Associates Inc.) at a bias of -0.6 V wrt Hg/HgO (in 1M KOH).

Active material loading (mg/cm^2)	R_s(Ω-cm^2)	R_f(Ω-cm^2)	CPE_{dl}		CPE_p		W_s			GE		W_{s-trap}			R_{trap}(Ω-cm^2)	CPE_{trap}	
			T ($*10^{-4}$)	Φ	T($*10^{-2}$)	Φ	R	T	Φ	T	Φ	R	T	Φ		T	Φ
0.05	4.68	2.50E-8	8.28	0.68	2.35	0.94	4.28	1.14	0.26								
0.10	4.02	2.92E-7	1.46	0.85	1.47	0.86	15.96	0.23	0.22								
0.25	3.60	0.404	1.73	0.85	12.67	0.95	1.81	0.84	0.28								
0.50	4.18	0.531	2.45	0.96	12.90	0.85	3.40	6.35	0.33								
0.80	3.52	0.608	49.46	0.23	36.51	0.09	2826	7.79	2.12	0.17	0.07	0.007	1	1	0.017	0.453	4.30

Table 15.Charge transfer parameters of ammonlysis derived VN electrodes at various voltages where Faradaic reactions are predominant (active material loading ~ 0.25 mg/cm^2).

Voltage (vs. Hg/HgO (in 1M KOH)	R_s(Ω-cm^2)	R_f(Ω-cm^2)	CPE_{dl}		CPE_p			W_s	
			T (*10^{-4})	Φ	T	Φ	R	T	Φ
0	4.32	1.19E-10	16.3	0.85	7.76E-02	0.88	2.83	4.33E-01	0.18
-0.3	3.67	4.72E-07	67.5	1.10	1.03E-01	0.93	4.10	3.99E+00	0.20
-0.6	3.60	0.404	17.33	0.85	1.27E-01	0.95	1.81	8.41E-01	0.28
-1	4.02	0.050	129.06	0.71	1.22E-01	0.91	0.82	1.39E-18	0.58

It is also possible to model the characteristic of the electrode using a Warburg and Gerischer impedance model similar to that used by Levi et al. to model magnesium ion charge storage in Chevrel phase molybdenum sulfide[362]. The use of the Gerischer impedance element (GE) is usually undertaken when there is a coupled chemical reaction along with an electrochemical reaction. **Table 14** shows the values of GE and though the contribution to impedance is not significant, it could shed light on the co-existing dissolution reaction in the ammonolysis derived VN. The effect while not present in thinner electrodes may possibly be occurring to a large extent in the thick electrodes as result of local pH changes being significant in the thicker electrodes. It is well known that vanadium oxide species can dissolve in aqueous media at very strongly basic or acidic pH[337]. Local pH changes occurring in macroscopic pores which might act as traps for ions could result in chemical dissolution occurring in tandem with electrochemical processes. In addition to the Gerischer element, ion trapping effects and charge-trapping mechanisms were also considered. Such an inclusion is based on consideration that the characteristic is similar to that observed as a result of charge-trapping in thiophene based systems and magnesium intercalation systems[362, 363]. The chemical origin of the same is not completely clear and further studies are warranted to achieve a complete understanding of the same. The change in electrochemical characteristic (especially a change in slope at low frequencies) when going from thin electrodes to thick electrodes has previously been observed and attributed to bulk electronic conductivity in addition to self-discharge processes[364, 365]. It is clear in the present case that the ammonlysis derived VN material suffers from poor electronic conductivity (see **Table 9**) which is amplified when thick electrodes of the same are prepared. Increase in mass transfer effects with increase in loading is a result of the inability of thicker electrodes to provide easy access to ions which travel to surface sites present in fine nanoparticles. The corresponding

increase in electrode resistance is a result of the poor electronic conductivity of the fine nanoparticles of VN formed by the two step ammonlysis which result in extended grain boundary regions. Such a phenomenon results in the poor capacitance retention with increase in scan rate and active material loading seen in **Figure 23a**. **Table 14** tabulates the vales of the various charge transfer parameters corresponding to **Figure 36a** and **Figure 36b**. **Figure 36b** is a magnified image of **Figure 36a** showing the characteristic high frequency semi-circle corresponding to the underpotential deposition like characteristic of the various electrodes made of ammonlysis derived VN.

Figure 36c, **Figure 36d** and **Table 15** demonstrate the Nyquist plot of ammonlysis derived VN at various potentials with respect to the Hg/HgO (in 1M KOH) reference electrode. The aim of this plot is to examine charge-storage behavior occurring at various potentials at a constant loading. Loading of ~0.25 mg/cm^2 was chosen since it was representative of a mediocre loading range seen in **Figure 36a**. The charge transfer characteristics are not seen to be significantly different barring the fact that charge transfer resistance and pseudocapacitance vary with potential. It can be seen that charge transfer and pseudocapacitance behavior is pronounced at -0.3 V, -0.6 V and -1 V as compared to 0 V. This is because the three predominant Faradaic reactions of surface vanadium oxide occur at these potentials with respect to Hg/HgO (in 1M KOH) as detailed in our previous reports[182, 235, 246]. These three reactions correspond to the transformation of vanadium from a +5 oxidation state to a ~+2 oxidation state. The occurrence of pseudocapacitance at -0.3 V is in contrast with the behavior of mechanochemically derived VN previously reported earlier by the Kumtagroup[246]. This characteristic of the ammonlysis derived VN possibly results in its poor fade characteristic as seen in **Figure 24**. It can be observed that there is a rapid fade in capacity over 30 cycles following which the capacity becomes stable.

This fade in capacity is believed to be the result of change of surface oxidation state i.e. instability of higher oxidation state vanadium in the very highly basic 1M KOH electrolyte (pH~14). This characteristic might be partially responsible for the presence of mass transfer effects seen in the impedance characteristic in **Figure 36a-Figure 36d**. The need of a Warburg diffusion characteristic was not necessary to model impedance characteristic of mechanochemically derived VN (see Ref. [246]). It is also possible that the Warburg element might have been necessitated by the simple fact that the particles of ammonlysis derived VN are much smaller, resulting in finer pores and associated mass-transfer effects. It is believed that the fade characteristic arising in **Figure 24** is partially responsible for the complicated impedance behavior observed in the thick electrodes seen in **Figure 36a**. Ion trapping and concentration changes associated with fade-reactions could possibly be a factor contributing to the reason for sluggish pronounced diffusion effects seen in thick electrodes. Another possible reason for the enhanced fade characteristics of the ammonlysis derived VN is the strain associated with surface phase change at such small nanoparticles. It is possible that the strain generated in surface pseudocapacitance reactions might result in irreversible detachment of the oxide layer from the nitride core resulting in a rapid reduction in capacity. It is however, more likely that the dissolution process has a greater dependence on surface composition as elucidated in the previous works reported by Choi et al.[182, 246] and by the fact that improvement in capacity retention has previously been observed in ammonlysis derived VN by shortening of the test window upto -0.3 V and also lowering the pH[182].

Table 16. Materials properties and their effect on capacitance behavior in different VN materials.

Material property	**Surface area**	**Crystallinity**	**Electronic conductivity**	**Surface oxide composition**
Synthesis method				
Two-step ammonlyis	High surface area resulting in high gravimetric capacitance	Nano-crystalline resulting in poor electronic conductivity and high surface area	Poor electronic conductivity resulting in poor rate capability	+5 surface oxide resulting in rapid fade
Mechano-chemical reduction	Mediocre surface area resulting in average gravimetric capacitance	Large nano-crystals resulting in higher electronic conductivity but less surface area	Improved electronic conductivity and superior rate capability. Low loading dependence resulting in high areal capacitance	+3/+4 surface oxide with improved stability

Table 16 (continued)

Commercial VN	Poor surface area resulting in poor capacitance	Very crystalline material i.e. low surface area	N/A	N/A
Commercial VN-milling	Milling improves surface area causing higher capacitance	Large nano-crystals with milling decreasing crystallinity	High electronic conductivity	N/A

Due to the complexities addressed above in the chemically synthesized material, the introduction of a simple, inexpensive synthesis procedure for producing nanomaterial transition metal nitrides is therefore currently one of the aims of the current work. Even though the nitride thus derived does not result in high capacitive charge storage, it is hoped that this work will be the harbinger for further studies into the development of low cost milled nitride materials with high capacitance behavior. The current work also provides an insight into the materials properties required to attain superior charge storage in nitride nanomaterials, i.e. crystallinity, surface area and surface oxidation state. **Table 16** shows the nature of the three nitride materials and the effect of this on capacitance behavior in various nityride materials. The capacitance values of ~1340 F/g reported by Choi et al. are at very low loadings. However, at high loadings of ~1 mg/cm^2, the capacitance of the milled nitride albeit a third of that of that reported by Choi et al. however results in excellent areal capacitance (see **Figure 25**).

4.1.5 Conclusions

An in-depth study into the capacitor behavior of vanadium nitride has been undertaken. Three different materials were compared and contrasted to highlight the effect of particle properties and electrode properties on nitride capacitance. The study has shown that nitride capacitance is directly proportional to surface area and inversely proportional to particle size. However very fine nanoparticles (~6nm) of vanadium nitride end up being rate limited on account of poor electronic conductivity. In addition, the capacitance behavior of ultra-fine nanoparticles of vanadium nitride has been shown to depend very much on electrode loading. Very thin films exhibit very high gravimetric charge storage on account of ease of electron conduction and ion accessibility into pores. However, thicker films end up being limited in their charge storage capability on account of the same. The cycling stability of vanadium nitride has also been shown to depend on particle size reflected as a possible difference in surface oxidation state. In conclusion, vanadium nitride has been shown to be a material of great promise for commercial capacitors though further studies are needed to understand surface properties and their effect on stability.

Mechano-chemically derived vanadium nitride has been synthesized and shown to have promising capacitance in the range of 25 to 60 F/g. Though the capacitance values are lower than those reported for chemically synthesized nanoparticulate VN, the ease of synthesis involved in milling induced mechano-chemical reduction, and an almost 5 minute preparation time makes mechanochemical reduction a very attractive method for large scale bulk synthesis of various nitrides. The study has also shown the effect of various materials parameters on VN capacitance. Importance of the reduced crystallite size and high surface area are highlighted in the study (**Table 16**). In addition, the nature of the surface oxide has been identified to be vital for

pseudocapacitance response of VN. It has also been identified that the presence of V_2O_5 in the chemically derived nano-particulate nitride previously reported by Choi *et. al.*, though leading to a presumable increase in capacitance is detrimental to the cycling stability of the nitride. Vanadium nitride synthesized by mechanochemical reaction however exhibits excellent cycling characteristics on account of the absence of the vanadium +5 oxidation-state surface oxide. Furthermore, it has been shown by various characterization techniques that VN derived by the mechanochemical synthesis has larger crystallites leading to better electronic conductivity, lower charge transfer resistance and thus better rate capability and cyclability as compared to chemically synthesized nanoparticulate VN. The combination of facile low-cost synthesis, good rate capability, cycling stability and excellent volumetric capacitance (**see Figure 25**) makes VN synthesized by mechano-chemical reduction a very attractive supercapacitor material amenable for scale-up and large scale industrial production. The issue of poor electronic conductivity of nanostructured VN, as outlined here which is vital is a topic that has been addressed in **Section 4.4**.

4.2 VANADIUM OXIDE CAPACITORS

Figure 37a shows the scanning electron microscope image of vertically aligned CNTs deposited by chemical vapor deposition on Ni substrate. The length of each individual tube has been identified to be about 200 microns. It is expected that the prolific length of the CNTs would help create a very good 3-D architecture which could be covered with a thin layer of the oxide to maximize the volumetric loading while at the same time ensuring that a very thick film does not cover the carbon nanotubes thereby impeding the proper electronic transport channel.

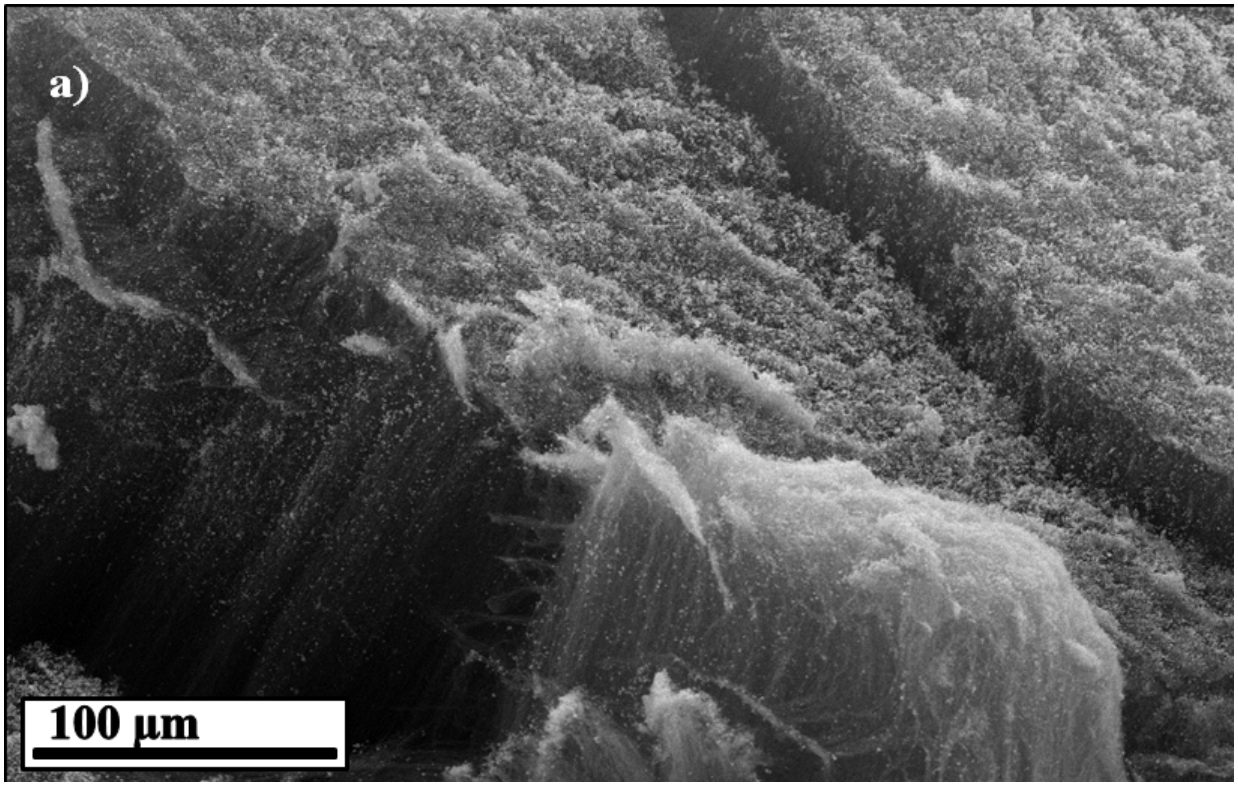

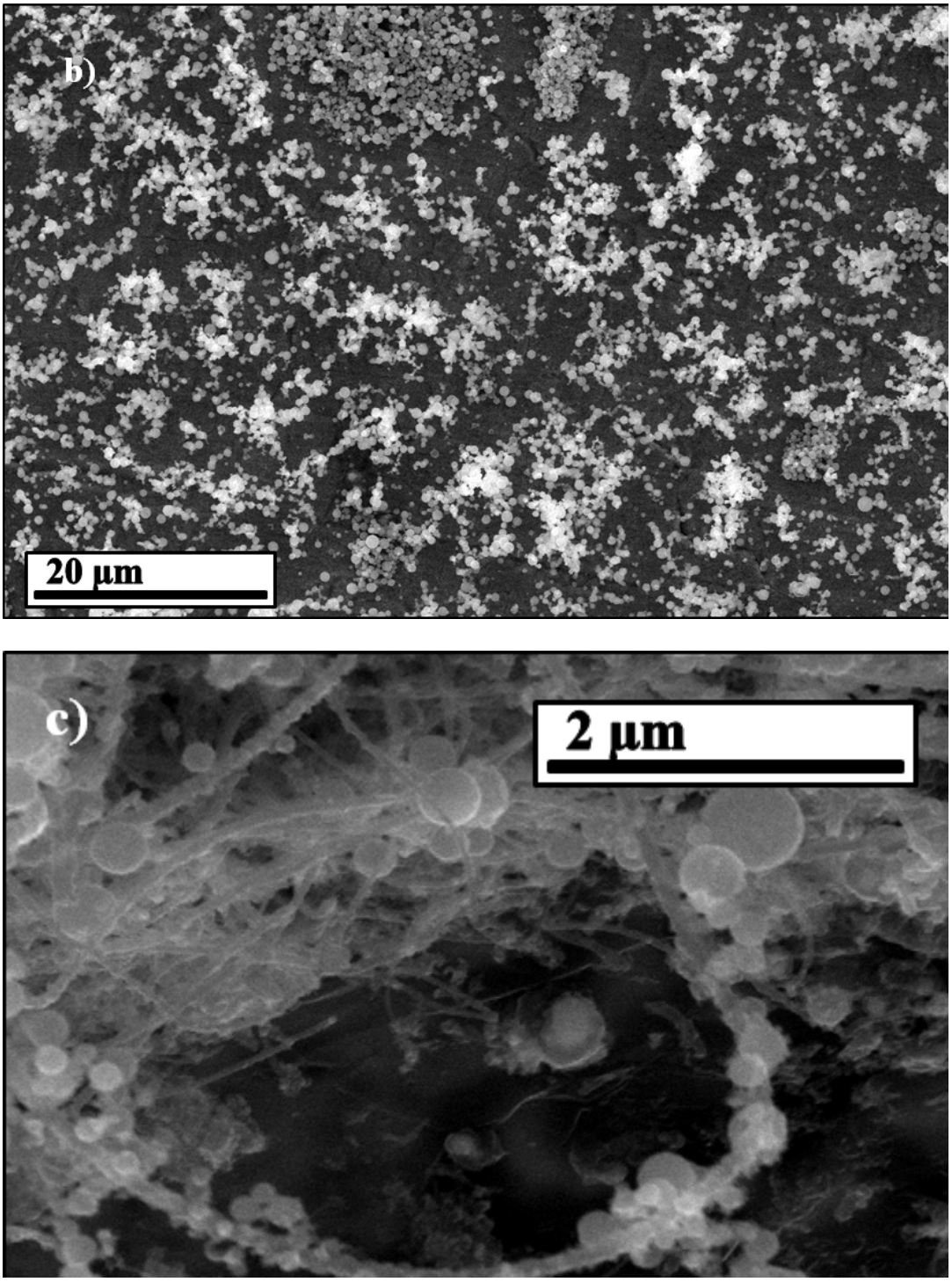

Figure 37. Scanning Electron Microscope images of (a) CVD derived Vertically Aligned Carbon nanotubes (b) CVD derived vanadium oxide thin film on Nickel substrate and (c) CVD deposited vanadium oxide-VACNT heterostructures.

The nature of the oxide film on Ni substrate can be seen in **Figure 37b.** It can be seen that the oxide is coated onto the nickel current collector in the form of a particle film of ~2 μm in thickness. **Figure 37c** shows the nature of the oxide deposited on the carbon nanotubes. From the figure it can be seen that the oxide deposited on the VACNTs is in the form of 0.2-0.5 micron diameter globules. The globules cover the length of the tube at regular spacing between each globule. This allows for maximum CNT-oxide electron transport minimizing electron transport through the oxide grain boundaries which naturally will act as a barrier to electron transport. The nanosphere morphology also leads to increased surface exposure of the oxide to the electrolyte i.e. maximizing the electrochemical surface area and thus affording maximum exploitation of the capacitance behavior.

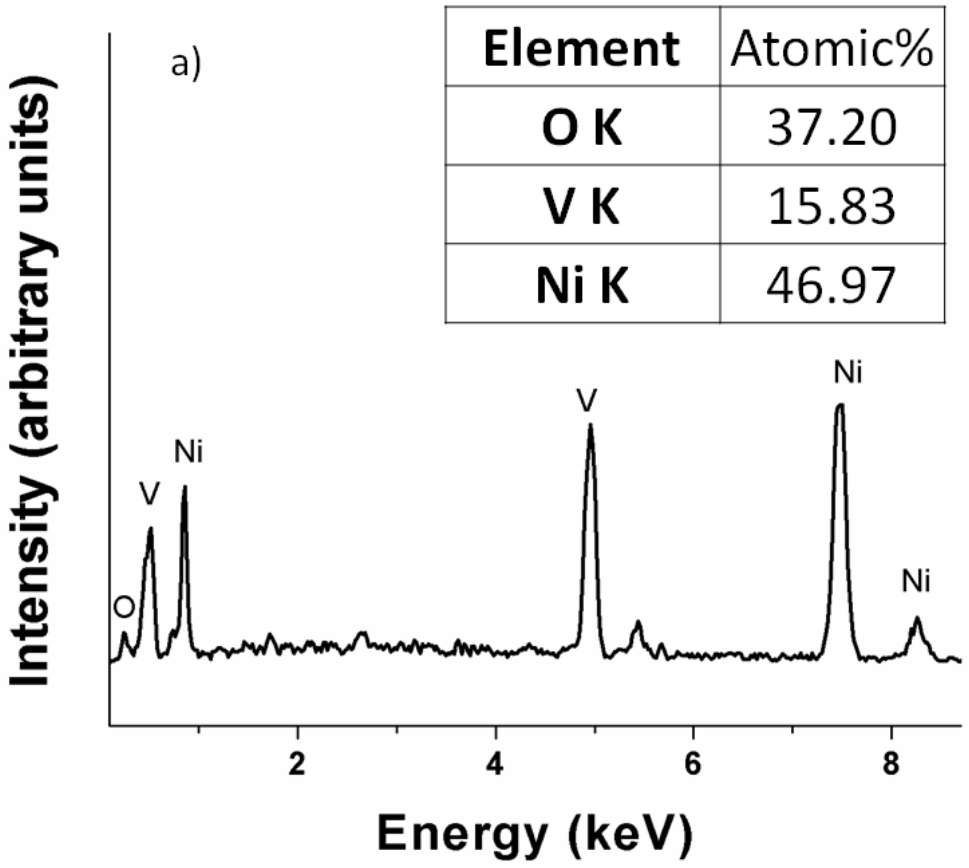
a)
Element
Atomic%
O K
37.20
V K
15.83
Ni K
46.97
Intensity (arbitrary units)
O
V
Ni
V
Ni
Ni
2
4
6
8
Energy (keV)

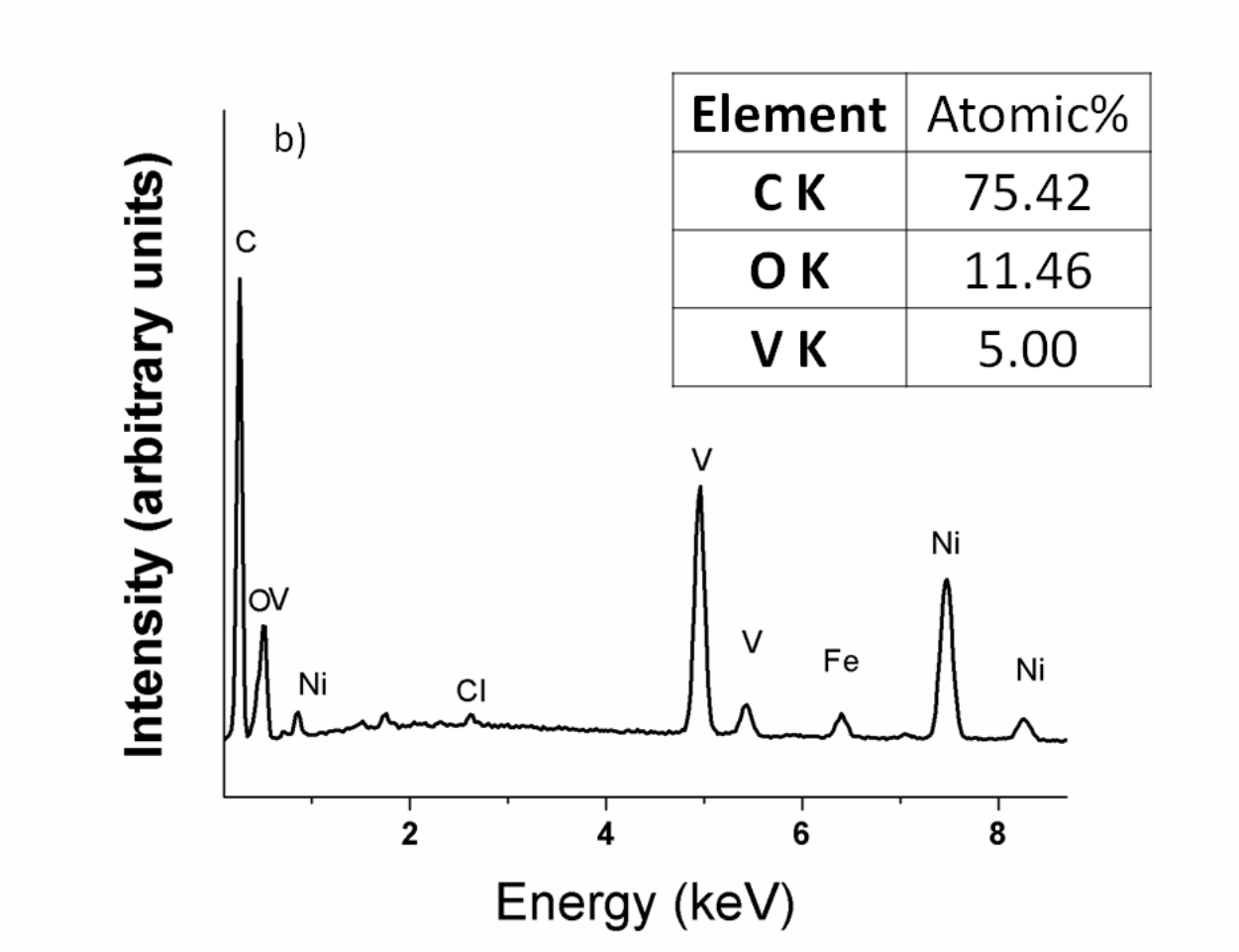

Element	Atomic%
C K	75.42
O K	11.46
V K	5.00

Figure 38. (a) EDAX spectra of the CVD deposited thin film on Nickel (b) EDAX spectra of CVD deposited -VACNT heterostructures

Figure 38a and **Figure 38b** show the EDAX analysis and the respective compositions of the oxide film deposited on Ni disk and the VACNT-oxide nanospheres, respectively. It can clearly be seen that the oxide has a composition of V_2O_{5-x} with x ~ 0.4 in both cases. This indicates that the moderately high temperature of 450^{o}C afforded by the CVD process allows for the synthesis of the oxide at its highest oxidation state with very few defects. A less defective structure at a higher oxidation state is ideal to achieve minimum electron conductivity losses with lower defects, and thus also contributing to better stability of the composition.

In order to confirm the composition and nature of the oxide deposited on the CNTs, Raman spectroscopic analysis was performed on the material. The Raman spectrum collected on the carbon nanotubes is shown in **Figure 39a**. The D, G and G' bands are clearly observed at 1250, 1650 and 2650 cm^{-1}, respectively. It is clearly observed that the G/D (I_g/I_d=1.59) ratio is much greater than one indicating few lattice defects in the graphene layers indicating the MWCNTs would have relatively high conductivity[366, 367]. **Figure 39b** shows the spectrum from 200 to 1000 cm^{-1} wavenumber range which has several peaks marked that have been identified to correspond closest to those of thin filmV_2O_5[368] and those of vanadium oxide corresponding to VO_x-carbon nanofibers reported previously[369].

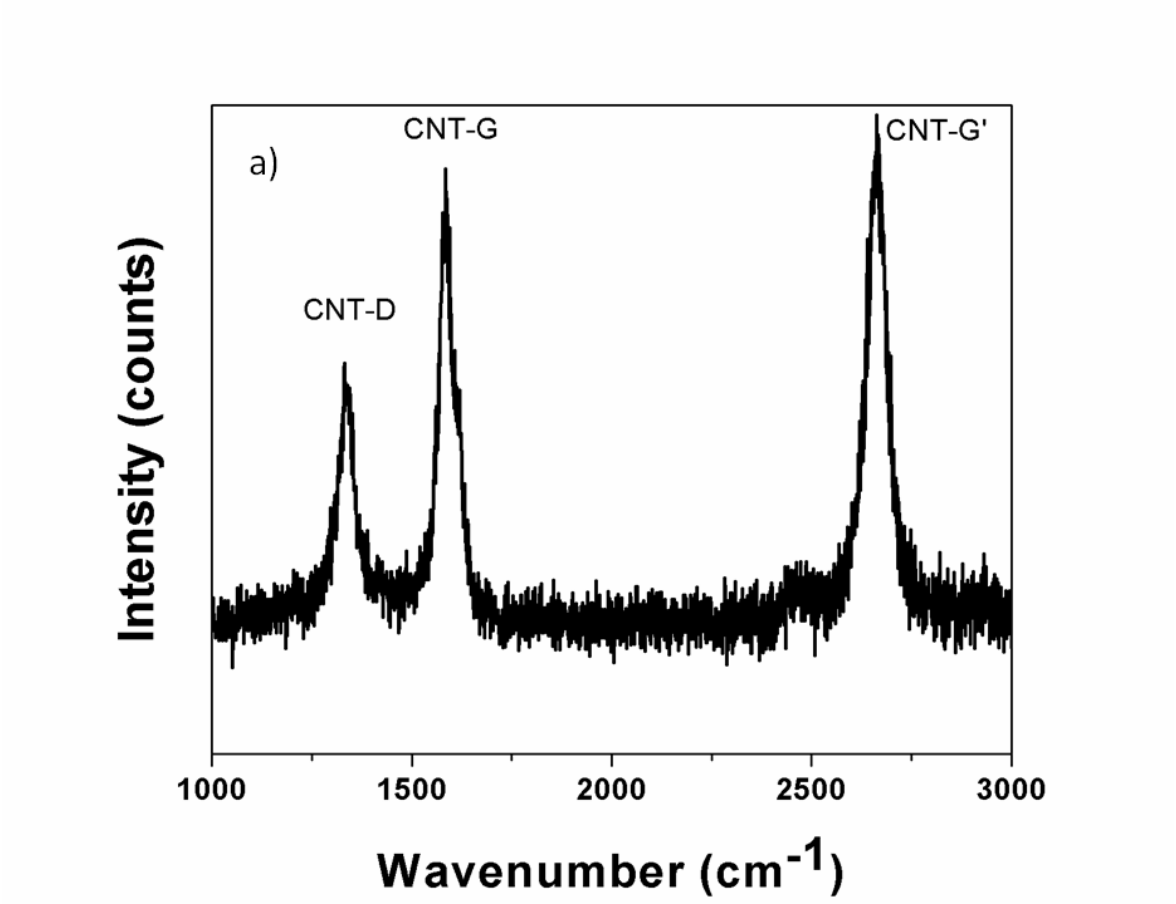

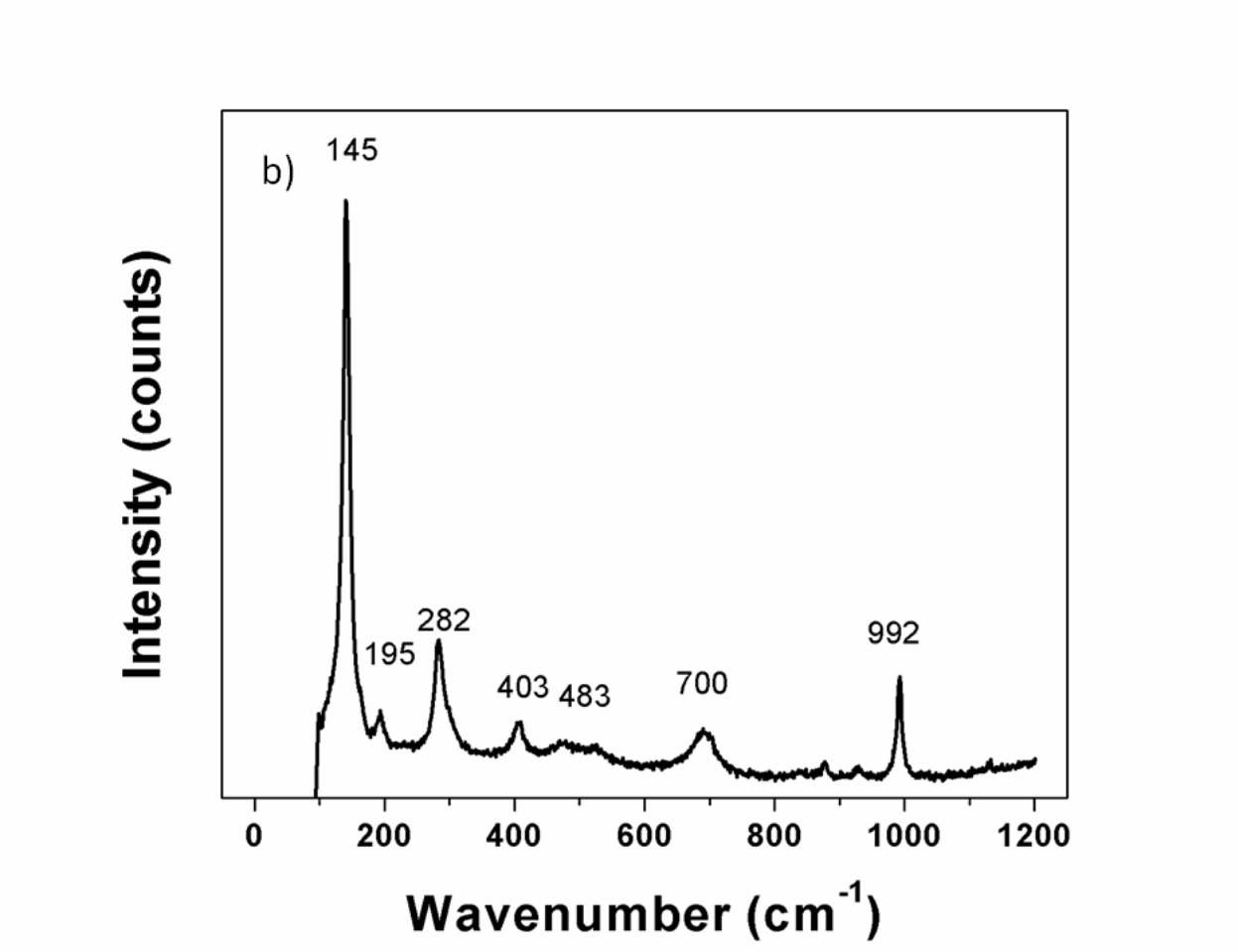

Figure 39. Raman spectra of (a) Vertically Aligned CNTs (VACNTs) and (b) Vanadium oxide coated on the CNTs.

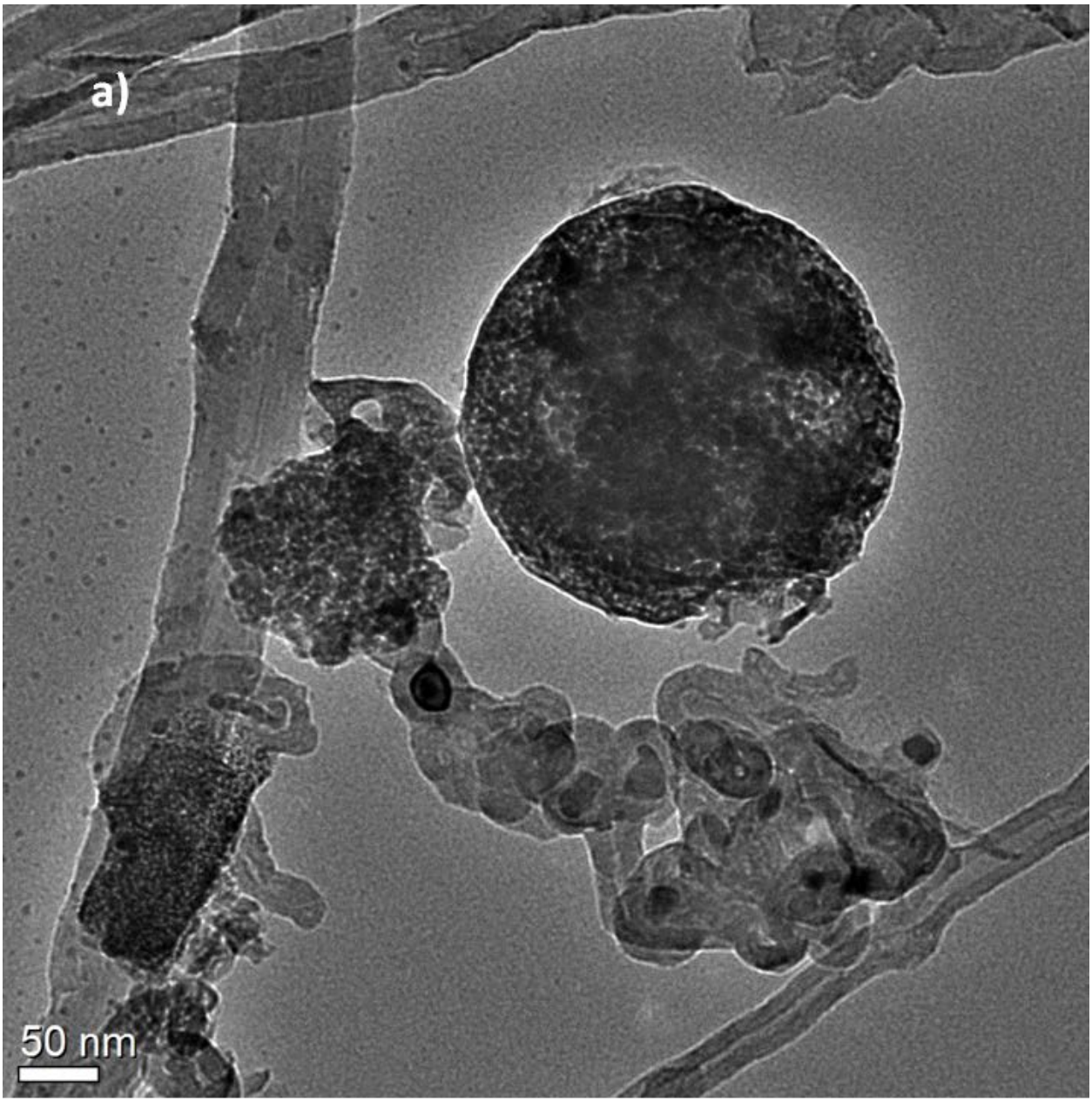
a)
50 nm

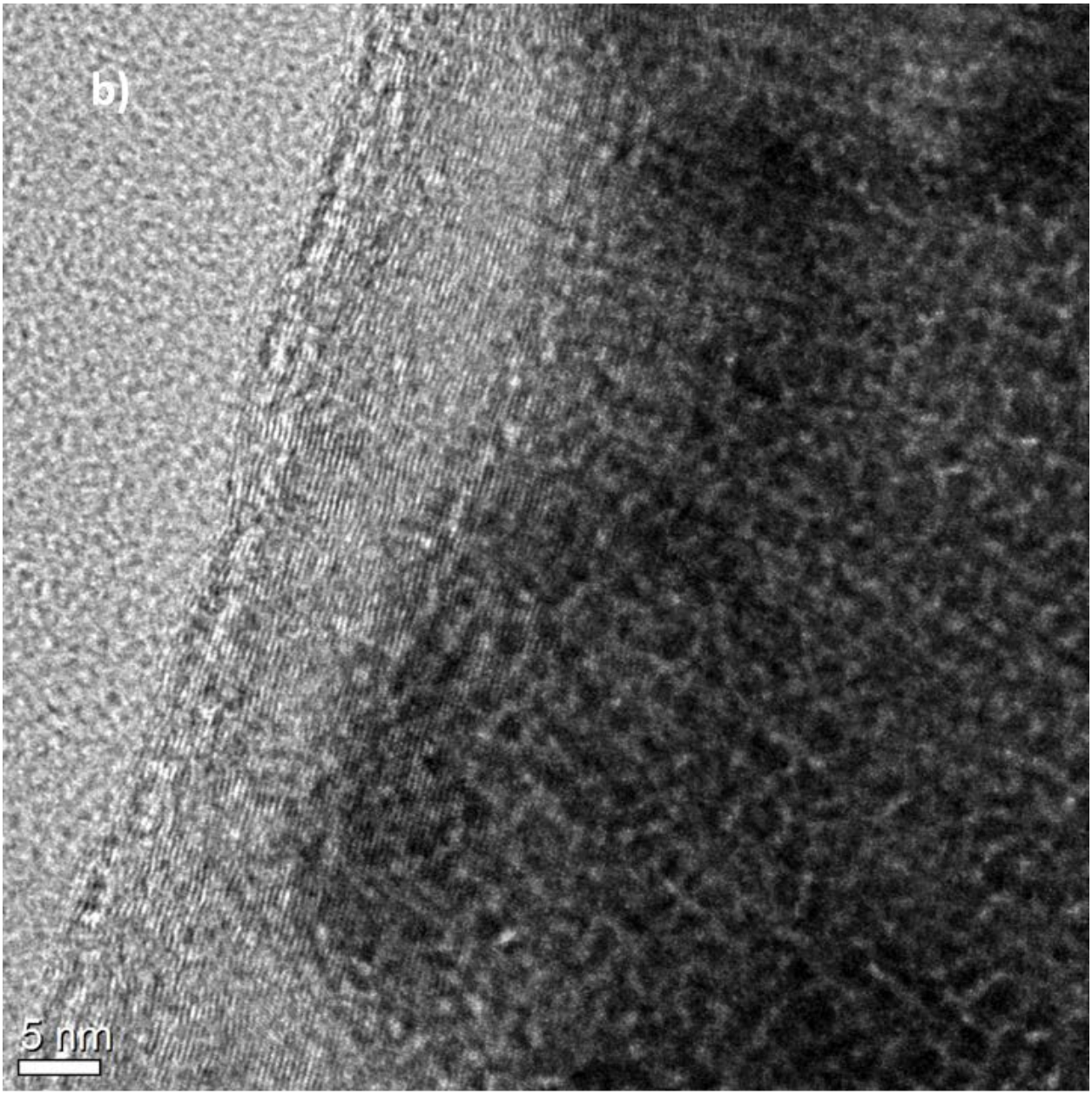

Figure 40. HRTEM images of the vanadium oxide nanospheres coated on Multiwall Carbon nanotubes.

In order to confirm the morphology of the nanospheres on the surface of the CNTs, high resolution transmission electron microscopy (HRTEM) was also performed on the samples that were scraped off and dispersed onto Cu grids. **Figure 40a** shows the image of a vanadium oxide

nanosphere covering a carbon nanotube. It can be seen that the diameter of the nanospheres is about 250 nm. Upon closer examination (**Figure 40b**), it can be seen that the oxide nanosphere has an amorphous morphology with no periodic arrangement. The interplanar separation between the CNT layers has been measured to be ~0.35 nm. This corresponds to the value reported for that of graphite (d002=0.35 nm) and multi wall CNTs of diameter 20 nm[370, 371].

The interface of the CNT and the oxide is an important factor that would determine the nature of the electron transport and stability of the oxide particle. On further observation of **Figure 41a** to **Figure 41d** and comparing with **Figure 40a**, the mechanism of growth of the oxide can be construed. **Figure 41a**-**Figure 41d** show the EDAX maps of the oxide coated on the carbon nanotubes. It can clearly be seen that the maps of both oxygen and vanadium are similar corresponding to superimposed regions of the nanospheres in **Figure 41a**. Chlorine though present in much lesser atomic percentages is more ubiquitous and is directly tethered to the CNTs. This indicates that the chloride precursor used in this reaction tethers to certain specific sites on the CNTs which in turn become nucleation sites for the formation and growth of the oxide. This theory is also supported by the TEM images which indicate the presence of a thin layer of the oxide on the CNTs over which the oxide spheres tend to develop.

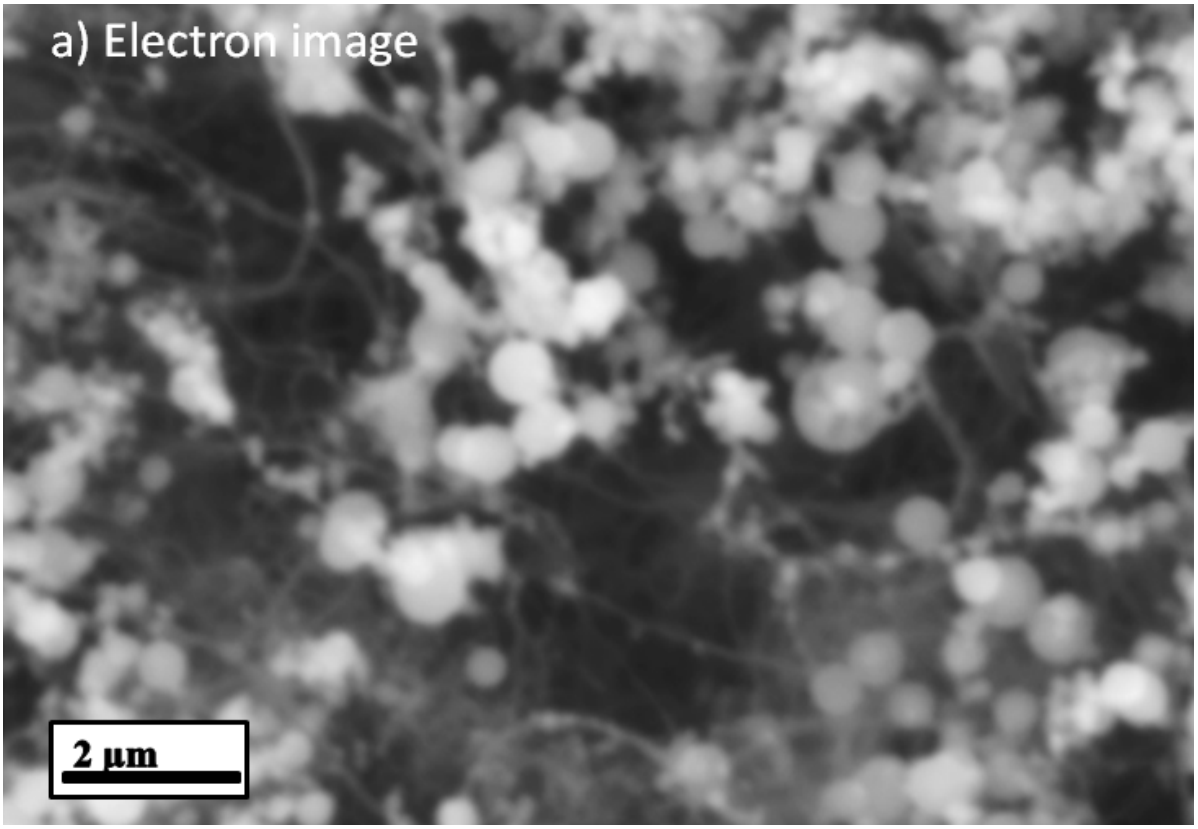
a) Electron image
2 µm

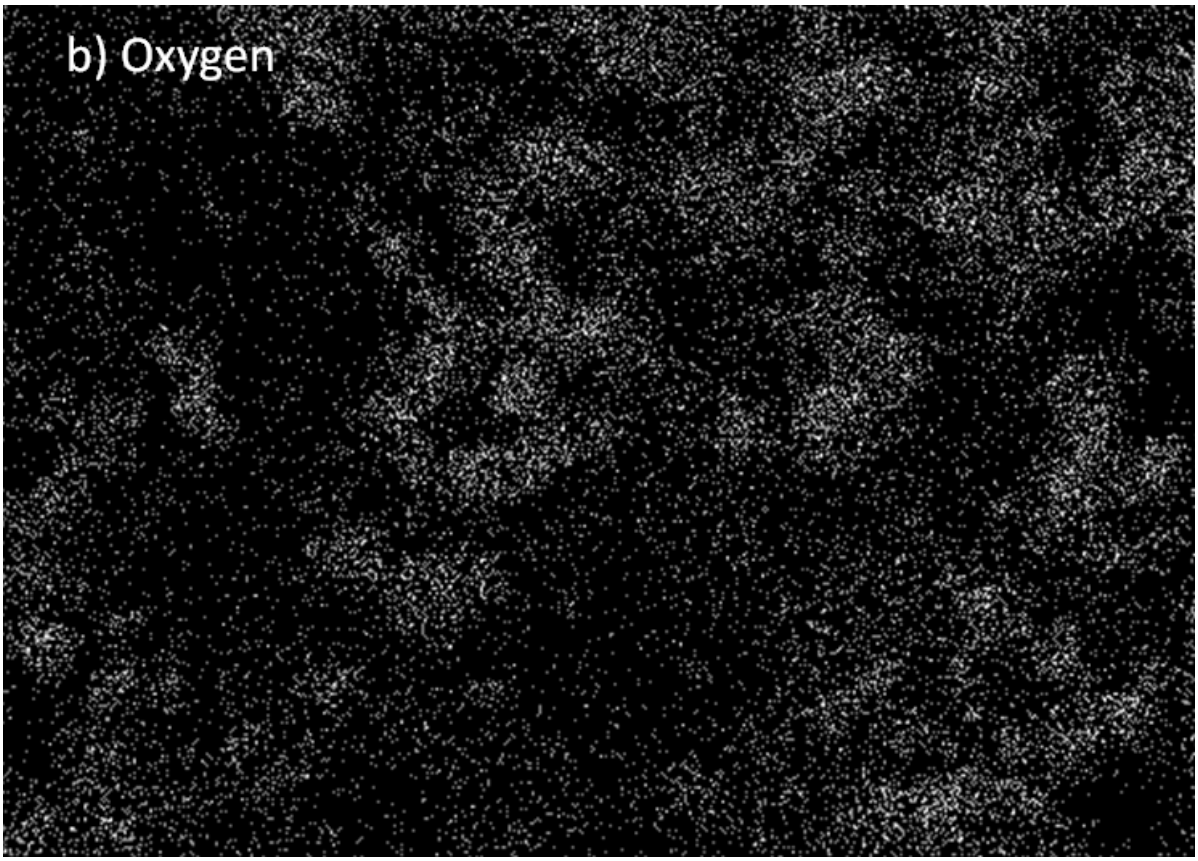
b) Oxygen

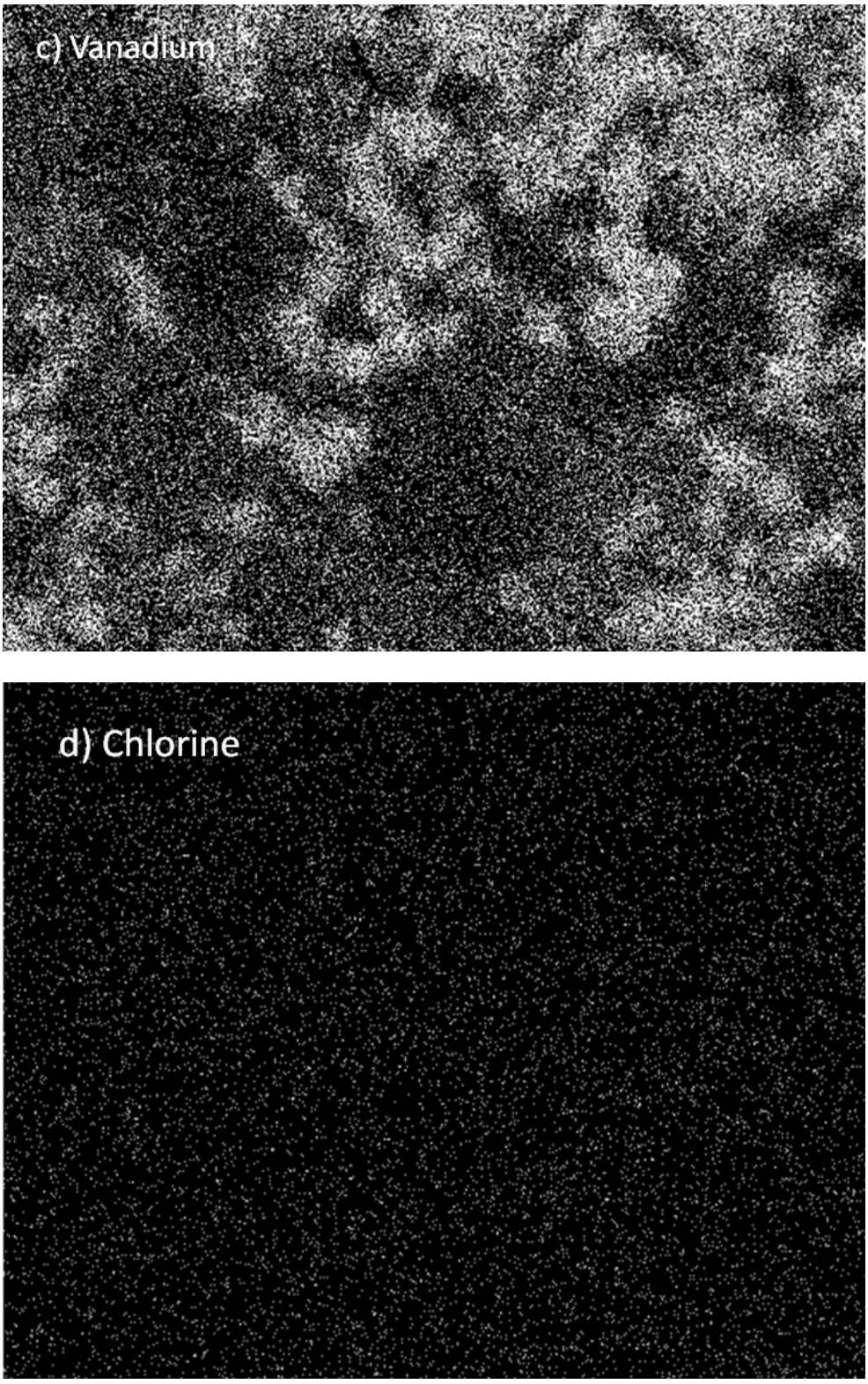

Figure 41. EDAX maps of the vanadium oxide coated CNTs.

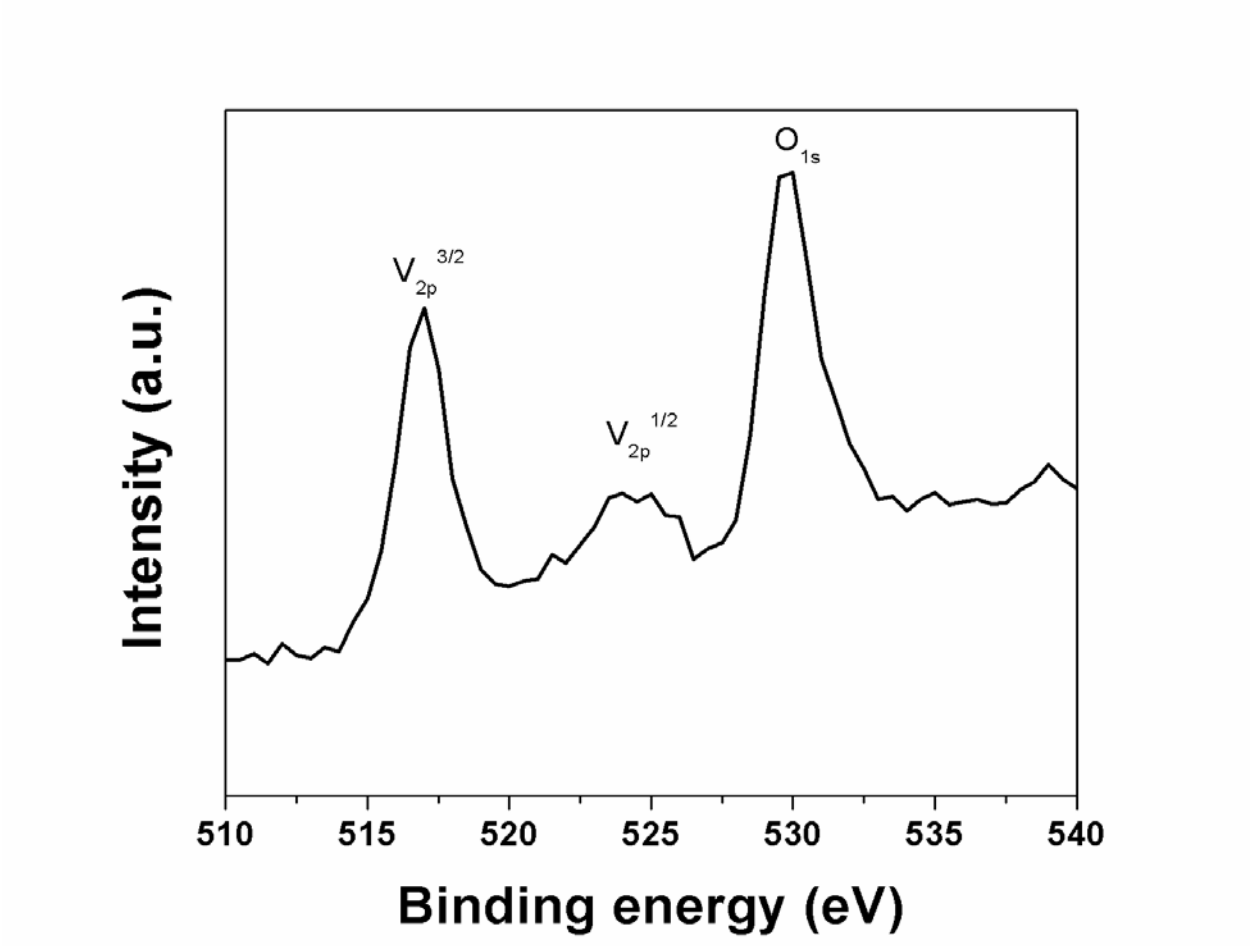

Figure 42. X-ray photoelectron spectrum of CVD deposited VACNT-oxide nanosphere heterostructures showing the peaks corresponding to the binding energies of vanadium and oxygen.

In order to determine the chemical oxidation states of V and O in the VACNT-oxide nanosphere composite electrode, x-ray photoelectron spectroscopy (XPS) techniques has been conducted on a Phillips PHI 5600 system. The XPS spectra of V_{2p} and O_{1s} peak of vanadium oxide are shown in **Figure 42**. As shown in **Figure 42**, the binding energy of vanadium [$V_{2p}^{3/2}$ (517.0 eV) and $V_{2p}^{1/2}$ (524.378 eV)] is indicative of V in the oxidation state between +4 and +5[347, 350]. The binding energy of oxygen O_{1s} (529.84 eV) corresponds to a high oxidation state of the metal around +4/+5 oxidation state. This binding energy of vanadium corresponds to that of

vanadium predominantly being present in a high oxidation state. It has previously been identified that high oxidation state of vanadium in vanadium oxide is amenable for improved supercapacitor performance. The vanadium oxide coated on the VACNTs synthesized by CVD possesses a high oxidation state mixture of V^{5+}/V^{4+} similar to that of other promising oxide materials used in supercapacitors[178, 343].

Four-probe conductivity measurements were performed on both, the thin film oxide and VACNT-supported vanadium oxide nanospheres. Sheet conductivity data was obtained using a Veeco- FPP 500 instrument wherein the coated Ni disks were suppressed onto standalone tips and voltage vs. current was measured. Sheet resistance data were multiplied with thickness to obtain bulk resistivity. Bulk resistivity values were then averaged and determined to be ~0.46 Ω-cm for the oxide nanospheres coated on CNTs as compared to ~7.5 Ω-cm for thin film oxide. Bulk oxide values reported in the literature range between 10^3 and 10^4 Ω-cm[185]. The electronic conductivity of the nickel disk was found to be $9.3 * 10^{-6}$ Ω-cm. This is in agreement with the hypothesis that the four-probe conductivity data does not bear an artifact from the current collector as the conductivity of the VACNT-oxide composite is ~5 orders of magnitude lower than that of the nickel disk itself. The deposition of oxide nanospheres on CNTs therefore leads to conductivities similar to those of vanadium oxide nanowires reported previously[372]. This increase in conductivity would thus likely lead to enhanced electron transport and higher rate capability as would be expected following the schematic shown in **Figure 16**.

Figure 43a and **Figure 43b** show the cyclic voltammograms of the oxide-nanosphere coated VACNTs and the thin film vanadium oxide. The effect of scan rate on both samples is evident in the change of slopes of the I-V curves. As the scan rate increases, the current response on scanning potential undergoes a transition from a flat capacitor type behavior to a resistor-like

dependence as is common for most pseudocapacitor materials. Reversible Faradaic peaks are observed at ~0.2V, 0.3V and 0.6 V on the positive scan and ~-0.1 V and 0.3 V on the negative scan in both materials (clearly seen in **Figure 43c**).

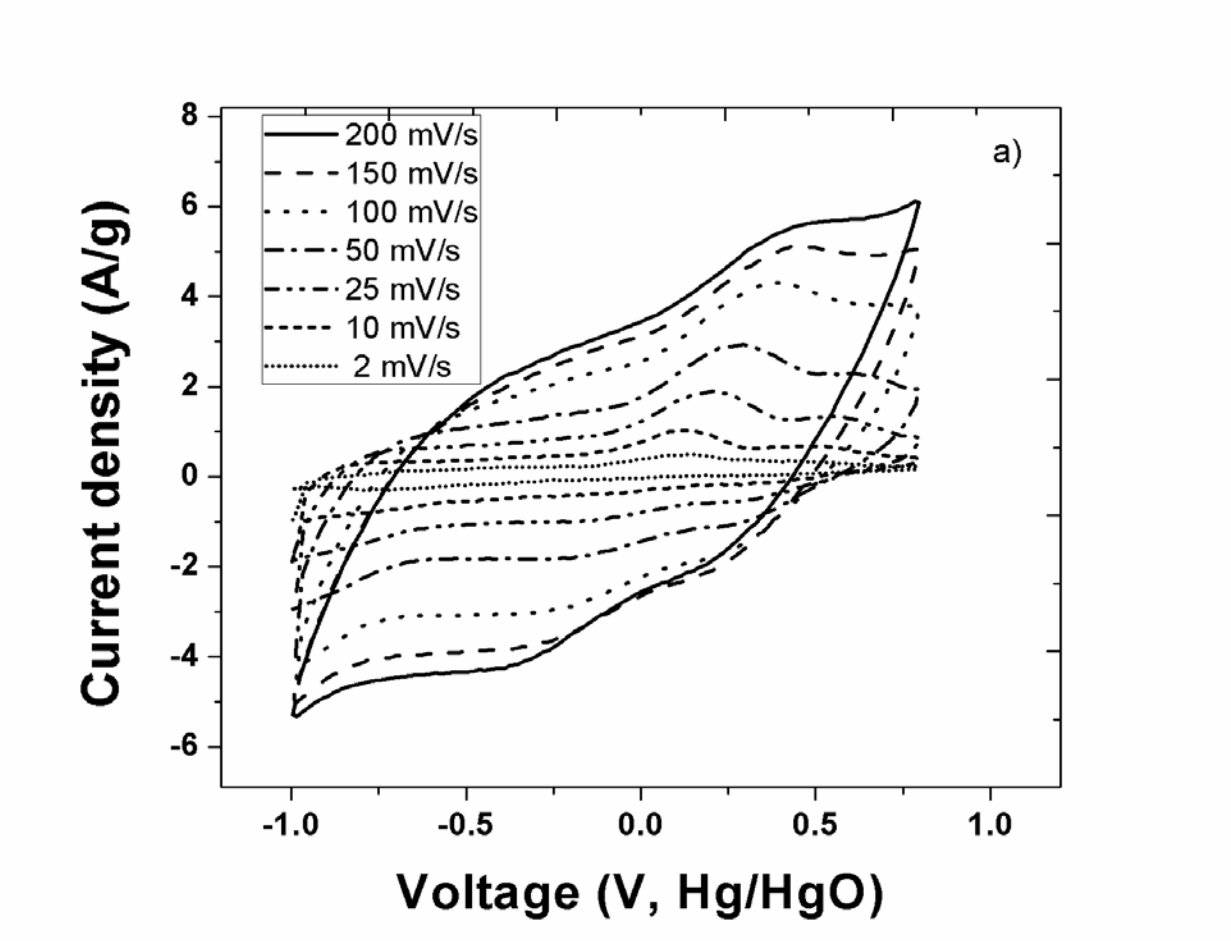

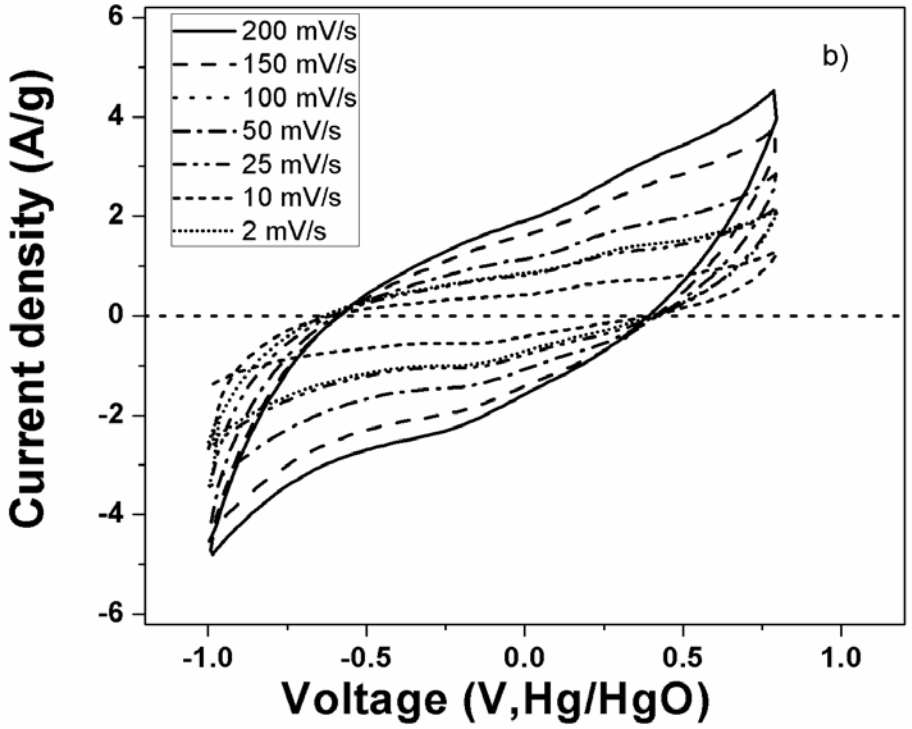
200 mV/s
150 mV/s
100 mV/s
50 mV/s
25 mV/s
10 mV/s
2 mV/s
b)
Current density (A/g)
Voltage (V,Hg/HgO)
6
4
2
0
-2
-4
-6
-1.0
-0.5
0.0
0.5
1.0

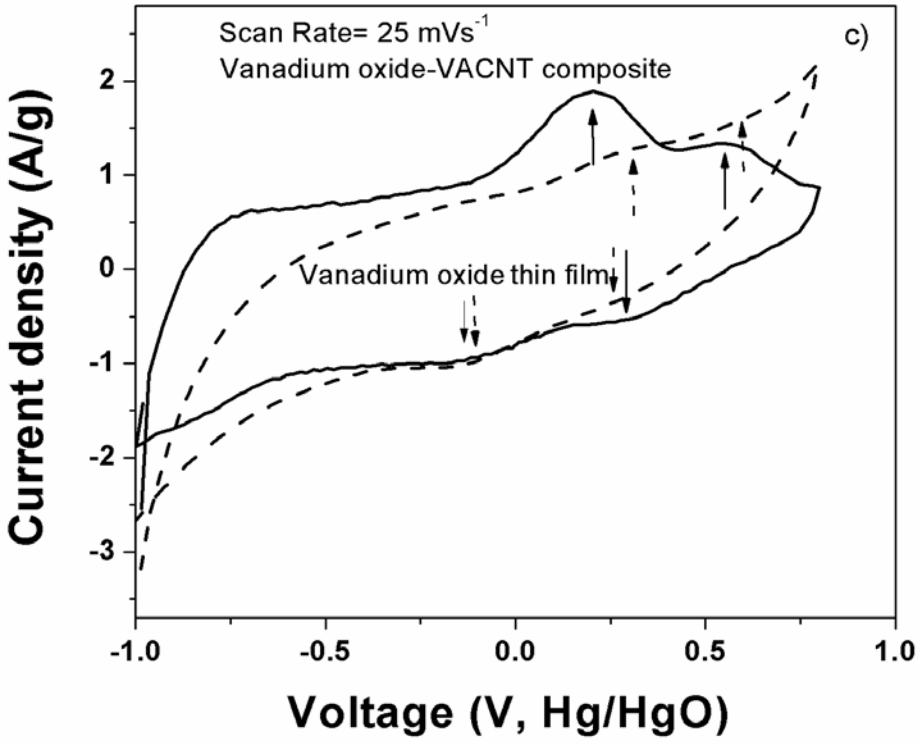
Scan Rate= 25 mVs-1
Vanadium oxide-VACNT composite
c)
Vanadium oxide thin film
Current density (A/g)
Voltage (V, Hg/HgO)
2
1
0
-1
-2
-3
-1.0
-0.5
0.0
0.5
1.0

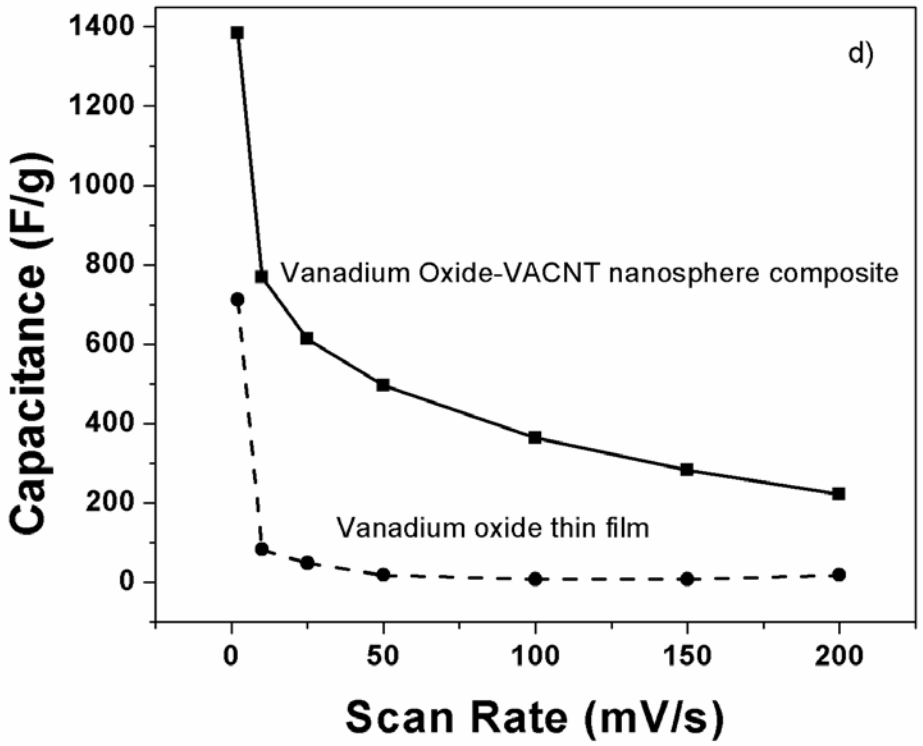
d)
Capacitance (F/g)
Scan Rate (mV/s)
Vanadium Oxide-VACNT nanosphere composite
Vanadium oxide thin film
0
200
400
600
800
1000
1200
1400
0
50
100
150
200

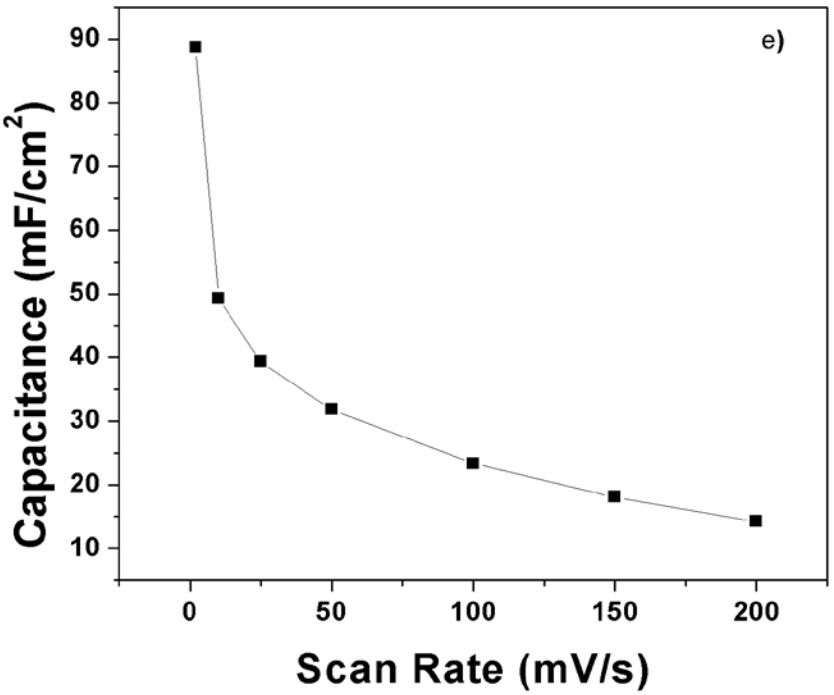
e)
Capacitance (mF/cm^2)
Scan Rate (mV/s)
10
20
30
40
50
60
70
80
90
0
50
100
150
200

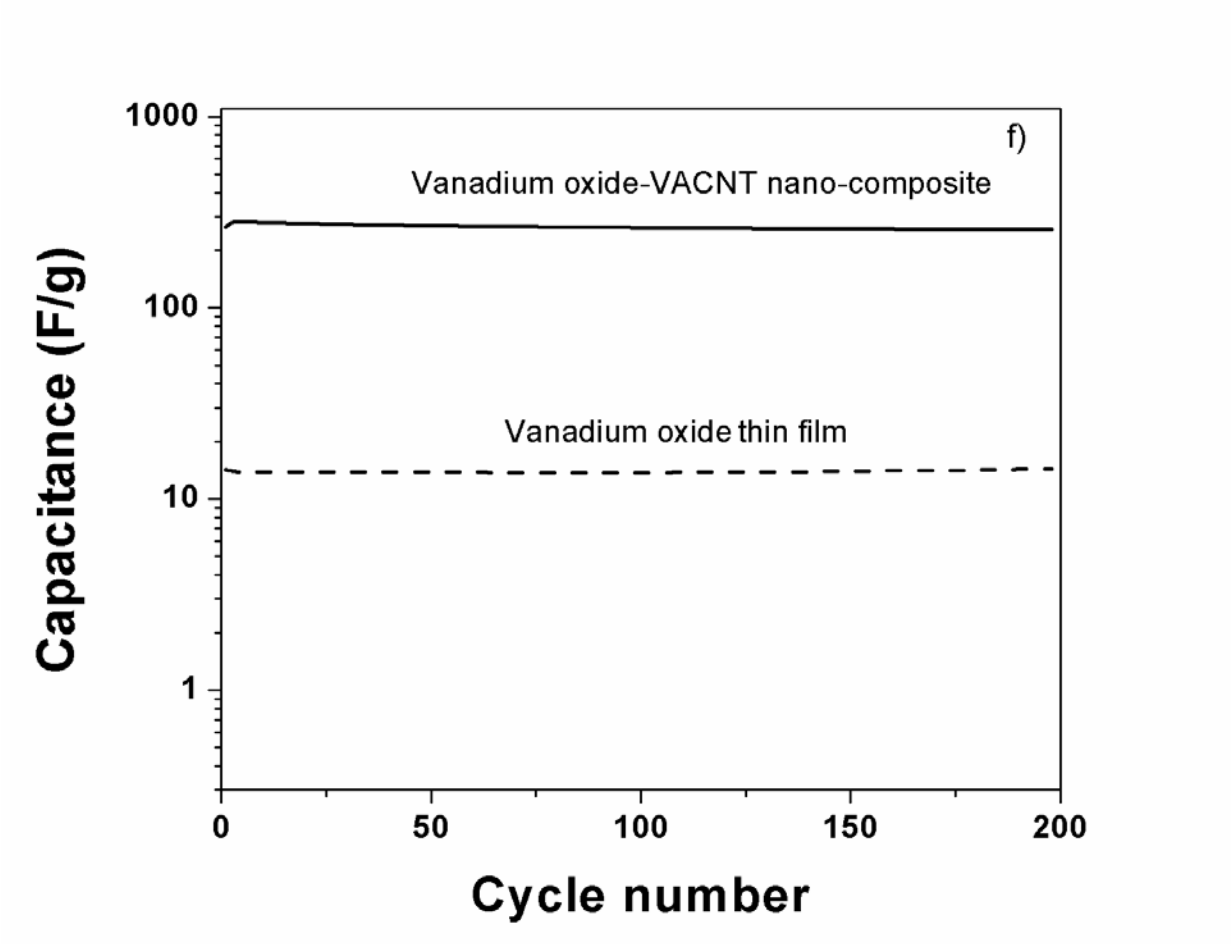

Figure 43. (a) Cyclic voltammograms of the CVD deposited oxide-VACNT heterostructures at different scan rates. (b) Cyclic voltammograms of the CVD deposited vanadium oxide thin film at different scan rates (c) Comparison of cyclic voltammograms of vanadium oxide-VACNT heterostructures and vanadium oxide thin film at a particular scan rate showing pronounced Faradaic response of CNT supported nanospheres (d) Capacitance behavior of vanadium oxide nanosphere-VACNT composite and vanadium oxide thin film with scan rates (Oxide loading=0.07 mg/cm^2, Oxide-CNT active material loading=1.1 mg/cm^2) (e) Areal Capacitance behavior of vanadium oxide nanosphere-VACNT composite calculated based on the total active material weight (f) Cycling behavior of vanadium oxide nanosphere-VACNT composite heterostructure and vanadium oxide thin film (Scan rate=150 mV/s, Oxide loading=0.07 mg/cm^2).

The potential dependent pseudocapacitance behavior present at these potentials is thought to correspond to a reversible transition of oxidation state of Vanadium from +5 to +3 most

commonly observed in aqueous systems at the almost neutral pH occurring in a 1M Na_2SO_4 solution[269, 373]. Upon comparing plots **Figure 43a** and **Figure 43b**, it can be seen that the Faradaic peak is more pronounced, at higher scan rates, in the VACNT-oxide spheres than in the thin film. This is due to the beneficial effect of the CNTs on the Faradaic capacitor processes occurring in vanadium oxide. The valuable effect of VACNTs is clearly evident in the capacitance plots seen in **Figure 43d**, in which the capacitance of the oxide nanospheres deposited on both the VACNTs and directly on the Ni substrate are plotted against the cyclic voltammetry scan rates. The effect of the resistance/capacitance behavior previously described is evident from the drop in capacitance with scan rate. This drop however, is more pronounced in the thin film material as compared to the oxide nanospheres supported on the VACNTs. Capacitances of upto 1400 Fg^{-1} (oxide loading basis, oxide loading~0.07 mg/cm^2, Oxide-CNT loading~1.1 mg/cm^2) have been observed at scan rates of 2 mVs^{-1} in the VACNT-oxide nano-composite material with good capacitance retention at higher rates compared to the oxide thin film on Ni substrates. **Figure 43e** shows the dependence of overall capacitance of the VACNT-oxide nano-composite material on scan rate in $mFarads/cm^2$. Areal capacitance is a very important characteristic when considering materials for industrial applications and it can be seen that the VACNT-oxide nano-composite material has excellent capacitances ranging from 89 $mFcm^{-2}$ (at 2 mVs^{-1}) to 14 $mFcm^{-2}$ (at 200 mVs^{-1}) which are superior to those reported for RuO_2 nanotubes (10-40 mF/cm^2) reported before[344]. The VACNT-vanadium oxide composite material however does not have areal capacitances as high as highly active ruthenium oxide supercapacitors (~160 mF/cm^2)[345, 346] but is still commercially viable on account of its relatively low cost as compared to ruthenium oxide (~0.193 $/gm as compared to ~10$/gm). The comparison of a relatively inexpensive vanadium oxide material possessing excellent areal

capacitance with that of a well-studied noble metal oxide such as ruthenium oxide is meant to provide a basis for comparison rather than to prove superiority in performance. Noble metal based capacitors as already mentioned in the introduction are expensive even though they have excellent charge storage properties. It is therefore the aim of this work to highlight the possibility of vanadium oxide having performance as good as that of a noble metal oxide. It should be noted that no claim is made to indicate that vanadium oxide is a better charge storage material compared to ruthenium oxide. Rather, the goal is to demonstrate the possibility of obtaining very high capacitance in vanadium oxide nanospheres in aqueous systems when they are decorated on vertically aligned carbon nanotubes.

The synergistic effect of the carbon nanotube-vanadium oxide junction has previously been studied for gas-sensing purposes[369, 374, 375]. It has been suggested that a p-n junction type interaction between the oxide and the CNT leads to increased catalytic response of the oxide while the multi walled CNTs, which acts as a p-type semiconductor help act as fast electron channels. This phenomenon can clearly be observed in **Figure 43d**. The performance of supercapacitor materials at high rates is most-often limited by the electronic conductivity of the material. The selection and presence of carbon nanotubes as a support structure for the oxide is essentially to provide to unidirectional electron transfer through the aligned CNTs[376] which then travel through the mini-oxide spheres and interact at the oxide-electrolyte interface where the charge is stored. It can be seen that the capacitance of the oxide-VACNT composite is ~ 80 Fg^{-1} when the total weight of the composite is considered. This drop in capacitance compared to the 18 fold increase in capacitance calculated on the basis of the active oxide material alone is due to the overwhelming weight of the CNTs which do not exhibit any pseudocapacitance behavior. Though excellent oxide capacitance behavior was demonstrated in the CVD derived vanadium

oxide material in the oxide-VACNT composite electrode, the overall capacitance is not very high when compared with other aqueous vanadium oxide supercapacitors[180]. There is therefore a need for further optimization of the system to identify an ideal oxide/CNT ratio so as to maximize capacitance whilst retaining the improvement in rate capability afforded by the high conductivity of the carbon nanotubes. The fade in capacitance with increase in scan rate is a phenomenon observed in supercapacitor materials as described by Conway et. al[58]. This is caused by the change in characteristic of the interface from that of a double layer capacitor to a resistor. This transition is a fundamental feature of all electrochemical double layers. Capacitance changes with scan rate with a factor s which varies from material to material. A similar characteristic in Faradaic reactions is the kinetic rate constant (k_0) which is a material property in a given electrode/electrolyte assembly. Pseudocapacitance reactions involving charge transfer by tunneling across the electrochemical interface have an inherent rate constant depending on the species involved in the charge transfer which could be limiting in the case of the current oxide coated on the CNTs. It could also be attributed to the nature of the oxide coating on the carbon nanotubes. It is observed that even though the carbon nanotubes have a vertical alignment, the nature of the tethering of the oxide nanoparticles on the carbon nanotubes needs to be improved to achieve better rate capability. In addition, the conductivity of undoped VACNTs themselves is limiting to some extent on account of presence of some amorphous carbon on the CNTs. Optimization of the system to improve oxide/VACNT loading and CNT conductivity would ideally increase both initial capacitance and rate capability. This is work in progress as part of the future work and will be the topic of work to be initiated and conducted in the near future.

Figure 43f shows the ability of the CVD deposited materials to retain charge over large cycles. Both the CVD deposited materials are seen to have exceptional capacitance retention

upto 200 cycles, at a scan rate of 150mVs^{-1} (oxide loading~0.07 mg/cm^2, Oxide-CNT loading~1.1 mg/cm^2). This excellent cyclability can be attributed to the reversible nature of the surface pseudocapacitance reactions occurring on the oxide. The thin film oxide on the other hand, has a relatively low capacitance at the same high rate of 150 mV/s at which cycling was performed as previously pointed out in **Figure 43d** but maintains stability with cycling. The oxidation state of the CVD deposited vanadium oxide is ~4.6 consisting predominantly of a +4/+5 oxide. According to the potential-pH diagram, vanadium oxide has stable insoluble phases between the potentials of ~0.5 V and -1 V wrt Ag/AgCl[269]. Above 0.5 V, the higher oxidation state oxide is considered soluble to form $HV_2O_5^-$ at a neutral pH. This should be reflected as loss in capacity with cycling. However, the onset potential of electrochemical reactions is known to vary with particle size and microstructure. It is believed that the amorphous nature of the oxide nanoparticles supported on the vertically aligned carbon nanotubes offsets the onset of such dissolution resulting in the very stable performance of the oxide in aqueous Na_2SO_4 seen in **Figure 43f**. It is also possible that the kinetics of the dissolution reaction might be sluggish and such a fade in capacity would probably be observed if the material were cycled over thousands of cycles.

It is common knowledge that thick films of nanoparticulate oxides especially amorphous oxides would be non-ideal to obtain high capacitances on account of the low inherent electronic conductivity, grain boundary diffusion and exposed surface of amorphous systems. On the other hand, the use of a relatively thin film on a supported structure affords us the benefits of high surface area, small particle size and direct contact of grains with the highly conductive carbon nanotubes. The accessible capacitance of vanadium oxide thick film is very limited when the material is synthesized as a thick film. However, thin film vanadium oxide has a high

capacitance as demonstrated in **Figure 43d**. This is improved even further when the VACNTs are used as a 3-dimensional support. These results are thus in agreement with trends observed in other pseudo-capacitor materials such as manganese oxide[377]. Though the overall capacitance reported here is lower than that reported in LiCl based systems by Hu et al.[178-181], t the unique synthesis method, morphology, electrode/electrolyte combination and an in-depth electrochemical characterization provided are original contributions to the best of the reported work in the literature accessed to date, enhancing the understanding of supercapacitor behavior in oxide systems. In addition, the observed fact that capacitance of the oxide material only when coated on the VACNTs is very high demonstrates that vanadium oxide is in fact, is a very promising material for aqueous supercapacitors. It is hoped that this would spur a renewed interest in vanadium oxide based aqueous capacitors to be further explored for commercial applications.

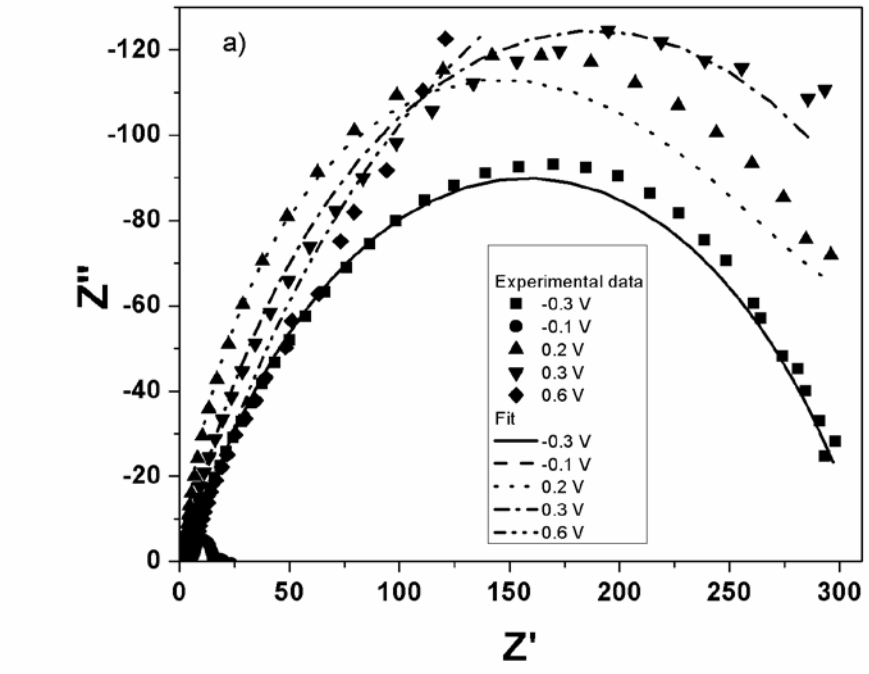

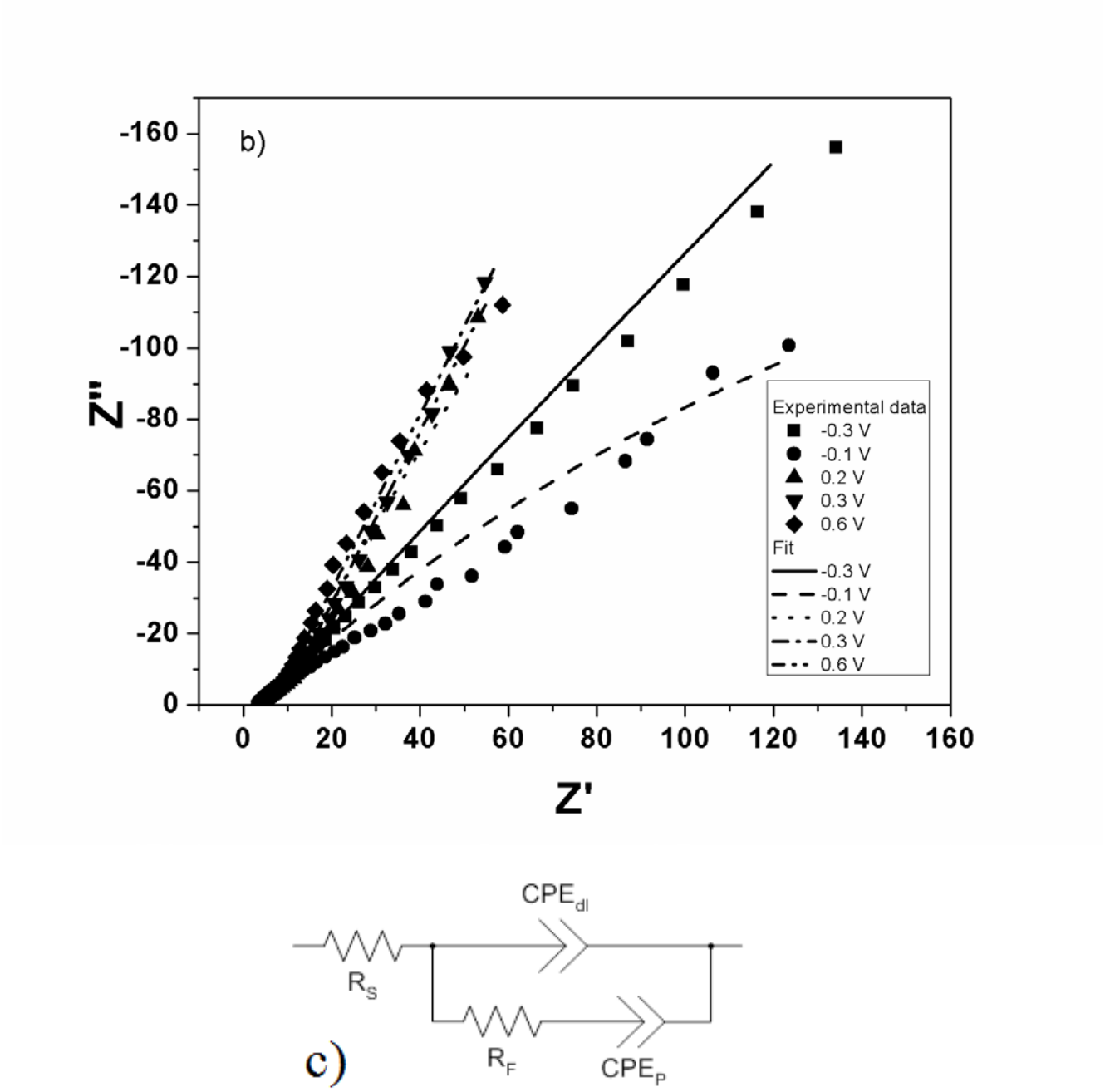

Figure 44. (a) Impedance behavior of thin film vanadium oxide and (b) Vanadium oxide nanosphere-VACNT composite heterostructure (Oxide loading=0.07 mg/cm^2, Oxide-CNT active material loading=1.1 mg/cm^2) (c) Underpotential deposition mechanism used to perform equivalent circuit modeling of electrochemical impedance spectra. Symbols mark the experimentally obtained data and the lines indicate the calculated fit from modeling of the equivalent circuit to the experimentally obtained curves.

In order to further establish the advantages yielded by the CVD deposition of vanadium oxide on CNTs, electrochemical impedance spectra were obtained on the nanospheres as well as oxide film and charge transfer characteristics were compared. **Figure 44a** and **Figure 44b** show the Nyquist plots of the thin film vanadium oxide and the oxide nanosphere-VACNT hybrid electrodes, respectively at different voltages over the window of interest. It can be observed directly that the impedance behavior of both materials is different especially at voltages close to the regions of the Faradaic peaks observed at 0.2, 0.3, 0.6, -0.3 V in the cyclic voltammograms (see **Figure 43c**) . At these potentials corresponding to the Faradaic charge transfer reactions, it can be seen upon comparing the response of oxide film and VACNT-oxide composite that the thin film oxide has a much larger charge transfer resistance. This is inferred from the large semi-circular arcs seen in **Figure 44a** as compared to **Figure 44b** wherein one can see that the Warburg tail being more prominent in the oxide-CNT hybrids as compared to the relatively much smaller semi-circular arcs. The large semi-circular arcs in a Nyquist plot are indicative of high charge transfer resistance which would result in the reduced Faradaic response as experimentally observed in the thin film oxide at higher scan rates as seen in **Figure 43c**. Pseudocapacitance performance which is usually prevalent in the 10^3 to 10^4 Hz region on account of electrode kinetic rate limitations[58] is much more prominent in the CNT-supported oxide as compared to the thin film oxide.

Equivalent Circuit modeling was performed using the Z-view software to obtain charge-transfer parameters of the oxide based capacitors. An underpotential deposition mechanism described by Conway et. al.[44, 58] was used to model the pseudocapacitance reactions occurring on both sets of electrodes as shown in **Figure 44c**. The mechanism considers both double layer capacitance (usually modeled as a capacitor (C_{dl}) in parallel with a resistor (R_F)) and

pseudocapacitance arising from surface reactions (C_p) on the electrode of interest. In addition, an electrochemical series resistance (R_s) common to all electrochemical systems is also considered. However, in porous electrode systems, the capacitor elements are usually modeled as constant phase elements [65, 360]. Constant phase elements are usually used to fit data having depressed semi-circular arcs on account of electrode porosity and roughness which leads to fractal character and inhomogeneity in response on account of presence of different crystallographic reaction sites. On account of such behavior noticeable in **Figure 44a** and **Figure 44b**, we have used constant phase elements, CPE-dl and CPE-p have been used to fit the data. The values of various charge transfer parameters obtained by fitting the equivalent circuit have been summarized in **Table 17**.

Table 17. Charge-transfer properties of the CVD derived oxide materials

Voltage	Series Resistance (R_s)-Ωcm^{-2}		Double layer Constant Phase Element (CPE-dl)				Pseudocapacitance Constant phase element (CPE-F)				Faradaic resistance (R_F)-Ωcm^{-2}	
	Nanospheres	Thin film	Nanospheres		Thin film		Nanospheres		Thin film		Nanospheres	Thin film
			T (*10^{-3})	φ	T (*10^{-3})	Φ	T(*10^{-2})	φ	T	Φ		
-0.8	0.73	0.78	1.99	0.86	1.44	0.61	2.32	0.50	1.62	0.00012	0.71	968.93
-0.3	0.70	0.56	3.28	0.76	1.21	0.67	2.63	0.57	0.14	0.7	0.30	58.80
0.2	0.71	0.31	56.18	0.52	0.38	0.88	1.07	1.09	0.02	0.9	13.74	58.19
0.3	0.70	0.26	32.54	0.69	1.58	0.76	2.99	0.77	0.03	0.92	3.89	67.13
0.8	0.68	0.86	1.06	0.94	22.20	0.70	1.25	0.63	0.51	3.43E-07	0.24	31.36

It can be seen that the series resistance is fairly constant in both systems and varies between 0.25 and 0.9 Ωcm^{-2} which is common in carbon based systems[361]. The most notable difference in behavior between the thin film oxide and the CNT-supported nanospheres is the charge transfer resistance R_F. R_F values are reduced by upto an order of magnitdude on account of the presence of CNTs. This can also be seen in **Figure 44b** where the oxide nanosphere based material has an almost 90 degree slope at low frequencies as compared to large semi-circles indicating high R_F values seen in **Figure 44a**[378]. This improvement in conductivity is reflected in the high capacitance response observed at high scan rates for the oxide nanosphere-VACNT heterostructures compared to the oxide thin film alone as seen in **Figure 43d**. ϕ refers to the phase angle of the constant phase element. It is a measure of the nature of the constant phase element used to replace the capacitor element on account of electrode porosity and roughness. ϕ values of >0.7 indicate a predominantly capacitor type response. However, in the case of thin film oxide made by CVD, at voltages of -0.8 V and 0.8 V, the values of ϕ are much less than 1 indicating that the response approaches that of a resistor particularly, at the fringe voltages. This can be accounted to by considering that the theoretical onset of electrolyte breakdown occurs around -0.65 V though the kinetics of the same is sluggish as seen in the cyclic voltammogram in **Figure 43c**. This is reflected as the low ϕ values seen in **Table 17**. This semi-resistive phenomenon is however absent in the oxide-VACNT composite as shown in **Table 17** indicating that an over-potential deposition mechanism need not be employed for accounting for all the phenomena involved in the composite electrode synthesized by the simple chemical vapor deposition approach.

4.2.1 Conclusions

Hot-wall chemical vapor deposition has for the first time been used to create a unique morphology consisting of vanadium oxide nanospheres tethered to carbon nanotubes. Such a CVD derived VACNT supported oxide nanosphere morphologies have been shown to exhibit excellent charge storage characteristics with capacitances of upto 1400 Fg^{-1} achieved at a scan rate of 2 mVs^{-1} based on the oxide loading. Moreover, the results indicate that carbon nanotubes serve to provide a strong complimentary effect on the rate capability of oxide capacitance as seen by comparing scan-rate dependent capacitance plots of CNT-oxide hybrid electrodes with pure oxide thin films. One of the highlights of this study is the ease of electrode fabrication. Chemical vapor deposition is a method amenable for continuous production of electrodes in an assembly-chain configuration in contrast with chemical and solid state methods typically used to produce oxides which require batch processes and in-turn also involve a second heat treatment step. The need for tedious slurry preparation method is eliminated and binder-free electrodes are thus generated. The CVD method could further be optimized to lead to electrodes with a good oxide/CNT ratio so as to maintain excellent capacitance yielded by the thin oxide layer as well as the rate capability enhancement provided by carbon nanotubes. Such studies will be valuable for generating capacitor devices at the industrial scale.

4.3 DOPED VANADIUM OXIDE CAPACITORS

Figure 45a shows the scanning electron microscope (SEM) image of vertically aligned CNTs (VACNTs) deposited by chemical vapor deposition on Ni substrate using a deposition time of 30 minutes for growth of carbon nanotubes. The carbon nanotubes grow on the nickel substrate supported by iron nanoparticles (from Ferrocene) which nucleate on the surface of the nickel as islands and in turn acting as growth sites for carbon[379, 380]. The carbon then grows in the form of nanotubes by progressive rise of the nucleated iron islands which continue to act as nucleation sites (floating catalyst mechanism) of carbon. Hence the length of the tubes can be controlled by varying the CVD deposition time. Accordingly, optimized deposition time of 30 minutes was used to obtain the vertically aligned tubes 120 micron in length. The hypothesis is that the prolific length of the CNTs would help create a very good 3-D architecture which when covered with a thin layer of the oxide would maximize the volumetric loading while at the same time ensuring that a very thick film does not cover the entire surface of the carbon nanotubes impeding electronic transport within the oxide itself.

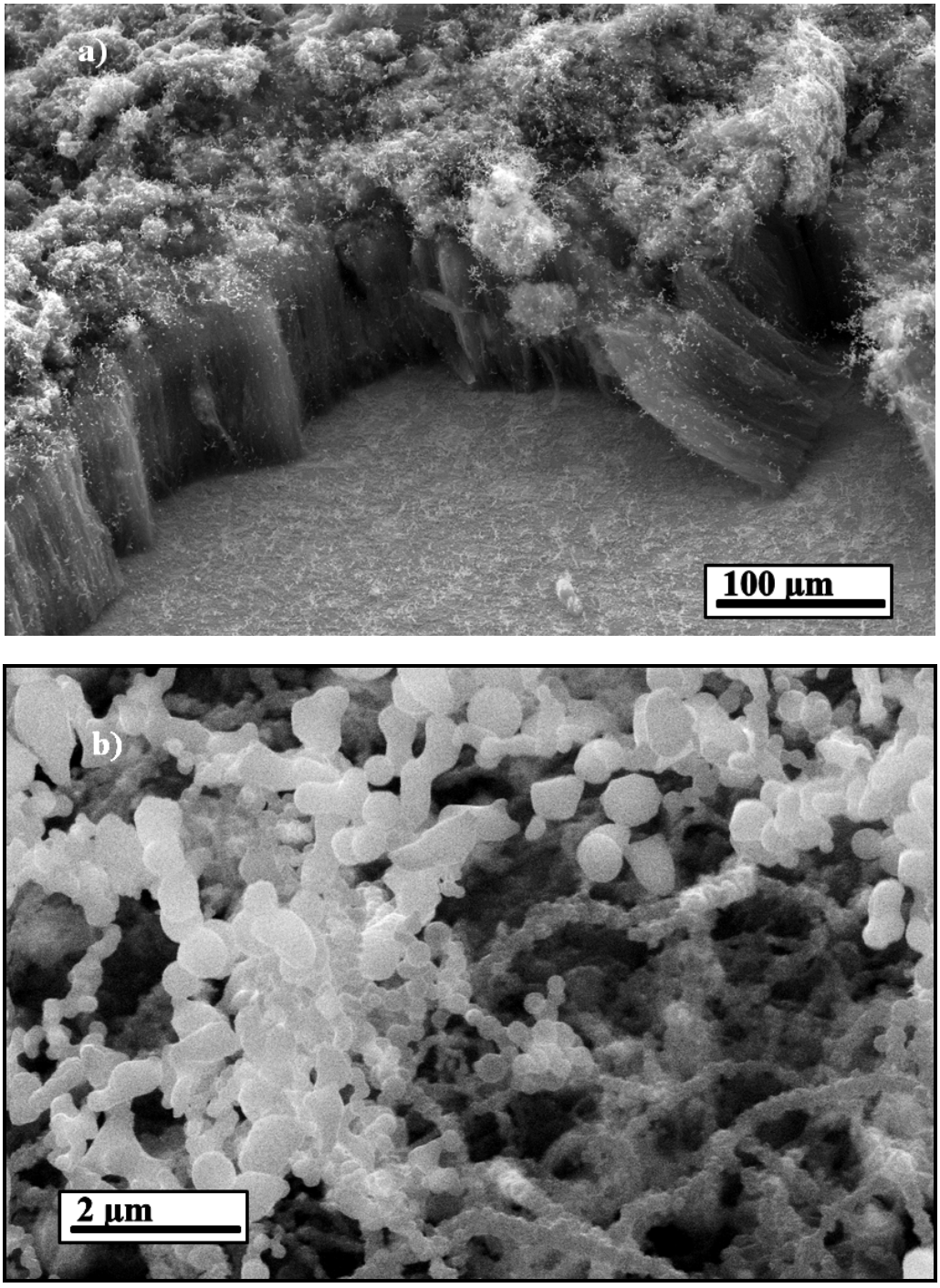

Figure 45. Scanning Electron Microscope image of (a) CVD derived Vertically Aligned Carbon nanotubes coated with titanium doped vanadium oxide showing forest of vertically aligned carbon nanotubes, and (b) Nanoparticulate titanium-doped vanadium oxide coated on the carbon nanotubes grown by chemical vapor deposition.

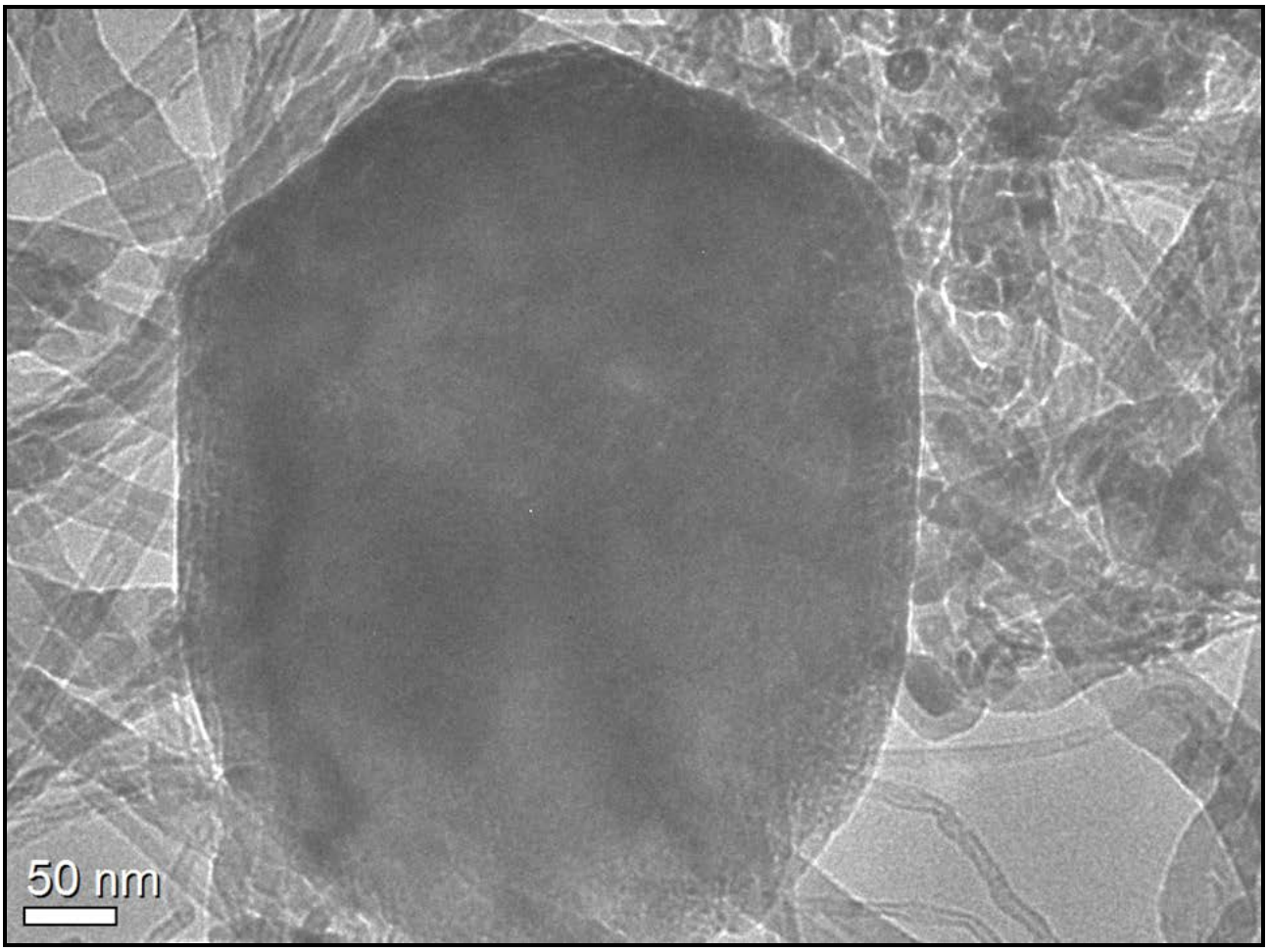

Figure 46. HRTEM images of the VO_x:Ti coated on the vertically aligned carbon nanotubes (VACNTs) showing nanoparticulate size of the oxide particles grown on the carbon nanotubes.

Figure 45b shows the SEM image of titanium doped vanadium oxide (VO_x:Ti) coating on the vertically aligned CNTs deposited by chemical vapor deposition using the pre-mixed chloride precursors and water which were aspirated using the CVD system described in **Figure 18b**. Deposition of the doped oxide using the pre-mixed chloride precursors and water aspirated in the CVD system was carried out for 20 minutes ensuring that the oxide is coated on the VACNTs in the form of a contiguous film consisting of a number of nanometer sized globules. **Figure 46** shows the bright field high resolution transmission electron microscopy (HRTEM)

image of VO_x:Ti-VACNT hybrid composite scrapped off the nickel substrate. The image confirms that the VO_x:Ti is deposited over the VACNTs in the form of a semi-contiguous film consisting of ~250 nm diameter amorphous globules evident by the lack of visible lattice fringes in the oxide particle seen in **Figure 46**.

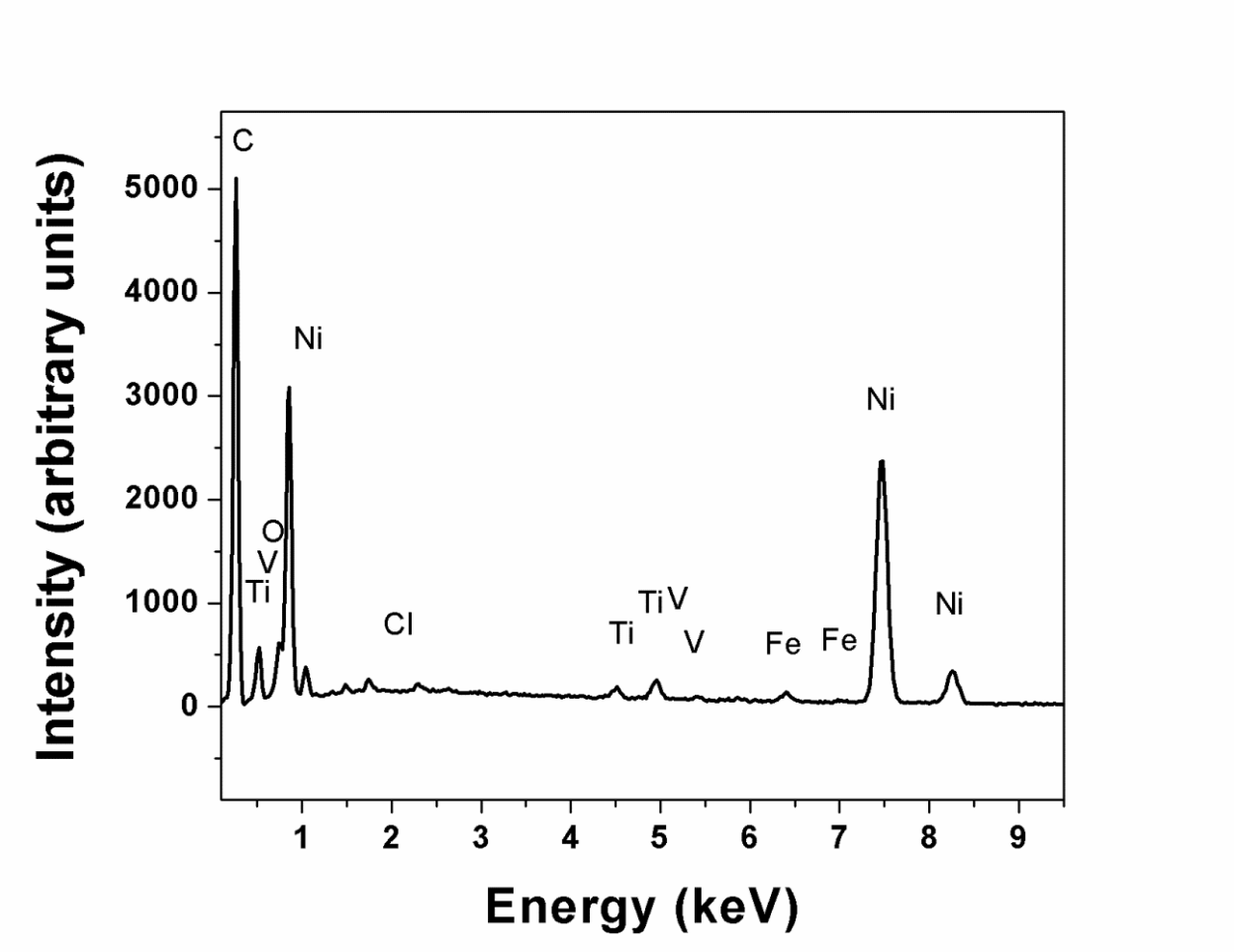

Figure 47. EDX spectra of the VO_x:Ti -VACNT composite heterostructures synthesized by CVD.

Energy dispersive x-ray analysis (EDX) was performed on the sample as shown in **Figure 47** since the composition of the CVD derived VO_x:Ti-VACNT could not be accurately confirmed by x-ray diffraction due to the amorphous nature of the oxide deposited on the

VACNTs (**Figure 46**). The presence of elemental V, O and Ti in the VO_x:Ti-VACNT heterostructures has been confirmed using the EDX configured to the SEM. The V and Ti ratio in the VO_x:Ti-VACNT is similar to the nominal composition used and is confirmed by EDX. Nickel is also observed in the EDX which is due to the substrate on which VO_x:Ti-VACNT is synthesized. It was found that the CVD derived doped oxide-VACNT composite heterostructure had a nominal composition of $V_{1.6}Ti_{0.4}O_{5-x}$ with x ~ 0.4. The vacancy rich oxide thus formed would correspond to a high oxidation state of vanadium which has previously been identified to be essential for achieving high capacity in vanadium oxide [178, 343].

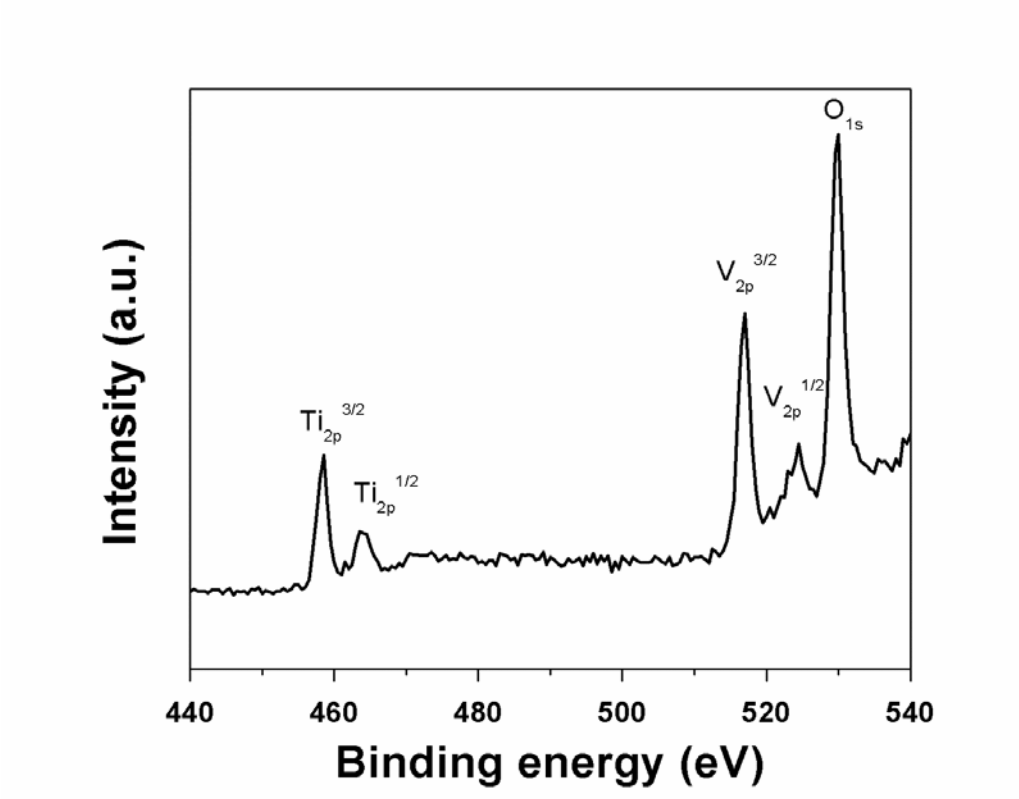

Figure 48. X-ray photoelectron spectrum of CVD deposited VACNT-titanium doped vanadium oxide composite heterostructure showing the peaks corresponding to the binding energies of vanadium, titanium and oxygen.

In order to determine the chemical oxidation states of V, Ti and O in the VACNT-doped oxide composite electrode, x-ray photoelectron spectroscopy (XPS) was conducted using a Phillips PHI 5600 system. The XPS spectra of V_{2p} and O_{1s} peak of vanadium oxide obtained are shown in **Figure 48**. As shown in the figure, the binding energy of vanadium [$V_{2p}^{3/2}$ (516.95 eV) and $V_{2p}^{1/2}$ (524.49 eV)] is indicative of V in the oxidation state between +4 and +5[347, 350]. The binding energy of titanium [$Ti_{2p}^{3/2}$(458.51 eV) and $Ti_{2p}^{1/2}$(463.83 eV)] in the CVD derived VACNT-doped oxide corresponds very closely to Ti existing in the stable +4 oxidation state[76]. The binding energy of oxygen O_{1s} (529.96 eV) corresponds to a high oxidation state of the metal, namely in the +4/+5 oxidation state. Both the vanadium and titanium are thus in their highest oxidation states which is conducive for achieving improved supercapacitor response. The Ti doped vanadium oxide coated on the VACNTs synthesized by the CVD approach exhibits V displaying a mix of high oxidation state of V^{5+}/ V^{4+} similar to that of other promising oxide systems used in supercapacitors[178, 343]. The XPS spectrum and binding energies match very closely that of Ti doped vanadium oxide reported earlier [381].

Raman spectra was collected on the VO_x:Ti-VACNT which is shown in **Figure 49a** since the x-ray diffraction pattern of the titanium doped vanadium oxide could not be acquired on account of the amorphous nature of the oxide grown on the VACNTs. The D, G and G' bands are observed at 1250, 1650 and 2650 cm^{-1}. The G/D (I_g/I_d=1.16) ratio is greater than one indicating few lattice defects in the graphene layers resulting in MWCNTs with relatively high conductivity[366, 367]. This would also have a positive effect on the capacitance behavior of the Ti doped vanadium oxide. **Figure 49a** shows several peaks marked that have been identified to correspond and match closest to those observed and reported in thin films of V_2O_5[368] and those of vanadium oxide corresponding to VO_x-carbon nanofibers reported previously[369]. **Table 18**

also shows the tabulated peak positions observed in **Figure 49a** and indicates the nature of the vibration resulting in the peaks seen in the Raman pattern of VO_x:Ti-VACNT. The V bonds which are characteristic of double and multilayer structures usually observed in V_2O_5 appeared at 404, 528 and 996 cm^{-1}[382, 383]. The peak at 700 cm^{-1} is indicative of stretching vibration of oxygen ions in bridging position between the three vanadia centers[383]. The peak observed at 477 cm^{-1} is at a similar position to that observed in V_2O_5 where oxygen ions are situated between the two vanadium centers[383].

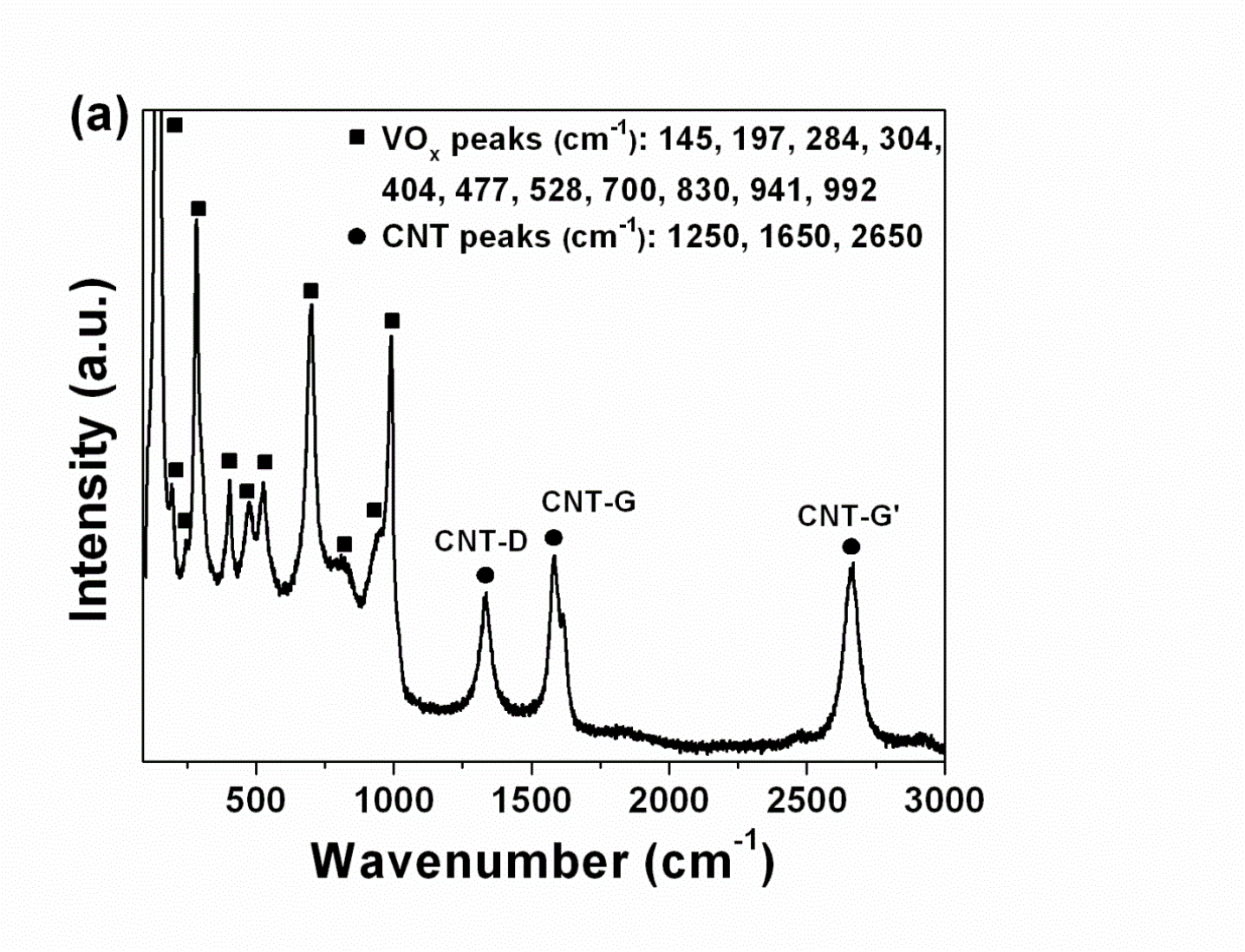

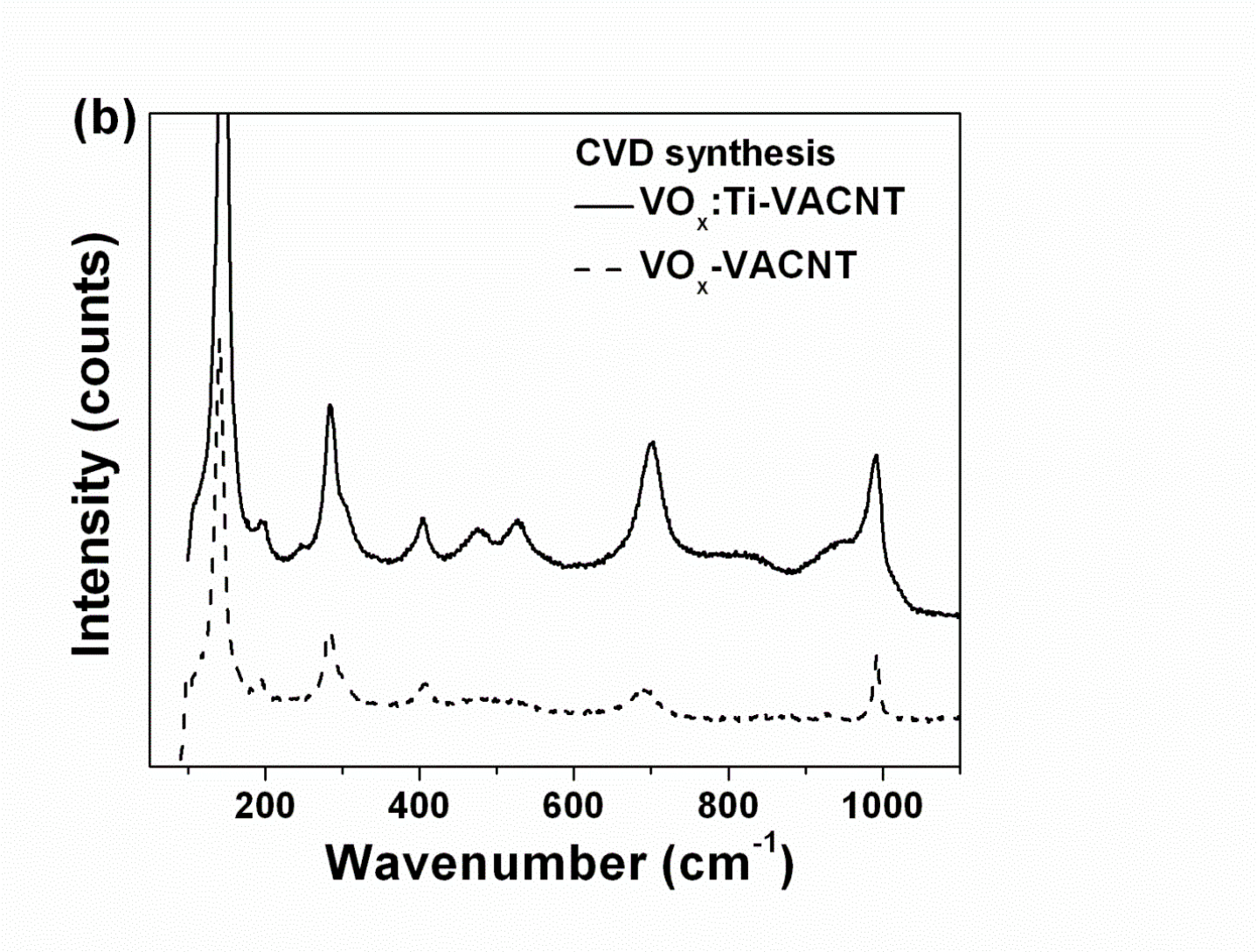

Figure 49. Raman spectra of vertically aligned CNTs coated with titanium doped vanadium oxide (VO_x:Ti-VACNT) over a frequency window of 100-3000 cm^{-1} showing the presence of oxide and CNT peaks (a), and comparison of Raman spectra of CVD derived VO_x:Ti and VO_x coated on VACNTs (b).

Titanium oxide conventionally has Raman peaks corresponding to the anatase phase at 142 cm^{-1} (E_g), 395 cm^{-1}(B_{1g}), 515 cm^{-1} (B_{1g}+A_{1g}) and 636 cm^{-1} (A_{1g}). Brookite (TiO_2) on the other hand, usually has a strong band at 153 cm^{-1}(E_g) and another at 320 cm^{-1} (B_{1g})[384, 385]. No Raman lines due to titanium oxide can be observed in the VO_x:Ti-VACNT samples, which proves that the titanium is dispersed very well in a homogeneous manner with no observed phase

separation and formation of any random individual titanium oxide clusters. It also confirms that titanium may be present in the substitutional positions in the lattice of the parent vanadium oxide.

Table 18. Peak positions observed in Raman spectrum of VO_x:Ti-VACNT and corresponding vibrations

Wavenumber (cm^{-1})	Vibration	References
145	$(V_2O_2)n$, bending	85
197	$(V_2O_2)n$, bending	85
284	V=O, bending	85
304	V_3-O, bending	369, 386
404	V=O, bending	369, 386
477	V-O-V, bending	369
528	V_3-O, stretching	369
700	V_2-O, stretching	369
830	V-O-Ti	382, 387
941	Bridging V-O-V vibrational bands	386-388
992	Symmetric stretching of V=O bond	386, 387
1250	CNT-D-band	78, 79
1650	CNT-G-band	78, 79
2650	CNT-G'-band	78, 79

As seen in **Table 18**, every single peak is seen to match with that of the linkages seen in the vanadia lattice. However, the peak occurring at 830 cm^{-1} does not match any of the vibrations of vanadium and oxygen. Nevertheless, it matches closely that of V-O-Ti as reported by Krykova et al.[387] (Ti-O-V linkage at a wavenumber of 860 cm^{-1} has been reported). The wavenumber of 830 cm^{-1} also matches that of rutile TiO_2 seen in TiO_2 supported V_2O_5[386]. However, none of the other vibrations of the rutile phase are present leading us to conclude that it is indeed a Ti-O-V bond rather than a secondary rutile phase. Titanium and vanadium have similar ionic radii which allows for the relative ease of doping and substitution of titanium on V sites in the vanadium oxide lattice. **Figure 49b** shows the comparison of Raman spectra seen in VO_x:Ti-VACNT and VO_x-VACNT. It can distinctly be observed that the peak at 830 cm^{-1} is absent in the VO_x-VACNT further corroborating the hypothesis that the peak position occurs as a result of a Ti-O-V vibration.

Table 19. Electronic conductivity data of various titanium doped vanadium oxide and undoped vanadium oxide and oxide-CNT composite electrodes.

Material	Resistivity (Ω-cm)
VO_x:Ti-VACNT	0.0182
VO_x-VACNT	0.46
VO_x:Ti	0.9
VO_x	7.5
Nickel current collector	$9.3 * 10^{-6}$

Four-probe conductivity measurements were also performed on both the thin film oxide and VACNT-supported VO_x:Ti nanocomposite heterostructures. Sheet conductivity data was obtained using a Veeco- FPP 500 instrument wherein the coated Ni disks were suppressed onto standalone tips and voltage *vs.* current was measured. Sheet resistance data was multiplied with the thickness to obtain bulk resistivity which is reported in **Table 19**. The electronic conductivity of the nickel disk was found to be almost 5 orders of magnitude larger than that of either the VO_x, VO_x:Ti, VO_x-VACNT or VO_x:Ti-VACNT composites indicating that the four-probe conductivity data does not bear any artifact arising from the current collector. The conductivity values fall within the range of resistivities reported ($10^1$and 10^4 Ω-cm[185, 389]) in the literature for various oxidation states of vanadium at room temperature. As expected, the electronic conductivity of the VACNT supported VO_x and VO_x:Ti is much higher than that of the respective thin film undoped and Ti doped vanadium oxides. The vertically aligned support structure provided by the VACNTs clearly allows for a thin film of oxide to be supported by highly conductive CNTs resulting in 1-D ballistic transport of electrons through the CNT channels reflected in the improved electronic conductivity. The Ti-doped VO_x supported on VACNT clearly demonstrates the combined benefits of doping as well as the CNT architecture together adding to the improved electronic conductivities even better by more than order of magnitude compared to undoped VO_x supported on VACNTs discussed in **Section 4.2**.

The deposition of oxide film on CNTs therefore leads to conductivities similar to those of vanadium oxide nanowires reported previously[372]. In addition, the electronic conductivity of the VO_x:Ti-VACNT can be seen to be almost one order higher than that of the VO_x-VACNT as mentioned above. Moreover, titanium and vanadium have similar ionic radii which allows for the relative ease of doping of titanium into the vanadium oxide lattice. Vanadium doping of titanium

oxide has also previously been proposed to result in increased electronic conductivity [387, 390]. The doping of titanium oxide with vanadium substantially changes its properties; i.e., the life time of charge carriers increases[391] resulting in increased electronic conductivity. It is expected that a similar phenomenon would be reflected to occur in the case of titanium doped vanadium oxide as well. Vanadium oxide is a well-known n-type semiconductor[329]. The presence of oxygen vacancies as observed in the EDX data would also contribute to increased electronic conductivity.

The doping of titanium into the vanadium oxide lattice it is believed would result in a vacancy mechanism as proposed in Equation (viii).

$$1.6VCl_4(g) + 0.4TiCl_4(g) + 5H_2O\ (g) = 1.6V_V^s + 0.4Ti_V^{i\prime} + 4.6O_O^x + 0.4\square_O^{\cdot\cdot} + 0.4e^{\prime} + 8HCl\ (g) + H_2(g)$$

Equation (viii)

The above proposed mechanism would result in an excess of n-type carriers further increasing the electronic conductivity of vanadium oxide. Furthermore, the doping of titanium into the vanadium oxide lattice also results in a shift of the d-band towards a more metallic state resulting in a further increase in electronic conductivity. This is reflected in **Table 19**, wherein both the VO_x: Ti-VACNT and VO_x-Ti have superior electronic conductivity of more than an order of magnitude in comparison to their undoped counterparts. This increase in electronic conductivity by doping with titanium would thus lead to enhanced inherent oxide electron transport and hence enhanced supercapacitor performance.

The marked improvement in electronic conductivity by serendipitous introduction of oxygen vacancies and Ti into the V_2O_5 oxide can be clearly demonstrated using first-principles

computational approaches implemented for calculations of the electronic structure of the pure and doped vanadium oxide (discussed on **Page 271**)

Figure 50a shows the cyclic voltammograms of the VO_x:Ti-VACNT at different scan rates ranging from 200mV/sec to 2mV/sec. The change in slopes of the I-V curves clearly shows the expected effects of scan rate. As the scan rate increases, the current response on scanning potential undergoes a transition from a flat capacitor type behavior to a resistor-like dependence as is common for most pseudocapacitor materials. The fade in capacitance with increase in scan rate is a phenomenon observed in all typical supercapacitor materials as described by Conway et. al[44]. This is caused by the change in characteristic of the interface from that of a double layer capacitor to a typical resistor due to the inherent limitations and complexities of charge transfer and electron mobility dynamics. This transition is a fundamental feature of all electrochemical double layer capacitors.

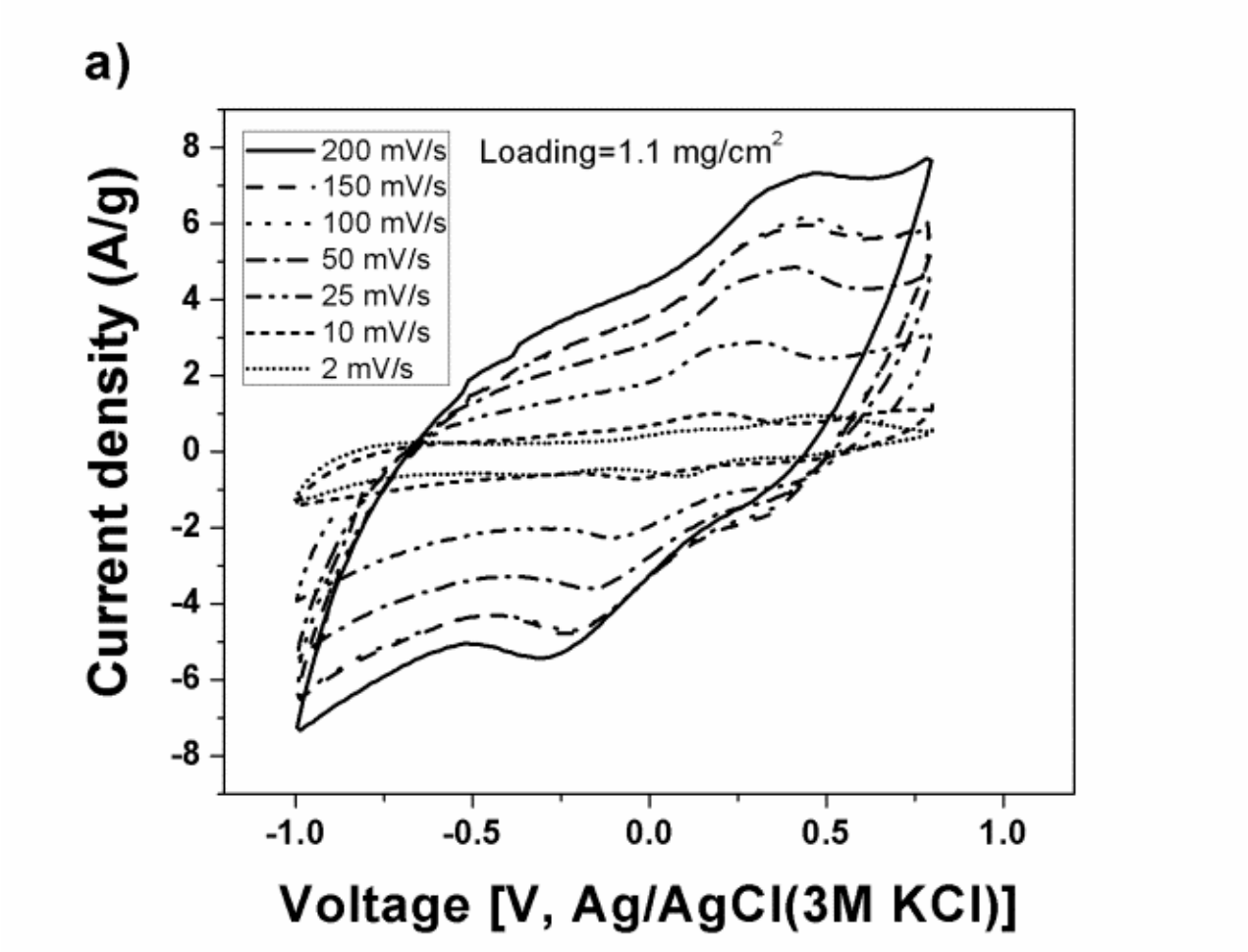
a)
Current density (A/g)
Voltage [V, Ag/AgCl(3M KCl)]
Loading=1.1 mg/cm2
200 mV/s
150 mV/s
100 mV/s
50 mV/s
25 mV/s
10 mV/s
2 mV/s
8
6
4
2
0
-2
-4
-6
-8
-1.0
-0.5
0.0
0.5
1.0

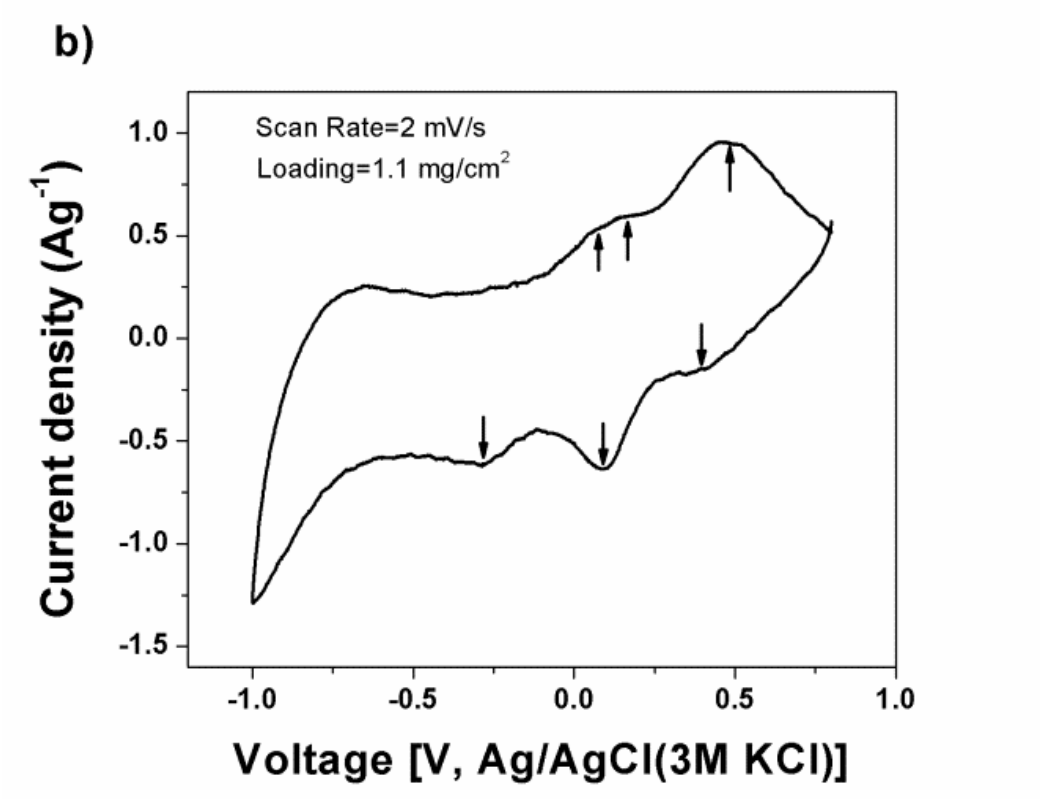
b)
Scan Rate=2 mV/s
Loading=1.1 mg/cm2
Current density (Ag-1)
1.0
0.5
0.0
-0.5
-1.0
-1.5
-1.0
-0.5
0.0
0.5
1.0
Voltage [V, Ag/AgCl(3M KCl)]

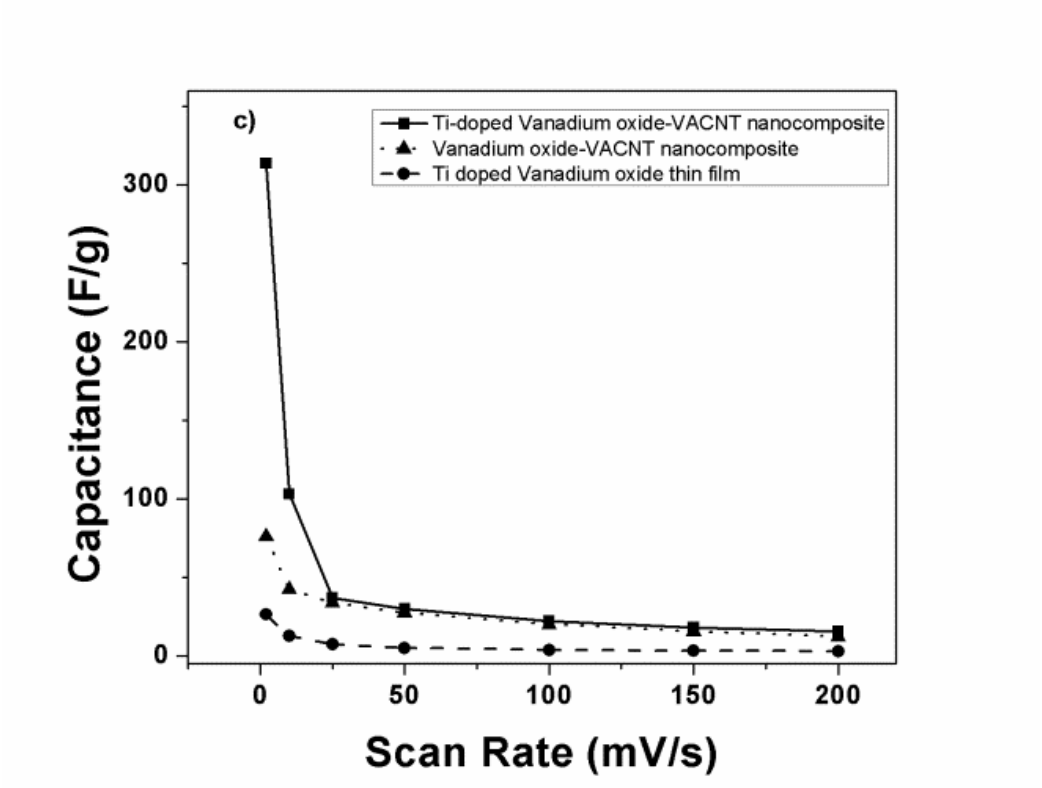
c)
Ti-doped Vanadium oxide-VACNT nanocomposite
Vanadium oxide-VACNT nanocomposite
Ti doped Vanadium oxide thin film
Capacitance (F/g)
300
200
100
0
0
50
100
150
200
Scan Rate (mV/s)

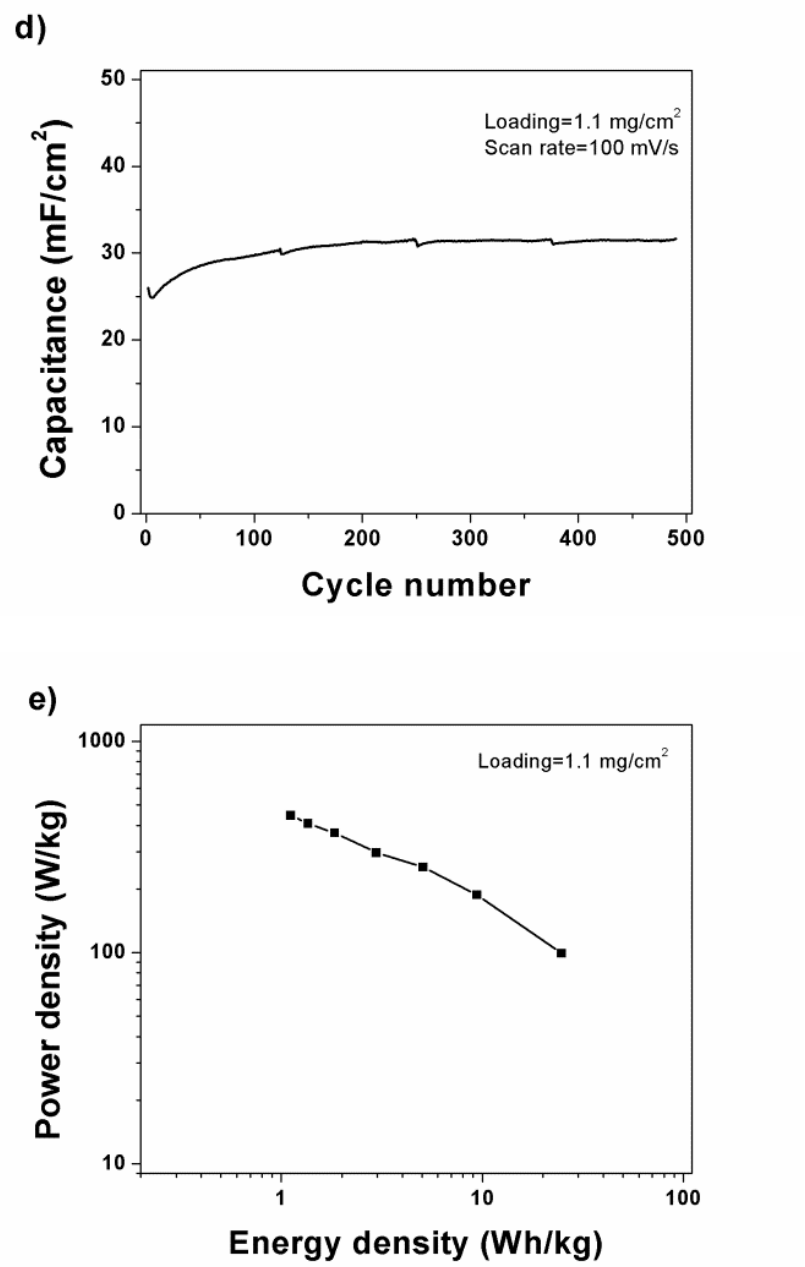

Figure 50. (a) Cyclic voltammograms of the VO_x:Ti-VACNT heterostructures at different scan rates, (b) Cyclic voltammograms of the VO_x:Ti-VACNT at 2mV/sec showing anodic and cathodic peaks for the reversible pseudocapacitive reactions, (c) Variation of gravimetric capacitance with respect to scan rate for VO_x:Ti-VACNT , VO_x-VACNT and thin film VO_x-Ti (oxide loading=0.55 mg/cm^2, Oxide-VACNT active material loading=1.1 mg/cm^2) (d) Cycling data showing capacitance as a function of cycle number conducted at a scan rate of 100mV/sec, and (e) Ragonne plot (power density *vs.* energy density) for VO_x:Ti-VACNT.

It is well known that the capacitance changes with scan rate and is a factor inherently dependent on the specific materials' characteristics. A similar characteristic in Faradaic reactions is the kinetic rate constant (k_o) which is a material property in a given electrode/electrolyte assembly. Pseudocapacitance reactions involving charge transfer by tunneling across the electrochemical interface have an inherent rate constant depending on the various species involved in the charge transfer which could be limiting in the case of the doped oxide coated on the CNTs. It is observed that even though the carbon nanotubes have a vertical alignment, the nature of the tethering of the oxide film on the carbon nanotubes needs to be improved to achieve better rate capability. Optimization of the system to improve the tethering of the doped oxide/VACNT and the CNT inherent conductivity would ideally increase both the initial capacitance as well as the rate capability, two of the most desired signatures characterizing the efficacy of a capacitor system. Such optimization studies are currently ongoing and will be reported in a forthcoming publication.

Figure 50b shows the slow scan rate cyclic voltammogram of the VO_x:Ti-VACNT composite electrode. Since voltammetry was performed at a slow rate, the Faradaic pseudocapacitance processes are hence not rate limited and distinct peaks occur corresponding to each Faradaic process is clearly visible. Reversible Faradaic peaks are observed at ~0.48V, 0.17V and 0.07V (*vs.* Ag/AgCl) on the positive scan and ~0.40V, 0.09V and -0.28V (*vs.* Ag/AgCl) on the negative scan in the VO_x:Ti-VACNT composite (see **Figure 50b** and **Table 20**).

Table 20 also shows tabulated the possible potential dependent pseudocapacitance type reactions present at these potentials corresponding to a reversible transition of oxidation state of vanadium from +5 to +3 most commonly observed in aqueous systems at the slightly alkaline pH

(~8.5) occurring in a 1M Na_2SO_4 solution[269, 373]. In addition, the onset of water electrolysis is seen to occur at about -0.75V (*vs.* Ag/AgCl) in **Figure 50b** at a low scan rate of 2 mVs^{-1}. This however is not observed at higher scan rates indicating that the kinetics of electrolysis are very sluggish on the VO_x:Ti-VACNT composite heterostructure electrodes, despite the improved electronic conductivity indicated in **Table 19**. We can therefore use this material over an extended window of ~1.8V with minimal or no electrolyte loss caused due to water electrolysis.

Table 20. Faradaic charge transfer processes observed in the titanium doped vanadium oxide-VACNT composite electrode.

Anodic scan peak potential (*vs.* Ag/AgCl)	**Cathodic scan peak potential (*vs.* Ag/AgCl)**	**Possible reaction mechanism**
~0.48V	~0.40V	$3V_2O_5\,(s) + 2H_2O + 4e^- \leftrightarrow V_6O_{13}\,(s) + 4OH^-$ $E = 0.8425 - 0.0591 \times pH$ (Volts vs. SHE) $E = 0.1302$ (Volts vs. Ag/AgCl (3M KCl))
~0.17V	~0.09V	$V_6O_{13}\,(s) + H_2O + 2e^- \leftrightarrow 3V_2O_4\,(s) + 2OH^-$ $E = 0.4352 - 0.0591 \times pH$ (Volts vs. SHE) $E = -0.2768$ (Volts vs. Ag/AgCl (3M KCl))
~0.07V	~-0.28V	$3V_2O_4\,(s) + 2H_2O + 4e^- \leftrightarrow 2V_3O_5\,(s) + 4OH^-$ $E = 0.3901 - 0.0591 \times pH$ (Volts vs. SHE) $E = -0.3222$ (Volts vs. Ag/AgCl (3M KCl))

I It should also be noted that in titanium oxide, the electronic state transition of Ti from +4 to +3 occurs generally at ~-0.6V (*vs.* Ag/AgCl) at pH ~ 8.5[77, 78]. However, these transitions are not observed (see **Figure 50a** and **Figure 50b**) indicating that the titanium is completely doped and in the VO_x lattice forming a solid solution with and no phase separation or secondary oxide formation. This further complements the Raman results confirming the Ti doping in the VO_x lattice.

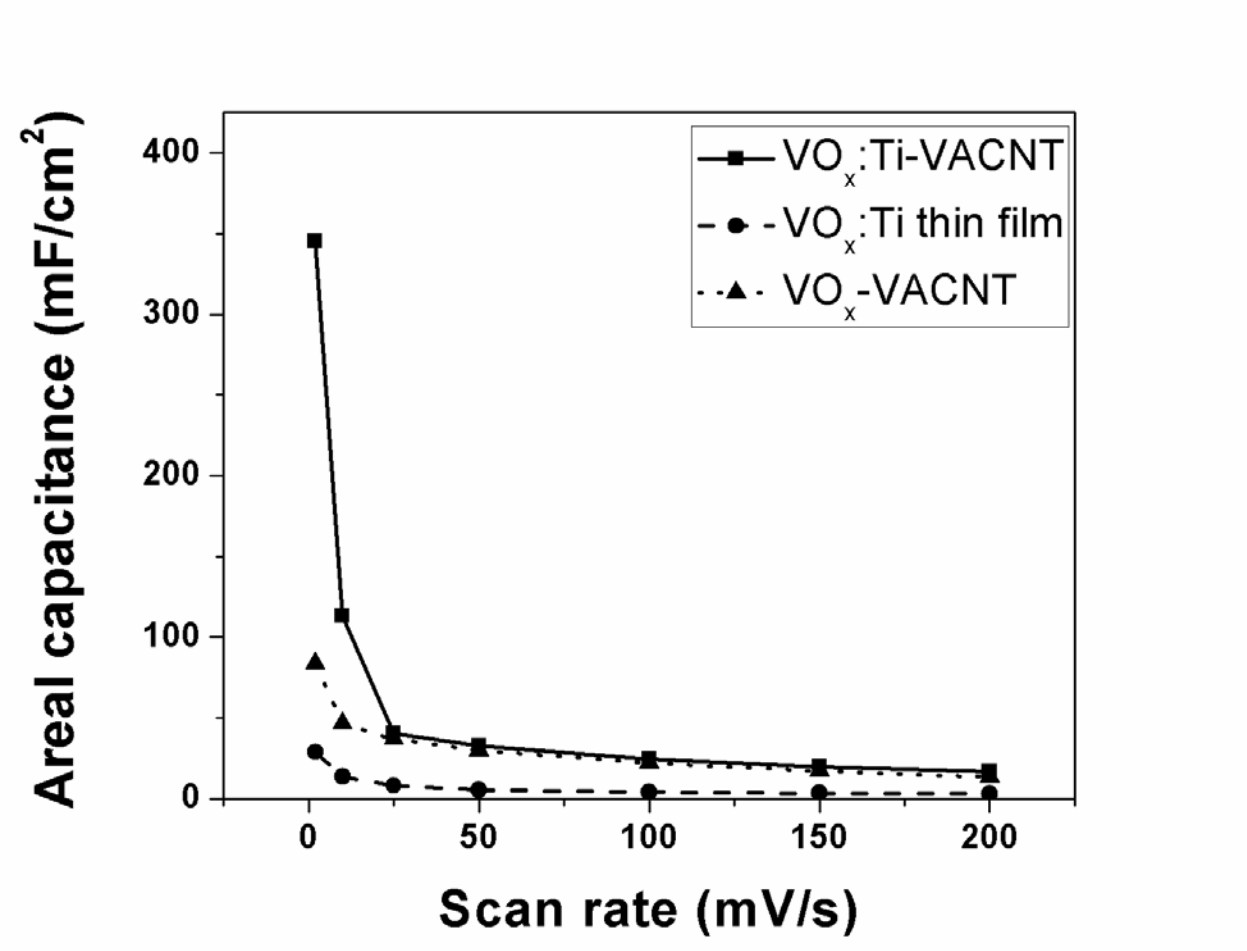

Figure 51. Variation of areal capacitance with respect to scan rate for VO_x:Ti-VACNT , VO_x-VACNT and thin film VO_x-Ti (oxide loading=0.55 mg/cm^2, Oxide-VACNT active material loading=1.1 mg/cm^2)

The variation of the capacitance of VO_x:Ti-VACNT, VO_x-VACNT and VO_x:Ti on Ni substrate with respect to scan rate is plotted in **Figure 50c** (oxide loading~0.55 mg/cm^2, oxide-VACNT loading~1.1 mg/cm^2). The drop in capacitance with scan rate is due to the effect of the resistance/capacitance behavior previously described. Capacitances of ~315 Fg^{-1} on the basis of the total active material loading (~1.1 mg/cm^2) (**not just vanadium oxide loading as seen in the case of the system discussed in Section 4.2**) has been observed at a scan rate of 2 mVs^{-1} in the VO_x:Ti-VACNT nanocomposite material with excellent capacitance retention at higher rates. Also, VO_x:Ti-VACNT has a higher capacitance not only at low scan rates but also at higher scan rates compared to VO_x: Ti thin film. The areal capacitance of the VO_x:Ti-VACNT is between 350 mFcm^{-2} and 30 mFcm^{-2} (see **Figure 51**) which is superior to that reported for other supercapacitor materials at similar scan rates[355, 392]. The performance of supercapacitor materials at high rates is most-often limited by the electronic conductivity of the material. The presence of VACNTs as a support structure for the oxide leads to unidirectional electron transfer through the VACNTs[376] which then travel through the semi-contiguous film and interact at the oxide-electrolyte interface where the charge is stored. This allows for maximum CNT-oxide electron transport while minimizing electron transport through the VO_x grain boundaries which act as a barrier to electron transport. The present morphology also leads to increased surface exposure of the oxide to the electrolyte *i.e.* maximizing the electrochemical surface area and affording maximum exploitation of the capacitance behavior.

The cycling stability of the VO_x:Ti-VACNT supercapacitor material to retain charge over 400 cycles at a scan rate of 100mV/sec is shown in **Figure 50d**. It can be observed that the areal capacitance increases initially stabilizing at a value of ~31 mF/cm^2. This excellent cyclability can be attributed to the reversible nature of the surface pseudocapacitance reactions of the oxide

(see **Table 20**). The slight initial increase in capacity is possibly a result of the gradual improvement in wetting of the VO_x:Ti-VACNT composite with the electrolyte. The oxidation state of the CVD deposited vanadium oxide is ~4.6 consisting predominantly of a +4/+5 oxide. According to the potential-pH diagram, at the pH of ~8.5, vanadium oxide has stable insoluble phases between the potentials of ~0.5 V and -1 V wrt Ag/AgCl[269]. Above 0.5 V, the higher oxidation state oxide is considered soluble to form $H_2VO_4^-$ at a neutral pH. This should be reflected as a loss in capacity with cycling. However, the onset potential of the electrochemical reactions is kinetically limited and is known to vary with particle size and the ensuing microstructure[235]. The Ti doped oxide is amorphous in the present work and most amorphous materials will be expected to exhibit lower stability compared to the crystalline counterpart due to the higher reactivity and defective state. However, the stronger Ti-O bonds and the overall higher cohesive energies for the crystalline counterpart translated to the amorphous state could likely contribute to the better stability of the system. Hence it is believed that the amorphous nature of the oxide nanoparticles supported on the vertically aligned carbon nanotubes could offset the onset of such dissolution resulting in the observed very stable performance of the oxide in aqueous Na_2SO_4 shown in **Figure 50d**. It is also possible that the kinetics of the dissolution reaction might be sluggish and such a fade in capacity would probably be observed if the material were cycled over several thousands of cycles which was not conducted in the present study since the objective was to demonstrate the performance of the doped system supported on VACNTs rather than demonstrate optimization of the system which will be part of the continued study that will be reported in subsequent publications.

The synergistic effect of the carbon nanotube-vanadium oxide junction has previously been studied for gas-sensing purposes [369, 374, 375]. It has been suggested that a p-n junction type

interaction between the VO_x and the CNT leads to increased catalytic response of the oxide while the multi walled CNTs, which acts as a p-type semiconductor facilitates the fast electron channels. A similar p-n type interaction can be expected to be observed in VO_x:Ti-VACNT composite as it is known that VO_x:Ti tends to exhibit predominantly n-type carrier behavior. All these factors are reflected in the improved electronic conductivity (**see Table 19**) contributing to achieving the improved rate capability, excellent supercapacitor response and cycling stability as seen in **Figure 50c and Figure 50d**. Improved charge storage behavior may also be attributed to electronic sensitization of the doped oxide by this effect as commonly observed in doped oxides used for gas sensing applications[393].

It is common knowledge that thick films of nanoparticulate oxides especially amorphous oxides would be non-ideal configurations to obtain high capacitances on account of the low inherent electronic conductivity, grain boundary diffusion and exposed surface area. On the other hand, the use of a relatively thin film on a supported structure affords the benefits of high surface area, small particle size and direct contact of grains with the highly conductive carbon nanotube surface. This accessible capacitance of vanadium oxide is very much limited when the electrode is cast as a thick film. However, thin film titanium vanadium oxide has a high capacitance when supported on VACNTs as demonstrated in **Figure 50c**. The VACNTs act as a 3-dimensional electronically conductive support resulting in enhanced electrochemical surface area reflected both in the improved performance and rate capability of the VO_x:Ti-VACNT heterostructure composite. The overall capacitance reported in this manuscript is however lower than that reported for vanadium oxide-CNT systems in LiCl based systems by Hu et al.[180], as there is no intercalation mechanism involved in tandem with the pseudocapacitance processes combined with double layer charge storage seen in the present VO_x:Ti-VACNT composite. Evaluation of

VO_x:Ti-VACNT and other doped vanadium oxide systems is ongoing in intercalation based electrolytes and it is expected that higher energy density can be obtained using this system. The unique synthesis method, composition, morphology, electrode/electrolyte combination and an in-depth electrochemical characterization provided in this detailed study are original contributions enhancing the understanding of supercapacitor behavior in early transition metal oxide systems to the best of the understanding known from the published literature to date.

The above-stated improvements in the VOx:Ti-VACNT are reflected as the excellent supercapacitor performance seen in the Ragone plot **Figure 50e**. The Ragone plot is conventionally used to represent the variation of energy density as a function of power density. An ideal device would maintain its energy density upon increasing power density. However, this is not very commonly observed as higher power densities indicate a greater diversion from equilibrium resulting in an L-shaped curve commonly seen showing higher power densities with low energy density and corresponding decrease in power densities with increasing energy density. In the case of the VO_x:Ti-VACNT high energy densities are sustained by the system with increasing power density although there is also observed a fade in energy density with rise in power density. The highest energy density of ~25 $Whkg^{-1}$ was obtained at a power density of ~100 Wkg^{-1}. This is comparable to noble metal oxide (~25 Wh/kg) and very thin film based oxide (~30 Wh/kg) supercapacitor electrodes[394-396] and superior to other oxide materials(10-20 Wh/kg) representing the novelty of the work conducted in this study[397].

In order to further establish the advantages yielded by the CVD deposition of VO_x:Ti on VACNTs, electrochemical impedance spectroscopy (EIS) analysis was conducted on the nanospheres as well as the doped oxide film and charge transfer characteristics were accordingly compared. **Figure 52a** and **Figure 52b** show the Nyquist plots of the VO_x:Ti -VACNT hybrid

and the VO_x:Ti thin film oxide, respectively at different voltages over the window of interest. It can be directly observed that the impedance behavior of both materials is different especially at voltages close to the regions of the Faradaic peaks observed at ~0.48 V, 0.17 V and 0.07 V on the anodic scan and ~0.40 V, 0.09 V and -0.28 V in the cyclic voltammograms (see **Figure 50b**). At these potentials corresponding to the Faradaic charge transfer reactions, it can be seen upon comparing the response of VO_x:Ti and VO_x:Ti-VACNT composite that the thin film oxide has a much larger charge transfer resistance similar to the results discussed in **Section 4.2**. This is inferred from the large semi-circular arcs seen in **Figure 52b** as compared to **Figure 52a** where one can see the Warburg tail being more prominent in **Figure 50a** as compared to the relatively much smaller semi-circular arcs (oxide loading~0.55 mg/cm^2, oxide-VACNT loading~1.1 mg/cm^2). The large semi-circular arcs in a Nyquist plot are indicative of high charge transfer resistance which would result in the reduced Faradaic response in the VO_x:Ti thin film oxide at higher scan rates as seen in **Figure 50c**. Pseudocapacitance performance which is usually prevalent in the 10^3 to 10^4 Hz region on account of the electrode kinetic rate limitations[58] is much more prominent in the VO_x:Ti-VACNT as compared to the VO_x:Ti.

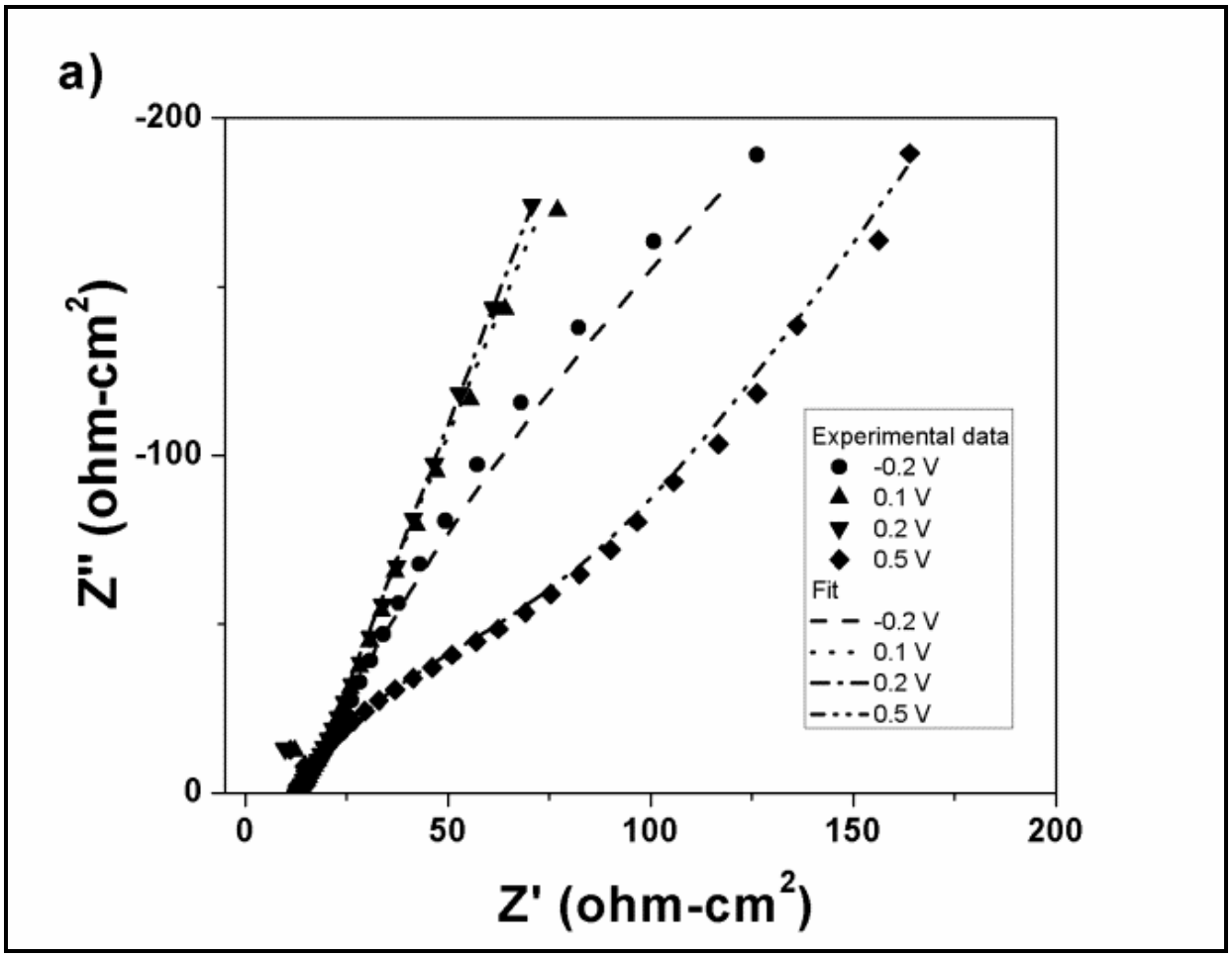
a)
-200
-100
0
Z'' (ohm-cm^2)
0
50
100
150
200
Z' (ohm-cm^2)
Experimental data
-0.2 V
0.1 V
0.2 V
0.5 V
Fit
-0.2 V
0.1 V
0.2 V
0.5 V

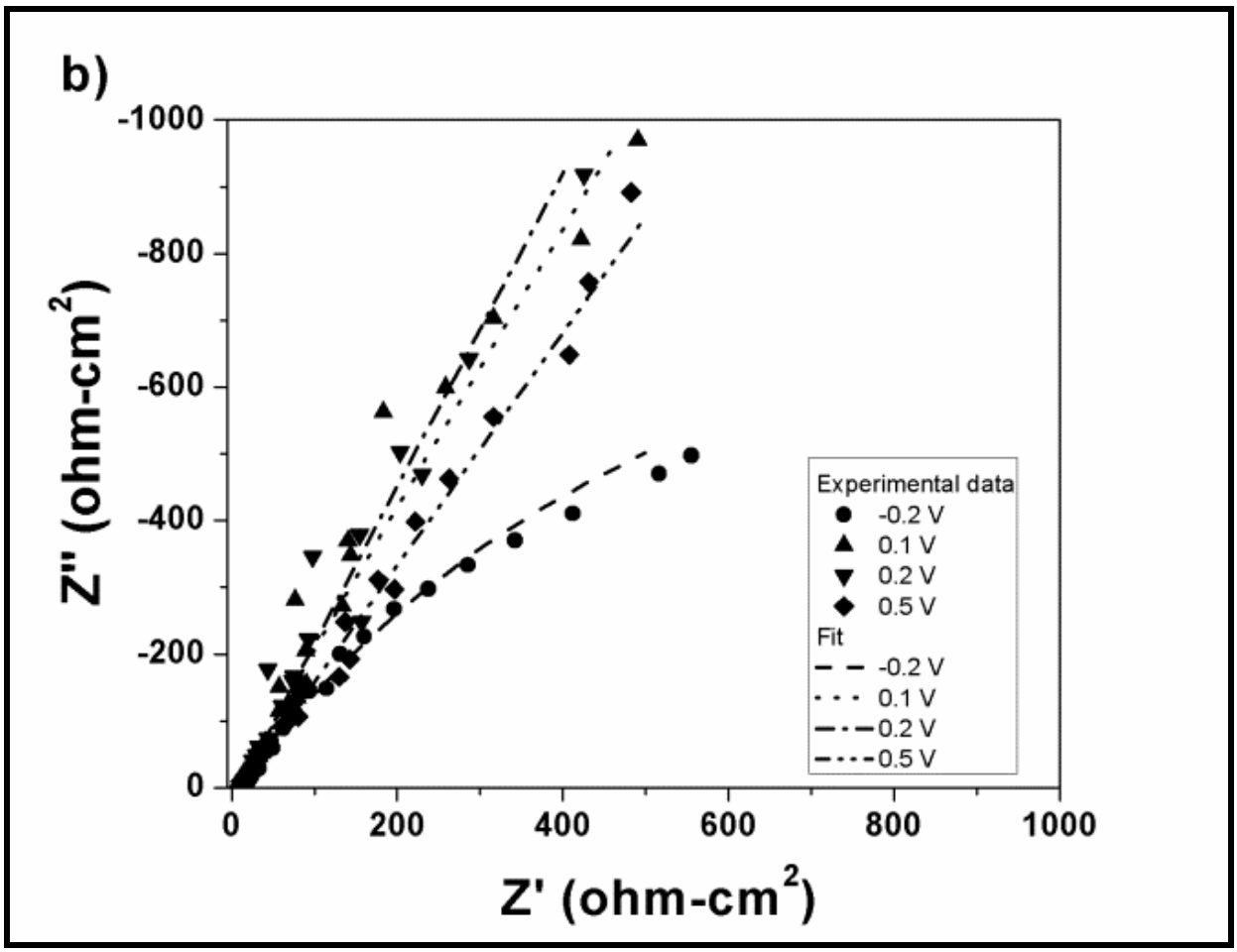

Figure 52. (a) Impedance behavior of VO_x:Ti-VACNT (oxide loading~0.55 mg/cm^2, oxide-VACNT loading~1.1 mg/cm^2) and (b) VO_x:Ti thin film.

Equivalent Circuit modeling was performed using the Z-view software to obtain charge-transfer parameters of the titanium doped vanadium oxide thin film and titanium doped vanadium oxide-VACNT composite electrodes. An under-potential deposition mechanism (**Figure 35**) described by Conway et. al.[44, 58] was used to model the pseudocapacitance reactions at both sets of electrodes. The mechanism considers both double layer capacitance (usually modeled as a capacitor (C_{dl}) in parallel with a resistor (R_F)) and pseudocapacitance arising from

surface reactions (C_p) on the electrode of interest. In addition, an electrochemical series resistance (R_s) common to all electrochemical systems is also considered. However, in porous electrode systems, the capacitor elements are usually modeled as constant phase elements[65, 360]. Constant phase elements (CPE) are usually used to fit data having depressed semi-circular arcs on account of electrode porosity and roughness which leads to fractal character and inhomogeneity in response on account of presence of different crystallographic reaction sites. On account of such behavior noticeable in **Figure 52a and Figure 52b**, we have used constant phase elements, CPE-dl and CPE-p to fit our data. The values of various charge transfer parameters obtained by fitting have been summarized in **Table 21**.

Table 21. Charge-transfer properties of the CVD derived titanium doped vanadium oxide materials.

Voltage	Series Resistance (R_s)-Ωcm^{-2}		Double layer Constant Phase Element (CPE-dl)				Pseudocapacitance Constant phase element (CPE-F)				Faradaic resistance (R_F)-Ωcm^{-2}	
	Ti-VO_x-VACNT	Ti-VO_x	Ti-VO_x-VACNT		Ti-VO_x		Ti-VO_x-VACNT		Ti-VO_x		Ti-VO_x-VACNT	Ti-VO_x
			$T*10^4$	φ	$T*10^4$	φ	$T*10^4$	Φ	$T*10^4$	Φ		
-0.2	2.46	1.67	6.14	0.86	4.22	0.60	23.37	0.71	0.24	0.98	0.86	9.68
0.1	2.51	1.7	3	0.98	0.04	0.96	19	0.77	1.17	0.72	0.94	1.06
0.2	2.51	1.69	6	0.90	0.05	0.94	16	0.77	1.01	0.73	1.44	1.09
0.5	2.46	2.01	23	0.74	0.57	0.84	56.95	0.71	1.11	0.75	24.06	37.83

It can be seen that the series resistance (R_s) is fairly constant in both systems and varies between 2 and 3 Ωcm^{-2} which is common in carbon based systems[361]. The most notable difference in behavior between VO_x:Ti and the VO_x:Ti-VACNT composite is the charge transfer resistance R_F. R_F values are reduced by up to an order on account of the presence of VACNTs. This can also be seen in **Figure 52a** wherein the oxide nanosphere-VACNT heterostructure based material has an almost 90 degree slope at low frequencies as compared to large semi-circles indicating high R_F values seen in **Figure 52b** [378]. R_F is the charge transfer resistance for electron tunneling from the electrode to the electrolyte i.e. the Faradaic pseudocapacitance process. R_F can usually be correlated with exchanged current density through the expression[58]:

$$R_F \text{ (in ohms)} = \frac{RT}{i_0 F} \qquad \text{Equation (ix)}$$

where

R= Gas constant ($Jmol^{-1}K^{-1}$)

T= Temperature (in Kelvin)

i_0= Exchange current density (in Amperes)

F= Faraday constant ($Coulomb\text{-}mol^{-1}$)

R_F as defined in Equation (ix) is the Faradaic charge-transfer resistance at reversible potential. A decrease in charge-transfer resistance thus indicates an increase in exchange current density resulting in increased rates of the Faradaic reactions. The value of R_F as defined in Equation (ix) is limited to the reversible potential of the particular reaction. Therefore, in addition to the above conclusion, one can understand that the Faradaic leakage current density and thus Faradaic charge-transfer resistance are overvoltage dependent[58]. The dependence of R_F on voltage can be seen in **Table 21**. **Table 21** compares the charge transfer resistance of the

VO_x:Ti-VACNT with that of VO_x:Ti at different voltages. The charge transfer resistance of VO_x:Ti –VACNT is less than or equal to that of VO_x:Ti at all the potentials indicating that electron tunneling across the electrochemical interface is more easily activated in the case of VO_x:Ti-VACNT than in the case of VO_x:Ti. The improvement in pseudocapacitance behavior can also be inferred by referring to the quantitative values of the constant phase elements (CPE-F) seen in **Table 21**. The doping of titanium into the vanadium oxide lattice thus enhances not only electronic conductivity but electrochemical performance to a certain extent resulting in the improved response seen in **Figure 50c**.

4.3.1 Conclusions

Hot-wall chemical vapor deposition has for the first time been used to create a unique morphology consisting of titanium doped vanadium oxide nanospheres on vertically aligned carbon nanotubes. Such a CVD derived VO_x:Ti-VACNT heterostructure composite has been shown to exhibit excellent charge storage characteristics with capacitances of up to 313 Fg^{-1} achieved at a scan rate of 2 mVs^{-1} in a thick oxide nanosphere film coated on the VACNTs. The doping of titanium into the vanadium oxide lattice has been shown to have a salutary effect on the electrochemical charge storage capability of vanadium oxide. One of the highlights of this study is the ease of electrode fabrication. Chemical vapor deposition is a method amenable for continuous production of electrodes in an assembly-chain configuration in contrast with chemical methods used to produce oxides which require batch processes and in-turn also involve a second heat treatment step. The need for slurry preparation is eliminated and binder-free electrodes are thus generated. The formation of a thick film with high loadings (upto 1.1 mg/cm^2) by a chemical vapor deposition method allows for tailoring of the morphology of the

oxide while maintaining sufficient active materials resulting in high areal capacitance of upto ~350 mF/cm^2. The CVD method could further be optimized to lead to electrodes with superior rate capability by tailoring the nature of the CNT-oxide interface by functionalization.

4.4 DOPED VANADIUM NITRIDE CAPACITORS

Figure 53a and **Figure 53b** show the X-ray diffraction patterns of the niobium doped VN and tungsten doped VN prepared by the two-step ammonolysis respectively. It can be observed that the X-ray patterns in the case of both dopants match very well that of cubic vanadium nitride (PDF 00-035-0768).

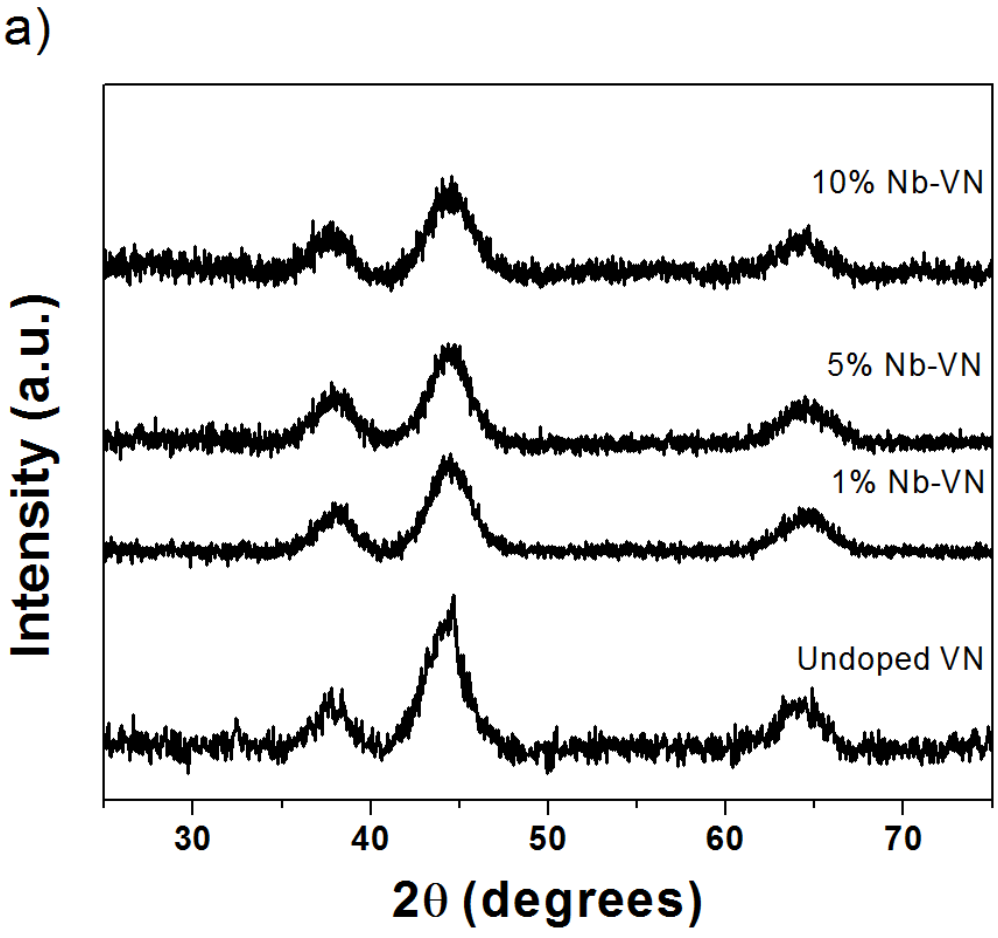

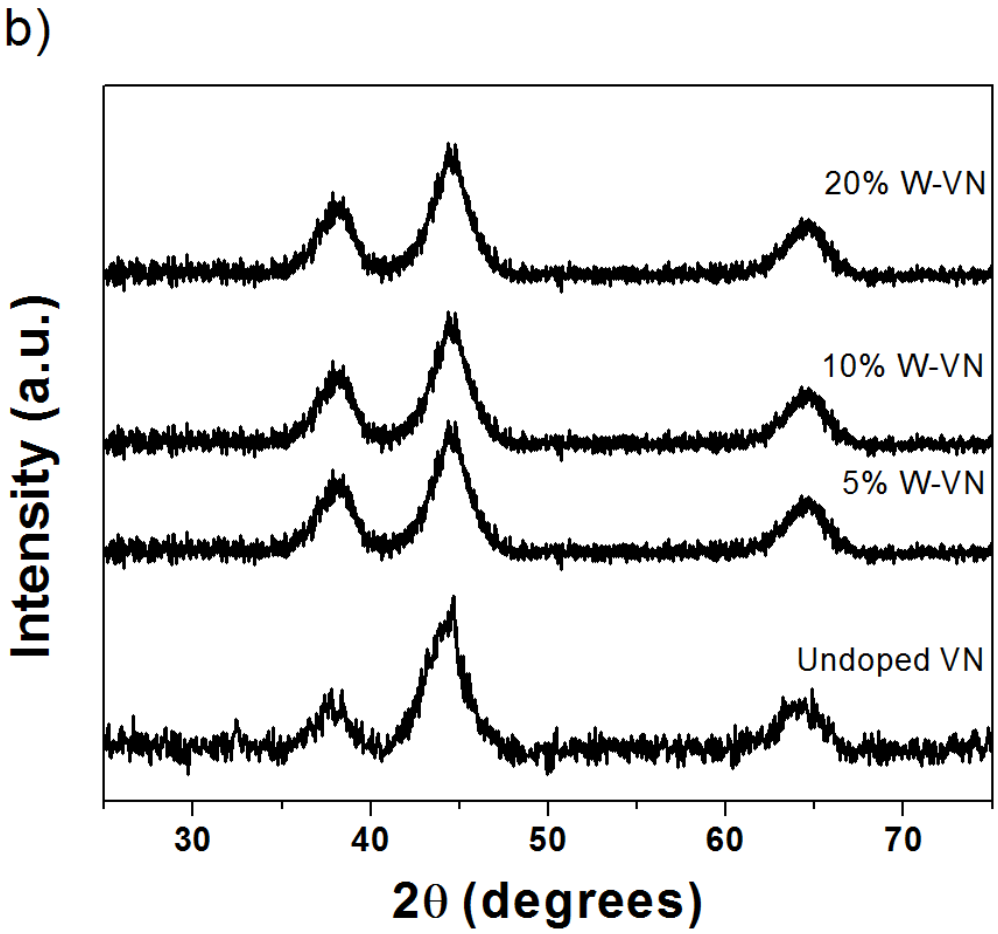

Figure 53. X-ray diffraction patterns of various compositions of (a) $V_xNb_{1-x}N$ (x=0.01-0.1) and (b) $V_xW_{1-x}N$ (x=0.05-0.2).

Table 22. Comparison of materials properties of the different doped vanadium nitride materials.

Nominal material composition	Crystallite size (nm)*	Lattice parameter (A^0)#	Molar volume (cm^3/mol)	BET surface area (m^2/g)	Experimentally derived composition	Average Vanadium oxidation state	Electronic conductivity (S/cm)
VN	4.10	4.066±0.027	10.12	28.80	$VN_{0.76}O_{0.24}$	3.48	81.8
$Nb_{0.01}V_{0.99}N$	2.28	4.066±0.041	10.12	29.85	$Nb_{0.01}V_{0.99}N_{0.61}O_{0.69}$	3.19	63.3
$Nb_{0.05}V_{0.95}N$	2.73	4.073±0.060	10.17	34.06	$Nb_{0.05}V_{0.95}N_{0.57}O_{0.53}$	2.65	86.5
$Nb_{0.10}V_{0.90}N$	2.64	4.036±0.058	9.90	42.63	$Nb_{0.14}V_{0.86}N_{0.73}O_{0.63}$	3.20	138.0
$W_{0.05}V_{0.95}N$	4.45	4.038±0.053	9.91	26.66	$W_{0.05}V_{0.95}N_{0.78}O_{0.63}$	3.47	946.5
$W_{0.10}V_{0.90}N$	4.09	4.083±0.146	10.25	31.29	$W_{0.13}V_{0.87}N_{0.69}O_{0.60}$	2.86	87.6
$W_{0.20}V_{0.80}N$	4.16	4.034±0.057	9.88	31.49	$W_{0.20}V_{0.80}N_{0.78}O_{0.52}$	2.73	104.1

*Calculated using single line approximation of (002) peak# Calculated using linear regression of a and $\cos^2\theta$.

The effective crystallite size of the various doped nitrides of vanadium calculated using the Scherrer formula, from the integral breadth of the Lorentzian contribution determined from the peak profile analysis using the single line approximation method after eliminating the instrumental broadening and lattice strain contribution[335, 336], are seen in **Table 22**. In addition, the lattice parameter and molar volume of the various nitride samples in **Figure 53** was calculated using the least square refinement technique and were found to be ~0.4083±0.0146nm and ~9.88-10.25cm^3/mol respectively. It is seen that the lattice parameter is in agreement with the bulk lattice parameter of cubic VN of 0.4105-0.414 nm[338, 339]. The multi-point BET surface area and four-probe electronic conductivity of the samples are also shown therein. It is observed that there is a change in crystallite size from 4.1 nm to ~2.5 nm upon doping the vanadium nitride with niobium while tungsten doped vanadium nitride did not result in any substantial decrease in crystallite size. No significant trends in surface area are seen therein. Though niobium doping is seen to result in a change in crystallite size, the surface area change however, does not parallel the same. **Table 22** also shows the dependence of electronic conductivity on the composition of the doped vanadium nitride. It can be seen that niobium doping results in a very slight decrease in conductivity with initial doping which increases thereon with further doping. Given that there is a drop in apparent crystallite size, the bulk electronic conductivity should decrease on account of induction of more grain boundaries. The trend observed shows a slight decrease with initial doping occurring as a result of the crystallite-size effects with an increase thereafter, indicating that niobium doping indeed results in generation of more carriers either as a result of inherent electronic changes in either the bulk nitride or surface oxide as predicted by the theoretical studies.

On the other hand, doping with tungsten results in a significant alteration in electronic conductivity especially at a dopant concentration of 5% W-VN wherein an impressive, almost one order increase in electronic conductivity is observed. W-doping of VN also results in no significant alteration of crystallite size as seen in **Table 22** indicating that W-doping indeed has a propitious effect on either bulk nitride conductivity/surface oxide conductivity or both as predicted by theory.

a)

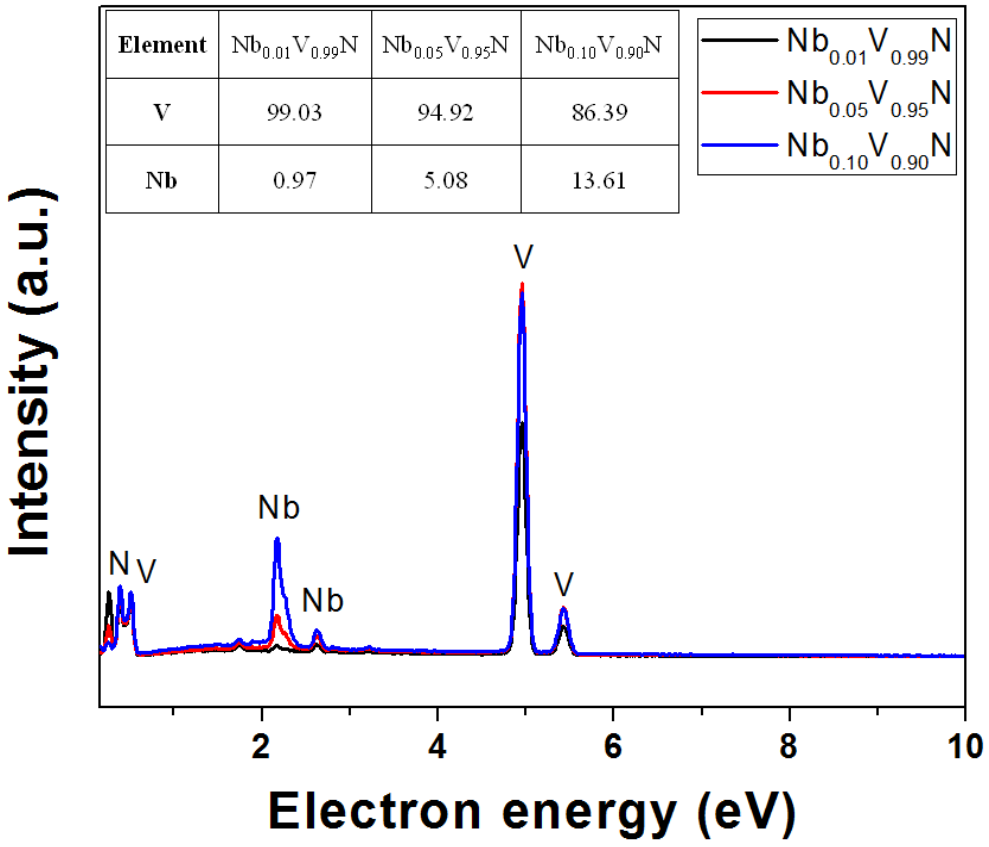

b)

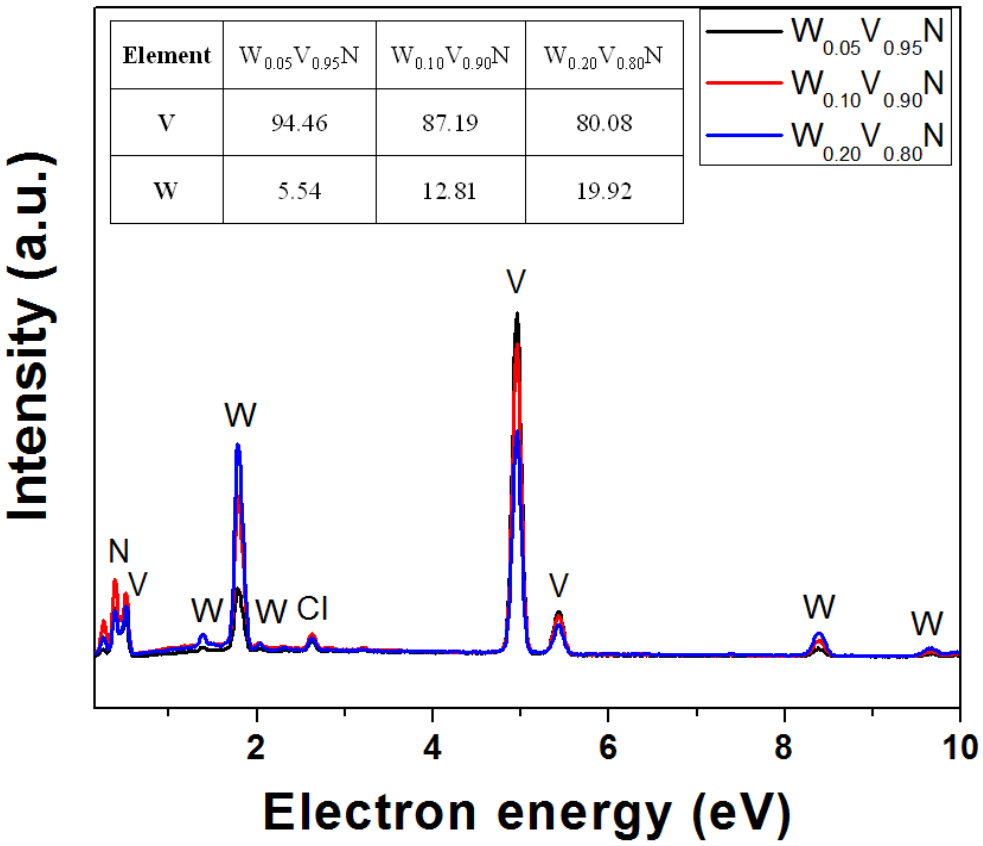

Figure 54. EDAX spectra of various compositions of (a) $V_xNb_{1-x}N$ (x=0.01-0.1) and (b) $V_xW_{1-x}N$ (x=0.05-0.2).

The composition of the various doped nitrides of VN as obtained from EDAX analysis and inert gas fusion analysis (LECO analysis, Alternative Testing Laboratories, Inc.) are shown in **Table 22**. **Figure 54a** and **Figure 54b** show the EDAX spectra of different doped compositions of niobium vanadium nitride and tungsten vanadium nitride respectively. Suitable calibration was performed before EDAX analysis using pure standards. It can be seen that there is a close match in the dopant metal: vanadium ratio with that of the expected nominal composition. The metal:metal composition reported in **Table 22** was obtained by EDAX

analysis. The oxygen and nitrogen content in the samples was obtained using inert gas fusion analysis since EDAX analysis would not yield error-free oxygen content as the L-edge of vanadium coincides with the peak of K-edge of oxygen. The peaks at 386 eV (N-K, L2, L3) and 513 eV (V, L3, M4, M5) have a broad band between them as a result of peaks occurring at 447 eV (V, L3, M1) and 454 eV (V, L2, M1) making de-convolution of the oxygen peaks [525 eV (O K-L2, L3) and 532 eV (O K)] impossible. On account of this overlap, it was not possible to draw conclusions about the oxygen presence from the EDAX data. Instead, inert gas fusion analysis was therefore used to determine the N and O content, and it can be seen that the doped materials contain both nitrogen and oxygen. From the prior studies, it was established that the surface oxide present on the nitride material is related to charge storage behavior as well as cycling stability[182, 235, 246]. The X-ray diffraction peaks do not show presence of any vanadium oxide and high temperature heat treatment does not result in formation of any discrete oxide phase. This indicates that the oxygen is distributed at the surface and the oxide exists in the form of either an oxy-nitride or surface hydroxide. Nitrogen/oxygen atomic ratio varies in all these materials between 0.7 and 1.1. The average vanadium oxidation state based on the composition calculated using EDAX and inert gas fusion analysis are seen in **Table 22**. There is no direct correlation between doping concentration and oxygen amount even though heat treatment and subsequent passivation was performed under near-identical conditions indicating that the surface oxide content depends on the stabilization of surface as preferred by the individual nitride material i.e. the surface oxygen content possibly depends on energy minimization based on crystallite size, presence of defects and other such factors which are not completely understood at this time. Molecular level simulation might help obtain further insight into the characteristic behavior of each surface oxide and its preferred stabilization. The effect of the same on surface charge

storage and capacitance could be correlated and experiments reported in this work could be verified using the same. At the present time however, such molecular simulations are beyond the scope of this study. **Figure 55a-Figure 55f** show the SEM images and EDAX maps of the various compositions of niobium and tungsten doped VN. It can clearly be observed that the dopant metal is uniformly distributed in the case of all the doped compositions.

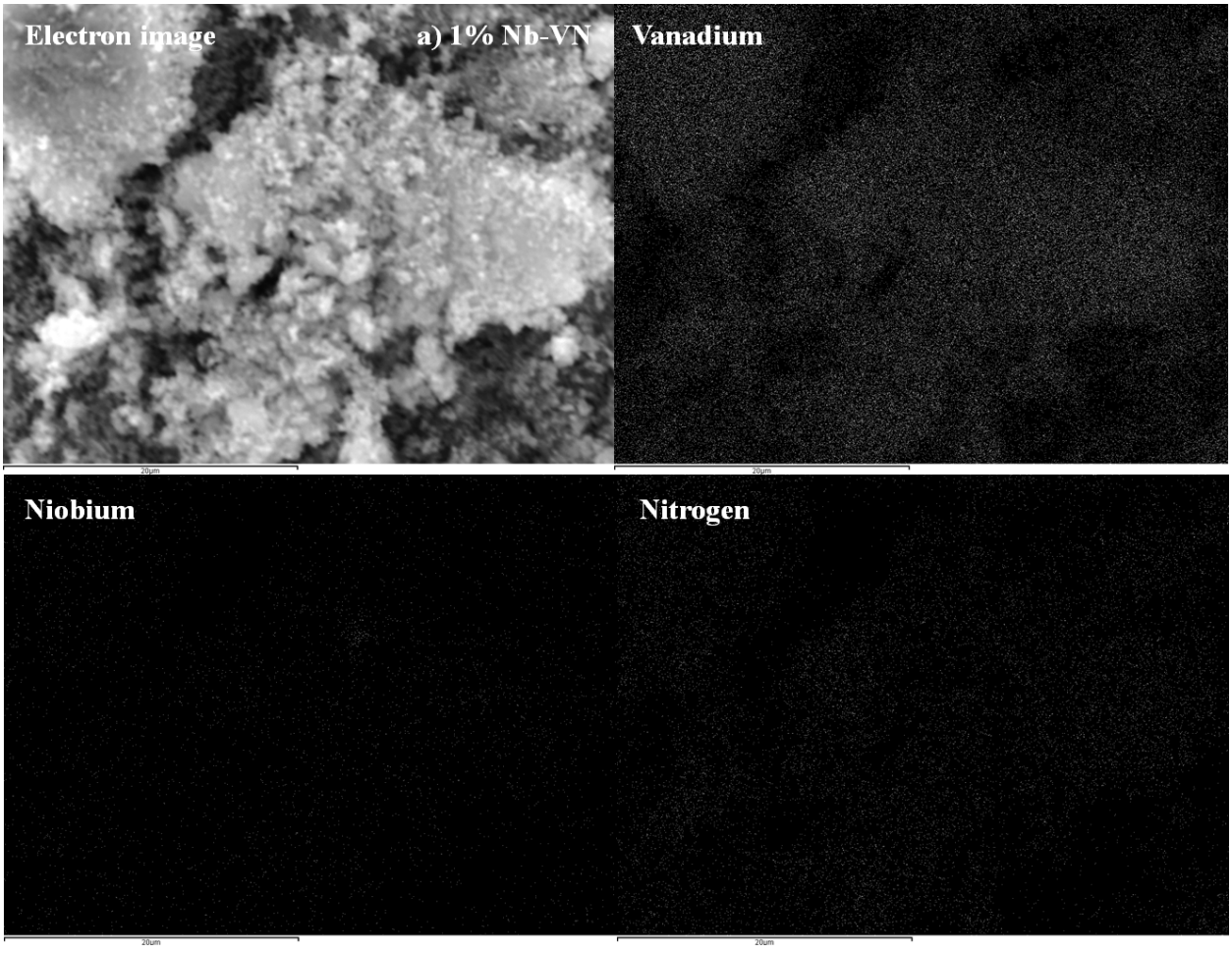

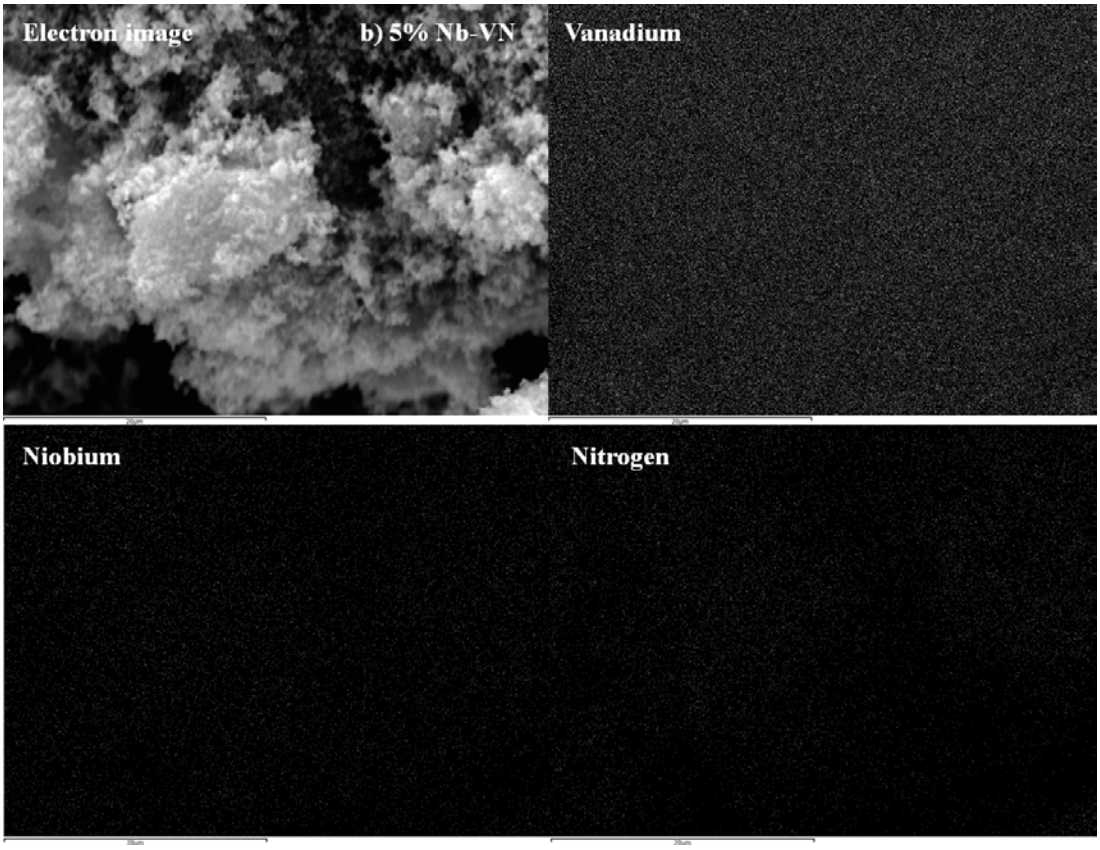
Electron image
b) 5% Nb-VN
Vanadium
Niobium
Nitrogen

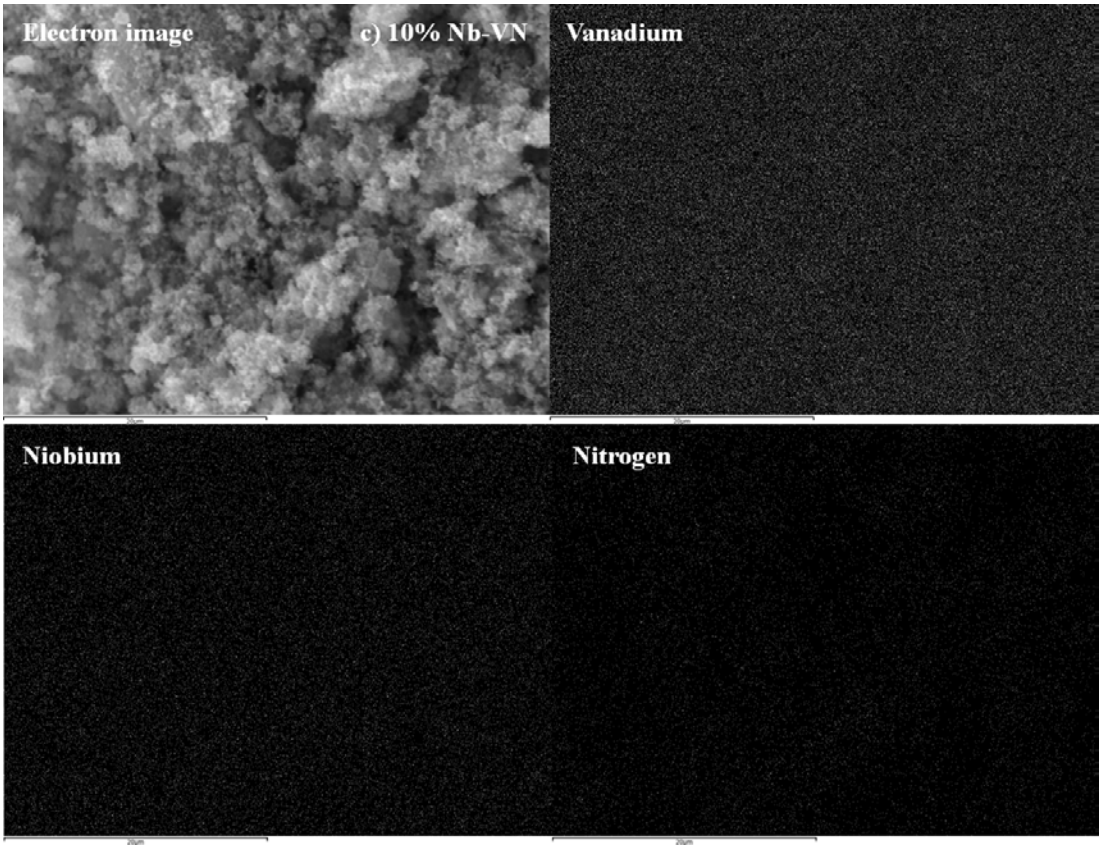
Electron image
c) 10% Nb-VN
Vanadium
Niobium
Nitrogen

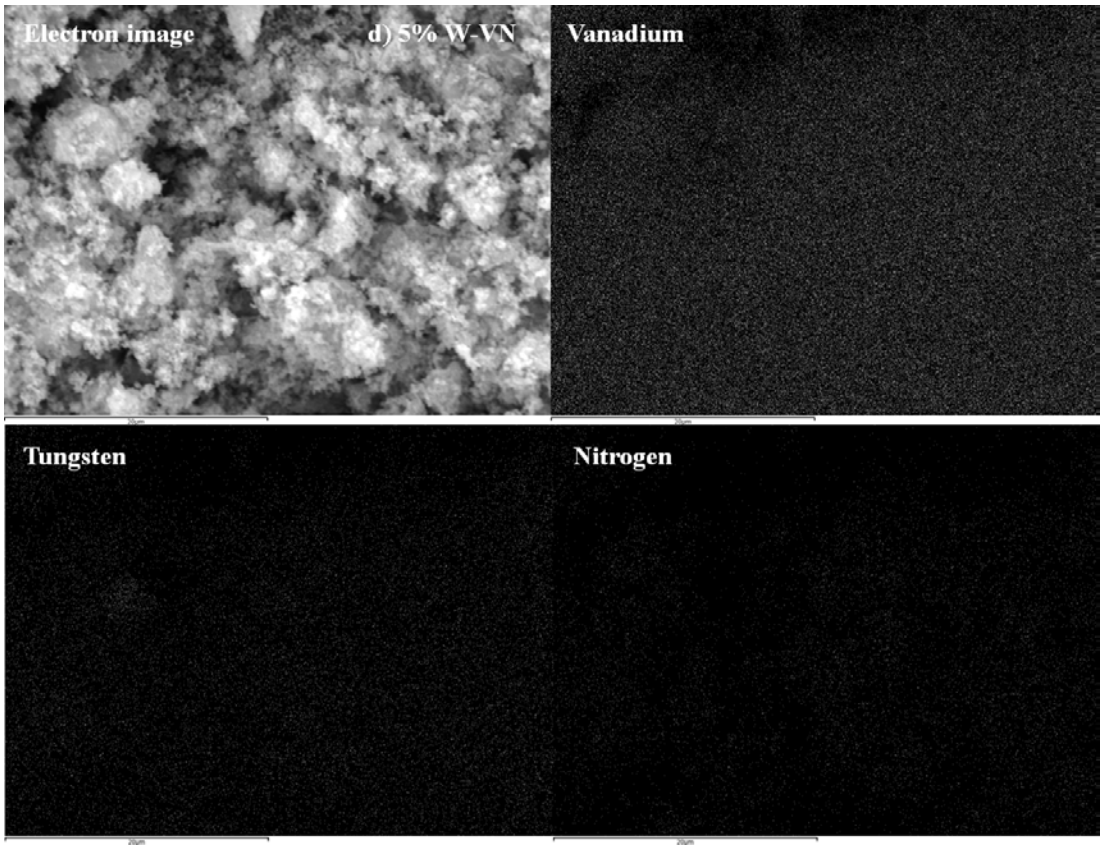
Electron image
d) 5% W-VN
Vanadium
Tungsten
Nitrogen

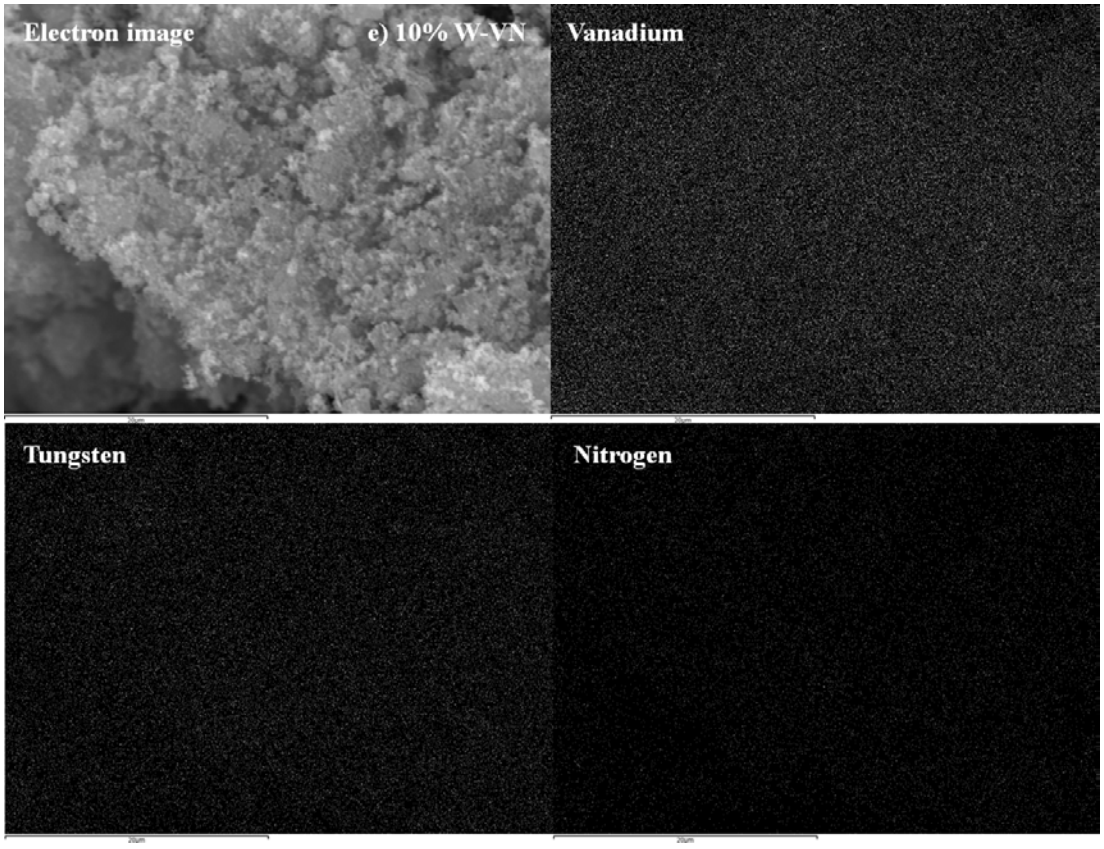
Electron image
e) 10% W-VN
Vanadium
Tungsten
Nitrogen

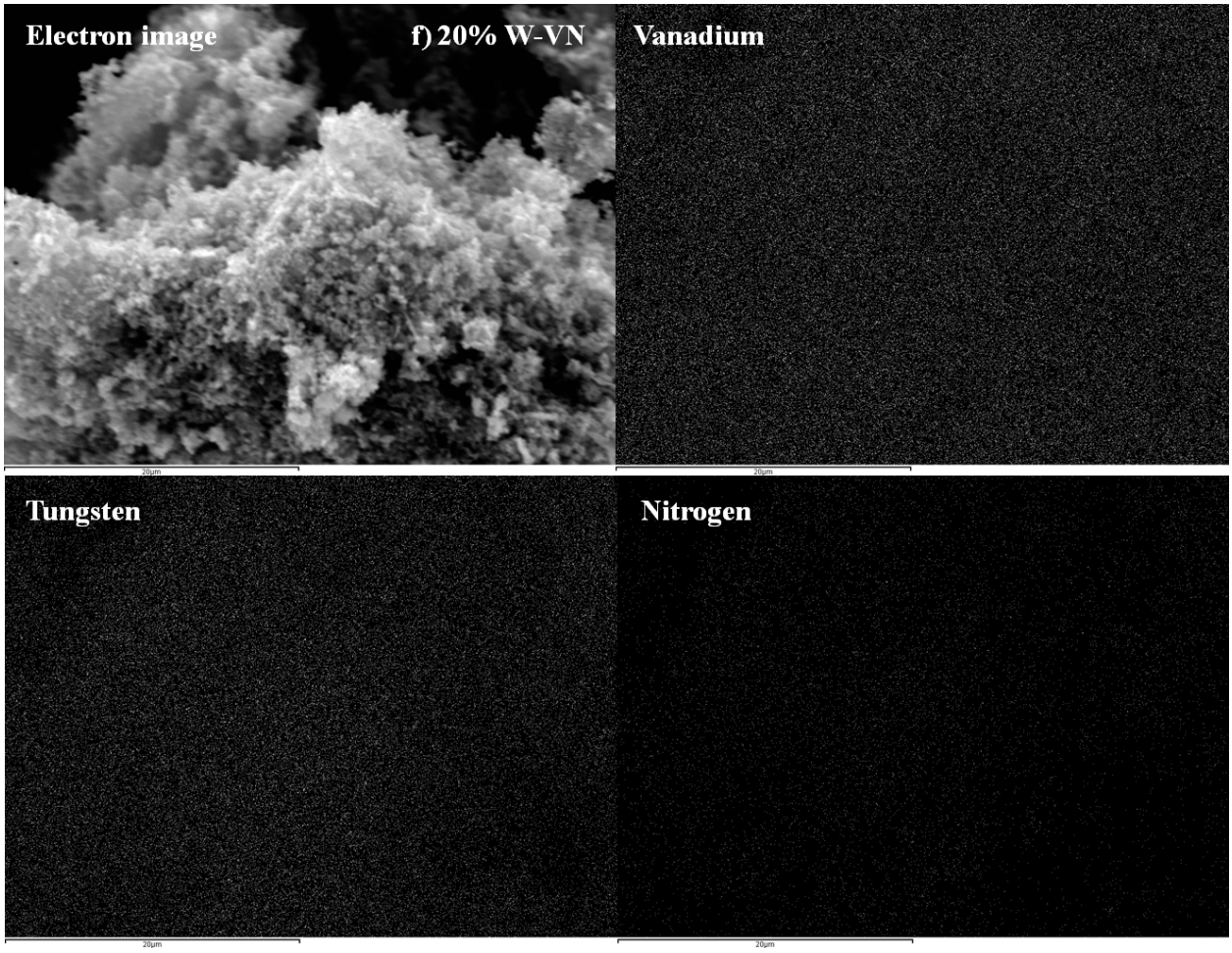

Figure 55. (a)-(f) EDAX maps of various compositions of Nb doped and W doped VN.

The HRTEM images of the various doped nitrides of vanadium are shown in **Figure 56a-Figure 56f**. The TEM image confirms the formation of nano-sized doped VN particles with a very fine particle size of 4-10 nm. Lattice fringes observed in each case correspond to the various planes of the face centered cubic VN. The d-spacings shown in **Figure 56a-Figure 56f** match those of cubic vanadium nitride (PDF 00-035-0768). The crystallite size of Nb doped VN seen herein is slightly larger than the values reported in **Table 22** obtained using X-ray diffraction data seen in **Figure 53a**. This is possibly a result of inhomogeneity in crystallite size as well as particle agglomeration which is distinctly observed in **Figure 56a-Figure 56f**.

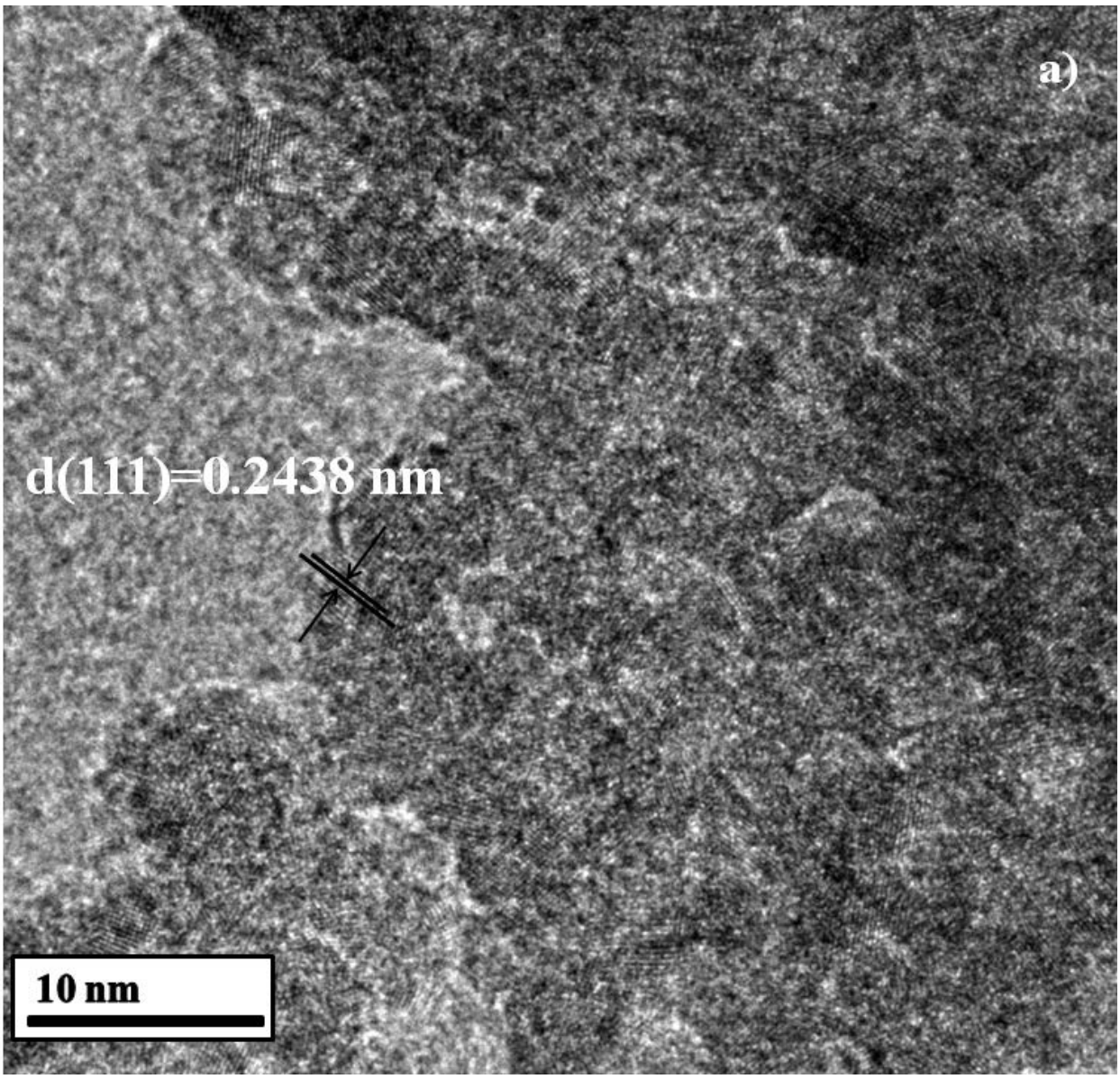
a)
d(111)=0.2438 nm
10 nm

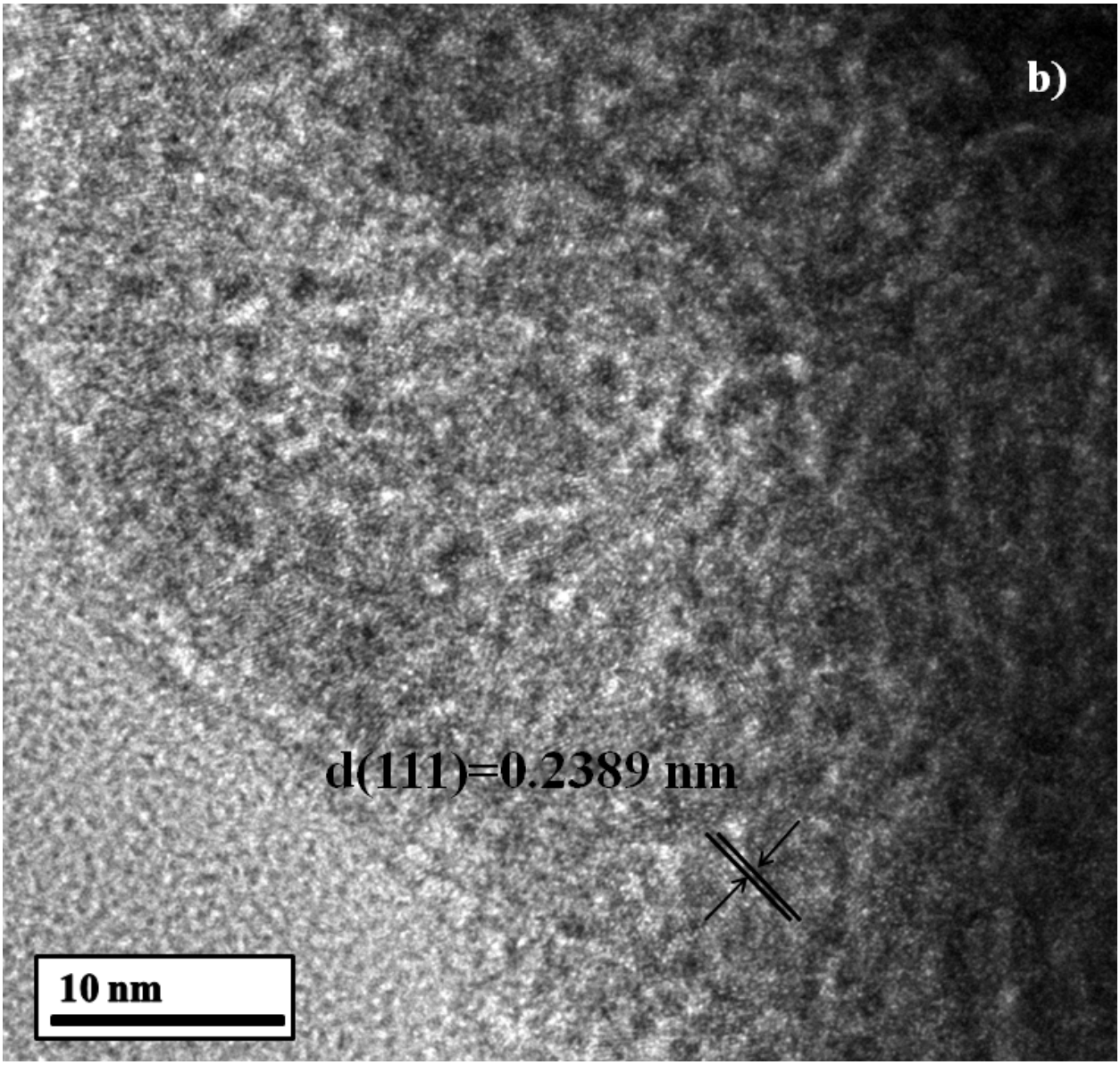
b)
d(111)=0.2389 nm
10 nm

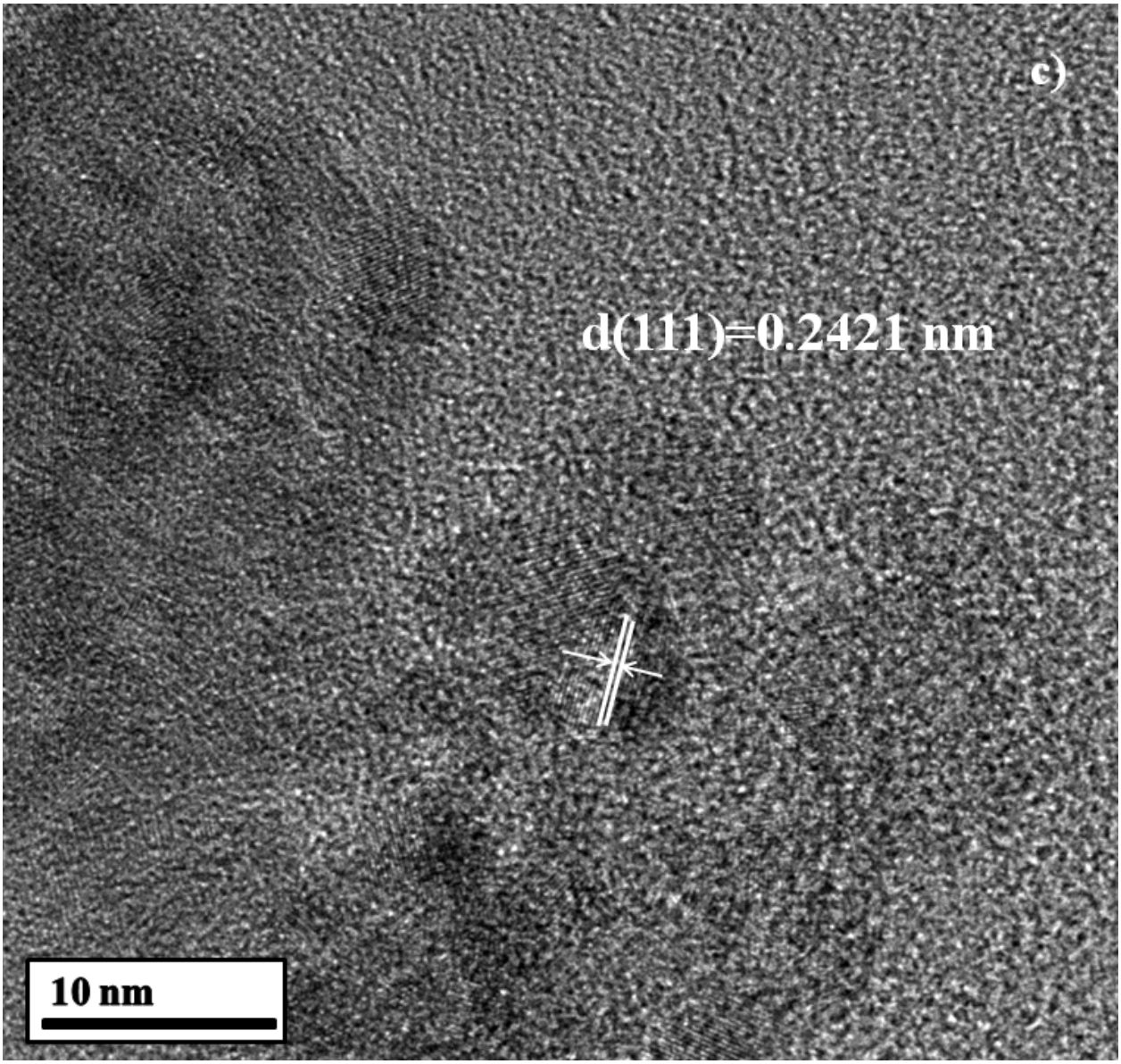
c)
d(111)=0.2421 nm
10 nm

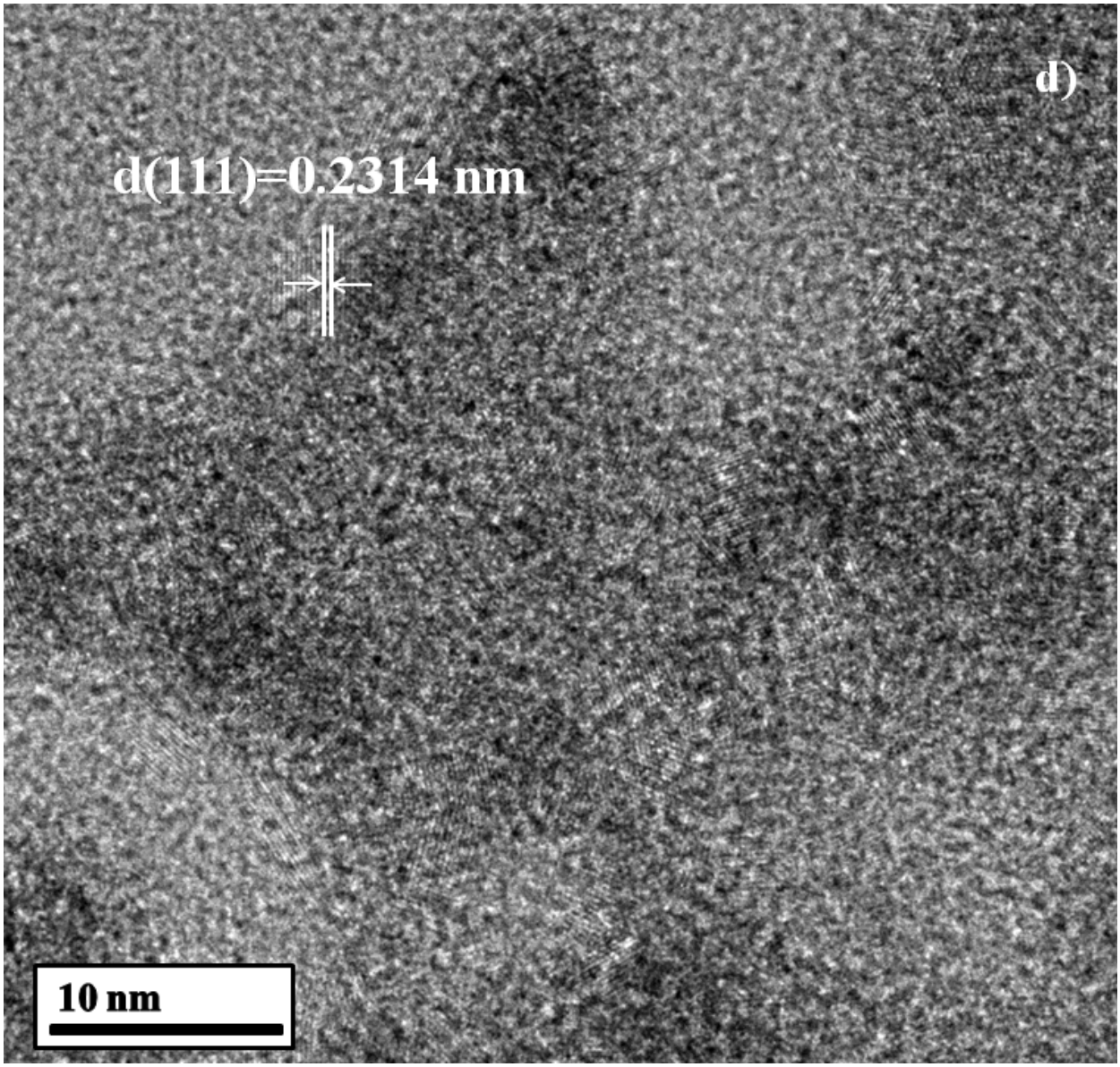
d)
d(111)=0.2314 nm
10 nm

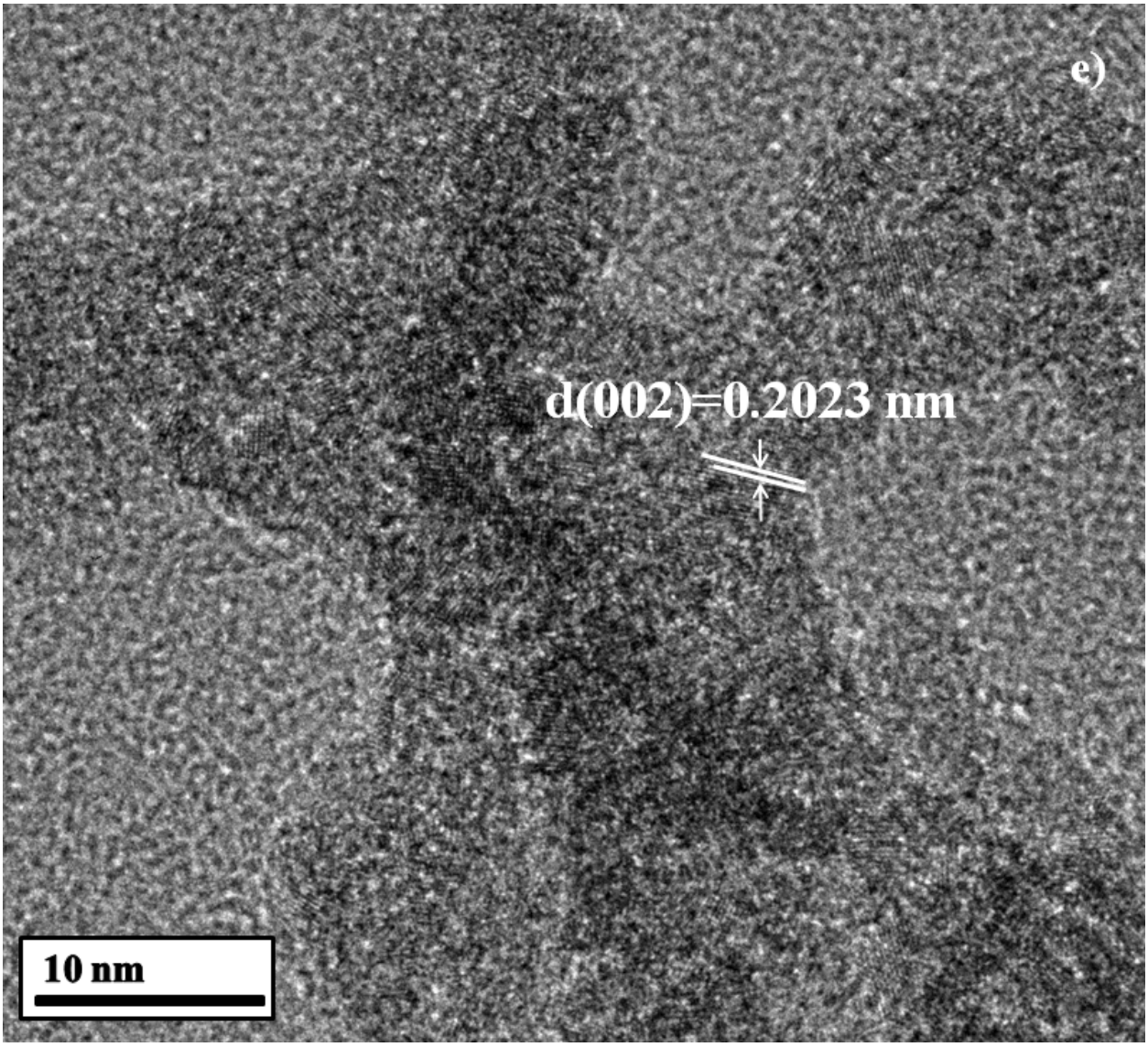
e)
d(002)=0.2023 nm
10 nm

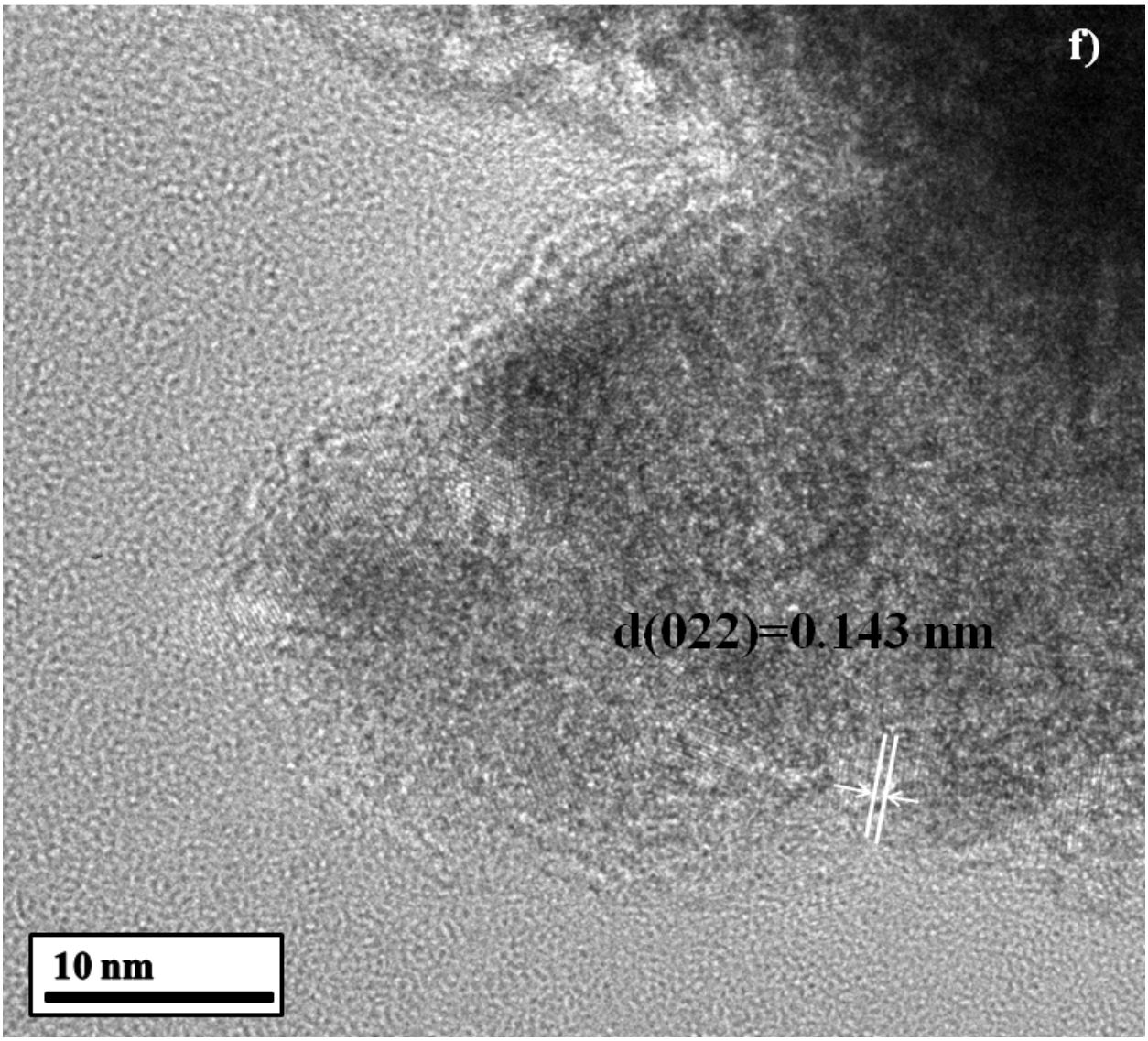

Figure 56. HRTEM images of various compositions of Nb doped and W doped VN (a) $Nb_{0.01}V_{0.99}N$ (b) $Nb_{0.05}V_{0.95}N$ (c) $Nb_{0.10}V_{0.90}N$ (d) $W_{0.05}V_{0.95}N$ (e) $W_{0.10}V_{0.90}N$ (f) $W_{0.20}V_{0.80}N$.

a)

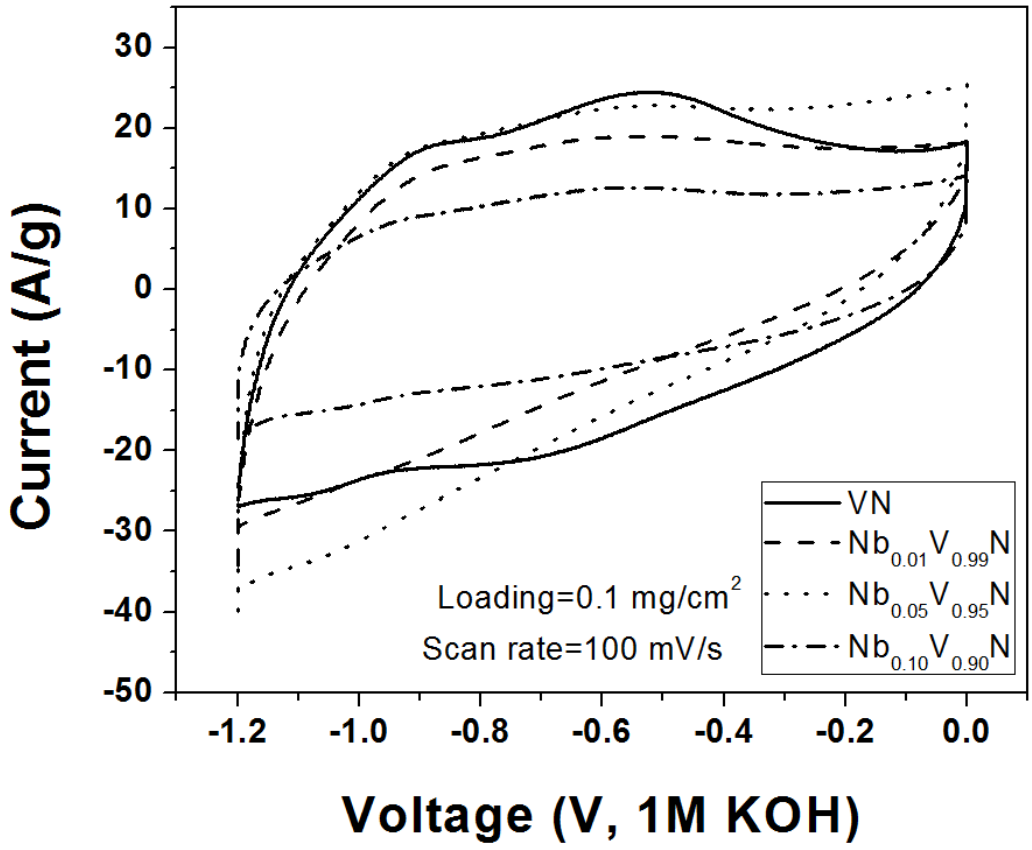
Current (A/g)
30
20
10
0
-10
-20
-30
-40
-50
-1.2
-1.0
-0.8
-0.6
-0.4
-0.2
0.0
Voltage (V, 1M KOH)
VN
Nb0.01V0.99N
Nb0.05V0.95N
Nb0.10V0.90N
Loading=0.1 mg/cm2
Scan rate=100 mV/s

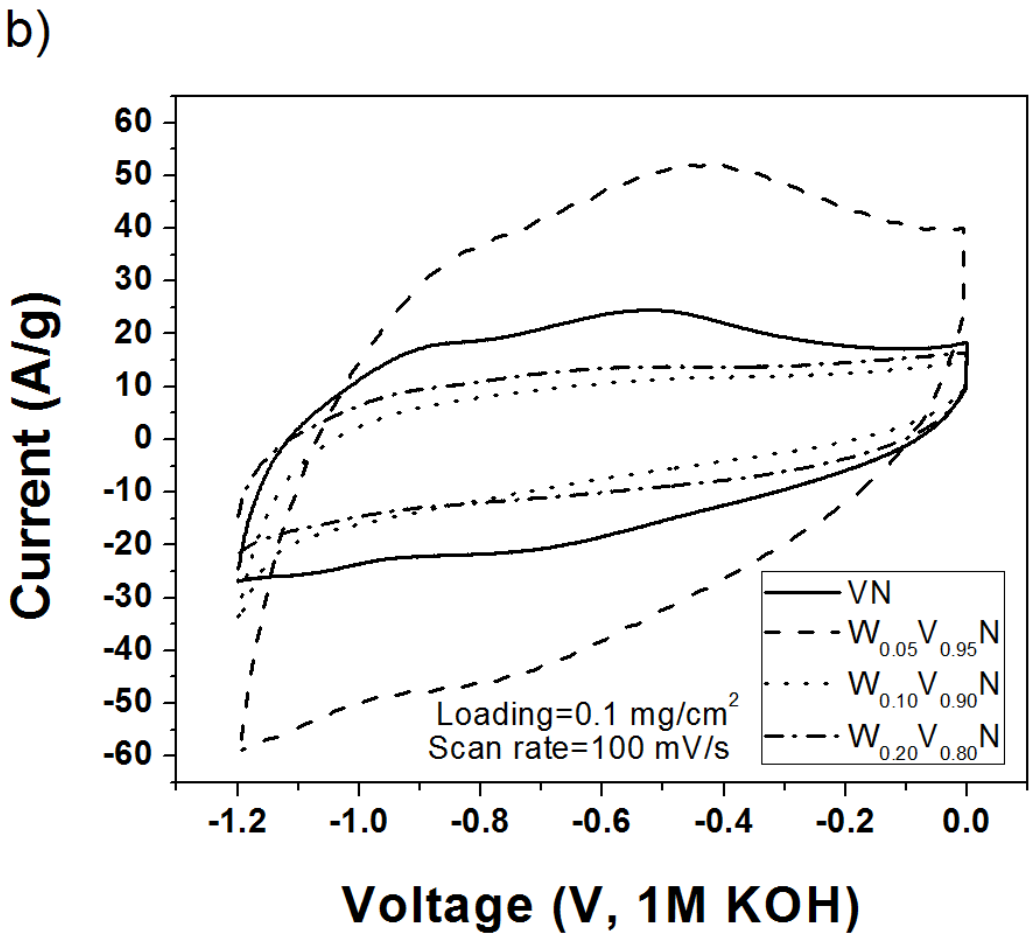

Figure 57. Cyclic voltammograms of various doped compositions of Nb doped and W doped VN (a) $V_xNb_{1-x}N$ (x=0.01-0.1) and (b) $V_xW_{1-x}N$ (x=0.05-0.2) -Active material loading=0.1 mg/cm^2-Scan rate=100 mV/s.

Figure 57a and **Figure 57b** show the cyclic voltammograms (CV) of the various niobium doped VN compositions and tungsten doped VN compositions respectively in 1M KOH over a voltage window of -1.2 V to 0 V with respect to Hg/HgO (scan rate=100 mV/s). As can be seen, both double layer and pseudocapacitor type response is visible in the CVs. It can be seen that reversible Faradaic reactions are observed to occur at the surface oxide layer covering the nitride with peaks in the vicinity of ~-0.9 V, -0.6 V, -0.1 V on the anodic scan and at and around -0.2V, -0.7 V and -1 V on the cathodic scan. These electrode potentials correspond closely with

the change in oxidation state of vanadium from +2 to +5 resembling those of mechanochemically derived VN previously reported by Jampani et al.[246] (**Section 4.1**) and VN reported by Choi et al.[182, 235]. From the potentials observed in the cyclic voltammogram, the predominant pseudocapacitance reactions occurring in the alkaline KOH solution at pH 14 can thus be attributed to the reversible cycling of the surface oxide between V_2O_5 and V_6O_{13}, V_2O_4 and V_6O_{13} , V_2O_3 and V_3O_5 (Equations (iii) to (vi)) and similar to those reported by Choi et al. [182, 235, 337]. It must also be noted that no additional peaks are observed within the same window indicating that the behavior of the doped nitrides predominantly resembles that of vanadium nitride. It also indicates the absence of impurity phases and undesirable side reactions. A distinct differenuce in character is observed in the various niobium-doped VN compositions. It can be seen that the $V_{.99}Nb_{.01}N$, $V_{.95}Nb_{.05}N$ compositions show almost square-wave forms with the Faradaic peaks being very weak while the $V_{.90}Nb_{.10}N$ doped VN has strong Faradaic peaks corresponding to the same reactions seen in VN. Tungsten doping on the other hand results in a significant increase in capacitive charge storage as seen in **Figure 57b**. $W_{0.05}V_{0.95}N$ shows a marked increase in both the double layer as well as pseudo-capacitive charge storage while the other two doped compositions have characteristics very similar to that of pure undoped VN. Faradaic peaks are observed at similar potentials as those seen in **Figure 57a**.

a)

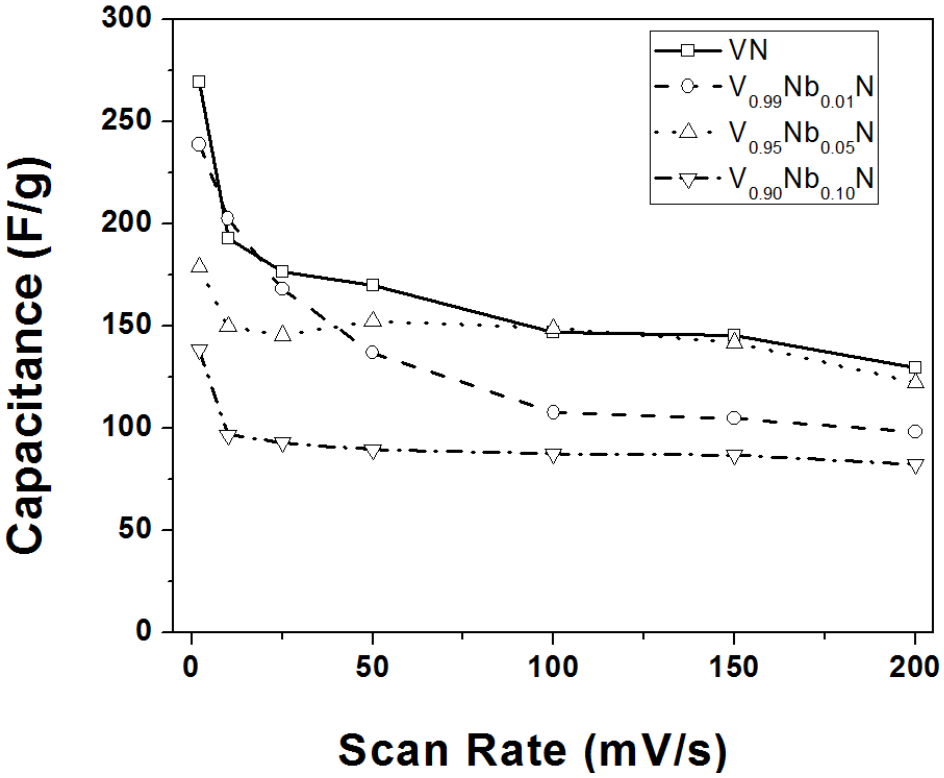
Capacitance (F/g)
Scan Rate (mV/s)
VN
V0.99Nb0.01N
V0.95Nb0.05N
V0.90Nb0.10N
0
50
100
150
200
250
300

b)

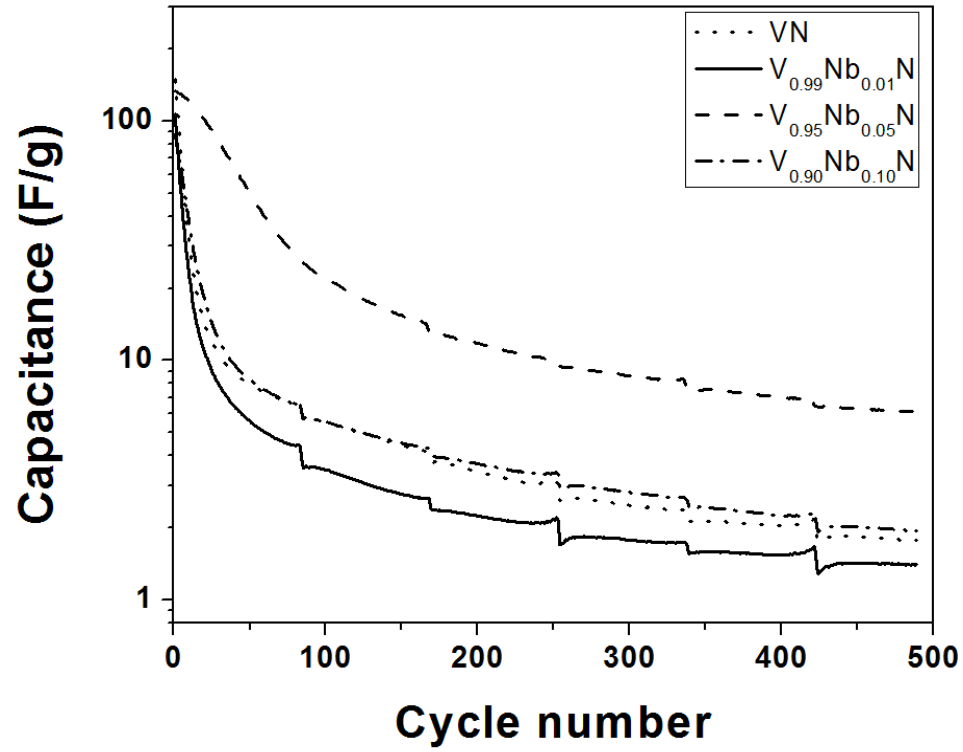
Capacitance (F/g)
Cycle number
VN
V0.99Nb0.01N
V0.95Nb0.05N
V0.90Nb0.10N
1
10
100
0
100
200
300
400
500

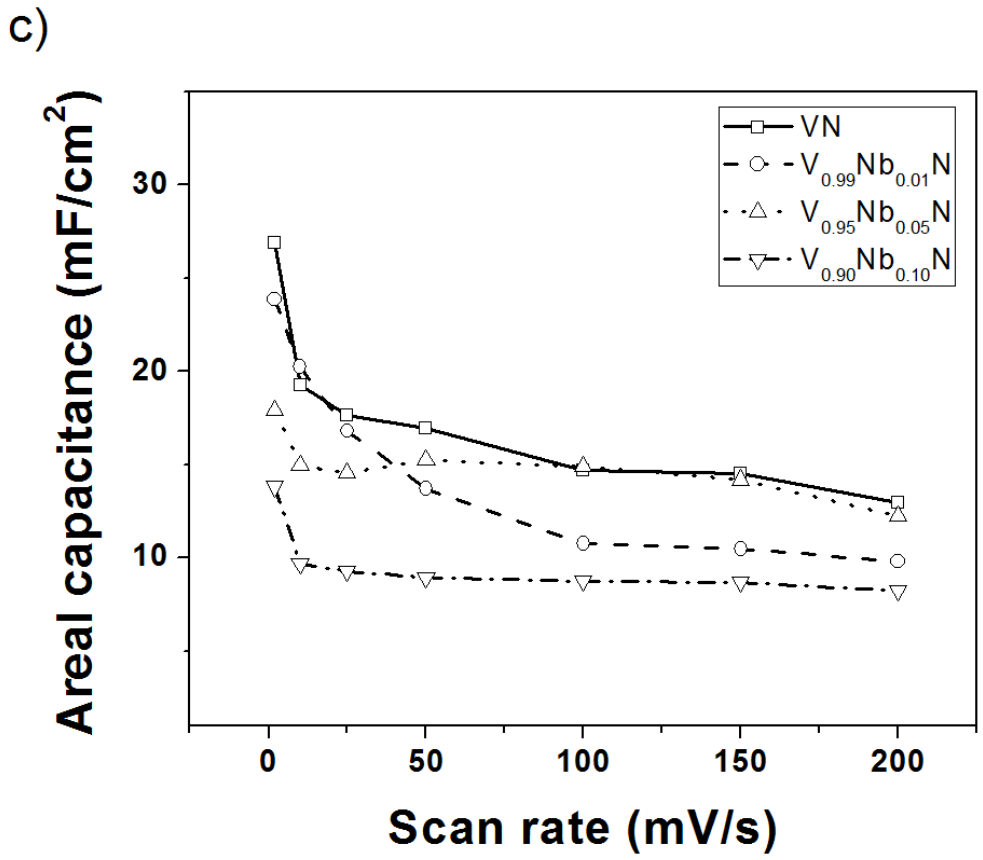

Figure 58. (a) Scan rate dependence of capacitance of various niobium doped compositions $Nb_xV_{1-x}N$ (x=0.01-0.1)-Active material loading=0.1 mg/cm^2 (b) Cycling stability of various niobium doped compositions $Nb_xV_{1-x}N$ (x=0.01-0.1)-Active material loading=0.1 mg/cm^2-Scan rate=100 mV/s (c) Areal capacitance of various niobium doped compositions $Nb_xV_{1-x}N$ (x=0.01-0.1)-Active material loading=0.1 mg/cm^2-Scan rate=100 mV/s.

Figure 58a depicts the scan rate dependent capacitance of various Nb doped VN compositions calculated by integrating the area under the cyclic voltammogram as previously reported by us[246] (see Equation (i)). It can be seen that niobium doping does not improve capacitance in any of the compositions reported herein. It can be seen that capacitance drops progressively with increasing niobium content possibly as a result of the larger size and atomic

weight of niobium and as a result of niobium resulting in stabilization of the oxide resulting in a greater activation to charge-transfer. The effect of electronic conductivity seen in **Table 22** is distinctly observed in **Figure 58a**. $V_{0.99}Nb_{0.01}N$ shows very poor capacity retention with increasing scan rate while $V_{.95}Nb_{0.05}N$ and $V_{0.90}Nb_{0.10}N$ have good capacity retention at higher rates. Though the electronic conductivity of all three compounds are in a similar regime, the trends in **Figure 58a** indicate that conductivity has a significant role to play in the charge storage response in Nb doped VN, especially with regards to the rate capability. Niobium is a heavier element with little inherent pseudocapacitance behavior. Niobium oxide is a very stable oxide with no dissolved states within a wide pH window in the voltage window of stability of aqueous electrolytes[269]. Niobium nitride is purely a double layer type capacitor with no Faradaic peaks in 1M KOH[234]. As a result of these factors, niobium doped vanadium nitride is a weaker pseudocapacitor than pure vanadium nitride. However, the inherent stability of niobium nitride is expected to result in an improved cyclability of the niobium doped vanadium nitride. Nevertheless, as seen in **Figure 58b**, doping of VN with niobium results in only a slight improvement in cycling stability. In fact, $V_{0.99}Nb_{0.01}N$ has a much lower capacity retention than VN. $V_{.95}Nb_{0.05}N$ and $V_{0.90}Nb_{0.10}N$ have better capacity retention though not significantly better. $V_{.95}Nb_{0.05}N$ has the best capacity retention among the four materials along with the best rate capability. Niobium doping of VN does not result in significant improvement in performance since niobium is an isoelectronic element with a higher molecular mass.

a)

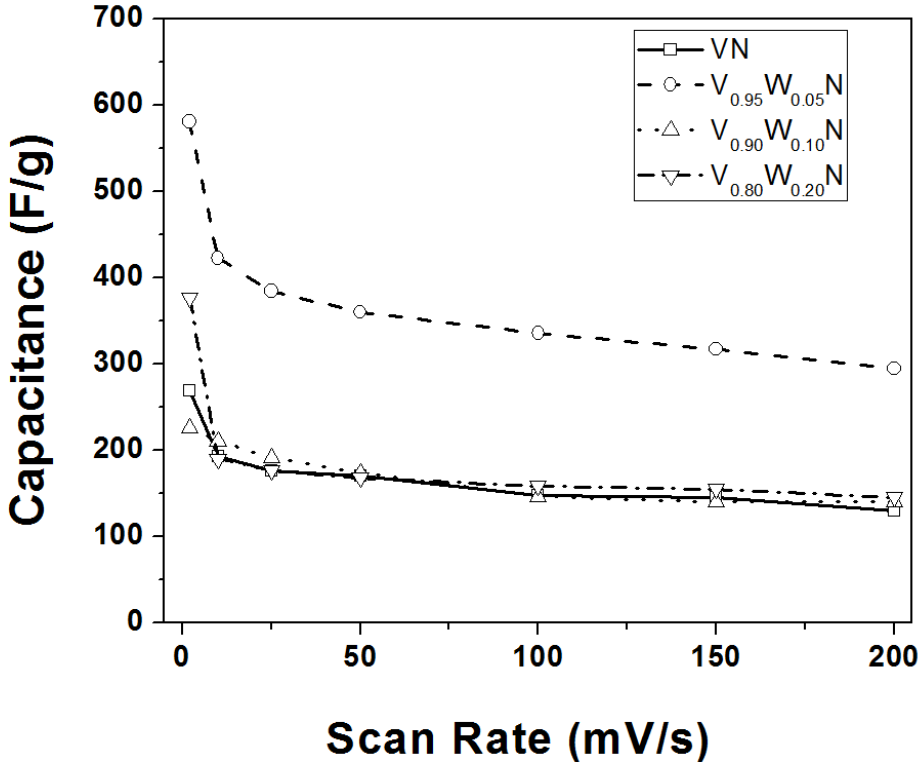
Capacitance (F/g)
Scan Rate (mV/s)
VN
V0.95W0.05N
V0.90W0.10N
V0.80W0.20N
0
100
200
300
400
500
600
700
0
50
100
150
200

b)

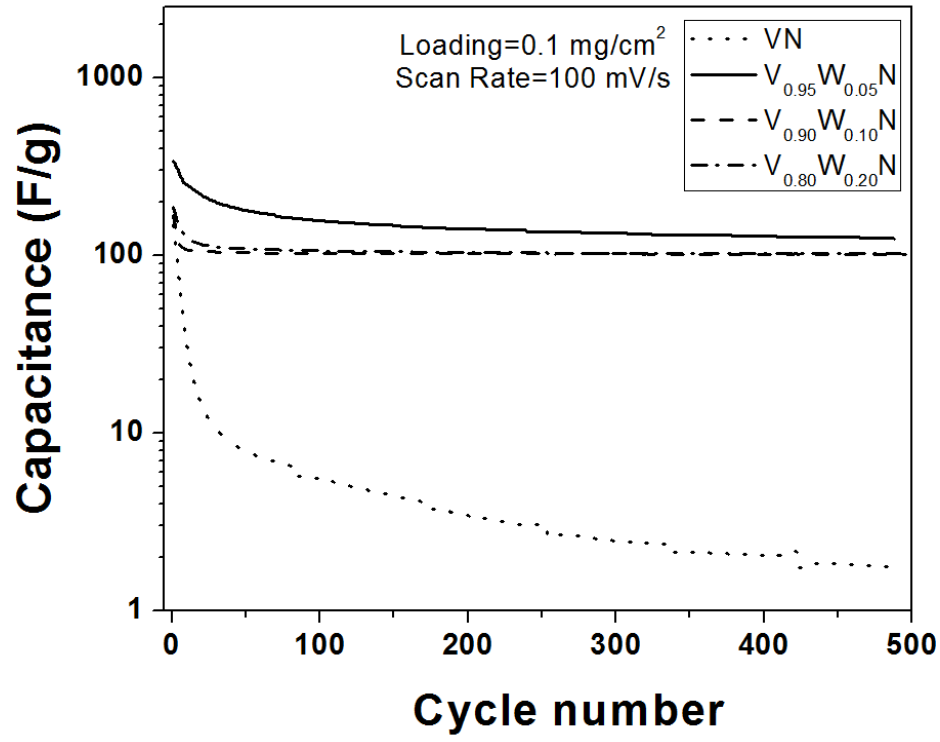
Loading=0.1 mg/cm2
Scan Rate=100 mV/s
VN
V0.95W0.05N
V0.90W0.10N
V0.80W0.20N
Capacitance (F/g)
Cycle number
1
10
100
1000
0
100
200
300
400
500

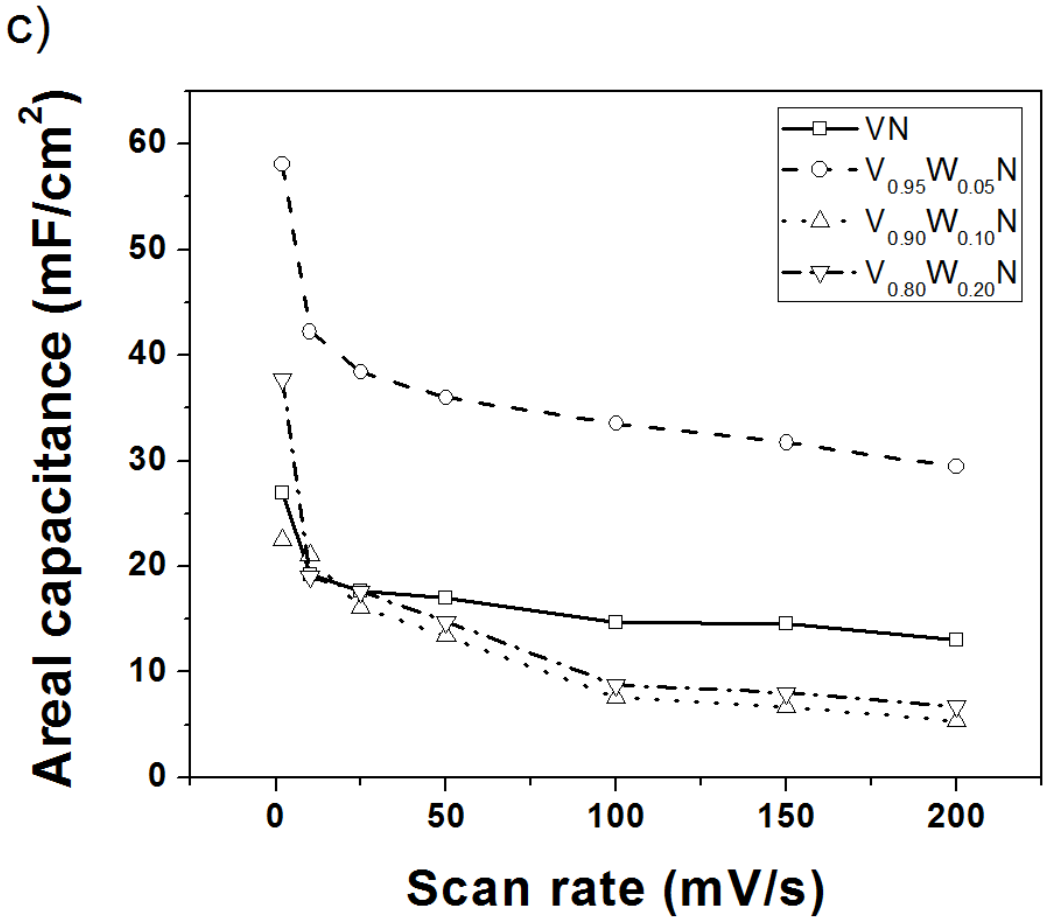

Figure 59. (a) Scan rate dependence of capacitance of various tungsten doped compositions $W_xV_{1-x}N$ (x=0.05-0.2)-Active material loading=0.1 mg/cm^2 (b) Cycling stability of various tungsten doped compositions $W_xV_{1-x}N$ (x=0.05-0.2)-Active material loading=0.1 mg/cm^2-Scan rate=100 mV/s (c) Areal capacitance of various tungsten doped compositions $W_xV_{1-x}N$ (x=0.05-0.2)-Active material loading=0.1 mg/cm^2-Scan rate=100 mV/s.

The behavior of tungsten doped vanadium nitride however, is very much in contrast with that of niobium doped VN as seen in **Figure 59a** and **Figure 59b**. Unlike niobium, doping of vanadium nitride with tungsten results in much improved capacitance and improvement in cycling stability at the same time. It can be seen that among the three doped compositions, both $W_{0.05}V_{0.95}N$ and $W_{0.20}V_{0.80}N$ have much higher gravimetric capacitances as compared to VN.

$W_{0.10}V_{0.90}N$ on the other hand demonstrates almost identical behavior as VN. It is believed that this is as a result of two disparate and complimentary phenomena. As shown in **Table 22**, doping of vanadium nitride with tungsten results in an increase in electronic conductivity. The trend in capacitance behavior of tungsten doped vanadium nitride very much follows the trend observed in electronic conductivity. Among the three tungsten doped vanadium nitride compositions, $W_{0.05}V_{0.95}N$ has the highest gravimetric capacitance while at the same time retaining the best capacitance response. Tungsten nitride has previously been shown to behave as a pseudocapacitor[235, 239] and doping of vanadium nitride with the same would result in increased charge storage possibly as a result of increased charge transfer kinetics caused by either chemical or electronic activation due to the dopant atom[208, 398]. The improvement in performance of the nitride could also be attributed to increased electronic conductivity and reactivity of the surface oxide. Tungsten doping has previously been shown to lead to conductivity increase in VO_2[320, 325-328]. This improvement in conductivity would result in improvement in performance as well. In addition to improvement in charge storage capability, the cycling stability of vanadium nitride is significantly increased by doping with tungsten. Tungsten nitride as a standalone supercapacitor electrode has been shown to exhibit fade in capacity with cycling though the retention in capacity is much better than that of vanadium nitride[16, 21]. $W_{0.05}V_{0.95}N$ and $W_{0.10}V_{0.90}N$ have superior cyclability than VN however possibly as a result of the stabilization of the structure and the surface oxide as discussed in the theoretical study below. The capacitance of $W_{0.05}V_{0.95}N$ approaches ~600 F/g at 2mV/s with good retention resulting in a capacity of ~300 F/g at 200 mV/s (active material loading~0.1 mg/cm^2). This is believed to be as a result of the strong pseudocapacitance behavior of the surface oxide as well as superior electronic conductivity of the material as shown in **Table 22**.

Figure 58c and **Figure 59c** depict the areal capacity of the various niobium doped VN and tungsten doped VN compositions respectively. It can be seen that the materials show high areal capacities superior to that of other capacitor materisls due to the high gravimetric capacitance of VN[267, 344]. The trends in areal capacitance mimic those in gravimetric capacitance since all materials were tested under identical conditions. Among the various doped materials $W_{0.05}V_{0.95}N$ demonstrates areal capacitances of ~60mF/cm^2 exceeding that of ruthenium oxide supercapacitors (12-30 mF/cm^2)[344]. However, areal capacitances were lower than that observed for VO_x:Ti-VACNT electrodes (~350 mF/cm^2) reported in **Section 4.3** and approach values of highly active ruthenium oxide (60-100 mF/cm^2) [345, 346]. Testing is ongoing with $W_{0.05}V_{0.95}N$ of higher loadings and it is expected that the material will retain its capacitance in very high loading electrodes due to its superior electronic conductivity and electrochemical activity. The effect of niobium and tungsten doping on the electronic structure of vanadium nitride and its surface oxide have been studied in tandem with the experimental evaluation performed above using first-principles computational approaches (see **Page 276**).

a)

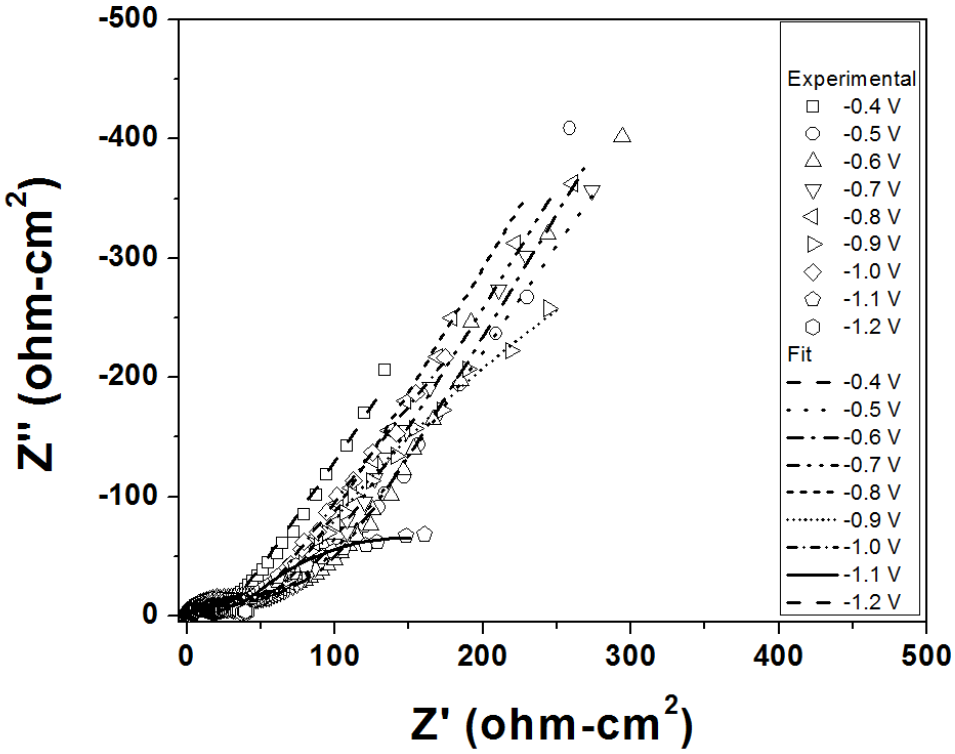
-500
-400
-300
-200
-100
0
0
100
200
300
400
500
Z'' (ohm-cm2)
Z' (ohm-cm2)
Experimental
-0.4 V
-0.5 V
-0.6 V
-0.7 V
-0.8 V
-0.9 V
-1.0 V
-1.1 V
-1.2 V
Fit
-0.4 V
-0.5 V
-0.6 V
-0.7 V
-0.8 V
-0.9 V
-1.0 V
-1.1 V
-1.2 V

b)

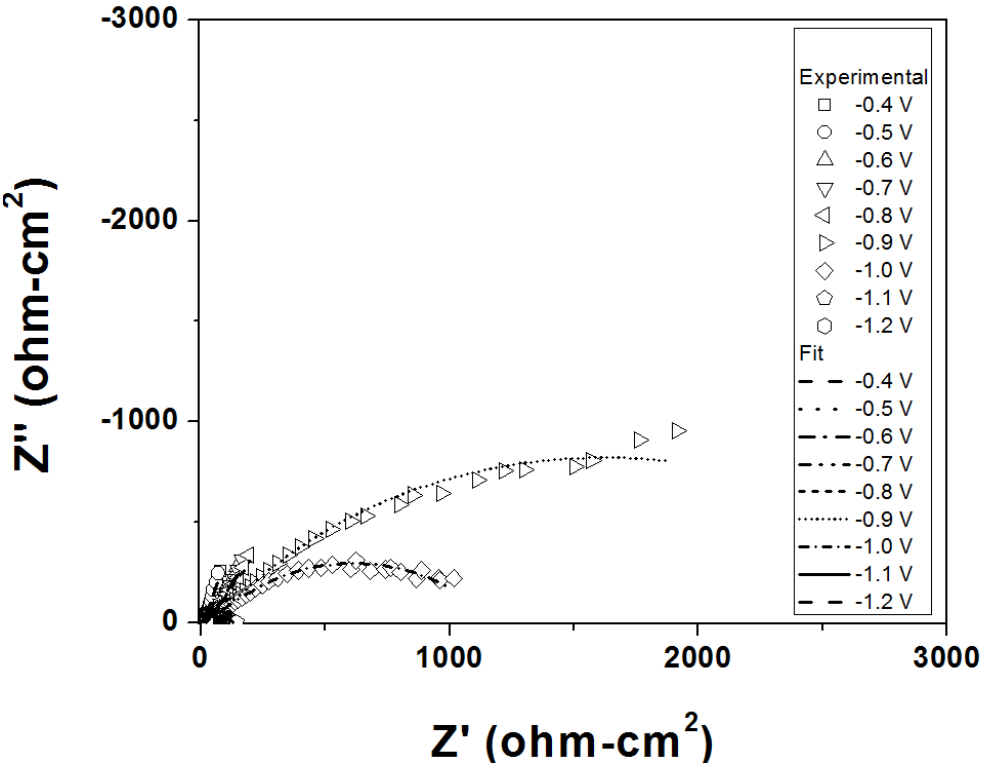
-3000
-2000
-1000
0
0
1000
2000
3000
Z'' (ohm-cm2)
Z' (ohm-cm2)
Experimental
-0.4 V
-0.5 V
-0.6 V
-0.7 V
-0.8 V
-0.9 V
-1.0 V
-1.1 V
-1.2 V
Fit
-0.4 V
-0.5 V
-0.6 V
-0.7 V
-0.8 V
-0.9 V
-1.0 V
-1.1 V
-1.2 V

c)

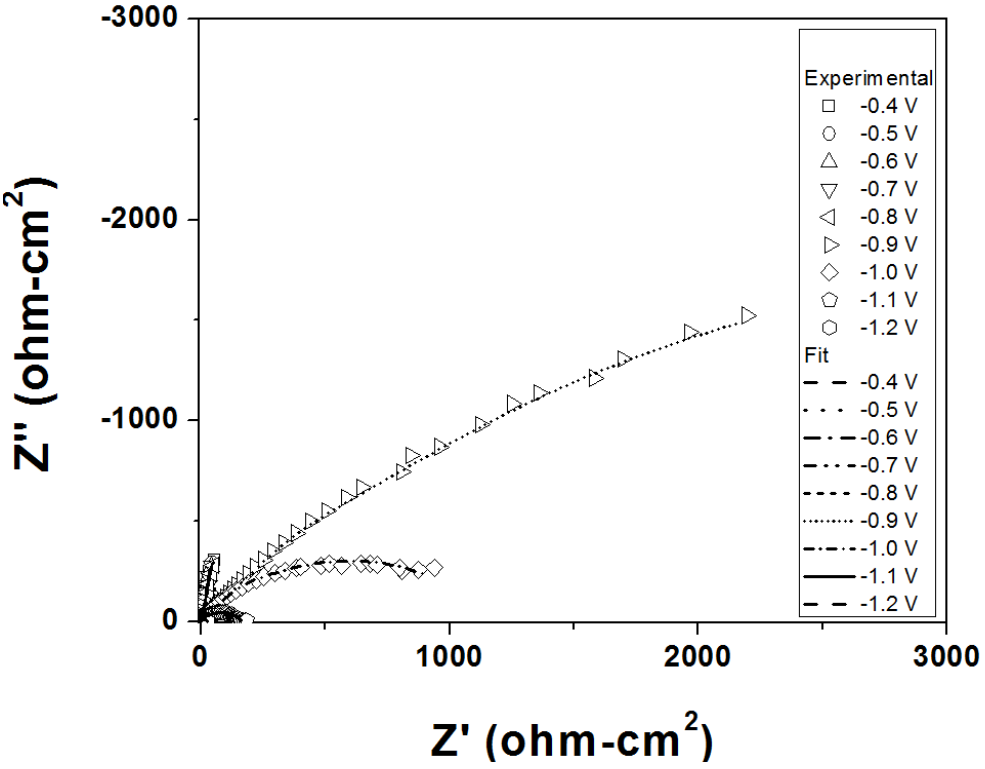
-3000
-2000
-1000
0
0
1000
2000
3000
Z'' (ohm-cm2)
Z' (ohm-cm2)
Experimental
-0.4 V
-0.5 V
-0.6 V
-0.7 V
-0.8 V
-0.9 V
-1.0 V
-1.1 V
-1.2 V
Fit
-0.4 V
-0.5 V
-0.6 V
-0.7 V
-0.8 V
-0.9 V
-1.0 V
-1.1 V
-1.2 V

d)

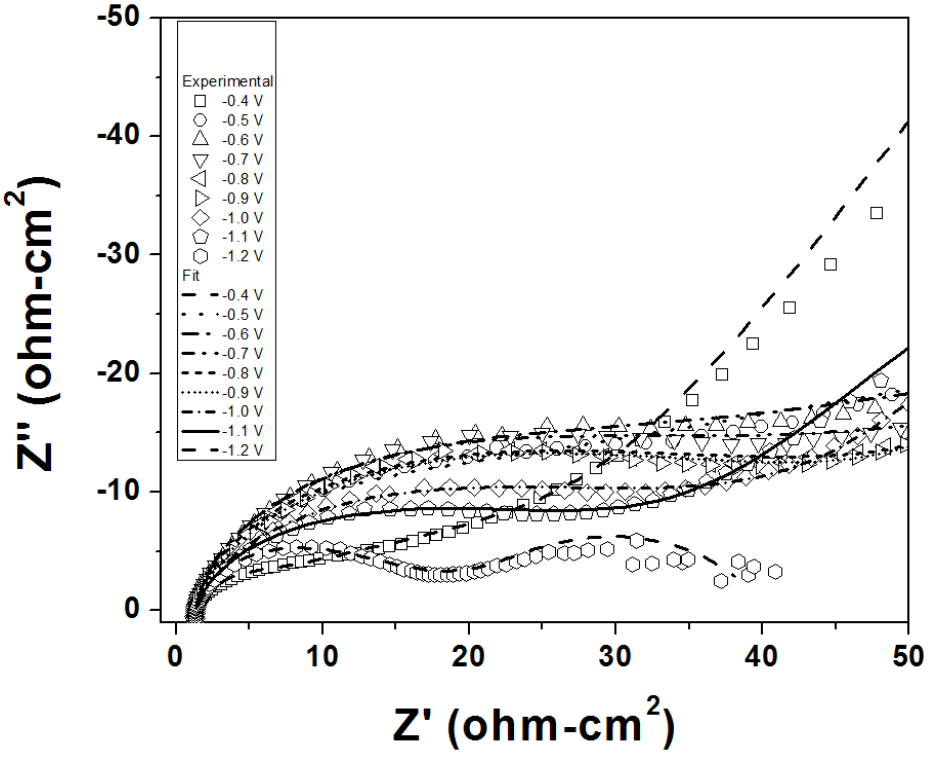
-50
-40
-30
-20
-10
0
0
10
20
30
40
50
Z'' (ohm-cm2)
Z' (ohm-cm2)
Experimental
-0.4 V
-0.5 V
-0.6 V
-0.7 V
-0.8 V
-0.9 V
-1.0 V
-1.1 V
-1.2 V
Fit
-0.4 V
-0.5 V
-0.6 V
-0.7 V
-0.8 V
-0.9 V
-1.0 V
-1.1 V
-1.2 V

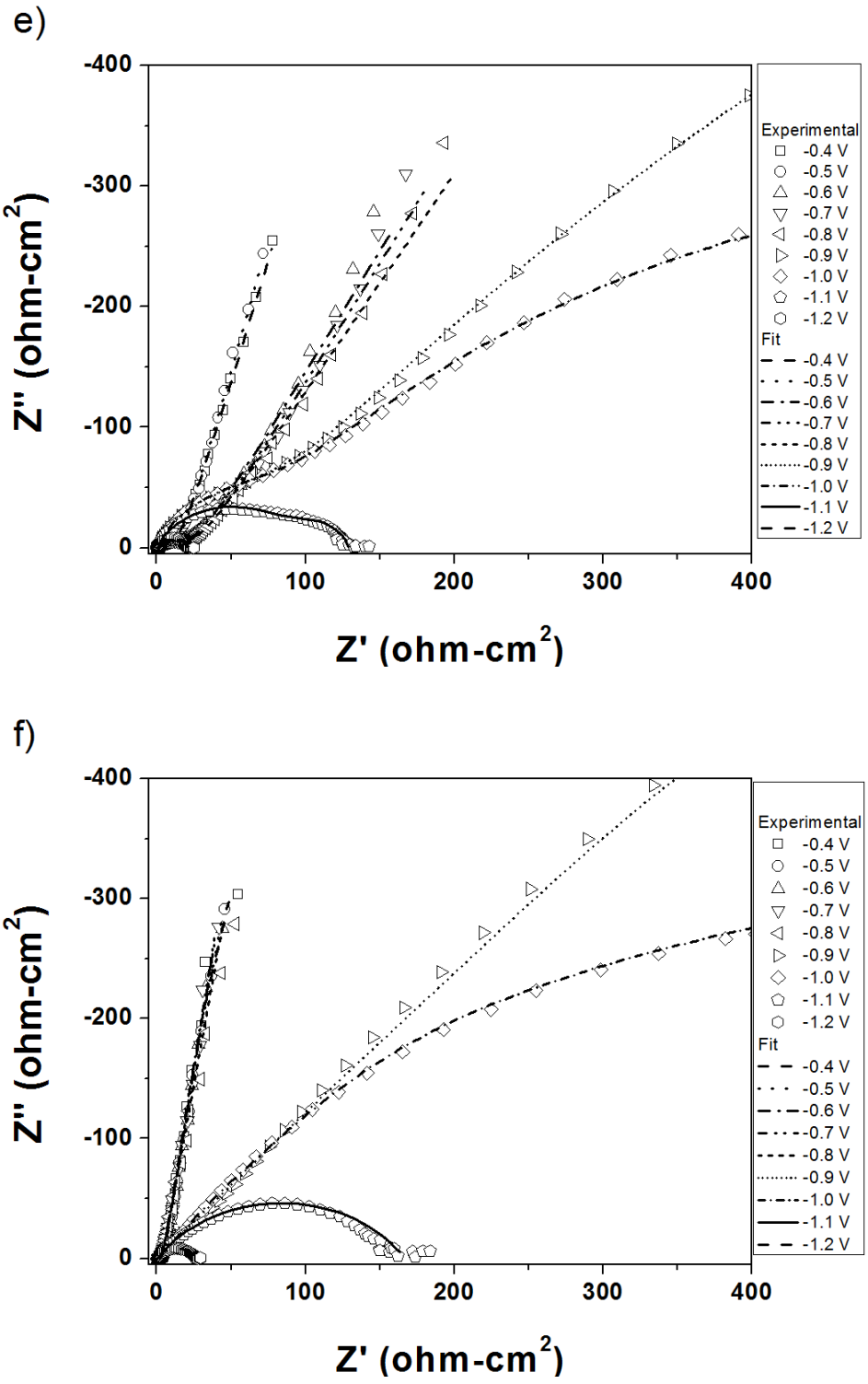

Figure 60. Nyquist plots of the various niobium doped nitride materials during 1st discharge (Active material loading~0.1 mg/cm^2) (a) $Nb_{0.01}V_{0.99}N$ (b) $Nb_{0.05}V_{0.95}N$ (c) $Nb_{0.10}V_{0.90}N$ and magnified high frequency-semicircle portion of plots (a), (b), (c) in (d), (e), (f) respectively.

To further understand charge storage behavior in the doped nitride materials and attempt to explain the trends in capacity between various dopant concentrations, electrochemical impedance spectroscopy was performed at various voltages during the 1st discharge cycle. The as-prepared electrodes had an open circuit potential (OCP) of ~0.35 V (wrt Hg/HgO (in 1M KOH)). The potential was scanned down slowly (0.1 mV/s) and allowed to stabilize at -0.4 V (wrt Hg/HgO (in 1M KOH)) and the impedance spectra were collected at every 100 mV thereon till -1.2 V (wrt Hg/HgO (in 1M KOH)). **Figure 60a-Figure 60c** depict the Nyquist plots of $Nb_xV_{1-x}N$ (x=0.01, 0.05, 0.10) at different potentials during the 1st discharge. It can be seen that in all doped VN compositions, capacitor type charge storage is observed resembling behavior of pure VN[246]. The EIS spectra are characteristic of most capacitor materials with a fairly small and constant series resistance, double layer capacitance, pseudocapacitance and charge transfer resistance. This behavior corresponds to the underpotential deposition mechanism (shown in **Figure 62a)** between -0.4 V and -0.8 V (wrt Hg/HgO (in 1M KOH)) and overpotential deposition (**Figure 62b**) thereafter. Underpotential deposition is the precursor to gas evolution in aqueous electrolytes and involves Faradaic pseudocapacitance arising as a result of bias applied. Beyond -0.9 V (wrt Hg/HgO (in 1M KOH)), gas evolution starts albeit a very low rate. This potential corresponds to the expected potential for hydrogen evolution in aqueous electrolytes[269]. This results in the 2nd arc seen in **Figure 60a-Figure 60c**. Inset in some of these figures shows the high frequency region where it is not distinctly visible. In addition to the elements of underpotential deposition (UPD) most commonly observed in aqueous pseudocapacitor systems[58], a Warburg element (W_s) has been introduced to account for mass transfer effects. Similar trends are observed in the case of $W_xV_{1-x}N$ (x=0.05, 0.1, 0.2) shown in **Figure 61a-Figure 61c**.

a)

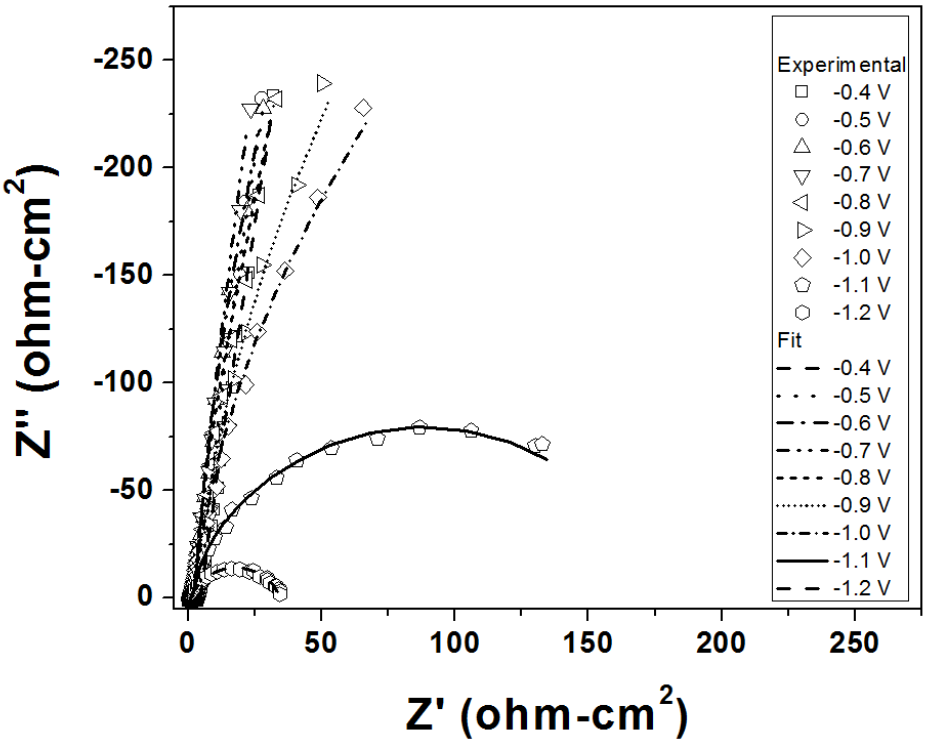
-250
-200
-150
-100
-50
0
Z'' (ohm-cm2)
0
50
100
150
200
250
Z' (ohm-cm2)
Experimental
-0.4 V
-0.5 V
-0.6 V
-0.7 V
-0.8 V
-0.9 V
-1.0 V
-1.1 V
-1.2 V
Fit
-0.4 V
-0.5 V
-0.6 V
-0.7 V
-0.8 V
-0.9 V
-1.0 V
-1.1 V
-1.2 V

b)

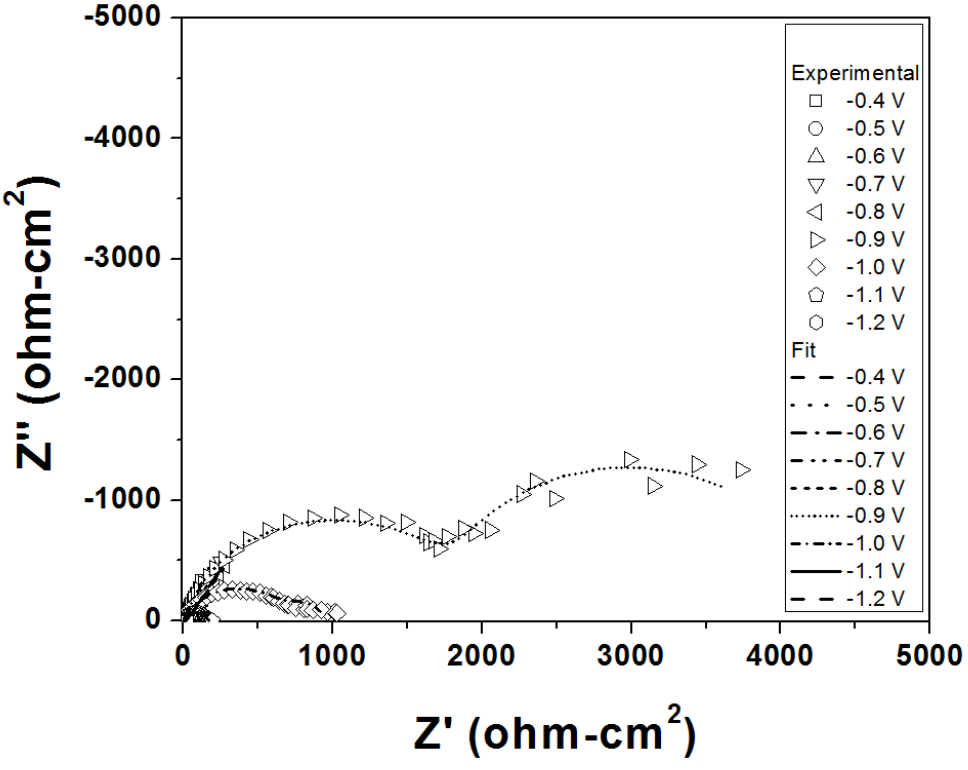
-5000
-4000
-3000
-2000
-1000
0
Z'' (ohm-cm2)
0
1000
2000
3000
4000
5000
Z' (ohm-cm2)
Experimental
-0.4 V
-0.5 V
-0.6 V
-0.7 V
-0.8 V
-0.9 V
-1.0 V
-1.1 V
-1.2 V
Fit
-0.4 V
-0.5 V
-0.6 V
-0.7 V
-0.8 V
-0.9 V
-1.0 V
-1.1 V
-1.2 V

c)

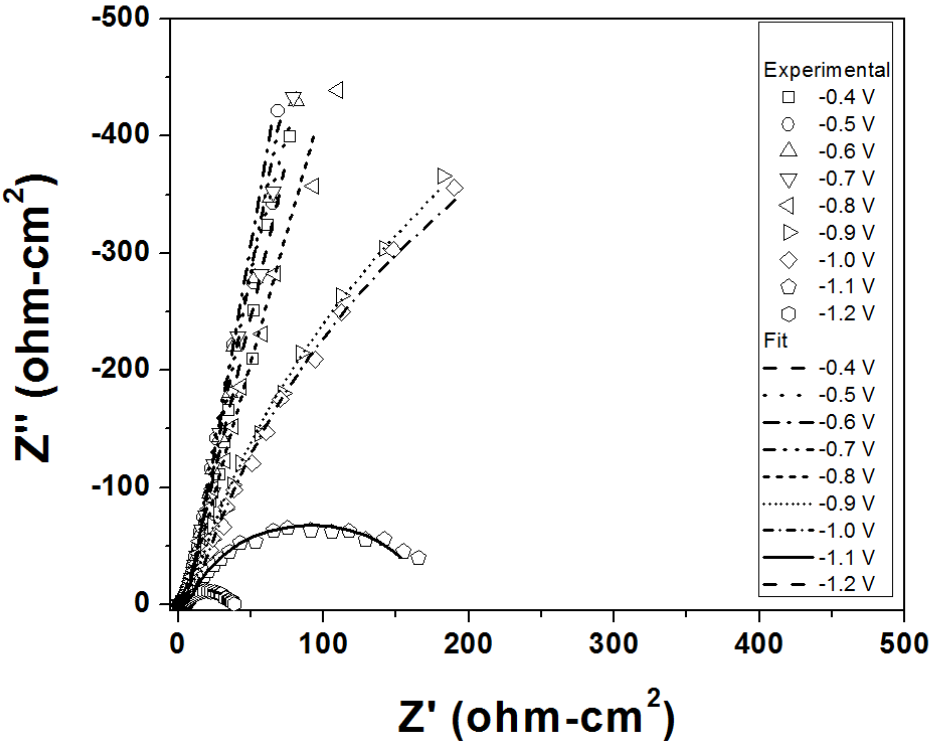
-500
-400
-300
-200
-100
0
Z'' (ohm-cm2)
0
100
200
300
400
500
Z' (ohm-cm2)
Experimental
-0.4 V
-0.5 V
-0.6 V
-0.7 V
-0.8 V
-0.9 V
-1.0 V
-1.1 V
-1.2 V
Fit
-0.4 V
-0.5 V
-0.6 V
-0.7 V
-0.8 V
-0.9 V
-1.0 V
-1.1 V
-1.2 V

d)

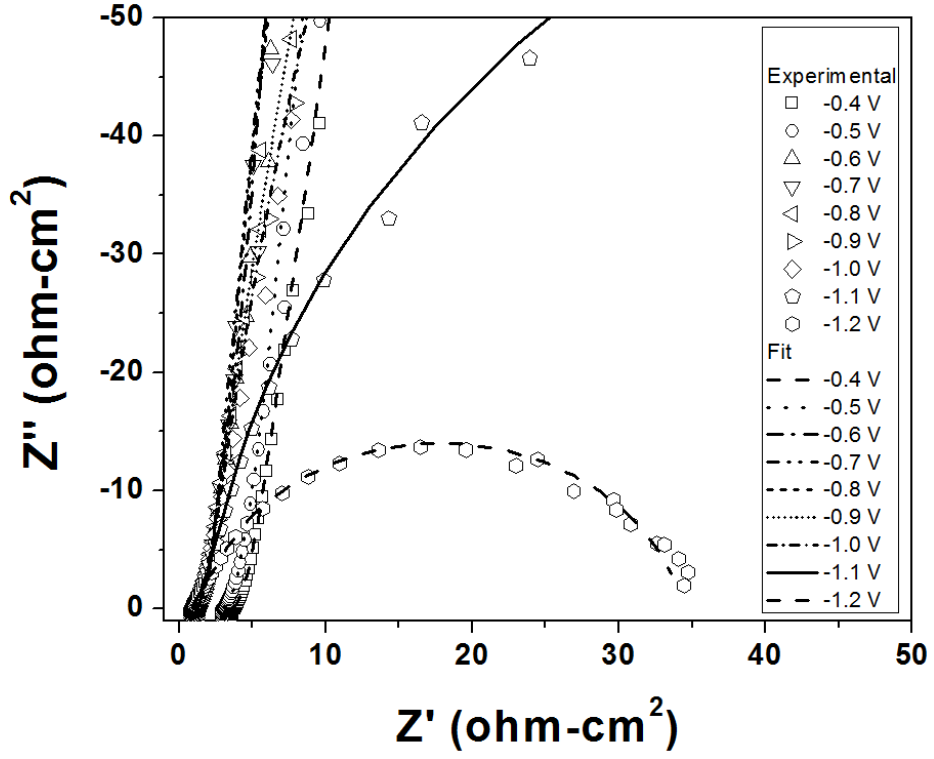
-50
-40
-30
-20
-10
0
Z'' (ohm-cm2)
0
10
20
30
40
50
Z' (ohm-cm2)
Experimental
-0.4 V
-0.5 V
-0.6 V
-0.7 V
-0.8 V
-0.9 V
-1.0 V
-1.1 V
-1.2 V
Fit
-0.4 V
-0.5 V
-0.6 V
-0.7 V
-0.8 V
-0.9 V
-1.0 V
-1.1 V
-1.2 V

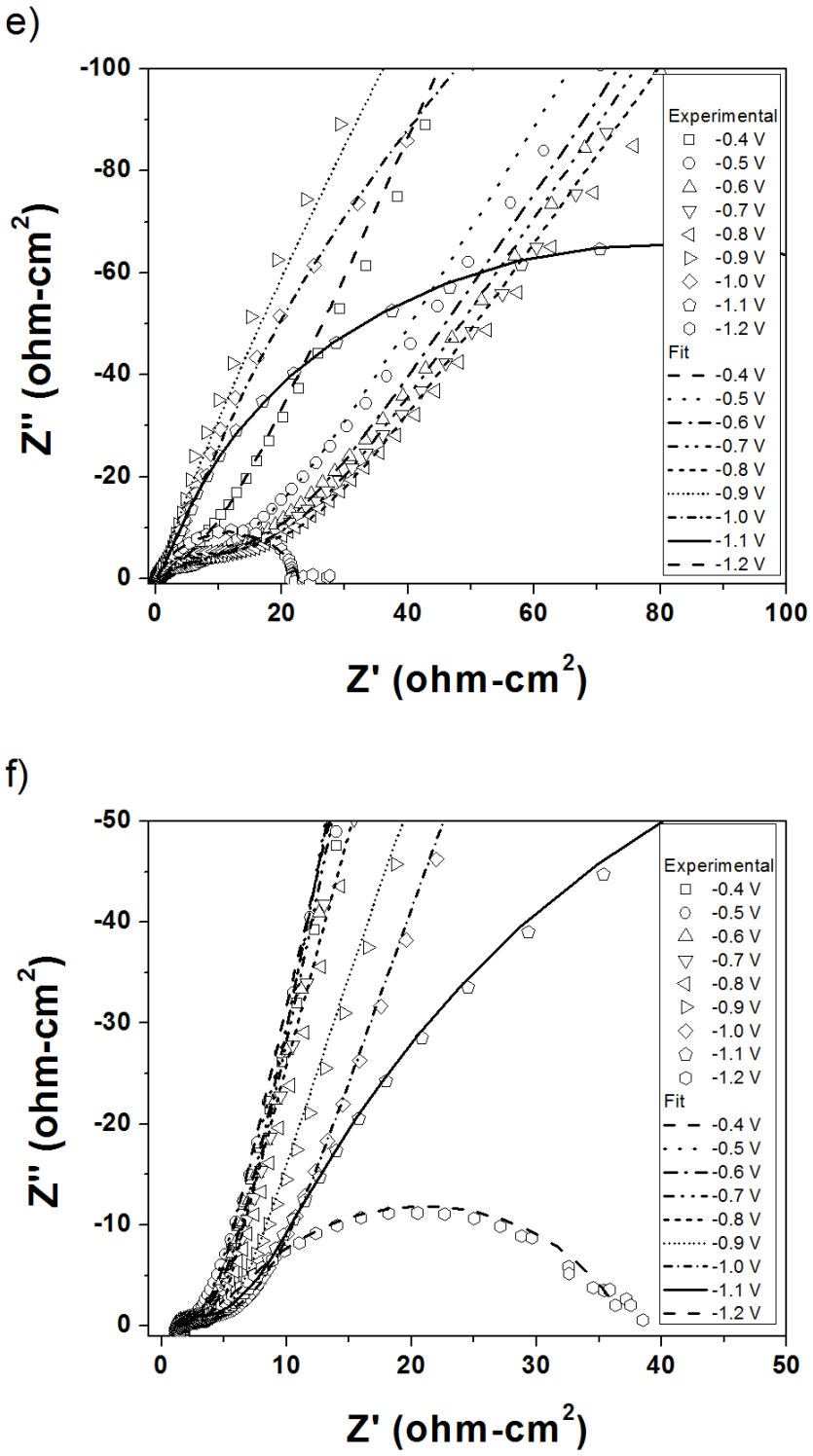

Figure 61. Nyquist plots of the various tungsten doped nitride materials during 1st discharge (Active material loading~0.1 mg/cm^2) (a) $W_{0.05}V_{0.95}N$ (b) $W_{0.10}V_{0.90}N$ (c) $W_{0.20}V_{0.80}N$ and magnified high frequency-semicircle portion of plots (a), (b), (c) in (d), (e), (f) respectively.

Table 23. Charge-transfer parameters of the doped nitrides of vanadium at different voltages during the 1st discharge (a) $Nb_{0.01}V_{0.99}N$ (b) $Nb_{0.05}V_{0.95}N$ (c) $Nb_{0.10}V_{0.90}N$ (d) $W_{0.05}V_{0.95}N$ (e) $W_{0.10}V_{0.90}N$ (f) $W_{0.20}V_{0.80}N$-Active material loading~0.1 mg/cm^2.

a) $Nb_{0.01}V_{0.99}N$												
Nominal voltage [wrt Hg/HgO (in 1M KOH)]	R_s(Ω-cm^2)	R_f (Ω-cm^2)	CPE_{dl}		C_{dl}^{eff} (*10^{-5}) (F)	CPE_p		C_p^{eff} (*10^{-3}) (F)	W_s			$R_{f'}$(Ω-cm^2)
			T(*10^{-5})	Φ		T(*10^{-2})	Φ		R	T	Φ	
-0.4	1.43	1.36E-07	1.23	0.99	1.14	2.66	0.68	5.90	30.19	0.16	0.23	
-0.5	1.35	2.46E-07	1.04	1.01	1.14	1.59	0.68	2.60	82.47	0.20	0.23	
-0.6	1.35	3.23E-07	1.87	0.97	1.29	1.78	0.72	4.26	100.40	0.50	0.20	
-0.7	1.36	3.85E-06	2.16	0.96	1.38	1.84	0.71	4.19	80.56	0.23	0.19	
-0.8	1.35	1.79E-05	2.59	0.95	1.44	1.88	0.72	4.41	62.43	0.07	0.21	
-0.9	1.37	6.61E-07	3.99	0.91	1.55	1.99	0.71	4.68	59.23	0.06	0.20	4011
-1	1.37	4.47E-07	5.64	0.89	1.77	2.75	0.70	6.65	51.14	0.12	0.19	1494

Table 23 (continued)

-1.1	1.36	2.53E-06	5.35	0.91	2.13	2.86	0.67	5.83	38.80	0.06	0.21	222.3
-1.2	1.35	8.54E-08	4.07	0.96	2.85	9.10	0.73	42.00	23.85	0.08	0.15	15.7
b) $Nb_{0.05}V_{0.95}N$												
-0.4	1.01	7.33E-10	20.70	0.86	5.42	4.09	0.85	23.10	17.20	0.85	0.25	
-0.5	1.05	4.37E-07	20.50	0.86	5.43	4.48	0.86	27.10	17.65	0.88	0.26	
-0.6	1.01	2.31E-07	1.65	1.01	1.76	2.45	0.71	5.40	30.89	0.32	0.20	
-0.7	0.97	2.29E-07	2.50	0.98	1.95	2.16	0.71	4.38	37.34	0.70	0.16	
-0.8	0.97	1.23E-06	2.37	0.99	2.08	1.88	0.68	2.88	30.99	0.08	0.17	
-0.9	0.98	6.49E-05	3.82	0.95	2.35	0.14	0.61	0.02	73.26	0.01	0.37	3118
-1	1.02	1.00E-09	3.98	0.95	2.33	0.14	0.62	0.02	75.46	0.01	0.39	1094
-1.1	1.05	1.72E-08	5.26	0.95	3.18	0.70	0.90	4.12	95.05	0.02	0.34	32.94
-1.2	1.02	4.99E-06	1.50	1.09	3.61	19.00	0.40	16.50	18.40	0.00	0.45	4.15
c) $Nb_{0.10}V_{0.90}N$												
-0.4	1.61	7.08E-01	658.00	0.66	61.30	4.97	1.07	58.20	101.20	66.23	0.54	
-0.5	1.20	9.03E-01	264.00	0.61	7.07	4.95	0.99	47.70	47.22	75.58	0.47	

Table 23 (continued)

-0.6	1.33	3.16E-01	1.04	1.13	3.82	4.72	0.92	37.00	4.72	10.00	0.22	
-0.7	1.23	4.39E-01	1.18	1.11	3.53	4.73	0.92	36.90	3.86	6.61	0.23	
-0.8	1.22	4.01E-01	0.81	1.14	3.32	4.42	0.91	33.00	3.12	6.23	0.20	
-0.9	0.95	2.94E+01	22.40	0.78	2.06	0.15	0.60	0.02	319.20	2.01	0.45	6679
-1	1.15	2.68E-01	0.11	1.31	2.53	0.21	0.62	0.05	45.10	1.01	0.56	1130
-1.1	1.08	3.69E-01	0.11	1.31	2.69	0.13	0.64	0.04	0.00	0.65	0.45	165.5
-1.2	1.09	4.67E-08	4.80E-04	1.80	2.23	0.07	0.74	0.06	1.44	0.00	0.64	24.6
d) $W_{0.05}V_{0.95}N$												
-0.4	3.71	260.32	2638.50	0.86	1832.29	3.09	1.00	30.87	5.14	1.28	0.33	
-0.5	3.06	0.16	2887.30	0.84	1833.33	3.38	1.09	40.90	10.40	2.63	0.42	
-0.6	1.17	1.11	4038.80	0.86	2419.32	2.84	1.25	55.93	30.55	3.78	0.52	
-0.7	1.16	1.49	3796.80	0.89	2617.12	2.59	1.05	30.55	6.11	0.66	0.34	
-0.8	1.15	2.48	4277.90	0.86	2661.20	2.04	1.26	43.79	25.31	2.38	0.48	
-0.9	1.15	15.91	2159.78	0.91	2435.12	2.63	0.98	24.56	3.99	0.33	0.32	1915

Table 23 (continued)

-1	0.89	2.04	2794.40	0.91	1966.03	2.82	0.97	25.20	4.68	0.37	0.32	1207
-1.1	0.91	1.92E+07	2354.90	0.91	1607.45	2.82	1.09	37.66	82.79	12.10	0.58	82.7
-1.2	0.89	2.16E+07	2162.50	0.89	1334.11	2.82	1.04	32.01	16.56	1.24	0.40	14.8
e) $W_{0.10}V_{0.90}N$												
-0.4	0.59	1.37E+00	867.00	0.72	117.00	1.68	0.72	2.83	0.00	1.00	1.00	
-0.5	0.62	4.86E-08	11.00	1.03	14.30	2.57	0.78	8.01	9.22	0.45	0.33	
-0.6	0.60	7.04E-07	0.10	1.29	2.51	1.71	0.71	2.75	19.23	0.30	0.24	
-0.7	0.59	1.69E-07	0.11	1.28	2.40	1.40	0.69	1.63	21.41	0.08	0.25	
-0.8	0.52	2.72E-08	0.47	1.14	2.24	1.36	0.69	1.47	25.21	0.11	0.22	
-0.9	0.50	6.02E-07	0.65	1.11	2.16	1.33	0.68	1.20	25.24	0.06	0.22	2312
-1	0.37	3.21E+01	11.40	0.86	2.30	0.40	1.01	4.16	1934.00	0.13	0.51	215.7
-1.1	0.39	2.66E-06	25.20	0.79	2.23	1.23	0.94	8.51	731.80	0.01	0.59	129.5
-1.2	0.58	1.25E-07	1.22E-03	1.74	3.48	0.02	0.92	0.08	37.58	0.18	0.48	22.08

Table 23 (continued)

f) $W_{0.20}V_{0.80}N$												
-0.4	1.95	5.62E-04	1.22E-03	0.70	5.59E-07	3.05	0.88	21.00	2.22	0.09	0.39	
-0.5	1.53	4.08E-01	686.00	0.67	74.40	2.69	1.06	32.00	19.04	2.69	0.44	
-0.6	1.56	5.09E-08	1.05	1.19	5.91	3.00	0.91	22.30	6.09	1.44	0.25	
-0.7	1.48	3.97E-08	0.27	1.25	3.19	2.91	0.90	20.80	5.98	1.53	0.20	
-0.8	1.27	2.27E+00	88.20	0.68	3.40	2.55	0.87	15.30	1.12	0.03	0.65	
-0.9	1.41	2.56E-07	0.75	1.10	2.11	2.58	0.87	15.50	7.56	1.48	0.15	1603
-1	1.36	1.25E-05	1.75	1.04	2.54	2.74	0.89	18.00	23.46	71.78	0.18	1317
-1.1	1.42	5.24E-08	1.11	1.10	2.93	2.33	0.90	15.70	24.74	34.89	0.21	151.3
-1.2	1.62	1.28E-07	0.91	1.16	4.34	2.56	0.88	16.50	13.03	2.44	0.26	23.04

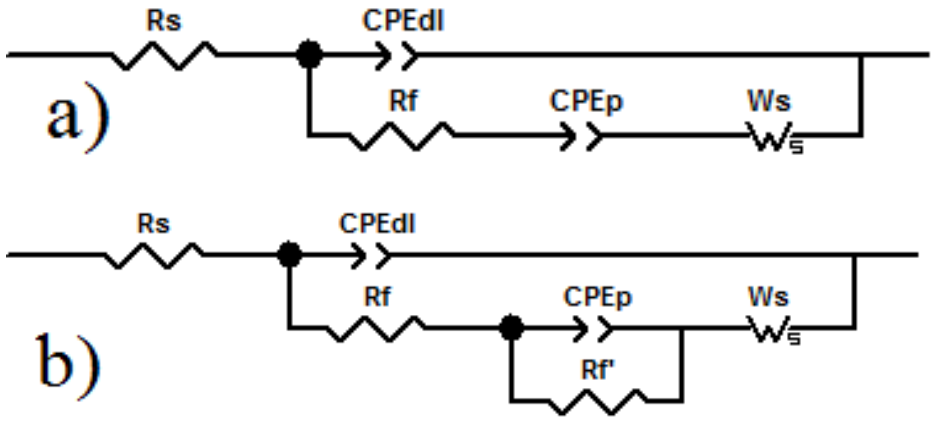

Figure 62. Equivalent circuit model used to fit the impedance plots seen in Figure 60 and Figure 61. Fit lines shown in those figures use the underpotential deposition mechanism (UPD) seen in Figure 62a between -0.4 V and -0.8 V wrt Hg/HgO (in 1M KOH) and overpotential deposition (OPD) mechanism seen in Figure 62b between -0.9 V and -1.2 V wrt Hg/HgO (in 1M KOH).

Table 23a-Table 23f depict the values of charge-transfer parameters for the different doped compositions of vanadium nitride during the 1st discharge. Charge-transfer parameters were obtained by equivalent circuit modeling of the experimentally obtained impedance data using either the underpotential deposition model shown in **Figure 62a** or the overpotential deposition model shown in **Figure 62b**. Fitting was performed over the whole frequency window and in each instance the goodness of fit was ensured using χ^2 values. The series resistance (R_s) occurring at the high frequency domain as a result of electrolyte conductivity and current collector resistances is seen to be very small (~1-4 Ω–cm^2) and appears to be constant over the whole voltage window. It can be seen that the charge-transfer resistances (R_f) seemingly varies without any noticeable trend over the whole voltage window. However, upon closer examination (**see Figure 63a**), it will be seen that charge-transfer resistances attain local minima at potentials [-0.5-0.7 V(wrt Hg/HgO (in 1M KOH)) and -0.9—1V (wrt Hg/HgO (in 1M KOH))] corresponding to Faradaic reactions in **Figure 57a** and **Figure 57b**. This is to be expected since

Faradaic reactions are voltage activated. The voltages at which minima occur are slightly different in the different compositions since standard reaction potential (E^0) is known to be composition dependent. The overlap of different Faradaic reactions is a characteristic of pseudocapacitor materials making the observed R_f values seemingly fluctuate over a couple of orders. In addition to Faradaic charge-transfer involving oxidation state changes of vanadium, electrolysis reactions start occurring in all the doped vanadium nitride compositions resulting in a change in mechanism to the overpotential deposition mechanism seen in **Figure 62b**. The secondary resistance R_f' corresponding to activation of water electrolysis indicates that though the onset of electrolysis occurs at -0.9 V (wrt Hg/HgO (in 1M KOH)) in all the electrode materials, the kinetics are severely limited upto -1.2 V (wrt Hg/HgO (in 1M KOH)). Such poor kinetics allow for the use of a voltage window upto -1.2 V (wrt Hg/HgO (in 1M KOH)). It can be seen that R_f' exhibits very high values of ~10^3-10^4 Ω–cm^2 gradually decreasing to ~10^1 Ω–cm^2 at -1.2 V (wrt Hg/HgO (in 1M KOH)). In addition to charge transfer resistance (R_f) and series resistance (R_s), one can obtain fundamental information about capacitive charge storage through the constant phase elements CPE_{dl} (constant phase element-double layer) and CPE_p (constant phase element-pseudocapacitance). Constant phase elements are commonly used in place of capacitor elements in porous electrodes as is the case here. It can be seen that in **Table 23a-Table 23f**, the phase angle Φ varies between 0.65 and 1.10 indicating that the fit is a good one. Calculation of effective capacitance from the constant phase elements has been reported before[399] using Equation (x) below:

$$C_{eff} = (CPE - T)^{1/(CPE-\Phi)} * R_s^{(1-CPE-\Phi)/(CPE-\Phi)} \qquad \text{Equation (x)}$$

Where CPE-T is the quantitative component of the constant phase element and CPE- Φ is its phase angle.

Table 24. Comparison of the charge-transfer properties of undoped VN and various doped compositions of the same at a potential of -0.6 V wrt Hg/HgO (in 1M KOH)- Active material loading~0.1 mg/cm^2.

Nominal composition	R_s(Ω-cm^2)	R_f (*10^{-7}) (Ω-cm^2)	CPE_{dl}		C_{dl}^{eff} (*10^{-5}) (F)	CPE_p		C_p^{eff} (*10^{-3}) (F)	W_s		
			T (*10^{-5})	Φ		T (*10^{-2})	Φ		R	T	Φ
VN	4.02	2.92	14.60	0.85	3.93	1.47	0.86	9.28	15.96	0.23	0.22
$Nb_{0.01}V_{0.99}N$	1.35	3.23	1.87	0.97	1.29	1.78	0.72	4.26	100.40	0.50	0.20
$Nb_{0.05}V_{0.95}N$	1.01	2.31	1.65	1.01	1.76	2.45	0.71	5.40	30.89	0.32	0.20
$Nb_{0.10}V_{0.90}N$	1.33	3.16E+06	1.04	1.13	3.82	4.72	0.92	37.02	4.72	10.00	0.22
$W_{0.05}V_{0.95}N$	1.17	1.11	4038.80	0.86	2419.32	2.84	1.25	55.93	30.55	3.78	0.52
$W_{0.10}V_{0.90}N$	0.59	1.69	0.11	1.28	2.40	1.40	0.69	1.63	21.41	0.08	0.25
$W_{0.20}V_{0.80}N$	1.56	0.51	1.05	1.19	5.91	3.00	0.91	22.33	6.09	1.44	0.25

a)

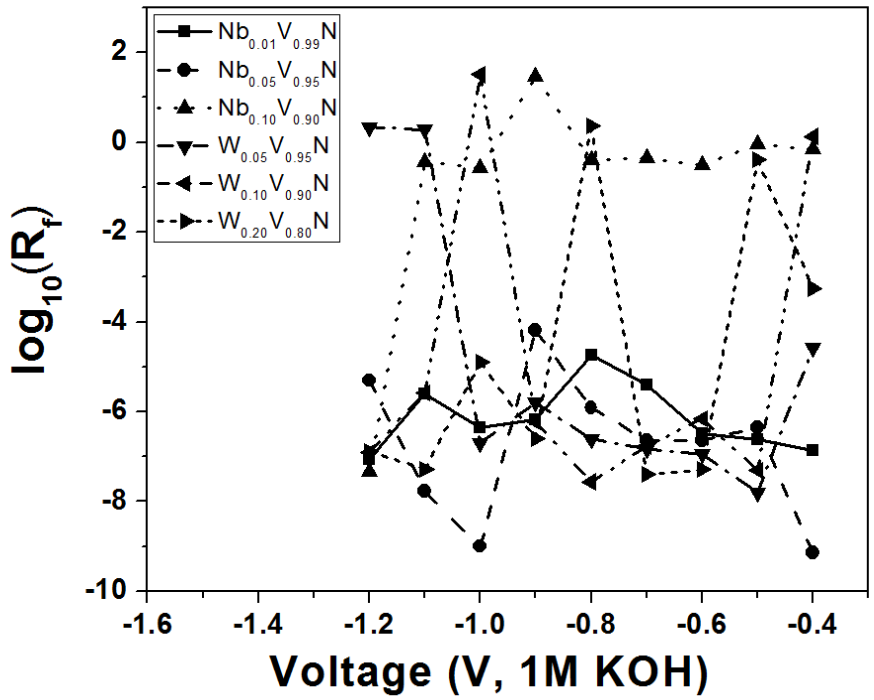
Nb0.01V0.99N
Nb0.05V0.95N
Nb0.10V0.90N
W0.05V0.95N
W0.10V0.90N
W0.20V0.80N
log10(Rf)
Voltage (V, 1M KOH)

b)

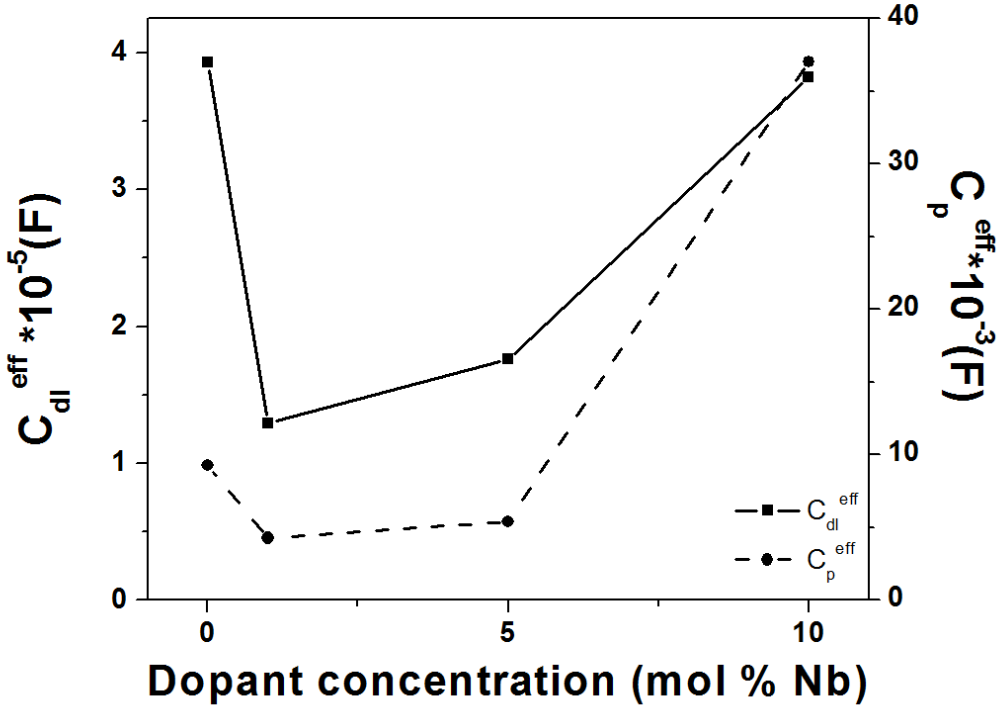
Cdl eff *10-5(F)
Cp eff*10-3(F)
Cdl eff
Cp eff
Dopant concentration (mol % Nb)

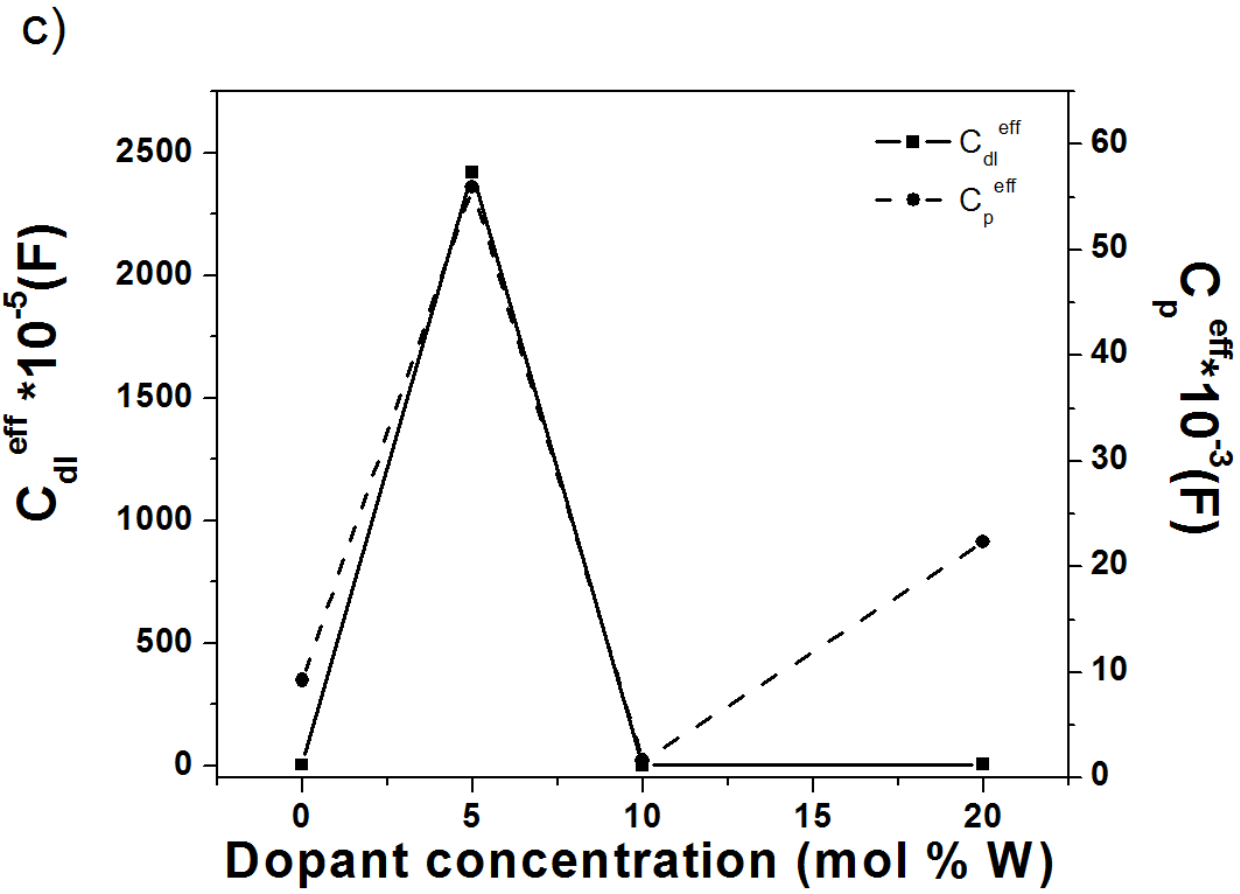

Figure 63. (a) Dependence of charge transfer resistance on potential in the different niobium and tungsten doped compositions of vanadium nitride. $\log_{10}R_f$ has been plotted against potential (wrt Hg/HgO (in 1M KOH)). (b,c) Dependence of effective capacitance (double-layer capacitance and pseudocapacitance) calculated from charge-transfer parameters shown in Table 23 on dopant concentration (b) $Nb_xV_{1-x}N$ (x=0.01-0.1) (c) $W_xV_{1-x}N$ (x=0.05-0.2). All values are at a potential of -0.6 V wrt Hg/HgO (in 1M KOH)- Active material loading~0.1 mg/cm^2.

Both the effective double layer capacitance (C_{dl}^{eff}) as well as the effective pseudocapacitance (C_p^{eff}) is seen in **Table 23a-Table 23f**. It can be seen that the effective pseudocapacitance values are almost two orders of magnitude greater than the effective double layer capacitance values in most of the doped VN compositions. This is to be expected since the

material is known to store charge predominantly through Faradaic reactions occurring on the surface oxide[182, 235]. The comparison between various charge-transfer parameters at a particular potential [-0.6 V (wrt Hg/HgO (in 1M KOH))] are seen in **Table 24**. This potential was chosen since it corresponds to a Faradaic peak potential in the cyclic voltammograms seen in **Figure 57a** and **Figure 57b**. The aim of impedance analysis was to obtain charge-transfer parameters and relate them with observed capacitance behavior in **Figure 58a** and **Figure 59a**, particle properties seen in **Table 22** and theoretically derived electronic properties seen in **Table 28** (see **Page 276**). **Figure 63b** and **Figure 63c** depict the dependence of effective double layer capacitance and effective pseudocapacitance on doping concentration in $Nb_xV_{1-x}N$ (x=0.01, 0.05, 0.10) and $W_xV_{1-x}N$ (x=0.05, 0.1, 0.2) respectively at the potential of -0.6 V (wrt Hg/HgO (in 1M KOH)). It can be seen that initial doping of VN with Nb results in a fade in both effective double layer capacitance and effective pseudocapacitance possibly as a result of the drop in electronic conductivity seen in **Table 22**. Niobium doped vanadium nitride demonstrates characteristic behavior of vanadium nitride with Faradaic peaks, but as seen in **Figure 57a**, the response is most predominant in $Nb_{0.05}V_{0.95}N$ while both $Nb_{0.01}V_{0.99}N$ and $Nb_{0.10}V_{0.90}N$ have weaker responses. This is found to be the case in **Figure 58a** as well wherein $Nb_{0.05}V_{0.95}N$ shows the most scan-rate stable capacitance with values higher than $Nb_{0.10}V_{0.90}N$. This behavior can be explained by examining the values of R_f in **Table 24** and the trend in C_{dl}^{eff} and C_p^{eff} seen in **Figure 63b**. $Nb_{0.01}V_{0.99}N$ has the least C_{dl}^{eff} and C_p^{eff} which keeps increasing with increasing doping concentration. However, $Nb_{0.10}V_{0.90}N$ has poor capacitance as compared to $Nb_{0.05}V_{0.95}N$. It can be seen that among the various materials, $Nb_{0.10}V_{0.90}N$ has a very high charge-transfer resistance. This is the case at all potentials as seen in **Figure 63a** and **Table 23c**. Though $Nb_{0.10}V_{0.90}N$ has a high electronic conductivity, it has a higher activation potential for Faradaic

processes which limits its capacity storage ability. This is possibly due to higher Nb content resulting in a more strongly bonded structure as predicted by the ab-initio first principle calculations seen in **Table 28** (see **Page 276**). Hence, 5% Nb doping results in a good rate capable material with slight improvement in cycling stability as seen in **Figure 58b**.

Figure 63c depicts the dependence of C_{dl}^{eff} and C_p^{eff} on W content in VN. It can be seen that $W_{0.05}V_{0.95}N$ has C_{dl}^{eff} and C_p^{eff} values much higher than those of the other two doped compositions. This is in line with the very high electronic conductivity observed in **Table 22** resulting in the high capacitance seen in **Figure 57b, Figure 59a, Figure 59b**. This high electronic conductivity of the doped VN resulting from electronic structure modifications as predicted by the ab-initio studies displayed in **Table 28** contributes to a very high capacity and retention of the high capacity even at high scan rates. The high conductivity and cycling stability of $W_{0.05}V_{0.95}N$ are possibly the result of a highly conductive nitride core with a reactive and conductive oxide exo-skeleton. The phenomenon however is not as pronounced in the other tungsten doped VN compositions. As seen in **Figure 63c**, $W_{0.10}V_{0.90}N$ has C_{dl}^{eff} and C_p^{eff} values reflecting those of undoped VN resulting in the capacitance behavior seen in Figure 7a. The C_p^{eff} of $W_{0.10}V_{0.90}N$ is slightly lower than that of undoped VN resulting in the slightly lower value of capacitance observed at low scan rates. At higher scan rates, both materials have almost identical capacity. However, $W_{0.10}V_{0.90}N$ is much more stable than VN possibly as a result of a stable surface oxide as predicted by first principle studies (**Table 28**). $W_{0.20}V_{0.80}N$ has similar C_{dl}^{eff} and slightly higher C_p^{eff} at -0.6 (wrt Hg/HgO (in 1M KOH)) as seen in **Figure 63c**. This results in a higher capacitance of ~380 F/g at 2 mV/s. However, the material does not retain this capacitance at higher rates possibly as a result of electronic conductivity being similar to that of VN. $W_{0.05}V_{0.95}N$, however reflects a composition wherein the interplay of a number of factors

including high electronic conductivity and high reactivity result in capacitances of ~580 F/g. The capacitance obtained is superior to that of the values reported for a number of VN compositions reported before[249, 400] and accompanying cycling stability result in a material of great promise for grid-scale supercapacitor charge storage. $W_{0.05}V_{0.95}N$ has high electronic conductivity and chemical stability as evidenced by **Table 22** and **Table 28**. The cohesive energy is higher and electronic conductivity is higher as experiementally observed and theoretically predicted. This results in the very high capacitance which is retained at high rates and with extended cycling. Further studies are ongoing to understand surface oxidation state of both V and dopant metal and attempts are on to correlate the same with observed capacitor characteristics. Post-cycling analysis using inductively-coupled plasma (ICP) method would aid in confirming the improved stability of the doped compositions and work is ongoing on the same.

4.4.1 Conclusions

It was demonstrated that by use of a doping strategy guided by first principles DFT studies various compositions of niobium-vanadium nitride and tungsten-vanadium nitride were synthesized. The aim of doping vanadium nitride was multi-pronged (a) to increase electronic conductivity and (b) to increase surface oxide stability. In the case of niobium doped vanadium nitride, it was found that there was no significant increase in electronic conductivity resulting in charge storage behavior slightly inferior to that of undoped vanadium nitride. However, it was found that doping increased the cycling stability with a doping concentration of 5 mol% Nb in VN resulting in slight improvement in cycling stability without significant loss in capacity. In the case of tungsten doped vanadium nitride materials however, it was determined that 5 mol% W in VN resulted in very high capacitances of upto 580 F/g with good scan rate stability and cycling

stability. Using impedance spectroscopy, it was demonstrated that the increased pseudocapacitive charge storage in the material was a result of facile reaction kinetics and high electronic conductivity of the surface oxide. The material also exhibited superior cycling stability, possibly as a result of improved lattice binding as evidenced by the cohesive energy calculations.

5.0 SUMMARY AND OUTLOOK

The design and development of novel nanomaterials for energy generation and storage applications is an urgent necessity from a socio-economic and environmental perspective due to the growing need for energy encountered as a result of ballooning global population. There are a number of challenges to the identification of cheap materials and te chnologies for energy applications. A lack of fundamental understanding into the nature of energy storage at nanostructured interfaces is one of the primary problems preventing the development of reliable, high performance systems on a large scale. Engineering of materials to match application requirements is possible only if structure-property relationships are well established. The multivariate nature of the problem however makes the establishment of broad governing principles very challenging. In this work, the gauntlet of tackling a unique problem was undertaken namely, one of storing and distributing energy at rapid rates. Supercapacitors are ideal for this purpose on account of their inherently facile charge storage mechanism. It was decided to constrain the problem to entail materials capable of storing enough charge to be of practical use with excellent reversibility to ensure longevity. In addition, it would be preferable if the material were to be inexpensive. Having thus defined the problem, an uncommon set of materials was selected namely, nanostructured nitrides and oxides as the primary subject. The choice was based on the constraints already listed i.e. cost, theoretical energy density and power density and cycling stability. The challenge that was faced in delivering a material capable of

matching all the above constraints was a lack of complete understanding into charge storage in these materials. Instead of taking it as an obstacle, it was decided to take it as an opportunity to try and understand mechanisms controlling charge storage. Using a multi-pronged approach, it was demonstrated that nitride charge storage is indeed a surface catalysis phenomenon very much dependent on the nature of surface oxide (**Section 4.1.2**). In addition, it was demonstrated that cost effective approaches can be designed to derive nitride nanomaterials with good energy storage (**Section 4.1.1.2**). The translation of material properties into electrode properties is of utmost importance and using electrochemical impedance spectroscopy, the factors limiting scale-up in nitride nanoparticle based systems (**Section 4.1.4**) including mass transport and electronic conductivity limitations in thick electrodes was demonstrated. In the process, criteria required to obtain very high capacitances (~1200 F/g) in nitride materials were also established.

As it was evident that nanoparticulate surface oxide is responsible for charge storage in nitride nanomaterials, it was therefore attempted to show that the oxide material could deliver such excellent charge storage due to its ability to undergo pseudocapacitance reactions reversibly but that it is the inherent conductivity that limits its charge storage in thick films. This was addressed by coating vanadium oxide (VO_x) onto a matrix of highly conductive vertically aligned carbon nanotubes (VACNT) and comparing charge storage with that of thin film vanadium oxide (**Section 4.2.1**). It was demonstrated that the VO_x-VACNT material could result in capacitances of ~1400 F/g due to the high electronic conductivity of the carbon nanotube matrix.

It was then decided to adopt doping strategies to tackle the problem of preparing scaleable electrodes with high energy density and power density. Using titanium doping and a simple chemical vapor deposition technique, thick electrodes of VO_x:Ti-VACNT with electrode-

level capacitances of ~315 F/g at a loading of ~1.1 mg/cm^2 were obtained.It was demonstrated that the improvement in electronic conductivity of the oxide coated on CNTs is important to achieve high capacities in oxide nanomaterials (**Section 4.3**). With the knowledge gained from doping studies on nanoparticulate transition metal oxides, it was decided to conduct a detailed study trying to engineer nitride nanoparticles to create a stable, conductive surface oxide coated on very fine nitride nanoparticles. ~5 nm niobium and tungsten doped VN nanoparticles were synthesized using a simple chemical reduction method. A detailed study was conducted to try to correlate structure and property. Using a combination of first principles studies, material characterization and electrochemical impedance spectroscopy, it was demonstrated that capacitance in doped nitride materials is the result of the interplay of a number of factors including (a) electronic conductivity (b) surface pseudocapacitance (c) good lattice cohesion and (d) surface reaction kinetics. In the process, it was realized that there was no one factor that can be used as a means to optimize the nitride charge storage without trading it for either loss in rate capability or cycling stability. However, it was possible to successfully demonstrate very high capacitances of ~580 F/g in thick electrodes of $W_{0.05}V_{0.95}N$ (**Section 4.4.1**). It was found that the introduction of W into VN, VO_x resulted in improvement in both electronic conductivity as well as cohesive energy, both of these factors playing a big role in the superior performance of $W_{0.05}V_{0.95}N$.

Figure 64 depicts the advantages and disadvantages of all the materials studied as part of this work in the form a flow sheet depicting the evolution of the current work from the early inception stage. The choice of materials was driven by new insights gained into materials properties obtained at different times during the work. The work started off as an attempt to understand structure-property relationships in vanadium nitride. Initial studies showed the

cycling instability of ammonolysis-derived VN which laid the initial foundations for the current work focused mainly at determining the causes and mechanisms behind the same. The importance of surface oxide and particle crystallinity on the capacitance was highlighted by these studies. Electronic conductivity and surface oxidation state of vanadium were found to primarily dictate the system properties. Mechanochemical sysnthesis was thus undertaken to identify a low cost method to prepare conductive VN and to demonstate the effect of surface oxide on cycling stability. The importance of pseudocapacitive charge storage in vanadium oxide (VO_x) was thus realized. Subsequent studies were then directed towards gaining an insight into the charge-storage mechanisms in VO_x. Using a simple-CVD procedure, the effect of conductive substrates such as CNTs was shown. It was observed that the CNTs contributed to overcoming the inherent oxide conductivity limitations to some extent and also aided in improving the electrochemical reaction kinetics. However, the overall capacitance was still observed to be low at high rates and in thick oxide coatings due to the inherent oxide-conductivity limitations. Doping of multivalent transition metal ions was therefore adopted as a strategy to improve the vanadium oxide capacitance in addition to the coating on CNTs. Very high gravimetric and areal capacitances were thus obtained as a result of doping of the surface oxide.

This study provided new understandings into the oxide charge-storage mechanism, i.e. the effect of coating doped oxides onto inherently conducting support-structures. It was evident that nitride materials which derive their primary pseudocapacitor characteristics from a surface oxide layer were ideal materials for studying the effect of oxide doping in very fine nanoparticles. It was also expected that the ammonlysis method would help obtain doped nitride nanoparticles with a stable surface doped oxide. Doped nitride nanoparticles of 3-6 nm were thus prepared with tungsten and niobium as dopants. Tungsten doping was found to improve the

electronic conductivity, electrode kinetics and cycling stability of the parent VN leading to excellent high capacitance and superior rate capability with long cycle lives. The insights gained at each stage of this study thus led to the evolution of this work culminating in the identification and synthesis of doped nitide nanoparticles with superior supercapacitor-type charge storage characteristics.

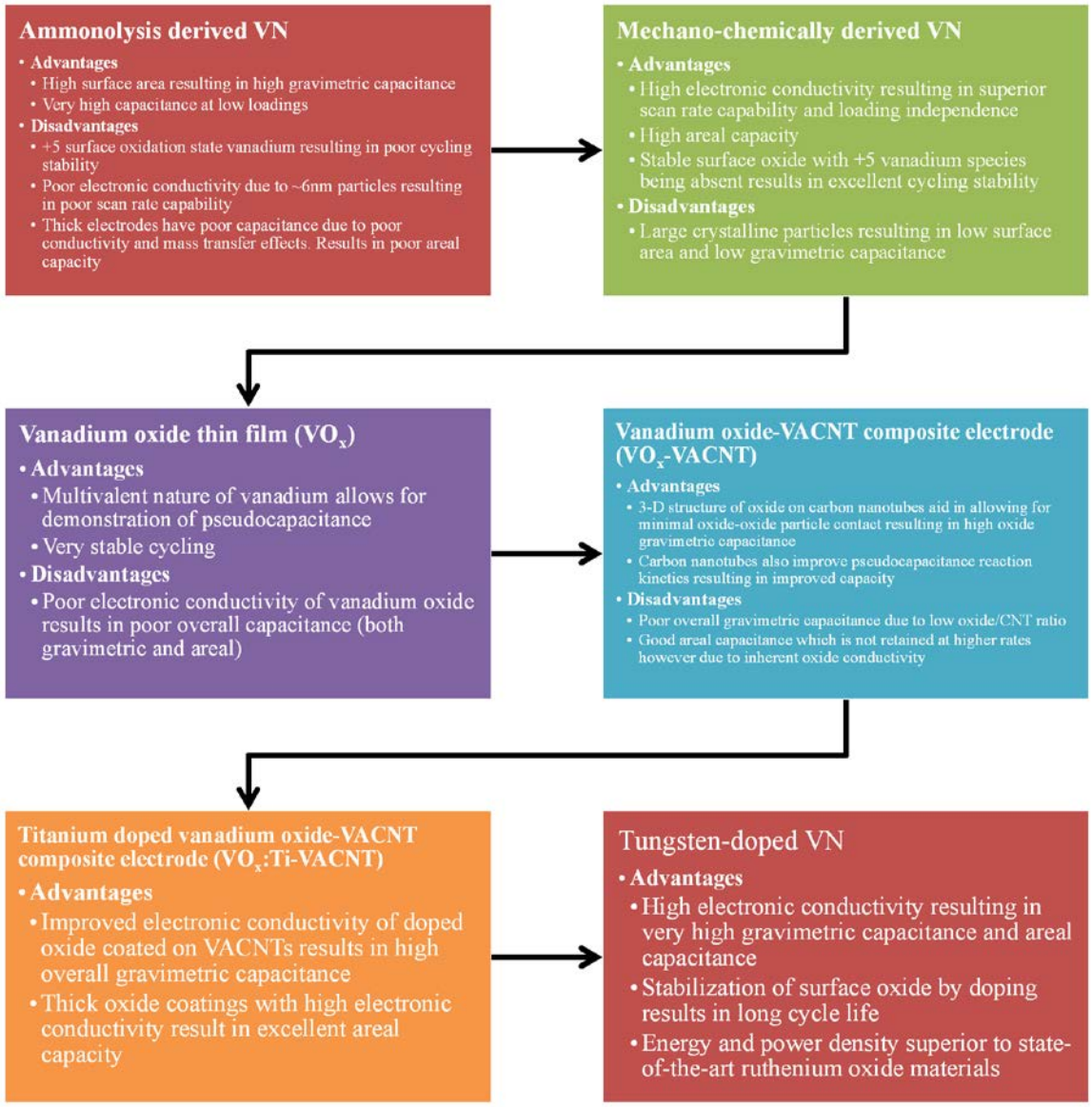

Figure 64. Flowchart showing the evolution of materials studied in this work.

There is however a need for a perspective in order to understand where the materials derived in this work stand with regards to performance targets and guidelines established in **Table 5**. The Ragone plot is a good means of comparing materials performance. **Figure 65** shows the Ragone plots of various materials in this study with the targets established in **Table 5** marked on the graph as well. It can be seen that among the various materials, mechano-chemically derived VN, VACNT-VO_x:Ti and $W_{0.05}V_{0.95}N$ have superior performance and are capable of matching the targets set for supercapacitor applications i.e. PAHEV (Power assist-Hybrid electric vehicle), TPA (Transient Power Assist) and SSA (Start-Stop Assist). $W_{0.05}V_{0.95}N$ as shown in this study far exceeds these targets and demonstrates almost a straight-line dependence of energy-density on power-density as shown in **Figure 65**. It can also be observed that $W_{0.05}V_{0.95}N$ charge-storage behavior exceeds the energy density and power density of RuO_2-graphene sheet composite electrodes (ROGSCs) reported before[401]. None of these materials however seem capable of meeting the EVP (electric vehicle power source) target of 350Wh/kg. As already pointed out, supercapacitors are unique devices suited to meet most of the requirements for high power applications and it is impractical to consider them yet as standalone power sources. They however serve a niche market and the materials derived and developed in this study demonstrate characteristics that are suitable for and are much better in meeting most of the requirements for these applications. In particular, TPA applications and grid-level applications are well within the reach of the materials developed in this study.

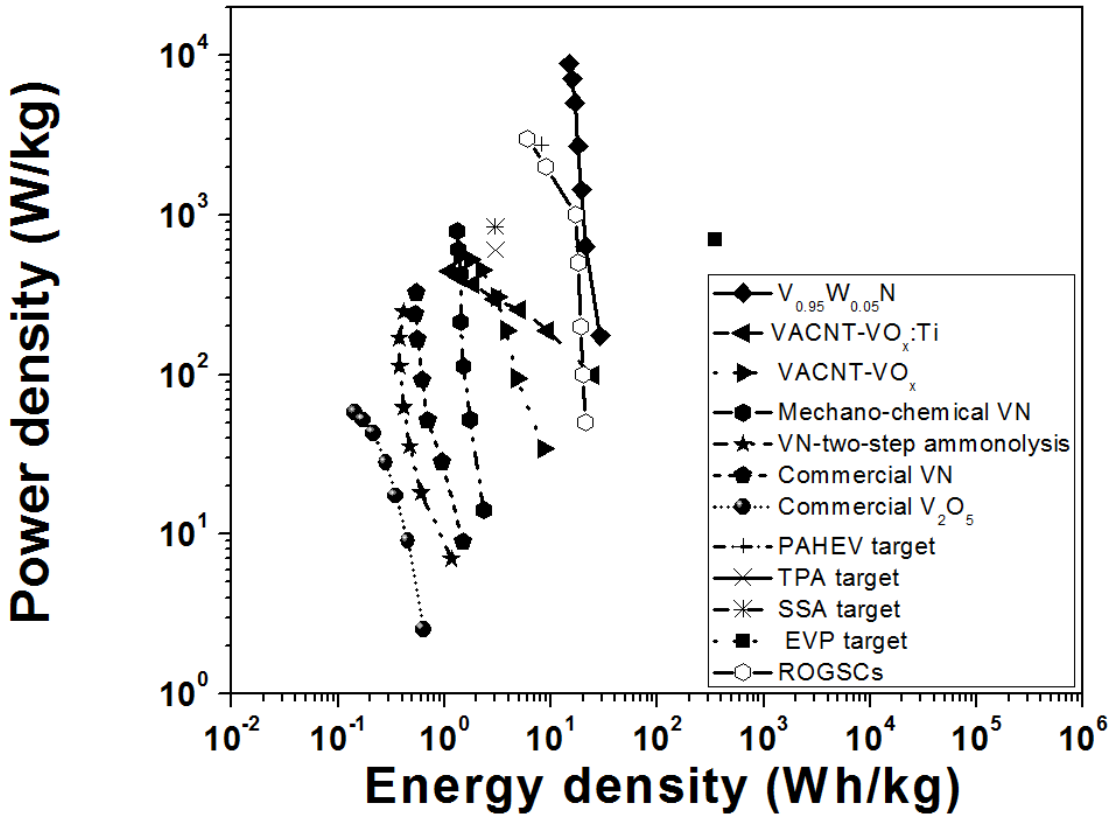

Figure 65. Ragone plot depicting the energy density and power density of the various supercapacitor materials.

Table 25. Cost of synthesis of various nanoparticulate oxides and nitrides.

Material	Energy density (Wh/kg)	Cost ($/gm)
Commercial RuO_2	5-20	55
Commercial V_2O_5	0.14-0.63	0.193
Commercial VN	0.5-1.49	60
VO_x-VACNT composite	1.37-8.55	24.7
VN: Mechano-chemical synthesis	1.3-2.34	5.3
VN: Ammonolysis method	0.41-1.16	36
VO_x:Ti-VACNT composite	1.12-24.74	30
$W_{0.05}V_{0.95}N$	14.73-29.04	37.5

Synthesized using a 10gm weight basis. Electricity cost of ~7 c/kWh was assumed in this calculation. Cost of precursors were obtained from Sigma Aldrich Inc. on 10 gm final VN yield assuming 100% conversion of reactants to products.

Another important aspect to consider is cost of synthesis of the nanomaterials. **Table 25** depicts the cost of synthesis of various nanomaterials which can be used as a tool to understand which among these materials bears the greatest promise. It can be seen that there is a tradeoff between cost and energy density. Commercially derived materials lack both performance characteristics while also being expensive. Amongst the in-house materials derived in this work, mechanochemically derived VN is the most cost effective material. An even better perspective however is obtained by looking at cost/energy as shown in **Figure 66**. T The modified Ragone

plot including cost/mWh shows that the ammonlysis derived VN and commercially procured VN provide very little energy/$ at all different power densities. On the other hand, VO_x-VACNT and VO_x:Ti-VACNT are relatively inexpensive but their cost/energy increases rapidly at high power densities. Commercial V_2O_5 is a material with little energy storage capability though it is cheap. Mechanochemically derived VN is inexpensive at all power rates but is limited in energy density. $W_{0.05}V_{0.95}N$ on the other hand is a superior material with very high energy density and cost/energy at very high power rates. This makes the material very promising from an application perspective.

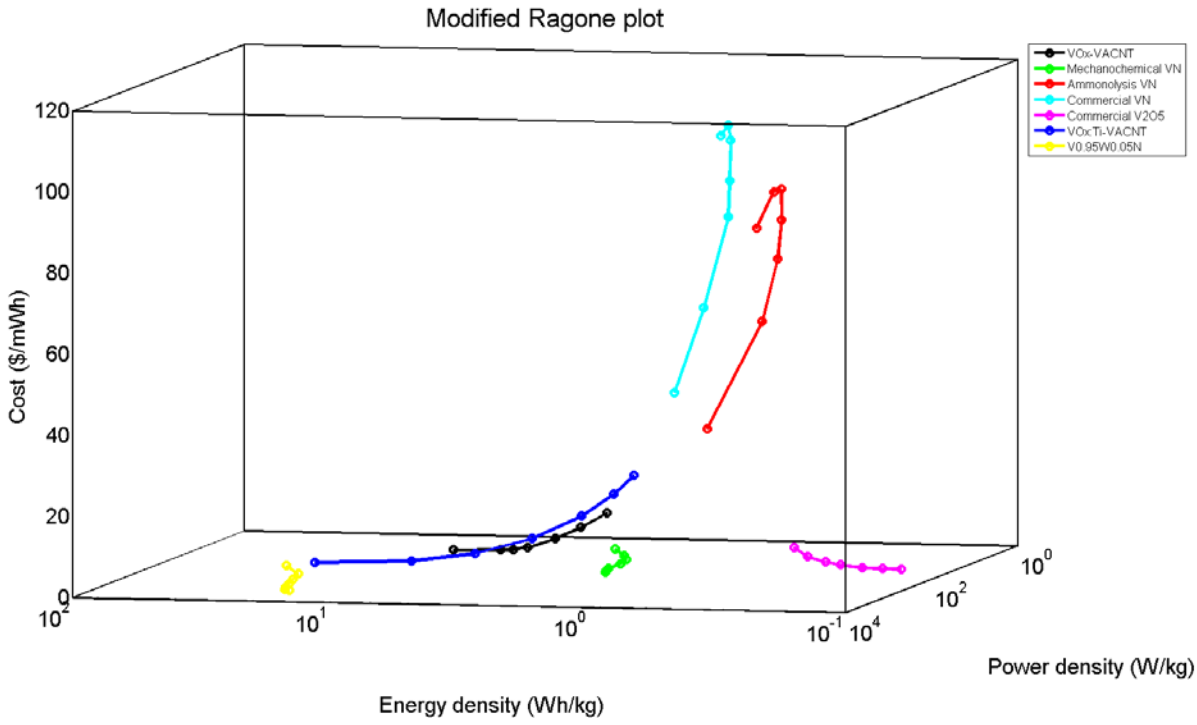

Figure 66. Modified Ragone plot of the different materials including cost of materials as a function of energy density.

In conclusion, it is possible to tailor the nanomaterials namely, oxides and nitrides for specific energy storage applications. Supercapacitor applications discussed in this study need high surface area, electronic conductivity and superior stability in conjunction with facile reaction kinetics in the case of supercapacitor materials. Doped materials using conductive supporting architectures bear the greatest promise. A first principles-driven approach in conjunction with experiment is required to be able to engineer materials with superior properties. With a view to the future, it is hoped that the data in the present work acts as a precursor to formulation of ab-initio strategies which allow for predictive materials selection in nitride and oxide nanomaterials as shown in **Figure 67**. It is hoped that these studies can be planned in the future to achieve the desired improved properties to meet the various challenging problems of energy storage systems.

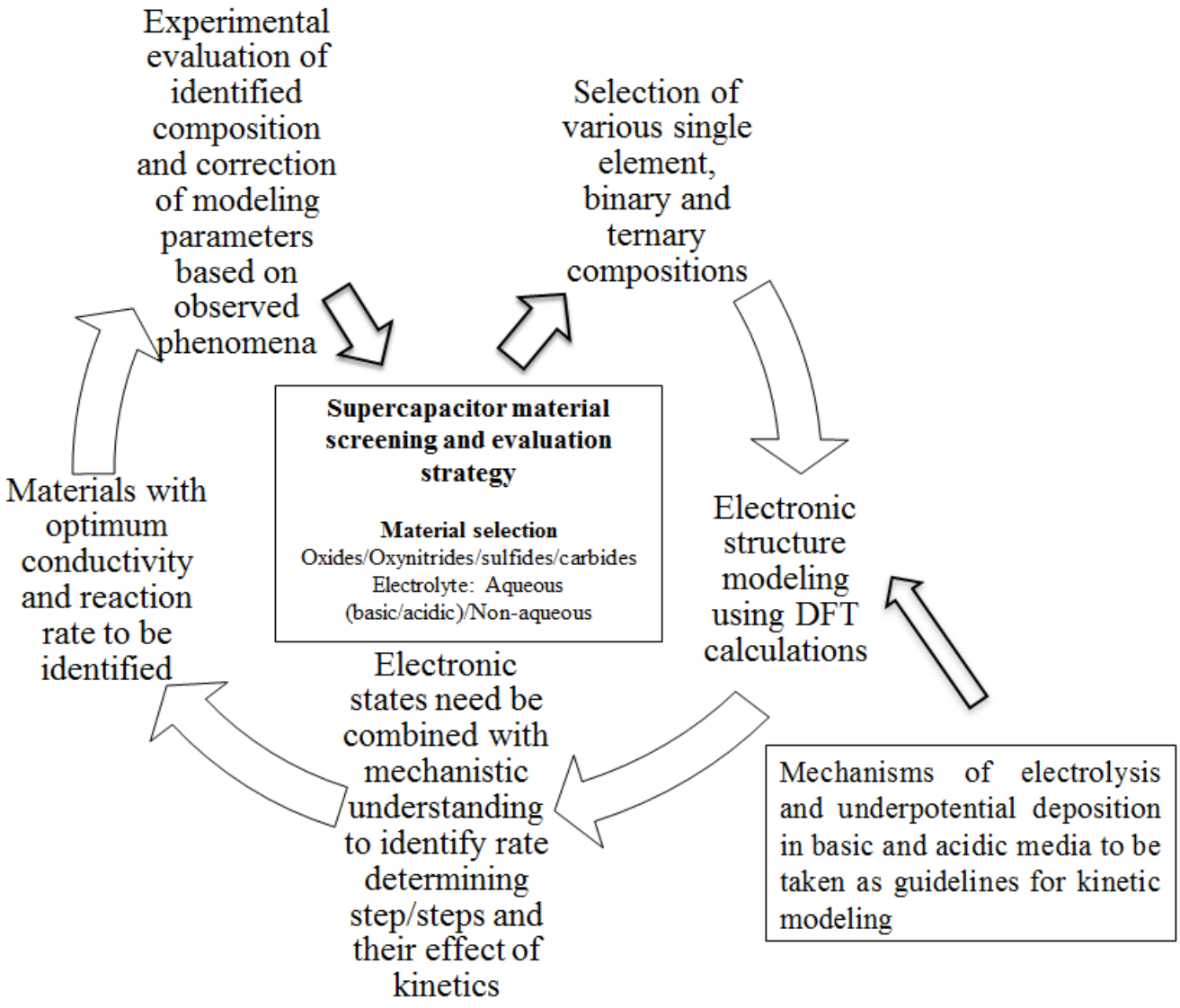

Figure 67. First-principles driven supercapacitor nanomaterials discovery and engineering as a strategy for future materials development.

APPENDIX A

SUPERCAPACITORS

A.1 FIRST PRINCIPLES CALCULATIONS

A.1.1 Doped vanadium oxide capacitors

Changes in the electronic structure of vanadium oxide with the introduction of oxygen vacancies and Ti-atoms in the oxide lattice results in substantial enhancement in the electronic conductivity of the material. For calculations of the total energy, density of electronic states and the cohesive energy (E_{coh} reflecting overall mechanical and chemical stability), the Vienna Ab-initio Simulation Package (VASP) based on the projector-augmented wave (PAW) formalism[402-404] within the generalized gradient approximation (GGA), for conducting the exchange-correlation corrections proposed by Perdew *et al.*[405], has been used in the present study. A plane-wave basis set with a cutoff energy of 520 eV and 184 *k*-points in the irreducible part of the Brillouin zone have been used to achieve an accuracy in the total energy of ~10^{-2} eV per formula unit, which is sufficient for a confident evaluation of the electronic structure, the cohesive energy and comparison of the results with corresponding experimental data.

V_2O_5 adopts an orthorhombic crystal structure with a space group D_{2h}^{13} - *Pmmn* (#59) with two formula units in the elementary unit cell. All structural parameters along with internal atomic Wyckoff positions are summarized in

Table 26 taken from the published report[406]. It should be noted, that there are three non-equivalent oxygen positions in the unit cell designated as bridge (O_b), vanadyl (O_v), and chain (O_c) oxygen sites.

Table 26. Crystal structure of V_2O_5[406]

Lattice constants (Å)		*a* = 11.512 Å	*b* = 3.564 Å	*c* = 4.368 Å
Atoms	Wyckoff positions	x	y	z
O_b	(2*a*)	0.0	0.0	0.001
O_v	(4*f*)	0.8543	0.0	0.531
O_c	(4*f*)	0.6811	0.0	0.003
V	(4*f*)	0.85118	0.0	0.8917

To simulate the experimentally studied materials, the following compounds have been constructed within one elementary unit cell containing 4 V and 10 O atoms: pure V_2O_5, $V_2O_{4.5}$ with one oxygen atom missing, and $V_{1.5}Ti_{0.5}O_{4.5}$ with one oxygen atom missing, and one V atom replaced for Ti. Such compositions although not exactly matching the actual experimentally generated systems, nevertheless could be very close approximations of the materials discussed in the present study: $V_2O_{4.6}$ and $V_{1.6}Ti_{0.4}O_{4.6}$. For $V_2O_{4.5}$ one vanadyl (O_v) atom has been removed to generate controlled defects, since previously there was shown in the computational study[407]

that vanadyl vacancy at the O_v site is the most favored among all other possible sites in the vanadium pentoxide. Also, for Ti-doped $V_2O_{4.5}$ a vanadium atom next to the vanadyl vacancy has been replaced to create the Ti substitution. All the considered structures were fully relaxed with respect to change in volume, shape, and ion positions within a certain unit cell during the self-consistent energy minimization.

The total density of electronic states calculated for pure V_2O_5, $V_2O_{4.5}$ and $V_{1.5}Ti_{0.5}O_{4.5}$ are shown in **Figure 68** with the Fermi level E_F set for zero. One can see that V_2O_5 (**Figure 68a**) is a semiconductor with a forbidden energy gap between the valence and conduction zones. The valence band consists primarily of strongly hybridized oxygen 2p- and vanadium 3d- electronic states with chiefly oxygen 2p-states, while the conduction band mainly consists of the vanadium 3d-states. This electronic structure correlates very well with results obtained in other theoretical studies on pure V_2O_5 previously published[407-409]. Our studies involving $V_2O_{4.5}$ and $V_{1.5}Ti_{0.5}O_{4.5}$ are unique however and provide new insight into the behavior of such doped structures. An internal analysis of the electronic structure showed that the valence band consisting primarily of O 2p states demonstrates a pronounced bonding character, while the conduction band comprises the anti-bonding states which was also noted in the work by Eyert et al.[408]. **Figure 68b** shows the total density of electronic states of $V_2O_{4.5}$. Since, one oxygen atom is missing, formally two vanadium 3d-electrons become free (unbounded) and thus fill the bottom of the previously empty conduction zone with these corresponding two electrons indeed rendering the material metallic. This phenomenon correlates well with results on the conductivity obtained in present study for $V_2O_{4.6}$ and discussed earlier.

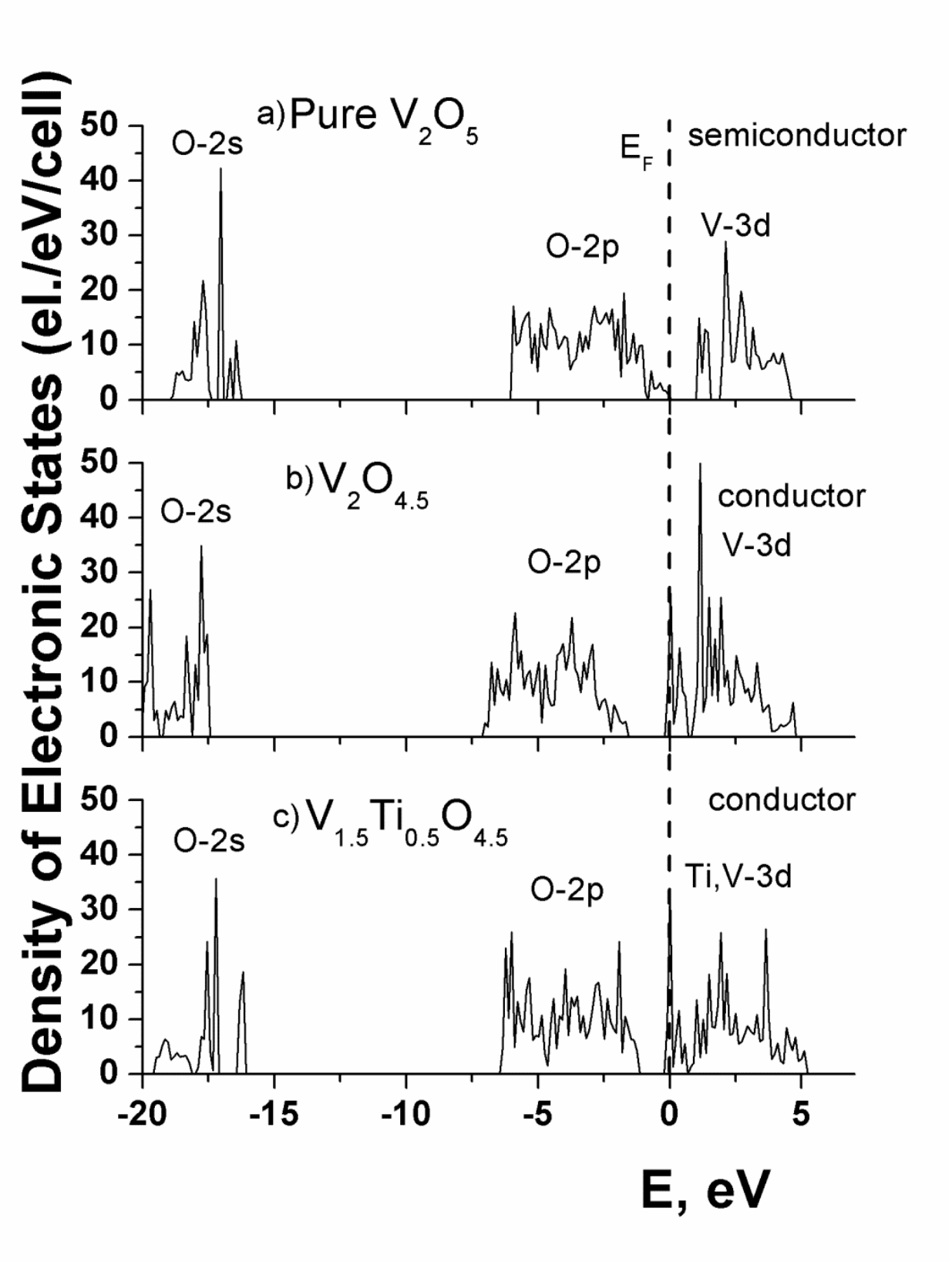

Figure 68. Total density of electronic states calculated for pure V_2O_5, $V_2O_{4.5}$ and $V_{1.5}Ti_{0.5}O_{4.5}$.

Figure 68c demonstrates the total density of states for $V_{1.5}Ti_{0.5}O_{4.5}$. One can see that in general, the electronic structure is very similar to the previous case of $V_2O_{4.5}$ containing the oxygen vacancy with the only difference that now there is one Ti atom substituting in place of a V. Comparing these two cases it can be noted that although one oxygen vacancy releases two vanadium electrons in the unit cell, the introduction of a Ti atom bears one electron less than that of V, therefore contributing to only one electron per unit cell capable of conducting the electric charge through the material. Thus, $V_{1.5}Ti_{0.5}O_{4.5}$ still remains electronically conductive.

The metallic conductivity is usually proportional to the density of states at the Fermi level $n(E_F)$ and hence it provides an opportunity to qualitatively evaluate the electronic conductivity of $V_2O_{4.5}$ and $V_{1.5}Ti_{0.5}O_{4.5}$ oxides. For these purposes **Table 27** collects $n(E_F)$ for these materials showing that $n(E_F)$ calculated for $V_2O_{4.5}$ is lower than that corresponding to $V_{1.5}Ti_{0.5}O_{4.5}$. The presence of Ti 3d-states increased to some extent the total density of states in the vicinity of the Fermi level thus rendering the material more electronically conductive than just the defective $V_2O_{4.5}$ oxide. This result is well confirmed by previously discussed experimental data summarized in **Table 19**.

Table 27. Comparison of density of states at Fermi energy level and cohesive energy between pure V_2O_5, vacancy-rich V_2O_5 and titanium doped vanadium oxide.

Materials	**$n(E_F)$, (el./(eV f.un.)**	**E_{coh} (eV/f.un.)**
V_2O_5	0 (band gap)	-42.17
$V_2O_{4.5}$	11.5	-39.05
$V_{1.5}Ti_{0.5}O_{4.5}$	15.5	-39.54

Further, as mentioned above, the material should demonstrate high stability in the voltage of interest. For these purposes the cohesive energy E_{coh} can be considered a measure of an overall structural and chemical stability of the material. A higher E_{coh} would therefore imply that more energy is required to break the primary chemical bonds of the compound during chemical reaction. Thus, the cohesive energies of all three compounds considered in the present theoretical study have been calculated and summarized in **Table 27**.

From **Table 27** it can be construed that pure V_2O_5 is the most stable material in comparison with both the doped and defective oxides. It is therefore expected that the defective oxide with oxygen vacancies $V_2O_{4.5}$ would be less stable due to filling up of the anti-bonding electronic states in the conduction band above the band gap and also because of lowering the total number of V-O bonds in comparison with non-defective V_2O_5. Thus, presence of O-vacancies decreases the overall stability of the material to some extent. The situation albeit improves with the introduction of the Ti-doping. Because Ti-O bonds are stronger than V-O (668 kJ/mol vs. 637 kJ/mol bond strength in Ti-O and V-O diatomic molecules, respectively[410]) the overall stability of the Ti-doped vanadium oxide is higher than the undoped oxide. Thus, in terms of the electronic conductivity and the overall stability the present theoretical study showcases $V_{1.5}Ti_{0.5}O_{4.5}$ as a promising super-capacitor material with excellent electrochemical properties.

A.1.2 Doped vanadium nitride capacitors

The effect of niobium and tungsten doping on the electronic structure of vanadium nitride and its surface oxide have been studied in tandem with the experimental evaluation performed above (**Section 4.4**) using first-principles computational approaches.

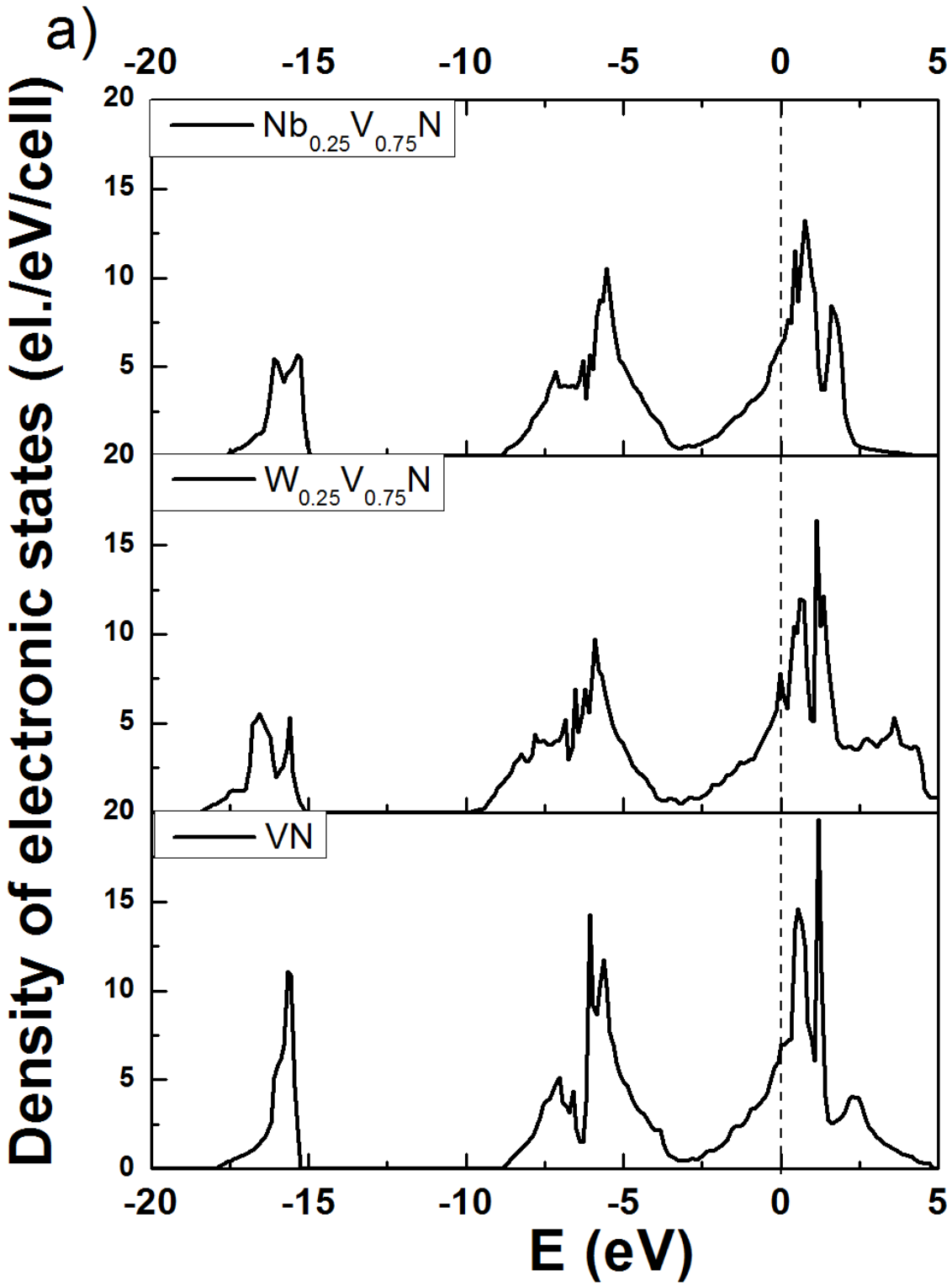
a)
Density of electronic states (el./eV/cell)
E (eV)
Nb0.25V0.75N
W0.25V0.75N
VN
-20
-15
-10
-5
0
5
0
5
10
15
20

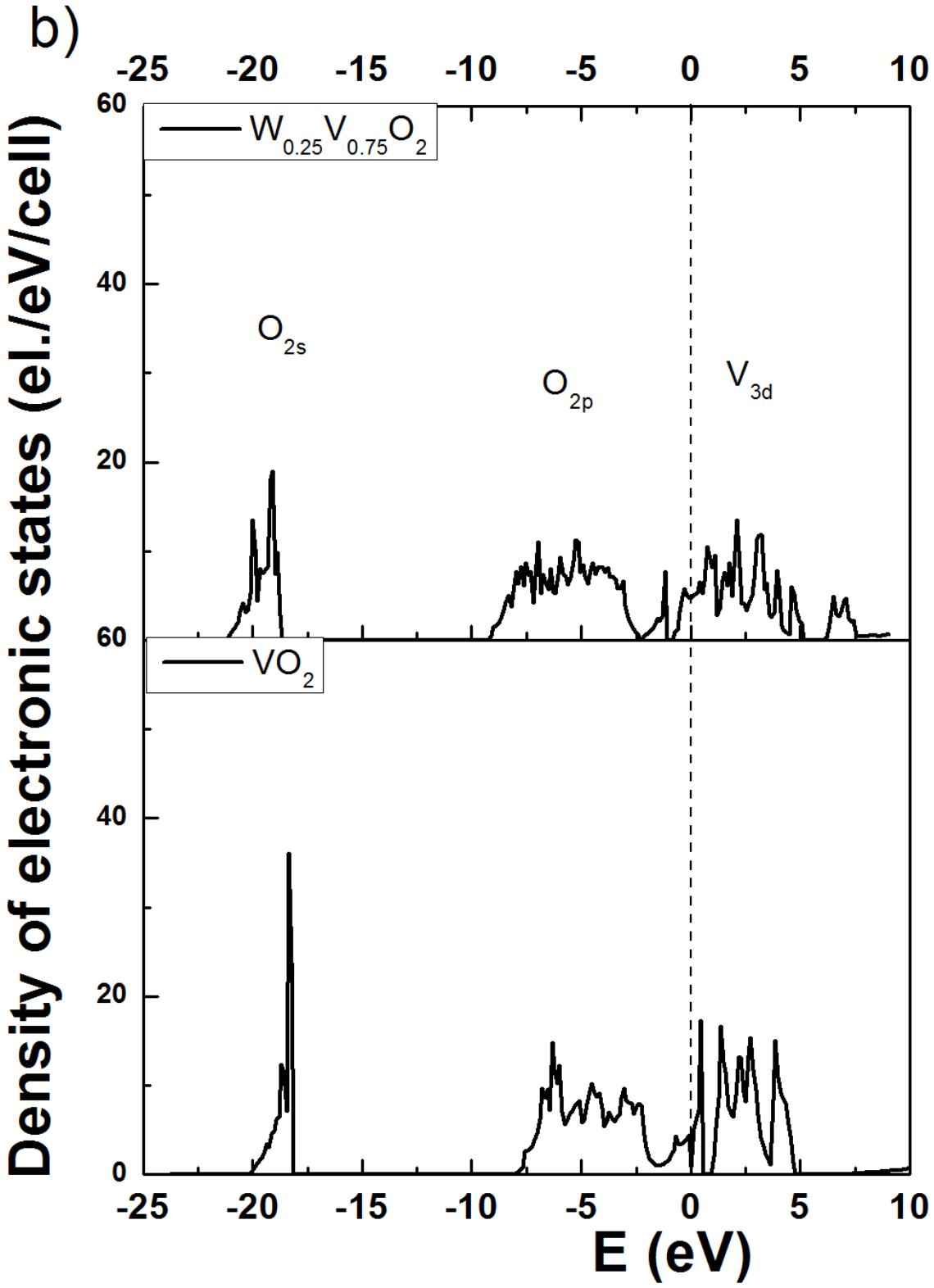
b)
-25
-20
-15
-10
-5
0
5
10
60
40
20
60
40
20
0
W0.25V0.75O2
VO2
O2s
O2p
V3d
Density of electronic states (el./eV/cell)
E (eV)

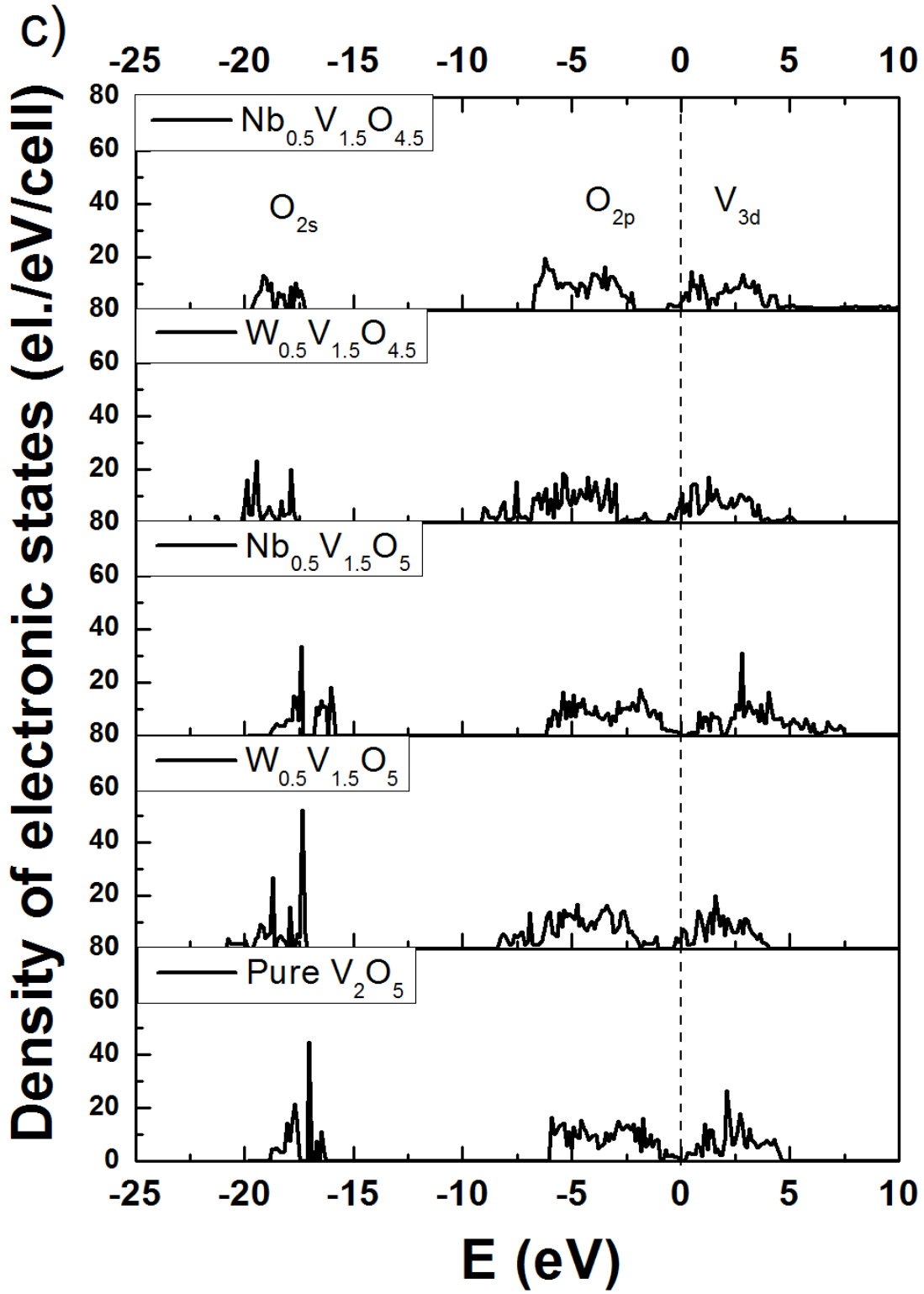

Figure 69. Total density of electronic states calculated for pure and doped compositions of (a) VN (b) VO_2 (c) V_2O_5.

Table 28. Comparison of density of states at Fermi energy level and cohesive energy between pure VN, V_2O_5, VO_2 and tungsten and niobium doped compositions of the same.

	$-E_{coh}$, (eV/f.unit)	**$N(E_F)$, el/eV/f.unit**
VN based compositions		
VN	12.51	1.8
$W_{0.25}V_{0.75}N$	12.71	2.05
$Nb_{0.25}V_{0.75}N$	12.77	1.60
VO_2 based compositions		
Pure VO_2	19.20	0 (insulator)
$W_{0.25}V_{0.75}O_2$	19.63	1.24
V_2O_5 based compositions		
Pure V_2O_5	42.17	0 (insulator)
$Nb_{0.5}V_{1.5}O_5$	43.94	0 (insulator)
$Nb_{0.5}V_{1.5}O_{4.5}$	40.49	1.52
$W_{0.5}V_{1.5}O_5$	43.57	2.23
$W_{0.5}V_{1.5}O_{4.5}$	39.80	4.81

Changes in the electronic structure of vanadium nitride with the introduction of tungsten and niobium into the lattice result in substantial alteration in the electronic properties of the material. For calculations of the total energy, density of electronic states and the cohesive energy (E_{coh} reflecting overall mechanical and chemical stability), the Vienna Ab-initio Simulation Package (VASP) based on the projector-augmented wave (PAW) formalism[402-404] within the generalized gradient approximation (GGA), for conducting the exchange-correlation corrections proposed by Perdew *et al.*[405], has been used in the present study. A plane-wave basis set with a cutoff energy of 520 eV and 184 *k*-points in the irreducible part of the Brillouin zone have been used to achieve an accuracy in the total energy of ~10^{-2} eV per formula unit, which is sufficient for a confident evaluation of the electronic structure, the cohesive energy and comparison of the results with corresponding experimental data.

The total density of electronic states calculated for pure VN, $Nb_{0.25}V_{0.75}N$ and $W_{0.25}V_{0.75}N$ are shown in **Figure 69a** with the Fermi level E_F set for zero. These compositions have been chosen as guides to obtain a fundamental understanding into how the dopant element alters the properties of the parent nitride. Though the compositions do not exactly match those of the experimentally utilized compositions, they were chosen for the simplicity to expediently gain an insight into the effect of doping. One can see that VN (**Figure 69a**) is a conductor and that the introduction of both tungsten and niobium into the lattice allows it to remain a metallic conductor. The metallic conductivity is usually proportional to the density of states at the Fermi level $N(E_F)$ and hence it provides an opportunity to qualitatively evaluate the electronic conductivity of VN, $Nb_{0.25}V_{0.75}N$ and $W_{0.25}V_{0.75}N$. **Table 28** shows the variation in $N(E_F)$ of the doped and undoped VN. It can be seen that introduction of niobium decreases conductivity slightly while tungsten increases the electronic conductivity of VN. **Figure 69b** and **Figure 69c**

depict the effect of W doping on the density of states of VO_2 and the effect of W doping and Nb doping on the electronic properties of V_2O_5 respectively. In addition to an understanding about the alteration of electronic structure of core nitride, an understanding into the effect of doping into the chemical stability and electronic conductivity of the surface oxide is important to obtain a composite picture. Both V_2O5 and VO_2 based compositions have been selected based on previous XPS studies which have shown that the oxide shell consists of a predominantly +4/+5 oxide in the case of nanoparticulate VN derived by the identical synthesis method[182, 235, 246]. In addition, **Figure 69c** depicts the effect of having a non-stoichiometric oxide on the surface with an oxidation state of 4.5. **Figure 69b** shows that pure VO_2 is almost an insulator which becomes a good conductor on the introduction of tungsten as a dopant. One can see that V_2O_5 (**Figure 69c**) is a semiconductor with a forbidden energy gap between the valence and conduction zones. The valence band consists primarily of strongly hybridized oxygen 2p- and vanadium 3d-electronic states with chiefly oxygen 2p-states, while the conduction band mainly consists of the vanadium 3d-states. This electronic structure correlates very well with results obtained in other theoretical studies previously published [407-409]. An internal analysis of the electronic structure showed that the valence band consisting primarily of O_{2p} states demonstrates a pronounced bonding character, while the conduction band comprises the anti-bonding states which was also noted in the work by Eyert et al.[408]. The introduction of niobium does not significantly alter the electronic conductivity of V_2O_5 since it is an isoelectronic element similar to the case of Nb doped VN seen in **Figure 69a**. Thus the $Nb_{0.5}V_{1.5}O_5$ ends up remaining an insulator similar to V_2O_5. Tungsten doping however shifts the Fermi-energy level rendering $W_{0.5}V_{1.5}O_5$ highly conductive. A non-stoichiometric vanadium oxide $V_2O_{4.5}$ is also highly conductive since one oxygen atom is missing, formally two vanadium 3d-electrons become free (unbounded) and thus

fill the bottom of the previously empty conduction zone with these corresponding two electrons indeed rendering the material metallic as shown and discussed in **Section 4.3**. This phenomenon correlates well with results on the conductivity obtained in the present study for $V_2O_{4.6}$ discussed in the previous reports of Jampani et al.[175]. Tungsten doping and niobium doping resulting in the formation of a non-stoichiometric surface oxide would thus significantly improve the electronic conductivity due to an increase of the charge carriers.

In addition to electronic conductivity, the material should demonstrate high stability in the voltage of interest. For these purposes the cohesive energy E_{coh} can be considered a measure of an overall structural and chemical stability of the material. A higher E_{coh} would therefore imply that more energy is required to break the primary chemical bonds of the compound during chemical reaction. Thus, the cohesive energies of all the compounds considered in the present theoretical study have been calculated and summarized in **Table 28**. From **Table 28** it can be construed that W and Nb both improve the overall stability of VN and VO_x due to the stronger interatomic bonds between W-N, Nb-N, W-O and Nb-O in comparison to corresponding bonds V-N and V-O[411]. Presence of oxygen vacancies in Nb and W doped vanadium oxides however decreases stability because of formation of dangling bonds in the $M\text{-}O_6$ crystal octahedrons. Upon comparing effects of W and Nb on the stability and conductivity of the oxides one can say that in all cases Nb improves the stability slightly better than W, while W improves the conductivity much better than Nb. This is due to the 6 valence electrons in W vs. 5 in Nb and V bringing more free charge carriers into the whole system. In fact, Nb and V are isoelectronic analogs and a simple substitution of V for Nb in the system does not make any substantial changes in the electronic structure of the material, thus keeping the conductivity virtually at the same level.

The trends in electronic conductivity seen in **Table 28** correlate very well with the experimentally measured electronic conductivity in the case of $W_xV_{1-x}N$ (x=0.05, 0.1, 0.2) shown in **Table 22**. In all the cases of tungsten doping the doped nitride material has higher electronic conductivity than the parent nitride material. The variation in conductivity with dopant concentration results possibly as a result of an interplay of a number of factors including thickness of surface oxide, presence of vacancies in the surface oxide and its overall oxidation state. The interphase between the oxide and the nitride may consist of an oxy-nitride material and its composition possibly plays a role in overall conductivity. The experimentally observed trends in capacitance seen in **Figure 59a** and **Figure 59b** can be correlated with the theoretically derived cohesive energy and $N(E_F)$. $W_{0.05}V_{0.95}N$ has superior supercapacitance behavior at various scan rates possibly as a result of the high electronic conductivity measured and shown in **Table 22**. Though the theoretical study does not match the exact composition, it has been shown that W doping leads to a shift in d-band resulting in improvement in the number of carriers in both the core nitride as well as the oxide shell. The very high capacitance observed reflects a surface oxide with a very high pseudocapacitance as discussed in a later section. At the same time, the material exhibits far superior cycling stability. This is a result of stabilization of surface oxide by doping as reflected by the increase in cohesive energy of both VN and VO_x by W doping (seen in **Table 28**). The improvement in stability is reflected in all the W doped VN compositions. However, $W_{0.10}V_{0.90}N$ and $W_{0.20}V_{0.80}N$ do not exhibit the very high supercapacitance seen in $W_{0.05}V_{0.95}N$ possibly as a result of lower electronic conductivity (**Table 22**) resulting in limited pseudocapacitance behavior. As stated earlier, this is an aspect that merits further studies and will be addressed in subsequent future studies planned. Niobium doping on the other hand has been shown to cause no significant change in electronic conductivity of core

nitride or oxide shell. This results in the experimentally observed conductivity values for $Nb_xV_{1-x}N$ (x=0.01, 0.05, 0.10) seen in **Table 22**. There is a gradual increase in electronic conductivity with increasing Nb doping possibly as an effect of formation of some amounts of non-stoichiometric surface oxide which is shown to increase $N(E_F)$. This does not however result in any significant improvement in charge storage capacity as seen in **Figure 58a**. Niobium doping is theoretically determined to help improve stability of VN. The effect is minimal as seen in **Figure 58b**. Capacity is retained better in $Nb_{0.05}V_{0.95}N$ possibly as the result of a more stable surface oxide formed in this composition.

A.2 VN-VACNT SUPERCAPACITORS

A.2.1 Abstract

One of the primary problems plaguing nanoparticulate pseudocapacitor materials is the low electronic conductivity associated with them. This is especially the case with ceramic oxide and nitride nanoparticles on account of their semiconducting nature. In this work, we demonstrate a facile chemical vapor deposition technique to synthesize Carbon nanotube supported Vanadium nitride heterostructures for use as electrodes in electrochemical supercapacitors. High electronic conductivity associated with vertically aligned CNTs has been exploited to create one-directional rapid electron transport into the coated Vanadium nitride layer. Rate capability issues encountered in nanomaterial nitride materials are thus overcome on account of high conductivity and 3-D architecture associated with the carbon nanotubes. We report capacitances as high as

650 F/g with good rate capability and excellent charge retention of the Carbon nanotube supported nitride heterostructures in KOH media. The electrochemical mechanisms and material properties influencing supercapacitor properties of CNT supported VN have also been reported.

A.2.2 Introduction

The need for high power energy storage devices for both stationary and mobile applications is being realized more and more of late[3-5]. One of the outstanding challenges in this regard is to have devices with sufficiently large amount of charge stored while at the same time being able to deliver the same at rapid rates. There is therefore an urgent need for supercapacitor materials with large energy storage capacities. Conventional dielectric and double layer electrochemical capacitors are generally incapable of storing such large amounts of charge. Pseudocapacitors involving a chain of successive reversible Faradaic reactions at the surface thus ensure short charging times and seemingly infinite cyclability with sufficiently large capacitances[44, 58, 65]. Transition metal oxides are very attractive for this kind of application on account of their ability to accept variable oxidation states. In addition, they have good bulk conductivity and atmospheric stability. Of particular interest to pseudocapacitor applications is the ability of the surface oxide to undergo reversible hydration as in Ruthenium oxide [44, 58]. The current-voltage characteristics of the successive oxidation/reduction reactions at the surface of the electrode resemble that of a capacitor, hence the term pseudocapacitor. Hydrous Ruthenium oxide is an excellent pseudocapacitor material with the ability to maintain stable capacitances of upto 900 F/g over a large number of cycles[69]. However, the prohibitive price of noble metal based capacitors impels the search for alternative materials with similar charge storage characteristics. Other non-noble metal oxides and hydroxyl-oxides have been widely explored in

this light including those of Mn, Ni and V[70-75]. However, most oxide materials have very limited energy densities. There is therefore an urgent need to explore novel chemistries to identify cheap pseudocapacitor materials with high energy densities and good rate capability.

Recent work by various groups has shown viability of nitrides, carbides and sulfides for catalysis and energy storage applications[243, 253, 254]. Transition metal nitrides were first shown to have promise as energy storage materials by various groups identifying Molybdenum nitride as a suitable pseudocapacitor material[240-244]. A thorough investigation into transition metal nitride supercapacitors was then undertaken by Choi et. al. and they found to be excellent supercapacitor materials in aqueous electrolytes [182, 235-238]. Among the various nitrides evaluated, VN was found to exhibit capacitances as high as 1350 F/g[182, 235, 238]. This exceptional performance has been attributed to a combination of both double layer type capacitance and pseudo-capacitance occurring at the nitride surface. Vanadium is an element in Group 5 of the periodic table with a half empty d-shell allowing it to accept valences of +2 to +5, thus allowing it to exhibit reversible Faradaic reactions yielding pseudocapacitance. Following this groundbreaking discovery, other groups have evaluated capacitor properties of VN and reported capacitances ranging between 150 and 250 F/g [249-251, 260, 261]. One of the primary reasons for the large disparity in capacitance is believed to be the nanoparticulate nature of the VN reported by Choi et. al. consisting of ~6nm VN crystallites[182, 235]. The nanoparticulate nature of the nitride yields large number of surface sites for the reversible faradaic reactions occurring at the nitride surface yielding very high pseudocapacitance. All the same, the very same nanoparticulate nature leads to an increased number of particle grain boundaries which act as electron conduction barriers causing a drop in overall conductivity of the nitride. This in-turn implies that the very high capacitance associated with the nanoparticulate VN can only be observed at low material

loadings and at low scan rates. In order to address this issue of rate-capability we have developed a novel architecture consisting of Vertically Aligned Carbon nanotube supported Vanadium Nitride. The high electronic conductivity of Carbon nanotubes could be exploited to create composite 3-D architectures to minimize nitride–nitride particle contact leading to efficient electron transport from current collector to the surface of the Vanadium nitride where pseudocapacitance behavior is exhibited.

Use of conducting architectures to increase capacity is a concept that has previously been explored in various oxide and conducting polymer based capacitors[158, 197, 412, 413]. Carbon based heterostructures have previously been shown to improve rate capabilities of various Lithium-ion and supercapacitor electrode materials including Silicon, Ruthenium oxide, Manganese dioxide and Nickel oxide[164, 186-193]. Electrodeposited amorphous hydrated Vanadium oxide coatings on CNTs were shown to have capacitances as high as 910 F/g by Kim et. al[170] and Balkus et.al.[194] in Lithium electrolyte cells. Recently, Sathiya et.al. have reported energy storage behavior of oxide coated carbon nanotubes in a Swagelok type cell with a Lithium electrolyte and a Lithium counter electrode and have reported capacities as high as 850 mAh/g with upto 60% of the energy storage being capacitive[195]. Vanadium oxide/CNT composites have also been tested for capacitance behavior in aqueous electrolytes and capacitances as high as 400 F/g have been reported [196]. A similar approach of using a 3-D conducting support to create conductive heterostructures was exploited by Yushin et. al. in their work Vanadium nitride thin films on Aluminum nanowires were also used as electrode materials in a Lithium ion based supercapacitor[197, 198]. Similar improvements in energy storage capacity were observed in single wall CNT, multi-wall CNT and polyaniline supoorted co-axial MnO_2 [158, 378, 413-415]. Recent work by Zhang et. al. has shown this concept to be lead to obtain improved capacitor performance in

uniform films of Vanadium nitride on functionalized Carbon nanotubes[248]. Vanadium Nitride was coated by vacuum sputtering on functionalized Carbon nanotubes and capacitances upto 289 F/g have been reported. Sputtering however a very low vacuum, high temperature technique is used to grow thin films and is not amenable for scale-up. CNT-supported VN prepared by solution based methods were also explored as supercapacitor electrode materials by Ghimbeu et. al. with capacitances of around 150 F/g reported in 6 M KOH[245]. In this work, we present a facile vapor deposition technique to synthesize unique Vanadium Nitride-Carbon nanotube morphologies. Chemical vapor deposition was chosen as the ideal method to grow CNT-nitride composites as other commonly used synthesis techniques for nitride synthesis usually involve very high temperature nitridation of the metal or oxide which is both energy inefficient and produces crystalline VN with very low surface areas, properties that are very undesirable for the above-stated applications[255, 260, 301, 302, 416]. These synthesis techniques are also not amenable for making composites with CNTs.

Chemical vapor deposition is an ideal method to obtain uniform architectures on Carbon structures[316, 317]. Chemical vapor deposition is a versatile synthesis method which could be used to tailor the nature of film deposition depending on deposition conditions. Various groups have previously reported chemical vapor deposition as a technique for growth of Vanadium nitride thin films[356, 417-421] using both chloride and metal organic precursors. Nitride thin films with differing conductivities have been reported depending on various deposition conditions including temperature[418]. Herein, a facile Atmospheric Pressure Chemical Vapor Deposition (APCVD) method was demonstrated to deposit Vanadium nitride on CNTs to obtain a novel morphology for use as a supercapacitor electrode in aqueous media. The use of CVD as a synthesis method

also yields us the advantage of avoiding binders which can consume upto 50% of the total weight of the electrode in high surface area systems[187, 317].

A.2.3 Experimental Methods

Materials Synthesis

A two-step CVD process was used to obtain Vanadium nitride-CNT heterostructures on Nickel substrate disks. 1" diameter Nickel disks were thoroughly cleaned using dilute acids, acetone and weighed for use as current collectors. Vertically Aligned Carbon nanotubes (VACNTs) were then deposited on the Nickel disks at 770 using an Ar/H_2 mixture with the ratio 85:15[330, 331]. A mixture of Ferrocene in m-Xylene was used as the Carbon source with Ferrocene acting as the catalyst for CNT nucleation and growth. The mixture was vaporized and bled into a pre-heated mixing zone at 200 C and then carried by the Ar/H_2 mixture into a hot-wall CVD tube maintained at 770 C. CNT coated disks were weighed to calculate CNT loading and Nitride/CNT ratio. Vanadium nitride films were then deposited onto the VACNTs using an atmospheric pressure hot-wall CVD process with Vanadium chloride (VCl_4, Sigma Aldrich) as the metal source and Hexamethyl disilazane ($C_6H_{19}NSi_2$, Sigma Aldrich) as the Nitrogen source. Both precursors were evaporated and carried into a hot wall CVD reactor, using two independent nitrogen gas streams, where the CNT coated Nickel disks were placed [418]. 550 C was chosen as the deposition temperature as this was reported to be the temperature where the nitride was most conductive. Deposition was carried for 20 minutes. Passivation was performed at room temperature using 0.1% O_2-Argon gas mixture for upto 2 h. The nitride coated disks were then weighed and characterized.

Materials Characterization

The nature of the deposition including morphology of the nitride on the CNTs needs to be understood for better understanding of the reasons for observed capacitance behavior. To investigate the microstructure of the CVD deposited VN, scanning electron microscopy (SEM) analysis was conducted on a Philips XL30 machine operating at 20 kV. The atomic composition of the film was also verified using EDAX. To identify the crystalline nature of the nitride coated on the CNTs and to identify any amorphous deposits other than the nitride present on the CNTs, micro-Raman spectroscopy was performed on a Reinshaw inVia Raman microscope. Raman spectra were obtained in air at room temperature using a 633 nm laser. Low laser intensities were chosen to avoid heating of the samples and spectra were obtained by averaging multiple scans over a frequency range of 3500-100 cm^{-1}.

To further characterize the nitride-CNT interface, High-resolution transmission electron microscopy was performed on a JEOL JEM-2100F microscope to observe the morphology of the film-CNT interface. HRTEM images could also give us an insight into the mechanism of growth of film on the CNTs. Vanadium nitride deposited CNTs were scraped off from the Nickel substrate and dispersed on 3.05 mm diameter copper grids (JEOL) containing a holey carbon film in methanol by sonication. The grids were then vacuum-dried for 24 h and used for TEM characterization.

Electrochemical Testing

Cyclic voltammetry was performed on the synthesized nitride materials to test their viability as high energy density supercapacitor materials. A three electrode cell configuration

was used to perform cyclic voltammetry and electrochemical impedance spectroscopy on the coated Ni disks to both understand electrochemical mechanisms involved and evaluate specific capacitance of the VN prepared by chemical vapor deposition. The cell was assembled with a Platinum counter electrode and Hg/HgO (in 1M KOH) reference electrode and active material coated Nickel disks described above as the working electrode. An aqueous KOH solution of unit molarity was used as the electrolyte.

Cyclic voltammetry tests were performed on a Princeton Applied Research Versastat-3 potentiostat from -0.9 V to 0 V with respect to reference to evaluate specific capacitance of VN made by CVD. Cycling was performed at different rates and area of the cyclic voltammogram was used to calculate capacitance. Gravimetric capacitance values were evaluated on the basis of both nitride weight as well as total active material weight.

The capacitance was calculated using the formula:

$$\text{Capacitance C (in F/g)} = \frac{\int I\,dV}{s \times 2 \times V \times m}$$

Where

$\int I\,dV$ = Area of the cyclic voltammogram

s= scan rate in V/s

V= voltage window =0.9 V

m= Mass of active material in grams

To further evaluate nature of the CVD-deposited VN as a supercapacitor, Electrochemical Impedance Spectroscopy was performed on the Versastat 3 over a frequency range of 0.01Hz-100 KHz. 5 mV amplitude was used and spectra were obtained between -0.9 and 0 V at voltages of interest. Impedance spectra were obtained on both the nitride and the

CNT-supported nitride hybrid electrodes to observe any noticeable changes in charge storage mechanism induced by the presence of Carbon nanotubes. Z-View (Scribner Associates, Inc.) software was used for circuit modeling of the impedance spectra.

A.2.4 Results and discussion

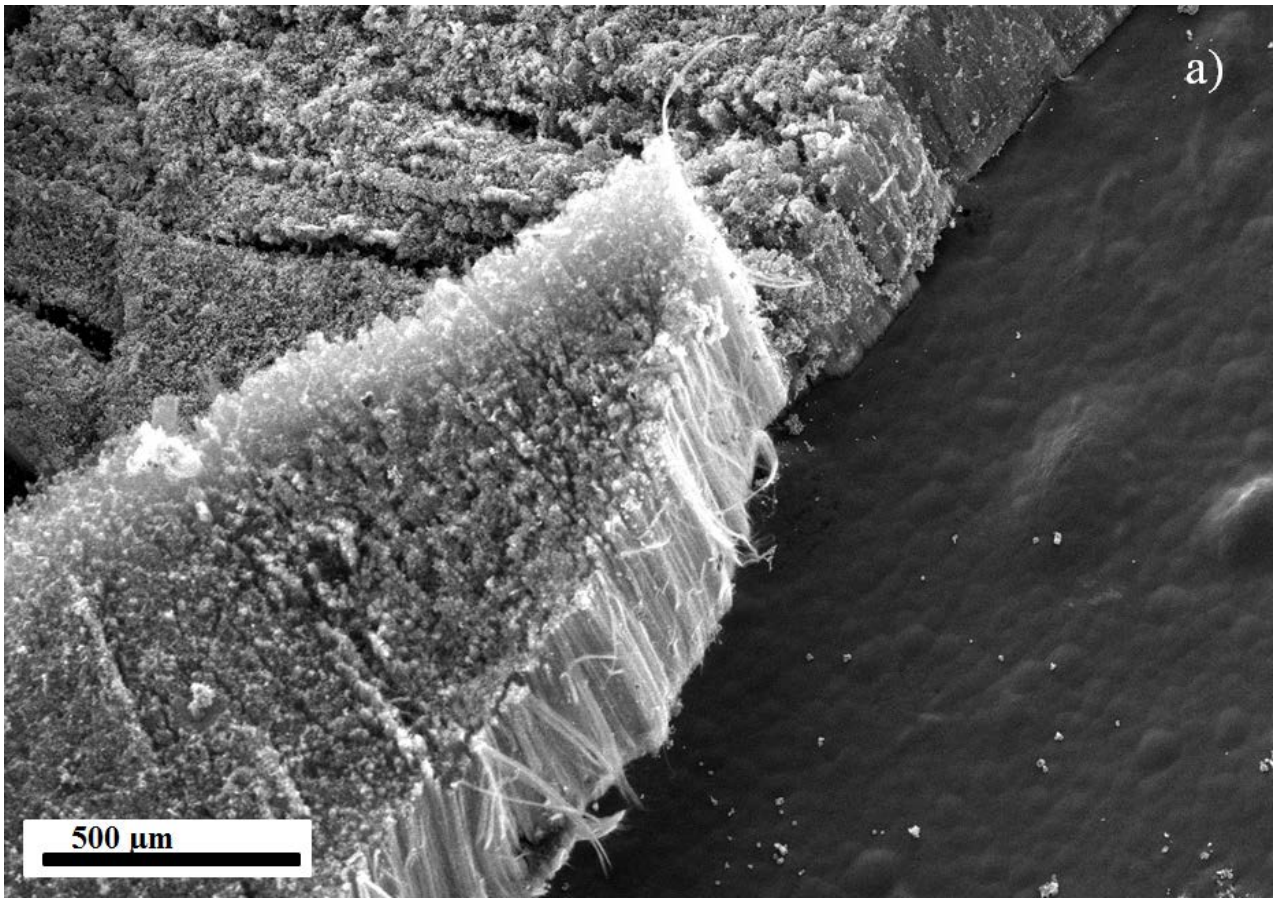

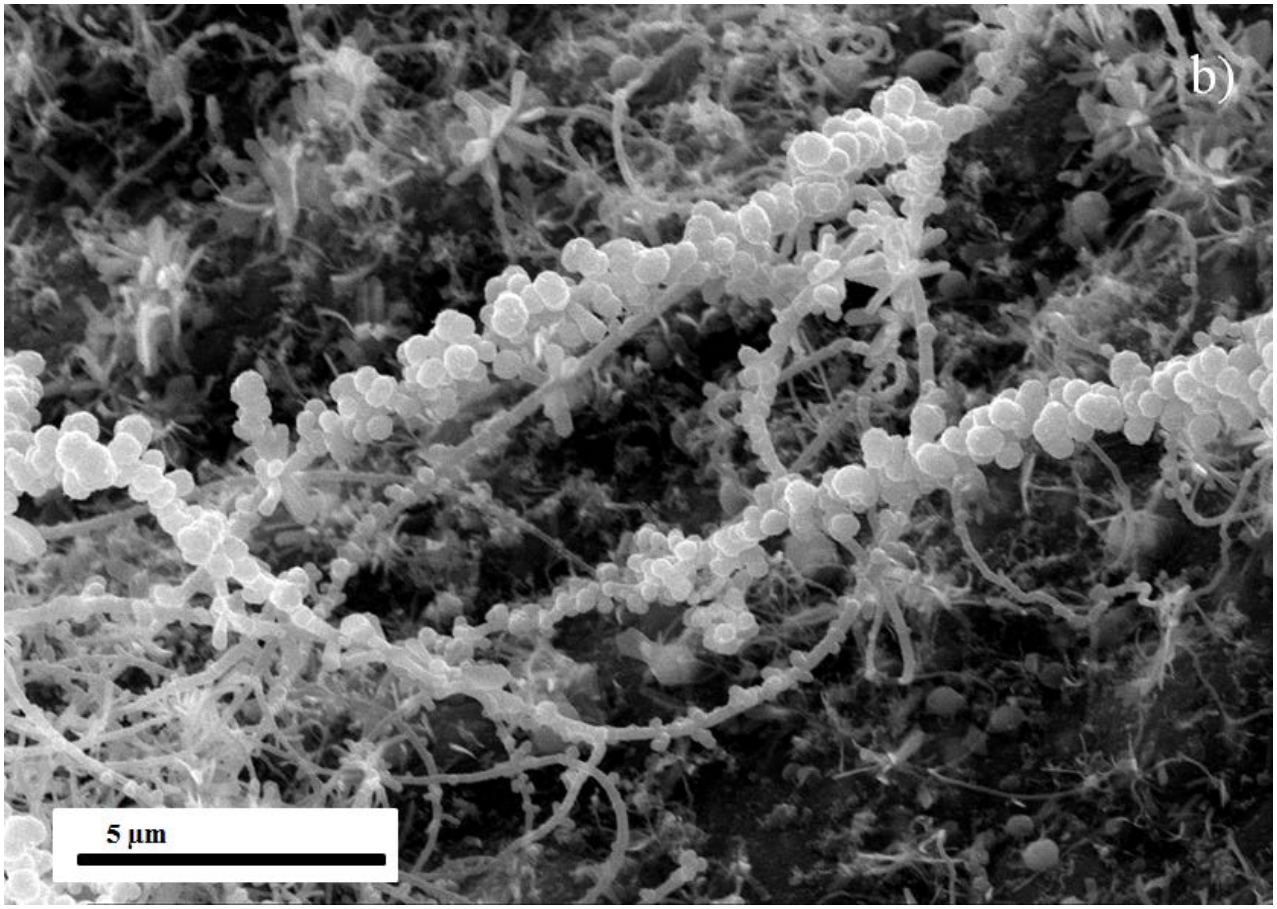

Figure 70. (a) Arrays of vertically aligned Carbon nanotubes coated on Nickel substrate (b) Scanning Electron Microscope Image of VN-coated CNTs with a novel architecture allowing rapid electron transport as well as higher surface contact with electrolyte.

Figure 70a shows the Scanning Electron Microscope image of Vertically Aligned CNTs deposited by Chemical vapor deposition on Nickel substrate. The vertically aligned forest of Carbon nanotubes seen in the figure is expected to provide an ideal template for deposition of a thin layer of nitride thus creating a conductive framework for the nitride, allowing it to overcome low rate capability issues with VN. It is also expected that the prolific length of the CNTs would help create a 3-D architecture which when covered with a thin layer of the nitride could maximize volumetric loading while at the same time making sure that a very thick film does not

cover the carbon nanotubes impeding proper electronic transport. **Figure 70b** shows the nature of the vanadium nitride deposition on the carbon nanotubes. As can be seen the deposition of the nitride is in the form of tiny globules covering the length of the tube with regular spacing between them. This allows for maximum CNT-nitride electron transport minimizing electron transport through nitride grain boundaries, which naturally act as barriers to electron transport. The film morphology also leads to increased surface exposure of nitride to electrolyte i.e. maximizing electrochemical surface area and allowing us to exploit maximum capacitance behavior. In order to confirm the morphology of the film on the surface of the CNTs, High resolution Transmission electron microscopy was performed on samples scraped off and dispersed onto a Cu grid. **Figure 71** shows the image of vanadium nitride nanospheres covering the length of the carbon nanotube. It can be seen that the nitride has a nanoparticle morphology with distinct rings indicating that the nitride is nanocrystalline.

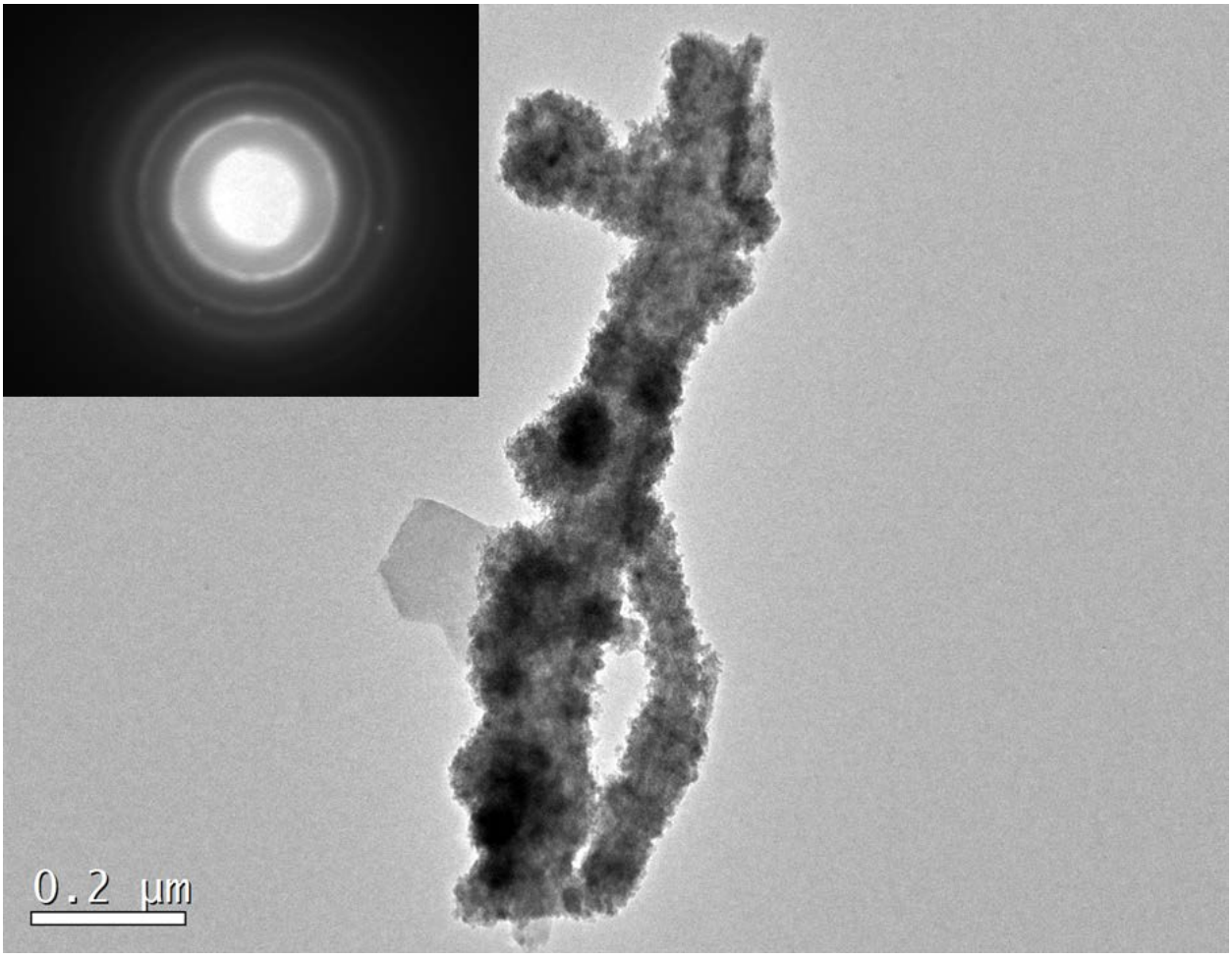

Figure 71. HRTEM images of the nitride film coated on Multiwall Carbon nanotubes.

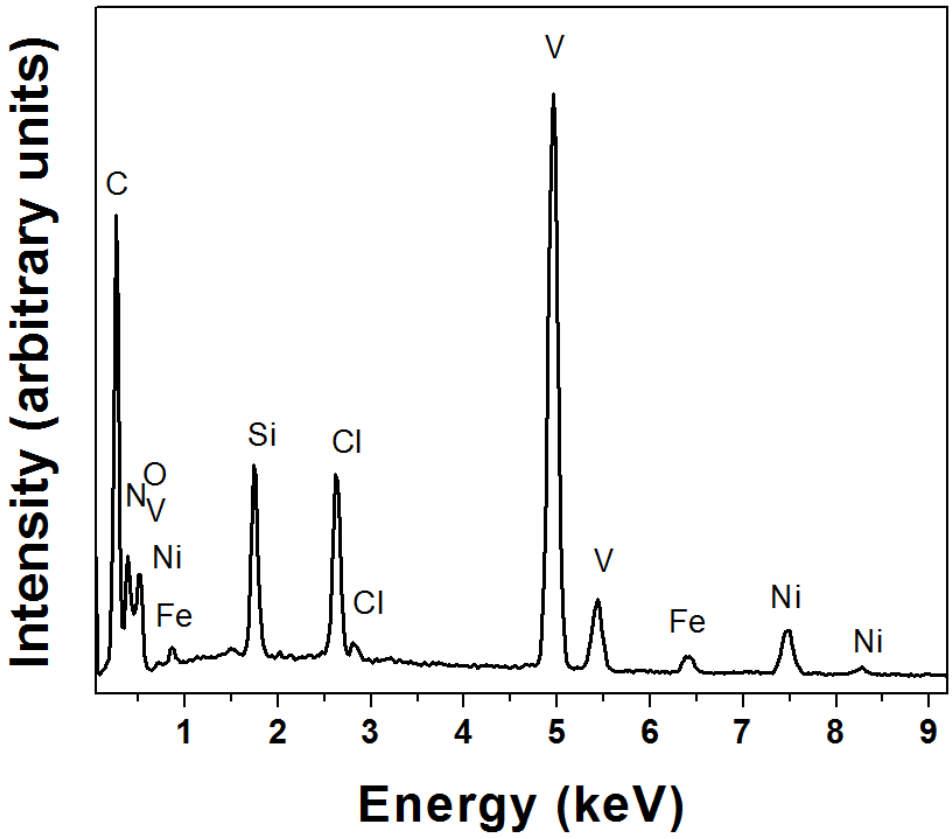

Figure 72. EDAX spectrum of vanadium nitride deposited on Nickel and Carbon nanotubes.

Figure 72 shows the EDAX compositions of the CNT supported nitride film deposited on Nickel disk. It can be seen that peaks corresponding to vanadium, nitrogen and oxygen are distinctly visible. In addition, a small amount of silicon and chlorine occurring as a result of the precursors used in the CVD approach is seen therein. Carbon and iron peaks corresponding to the CNTs are also visible. In order to confirm the composition and nature of the nitride deposit on CNTs, Raman spectroscopic analysis was performed on the material. The Raman spectrum of the Carbon nanotubes is shown in **Figure 73**. The D, G and G' bands corresponding to carbon nanotubes are clearly observed at 1250, 1650 and 2650 cm^{-1} respectively. It is clearly observed

that the G/D ratio is much greater than one indicating few lattice defects in the graphene layers indicating the MWCNTs would have relatively high conductivity[366, 367]. The spectrum from 200 to 1000 cm^{-1} wavelength range has several peaks marked that have been identified to correspond closest to those of Vanadium nitride of thin film VN[422], V-O-N band energies and closely to those of VO_x-Carbon nanofibers reported previously[245, 353, 369, 423, 424]. Surface peaks corresponding to vanadium-oxygen bond stretching and bending have been indicated in **Figure 73.**

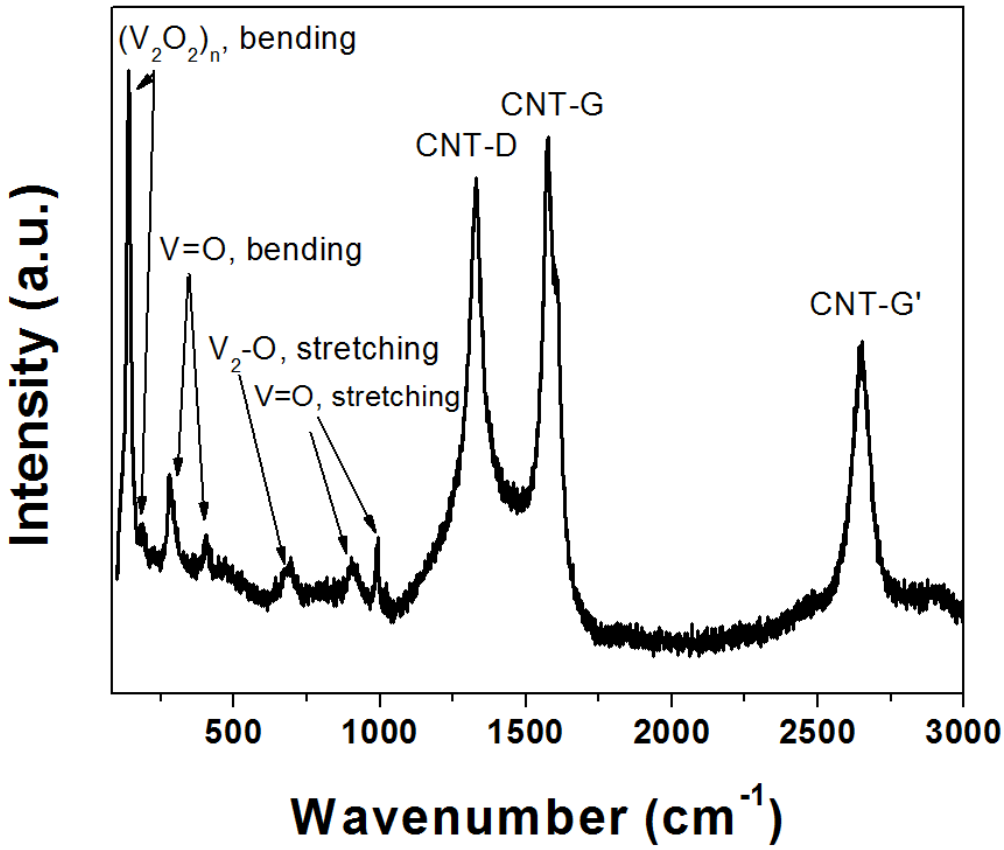

Figure 73. Raman spectrum of vanadium nitride coated on the VACNTs.

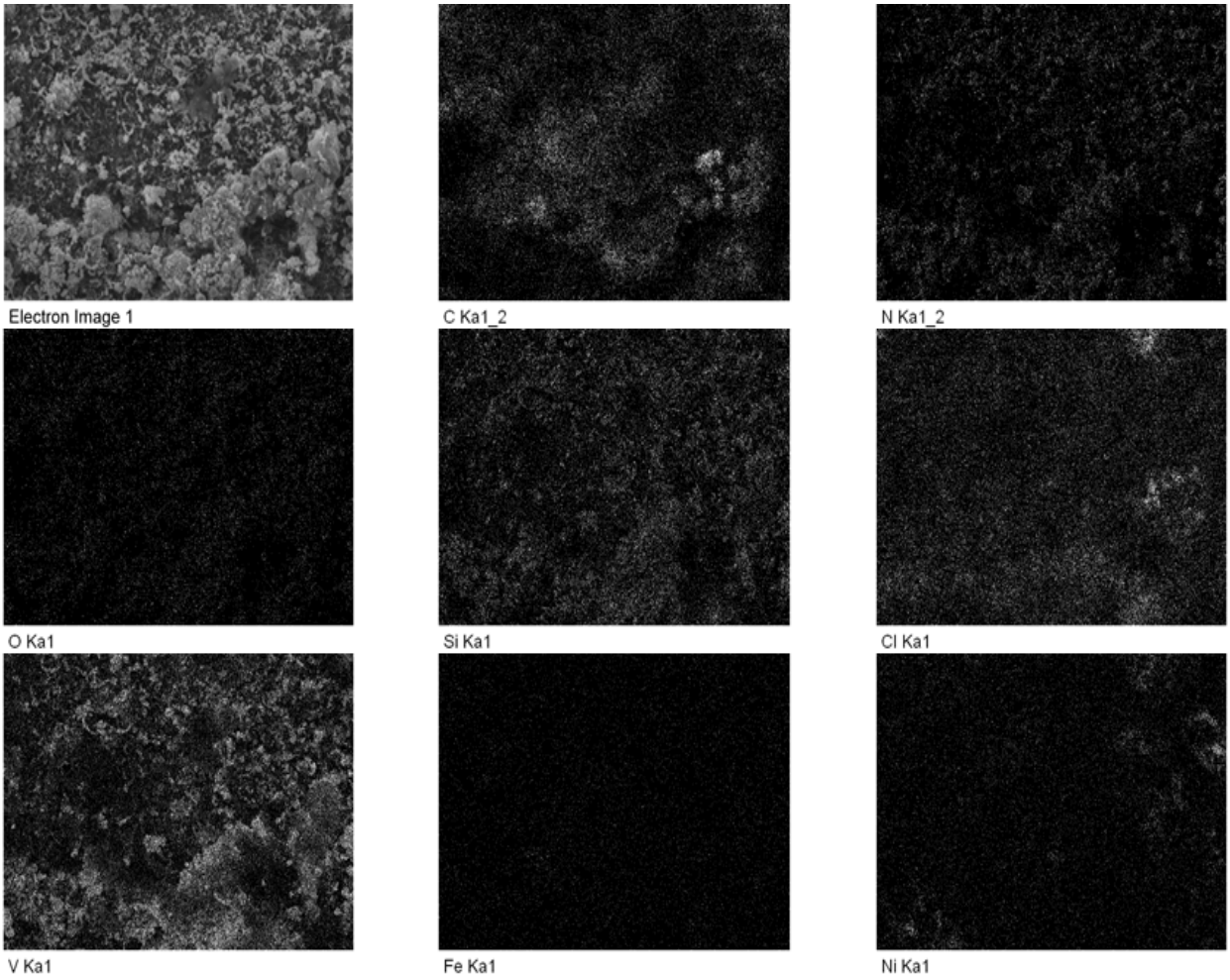

Figure 74.EDAX maps of the nitride coated CNTs.

The interface of the CNT and the nitride is an important factor that would determine the nature of electron transport and stability of the nitride particle. **Figure 74** shows the EDAX maps of nitride coated on the Carbon nanotubes. It can clearly be seen that the maps of both nitrogen and vanadium are similar corresponding to the regions of the film. The chloride though present in much lesser atomic percentages is more ubiquitous and is directly tethered to the CNTs. This indicates that the chloride precursor used in this reaction tethers to specific sites on the CNTs which in turn become growth sites for the nitride. This theory is also supported by the TEM images which indicate that a thin layer of the nitride on the CNTs on which the nitride spheres

tend to develop. In addition, oxygen elemental map corresponds to the same location as the vanadium and nitrogen indicating that the nitride consists possibly of a surface oxide occurring as a result of passivation.

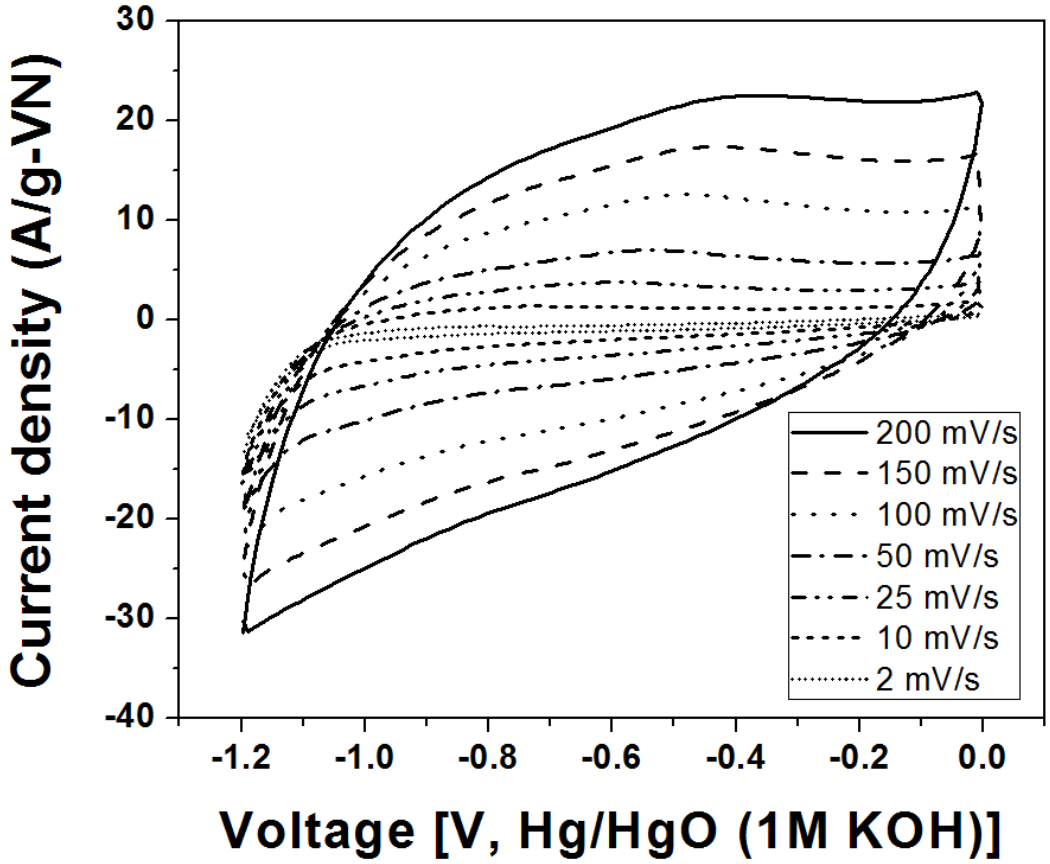

Figure 75. Cyclic voltammograms of the VN-CNT composite electrodes (VN loading=0.14 mg/cm^2. Active material loading=1.07 mg/cm^2).

Figure 75 shows the cyclic voltammograms of the nitride-nanosphere coated CNTs at various scan rates. The effect of scan rate on both samples is evident in the change of slopes of the I-V curves. As the scan rate increases, the current response on scanning potential undergoes a

transition from a flat capacitor type behavior to a resistor-like dependence as is common for most pseudocapacitor materials. Reversible Faradaic peaks are observed though they are not as prominent as seen in previously reported VN nanoparticles[182, 235]. The potential dependent pseudocapacitance behavior present at these potentials is thought to correspond to a transition of oxidation state of Vanadium from +5 to +3 most commonly observed in aqueous systems at the almost neutral pH occurring in a 1M KOH solution. Peaks are not as prominent as in VN nanoparticles previously reported possibly as a result of difference in particle size and surface area.

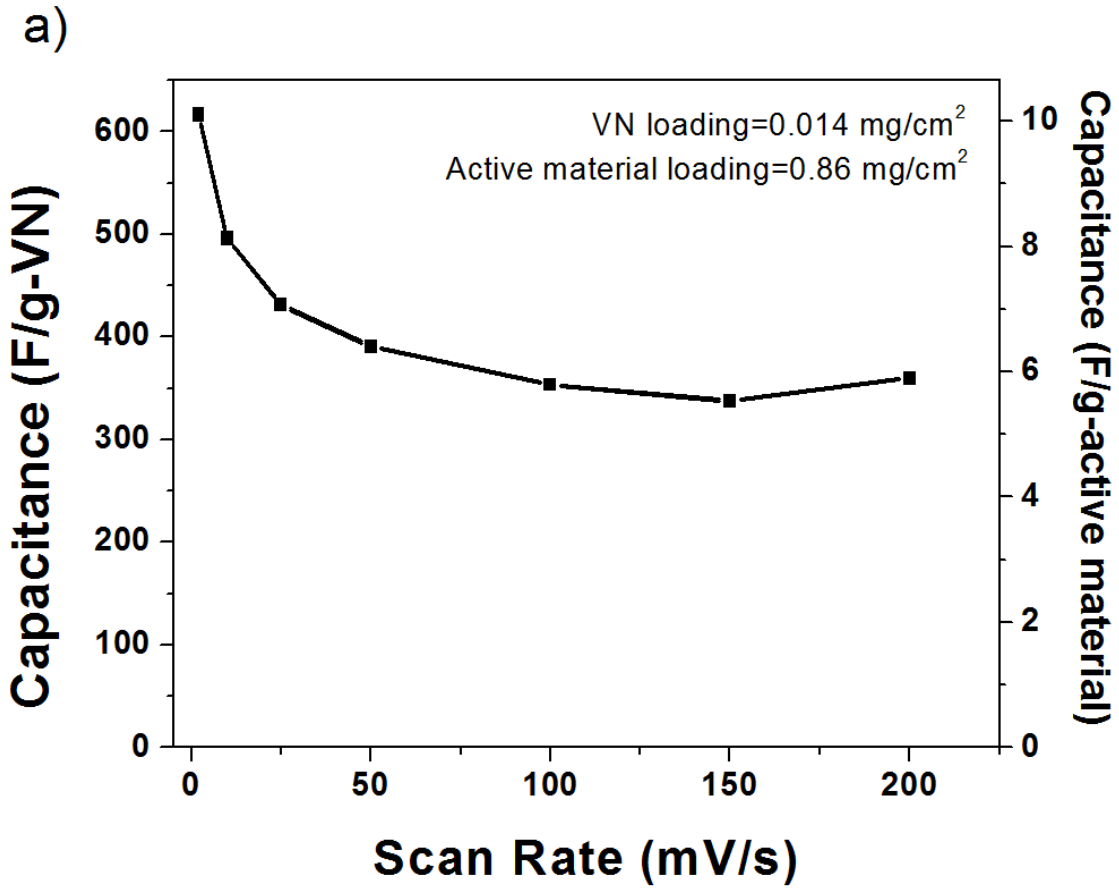

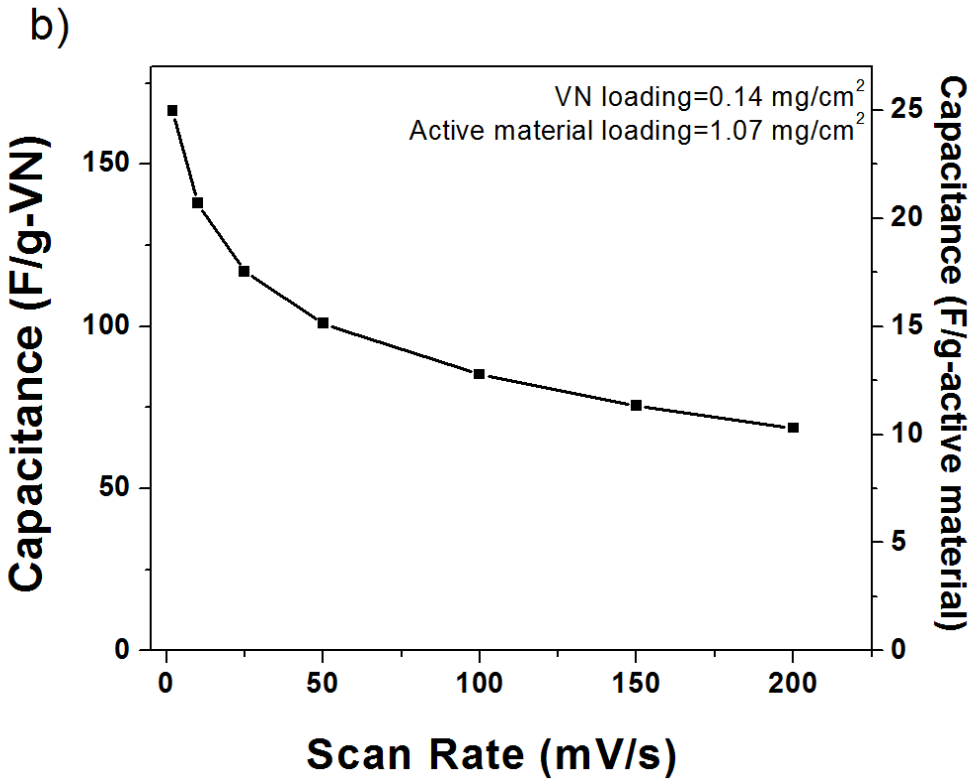

Figure 76. Capacitance behavior of VN-VACNT composite electrodes.

Figure 76 depicts the scan-rate dependent capacitance of the VN-CNT electrodes at different loadings. It can be seen that the VN-CNT electrodes have very high capacitances approaching ~600 F/g-VN at 2mV/s when the film thickness is very small (VN loading=0.014 mg/cm^2). As loading increases however, the capacitance drops to only 165 F/g at 2mV/s. This indicates that thick films of VN are not amenable to obtaining high capacitance. It can be seen that the overall capacitance of both materials is very poor indicating that coating of VN onto CNTs is not useful in improving the overall capacitance. The electrodes with thicker coatings show higher overall capacitances as is to be expected. Though the coating of vanadium oxide onto CNTs has been shown to result in very high capacitances as discussed in earlier chapters, the same effect is not as prominent in the case of VN-CNTs. It is believed that the reason for the

same is that pseudocapacitance arises primarily from the oxide layer present on the surface of nitride materials. In the case of VN-CNTs, the exposed surface area of oxide layer is much smaller than that of the case of ~6 nm particles reported in **Section 4.1**. At the same time, the oxide layer thickness is much smaller than that reported in **Section 4.2**. Therefore, both overall capacitance and nitride capacitance are lesser than that of pure nanocrystalline nitride and VO_x-VACNT respectively. More work is currently ongoing to understand mechanisms resulting in this limited performance.

A.2.5 Conclusions

Hot-wall Chemical Vapor deposition has for the first time been used to create a unique morphology consisting of Vanadium nitride film tethered to Carbon nanotubes. Such a CVD-coated-CNT supported nitride has been shown to have excellent charge storage characteristics with capacitances of upto 650 F/g achieved at a scan rate of 2 mV/s. One of the highlights of this works is the ease of electrode fabrication. Chemical vapor deposition is a method amenable for continuous production of electrodes in an assembly-chain configuration in contrast with chemical methods used to produce nitrides which require batch processes and in-turn also involve a second heat treatment step. The need for slurry preparation is eliminated and binder-free electrodes are thus generated. The CVD method could further be optimized to lead to electrodes with a good nitride/CNT ratio so as to maintain excellent capacitance yielded by the thin nitride layer as well as the rate capability boost provided by Carbon nanotubes. Efforts are on to achieve the same and will be reported in forthcoming publications.

APPENDIX B

LITHIUM, SODIUM & MAGNESIUM BATTERIES

B.1 LITHIUM-SULFUR BATTERIES

B.1.1 Introduction

Lithium-ion batteries with their unique high voltage, high energy density chemistries have come to fruition due to the decades of fundamental research conducted in electrochemical systems and more importantly, materials discovery. The development of a number of plug-in hybrid and fully electric vehicles (EV) using lithium-ion technology and their favorable market response is the harbinger of a long-awaited transition in automotive technology. Despite these advances, there is still a genuine need for increasing the energy densities for achieving a successful transition to EVs [425-427]. Advances in lithium-ion anode technology have made it possible to obtain ~1500 mAh/g anodes with superior cycle life [316, 428, 429]. However, cathode research has been rather stymied in contrast, on account of the challenges faced in designing stable, conductive materials with high capacities. Cathode capacities thus far have been limited to ~ 300 mAh/g in high voltage [425, 430] lithium manganese-nickel-cobalt oxide chemistries. Lithium sulfur and lithium-air batteries on the other hand, hold much more promise towards matching anode capacities on

account of their theoretical specific energy densities of 2567 and 3505 Wh/kg, respectively[426]. The dissolution of sulfur through the formation of soluble polysulfides and the poor electronic conductivity of sulfur are however, well known but major problems still persisting and hindering the much awaited progress of Li-S batteries [426, 431, 432]. In addition, particle fracture and delamination as a result of the repeated volumetric expansion and contraction have also been identified as factors responsible for poor long term performance[433, 434].

It has previously been demonstrated that the use of highly conductive porous carbon matrix and carbon nanotubes can help circumvent these issues [435-440]. The use of egg-shell type morphologies using graphene and titanium oxide have also been shown to aid in retaining stability and high Columbic efficiency through both polysulfide retention and particle-coating lamination over extended cycling[433, 434]. In addition, the use of a carbon matte as a barrier layer to polysulfide transport has been demonstrated to be effective in retaining the high capacity[441]. There is however a need to translate this design into thick electrodes capable of delivering high overall electrode capacity.

In this study, we coat pristine sulfur particles with carbon and a lithium ionically conducting (LIC) matrix as shown in **Figure 77**. Extensive research has been undertaken into development of solid state electrolytes for lithium-sulfur batteries [442-446]. Such solid electrolytes act as porous lithium ion conducting channels while at the same time preventing dissolution of polysulfides (as known to ubiquitously occur in liquid electrolytes). Super-ionic lithium ion conductors with conductivities between 10^{-3} and 10^{-7} S/cm have previously been developed [442-448]. The primary problem with solid electrolyte based systems however, is the limited rate capability as a result of the ion mobilities, as expected being lower than that of organic liquid electrolytes. In addition, cell fabrication becomes complicated and hence, ensuring low contact

resistances becomes essential. Use of thick electrodes becomes impossible and this leads to low areal capacities. In the present work, a simple solid state fabrication method was used to develop architectures shown in **Figure 77**. With such composite multilayer architectures, the feasibility of very thick electrodes possessing excellent cycling stability, areal capacity and rate capability was demonstrated. A novel lithium ion conducting (LIC) matrix (lithium orthosilicate) was used to prepare the 'composite multilayer electrodes' system and were tested in commonly used organic liquid electrolytes. The use of this matrix ensures that channels exist for lithium ion conduction while polysulfides (even when dissolved) cannot travel across to the bulk electrolyte. The lithium orthosilicate as the coating of choice was chosed because it has previously been shown to be an excellent lithium ion conductor[449, 450]. In fact, it has previously been shown that lithium electrodes when covered with lithium orthosilicate become immune to air oxidation[451]. In this study accordingly, the superior performance of above-stated morphology was demonstrated and the reason for the same was examined. A straight-forward method was also demonstrated for synthesizing nano-sulfur using a chemical reduction method. The nano-sulfur prepared by this method exhibits superior charge storage characteristics. When used in combination with the lithium orthosilicate as a 'composite multilayer electrode', it was possoble to overcome fade issues occurring as a result of the higher surface area of nano-sulfur and therefore demonstrate excellent stability of the high capacity electrodes.

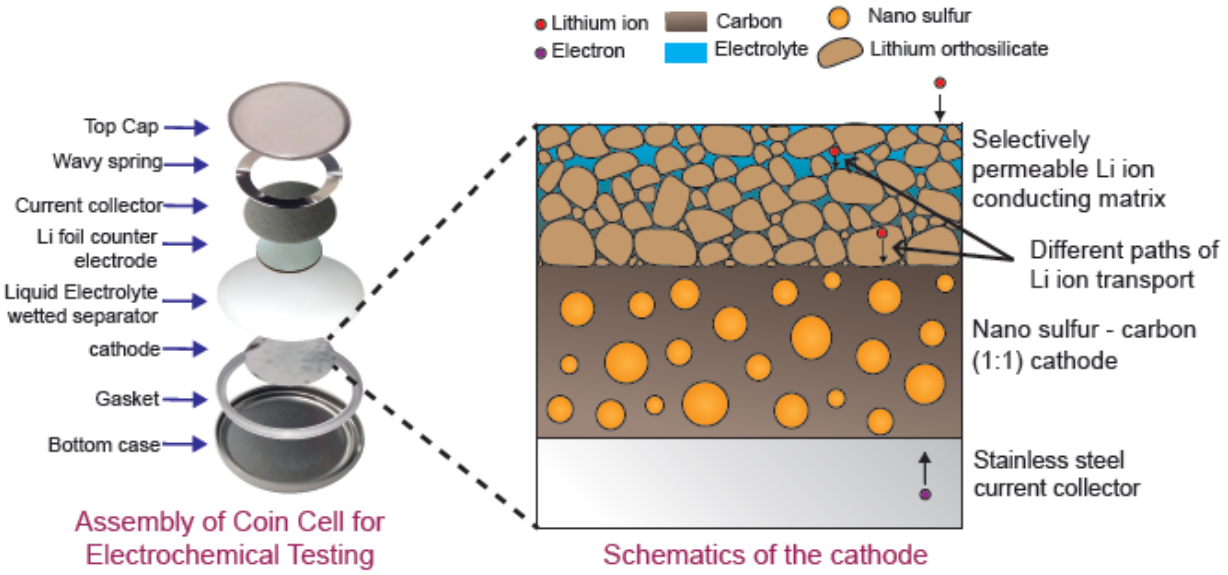

Figure 77. Schematic of the 'composite multi-layer electrode' assembly designed to prevent direct contact between sulfur and liquid electrolyte while at the same time ensuring short lithium diffusion distances through a solid phase. The lithium ion conducting (LIC) matrix used in the present study is lithium orthosilicate. Inset shows the pore structure existing within the lithium orthosilicate which we believe leads to short lithium ion solid-state diffusion distances.

B.1.2 Experimental

Nano-sulfur was prepared by a simple chemical procedure involving dissolution and reprecipitation of sulfur[452]. Commercial sulfur powder (~325mesh, Sigma Aldrich, Inc, 99% wt) was dissolved (5% wt/vol) in 1 M KOH solution (pH~=14) at a temperature of ~120^{o} C for four hours under constant stirring to obtain a reddish brown solution of potassium thio sulfate ($K_2S_2O_3$) and potassium sulfide (K_2S_3). The above solution was then cooled to room temperature, filtered and neutralized by the addition of 1M HCl equivalent to KOH to obtain a white colloidal solution of nano-sulfur along with the evolution of hydrogen sulfide and sulfur

dioxide gas. These sulfur nanoparticles in the colloidal solution subsequently settle down due to the increase in particle size caused by agglomeration when the solution is left undisturbed. The sulfur powder was filtered, repeatedly washed with water, isopropyl alcohol and then finally allowed to dry under vacuum at room temperature or 27^{o}C. A simple pellet pressing procedure was used to prepare electrodes for battery testing. Two different morphologies were used for the same. In the first morphology the nano-sulfur was mixed with conductive carbon additive (super-P, Timcal Graphite & Carbon) and binder [poly-vinyledene fluoride (PVDF)] in a suitable ratio of (1:1:1) and pressed into a pellet in a 1 cm diameter stainless steel (Carver Inc.) Carver press die employing a 5 ton load. The second sample was prepared resembling the morphology shown in **Figure 77**. Herein a layer of lithium orthosilicate (Alfa Aesar, 99.9% metals basis) as the lithium-ion conducting (LIC) matrix was pre-pressed in the Carver press. The mixture of nano-sulfur-binder-carbon additive was then pressed with the orthosilicate pellet to obtain the morphology shown in **Figure 77**. Similar pellets were prepared with commercial sulfur powder to evaluate the change in electrochemical performance induced by the use of synthesized nano-sulfur. Conventional slurry casting procedure was performed to prepare the electrodes for comparison with the pellet-pressed electrodes. Sulfur powder was mixed with super-P carbon and PVDF, and then dispersed in N-methyl pyrollidone (NMP). The dispersion was allowed to stir till a uniform slurry was obtained. The slurry was cast onto aluminum current collector foils (MTI Corp., ~15 μm thickness) using a tape casting machine (MTI Corp.). The coated foils were then dried in air and electrodes of ~1 cm diameter were punched.

In order to perform qualitative phase analysis, the sulfur materials were characterized by X-ray diffraction (XRD) using Philips XPERT PRO system employing CuK_{α} (λ = 0.15406 nm) radiation with operating voltage and current set at 45kV and 40mA, respectively. The XRD peak

profile was analyzed using the Pseudo-Voigt function to determine the Lorentzian and Gaussian contribution of the peaks. The integral breadth of the Lorentzian contribution, determined from peak profile analysis using single line approximation method after eliminating the instrumental broadening and lattice strain contribution, was implemented to calculate the lattice parameter and molar volume of the powder samples using least square refinement techniques [335, 336]. Scanning electron microscopy (SEM) was conducted to investigate the microstructure of the commercial sulfur powder, nano-sulfur powder and pellet electrodes. The powder samples were pre-dispersed in isoproponal by sonication for 30mins, followed by drying and then coated onto the carbon tape for SEM analysis. A thin palladium coating was performed onto the coated powder samples using Argon plasma in a sputter coater (Cressington sputter coater 108auto) to enhance conductivity of the powder samples for SEM imaging, to avoid charging effects. Elemental mapping was performed using the energy dispersive X-ray spectroscopy (EDAX) analyzer integrated into the SEM machine. Philips XL-30FEG equipped with an EDAX detector system comprised of an ultrathin beryllium window and Si (Li) detector operating at 20 kV was employed for executing the secondary electron (SE) image and elemental analyses. Finally, dynamic light scattering (DLS) experiments were conducted in a Malvern Zetasizer Nano zs90, for both commercial and nano-sulfur dispersed in DI water (0.01g/ml) after being wetted in iso-propanol to determine the average particle size.

Coin cells were assembled using the electrodes prepared by both methods. 2025 type cells were used with lithium as the counter/reference electrode and lithium trifluoro-methanesulfonate [1.8M $LiCF_3SO_3$ in 1, 3 dioxolane and 1, 2 dimethoxyethane (1:1 by vol.); with 0.1 M $LiNO_3$] as the electrolyte. All the cells tested in this study were cycled at room temperature (~298 K) within the 1.7–2.6 V (with respect to the lithium counter/reference

electrode) range employing the discharge/charge rates of ~50–2000 μA/cm^2 with a minute rest period between the charge/discharge cycles using a multichannel battery testing system (Arbin BT2000 instrument). It is common practice to allow for the system to equilibrate to open-circuit voltage between charge and discharge cycles[453]. Such a relaxation behavior allows for the response to be guided by material properties rather than switching processes. Continuous charge/discharge is a good indication of abuse tolerance and in the case of our study we performed evaluation of the multilayer composite electrodes using both rest/no-rest periods and found no significant difference in cycling behavior. Independent evaluation was performed on two separate Arbin cyclers and data reported herein was found to be reproducible in a number of coin cells. The specific capacity of the cathode materials has been reported as an areal capacity (mAh/cm^2) which has been calculated using the area of the electrodes, respectively. Areal capacity is a measure of the amount of charge that can be stored per unit area of an electrode. Areal and volumetric capacity values are of much greater importance than gravimetric capacity for commercial applications[454, 455]. Insulating and semiconducting materials (such as sulfur) when packed as thick films exhibit poor charge storage behavior since the thickness of the films limits flow of electrons to a large part of the electrode. The complications arising from preparing thick films makes it imperative to report areal capacity values. Gravimetric capacity is very much a property whose value varies with thickness of electrodes and though it is an important parameter to understand charge storage behavior, areal capacity is a parameter of more relevance to energy density of the system. In addition to the areal capacity, the gravimetric capacity (mAh/g), calculated on the basis of sulfur loading and overall active material have also been calculated and reported herein. To further evaluate the nature of the composite electrode shown in **Figure 77**, electrochemical impedance spectroscopy (EIS) was performed on the Versastat 3

over a frequency range of 2 Hz-100KHz. A.C. amplitude of 5 mV was used and the spectra were obtained between the open circuit potential and 1.7 V (with respect to lithium counter/reference) at intervals of 100 mV during the 1st discharge. The Z-View (Scribner Associates, Inc.; version 3.3c) software was used to design the equivalent circuit model for proper interprestation and analysis of experimentally obtained impedance spectra.

B.1.3 Results and discussion

Sulfur is known to dissolve in hot alkaline solutions to form polysulfides and $K_2S_2O_3$ as displayed in Equation (xi) below. The formation of nanoparticulate sulfur during the neutralizing reactions represented by Equation (xii) and Equation (xiii) below, is a result of the careful manipulation of temperature, concentrations of the reacting species and pH, which affect the nucleation and growth kinetics of the nanoparticles. During the precipitation reaction, the sulfur particles tend to agglomerate with time to reduce the surface energy and hence, settle down as precipitates in the solution from the white colloidal solution.

$$8\,S + 6\,KOH \xrightarrow{120^{o}C,\ stirring} 2\,K_2S_3 + K_2S_2O_3 + 3H_2O$$

Equation (xi)

$$K_2S_3 + 2HCl \xrightarrow{27^{o}C} 2S\downarrow + 2KCl + H_2S\uparrow$$

Equation (xii)

$$K_2S_2O_3 + 2HCl \xrightarrow{27^{o}C} S\downarrow + 2KCl + H_2O + SO_2\uparrow$$

Equation (xiii)

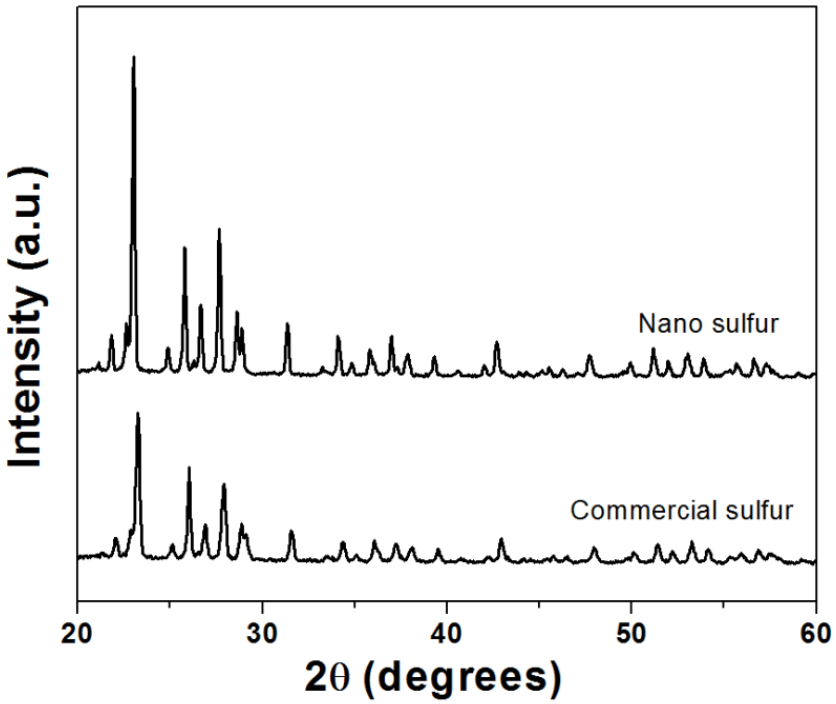

Figure 78. X-ray diffraction patterns of chemically derived nano-sulfur and commercially procured sulfur.

Figure 78 shows the X-ray diffraction pattern of nano-sulfur derived by the chemical method. It can be observed that the X-ray pattern matches very well that of orthorhombic sulfur (PDF 00-042-1278) and that of commercially procured sulfur (~325 mesh, Sigma Aldrich, Inc., 99% wt.). The absence of any impurity phase can be inferred from the XRD pattern. The lattice parameter and molar volume of the sulfur samples were calculated using the least square refinement technique and were found to be in good agreement with the bulk lattice parameter of orthorhombic sulfur. Peak broadening commonly observed as a result of the formation of nanoparticles is only significant when crystallite size goes to a <50 nm dimension. Such behavior has not been observed in X-ray diffraction patterns in **Figure 78** since the reduction in particle size is from 2μm to about 150 nm. No significant peak broadening is observed therein indicating that the nano-sulfur particles formed from the re-precipitation reaction have similar crystalline

domains as the commercially procured sulfur. Since no significant peak broadening was observed in the XRD patterns, DLS experiments were conducted to identify the size of the individual particles of nano-sulfur. The as-prepared powder was wetted in iso-propanol for 30 minutes with water as the dispersion medium since nanoparticulate sulfur is known to agglomerate easily upon drying. The average particle size of the sulfur nano particles increases with time from 130 nm after the first 2 minutes, to 320 nm in next 5 minutes and then to 610 nm after 15 minutes, a phenomenon similar to that observed by Massalimov et.al[452]. The driving process for agglomeration is the combined interaction of the van der Waal's attractive forces and electrostatic repulsive forces due to the surface charge on the particles. There is however, no significant mass transport between the surfaces of the synthesized and aggregated particles. As a result, these agglomerates are fragile and soft thus being susceptible for easy disintegration in different media using ultrasonication. In the dried powdered state the sulfur particles exist as micron sized agglomerates (~2 μm) and hence, the X-Ray diffraction analysis does not indicate the real difference between the synthesized nano-sulfur and commercial sulfur. Due to the large particle size of the commercial sulfur the dispersions obtained in isopropanol were unstable for DLS measurements. However, the drastic difference in the particle size of precipitated and commercial sulfur is clearly evident from the SEM images.

Figure 79a and **Figure 79b** show the SEM images of nano-sulfur and commercial sulfur, respectively. The difference in particle size is distinctly observed by comparing the two images. The nano-sulfur particles formed by the chemical re-precipitation procedure have agglomerated particle sizes of ~500 nm-2 μm as seen in the SEM micrograph in **Figure 79a**. Commercially obtained sulfur particles used as precursors to the chemical re-precipitation reaction on the other hand, have a wide particle size distribution consisting of 20-150 micron particles as seen in

Figure 79b. The particle size distribution obtained from DLS corroborates with the observation in **Figure 79a** and **Figure 79b**.

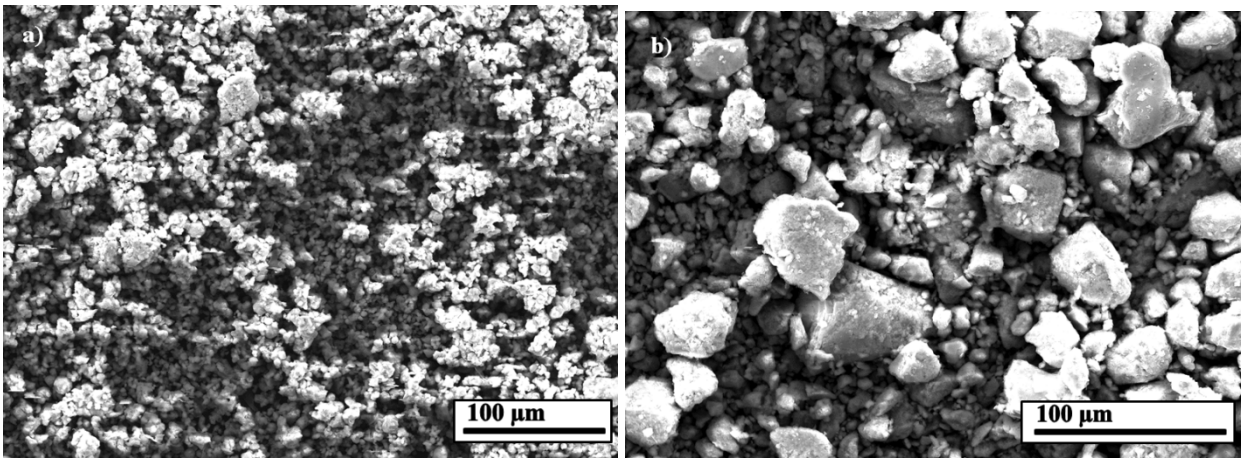

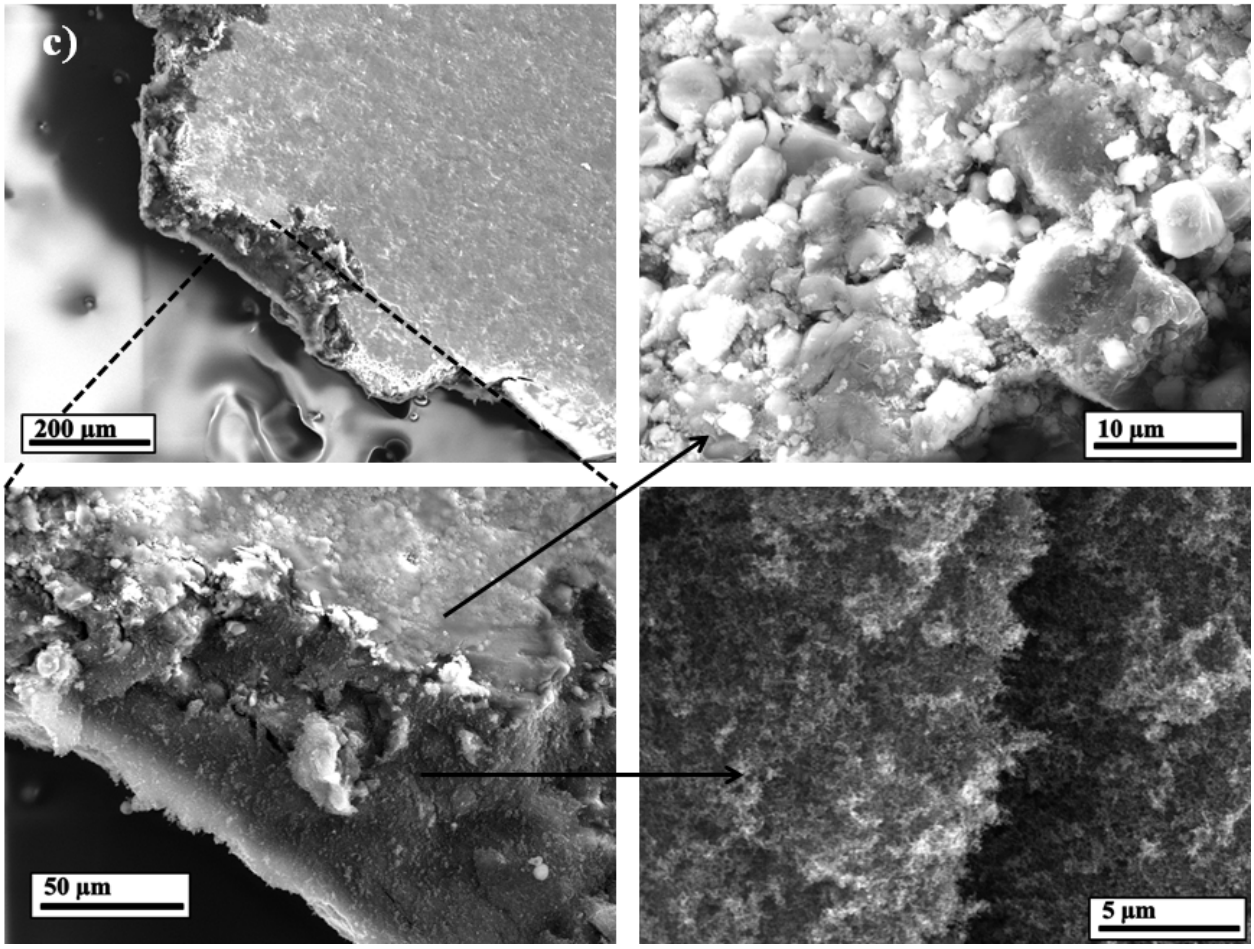

Figure 79. Scanning electron microscope images of (a) Chemically derived nano sulfur; (b) Commercially procured sulfur; (c) Composite multilayer electrode architecture with a uniform coating of lithium orthosilicate on a sulfur-carbon mixture. The layer structure is clearly visible in the inset image. The top layer of orthosilicate is porous and consists of macroscopic particles fused as a result of the mechanical pressing. The soft sulfur-carbon inner layer consists of much finer particles of distinctly different morphology.

The fine particles of nano-sulfur are expected to have exceptional exposure to the lithium conducting (LIC) layer/conductive additive resulting in high capacity. Similar to the case of nanoparticle amorphous silicon anodes studied for Li-ion, reversible expansion and contraction would not result in particle fracture and accompanying capacity fade[456]. **Figure 79c** shows the

morphology of the composite multilayer electrode assembled by the pellet pressing method. It can be seen that the morphology resembles that proposed and schematically shown in **Figure 77**. The pellet consists of a thin layer of lithium orthosilicate coating the mixture of sulfur and carbon. The uniformity of the coating and lack of macroscopic cracks are confirmed from the same. The inset images depict the disparate architecture existing within the orthosilicate layer and the sulfur-carbon layer. The orthosilicate layer consists of macroscopic particles fused together as a result of the mechanical pressing process. It can also be seen that the layer consists of macroscopic pores ideal for liquid electrolyte percolation. Short solid-state diffusion distances would result and the common issues typically experienced in solid electrolyte based lithium-sulfur batteries would thus be circumvented. The orthosilicate layer is a few microns thick ensuring that sulfur particles are not directly exposed to the liquid electrolyte thus serving to protect and prevent any dissolution of the polysulfides formed. The channel structure existing in the electrode would thus ensure minimal percolation of liquid electrolyte to sulfur particles. In addition to the protection offered by the orthosilicate layer, the pressing procedure ensures the formation of an elegant carbon coating on the sulfur particles. The carbon networks thus act both as electron conduction and lithium ion conduction (LIC) channels. Solid-state lithium ion diffusion through carbon is not sluggish and should not pose as a barrier to the ensuing intercalation and de-intercalation processes [457, 458].

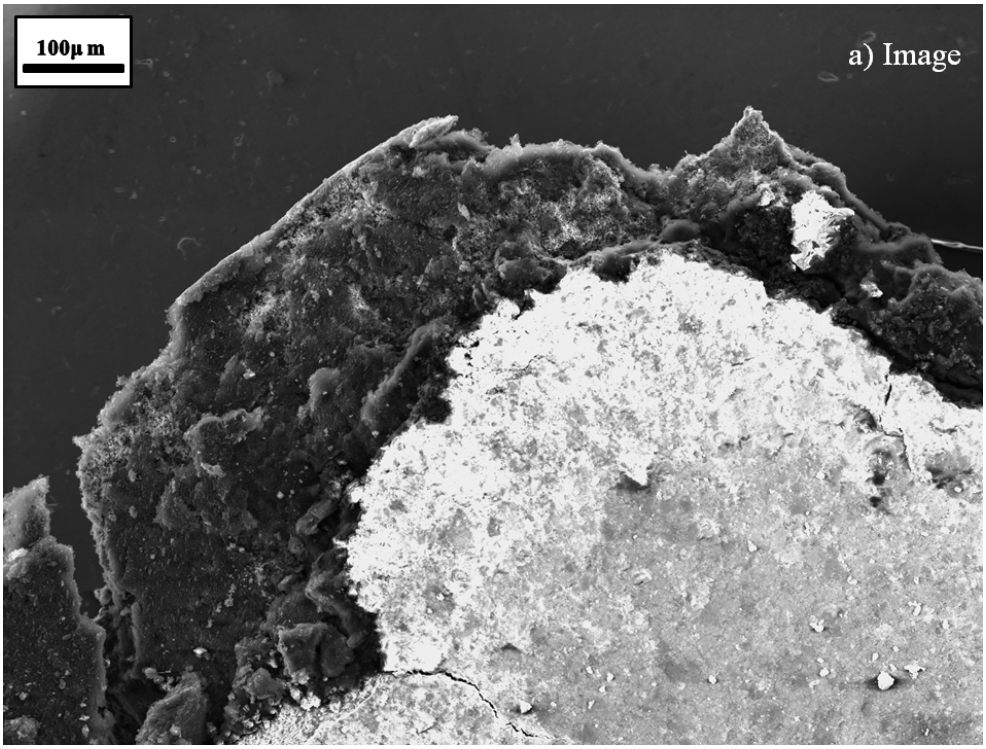
100µm
a) Image

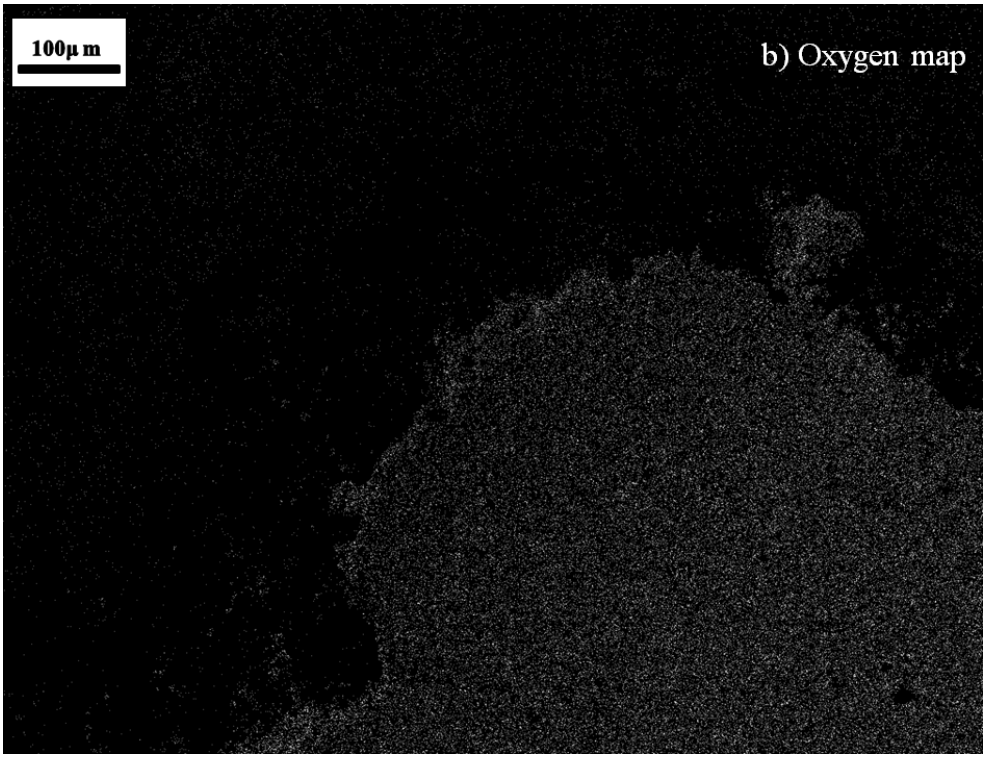
100µm
b) Oxygen map

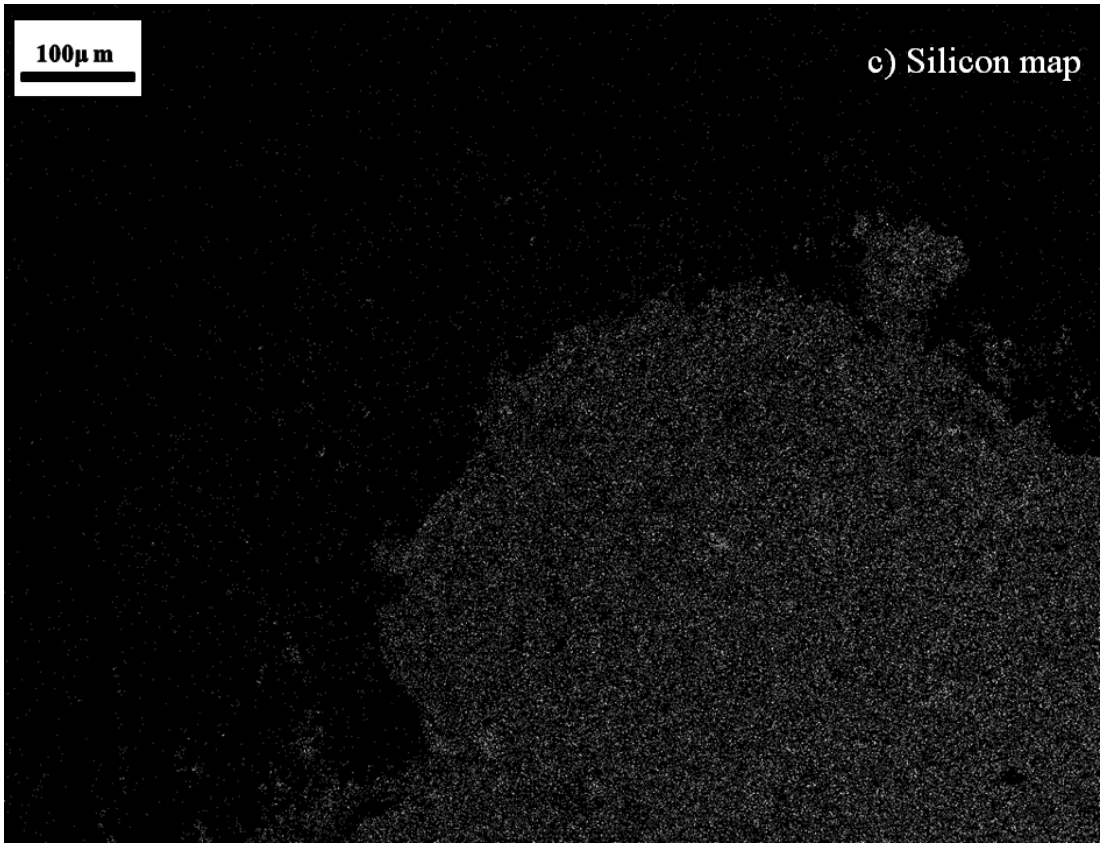
100µ m
c) Silicon map

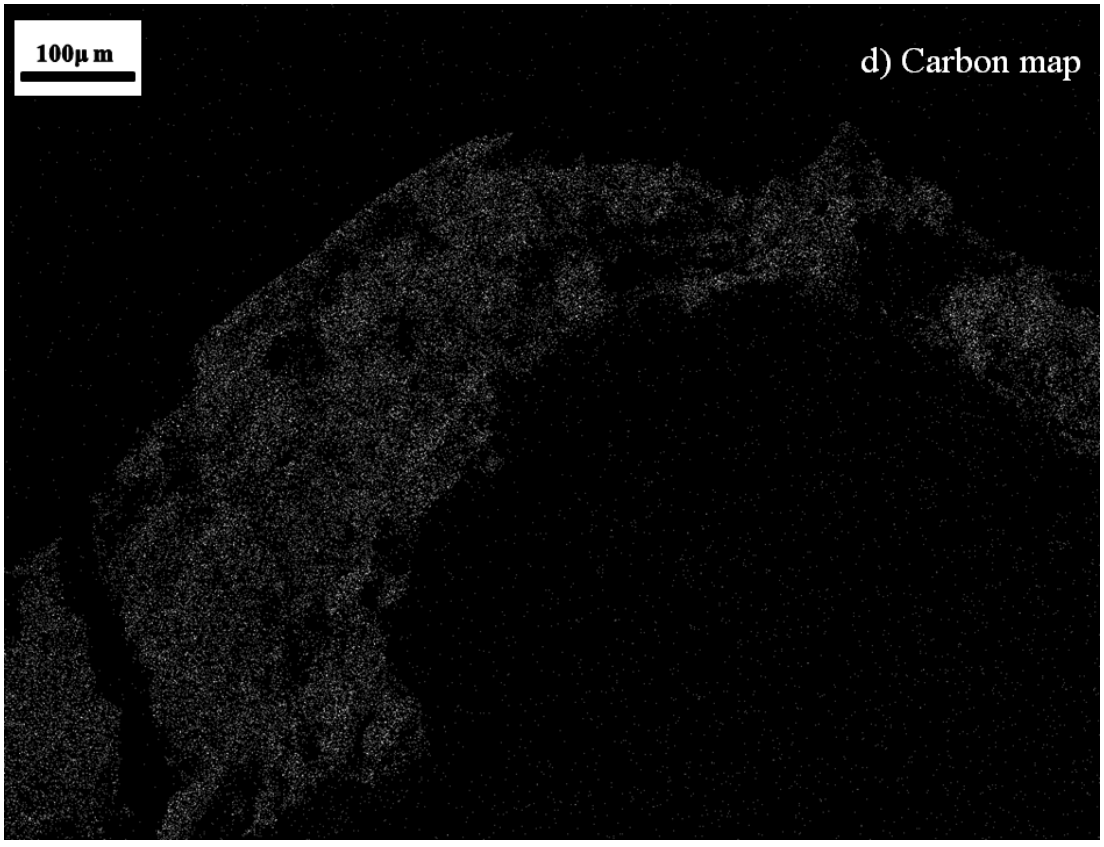
100µ m
d) Carbon map

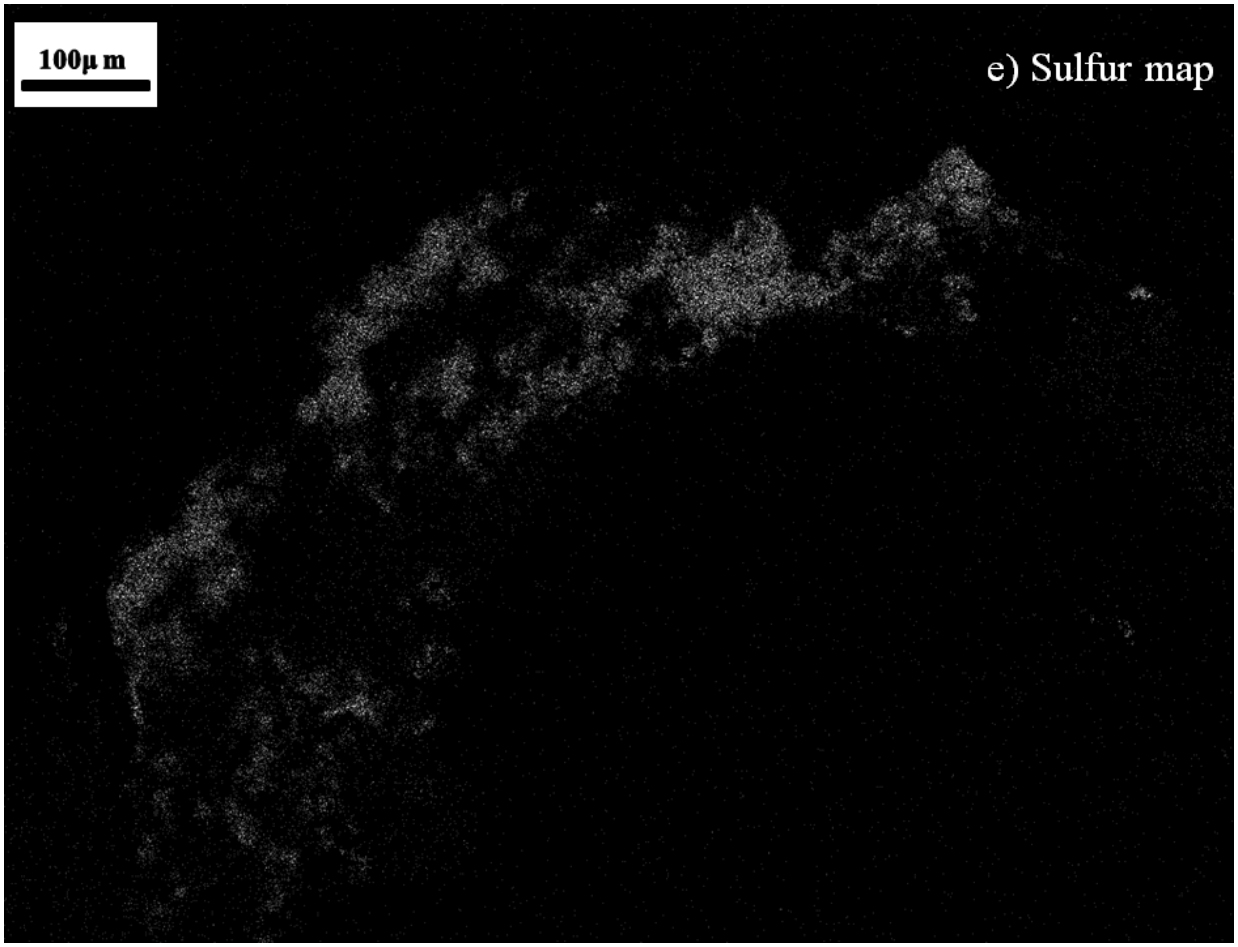

Figure 80. EDAX maps of the composite multilayer electrode showing (a) secondary electron image; (b) oxygen elemental map; (c) silicon elemental map; (d) carbon elemental map; (e) sulfur elemental map.

Figure 80a-Figure 80e show the EDAX image and elemental maps of the various elements present in the orthosilicate coating and the sulfur-carbon active phase present in the composite multilayer electrode. It can clearly be observed that the sulfur and carbon layer is distinct from the orthosilicate layer. The elemental composition of the top layer is also confirmed by the Si and O elemental maps clearly indicating the formation of the orthosilicate surface on top of the intricately mixed S and carbon electrode. It can be seen that there is very little intermixing of phases. The sulfur particles of the inner electrode are thus not directly exposed to the liquid electrolyte as a result of the lithium orthosilicate LIC coating. The carbon layer also

acts as an additional protection while also contributing to the electron conduction. Both the orthosilicate and the carbon serve as good solid state lithium diffusion media and would together contribute to good cycling stability of the composite multilayer electrode.

Evaluation of electrochemical performance of the various sulfur materials as cathodes was thus performed for the electrodes generated following the two methods described above. Electrodes of sulfur-carbon (1:1) were prepared by tape casting from the organic solvent based slurries and mechanically pressed pellets. **Figure 81a** shows the 10^{th} cycle charge-discharge profiles of the various sulfur-carbon materials. Characteristic plateaus corresponding to polysulfide formation and subsequent conversion to dilithium disulfide (Li_2S_2) and dilithium sulfide (Li_2S) are observed in all the materials. The composite multilayer electrode can be seen to exhibit however, the highest gravimetric capacity of the various materials after 10 cycles as a result of the high capacity yielded by the nano-sulfur (as shown in **Figure 81b** also). The nano-sulfur slurry electrode also displays a high capacity as compared to the commercial sulfur pellet and the slurry made from commercially obtained sulfur powder. The cycling stability of the various materials is plotted in **Figure 81b and Figure 81c** (specific gravimetric and areal capacity, respectively). Among the slurry cast electrodes, it can be seen that the nano-sulfur demonstrates the higher capacities and better fade characteristics in comparison to the commercially obtained sulfur. The improvement in capacity can be attributed to the change in particle size seen in **Figure 79a** and **Figure 79b**. The higher surface area of the 0.3-2 μm particles (as confirmed by DLS) results in enhanced reactivity and thus better capacity. The improvement in cycling performance observed there-in could be attributed to reduced particle stresses in smaller particles resulting in lesser fracture and delamination. In addition, the fine particle size would ensure good contact with the conductive additive preventing particles

becoming inactive over time as a result of fracture. The crystalline nature of the fine nanoparticles would at the same time, ensure that the particles would not be completely insulating. The slurry cast nano-sulfur electrode thus has a high initial capacity of ~1125 mAh/g-S and a fade rate of 0.86%/cycle as seen in **Table 29** and **Figure 81b**. This superior performance indicates that sulfur behaves similar to silicon with respect to charge storage capability and cycling stability in that the reduction of particle size aids both those characteristics. The straightforward chemical re-precipitation reaction used in this work is a useful tool, which when optimized can be used to further enhance the capacity of sulfur further towards achieving the maximum theoretical capacity of 1675 mAh/g. The nano-sulfur slurry cast electrode has a high initial areal capacity of 3.5 mAh/cm^2, stabilizing at ~1.4 mAh/cm^2, upon further cycling.

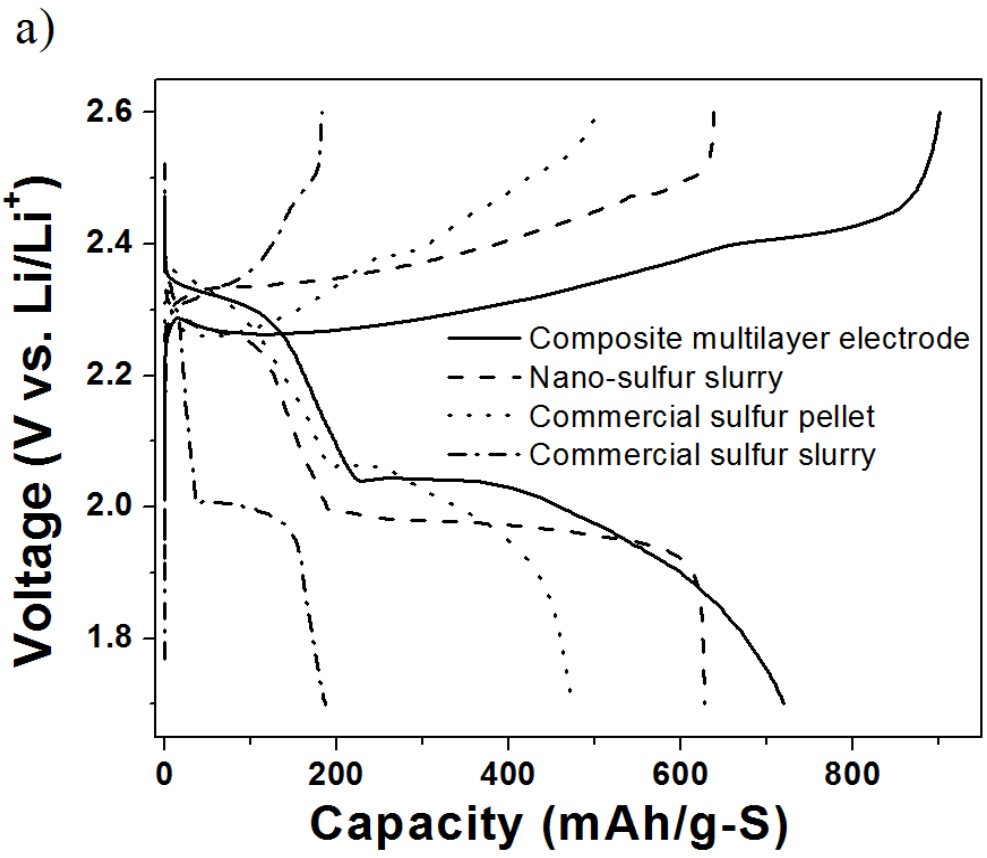

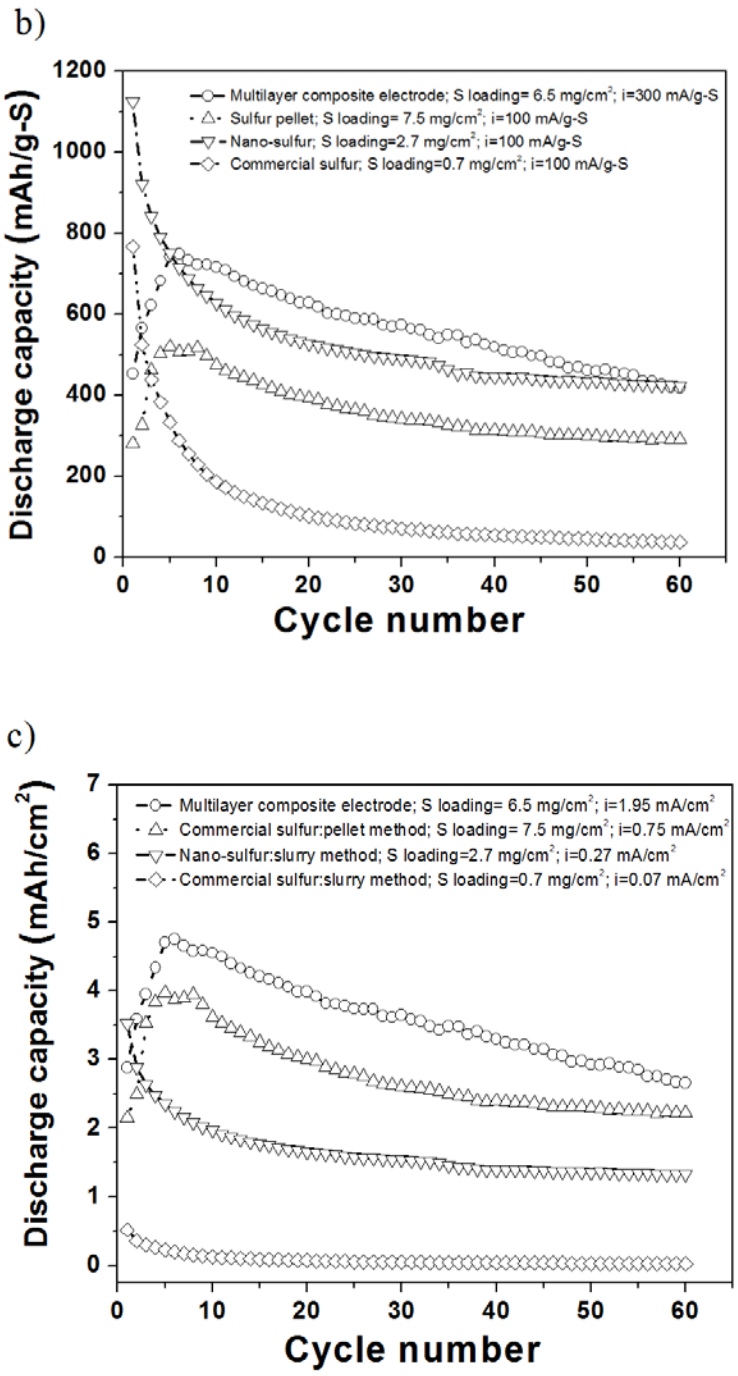

Figure 81. (a) Charge-discharge profiles (sulfur basis gravimetric capacity) of the various electrode architectures; (b) Comparison of cycling behavior of the commercial sulfur, nano-sulfur prepared by slurry method, pellet method and the multilayer composite electrode; (c) Comparison of cycling behavior (overall electrode areal capacity basis) of the various electrodes.

Table 29. Charge storage behavior of the various sulfur based electrodes.

Material	Initial discharge capacity (mAh/g-S)	Fade rate* (% capacity/cycle)
Commercial sulfur-slurry method	766.3	1.76
Nano-sulfur-slurry method	1125.8	0.86
Commercial sulfur-pellet method	519.3	0.87
Multilayer composite electrode	748.2	0.79

**Fade rate calculated on the basis of 5^{th} cycle capacity and 55^{th} cycle capacity.*

In addition to the slurry cast electrodes, solid state pellet pressing was used to prepare electrodes of the commercially obtained sulfur and the multilayer composite electrode schematically shown in **Figure 77**. The pellet pressing procedure allows for the ability to prepare very thick electrodes consisting of sulfur-carbon and PVDF binder. The compaction yielded by the pressing procedure results in better cycling stability as observed in **Figure 81b** and **Table 29**. The commercially obtained sulfur, which undergoes very rapid capacity fade when slurry casted, exhibits superior capacity retention (0.87%/cycle) when pressed into pellets to form thick electrodes. The improved performance may be attributed to the thick nature of the electrode. Even though the liquid electrolyte comes in contact with the sulfur, the thick electrode possibly ensures that the dissolved polysulfides have an increased residence time in close proximity with the carbon (through which electron transfer occurs). Though the behavior has not been completely explored in this study, it is believed that the behavior may be similar to that reported

by Nazar et al. in the case of mesoporous carbon-sulfur electrodes with tailored porosity[436]. Further studies are ongoing to understand this behavior and optimize the electrode/sulfur particle/carbon porosity, particle size and configuration, the results of which will be reported subsequently. As a part of exploration into this paradigm, we engineered the composite multilayer electrode further by having an additional protective layer of lithium-ion conducting (LIC) membrane (see **Figure 77**). This novel electrode architecture allows the liquid electrolyte molecules to very closely approach the nano-sulfur particles without actually coming in contact with the sulfur. Lithium undergoes solid-state diffusion through the membrane and the carbon layer to reach and react with the inner sulfur. The sulfur undergoes lithiation through two steps seen in **Figure 81a**. The initial lithiation to form polysulfides (LiS_x) (which in the absence of the protective membrane dissolves into the liquid lithium electrolyte) is very rapid. The protective membrane, we suspect acts both as a physical barrier for polysulfide transport to the liquid electrolyte as well as offering a superior lithium ion channel for transport to the sulfur/polysulfide species in contact with the carbon. The use of a liquid electrolyte in tandem with the lithium ion conducting porous coating on the sulfur electrode allows for reduced contact between sulfur particles and the liquid electrolytes, while at the same time ensuring that the lithium ion diffusion distances are not significant. In the current study, lithium orthosilicate was chosen as the thin solid lithium-ion conducting (LIC) barrier layer, though conceivably any good lithium ion conductor with good mechanical stability, small to medium pore size and minimal free volume within its lattice can also be used for the same.

Ordered lithium orthosilicate Li_4SiO_4 adopts a monoclinic crystal structure with space group $P2_1/m$ and a = 11.546, b = 6.090, c = 16.645 Å, β = 99.5°[459]. In **Figure 82** the crystal structure is shown along the [010] direction with the relative ionic sizes of lithium and oxygen

corresponding to the real ionic radii taken from experimental data and collected in Ref.[460] by R.D. Shannon (R_{Li} = 0.59 Å and R_O = 1.38 Å). One can see that along this direction there are some channels (or tunnels) formed by oxygen ions with internal sizes approximately equal to the corresponding diameters of Li-ions. Such a structural geometry allows Li-ions to migrate through the host material relatively easily, while for larger molecules of the organic solvent and electrolyte the structure remains impermeable. Thus, from **Figure 82** it is clearly visible that Li_4SiO_4 may well serve as a molecular sieve or filter for separation of Li-ions from the electrolyte. In addition, it is well known that lithium diffusion through orthosilicate structure is rapid[449, 450]. Thus it was selected as the material for serving as the protective barrier layer in this work.

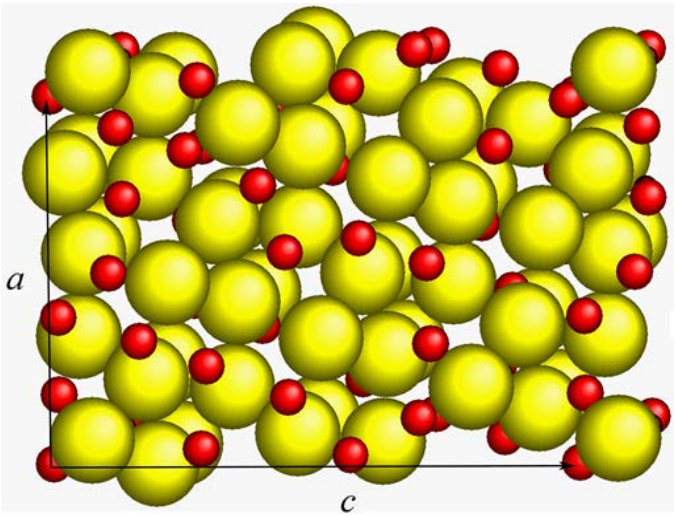

Figure 82. Li_4SiO_4 crystal structure indicating its suitability for use as a protective barrier layer while at the same time ensuring rapid solid-state diffusion of lithium. Projected view along [010] direction. Large balls – oxygen ions, small balls – Li. Si ions are not visible at this projection.

The improvement in charge storage as a result of utilizing the pellet-pressing procedure, especially the composite multilayer electrode architecture is seen both in **Figure 81b** and **Table**

29. The use of the pellet pressing procedure yields us thicker electrodes, while at the same time allowing for better capacity retention. This results in the significantly higher areal capacities seen in **Figure 81c**. The thick electrodes made from commercially obtained sulfur have an initial areal capacity of ~4 mAh/cm^2 while the composite multilayer electrode has a capacity of ~4.75 mAh/cm^2. These are values corresponding to the 5th cycle since these thick electrodes suffer from poor wetting in the initial cycles as would be expected. It should be noted that the charge capacity is greater than the discharge capacity in the charge-discharge profiles in **Figure 81a**. This characteristic of the charge-discharge profile is routinely encountered and widely reported in the literature[433, 436, 441, 455, 461, 462], and it is believed that this is a result of delithiation of polysulfides which dissolve/do not get completely converted to dilithium sulfide but remain in close proximity of the electrode to get converted back to sulfur. This phenomenon is pronounced in the case of the pellet made from commercially obtained sulfur and the composite multilayer electrode indicating its effectiveness in retaining the polysulfide species thus preventing dissolution. With further optimization, it is believed that the capacity and cyclability of the electrodes can be improved by ensuring such polysulfides would not contribute to loss of electrical contact and would thus get completely converted to Li_2S. Even so, the capacity at the 5th cycle is much higher than the current EERE-OVT (Office of Energy Efficiency & Renewable Energy-Office of Vehicle Technologies)[100] target for areal capacity of electrodes of 4 mAh/cm^2. It should be also noted that the areal capacities and sulfur loadings on the electrode exceed those previously reported though further optimization is ongoing to improve the overall sulfur weight percentage (to reduce overall electrode thickness)[455, 461]. Both electrodes exhibit superior cycling stability as outlined in **Table 29**.

The composite multilayer electrode has the best capacity retention with a fade rate of ~0.79%/cycle at a current density of ~1.95 mA/cm^2 which is comparable to that reported in the literature[455, 461]. The simplicity of the design and the relative ease of fabrication of the same make the procedure in this work unique and with considerable promise. This work entails initial investigation into the formation of a very thin coating of lithium ion conducing material (LIC) on sulfur-carbon and demonstrating that such a coating has a salutary effect as far as capacity retention is concerned. The LIC coating demonstrated in the current manuscript has yet to be optimized for porosity and thickness. Without such optimization, we believe there exist some porous channels which act like leaks and allow for contact of liquid lithium electrolyte with sulfur particles resulting in a gradual fade as observed in **Figure 81b**. However, the gravimetric capacity of the LIC coated sulfur electrode is superior to the slurry cast film for upto 60 cycles and its areal capacity is almost double that of the slurry cast electrode after 60 cycles. From a practical perspective, areal capacity is the observed and attainable charge and the LIC coated electrode retains higher areal capacity than both the coating-free pellet electrode and the nanoparticle slurry. This work is a proof of concept study and further optimization is necessary for the LIC coating to be of significant value for long term cycling upto 1000 cycles. There is however, scope for further optimization which is part of the on-going work. The porosity of the protective layer, thickness, composition and the particle properties of the nano-sulfur could be further optimized to increase the sulfur weight percentage, improve cyclability and decrease the electrode thickness. Work is ongoing on the same.

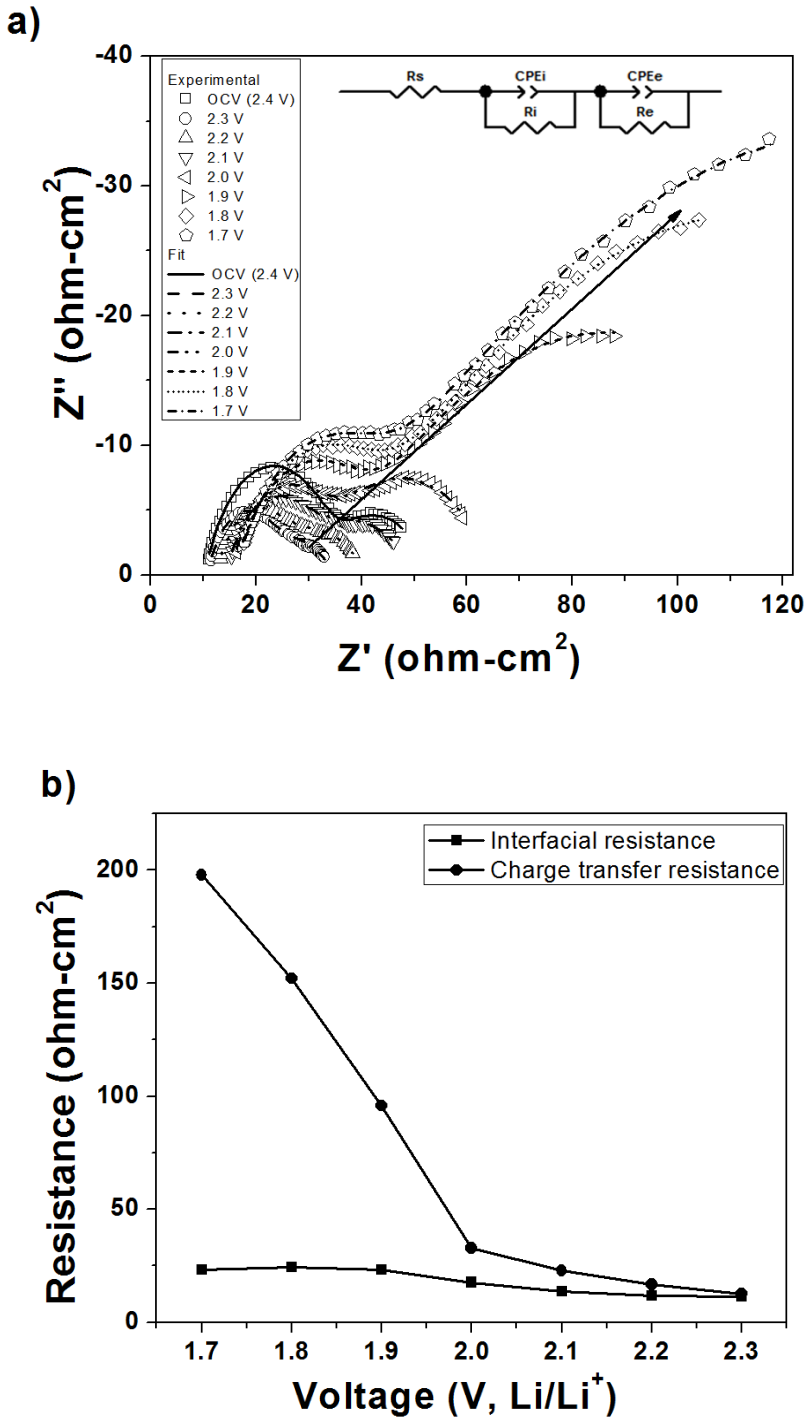

Figure 83. (a) Nyquist plot of the multilayer composite electrode at various potentials (with respect to Li/Li^+) during discharge (Inset shows the Randall's circuit used to model the system); (b) Variation of interface resistance and electrode resistance during 1st discharge.

Table 30. Charge storage characteristics of the multilayer composite electrode (calculated using the model shown in Figure 83a

	Voltage (V, Li/Li^+)	R_s (ohm-cm^2)	CPE_i-T	CPE_i-P	R_i (ohm-cm^2)	CPE_e-T	CPE_e-P	R_e (ohm-cm^2)
OCV	2.4	10.28	2.50E-5	0.75	23.43	5.90E-3	0.53	19.42
1^{st} Discharge	2.3	10.57	2.75E-5	0.77	11.52	4.88E-3	0.44	12.74
	2.2	12.25	3.04E-5	0.75	11.8	3.96E-3	0.45	16.79
	2.1	13.99	2.81E-5	0.75	13.63	4.28E-3	0.42	22.99
	2	14.94	3.17E-5	0.72	17.7	2.31E-3	0.52	32.81
	1.9	15.52	3.91E-5	0.68	23.3	3.01E-3	0.47	95.76
	1.8	15.79	3.44E-5	0.70	24.45	2.78E-3	0.45	152.1
	1.7	15.65	3.23E-5	0.71	23.27	2.47E-3	0.43	197.9

In order to further characterize the charge storage behavior of the composite multilayer electrode, electrochemical impedance spectroscopy (EIS) was performed over a frequency range of 100 KHz-2 Hz with an A.C. amplitude of 5 mV at different potentials during the 1^{st} discharge. The electrode was allowed to wet for over 24 hours to allow for complete wetting in order to obtain a representative picture of the charge storage process. The Nyquist plot of the electrode is shown at various potentials (with respect to Li/Li^+) in **Figure 83a**. Two distinct semi-circular arcs are observed at all potentials in addition to the very high frequency solution resistance term (R_s). Both semi-circular arcs are depressed which is typically observed in porous electrodes. The Randall's equivalent circuit modeling was performed using the model shown (see inset) in **Figure 83a**. It can be seen that the experimental data is in good agreement with the equivalent

circuit model by considering the two R-C elements in series with the solution resistance. In addition, the constant phase elements (CPE) was used in lieu of the usual capacitive elements as is common practice in modeling of porous electrodes. The 1st R-C element with R_i (interfacial resistance) and CPE_i (interfacial constant phase element) is indicative of the resistance yielded by the coating in addition to any other secondary interfaces formed during cycling. The second semi-circle corresponds to the charge transfer process and it is represented herein as R_e (resistance to electron transfer) and CPE_e (electron transfer constant phase element). It can be seen in **Figure 83a** that the interfacial resistance increases slightly with lithiation while the change in electron transfer resistance is more significant. **Figure 83b** plots the change in both parameters with voltage and their values combined with other charge transfer parameters are indicated in **Table 30**. It can be seen that the interfacial resistance (R_i) increases slightly with intercalation as is expected from the constant nature of the resistance arising from the lithium-ion conducting (LIC) protective barrier layer. The slight increase could be attributed to small amounts of secondary interface formation during the 1st discharge. On the other hand, the electron transfer resistance (R_e) undergoes almost a one order change with intercalation. The electron transfer resistance is a measure of kinetics of the reaction and the trend observed herein is to be expected as it is well known that the initial kinetics of polysulfide formation is rapid while the kinetics of conversion of lithium polysulfides to Li_2S is a sluggish process[426, 432]. In addition, lithiated species become successively harder to further lithiate as is commonly observed in lithium ion batteries [463, 464]. It can thus be concluded that the interfacial resistance provided by the protective barrier layer consisting of the lithium orthosilicate LIC does not significantly increase the overall resistance of the electrode though it helps to improve the

performance by facilitating the shuttling of lithium ions thus validating the proposed novel concept.

B.1.4 Conclusions

In the present work, it was demonstrated that the three different concepts outlined as under which when combined together allow to tailor electrodes for lithium-sulfur batteries with very high areal capacities higher than hitherto reports to the best of what is known to be reported in the literature while providing also good capacity retention.

a) Nano-particulate sulfur has been synthesized and shown to result in higher capacities without significant increase in fade rate.
b) Solid state processing i.e. pellet pressing has been shown to be an effective method to improve the capacity retention in lithium sulfur batteries in comparison to the conventional slurry casting procedure.
c) A thin coating of solid state lithium-ion conductive (LIC) layer allows for minimal contact of liquid electrolyte with sulfur preventing dissolution of the polysulfides formed during lithiation of sulfur, while at the same time not presenting problems observed with the use of purely solid state electrolytes

On the basis of the above three insights provided by our work, a multilayer composite electrode has been tailored and prepared by pellet pressing using lithium orthosilicate as the solid state lithium-ion conduction layer and nano-sulfur/carbon as our active material mix. It was demonstrated that this composite electrode exhibits very high areal capacity (~4.75 mAh/cm^2 at a current density of 1.95 mA/cm^2) with good capacity retention and cyclability. Using

electrochemical impedance spectroscopy (EIS), it was further characterized that the charge storage behavior of the composite multilayer electrode validates the beneficial aspect of LIC demonstrating that the layer does not act as a significant source of impedance.

B.2 MAGNESIUM BATTERIES

B.2.1 Introduction

Electrochemical energy storage technologies based on rechargeable batteries are considered as one of the leading emerging technologies for stationary power application. Current battery technologies based on lead acid, nickel metal hydride, sodium-sulfur, and vanadium flow systems used for stationary power applications suffers due to various environmental and economic concerns [465]. Li-ion batteries used for mobile electronics and electric vehicles can offer high energy density, however, with lithium's geographically constraint reserve and high cost makes it imperative to explore alternative battery technologies [14]. Recently, energy storage systems based on bivalent Mg^{2+} ions is being touted as a promising high energy density alternative battery system among others [466, 467]. Magnesium (Mg) has several positive attributes which set it apart from Li-ion battery system [468]. It is environmental friendly, cost effective (~$ 2700/ton for Mg compared to $64,000/ton for Li) and is relatively more abundant in the earth's crust (~13.9% Mg compared to ~0.0007% of Li) compared to hitherto used popular systems [469-471]. Additionally, magnesium is more stable in air compared to lithium, and is theoretically capable of rendering higher volumetric capacity (3832 mAh/cc for Mg vs. 2062 mAh/cc for Li). Furthermore, magnesium is not plagued by dendrite formation unlike lithium metal batteries

which led to initial safety concerns that was thankfully obviated by the intercalation of Li into graphite [472, 473].

Earlier studies shows that conventional salts such as $Mg(ClO_4)_2$, $Mg(CF_3SO_3)_2$, $Mg[(CF_3SO_2)_2N]_2$ etc. dissolved in various non-aqueous solvents develop surface passivation on the Mg anode and effectively block Mg^{2+} ion transport [474-476]. On the other hand, Grignard's reagents (RMgX, R alkyl or aryl; X = Cl, Br) dissolved in ethereal solvents are well-known and are capable of electrochemically depositing and dissolving magnesium [477]. However, the limited electrochemical window (~ 1.5V) of Grignard's reagents imposes a major barrier for their use in practical cell assemblies. Aurbach *et al.* [478, 479] first invented Mg organohaloaluminate salts $(R_2Mg)_n(AlCl_{3-n}R_n)_m$ dissolved in ethereal solvents, capable of reversibly depositing and dissolving Mg yielding a 100% Coulombic efficiency in the electrochemical potential window ~ 2.2 V. Following Aurbach's successful invention, the interest for developing high energy density Mg storage systems has increased steadily over the past few years [480].

Aurbach also developed a prototype Mg cell using the Mo_6S_8 Chevrel Phase (CP) - a new class of cathodes, Mg anode, and the 0.25 molar $Mg(AlCl_2EtBu)_2$/tetrahydrofuran electrolyte where Mg^{2+} can be (de)intercalated reversibly ~ 1-1.2 V offering an energy density ~ 60 $Whkg^{-1}$ up to 2000 cycles with little fade in capacity [478, 481]. Chevrel phases, Mo_6T_8 (T = S, Se, Te) is an unique class of compounds that can accommodate multivalent cations within the Mo_6 anionic framework [482]. Relatively fast and easy intercalation of Mg^{2+} ions at room temperature makes CPs a preferred choice of cathode for magnesium battery. However, Mo_6S_8 is a metastable phase at room temperature, and is therefore indirectly stabilized when generated via leaching of the metal from the thermodynamically stable ternary Chevrel phase compounds, $M_xMo_6T_8$ (M = metal, T = S, Se, Te) [483]. Typically, $Cu_xMo_6S_8$ (Cu_xCP) are synthesized by high temperature

solid state reactions of elemental blends of copper, molybdenum, and sulfur powders in an evacuated quartz ampoules (EQA) at ~1423K for 7 days [466, 478] or by a molten salt route (MS) using Mo-MoS_2-CuS reactants in a KCl salt, and heat treating the reaction mixtures at ~1123K for 60h in an Ar atmosphere [481]. Both approaches are extremely tedious requiring chemical leaching either in 6M HCl/H_2O or 0.2 M I_2/acetonitrile solution for several days at room temperature for complete removal of copper [484]. The MS approach for synthesizing the Cu_xCP phase offers much improvement in terms of synthesis time (60h vis-à-vis 7 days at a 300^oC lower temperature of 1123K) compared to the EQA approach however, the total time of ~two and a half days required for the synthesis of Mo_6S_8 will likely increase the energy consumption and associated manufacturing costs. A recent report on ultra-fast synthesis of $Cu_{1.8}Mo_6S_8$ by self-propagating high-temperature synthesis (SHS) or thermal explosion method from elemental mixtures of Cu-Mo-S inside an Argon sealed Swagelok vessel successfully reduces the total synthesis time to 20 min at 1273K [485]. However, Mo_6S_8 a well-known model cathode for magnesium battery will continue to serve as the baseline system to evaluate the suitability of new magnesium electrolytes [486]. Thus, alternative methods to synthesize Mo_6S_8 Chevrel phase from its stable high temperature ternary Chevrel phase will be paramount importance in future. With this in mind, in the present work, we exploit an alternative solution chemistry route for the synthesis of Mo_6S_8 following modification of a previous manuscript [487] which reported the synthesis of the Cu analog of the Mo_6S_8 phase. However, the approach was never explored for the generation of the Mo_6S_8 phase devoid of Cu which is described in this work. More importantly, there has been no report exploring the ability of the material derived from this approach for cycling Mg. In this report, the cycling performance of the chemically synthesized Mo_6S_8 following removal of copper was evaluated in a Mg cell at various C- rates was discussed.

The results indicate that the sulfide phase derived by this solution route exhibits different morphologies than the other reported approaches in the literature while also displaying a competitive electrochemical response with a much improved and noteworthy rate capability compared to reports in the literature [466, 478].

B.2.2 Experimental

Material Preparation

$Cu_2Mo_6S_8$ (Cu_2CP) was synthesized according to the method outline by Nanjundaswamy *et al.* [487]. In a 3-neck round bottom flask, stoichiometric amount of ammonium tetrathiomolybdate (4g, 15.37 mmol; Alfa-Aesar 99.95%) and anhydrous copper(II) chloride (0.6890 g, 5.12 mmol, Alfa-Aesar 99.985%) was added to *N.N*, dimethylformamide, DMF (130 ml) solution. The resultant mixture was heated over a hot plate (~363K) for 6h under constant N_2 bubbling. After complete reaction, the mixture turned deep red which was filtered, and tetrahydrofuran (1:5 by volume) was added immediately to the filtrate to initiate precipitation. A fine black precipitate was immediately formed which was kept overnight to settle at the bottom of the flask. The precipitate collected, washed with tetrahydrofuran and methanol followed by drying 12h at room temperature [488]. The dried solid agglomerate was ground and heated at ~1273K for 5h under UHP Ar + 6.5%H_2 atmosphere which directly yielded the desired ternary Chevrel Phase $Cu_2Mo_6S_8$ [487]. It should be noted that Nanjundaswamy *et al.*[487] only synthesized the ternary Chevrel phase ($Cu_2Mo_6S_8$) and studied the variation of electrical resistivity with temperature. The approach was however never explored for generation of the de-cuprated Mo_6S_8 form. We further leached copper from the $Cu_2Mo_6S_8$ by acid treatment (bubbling a solution of 6 M HCl/O_2 for 8h) in ambient atmosphere [484]. After complete removal of copper from $Cu_2Mo_6S_8$,

the acid solution containing the residue was centrifuged, washed with the de-ionized water three times and dried in an oven at ~323K. In order to perform qualitative phase analysis, X-ray diffraction (XRD) was carried out using the Philips PW1830 system employing the CuK_{α} (λ=0.15406nm) radiation. Microstructural analysis of the $Cu_2Mo_6S_8$ and Mo_6S_8 were performed using a scanning electron microscopy (JSM-6610, JEOL) operating at 10kV.

Electrochemical Characterization

Electrode slurry was prepared by mixing 80 wt.% of the Mo_6S_8 powder (-325 mesh), 10 wt.% Super P, 10 wt.% polyvinylidene fluoride (PVDF) dissolved into a solution of *N*-methylpyrrolidinone (NMP) to prepare a homogeneous solution. The slurry was coated onto a graphite foil and dried at ~383K in a vacuum oven. Electrochemical characterization was conducted at room temperature with 2016 coin cells assembled inside an argon-filled MBraun Inc. glove box (< 0.1 ppm each of O_2 and H_2O) employing magnesium foil as the counter electrode and cellgard separator soaked in an electrolyte solution of 0.4 molar 2(PhMgCl)-$AlCl_3$ in tetrahydrofuran. Cyclic voltammogram (CV) was performed using an electrochemical workstation (VersaSTAT 3, Princeton Applied Research) between 0.5-1.75 V at a constant sweep rate of ~0.01 $mVs^{-1.}$ Galvanostatic charge-discharge cycles were carried out employing various current rates ~20-120 mA/g within 0.5-1.5 V, employing a short rest period between the charge/discharge cycles using a multichannel battery testing system (Arbin BT2000 instrument).

Electrochemical impedance spectroscopy (EIS) was carried out on the Mo_6S_8 electrode both before and after cycling in order to obtain a fundamental understanding into the nature of Mg^{2+}-ion charge storage mechanisms. EIS was performed using the Versastat 3 (Princeton Applied Research Inc.) potentiostat over a frequency range of 0.01Hz-100KHz. A.C. amplitude of 5 mV was used and the spectra were obtained before cycling and subsequent to 1^{st} and 2^{nd}

discharge cycle. Electrode potential was stabilized after discharge cycle and EIS was performed (EIS was performed immediately so that no significant relaxation processes and equilibrium phase changes occurred) to observe any noticeable changes in the charge storage mechanism upon cycling. The effect of cycling on charge transfer parameters was also analyzed by performing EIS. Z-View (Scribner Associates, Inc.; version 3.3) software was used for Randall's equivalent circuit modeling of the experimentally collected impedance spectra.

B.2.3 Results and Discussion

The dried solid agglomerate obtained after 12h drying at room temperature was subjected for XRD analysis. Powder XRD pattern shows the formation of an X-rays amorphous compound (see **Figure 84a**). The Bragg's diffraction lines were broad and not well-defined due to low crystallinity of the phase formed at room temperature, and could not be indexed with standard JCPDS file (ICDD database). However, according to Nanjudwaswamy *et al*. [487] the solid product obtained after drying the black precipitate at room temperature is a compound of formula $Cu(NH_4)_qMo_3S_9$. Nanujudswamy *et al*.[487] confirmed the composition of this compound by infrared spectroscopy and chemical analysis. The $Cu(NH_4)_qMo_3S_9$ compound upon heating at 1273K for 5h under 6.5%H_2 + UHP Ar atmosphere directly yields $Cu_2Mo_6S_8$ Chevrel phase according to the following formula:

$$2Cu(NH_4)_qMo_3S_9 + 10H_2 = Cu_2Mo_6S_8 + 10H_2S + 2qNH_3 + qH_2 \qquad \text{Equation(xiv)}$$

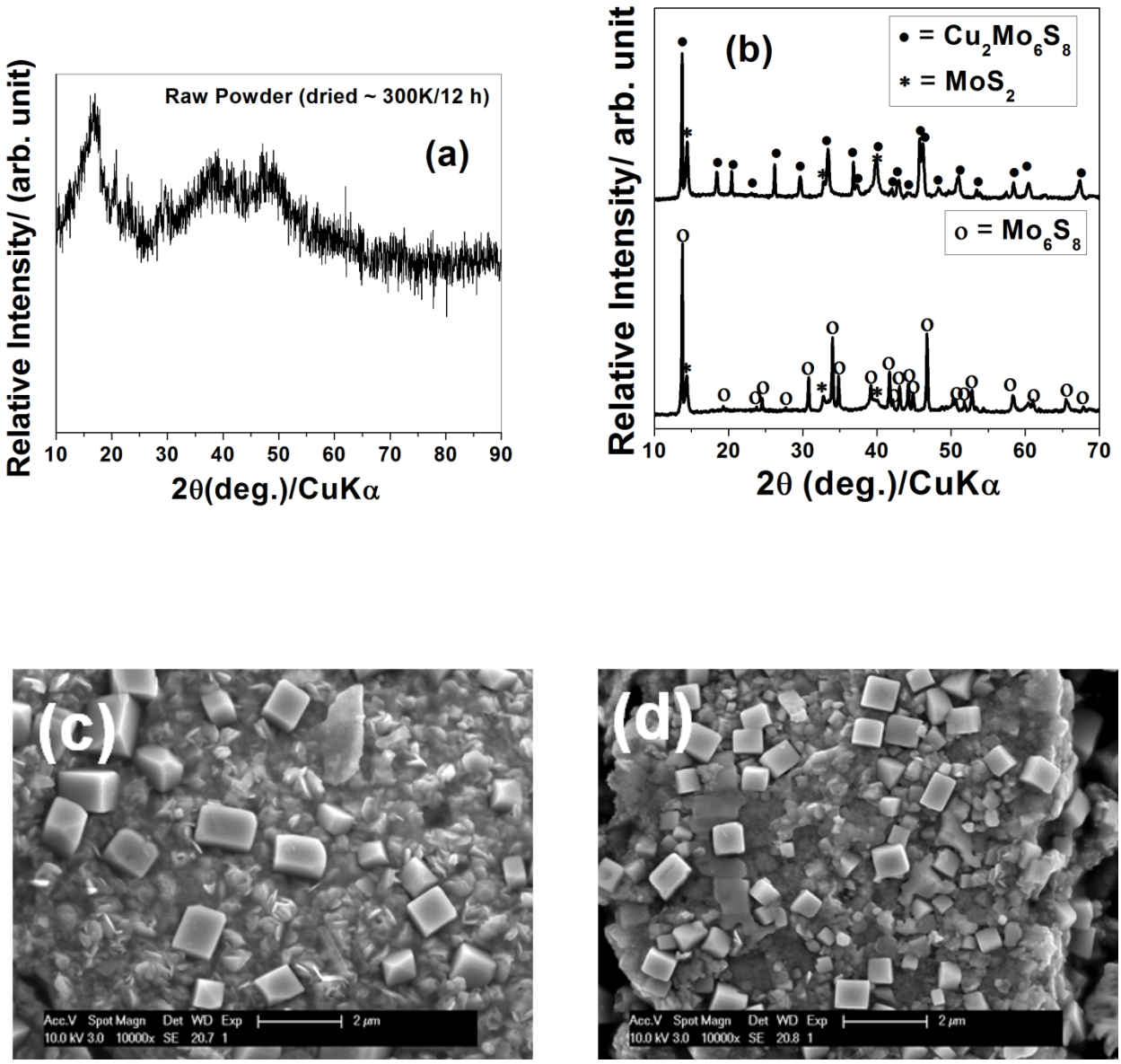

Figure 84. Powder XRD pattern of (a) as-prepared powder dried at room temperature for 12h, (b) heat treated powder showing the formation of $Cu_2Mo_6S_8$ (top) and acid leached showing the formation of Mo_6S_8 (bottom) (c) SEM images of $Cu_2Mo_6S_8$ and (d) Mo_6S_8 obtained after removing copper using acid treatment.

The heat treatment is a necessary step to form the cuprated Chevrel phase, Cu_2CP ($Cu_2Mo_6S_8$) from the $Cu(NH_4)_qMo_3S_9$ compound, which in fact is the basis of the current work to

synthesize Cu_2CP. **Figure 84b** shows the XRD pattern of the heat-treated Cu_2CP powder obtained by the precursor route. The Bragg diffraction lines were indexed to a hexagonal-rhombohedral symmetry unit cell of $Cu_2Mo_6S_8$ (space group: *R-3*; number: 148; JCPDS-ICDD: 00-047-1519). Lattice parameter(s) calculated using the least-square method of the experimental data (a = 0.96245 nm, c = 1.01987 nm, and unit cell volume = 818.14 × 10^{-3} nm^3) was in good agreement with the standard $Cu_2Mo_6S_8$ unit cell parameters (a = 0.9584 nm, c = 1.025 nm, unit cell volume = 815.36 × 10^{-3} nm^3). Similarly, **Figure 84b**-bottom exhibits the XRD pattern obtained after removal of copper from the heat-treated powder using hydrochloric acid treatment. The Braggs lines were indexed with the hexagonal-rhombohedral symmetry unit cell of Mo_6S_8 phase (space group: *R-3*; number: 148; JCPDS-ICDD: 00-027-0319), and the calculated lattice parameter(s) (a = 0.91944 nm, c = 1.08732 nm, and unit cell volume = 796.0424 × 10^{-3} nm^3) matched quite well with standard unit cell parameters of Mo_6S_8 obtained from the above ICDD database (a = 0.92 nm, c = 1.088 nm, unit cell volume = 797.51 × 10^{-3} nm^3). The calculated lattice parameters values are consistent with the standard lattice parameter(s) values of pristine $Cu_2Mo_6S_8$ and acid leached Mo_6S_8 powder obtained from the JCPDS-ICDD database which suggests that the solution chemistry route is a convenient approach for directly synthesizing the ternary Chevrel phase compounds; although, MoS_2 (space group: P63/mmc, number: 194, JCPDS number: 01-073 1508) phase was also formed as a minor second phase in both $Cu_2Mo_6S_8$ and Mo_6S_8 structures identified by the presence of peaks at 2θ = 14.4°, 32.8°, and 39.6°. Structural refinement of the powder XRD data conducted shows the formation of 1.4% MoS_2 as a second phase (not shown here). However, it can be seen from the XRD pattern of the Mo_6S_8 phase obtained following removal of Cu (shown above **Figure 84b**-bottom); the MoS_2 peak intensities are considerably reduced. We therefore believe that there is no detrimental effect of

the minor MoS_2 phase on the electrochemical performance of Mo_6S_8. The SEM images of $Cu_2Mo_6S_8$ and Mo_6S_8 powder shown in **Figure 84c** and **Figure 84d**, respectively, indicate that the sulfide formed exhibits unique cuboidal shaped particles in the ~1-1.5μm size range different from the morphology reportedly seen in other approaches. Removal of Cu does not alter the morphology of the particles indicating the pseudo-amorphous nature of the Cu removal leaching reaction although there may be a slight alteration in the particle sizes due to the change in the lattice parameter.

Figure 85a shows the cyclic voltammogram, recorded between 0.5-1.75 V employing a scanning rate of 0.01 mVs^{-1}, for the electrode (comprising 80% Mo_6S_8, 10% PVDF, 10% Super-P) utilzing a 0.4 M THF/2(PhMgCl)-$AlCl_3$ electrolyte solution. The CV curve indicates a highly reversible behavior for magnesium-ion insertion/extraction in the Mo_6S_8 phase similar to the expected electrochemical reactions observed in the literature [466, 479]. The anodic and cathodic peaks observed at ~ 1.05 V and ~ 1.17 V, correspond to the Mg^{2+} insertion/removal into/from the $Mg_xMo_6S_8$ ($0 < x < 2$) phase. Based on the cyclic voltammogram, it can be seen that there is no reaction occurring above 1.5V. Hence galvanostatic cycling was conducted only in the 0.5-1.5 V range. **Figure 85b** exhibits the variation of specific capacity *versus* cycle number along with Coulombic efficiency of the Mo_6S_8 electrode, cycled at a constant current of ~20mAg^{-1}(~C/6 rate) in the potential window of 0.5-1.5 V. As observed in **Figure 85b**, the 1st cycle discharge and charge capacity of the Mo_6S_8 electrode is ~ 116 $mAhg^{-1}$ and ~104 $mAhg^{-1}$, respectively, with a 1st cycle irreversible loss of ~ 10.3% (or Coulombic efficiency of ~89.7%). However, from the 2nd to 50th cycle we can see a stable charge and discharge capacity of ~80 $mAhg^{-1}$ and ~76 $mAhg^{-1}$, respectively with an improvement in Coulombic efficiency to ~95% similar to reports in

the literature. The 5% loss in Coulombic efficiency with each cycle could be attributed to ionic and electronic transport limitations.

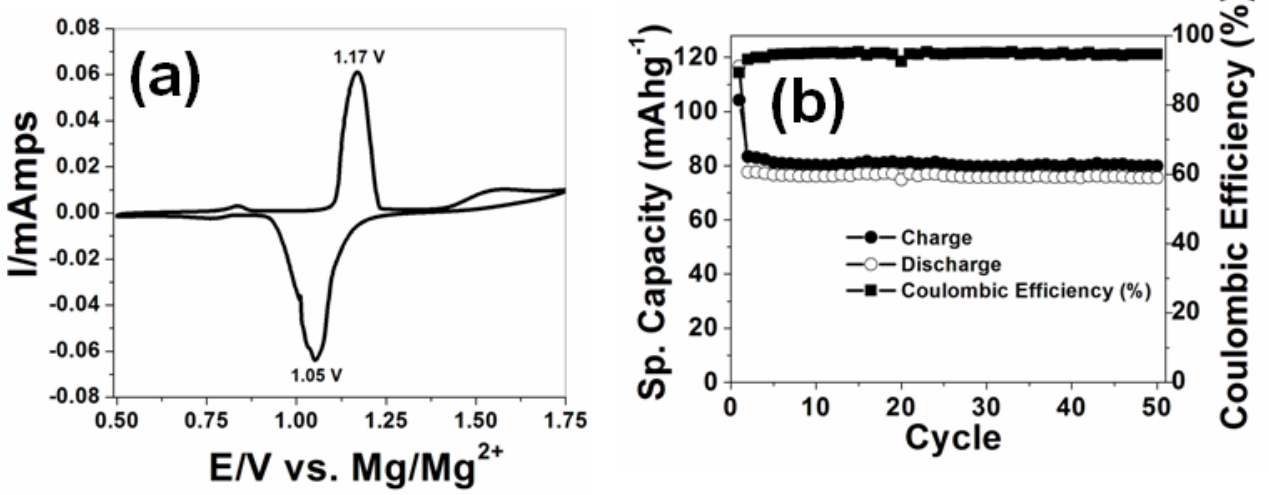

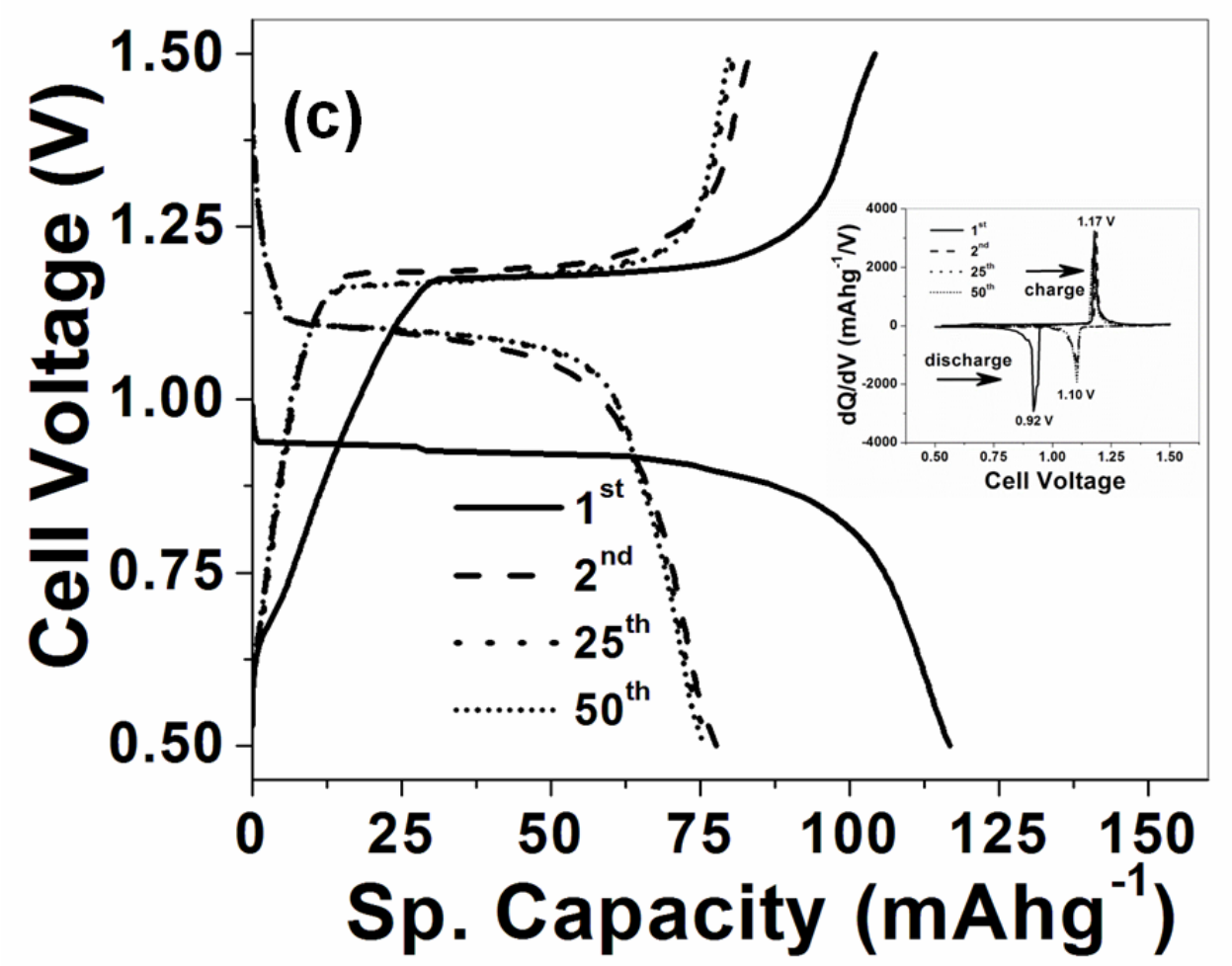

Figure 85. (a) A typical cyclic voltammogram (scan rate ~0.01 mVs^{-1}) of Mo_6S_8 electrode (active material ~3.92 mg/cm^2) coated on to graphite foil showing the reversible reactions, (b) Specific charge-discharge capacity and Coulombic efficiency *vs.* cycle number curves of Mo_6S_8 electrode cycled at a constant current of ~20mAg^{-1} in the potential window 0.5V-1.5V, (c) charge-discharge profiles (1^{st}, 2^{nd}, 25^{th}, and 50^{th} cycle) of the electrode comprising Mo_6S_8 at constant current rate of ~20 mAg^{-1}(~C/6 rate), and (inset) Differential capacity *vs.* cell potential curves of Mo_6S_8 electrode obtained after 1^{st}, 2^{nd}, 25^{th}, and 50^{th} cycle cycled at ~20mAg^{-1} in the potential window 0.5V-1.5V.

Figure 85c shows the galvanostatic charge-discharge profiles (1^{st}, 2^{nd}, 25^{th} and 50^{th} cycle) of the Mo_6S_8 electrode performed at a constant current rate ~ 20 mAg^{-1} (~C/6). It should be noted

that during the 1st cycle, Mg^{2+} insertion and extraction is observed at ~0.9 V, and ~1.2 V, respectively, whereas in the 2nd, 25th, and 50th cycles the reaction plateaus are observed at ~ 1.1 V (Mg^{2+} insertion) and at ~1.2 V (Mg^{2+} extraction), respectively. In order to identify the specific reaction voltages, the differential capacity versus voltage (dQ/dV vs. V) plots were plotted for the 1st, 2nd, 25th, and 50th cycle [shown in **Figure 85c**-inset]. It is observed that during the 1st discharge and charge cycle, magnesiation/demagnesiation occurs at 0.92 V and at 1.17 V respectively. However, from the 2nd cycle onwards the magnesiation reaction plateaus were shifted towards a higher voltage and the reaction peak was observed at 1.10 V (magnesiation) and at 1.17 V (demagnesiation) for the 2nd, 25th, and 50th cycles. A careful analysis of the charge-discharge profiles and dQ/dV (**Figure 85c**) versus voltage curves suggest that the initial Mg^{2+} insertion into Mo_6S_8 is kinetically limited, and thus intrinsically very slow at the current rate employed, requiring a slight overvoltage of ~ 200 mV from the equilibrium magnesiation potential of ~ 1.10 V [489].

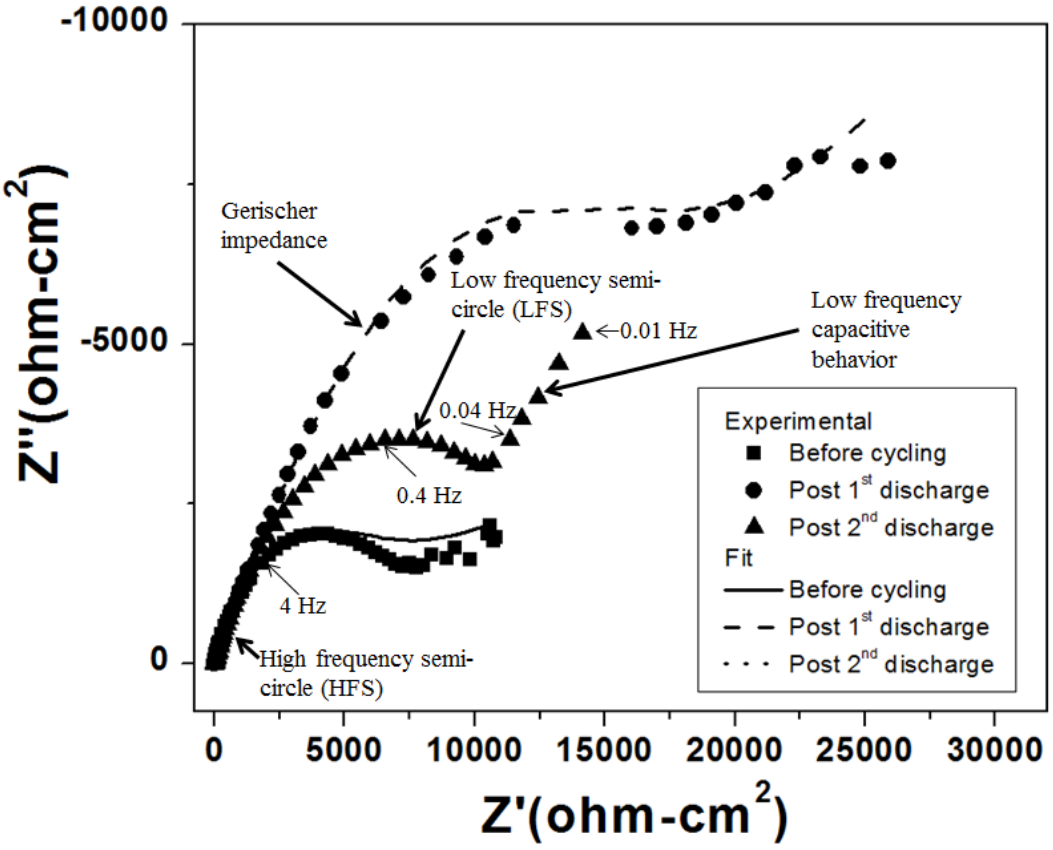

Figure 86. Nyquist plot of Chevrel phase electrode at different discharge states tested in a 2016 coin cell using 0.4 molar 2(PhMgCl)-$AlCl_3$ in tetrahydrofuran electrolyte over a frequency range of 100 KHz-0.01 Hz. The plot shows charge storage characteristics at different stages of cycling.

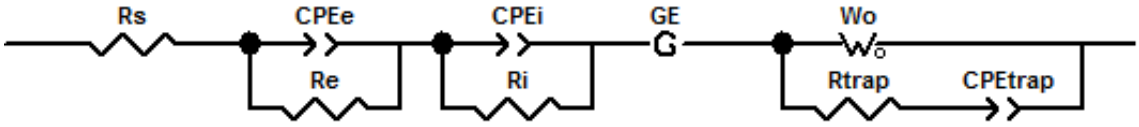

Figure 87. Randall's circuit used to model the experimentally obtained impedance data for magnesium insertion/extraction into the Chevrel phase. The model employed considers both charge transfer and mass transfer phenomena contributing to the electrode impedance.

In order to understand the discharge-charge phenomena and related loss in capacity during the 1st and 2nd cycle, electrochemical impedance study (EIS) was performed on the freshly prepared Mo_6S_8 electrode as well as cycled Mo_6S_8 electrode at the magnesiated (discharged) and de-magnesiated (charged) states assembled in a 2016 coin cell using magnesium foil as the counter and reference electrodes, Mo_6S_8 composite electrode as the working electrode and 0.4 molar 2(PhMgCl)-$AlCl_3$ in tetrahydrofuran as the electrolyte. **Figure 86** below depicts the Nyquist plot of the electrode prepared using the Chevrel phase (Mo_6S_8) at different stages. A clear transition in behavior can be observed upon cycling. The impedance behavior observed herein is in accordance with the previous published reports for Mg^{2+}-ion insertion-extraction phenomena observed in the Mo_6S_8 Chevrel phase [362, 490]. The impedance behavior depicted in **Figure 86** can be modeled using the circuit shown in **Figure 87**. The Randall's circuit shown therein considers a number of electrochemical phenomena including:

a) High frequency series resistance (R_s)
b) High frequency semi-circle (HFS) due to sluggish charge and electron transfer kinetics (CPE_e and R_e)
c) Gerischer impedance as a result of the coupling of a chemical and an electrochemical process (GE)
d) Low frequency semi-circle (LFS) due to Mg-ion trapping in the Chevrel phase (Mo_6S_8) host (CPE_i and R_i)
e) Diffusion characteristic and associated ion-trapping (W_o, R_{trap}, CPE_{trap})

Table 31. Charge transfer parameter(s) of the Chevrel phase electrode at different stages obtained from Randall circuit model of Figure 86

	R_s	CPE_e-T	CPE_e-P	R_e	CPE_i-T	CPE_i-P	R_i	GE-T	GE-P	W_o-R	W_o-T	W_o-P	R_{trap}	CPE_{trap}-T	CPE_{trap}-P
Before cycling	10.27	8.03E-06	0.974	286.4	8.49E-06	1.009	53.28	0.693	0.134	5.041	4.22E-06	0.393	2.32E-04	1.318E-04	0.125
After 1st discharge	12.36	4.88E-06	0.941	182.6	7.23E-05	0.821	9748	5.195	0.089	0.205	1.61E-07	0.416	3.01E-05	1.287E-04	0.294
After 2nd discharge	12.94	4.29E-05	0.76	921.2	1.14E-05	0.881	65.09	3.849	0.728	0.135	1.08E-07	0.375	8855	5.813E-04	0.479

In the case of the Chevrel phase host, it can be observed that a model comprised of all these elements can be used for circuit modeling. Unlike previous reports using only capacitance elements in the circuit shown in **Figure 87**, constant phase elements (CPEs) was incorporated on account of the porous nature of our electrodes. In addition, it was observed that the Gerischer impedance element (GE) reported to be a significant term during Mg^{2+}-ion insertion/extraction was found to be very small and insignificant in the case of the present electrode.

Figure 86 shows the effect of insertion/extraction on the impedance profile of the synthesized electrode materials. It can be clearly observed that the material exhibits a significant increase in overall impedance after the initial Mg^{2+}-ion insertion after the 1^{st} discharge cycle. **Table 31** depicts the values of resistances obtained as a result of Randall's circuit modeling. The solution resistance (R_s) is almost invariable. On the other hand, the charge transfer resistance (R_e) which is a characteristic of electron and ion transfer differs, pre and post Mg^{2+}-ion insertion stage. There is a drop in R_e post 1^{st} discharge and an increase from subsequent to 2^{nd} discharge. On the other hand, interfacial resistance increases post 1^{st} discharge and decreases subsequent to 2^{nd} discharge. Charge trapping (R_{trap}) which remains very small before cycling and post 1^{st} discharge, increases by almost 8 orders, post 2^{nd} discharge. The transition in these three parameters allows us to gain an insight into the Mg^{2+} charge storage mechanisms occurring in the Chevrel phase. The significant increase in overall impedance subsequent to first discharge indicates that the Mg^{2+}-ion insertion is accompanied by a rate limiting phenomenon. This in turn is seen by the two order rise in interfacial resistance (R_i) subsequent to 1^{st} discharge. The electrode resistance however, maintains the same order indicating that post-insertion in the 1^{st} discharge cycle, the electrode becomes kinetically limiting for electrochemical charge transfer processes as a result of the formation of either a secondary interface or a phase change. After the

2^{nd} discharge, however, the R_i is small but R_{trap} and R_e increase indicating that part of the layer is either inactive or becomes a barrier to solid state diffusion of Mg^{2+}. This mass transfer limitation and loss in magnesium trapped irreversibly as a result of the phase change occurring in the 1^{st} discharge cycle, we believe is the reason for the low capacity occurring from the 2^{nd} cycle onwards.

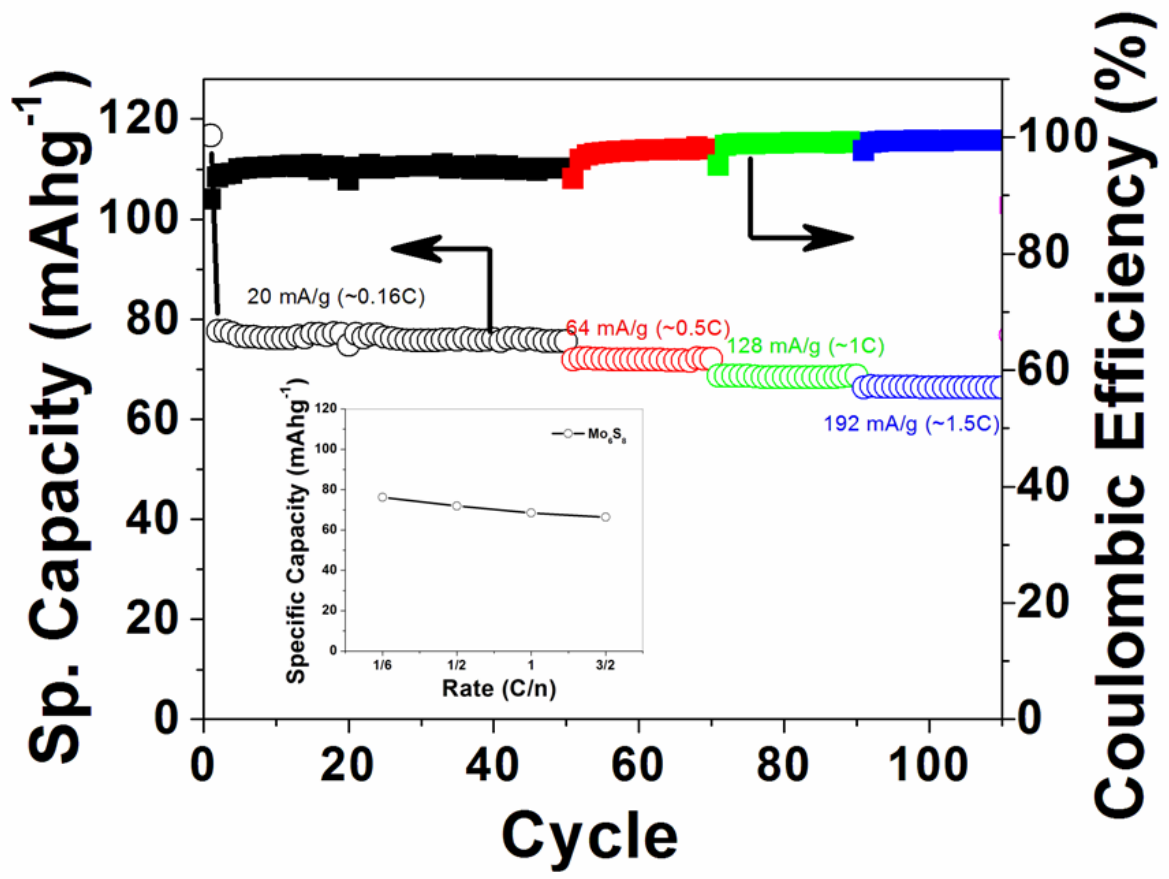

Figure 88. Rate performance of Mo_6S_8 electrode synthesized by solution precursor route cycled at various current rate of 20 mAg^{-1} (~C/6), 64 mAg^{-1} (~C/2), 128 mAg^{-1} (~C) and 192 mAg^{-1} (~1.5C), and (inset) Comparison between capacity vs. current rate.

In order to determine the electrochemical rate performance, the Mo_6S_8 electrode was cycled at various current rates. **Figure 88** shows the rate capabilities of the Mo_6S_8 electrode

tested at various current rates of 20 mAg^{-1} (~C/6), 64 mAg^{-1} (~C/2), 128 mAg^{-1} (~1C), and 192 mAg^{-1} (~1.5C). The discharge capacities at C/6, C/2, 1C and 1.5C rates were ~ 76 $mAhg^{-1}$, ~72 $mAhg^{-1}$, ~68 $mAhg^{-1}$, and ~66 $mAhg^{-1}$, respectively. It is observed that the capacity retention of the Mo_6S_8 electrode derived by the solution chemistry approach reported herein is excellent at various current rates. Moreover, it should be noted that the rate capability reported herein is much more improved compared to reported values in the literature to the best of the known information in the pubished literature. The Coulombic efficiency at ~C/6, ~C/2, ~1C, and ~ 1.5 C rate is observed to be 95%, 97.8%, 98.9%, and 99.3% respectively. It should be noted that a decrease in Coulombic efficiency with increasing C-rates is ordinarily to be expected. However, for the present scenario it is important to note that a relatively fast insertion/extraction of Mg^{2+} ions was evident within the Mo_6S_8 network at ambient temperature resulting in an improved Coulombic efficiency. Indeed, it is observed thus that at ~1.5C current rate, Mo_6S_8 electrode shows only 13% decrease in capacity from the initial capacity of ~66 mAh/g, compared to the discharge capacity of ~76 $mAhg^{-1}$ observed at ~C/6 rate [see **Figure 88** (inset)].

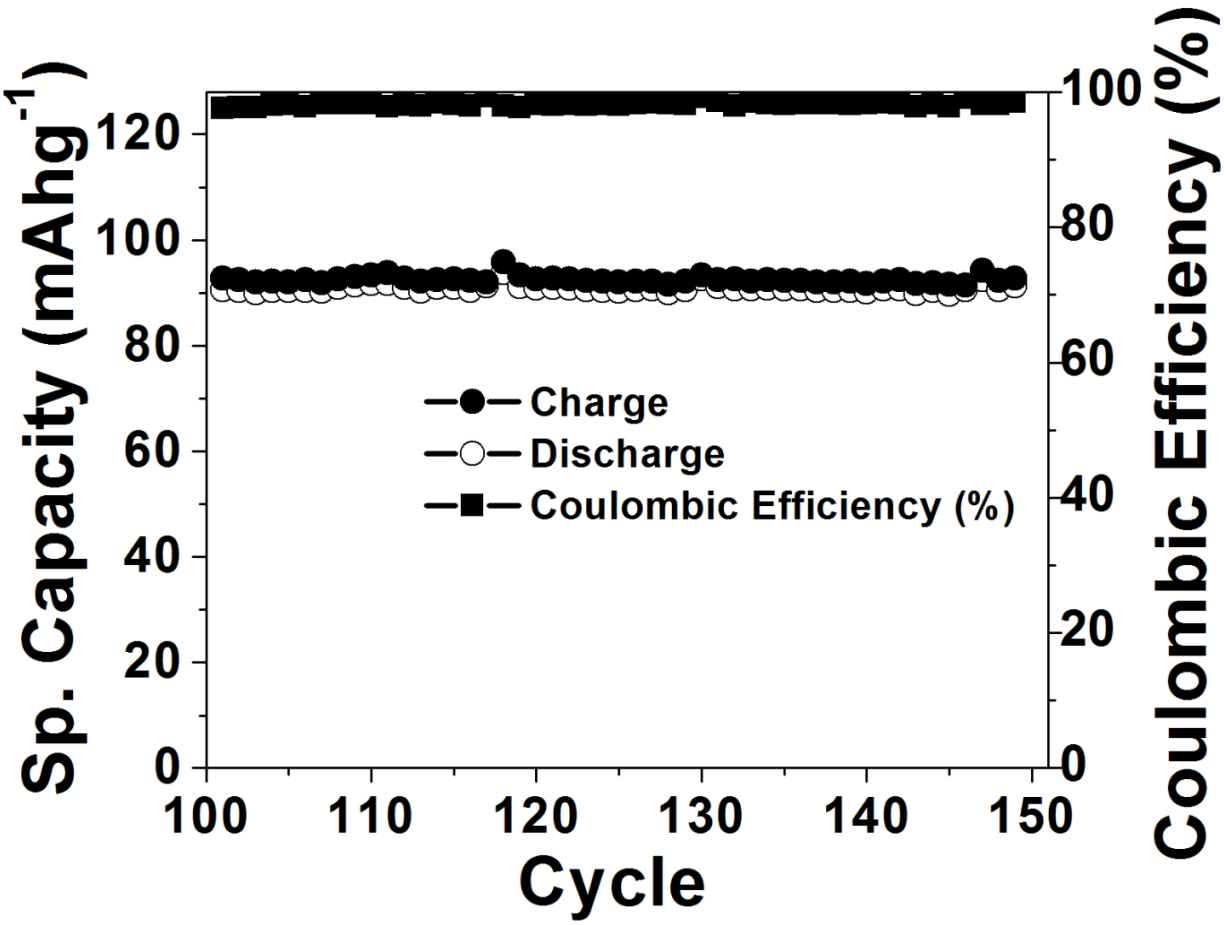

Figure 89. Specific charge-discharge capacity and Coulombic efficiency *vs.* cycle number curves of Mo_6S_8 electrode cycled at a constant current of ~20mAg^{-1} in the potential window 0.5 V-1.8 V.

It is established that Mg^{2+} insertion into the Mo_6S_8 Chevrel phase occurs in two stages, and theoretically can offer a capacity ~ 128 mAhg^{-1}. However, due to partial charge entrapment commensurate with EIS data discussed above, after initial magnesiation only 60-80% magnesium-ion can be extracted during the first charge, resulting in a 20-25% capacity loss from the theoretical value (~128 mAhg^{-1}) [491]. Indeed, it is true that the complete removal of Mg^{2+} ion is therefore not possible at ambient temperature due to the partial trapping of Mg^{2+} in the Mo_6S_8 host lattice as observed in the literature [492]. The second Mg-ion can only cycle when the cell operates at elevated temperature (~323-343K) primarily due to improved kinetics of Mg-ion

diffusion into Mo_6S_8 phase and consequently the loss in capacity can be salvaged [493]. Since, the 2016 coin cell was cycled at ambient condition; the Mg^{2+} trapping observed after the 1st discharge cycle (magnesiation) is certainly to be expected. Moreover, cyclic voltammetry conducted between 0.5-1.75 V shows the 2 step Mg-ion insertion/extraction peaks although careful observation suggests that the second Mg-ion extraction peak is observed ~1.47 V which is within the potential limit of galvanostatic cycling data between 0.5-1.5 V. Nevertheless, to obtain a better understanding, the 2016 coin cell was cycled between 0.5-1.8 V at room temperature under identical galvanostatic conditions (current rate ~20mA/g or ~C/6 rate). **Figure 89** shows the typical galvanostatic charge-discharge cycling curve along with Coulombic efficiency from 101-150 cycles indicating marginal improvement in terms of electrochemical performance (specific discharge capacity ~90.8 mAh/g, specific charge capacity ~ 92.5 mAh/g and Coulombic efficiency = 98.2%). All of the above electrochemical results observed in the present study therefore truly indicate the excellent capacity retention of the Mo_6S_8 phase probably due to the formation of micrometer sized cuboidal shaped Mo_6S_8 crystals allowing better wetting characteristics of the active electrode with the electrolyte while also enabling rapid transport of the Mg^{2+} ions.

B.2.4 Conclusion

In summary, unique cuboidal shaped ~1-1.5 μm sized Mo_6S_8 Chevrel phase crystals was synthesized using a rapid solution chemistry route followed by heat treatment under 6.5%H_2 and UHP Ar atmosphere. X-ray diffraction data shows that the calculated unit cell parameters of $Cu_2Mo_6S_8$ and copper leached Mo_6S_8 powder is consistent with the standard unit cell parameters, suggesting that the present method offers a convenient approach for the synthesis of Chevrel

compounds. Electrochemical measurements of Mo_6S_8, obtained by acid leaching of copper from $Cu_2Mo_6S_8$, exhibited excellent galvanostatic cycling performances such as rate capability and high discharge capacity (~76 $mAhg^{-1}$ at C/6 rate). Mo_6S_8 when assembled in a prototype 2016 coin cell delivered a capacity of ~ 66 $mAhg^{-1}$ at ~1.5 C rate with ~99.3% Coulombic efficiency at ambient temperature indicating a much higher rate capability response compared to previous reports thus rendering the solution chemistry route an attractive and convenient approach for likely scaled up synthesis of Mo_6S_8 and other electrochemically active Chevrel phase compounds for magnesium battery.

B.3 SODIUM BATTERIES

B.3.1 Introduction

The worldwide electricity consumption is predicted to triple by the end of century warrant a clear roadmap for economical and sustainable energy solution for future generation due to increasing global population [494]. Renewable energy sources such as solar and wind generates electricity intermittently and forecasted to meet the future energy demand at affordable cost. However, electricity generated from intermittent energy sources require stationary EES devices work in tandem for effective storage and uninterrupted delivery of power during demand[14, 293, 339, 495]. Chemical energy storage based rechargeable batteries can fulfill the above dream and afford a cost-effective solution[14, 293, 339, 495, 496]. However, the technologically superior advanced Li-ion batteries (LIB) developed for portable electronics and electric vehicles are still under consideration for stationary EES stringent requirements of low cost ($100/kWh) and safety[496-498].

NaS, ZEBRA, vanadium-redox flow batteries although successfully demonstrated as large-scale EES, however, require high temperature for operation and has safety issues [465]. Therefore there is a need to make provision for alternative chemistries to enter into the market beyond LIBs which are cheaper and have abundant global reserve [498].

Recently, sodium-ion batteries (SIB) generated lot of interest due to various technical reasons[498-501]. Sodium and lithium both are group-1 elements and possess identical chemical properties. Sodium has almost inexhaustible natural reserve (sodium is 4th most abundant on earth, ~2.6% by weight of the earth's crust; whereas lithium present ~0.0007% by weight of the earth's crust) and touted to be cheaper (cost equivalent of dollars for bulk metal: Na: 0.075, Li: 0.50)[174, 502-504]. In addition, Na-ion is also chemically more stable compared to Li-ion system and environmentally benign in nature [504]. Based on the several above factors ambient temperature SIB's appears lucrative and provide ample rationale for use in stationary EES in the future. [174, 502-505].

Various high capacity anodes have been proposed for Na-ion batteries that can deliver a specific capacity ~200-600 $mAhg^{-1}$ based on sodium alloying/de-alloying principle for metal Sn [506], Sb [507] anodes or Na-ion adsorption phenomena in the nanopores of hard carbon [508]. Contrary to the Li-ion battery system, the research and development efforts for developing high voltage and high capacity cathode materials for sodium-ion battery are limited. A large number of oxide cathode materials have been extensively investigated and proposed as potential electrodes for sodium-ion batteries, such as P2-Na_xCoO_2 [509], P2-$Na_{2/3}[Ni_{1/3}Mn_{2/3}]O_2$ [510], $Na_{0.44}MnO_2$ [511-513], P2-$Na_x[Fe_{1/2}Mn_{1/2}]O_2$ [501], P2-$Na_{2/3}[Co_{2/3}Mn_{1/3}]O_2$ [514]. Among them, Layered Na_xMnO_2 ($0 < x \leq 1$; M = Mn, Ni, Co) has received considerable interest as a promising cathode material for Na-ion battery due to its structural similarity with well known Li-ion battery electrodes $LiMO_2$ (M =

Mn, Ni, Co). Depending on the sodium content in the Na_xMnO_2, three dimensional orthorhombic tunnel structures of *Pbam* symmetry (Na/Mn < 0.45) or two dimensional monoclinic layered phases (0.45 ≤ Na/Mn ≤ 0.7) are obtained during synthesis reported in literatures [515, 516]. The nomenclature of these layered compounds includes an alphabet and number that denotes the distinguishable crystal structure and alkali metal present in the layers first used by Delmas and co-workers (e.g. P3 means that the environment is prismatic and the unit cell is consists of three MnO_2 sheets) [517]. The P2-type proved the best choice in terms of battery performance among the different Na_xMnO_2 phases and able to deliver sp. capacity ~120 $mAhg^{-1}$ with the Na^+ de-intercalation/intercalation reaction occurring between ~2.0-3.8V. However, there was rapid capacity decay after first few cycles in the P2-type Na_xMnO_2 phase due to structural instability caused by Jahn-Teller distortion of Mn^{3+} [518]. Another practical issue plauging the layered P2-type Na_xMnO_2 phases is the presence of hydrated phases and the difficulty associated to remove the water molecules present which inevitably collapse the layer framework. The O3-type layered Na_xMnO_2, $NaNi_{0.5}Mn_{0.5}O_2$, or $NaNi_{1/3}Mn_{1/3}Co_{1/3}O_2$ also exhibits capacity of 105-125 $mAhg^{-1}$ when cycled between 2.2-3.8V. Komaba *et al.* [519] showed that layered O3-type $Na_1Ni_{0.5}Mn_{0.5}O_2$ (space group: $R\bar{3}m$) able to deliver 1st cycle capacity ~185 $mAhg^{-1}$ when charged to ~4.5 V but leads to structural transformation from O3 to O′3, P3, P′3, and finally to monoclinic P3″ phase during progressive sodium extraction and marked by concomitant changes in the stacking sequences of $[Ni_{0.5}Mn_{0.5}]O_2$ slab distances leading to rapid decay in capacity after 10 cycles. On the other hand, orthorhombic $Na_{0.44}MnO_2$ (*Pbam* symmetry) which consist of MnO_6 octahedra and MnO_5 square pyramids forming S-shape tunnels for Na ion hopping [511, 513, 520, 521] showed a constant biphasic phenomena during sodium-ion extraction/insertion between 2-3.8V leading to very low specific capacity for practical use. Pyrophosphates family of compounds $Na_2MP_2O_7$ (M

= Fe, Mn, Co etc.) first proposed by Yamada *et al*. [522] showed a specific capacity ~80-90 $mAhg^{-1}$ when cycled at slow current rate of ~C/20. Apart from the oxide and phosphate mentioned above, NASICON compounds- $Na_3M_2(PO_4)_3$ [M = transition metals], fluorophosphates- $NaVPO_4F$ [523], $Na_3V_2(PO_4)_2F_3$ [524], Na_2FePO_4F, [525] Na_2MnPO_4F, $Na_2(Fe,Mn)PO_4F$] [526], and Prussian blue derivative compounds- $KMnFe(CN)_6$, $Na_xMnFe(CN)_6$ [527-529] have been proposed as high voltage cathodes for sodium-ion batteries. However, most of the layered oxides, phosphates, NASICON compound exhibit irreversible phase transformation, sloping voltage plateaus; large difference in voltages during Na^+ intercalation/de-intercalation phenomena preclude their use as cycle stable cathodes for Na-ion batteries.

In addition to the sodium bearing oxides, phosphates, fluorophosphates, insertion type host such as Fe_3O_4 [530], MoS_2 [531], FeF_3 [532], etc. are also considered promising cathodes for Na-ion batteries. Among them, Chevrel phase Mo_6T_8 (T =S, Se) materials family are well-known compounds which can intercalate univalent (Li^+, Na^+, Cu^+), bivalent (Zn^{2+}, Cd^{2+}, Ni^{2+}, Mg^{2+}) cation at room temperature within the Mo_6T_8 open, rigid framework (comprising Mo_6-clusters within anion cubes) due to their intrinsic high electronic conductivity [533]. Recently, Mo_6S_8 has been proposed as a model cathode for magnesium battery [478]. However, Mo_6S_8 and Mo_6Se_8 Chevrel phases have never been fully explored as potential Na-ion host. Gocke [534] and Tarascon [535] in the late eighties studied the electrochemical Na-ion intercalation phenomena in the Chevrel phases and provided information about the irreversible sodium intercalation behavior, occurrence of partial charge trapping during 1^{st} sodiation in Chevrel phase etc. Inspired from the above work, it was decided to extend the electrochemical investigations on Mo_6S_8 phase prepared by the time saving wet chemistry, molten salt (MS) route and Mo_6Se_8 developed by the high energy mechanical milling (HEMM) route as potential Na-ion host for room temperature sodium ion

battery (SIB). The electrochemical behaviors of Na/Mo_6S_8 and Na/Mo_6Se_8 cell were evaluated using CV, galvanostatic cycling at different C-rates, EIS and discussed in details.

B.3.2 Experimental Section

Synthesis of $Cu_xMo_6S_8$ Chevrel phase

$Cu_xMo_6S_8$ (Cu_xCP-1) and Mo_6S_8 (CP-1) obtained by leaching copper from the parent phase were synthesized by two different established routes. In the first case, $Cu_xMo_6S_8$ was synthesized by two-step solution chemistry route reported elsewhere [536]. Briefly, in a 3-neck flask, stoichiometric amount of ammonium tetrathiomolybdate (4g, 15.37mmol; Alfa-Aesar 99.95%) and anhydrous copper (II) chloride (0.6890g, 5.12mmol, Alfa-Aesar 99.985%) was added to *N.N*, dimethylformamide, DMF (130ml) solution. The resultant mixture was heated over a hot plate (~363K) for 6h under constant N_2 gas. After complete reaction, the deep red mixture was filtered, tetrahydrofuran (~5 times by volume) was added to the filtrate to incipient precipitation. The resultant black precipitate was collected, washed with tetrahydrofuran and methanol followed by 12h drying at room temperature [488]. The dried agglomerate upon heating at ~1273K for 5h under ultra-high purity Ar + 6.5% H_2 atmosphere yielded the ternary Chevrel Phase $Cu_{1.8}Mo_6S_8$ [487]. Cu_xCP-1 was also synthesized by MS route according to the method outline by Lancry *et al*. [481]. Potassium chloride-KCl (99.7% JT Baker) was used as solvent and dried for 3h at 423K prior to use. Molybdenum disulfide (1g, 99% Alfa Aesar), cupric sulfide (0.398g, 99.8% Alfa Aesar) and molybdenum powder (0.602g, 99.9% Alfa Aesar) were hand ground with 4g KCl in a mortar pestle for 15 min and immediately transferred into a corundum crucible. The salt mixture was then heated to 1123K at a ramp of 423K/h and held for 60h followed by furnace cooling to room temperature under ultra-high purity Ar atmosphere. The obtained product was

washed with de-ionized water four times and ultra sonicated for 20min to wash any remaining salt and de-agglomerate the particles.

Novel Approach to synthesis of $Cu_xMo_6Se_8$ Chevrel phase

$Cu_xMo_6Se_8$ (Cu_xCP-2) was synthesized for the first time using the HEMM approach. Stoichiometric amount of $MoSe_2$ (1.141g, 99.9% Alfa Aesar), Mo (0.432g, 99.9% Alfa Aesar), and CuSe (0.427g, 99.5% Alfa Aesar) were batched in a stainless steel vial (powder: ball ratio = 1:10). The powders were mechanically milled for 1h, 2h, and 3h duration and subjected for XRD analysis. After 3h milling, the powder was heat-treated at 1273K for 5h under ultra-high purity(UHP) Argon atmosphere to yield the Cu_xCP-2. Copper-ions were leached from both solution chemistry and molten salt derived Cu_xCP-1 and HEMM derived Cu_xCP-2 phase using 6 MHCl solution under constant bubbling of oxygen for 8h in ambient atmosphere [484]. After complete removal of copper from the parent phase, the acid solution containing the residue was centrifuged, washed with the de-ionized water three times and dried in an oven at ~323K. Powder X-ray diffraction (XRD) was carried out using the Philips PW1830 system employing the CuK_α (λ=0.15406nm) radiation. Quantitative phase analysis was carried out using PANalytical X'Pert HighScore-Plus Rietveld program on the powder XRD patterns. Microstructural analyses of the Chevrel phases were performed using a scanning electron microscopy (JSM-6610, JEOL) operating at 10kV and high resolution transmission electron microscopy-HRTEM (JEOL JEM 2000FX) operating at 200 kV.

Electrochemical Characterization

Electrode slurry was formulated by mixing 80 wt.% of active material (-325 mesh), 10 wt.% Super-P carbon, 10 wt.% polyvinylidene fluoride (PVDF) binder with *N*-methylpyrrolidinone (NMP) solvent together in a glass vial with constant magnetic stirring for 24h. The slurry thus

obtained was coated (50 μm thick) onto graphite foil acting as a current collector and dried at ~383K overnight in a vacuum oven. Further, the dried electrodes were uniaxially pressed at ~5 MPa to improve the particle contact and then disks (Θ = 11.28 mm) were punched with an active material loading ~1-3 mg/cm^2. Electrochemical test was carried out at room temperature with 2016-type coin cells assembled inside an argon-filled MBraun Inc. glove box (< 0.1 ppm each of O_2 and H_2O) employing sodium metal foil as the counter and reference electrode, electrode disks as working electrode, and Celgard® separator soaked in an electrolyte solution of 1 M $NaClO_4$ in ethylene carbonate: dimethyl carbonate (v:v = 1:2 ratio). Cyclic voltammogram (CV) was acquired using an electrochemical workstation (VersaSTAT 3, Princeton Applied Research) between 1.2-2.2V at a constant sweep rate of ~$0.001Vs^{-1}$. Galvanostatic charge-discharge cycles were carried out at various rates ~20-240 mAg^{-1} within 1.2-2.2V, employing a short rest period between the charge/discharge cycles using a multichannel battery testing system (Arbin BT2000 instrument). Electrochemical impedance spectroscopy (EIS) was performed to obtain a fundamental understanding of charge storage mechanisms at different stages of cycling and to monitor the electrode interfacial impedance in both the solution chemistry derived CP-1 and the HEMM derived CP-2 Chevrel phases. Electrochemical impedance spectroscopy (EIS) was performed on the Versastat 3 over a frequency range of 0.01Hz-100KHz. A.C. amplitude of 5 mV was used and the spectra were obtained at different voltages during 1^{st} and 2^{nd} charge/discharge cycles. (Dis)charge in these cases was performed by linear scan voltammetry at $0.0001Vs^{-1}$ and electrode potential was stabilized before EIS was performed (immediately so that no significant relaxation processes and equilibrium phase changes occurred). The charge transfer characteristics and accompanying parameters were analyzed by equivalent circuit modeling using Z-View (Scribner Associates, Inc.; version 3.3).

B.3.3 Results and Discussion

Synthesis of $Cu_xMo_6S_8$/Mo_6S_8 and electrochemical performance of Mo_6S_8 *versus* sodium

Figure 90a depicts the XRD pattern of the Cu_xCP-1 obtained by solution chemistry approach. The essence of solution chemistry approach is that it reduces the total furnace heating time down to 5h compared to 60h required for molten salt (MS) route for direct synthesis of ternary CP [536]. The Bragg peaks of the XRD pattern recorded between 2θ values of 10°-90° matches quite well with the ternary copper Chevrel phase of $Cu_{1.8}Mo_6S_8$ composition.

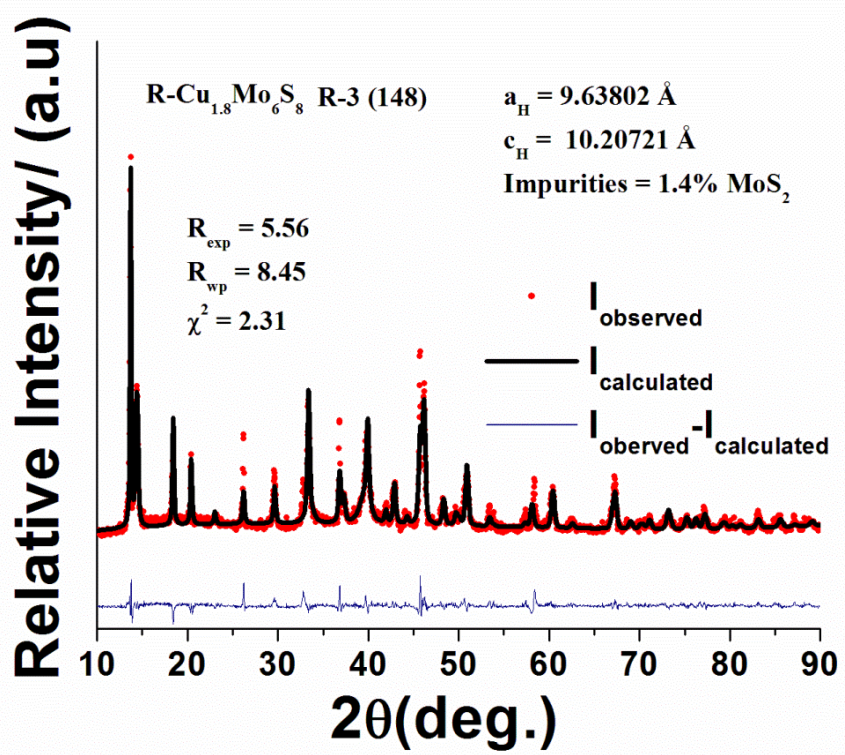

a)

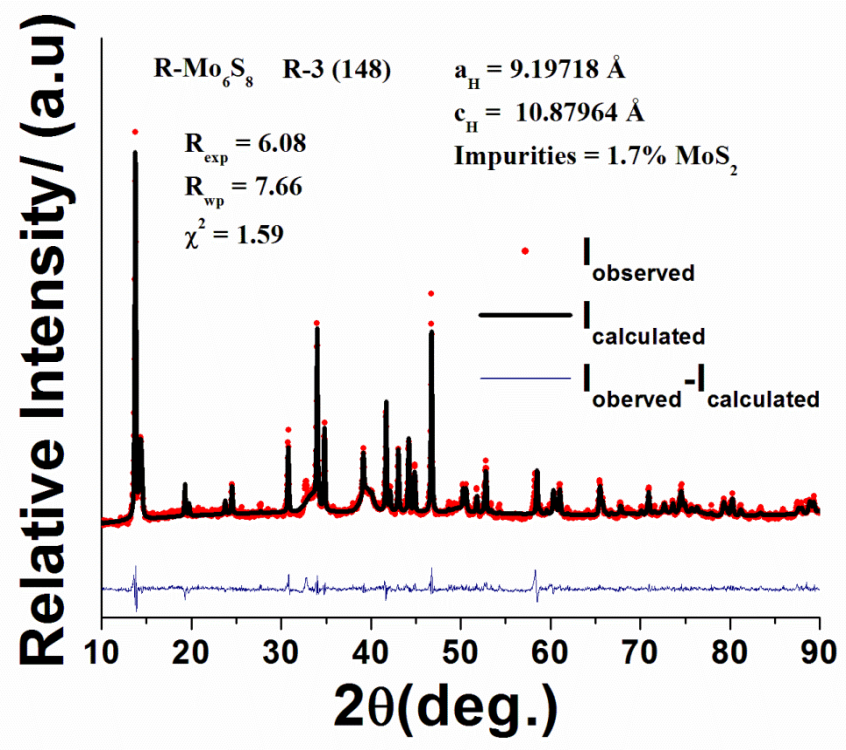

b)

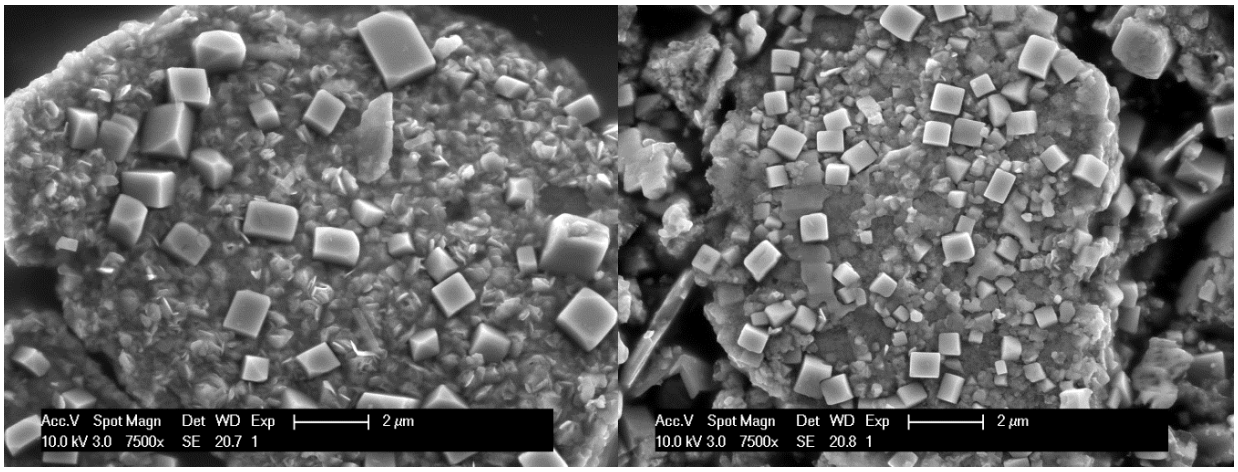

c) d)

Figure 90. Powder XRD patterns and the Rietveld refinement results using Le Bail fit for (a) $Cu_{1.8}Mo_6S_8$, (b) Mo_6S_8 and SEM images for (c) $Cu_{1.8}Mo_6S_8$, and (d) Mo_6S_8 obtained from wet chemistry route.

The peaks were indexed with the rhombohedral phase (*R-3*) of $Cu_{1.8}Mo_6S_8$ (JCPDS-ICDD: 98-012-1726) and minor MoS_2 impurity phase (JCPDS-ICDD: 98-008-3546) crystallized in hexagonal symmetry (*R3m*). The experimental XRD pattern was refined according to the Le-Bail model using structural parameters of $Cu_{1.8}Mo_6S_8$ in hexagonal symmetry [space group: *R-3*] and MoS_2 [space group: *R3m*]. The major parameter(s) refined were scale factors, zero shifts, unit cell, and Pseudo-Voigt peak shape and profile parameters. The agreement indices in the simulated pattern gives the best-fit value of weighted R profile- R_{wp} =8.45%, R expected- R_{exp} = 5.56%, and goodness of fit- $\chi 2$ = 2.31 with 98.6% of $Cu_{1.8}Mo_6S_8$ and 1.4% of MoS_2 phase. Calculated lattice parameter(s) obtained from simulating the experimental data were (*a* = 0.963802 nm, *c* = 1.020721 nm, and unit cell volume = 821.1325 × 10^{-3} nm^3) for $Cu_{1.8}Mo_6S_8$ phase. The de-cuprated Chevrel phase (Mo_6S_8) XRD pattern resemble quite well with Mo_6S_8 pattern (JCPDS-ICDD 27-0319) and with minor unreacted MoS_2 as shown in **Figure 90b**. The agreement indices were found in the simulated as weighted R profile- R_{wp} =7.66%, R expected- R_{exp} = 6.08%, and goodness of fit- $\chi 2$ = 1.59 with 98.3% of Mo_6S_8 and 1.7% of MoS_2 phase. Lattice parameter(s) obtained from simulating the experimental data were (*a* = 0.919718 nm, *c* = 1.087964 nm, and unit cell volume = 796.993 × 10^{-3} nm^3) for Mo_6S_8 was in agreement with the standard values. The SEM image of the $Cu_{1.8}Mo_6S_8$ phase shown in **Figure 90c** obtained during solution chemistry approach shows the formation of cuboidal shape particles between ~1-1.5μm ranges. The cuboidal shape particles retain its morphology in the leached product but appears slightly rectangular in shape due to expected increase in the c/a ratio of Mo_6S_8 phase from the $Cu_{1.8}Mo_6S_8$ phase illustrated in **Figure 90d**.

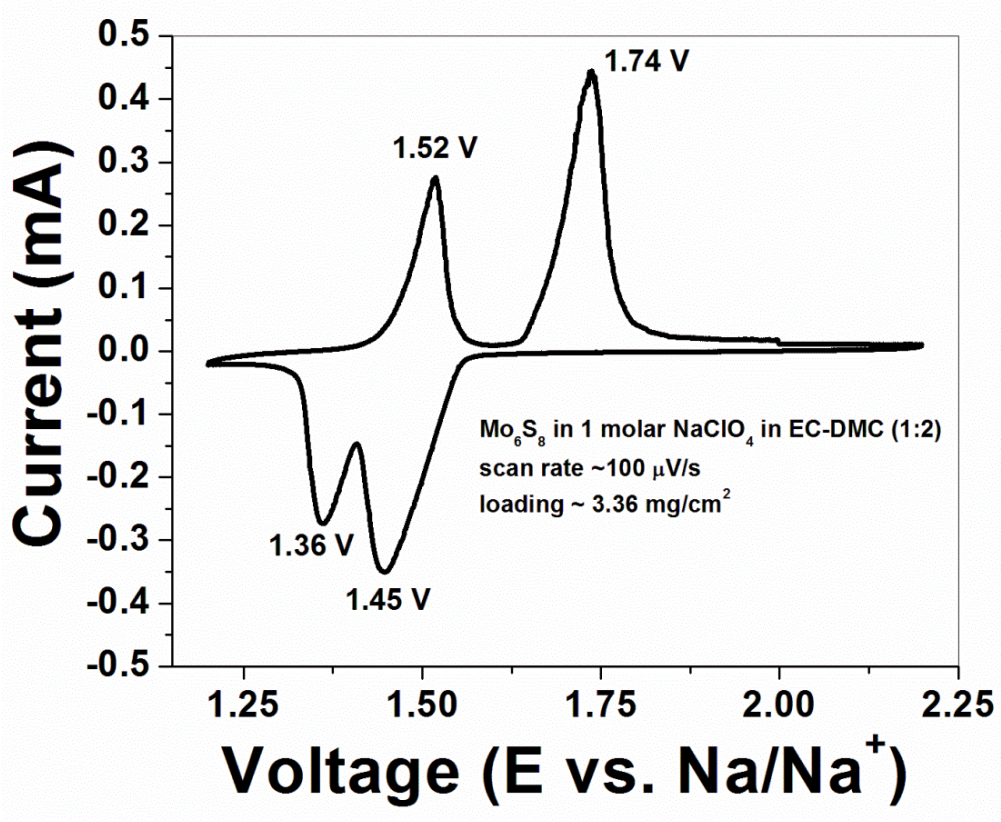
Current (mA)
Voltage (E vs. Na/Na+)
1.74 V
1.52 V
1.36 V
1.45 V
Mo6S8 in 1 molar NaClO4 in EC-DMC (1:2)
scan rate ~100 μV/s
loading ~ 3.36 mg/cm2

a)

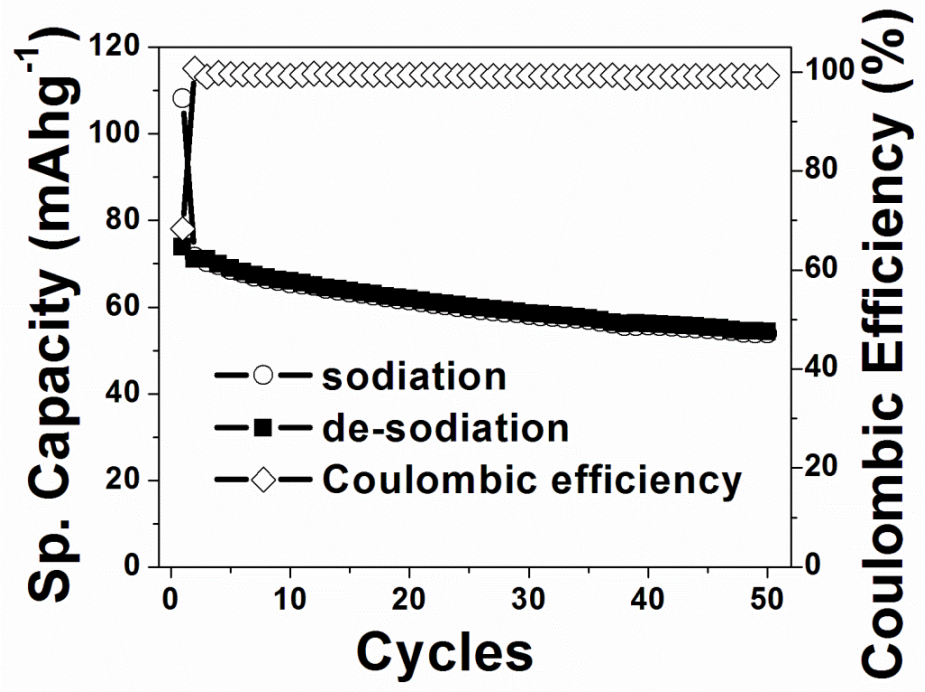
Sp. Capacity (mAhg-1)
Coulombic Efficiency (%)
Cycles
sodiation
de-sodiation
Coulombic efficiency

b)

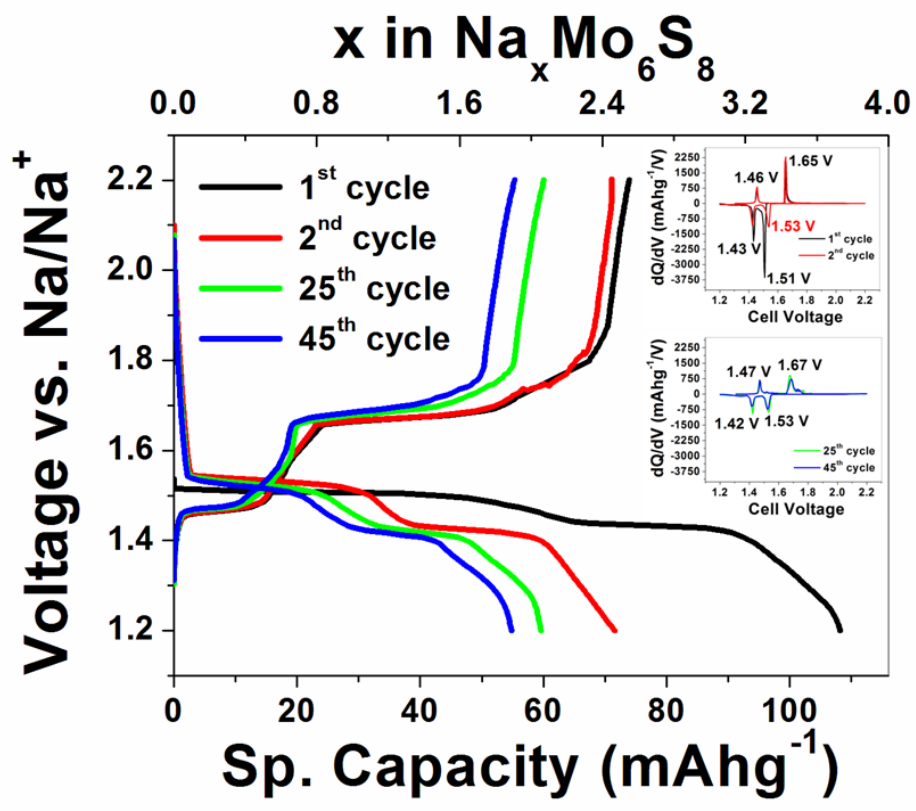
x in Na$_x$Mo$_6$S$_8$
0.0
0.8
1.6
2.4
3.2
4.0
Voltage vs. Na/Na$^+$
2.2
2.0
1.8
1.6
1.4
1.2
1st cycle
2nd cycle
25th cycle
45th cycle
0
20
40
60
80
100
Sp. Capacity (mAhg^{-1})
dQ/dV (mAhg^{-1}/V)
1.46 V
1.65 V
1.53 V
1.43 V
1.51 V
1st cycle
2nd cycle
Cell Voltage
1.47 V
1.67 V
1.42 V
1.53 V
25th cycle
45th cycle
Cell Voltage

c)

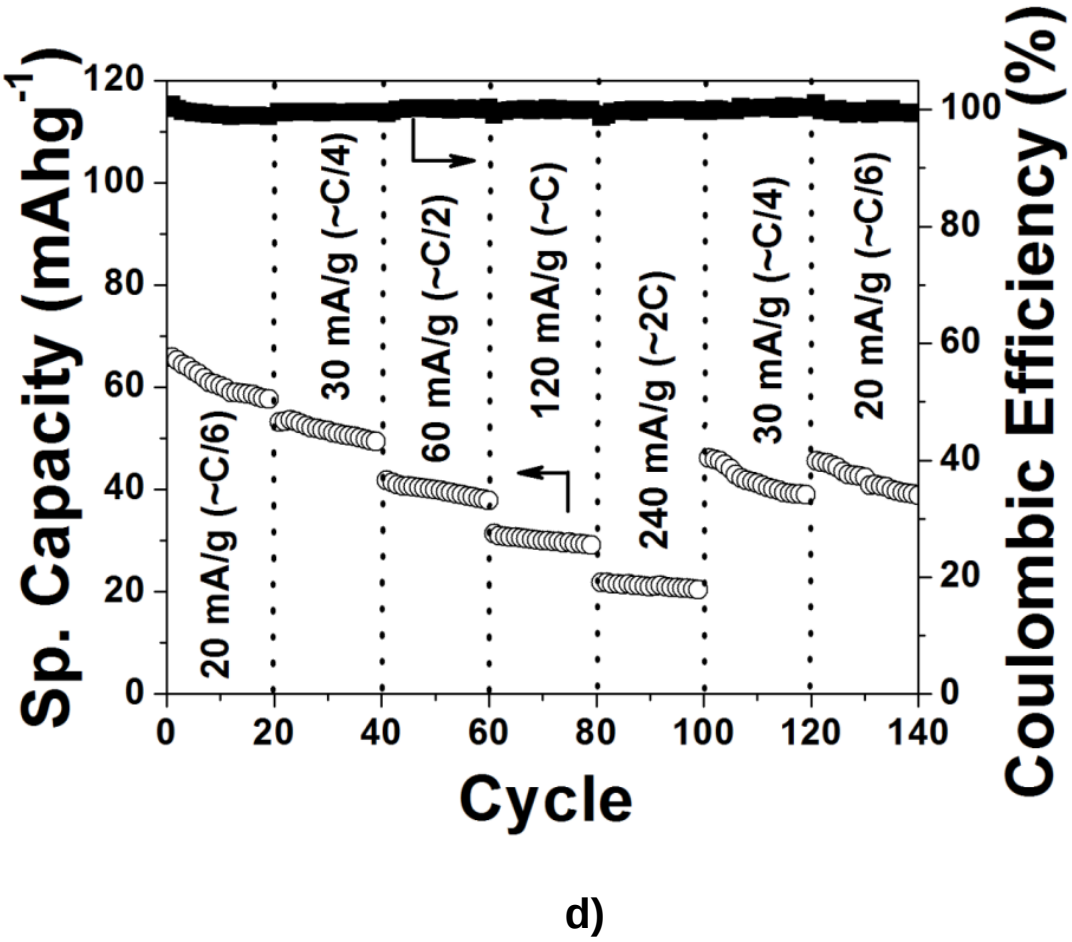

d)

Figure 91. (a) Cyclic voltammogram at a scan rate of 0.0001Vs^{-1}, (b) charge/discharge capacity versus cycle number curve along with Coulombic efficiency, (c) voltage versus capacity profile along with dQ/dV versus voltage (inset), and (d) rate performance of wet chemistry derived Mo_6S_8 electrodes.

A typical CV curve presented in **Figure 91a** indicates a highly reversible two-step Na-ion insertion/extraction behavior in the Mo_6S_8 phase. The cathodic peaks observed at ~1.45V and ~1.36V, correspond to the Na-ion insertion into the $Na_xMo_6S_8$ ($0 < x < 4$). Similarly, the anodic peaks observed at ~1.52V and ~1.74V correspond to the removal of Na-ion from the sodiated Chevrel phase $Na_xMo_6S_8$. **Figure 91b** exhibits the variation of specific capacity *versus* cycle number along with Coulombic efficiency of the Mo_6S_8 electrode. The 1st cycle sodiation and de-sodiation capacity of the Mo_6S_8 electrode is ~108 mAhg^{-1} (~93% of theoretical capacity ~116

$mAhg^{-1}$) and ~74 $mAhg^{-1}$, respectively, with a 1st cycle Coulombic efficiency of ~68.3%. From the 2nd to 50th cycle it can be seen that an average discharge (sodiation) and charge (de-sodiation) capacity of ~60.7 $mAhg^{-1}$ and ~60.3 $mAhg^{-1}$, respectively, was obtained with an improvement in Coulombic efficiency to ~99.3%. **Figure 91c** depicts the voltage versus capacity plots of 1st, 2nd, 25th, and 45th cycle. A two-steps reaction observed during 1st sodiation cycle, where Na-ions insert into open channels of Mo_6S_8 phase at two different voltages; corresponding to a total 3.7 Na-ions insertion according to the following formula.

$$3.7Na^+ + Mo_6S_8 + 3.7e^- = Na_{3.7}Mo_6S_8$$

Figure 91c shows that during 1st cycle sodiation, two voltage plateaus [similar to the peaks in dQ/dV *versus* voltage curves shown in **Figure 91c(inset**)] observed in the voltage versus capacity curve are lies at ~1.51V, and ~1.43V. The complete 1st discharge profile can be decoupled into two parts and it appears that the 1st sodiation occur at ~1.51V to deliver a total capacity of ~ 59 $mAhg^{-1}$ (equal to 2Na-ions intercalation into Mo_6S_8 host) and the 2nd sodiation occur ~1.43V with a specific capacity of ~ 49 $mAhg^{-1}$ (equal to 1.7Na-ions intercalation into Mo_6S_8 host). Two different 1st cycle sodiation reactions can therefore be expressed according to the following formula.

$$2Na^+ + Mo_6S_8 + 2e^- = Na_2Mo_6S_8 \text{ observed at ~1.51V versus } Na^+/Na$$

$$1.7Na^+ + Na_2Mo_6S_8 + 2e^- = Na_{3.7}Mo_6S_8 \text{ observed at ~1.43V versus } Na^+/Na$$

$$\text{Total: } 3.7Na^+ + Mo_6S_8 + 4e^- = Na_{3.7}Mo_6S_8 \qquad \text{Equation (xv)}$$

However, during the reverse 1st charge cycle (de-sodiation) there was a loss in capacity and the observed capacity was ~74 $mAhg^{-1}$ (see **Figure 91c)**. The associated Na-ion extraction or de-sodiation reactions from the $Na_{3.7}Mo_6S_8$ phase occur at two different voltages of ~1.46V and ~1.65V, respectively, as exhibited in dQ/dV versus voltage curves in **Figure 91c(inset**). Similar

to the 1st cycle discharge profile, the charge profile can also be decoupled into two parts, where 1st de-sodiation occurs at ~1.46V with an associated capacity of ~ 24 $mAhg^{-1}$ (equal to $0.83Na^{+}$-ions extraction from $Na_{3.7}Mo_6S_8$) and the 2nd de-sodiation occurs at ~1.65V with an associated capacity of ~ 50 $mAhg^{-1}$ (equal to $1.7Na^{+}$-ions extraction from $Na_{2.87}Mo_6S_8$). The complete de-sodiation reactions can thus be expressed as follows:

$$Na_{3.7}Mo_6S_8 - 0.83Na^{+} - 0.83e^{-} = Na_{2.87}Mo_6S_8 \text{ observed at ~1.46V versus } Na/Na^{+}$$

$$Na_{2.87}Mo_6S_8 - 1.7Na^{+} - 1.7e^{-} = Na_{1.17}Mo_6S_8 \text{ observed at ~1.65V versus } Na/Na^{+}$$

$$\text{Total: } Na_{3.7}Mo_6S_8 - 2.53Na^{+} - 2.53e^{-} = Na_{1.17}Mo_6S_8 \qquad \text{Equation (xvi)}$$

The reaction voltage observed during 2nd cycle sodiation/de-sodiation was similar to that of 1st cycle. However, a careful analysis of the 2nd cycle charge-discharge curves in **Figure 91c** and dQ/dV versus voltage profiles in **Figure 91c (inset)** clearly demonstrates that the first sodiation reaction was shifted towards slightly higher voltage (~0.02V) for the 2nd cycle and occur at ~1.53V, but there was no change however, in the remaining sodiation and de-sodiation reactions which was evident in the plateaus of voltage versus capacity curve or peaks into dQ/dV *versus* voltage profile (red line). It is believed that the slight difference in the reaction voltage between first sodiation in the 1st and 2nd cycle (~0.02V) may arise due to different chemical potential for Mo_6S_8 and $Na_{1.17}Mo_6S_8$. The observed sodiation and de-sodiation capacity in the 2nd cycle was ~71.6 $mAhg^{-1}$ and ~71.1 $mAhg^{-1}$, with ~99.3% Coulombic efficiency suggests that Na-ion insertion into Mo_6S_8 is highly reversible in nature. It also gives an indication that from the 2nd cycle onwards, $Na_{\sim 3.7}Mo_6S_8$ and $Na_{\sim 1.2}Mo_6S_8$ phase become stable between the two extremities of sodiation/de-sodiation reactions indicating the ability to cycle ~2 Na-ions in reversible manner. The sodiation capacity although drops to ~60 $mAhg^{-1}$ and ~55 $mAhg^{-1}$ in the 25th and 45th cycles respectively, which may be due to ionic or electronic transport limitation or partial

entrapment of Na-ions within the Mo_6S_8 framework during progressive cycles. This can be best argued as there was no apparent change in the cathodic/anodic peaks corresponding to sodiation and de-sodiation for 25^{th} and 45^{th} cycle as evident from dQ/dV versus voltage curves. The electrochemical rate performance of the Mo_6S_8 electrode was also excellent when cycled at various current rates.**Figure 91d** shows the rate capabilities of the Mo_6S_8 electrode tested at various current rates of 20 mAg^{-1} (~C/6), 30 mAg^{-1} (~C/4), 60 mAg^{-1} (~C/2), 120 mAg^{-1} (~1C), and 240 mAg^{-1} (~2C). The average discharge capacities at C/6, C/4, C/2, 1C and 2C rates were ~60.8 $mAhg^{-1}$, ~51.5 $mAhg^{-1}$, ~39.8 $mAhg^{-1}$, ~30.1 $mAhg^{-1}$ and ~21.1 $mAhg^{-1}$, respectively. It is observed that the capacity retention of the Mo_6S_8 electrode derived by the solution chemistry approach is excellent at various current rates. The Coulombic efficiency at ~C/6, ~C/4, ~C/2, ~1C, and ~2C rate was found to be 99.2%, 99.5%, 99.9%, 99.8%, and 99.7%, respectively.

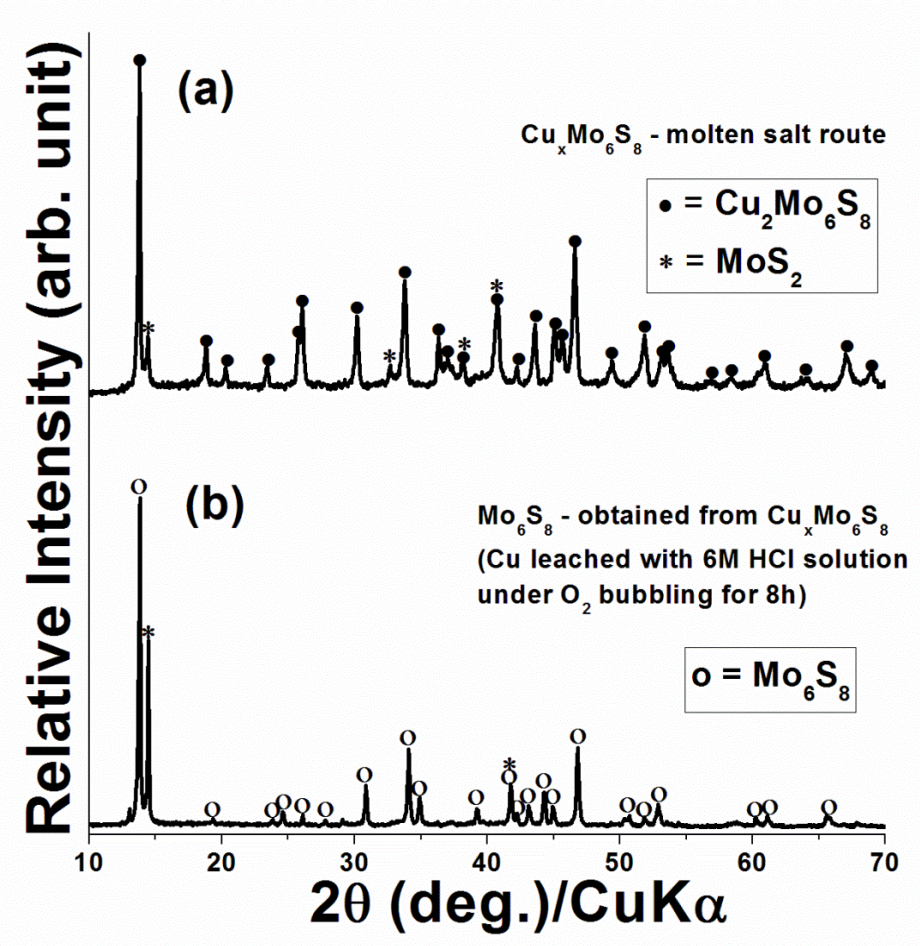

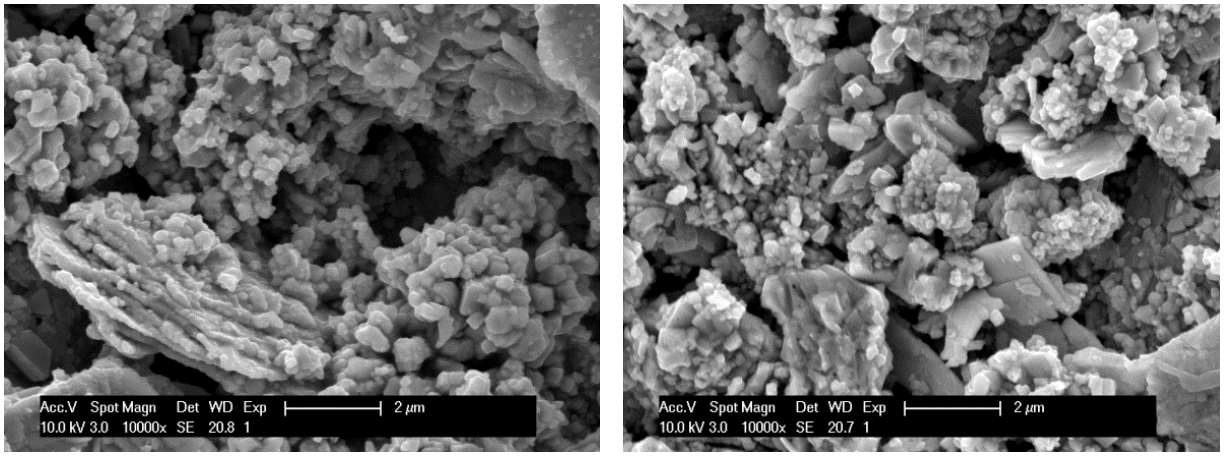

c) d)

Figure 92. Powder XRD patterns for (a) $Cu_2Mo_6S_8$ (b) Mo_6S_8 and SEM images for (c) $Cu_2Mo_6S_8$ and (d) Mo_6S_8 obtained from molten salt route.

In order to verify the accuracy of the electrochemical (de)sodiation data observed on wet chemistry derived Mo_6S_8 phase, electrochemical performance was also evaluated on Mo_6S_8 derived by the known molten salt (MS) synthesis route found in literature[481] and compared with solution chemistry approach. **Figure 92a-Figure 92b** shows the XRD pattern of the MS route derived Cu_xCP-1 and CP-1 phase, respectively. The major Bragg peaks of the XRD pattern was in good agreement with the synthetic product of Lancry *et al.* [481] and can be indexed with the rhombohedral phase (R-3) of $Cu_2Mo_6S_8$ and Mo_6S_8 with slight presence of minor unreacted MoS_2. It is important to note that Lancry *et al.* [481] also observed similar XRD pattern after the Cu-ions were leached using acid treatment. **Figure 92c and Figure 92d** show the SEM image of the heat treated powder of Cu_xCP-1 and CP-1 phase, respectively. It appears that irregular spherical particles of $Cu_2Mo_6S_8$ were formed which retains this morphology completely in the de-cuprated Chevrel phase. Electrochemical performance of the molten salt derived de-cuprated Mo_6S_8 phase was examined at room temperature (~300K) in a 2016 coin cell. The electrochemical performance was excellent and a similar trend with that of the solution chemistry derived de-cuprated Mo_6S_8 phase discussed earlier. Specific capacity and Coulombic efficiency versus cycle plot illustrated in **Figure 93a** shows the 1st cycle sodiation and de-sodiation capacity was ~84 mAhg^{-1} and ~74 mAhg^{-1} with 1st cycle Coulombic efficiency ~ 88.2%. The observed sodiation and de-sodiation capacity in the 2nd cycle was ~76.5 mAhg^{-1} and ~74.7 mAhg^{-1}, with ~97.7% Coulombic efficiency. From the 6th cycle onward a steady and stable Coulombic efficiency close to ~99.7% was observed. The observed average sodiation (~64.2 mAhg^{-1}) and de-sodiation capacity (~64.0 mAhg^{-1}) between 6th and 46th cycles were remain extremely stable with ~0.3% minimal irreversible loss per cycle. The voltage versus sp. capacity curves of 1st, 2nd, 25th, and 45th cycles presented in **Figure 93b** also shows a two-steps

sodiation/de-sodiation reaction similar to the reaction patterns shown in **Figure 91c**. The above results clearly showcase that ~2Na-ion can electrochemically inserted/extracted from Mo_6S_8 host in reversible manner irrespective of the synthesis route.

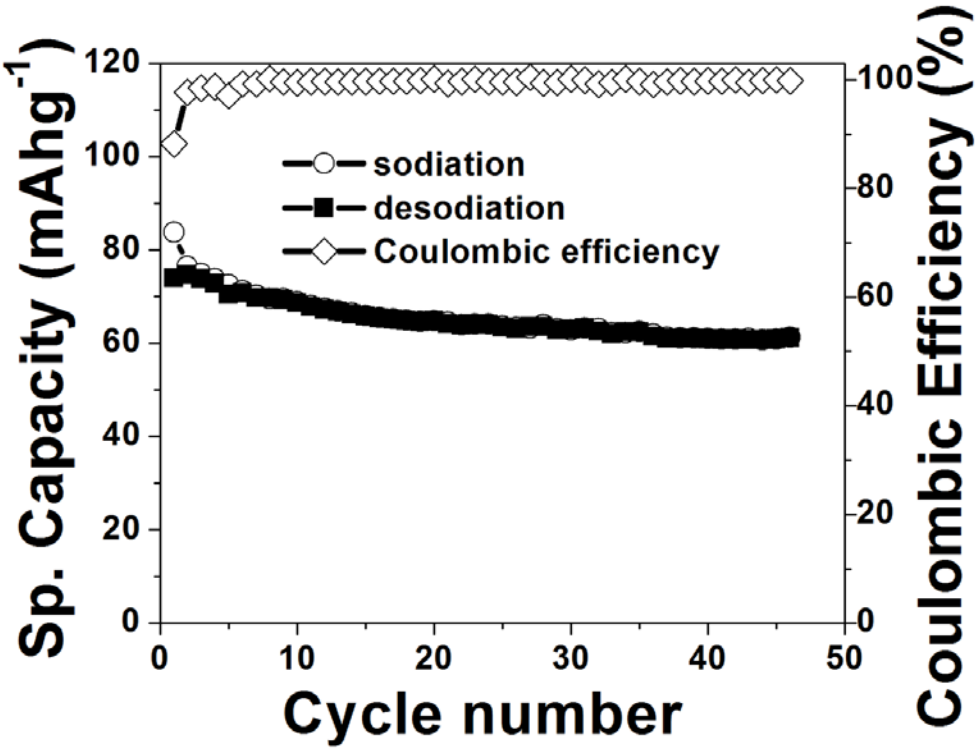

a)

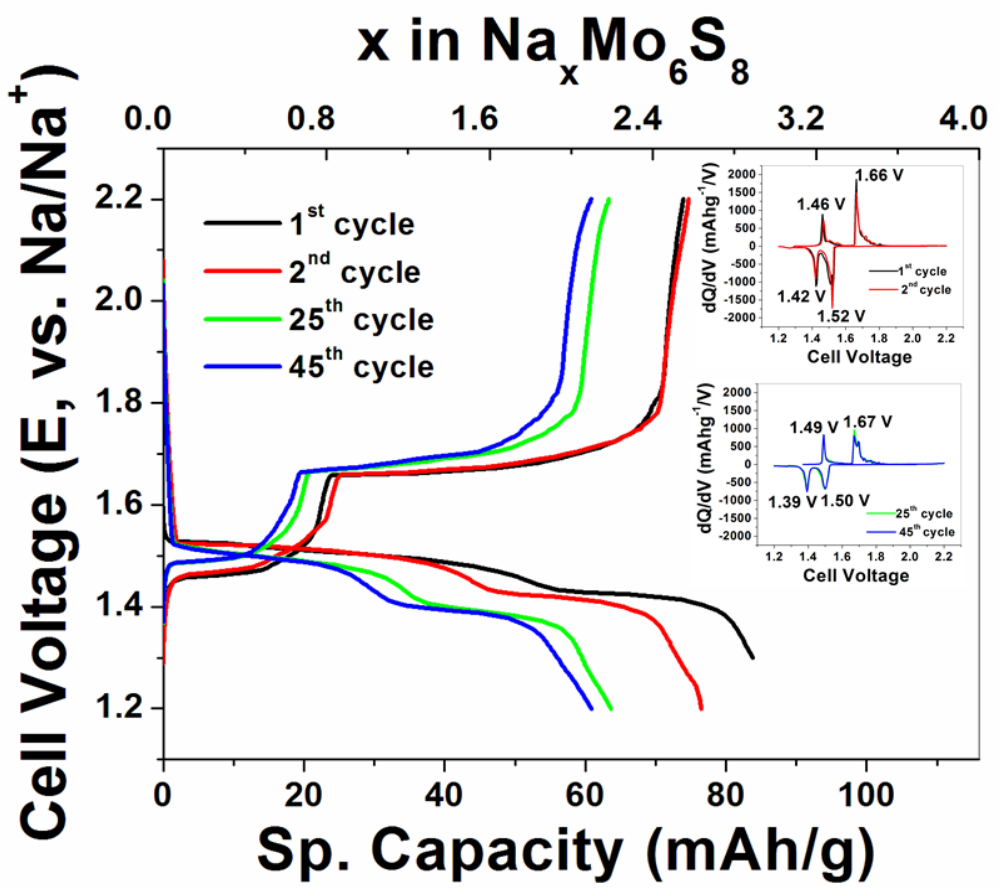

b)

Figure 93. (a) Charge/discharge capacity versus cycle number curve along with Coulombic efficiency, (b) voltage versus capacity profile along with dQ/dV versus voltage (inset), of molten salt derived Mo_6S_8 electrodes.

HEMM Synthesis of $Cu_xMo_6Se_8$/Mo_6Se_8 and electrochemical performance of Mo_6Se_8 *versus* sodium

$Cu_xMo_6Se_8$ (Cu_xCP-2) was also synthesized first time by high energy mechanical milling (HEMM) approach using CuSe, $MoSe_2$ and Mo precursor powder. In order to understand the effect of milling on the phase formation, each commercial powder (as-received) was subjected for XRD pattern and compared along with the 3h mechanically milled powder. **Figure 94a**

shows the XRD patterns of 3h mechanically milled powder along with the commercial powders. It appears that 3h mechanically milling induces a homogeneous mixture where the Bragg reflection of high intensity peaks from $MoSe_2$, Mo and CuSe are evident. However, 3h mechanical milling induces broad X-rays peaks indicating the formation of pseudo-amorphous $MoSe_2$ and CuSe phases may be due to formation of ultrafine particles which significantly decrease the peak intensity. On the contrary, the Braggs reflection from (011), (002), (112), and (022) planes scattered from elemental Mo were found relatively intense. The difference in peak intensities was largely due to ductile and hard Mo metal powder repeatedly get fractured and cold welded whereas brittle and soft $MoSe_2$, and CuSe ceramic phase get fragmented and embedded within the ductile Mo matrix during milling operation[537]. Importantly, absence of any oxides of copper and molybdenum during milling operation suggest that HEMM yielded a phase pure homogeneous mixture between the constituents. However, it is to be noted that direct mechanical milling do not form the desired ternary CP which require heating at elevated temperature under inert atmosphere to form the desired phase.

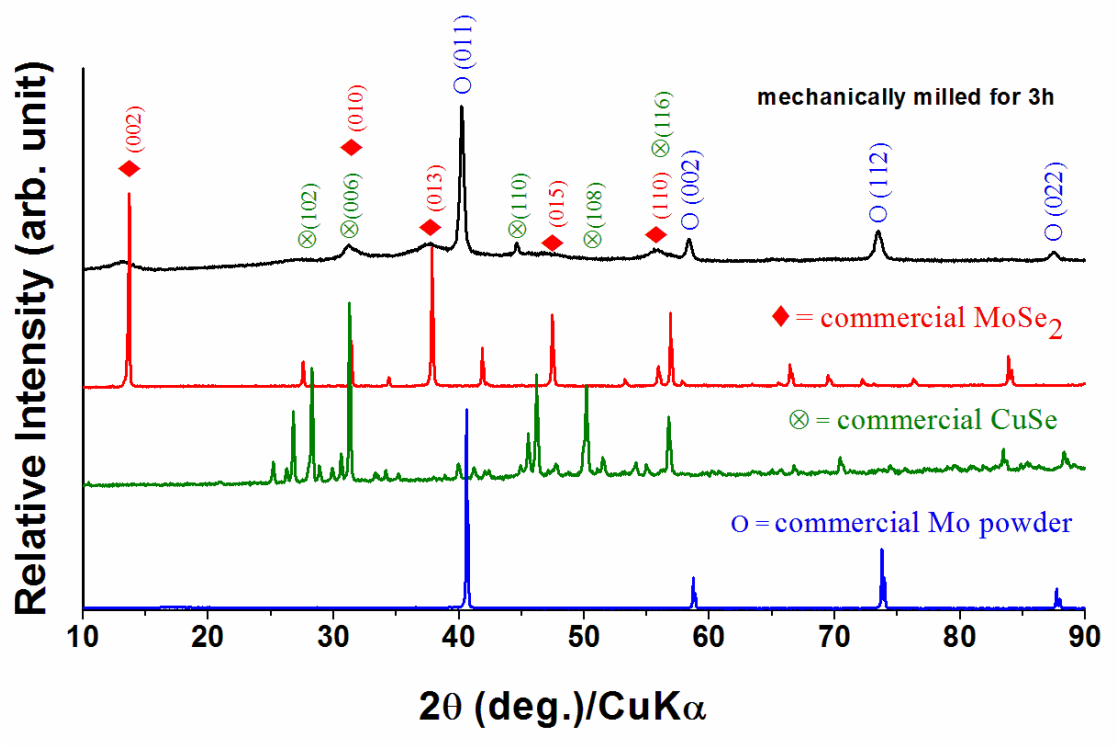
mechanically milled for 3h
(002)
(010)
O (011)
⊗(102)
⊗(006)
(013)
⊗(110)
(015)
⊗(108)
(110)
⊗(116)
O (002)
O (112)
O (022)
♦ = commercial MoSe2
⊗ = commercial CuSe
O = commercial Mo powder
Relative Intensity (arb. unit)
2θ (deg.)/CuKα

a)

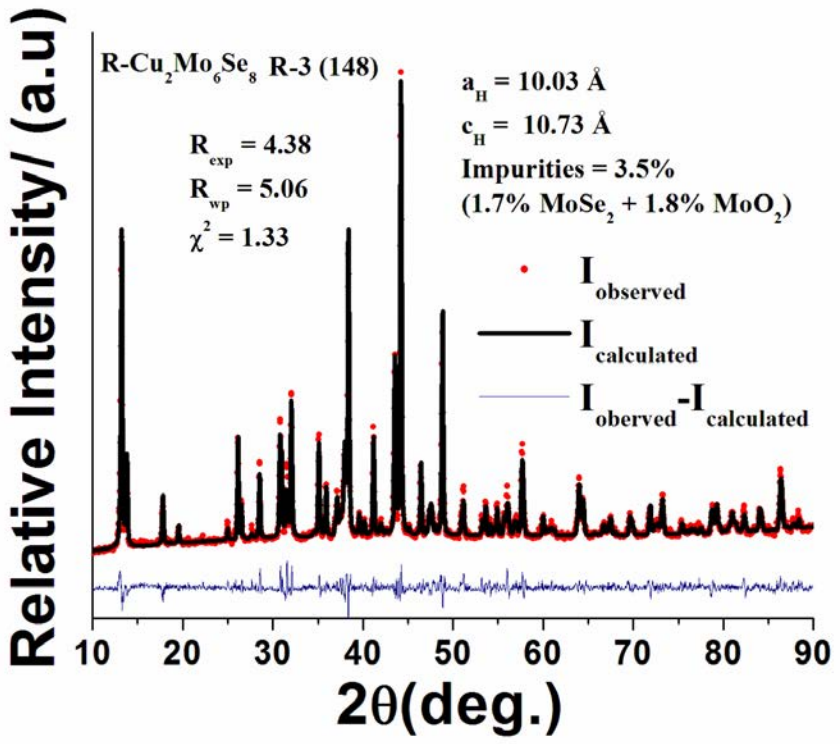
R-Cu2Mo6Se8 R-3 (148)
aH = 10.03 Å
cH = 10.73 Å
Rexp = 4.38
Rwp = 5.06
χ2 = 1.33
Impurities = 3.5%
(1.7% MoSe2 + 1.8% MoO2)
Iobserved
Icalculated
Iobserved-Icalculated
Relative Intensity/ (a.u)
2θ(deg.)

b)

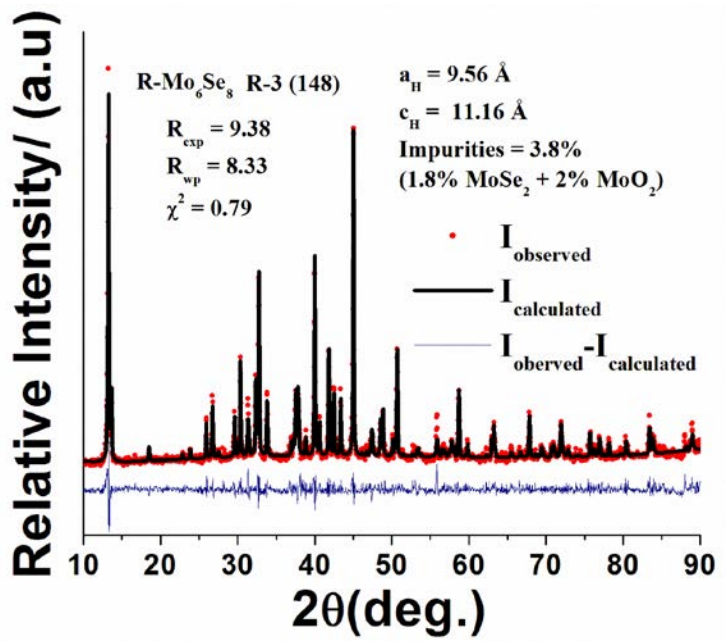

c)

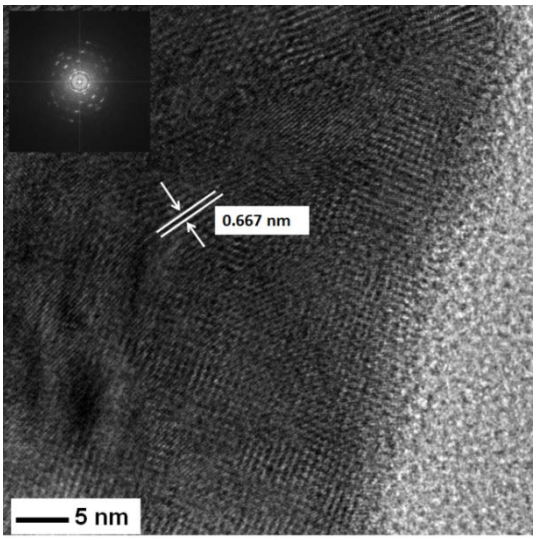

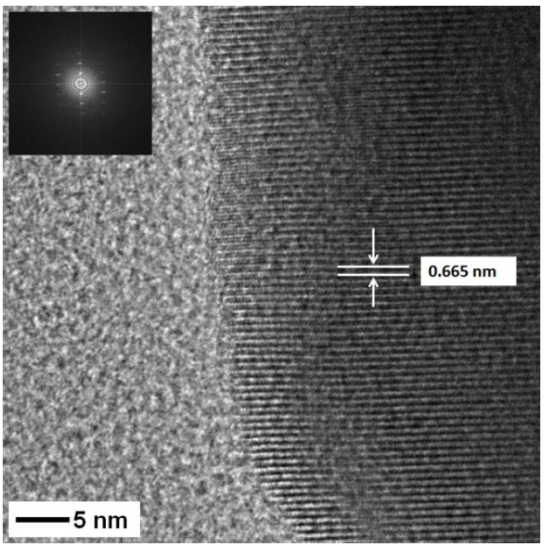

d) e)

Figure 94. (a) Powder XRD patterns of 3h mechanically milled powder of stoichiometric composition of (CuSe+Mo+$MoSe_2$), along with commercial powder of $MoSe_2$, Mo, and CuSe, Rietveld refinement results using Le Bail fit of (b) $Cu_2Mo_6Se_8$, (c) Mo_6Se_8 and HRTEM image showing lattice fringes of (101) planes from (d) $Cu_2Mo_6Se_8$ and (e) Mo_6Se_8.

The powder XRD pattern of $Cu_2Mo_6Se_8$ obtained upon heating the 3h mechanically milled powder at 1273K for 6h in UHP Ar atmosphere was refined using the Rietveld method following the standard guidelines and the method outlined by Le-Bail and others[538, 539]. The standard unit cell parameters, crystal symmetry, and Wyckoff positions [including x, y, z co-ordinates, site occupancy factors, and thermal parameter] were obtained from literature[540, 541]. The parameter(s) refined were zero shifts, cell parameters, peak width by Caglioti function, and peak shape by Pseudo-Voight polynomial functions. **Figure 94b** present the fitting of the XRD pattern recorded between 10°-90° at room temperature. The refinement in the hexagonal-rhombohedral symmetry converged on a = 1.003 nm, c = 1.073 nm, unit cell volume = 933.48 × 10^{-3} nm^3, R_{wp} ~ 4.38% and R_{exp} ~ 5.06%, and χ^2 ~ 1.33%. The presence of slight impurities including layered $MoSe_2$ (1.7%) and MoO_2 (1.8%) was evident and cannot be avoided due to oxidation of molybdenum and unreacted $MoSe_2$ present during heat treatment in the furnace. The copper leached Mo_6Se_8 Chevrel phase was also fitted using Le Bail method in order to check the phase formation and purity of the leached product as well to electrochemically verify the feasibility of the material as a suitable Na-ions insertion host. The Rietveld refined parameter in the simulated XRD pattern of Mo_6Se_8 phase shown in **Figure 94c** found the following: weighted R profile- R_{wp} =9.38%, R expected- R_{exp} = 8.33% and goodness of fit- $\chi 2$ = 0.79 with 96.2% of Mo_6Se_8, 1.8% of MoS_2 and 2.0% of MoO_2 phase. Lattice parameter(s) obtained from simulating the experimental data were (a = 0.956 nm, c = 1.176 nm, and unit cell volume = 883.38 × 10^{-3} nm^3) for Mo_6Se_8 phase. The excellent agreement of the lattice parameter(s) of Cu_xCP-2 and CP-2 suggests that HEMM is scalable high throughput approach for direct synthesis of ternary CP-$Cu_2Mo_6Se_8$ in a time saving manner. **Figure 95a and Figure 95b** shows the elemental x-ray mapping *i.e.* the distribution of Cu, Mo, and Se atoms in the heat treated powder of Cu_xCP-2 and copper leached powder of CP-

2 phase, respectively. Elemental x-ray maps confirm that all the elements *viz.* are homogeneously distributed within the particle aggregates without segregation on any specific site. Quantitative elemental composition of the powders obtained by EDX analyses (see **Figure 95c**) further shows that the measured atomic percent of Cu, Mo, and Se are close to the nominal composition of $Cu_2Mo_6Se_8$ and Mo_6Se_8 phase, respectively. **Figure 94d and Figure 94e** show the HRTEM images of a single $Cu_2Mo_6Se_8$ and Mo_6Se_8 particle, respectively. Fast Fourier transform (FFT) shown in the **inset** of each figure was used to calculate the lattice spacing of the nanocrystalline particle. The lattice fringe spacing was found to be ~0.667nm for $Cu_2Mo_6Se_8$ and ~0.665nm for Mo_6Se_8 corresponding to the interplanar d-spacing of (101) planes (hexagonal crystal system: space group *R-3*).

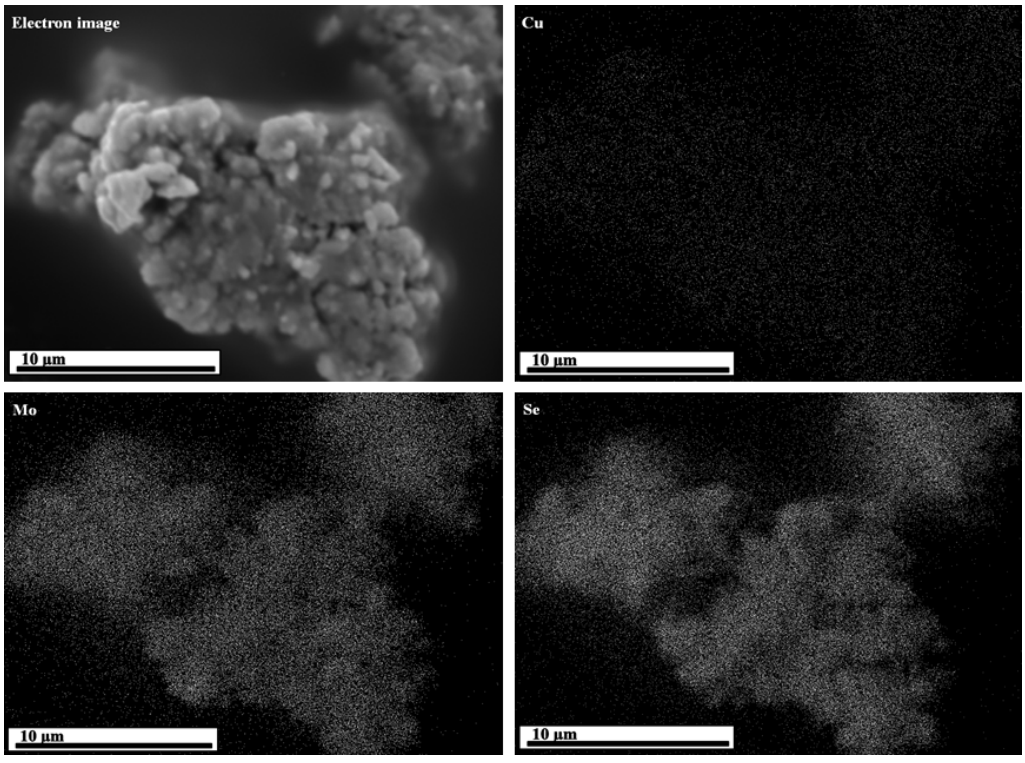

a)

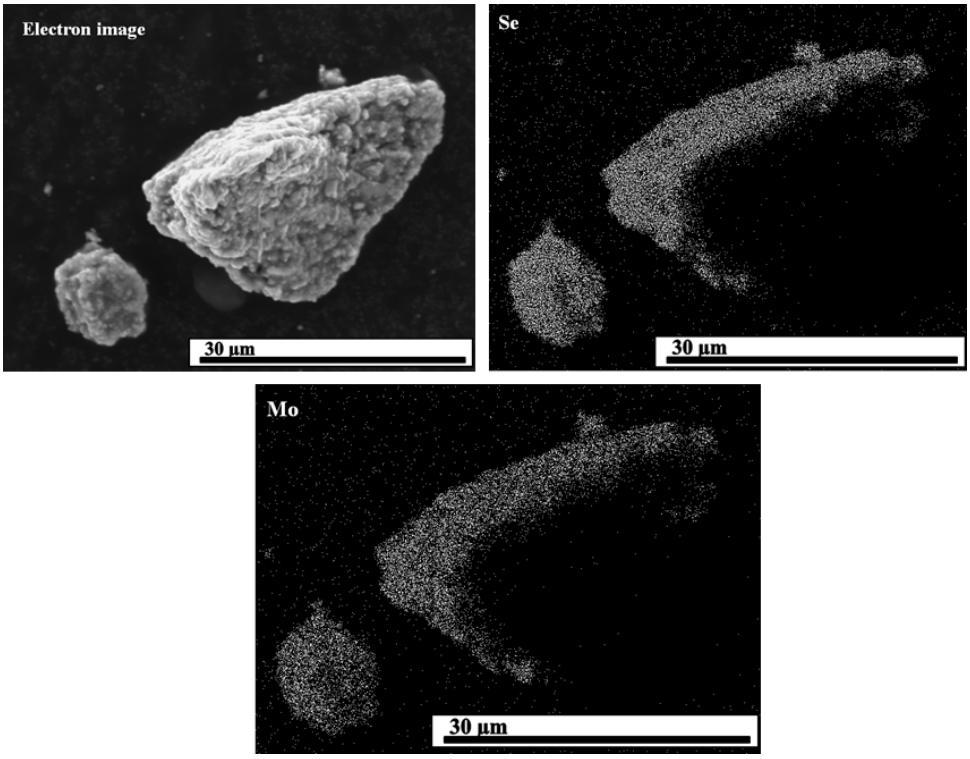

b)

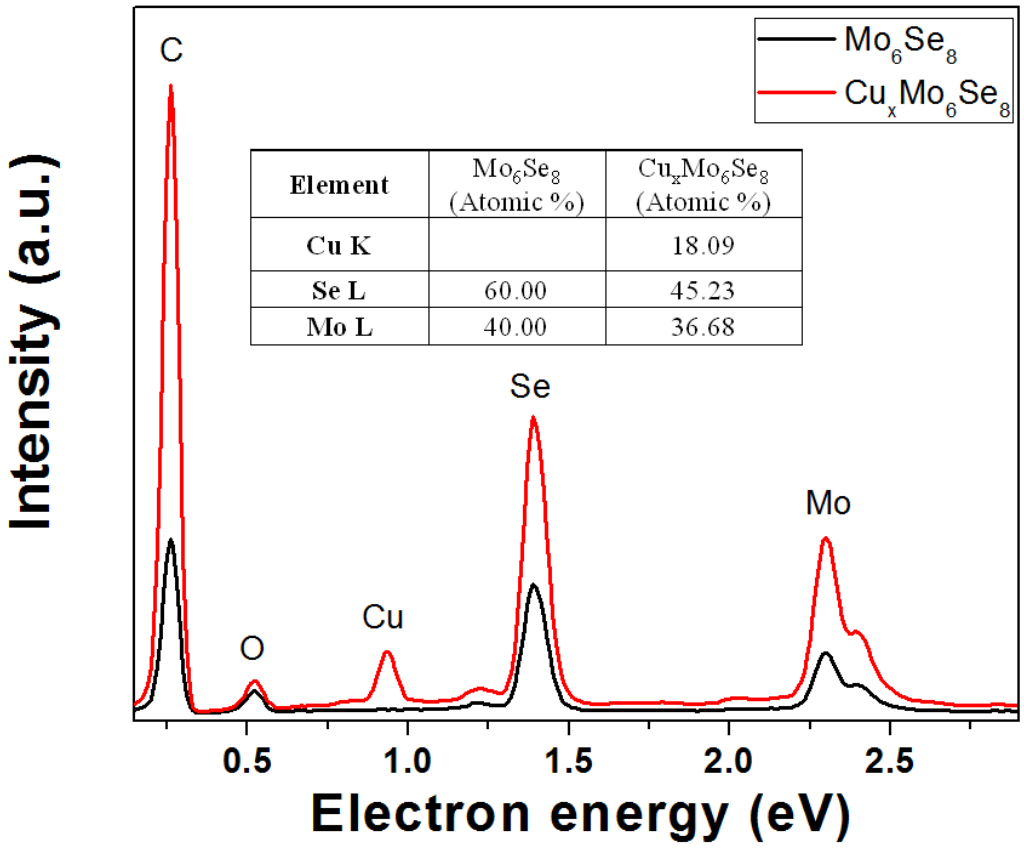

Element	Mo_6Se_8 (Atomic %)	$Cu_xMo_6Se_8$ (Atomic %)
Cu K		18.09
Se L	60.00	45.23
Mo L	40.00	36.68

c)

Figure 95. The elemental x-ray mapping of (a) Cu, Mo, Se in $Cu_xMo_6Se_8$ and (b) Mo, and Se in Mo_6Se_8 phase, and (c) EDS full frame analyses of $Cu_xMo_6Se_8$ and Mo_6Se_8 phase showing composition.

Similar to Mo_6S_8 phase, electrochemical performance of the HEMM derived de-cuprated Mo_6Se_8 phase was also verified at room temperature (300K) in a 2016 coin cell. **Figure 96a** shows a typical CV curve indicating reversible two-steps Na-ion insertion/extraction phenomena in Mo_6Se_8 phase. The cathodic peaks observed during sodiation at ~1.32V and ~1.37V, and the corresponding anodic peak observed at ~1.38V and ~1.56V exhibits the reversible insertion/extraction of Na-ion from the Mo_6Se_8 Chevrel phase. **Figure 96b** present the specific capacity and Coulombic efficiency *versus* cycle plot at constant current rate of ~30 mAg^{-1}

(~C/3). The 1st sodiation and de-sodiation capacity was ~69 $mAhg^{-1}$ (~84% of theoretical capacity ~82 $mAhg^{-1}$) and ~49 $mAhg^{-1}$ with 1st cycle Coulombic efficiency ~ 71%. In the 2nd cycle, the sodiation and de-sodiation capacity was ~47.6 $mAhg^{-1}$ and ~42 $mAhg^{-1}$ with 2nd cycle Coulombic efficiency ~ 88.4%. Whereas, in the 3rd cycle, the sodiation and de-sodiation capacity was ~39.7 $mAhg^{-1}$ and ~38.7 $mAhg^{-1}$ with 3rd cycle Coulombic efficiency ~ 97.6%. The capacity loss from the first three cycles may stem from the partial entrapment of Na-ion in the open channels of Mo_6Se_8 phase. From the 4th cycle onward a steady and stable sodiation capacity of ~34.7 $mAhg^{-1}$ and Coulombic efficiency close to ~99.33% was observed. The observed sodiation and de-sodiation capacity between 4th and 20th cycles was stable with ~0.67% minimal irreversible loss per cycle. The expected drop in overall gravimetric capacity in Mo_6Se_8 compared to Mo_6S_8 was mainly due to heavy selenium atom compared to sulfur atom and associated difference in molecular weight of Mo_6S_8 and Mo_6Se_8 phase. In order to understand the reaction phenomena during sodiation/de-sodiation into/from the Mo_6Se_8 phase, voltage *versus* specific capacity of different cycles were plotted and analyzed. **Figure 96c** shows the voltage *versus* capacity curves of 1st, 2nd, 3rd, 5th, 10th, and 20th cycle and the number of Na-ion that can be inserted in the Mo_6Se_8 phase. Similar to Mo_6S_8 phase, It is apparent that 1st sodiation into Mo_6Se_8 phase is a two-steps reaction where Na-ion insert at two different voltage and commensurate with total ~3.3 Na-ions insertion into the Mo_6Se_8 host according to the following formula.

$$3.3Na^{+} + Mo_6Se_8 + 3.3e^{-} = Na_{3.3}Mo_6Se_8$$

The dQ/dV *versus* voltage curves presented in **Figure 96c** reveals that the 1st cycle sodiation reaction occur in two stages wherein the 1st reaction occurs at ~1.4V and corresponds to a capacity of ~ 42 $mAhg^{-1}$ (equal to 2Na-ions intercalation into the Mo_6Se_8) and the 2nd

reaction occurs ~1.33V and gives a capacity of ~ 27 $mAhg^{-1}$ (equal to 1.3Na-ion intercalation into the Mo_6Se_8).

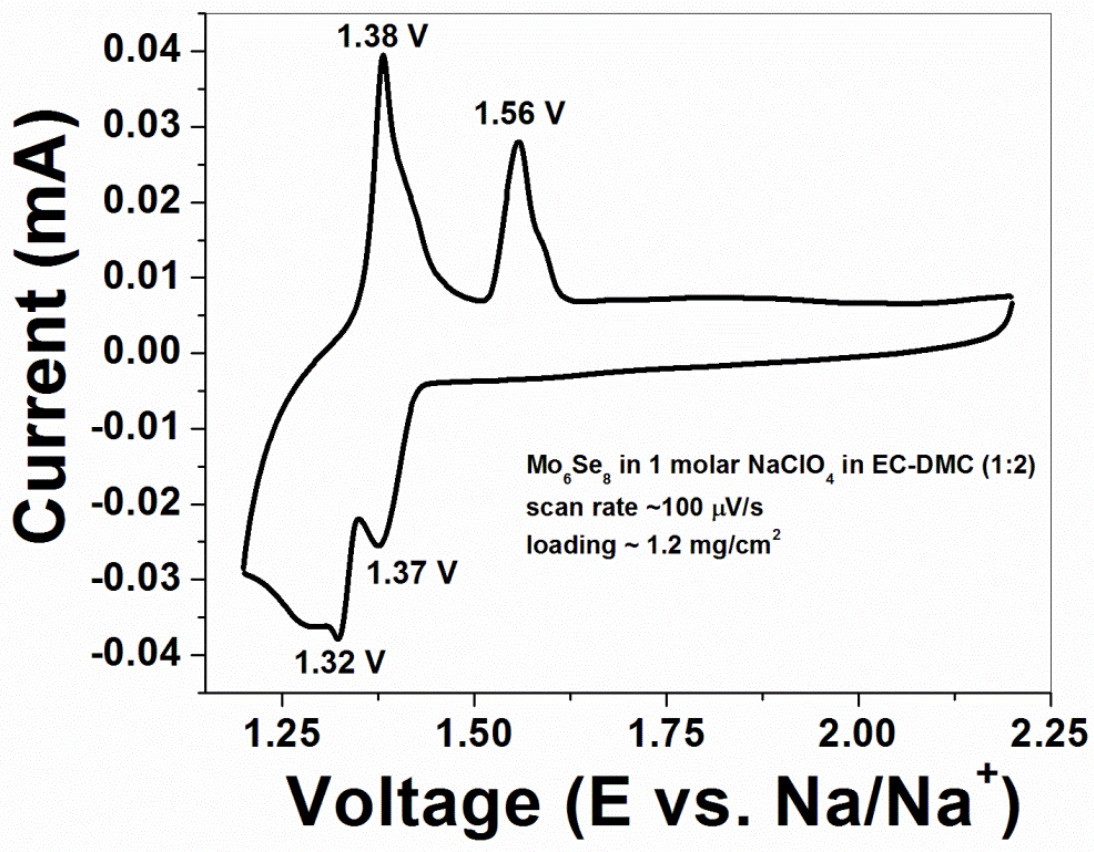

a)

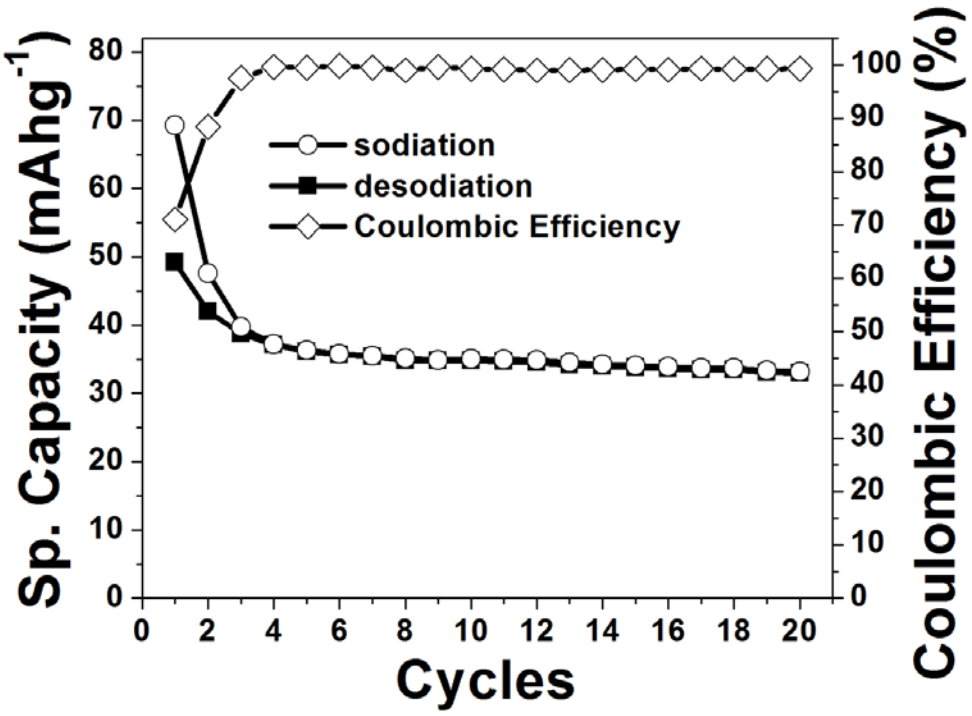
Sp. Capacity (mAhg-1)
Coulombic Efficiency (%)
Cycles
sodiation
desodiation
Coulombic Efficiency

b)

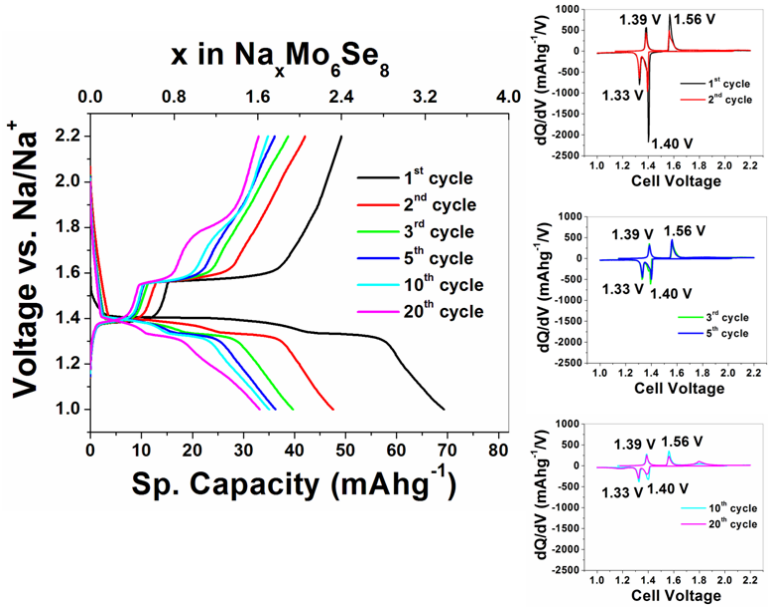
x in NaxMo6Se8
Voltage vs. Na/Na+
Sp. Capacity (mAhg-1)
1st cycle
2nd cycle
3rd cycle
5th cycle
10th cycle
20th cycle
dQ/dV (mAhg-1/V)
Cell Voltage
1.39 V
1.56 V
1.33 V
1.40 V

c)

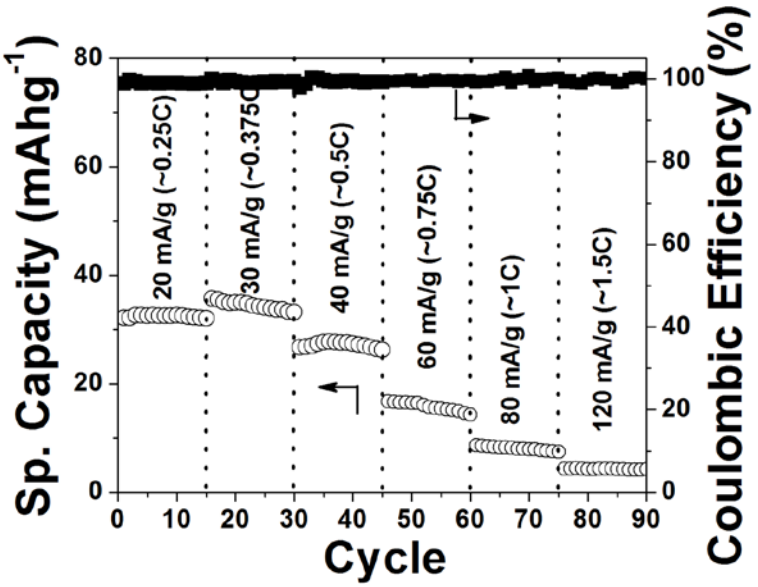

d)

Figure 96. (a) Typical cyclic voltammogram at a scan rate of 0.0001Vs^{-1} (b) charge/discharge capacity versus cycle number curve along with Coulombic efficiency, (c) voltage versus capacity profile along with dQ/dV versus voltage (inset), and (d) rate performance of HEMM derived Mo_6Se_8 electrodes.

The reaction for each voltage plateau observed in the specific capacity *versus* voltage profile in **Figure 96b** can be summarized according to the following formula.

$$2Na^+ + Mo_6Se_8 + 2e^- = Na_2Mo_6Se_8 \text{ observed at ~1.4V versus } Na^+/Na$$

$$1.3Na^+ + Na_2Mo_6Se_8 + 1e^- = Na_{3.3}Mo_6Se_8 \text{ observed at ~1.33V versus } Na^+/Na$$

$$\text{Total: } 3.3Na^+ + Mo_6Se_8 + 3.3e^- = Na_{3.3}Mo_6Se_8$$

Similarly, during 1st cycle de-sodiation reaction two stage reactions occur (see the dQ/dV *versus* voltage curve in **Figure 96c**. The associated Na-ions de-sodiation reactions from the $Na_{3.3}Mo_6Se_8$ phase occur at ~1.39V (removal of ~0.75Na-ion with associated capacity of ~15 mAhg^{-1}) and ~1.56V (removal of ~1.6 Na-ion removal with associated capacity ~34 mAhg^{-1}), respectively. The reactions can be expressed as follows:

$$Na_{3.3}Mo_6Se_8 - 0.75Na^+ - 0.75e^- = Na_{2.55}Mo_6Se_8 \text{ observed at } \sim 1.39V \text{ versus } Na/Na^+$$

$$Na_{2.55}Mo_6Se_8 - 1.6Na^+ - 1.6e^- = Na_{0.95}Mo_6Se_8 \text{ observed at } \sim 1.56V \text{ versus } Na/Na^+$$

$$\text{Total: } Na_{3.3}Mo_6Se_8 - 2.35Na^+ - 2.35e^- = Na_{0.95}Mo_6Se_8$$

The reaction profiles observed during 2nd, 3rd, and 5th cycle sodiation/de-sodiation was similar to that of the 1st cycle. It appears from the 2nd cycle onwards, $Na_{\sim 3.3}Mo_6Se_8$ and $Na_{\sim 1}Mo_6Se_8$ become two stable phases during discharge/charge cycle and capable of cycling ~2.0Na-ions in reversible manner. However, the sodiation capacity gradually drops to ~33 $mAhg^{-1}$ in the 20th cycle either due to ionic or electronic transport limitation or Na-ions entrapment within the Mo_6Se_8 framework during progressive cycles. The electrochemical rate performance of the Mo_6Se_8 electrode cycled at various current rates is presented in **Figure 96d**. The average discharge capacities at ~0.25C, ~0.375C, ~0.5C, ~0.75C, ~1C and ~1.5C rates were ~32.4 $mAhg^{-1}$, ~34.5 $mAhg^{-1}$, ~27.2 $mAhg^{-1}$, ~15.8 $mAhg^{-1}$, ~8 $mAhg^{-1}$, and ~4.3 $mAhg^{-1}$, respectively. The capacity retention of the Mo_6Se_8 electrode reported here decent at various current rates. The Coulombic efficiency at ~0.25C, ~0.375C, ~0.5C, ~0.75C, ~1C and ~1.5C rate was found to be 99%, 99.3%, 99.5%, 99.5%, 99.7%, and 99.5%, respectively. It appears that rate capability of Mo_6Se_8 phase is not excellent and drops to low values at high current rate. In other words, it indicates that there exist a kinetic or charge transfer barriers which limits the Na-ion insertion in the Mo_6Se_8 phase.

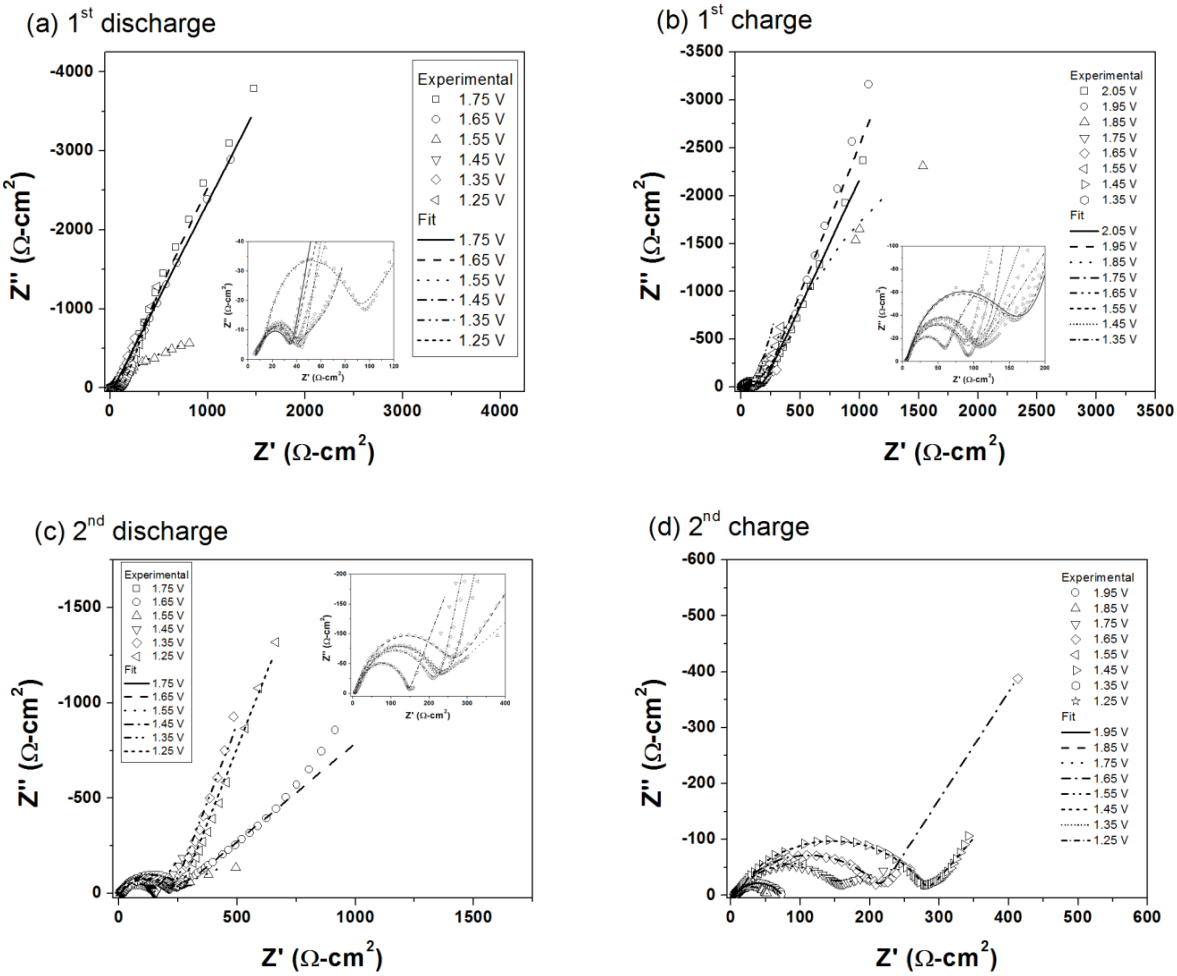

Figure 97. Nyquist plot of wet chemistry derived Mo_6S_8 Chevrel phase electrode in a sodium cell at (a) 1st discharge, (b) 1st charge, (c) 2nd discharge, and (d) 2nd charge cycle obtained over a frequency range of 100 KHz-0.01 Hz.

Table 32. Charge transfer parameter(s) of wet chemical derived Mo_6S_8 electrode obtained from Randall circuit modeling of Figure 97a -Figure 97d.

Voltage (V, *vs.* Na/Na^+)	R_s	CPE_i		R_i	CPE_e		R_e	W_o			R_{trap}	CPE_{trap}	
		T	P		T	P		R	T	P		T	P
1^{st} discharge Mo_6S_8													
1.75	1.19	7.68E-06	0.82	5.66	2.64E-05	0.78	24.76	2.78E-05	1.00E-20	0.36	3.48	2.16E-03	0.75
1.65	5.30	4.24E-06	0.90	3.26	2.30E-05	0.81	27.64	1.97E-03	6.13E-08	0.37	691.60	7.33E-04	0.97
1.55	5.42	3.63E-06	0.91	3.12	2.73E-05	0.81	31.90	2.40E-03	4.60E-08	0.35	5.14E-05	1.00E-03	0.18
1.45	5.27	5.48E-06	0.87	3.92	2.10E-05	0.85	25.59	4.98E-03	2.09E-10	0.22	79.19	1.79E-02	0.80
1.35	1.81	6.77E-06	0.89	3.32	5.83E-05	0.73	35.63	1.23E-01	1.00E-20	0.16	3.85	1.46E-02	0.77

Table 32 (continued)

1.25	4.32	1.58E-05	0.79	7.32	1.94E-05	0.93	64.62	1.60E+02	1.29E+00	0.41	N/A		
1^{st} charge Mo_6S_8													
1.35	4.62	1.15E-05	0.82	5.74	2.52E-05	0.88	70.52	1.18E+02	2.03E+00	0.43	N/A		
1.45	4.86	1.34E-05	0.83	3.67	2.80E-05	0.86	78.88	2.26E-10	5.94E-18	0.33	16.38	9.09E-02	0.76
1.55	0.22	7.00E-06	0.90	2.44	4.14E-05	0.82	99.59	1.23	1.00E-20	0.16	4.65	9.69E-03	0.66
1.65	2.60	3.54E-05	0.77	3.20	2.85E-05	0.87	90.63	3.37	1.00E-20	0.05	2.12	1.41E-02	0.48
1.75	2.73	3.84E-05	0.78	2.84	3.57E-05	0.85	51.69	1.85	1.00E-20	0.04	2.06	3.20E-03	0.77
1.85	2.03	1.55E-05	0.87	2.11	4.16E-05	0.83	84.31	0.93	1.00E-20	0.06	2.66	3.45E-03	0.81

Table 32 (continued)

1.95	4.34	1.34E-06	1.15	0.62	2.63E-05	0.88	117.00	1.74E+02	4.47E-01	0.40	N/A
2.05	4.22	3.77E-07	1.28	0.38	2.53E-05	0.88	120.70	1.61E+02	4.00E-01	0.38	N/A
2^{nd} discharge Mo_6S_8											
1.65	3.46	1.70E-07	1.95	0.35	3.41E-05	0.82	231.60	1.76E+01	4.73E-03	0.26	N/A
1.55	4.30	1.95E-06	1.12	0.65	3.16E-05	0.83	189.20	4.54E-02	6.48E-11	0.17	
1.45	4.84	3.59E-05	0.76	3.48	3.34E-05	0.80	136.50	2.94E+00	2.95E-02	0.33	
1.35	4.60	2.49E-05	0.76	7.27	3.26E-05	0.82	179.90	1.01E+02	1.05E+00	0.40	
1.25	4.51	1.46E-05	0.81	10.20	3.13E-05	0.83	189.10	1.62E+02	1.20E+00	0.40	

Table 32 (continued)

2^{nd} charge Mo_6S_8										
1.45	4.77	7.48E-05	0.70	5.38	4.05E-05	0.79	268.3	6.35E+00	1.07E-01	0.31	N/A
1.55	5.03	4.81E-05	0.76	3.87	5.26E-05	0.76	166.9	7.54E-06	2.19E-01	0.51	
1.65	4.95	8.09E-05	0.71	4.53	4.85E-05	0.78	203.1	3.33E-04	2.77E-08	0.35	
1.75	4.97	1.67E-04	0.64	4.20	4.12E-05	0.80	135.2	2.65E-03	1.21E-11	0.20	
1.85	4.39	3.60E-04	0.59	4.72	7.50E-05	0.76	44.43	3.48E-09	1.08E-17	0.04	
1.95	4.87	3.52E-05	0.85	2.10	6.88E-05	0.75	64.17	4.36E-03	3.12E-09	0.19	

Electrochemical Impedance behavior of Mo_6S_8 Chevrel phase

Electrochemical impedance spectroscopy (EIS) was performed to gain further understanding of the charge-storage mechanisms observed during the charge-discharge behavior. **Figure 97a-Figure 97d** depicts the Nyquist plots of the solution chemistry derived Mo_6S_8 electrode at different potentials during the 1^{st} and 2^{nd} sodiation (discharge) and de-sodiation (charge) steps. Characteristic semi-circular arcs are observed at all the potential steps during charge/discharge cycle. In addition to the charge transfer based semicircles, straight lines are observed at low frequencies corresponding to the mass transfer effects. **Figure 98a** and **Figure 98b** depict the two circuit models used to fit the experimental impedance data. In all the cases, it was ensured that the fit had a χ^2 value between 10^{-3} and 10^{-4}. The Randall's circuit shown therein considers a number of electrochemical phenomena including series resistance (R_s), charge and electron transfer kinetics (CPE_e and R_e), interfacial resistances (CPE_i and R_i), diffusion characteristics and associated ion-trapping (W_o, R_{trap}, CPE_{trap}). Both models are variants of previously reported magnesiation and lithiation phenomena observed into Chevrel phase discussed in earlier chapters [362, 536, 542]. To the best of the reports in the open literature, charge transfer processes involving sodiation/de-sodiation into Chevrel phases have seldom been studied in such detail using EIS and it is the main aim to setup a template for further studies of the system[543].

The two models that have used in this study differ primarily in that one consider ion trapping and solid-state diffusion effects shown in **Figure 98a** whereas the second one neglect the same in the model shown in **Figure 98b** (which has previously been used to accurately predict the lithiation/de-lithiation phenomena into/from the Mo_6S_8 Chevrel phase cathode [542]). The constant phase elements (CPE) used in the present study instead of capacitor elements serve to model the

behavior of the charge transfer processes since porous electrodes seldom exhibit ideal capacitor behavior and are often replaced by a constant phase element [65, 360].

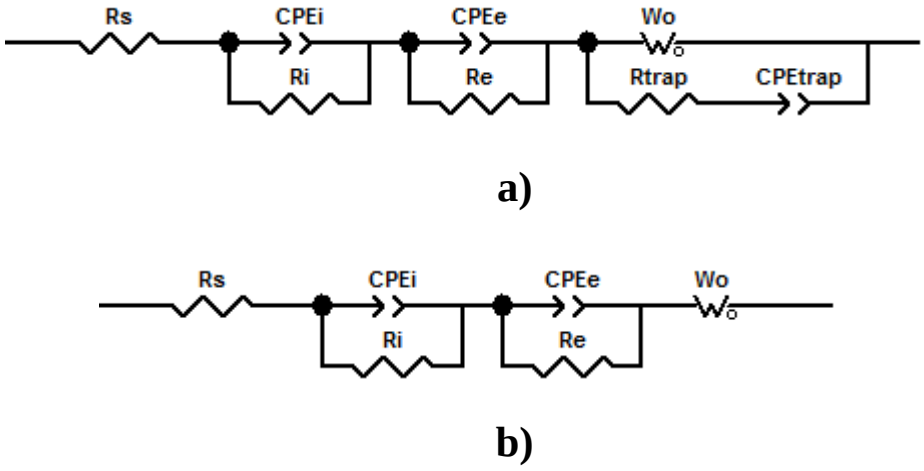

Figure 98. Randall's circuit used to model the experimentally obtained impedance data for sodium-ion insertion/extraction into/from the Mo_6S_8 and Mo_6Se_8 Chevrel phases. The model employed herein considers charge transfer, mass transfer phenomena contributing to the electrode impedance, in addition with (a) and without (b) partial charge trapping phenomena.

These models have been adopted to represent the behavior of insertion/extraction of sodium-ion into the Chevrel phase since it is expected that sodium-ion being of an equal valence as lithium-ion would behave in a somewhat similar manner. It is however to be expected that ion trapping known to occur in the Chevrel phase would be more pronounced in the case of sodium-ion insertion/extraction than that observed in lithium-ion on account of its larger ionic radius (Na-ion: 1.02Å, Li-ion: 0.76Å). The impedance behavior of the Chevrel phase electrodes differs significantly for the case of sodiation from that of magnesiation reported by us previously [536]. This is to be expected since magnesiation has previously been shown to have significant charge-

transfer barriers, ion trapping and co-existing chemical reactions (Gerischer type impedance) resulting in poor charge storage characteristics and very high impedances[362]. **Table 32** reflects the charge-transfer parameters obtained by equivalent circuit modeling of the experimentally obtained Nyquist plots shown in **Figure 97a-Figure 97d**. It can be seen from **Table 32** that the data in the 1st discharge and 1st charge cycle matches closely that of the model shown in **Figure 98a**. In contrast, we were able to model the characteristic of the 2nd discharge/charge cycle exclusively using the model shown in **Figure 98b.** The primary difference in both models is the presence/absence of Na-ion trapping in the Chevrel phase host. We ensure good fitting parameters in both cases including χ^2 values approaching 10^{-4}. This indicates an initial trapping of sodium-ions which subsides rapidly and allows for reversible charge storage. This observation corroborates the previously discussed irreversibility accompanying sodium-ion insertion resulting in the formation of the thermodynamically stable $Na_{\sim 1}Mo_6S_8$ rather than Mo_6S_8 phase (if complete removal of Na-ion occurred from $Na_{\sim 3.7}Mo_6S_8$) at the end of 1st charge cycle. It is believed that the irreversible capacity loss and Coulombic inefficiency observed in **Figure 91b** are consequence of the partial entrapment of sodium-ions in the Chevrel phase. The 2nd cycle however does not show such trapping behavior as seen in **Table 32**. In all the cases, the series resistance is low (varies between 1-6 Ω cm^{-2}). During 1st discharge cycle, trapping of sodium-ions occurs from the open circuit potential ~1.75V to ~1.35V. At the final discharge potential ~1.25V, significant trapping is not observed possibly because sodiation reaction occurs between ~1.5V and ~1.4V as seen in **Figure 91c**. Similar to the case of the 1st discharge, no significant sodium-ion trapping phenomena is observed at the fringe voltages (~1.35 V, ~1.95 V, and ~2.05 V). During 1st charge cycle which corresponds to extraction of sodium ions, trapping mechanism found to be predominant as seen in **Figure 98a**. This correlates well with the irreversible

capacity loss observed in **Figure 91c**. However the presence of ion trapping observed during the 1st discharge cycle (sodiation phenomena) is intriguing. There is reason to believe that this is the effect of charge trapping at inner rings of Mo_6S_8 make it difficult for Na-ions to diffuse into the bulk of the Mo_6S_8 host lattice. Further materials characterization (possibly *in-sit* XRD), however is warranted to understand this phenomenon which is not the focus of the present study. Subsequent to the 1st charge and discharge cycle, no obvious sodium-ion trapping phenomena observed as the $Na_{\sim 1}Mo_6S_8$ phase becomes thermodynamically stable and galvanostatic cycling occurs between $Na_{\sim 1}Mo_6S_8$ and $Na_{\sim 3.7}Mo_6S_8$ phase. The interfacial resistance (R_i) during the entire charge/discharge cycle is not significant indicating that solid electrolyte Interphase (SEI) layer formation is minimal. There is no significant variation of R_i, either at different stages in each cycle or between the two cycle which indicates that the SEI layer formation therein is unmodified with cycling. Compared to magnesiation[536], sodiation into solution chemistry derived Mo_6S_8 Chevrel phase was found to be facile resulting in the superior rate retention seen in **Figure 91d**. However, there is a gradual increase in R_e (charge transfer resistance) in each progressive step of cycling indicate that with each sodiation/de-sodiation, kinetics become progressively harder. This possibly evolves as a result of charge shielding caused by the trapped sodium-ions. The increase in R_e is very gradual and does not alter the characteristic of charge storage phenomena observed in **Figure 91d** to a great extent.

Electrochemical Impedance behavior of Mo_6Se_8 Chevrel phase

The charge storage behavior of Mo_6Se_8 Chevrel phase is very different from Mo_6S_8 as seen in **Figure 99a-Figure 99d** and **Table 33**. The low frequency behavior in the case of Mo_6Se_8 can only be modeled using the trapping based model shown in **Figure 98a**. Alteration from a purely Warburg-type behavior is distinctly observed as a result of the partial trapping of sodium-ions in

the charge and discharge steps of both 1st and 2nd cycle at all the voltages considered. Though R_s and R_i are not significant in the case of the Mo_6Se_8 Chevrel phase, R_e is larger than that observed in the Mo_6S_8 Chevrel phase derived using solution chemistry method. However, the charge transfer resistance, R_e does not increase progressively with cycling. Although, partial trapping of sodium-ions continues to exist till 2nd cycle resulting in the capacity fade behavior seen in **Figure 96a and Figure 96b**. The higher charge transfer resistance, R_e also results in slightly poorer capacity retention at higher rates. Sodium-ion diffusion and partial trapping effects render the Mo_6Se_8 Chevrel phase slightly less promising than the Mo_6S_8 Chevrel phase cathode for sodium-ion battery applications. The difference in charge storage behavior between the sodium and selenium Chevrel phase occurs possibly as a result of the difference in ionic radii between the two atoms. The larger selenium ion based Chevrel phase has slower ionic transport and increased sodium-ion trapping due to the same reason. Larger unit cell volume and corresponding free space in the tetrahedral and octahedral sites allow for a much larger amount of sodium-ions trapping in Mo_6Se_8 phase to occur. However, it is unclear at this point why that partial charge trapping continues to occur following the 1st cycle in the selenium CP while it is minimal in the sulfur CP. There is therefore a need for fundamental *in-situ* materials structural characterization studies to be conducted to understand the nature of the partial ion trapping and diffusion barriers which limit the properties of this material. These studies are part of the future studies to be conducted.

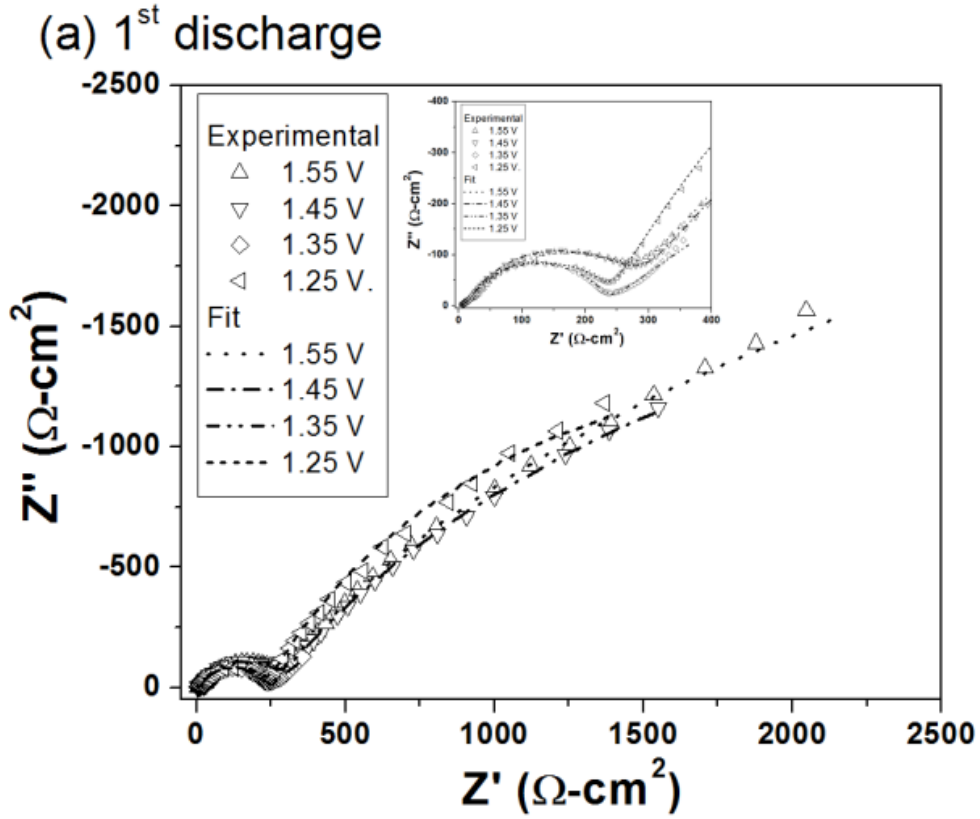
(a) 1st discharge
Experimental
1.55 V
1.45 V
1.35 V
1.25 V.
Fit
1.55 V
1.45 V
1.35 V
1.25 V
Z'' (Ω-cm2)
Z' (Ω-cm2)
-2500
-2000
-1500
-1000
-500
0
0
500
1000
1500
2000
2500

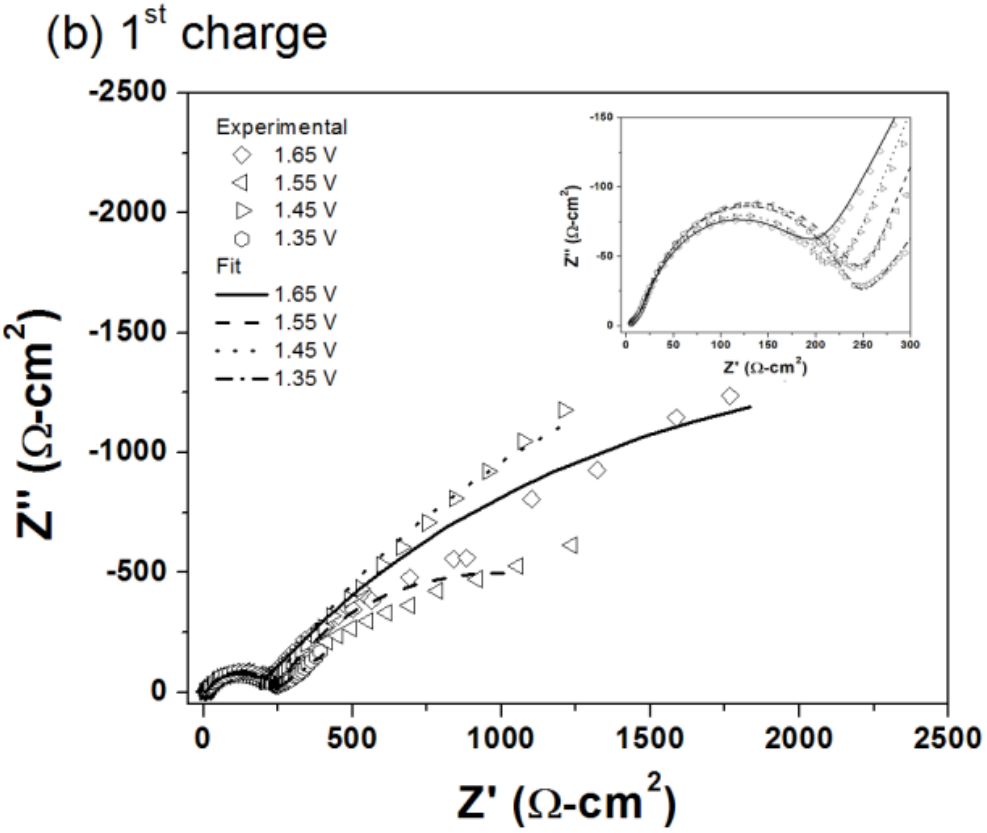
(b) 1st charge
Experimental
1.65 V
1.55 V
1.45 V
1.35 V
Fit
1.65 V
1.55 V
1.45 V
1.35 V
Z'' (Ω-cm2)
Z' (Ω-cm2)
-2500
-2000
-1500
-1000
-500
0
0
500
1000
1500
2000
2500

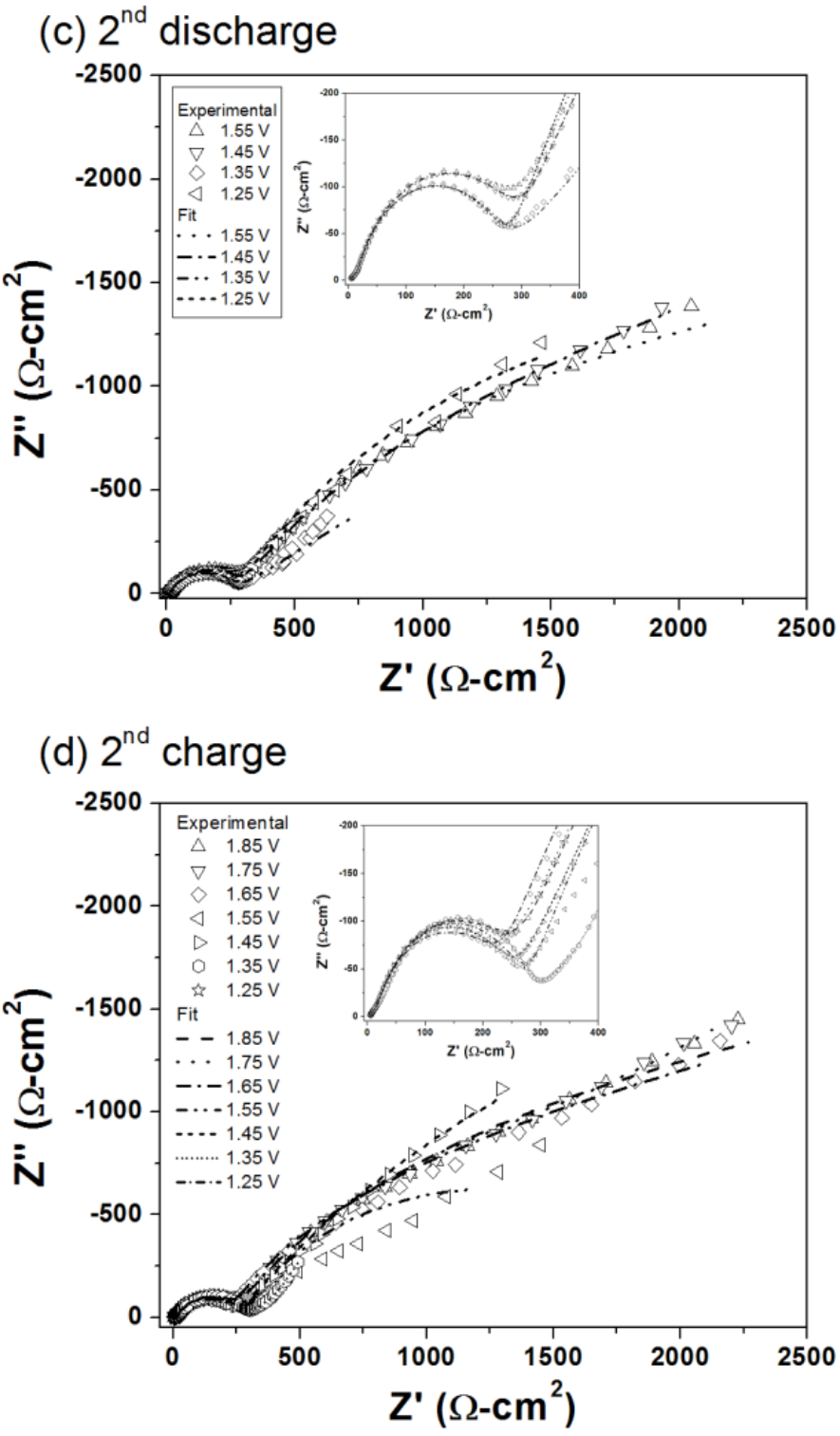

Figure 99. Nyquist plot of high energy mechanical milling derived Mo_6Se_8 Chevrel phase electrode in a sodium cell at (a) 1st discharge, (b) 1st charge, (c) 2nd discharge, and (d) 2nd charge cycle obtained over a frequency range of 100 KHz-0.01 Hz.

Table 33. Charge transfer parameter(s) of HEMM derived Mo_6Se_8 electrode obtained from Randall circuit modeling of Figure 99a-Figure 99d.

Voltage (V, *vs.* Na/Na^+)	R_s	CPE_i		R_i	CPE_e		R_e	W_o			R_{trap}	CPE_{trap}	
		T	P		T	P		R	T	P		T	P
1^{st} discharge Mo_6Se_8													
1.55	1.16E-06	4.16E-06	0.85	19.71	4.77E-05	0.81	251.30	3.03E-01	7.60E-19	0.11	4.35E+00	1.47E-03	0.72
1.45	3.77	9.65E-05	0.62	13.95	4.28E-05	0.83	254.70	2.71E+01	3.42E-14	0.07	5.72E-04	2.15E-03	0.69
1.35	3.75	8.11E-05	0.63	12.92	4.28E-05	0.83	210.60	4.38E-03	1.44E-10	0.23	8.06E-04	1.26E-02	0.46
1.25	3.48	1.07E-04	0.61	14.46	4.08E-05	0.83	216.80	2.93E+03	2.94E+04	0.00	2.03E-01	3.71E-03	0.74
1^{st} charge Mo_6Se_8													
1.35	2.65E-06	4.91E-05	0.69	8.92	4.53E-05	0.82	223.60	8.28E+00	1.40E-19	0.33	4.08	1.68E-02	0.49

Table 33 (continued)

1.45	3.94	6.08E-05	0.66	9.58	4.77E-05	0.81	204.80	7.44E+02	1.00E-20	0.02	8.17E-04	3.87E-03	0.70
1.55	2.49	6.84E-05	0.65	10.20	4.71E-05	0.81	232.90	2.49E+02	1.00E-20	0.01	1.49	5.11E-03	0.77
1.65	1.95	8.94E-05	0.63	11.85	4.30E-05	0.83	173.60	2.77E+01	1.00E-20	0.03	1.98	1.89E-03	0.66
2^{nd} discharge Mo_6Se_8													
1.55	5.96E-08	9.03E-06	0.83	8.35	5.10E-05	0.79	280.40	2.62E-01	1.29E-18	0.11	5.24E+00	1.13E-03	0.78
1.45	3.99	9.77E-05	0.62	12.64	4.47E-05	0.82	278.50	3.35E-01	2.12E-13	0.14	3.15E-08	1.38E-03	0.80
1.35	0.83	1.70E-05	0.80	7.24	4.44E-05	0.83	236.70	6.44E-01	1.00E-20	0.14	3.62E+00	5.40E-03	0.42
1.25	3.99	1.13E-04	0.61	13.40	4.22E-05	0.83	251.20	8.80E+02	1.00E-20	0.01	1.39E-03	3.31E-03	0.71

Table 33 (continued)

2nd charge Mo_6Se_8													
1.35	3.55	1.14E-04	0.58	28.92	4.00E-05	0.84	255.70	1.19E-03	1.41E-08	0.32	2.19E+02	1.41E-02	0.73
1.45	4.40	7.83E-05	0.66	12.47	4.34E-05	0.83	224.70	1.08E+03	1.00E-20	0.01	7.90E-03	3.14E-03	0.62
1.55	4.29	9.58E-05	0.64	12.56	4.82E-05	0.81	254.10	7.26E-02	1.29E-05	0.36	2.58E+01	5.14E-04	1.15E-09
1.65	4.50	5.85E-05	0.69	12.22	4.67E-05	0.81	211.00	4.21E-01	6.55E-05	0.40	1.94E-03	7.44E-04	0.25
1.75	3.27	2.35E-03	0.76	1104.00	3.49E-05	0.89	193.00	3.01E-02	9.75E-11	0.24	3.64E+01	2.52E-03	0.57
1.85	4.83E-08	1.85E-05	0.80	10.17	4.72E-05	0.80	238.40	1.89E-01	2.11E-18	0.11	5.31E+00	1.06E-03	0.77

B.3.4 Discussion

Generally, binary Chevrel phase compound of formula Mo_6T_8 (T =S, Se) consist of building blocks of Mo_6T_8 of Mo_6- octahedron cluster and surrounded by eight sulfur/selenium anions forming a cube. The three-dimensional structure of Mo_6T_8 clusters has empty cavities formed by face-sharing pseudo-cubic cavities 1 and 2 available for cation insertion (a strong repulsion between the Mo atoms and inserting cations does not allow the occupation of cavity 3)[482]. According to the cationic arrangements in the CPs, large cations such as Pb^{2+}, Sn^{2+} (radius > 1 Å) generally occupy the origin of the pseudo-cubic cavities characterized as the type I CPs, whereas small cations such as Cu^{+}, Li^{+} (radius < 1Å) delocalized and randomly distributed in the concentric rings (so-called inner and outer rings) of twelve tetrahedral sites form the type II CPs. Sodium-ion intercalation into Mo_6S_8 phase proceed in two stages accompanied by phase transformation from the initial Mo_6S_8 phase (hexagonal-rhombohedral, *R-3*, 148) to $Na_{\sim 1}Mo_6S_8$ phase(hexagonal-rhombohedral, *R-3*, 148 with increase in a_H, and c_H values) and then $Na_{\sim 3.7}Mo_6S_8$ phase (triclinic, *P1/1*). However, upon de-intercalation the fully sodiated $Na_{\sim 3.7}Mo_6S_8$ phase convert to thermodynamically stable $Na_{\sim 1}Mo_6SS_8$ (type I classic CP) phase rather than forming the Mo_6S_8 phase again. Following the initial sodiation/de-sodiation, the $Na_{\sim 1}Mo_6S_8$ phase becomes stable and thereafter sodium intercalation/de-intercalation reaction is found to be nearly reversible and proceed in the x ~1 to ~3.7 region in $Na_xMo_6S_8$ phase. According to Gocke *et al.* [544] re-oxidation of $Na_{\sim 3}Mo_6S_8$ phase leads to the formation of stable rhombohedral $Na_{\sim 1}Mo_6S_8$ phase a_R =90° where the sodium atom is located at the unit cell origin and becomes immobile (type I classic CP) for further oxidation to form the Mo_6S_8 phase. However, $Na_{\sim 1}Mo_6S_8$ phase can be reduced under galvanostatic condition to $Na_{\sim 3.7}Mo_6S_8$ phase

while cycling ~2.5Na-ions in reversible manner. Tarascon *et al.* [535] also observed by in situ XRD measurements during 1st cycle sodiation that initial rhombohedral Mo_6S_8 phase (denoted as R_0) undergoes phase transformation and forms an intermediate stable phase $Na_{\sim 3.1}Mo_6S_8$ phase (crystallized in a triclinic crystal structure denoted as T_1) and finally to $Na_{\sim 3.9}Mo_6S_8$ phase (crystallized in another triclinic crystal structure denoted as T_2). Upon de-sodiation, complete removal of ~3.9 Na-ion was impossible under galvanostatic condition and one Na-ion falls into a combined steric/energetic trap. Thus, $Na_{\sim 1}Mo_6S_8$ (denoted as R_1) becomes the stable phase with almost 25% irreversible loss in capacity during 1st cycle. Similar observation has been observed during sodiation/de-sodiation in the solution chemistry derived Mo_6S_8 phase and the galvanostatic behavior correlates well with observation made by others [535,544]. In addition electrochemical impedance spectroscopy (EIS) study of the Na/Mo_6S_8 cell in the entire discharge/charge window of 1st and 2nd cycle was able to model the partial charge-trapping phenomena. The 0.7% irreversible loss per cycle beyond 1st cycle may be best described in terms of the expansion/contraction in the unit cell parameter(s) and associated phase transformation observed by Tarascon *et al.* [535]. The calculated molar volume of Mo_6S_8 (R_0), $Na_{\sim 1}Mo_6S_8$ (R_1), $Na_{\sim 3}Mo_6S_8$ (T_1) and $Na_{\sim 3.9}Mo_6S_8$ (T_2) are ~80.06 cm^3/mol, ~124.86 cm^3/mol, ~185.98 cm^3/mol, and ~203.46 cm^3/mol, respectively. The associated volume expansion/contraction during galvanostatic cycling between R_1 and T_1 phase is ~49% may add mechanical strain on the electrode surface that leads to cracking and loss of electrical contact with the current collector. The peculiarities of the CP-1 are that partial charge-trapping occurs only in the 1st cycle until the $Na_{\sim 1}Mo_6S_8$ becomes stable at the onset of 2nd cycle which agrees well with observation made by others[535, 544]. On the other hand, partial charge-trapping continues to occur in the 1st and 2nd cycle

in the case of CP-2 (Mo_6Se_8) phase due to triclinic distortion of the sodiated Mo_6Se_8 phase rendering it difficult for complete removal of Na causing partial trapping[533].

B.3.5 Conclusion

$Cu_xMo_6S_8$ and $Cu_xMo_6Se_8$ ternary Chevrel phases were synthesized by wet chemistry and higher energy mechanical milling routes. X-rays diffraction and scanning electron microscopy results show the formation of cuboidal shape micrometer sized particles (1-1.5 μm) in the case of $Cu_xMo_6S_8$ and microcrystalline particles for $Cu_xMo_6Se_8$ phase. Le Bail fitting of the experimental powder XRD patterns confirms the formation of ternary CPs with the presence of impurities (<4%). Electrochemical performances of de-cuprated Mo_6S_8 phase in a sodium cell exhibits 1st cycle sodiation and de-sodiation capacity of ~108 $mAhg^{-1}$ and ~74 $mAhg^{-1}$ with Coulombic efficiency ~ 68.3%. A stable capacity of ~60 $mAhg^{-1}$ was obtained up to 50th cycle with 0.7% minimal capacity loss per cycle where ~ 2Na-ion able to cycle reversibly between two terminal composition of $Na_{\sim 1}Mo_6S_8$ and $Na_{\sim 3}Mo_6S_8$ phase. Similar electrochemical test with HEMM derived de-cuprated Mo_6Se_8 show slightly inferior capacity largely due to heavy molecular weight of selenium bearing CP over its sulfur counterpart. 1st cycle sodiation and de-sodiation capacity of Mo_6Se_8 phase was ~69 $mAhg^{-1}$ and ~49 $mAhg^{-1}$ with Coulombic efficiency ~ 71%. Stable capacity of ~35 $mAhg^{-1}$ was observed till 20th cycle with Coulombic efficiency ~99.33%. Electrochemical impedance spectroscopy (EIS) of Na/Mo_6S_8 and Na/Mo_6Se_8 cell during 1st and 2nd cycle was used to model the charge storage phenomena in the CPs. EIS show that partial charge trapping of Na-ions occurs in the CPs primarily in the 1st cycle with an increase in charge transfer resistance (R_e), which was the principle reason for 1st cycle irreversible capacity loss (~30%). The sodiated CPs beyond 1st cycle remain electrochemically

stable with two terminal composition with Na =1 and =3. In summary, sulfur and selenium ternary CPs have been synthesized by a time efficient wet chemistry and HEMM route, respectively, and the CPs obtained by acid leaching of copper thereafter clearly show promise as low voltage, cycle stable Na-ion cathode suitable for land based grid-scale electrical energy storage applications. Further studies are clearly warranted to further improve the systems based on the analyses reported in this study which is part of the future work.

PERMISSIONS

The thesis has text, figures and tables reprinted / reproduced with permission from several publishing companies and societies. Suitable permissions have been obtained for reproduction of figures where I am not an author/co-author and have been marked in the caption of the respective figures. In addition, content has been reused as-is or with slight modification from papers where I (*Prashanth Jampani Hanumantha*) am an author/co-author.

The journal papers listed below have been used in **Section 4.0** :

1. *Prashanth Jampani*, Karan Kadakia, Dae Ho Hong, Rigved Epur, James A. Poston, Ayyakkannu Manivannan, Prashant N. Kumta, "CVD derived vanadium oxide nano-sphere-carbon nanotube (CNT) nano-composite hetero-structures: High energy supercapacitors", *Journal of the Electrochemical Society*, 160[8] (2013) A1-A10, Copyright © 2013, Reproduced with permission of ECS - The Electrochemical Society.
2. *Prashanth Jampani*, Moni K. Datta, Karan Kadakia, Dae Ho Hong, Sung Jae Chung, Michael C. Tam, James A. Poston, Ayyakkannu Manivannan, Prashant N. Kumta, "A simple low temperature synthesis of nanostructured vanadium nitride for supercapacitor applications", *Journal of the Electrochemical Society*, 160[11] (2013) A2195-A2206, Copyright © 2013, Reproduced with permission of ECS - The Electrochemical Society.

The journal papers listed below has been used in **Appendix B** :

1. *Prashanth Jampani*, Bharat Gattu, Oleg Velikokhatnyi, Moni K. Datta, Sameer S. Damle, Prashant N. Kumta, "Heterostructures for improved stability of Lithium sulfur batteries",

Journal of the Electrochemical Society, 161[6] (2014) A1173-A1180, Copyright © 2014, Reproduced by permission of ECS - The Electrochemical Society.

2. Partha Saha, *Prashanth Jampani*, Moni K. Datta, Chris U. Okoli, Ayyakkannu Manivannan, Prashant N. Kumta, “A convenient approach to Mo6S8 Chevrel phase cathode for rechargeable magnesium battery”, *Journal of the Electrochemical Society*, 161[4] (2014) A593-A598, Copyright © 2014, Reproduced by permission of ECS - The Electrochemical Society.

BIBLIOGRAPHY

1. R. E. Smalley, *Mrs Bulletin*, 2005, **30**, 412-417.

2. N. S. Lewis, *MRS bulletin*, 2007, **32**, 808-820.

3. P. Simon and Y. Gogotsi, *Nature Materials*, 2008, **7**, 845-854.

4. J. R. Miller, *Science*, 2012, **335**, 1312-1313.

5. R. Kötz and M. Carlen, *Electrochimica Acta*, 2000, **45**, 2483-2498.

6. J. N. Armor, *Catalysis Today*, 2014.

7. B. K. Bose, *Industrial Electronics, IEEE Transactions on*, 2013, **60**, 2638-2651.

8. T. F. Stocker, 2013.

9. G. P. Peters, R. M. Andrew, T. Boden, J. G. Canadell, P. Ciais, C. Le Quere, G. Marland, M. R. Raupach and C. Wilson, *Nature Clim. Change*, 2013, **3**, 4-6.

10. K. Caldeira, A. K. Jain and M. I. Hoffert, *Science*, 2003, **299**, 2052-2054.

11. T. M. L. Wigley, R. Richels and J. A. Edmonds, *Nature*, 1996, **379**, 240-243.

12. S. Chu, *Science*, 2009, **325**, 1599.

13. M. E. Boot-Handford, J. C. Abanades, E. J. Anthony, M. J. Blunt, S. Brandani, N. Mac Dowell, J. R. Fernández, M.-C. Ferrari, R. Gross and J. P. Hallett, *Energy & Environmental Science*, 2014, **7**, 130-189.

14. B. Dunn, H. Kamath and J.-M. Tarascon, *Science*, 2011, **334**, 928-935.

15. S. Perathoner and G. Centi, in *Global Change, Energy Issues and Regulation Policies*, Springer, 2013, pp. 143-160.

16. N. MacDowell, N. Florin, A. Buchard, J. Hallett, A. Galindo, G. Jackson, C. S. Adjiman, C. K. Williams, N. Shah and P. Fennell, *Energy & Environmental Science*, 2010, **3**, 1645-1669.

17. S. Bhavsar, M. Najera, R. Solunke and G. Veser, *Catalysis Today*.

18. F. Orr and J. Taber, *Science*, 1984, **224**, 563-569.

19. H. J. Herzog, *Environmental Science & Technology*, 2001, **35**, 148A-153A.

20. B. Koelbl, M. Broek, A. C. Faaij and D. Vuuren, *Climatic Change*, 2014, **123**, 461-476.

21. L. Barreto, A. Makihira and K. Riahi, *International Journal of Hydrogen Energy*, 2003, **28**, 267-284.

22. G. W. Crabtree, M. S. Dresselhaus and M. V. Buchanan, *Physics Today*, 2004, **57**, 39-44.

23. M. Balat, *International Journal of Hydrogen Energy*, 2008, **33**, 4013-4029.

24. L. Schlapbach and A. Zuttel, *Nature*, 2001, **414**, 353-358.

25. P. D. Bossel, Ulf, P. D. Eliasson, Baldur and G. Taylor, *Cogeneration and Distributed Generation Journal*, 2003, **18**, 29-70.

26. U. Bossel, *Proceedings of the IEEE*, 2006, **94**, 1826-1837.

27. A. Mohd, E. Ortjohann, A. Schmelter, N. Hamsic and D. Morton, Challenges in integrating distributed Energy storage systems into future smart grid, 2008.

28. Z. Yang, J. Zhang, M. C. Kintner-Meyer, X. Lu, D. Choi, J. P. Lemmon and J. Liu, *Chemical Reviews*, 2011, **111**, 3577-3613.

29. M. Winter and R. J. Brodd, *Chemical reviews*, 2004, **104**, 4245-4270.

30. H. Chen, T. N. Cong, W. Yang, C. Tan, Y. Li and Y. Ding, *Progress in Natural Science*, 2009, **19**, 291-312.

31. M. Anisur, M. Mahfuz, M. Kibria, R. Saidur, I. Metselaar and T. Mahlia, *Renewable and Sustainable Energy Reviews*, 2013, **18**, 23-30.

32. A. Sharma, V. V. Tyagi, C. R. Chen and D. Buddhi, *Renewable and Sustainable Energy Reviews*, 2009, **13**, 318-345.

33. C. Liu, F. Li, L.-P. Ma and H.-M. Cheng, *Advanced Materials*, 2010, **22**, E28-E62.

34. S. E. Wright, *Renewable Energy*, 2004, **29**, 179-195.

35. A. E. Lutz, R. S. Larson and J. O. Keller, *International Journal of Hydrogen Energy*, 2002, **27**, 1103-1111.

36. T. Christen and M. W. Carlen, *Journal of Power Sources*, 2000, **91**, 210-216.

37. P. Jampani, A. Manivannan and P. N. Kumta, *Electrochemical Society Interface*, 2010, **19**, 57-62.

38. G. Allen, *Nanomarkets Smart Grid Analysis Group Issues, Papers on Smart Grid Sensors and Smart Grid Supercapacitors*, 2009.

39. M. Conte, *Fuel Cells*, 2010, **10**, 806-818.

40. J. Liu, J.-G. Zhang, Z. Yang, J. P. Lemmon, C. Imhoff, G. L. Graff, L. Li, J. Hu, C. Wang, J. Xiao, G. Xia, V. V. Viswanathan, S. Baskaran, V. Sprenkle, X. Li, Y. Shao and B. Schwenzer, *Advanced Functional Materials*, 2013, **23**, 929-946.

41. J. Manuel Carrasco, L. Garcia Franquelo, J. T. Bialasiewicz, E. Galvan, R. C. Portillo Guisado, A. Martin Prats, J. Ignacio Leon and N. Moreno-Alfonso, *Ieee Transactions on Industrial Electronics*, 2006, **53**, 1002-1016.

42. S. Vazquez, S. M. Lukic, E. Galvan, L. G. Franquelo and J. M. Carrasco, *Ieee Transactions on Industrial Electronics*, 2010, **57**, 3881-3895.

43. A. S. Arico, P. Bruce, B. Scrosati, J. M. Tarascon and W. Van Schalkwijk, *Nature Materials*, 2005, **4**, 366-377.

44. B. E. Conway, *Journal of the Electrochemical Society*, 1991, **138**, 1539-1548.

45. G. Allen, 2009.

46. L. Y. Qu and W. Qiao, *IEEE Trans. Ind. Appl.*, 2011, **47**, 359-367.

47. M. LaMonica, Supercapacitor-Enhanced Hybrid Storage to Earn Cash for Subways, http://spectrum.ieee.org/energywise/energy/the-smarter-grid/supercapacitor-enhanced-hybrid-storage-could-earn-cash-for-subways.

48. P. Ball and Y. Gogotsi, *MRS bulletin*, 2012, **37**, 802-803.

49. R. Perez, K. Zweibel and T. E. Hoff, *Energy Policy*, 2011, **39**, 7290-7297.

50. http://www.maxwell.com/ultracapacitors/, http://www.maxwell.com/ultracapacitors/, Accessed May 14, 2014.

51. *Basic Research Needs for Electrical Energy Storage*, Office of Basic Energy Science, US Department of Energy, Washington, DC, 2007.

52. R. M. Dell, *Solid State Ionics*, 2000, **134**, 139-158.

53. A. S. Arico, P. Bruce, B. Scrosati, J.-M. Tarascon and W. van Schalkwijk, *Nat Mater*, 2005, **4**, 366-377.

54. P. Simon, Y. Gogotsi and B. Dunn, *Science*, 2014, **343**, 1210-1211.

55. J. Hopkinson, *Philosophical transactions of the royal society of London*, 1877, **167**, 599-626.

56. W. Mordey, *Electrical Engineers, Journal of the Institution of*, 1909, **43**, 618-628.

57. J. Ho, T. Jow and S. Boggs, *Electrical Insulation Magazine, IEEE*, 2010, **26**, 20-25.

58. B. E. Conway, *Electrochemical Supercapacitors: Scientific Fundamentals and Technological Applications*, Kluwer Academic/Plenum Publishers, New York, 1999.

59. *United States Pat.*, 1966.

60. *United States Pat.*, 1970.

61. *United States Pat.*, 1957.

62. T. C. Liu, W. G. Pell, B. E. Conway and S. L. Roberson, *Journal of the Electrochemical Society*, 1998, **145**, 1882-1888.

63. W. G. Pell and B. E. Conway, *Journal of Electroanalytical Chemistry*, 2001, **500**, 121-133.

64. B. Conway and W. Pell, *Journal of Solid State Electrochemistry*, 2003, **7**, 637-644.

65. P. S. Germain, W. G. Pell and B. E. Conway, *Electrochimica Acta*, 2004, **49**, 1775-1788.

66. *United States Pat.*, 1996.

67. J. O. M. Bockris and A. K. N. Reddy, *Modern Electrochemistry*, Kluwer Academic/Plenum Publishers, 1998.

68. A. J. Bard and L. R. Faulkner, *Electrochemical Methods: Fundamentals and Applications*, Wiley, 2001.

69. J. W. Long, K. E. Swider, C. I. Merzbacher and D. R. Rolison, *Langmuir*, 1999, **15**, 780-785.

70. M. Toupin, T. Brousse and D. Belanger, *Chemistry of Materials*, 2002, **14**, 3946-3952.

71. C. C. Hu and T. W. Tsou, *Electrochemistry Communications*, 2002, **4**, 105-109.

72. V. Subramanian, H. W. Zhu, R. Vajtai, P. M. Ajayan and B. Q. Wei, *Journal of Physical Chemistry B*, 2005, **109**, 20207-20214.

73. H. Wang, H. S. Casalongue, Y. Liang and H. Dai, *Journal of the American Chemical Society*, 2010, **132**, 7472-7477.

74. K. W. Nam and K. B. Kim, *Journal of the Electrochemical Society*, 2002, **149**, A346-A354.

75. T. Kudo, Y. Ikeda, T. Watanabe, M. Hibino, M. Miyayama, H. Abe and K. Kajita, *Solid State Ionics*, 2002, **152**, 833-841.

76. M. Galiński, A. Lewandowski and I. Stępniak, *Electrochimica Acta*, 2006, **51**, 5567-5580.

77. M. Armand, F. Endres, D. R. MacFarlane, H. Ohno and B. Scrosati, *Nature Materials*, 2009, **8**, 621-629.

78. A. Balducci, U. Bardi, S. Caporali, M. Mastragostino and F. Soavi, *Electrochemistry Communications*, 2004, **6**, 566-570.

79. E. Frackowiak, G. Lota and J. Pernak, *Applied Physics Letters*, 2005, **86**, 1-3.

80. A. A. Kornyshev, *The Journal of Physical Chemistry B*, 2007, **111**, 5545-5557.

81. U. S. A. B. Consortium, Department of Energy, 2006.

82. G. Wang, L. Zhang and J. Zhang, *Chemical Society Reviews*, 2012, **41**, 797-828.

83. Y. Zhang, H. Feng, X. Wu, L. Wang, A. Zhang, T. Xia, H. Dong, X. Li and L. Zhang, *International Journal of Hydrogen Energy*, 2009, **34**, 4889-4899.

84. P. Sharma and T. S. Bhatti, *Energy Conversion and Management*, 2010, **51**, 2901-2912.

85. J. Chmiola, G. Yushin, Y. Gogotsi, C. Portet, P. Simon and P. L. Taberna, *Science*, 2006, **313**, 1760-1763.

86. J. Lee, J. Kim and T. Hyeon, *Advanced Materials*, 2006, **18**, 2073-2094.

87. C. Liu, F. Li, L.-P. Ma and H.-M. Cheng, *Advanced Materials*, 2010, **22**, E28-+.

88. A. G. Pandolfo and A. F. Hollenkamp, *Journal of Power Sources*, 2006, **157**, 11-27.

89. D.-W. Wang, F. Li, M. Liu, G. Q. Lu and H.-M. Cheng, *Angewandte Chemie-International Edition*, 2008, **47**, 373-376.

90. L. L. Zhang and X. S. Zhao, *Chemical Society Reviews*, 2009, **38**, 2520-2531.

91. Y. Zhu, S. Murali, M. D. Stoller, K. J. Ganesh, W. Cai, P. J. Ferreira, A. Pirkle, R. M. Wallace, K. A. Cychosz, M. Thommes, D. Su, E. A. Stach and R. S. Ruoff, *Science*, 2011, **332**, 1537-1541.

92. E. Frackowiak and F. Béguin, *Carbon*, 2001, **39**, 937-950.

93. C. D. Lokhande, D. P. Dubal and O.-S. Joo, *Current Applied Physics*, 2011, **11**, 255-270.

94. W. Wei, X. Cui, W. Chen and D. G. Ivey, *Chemical Society Reviews*, 2011, **40**, 1697-1721.

95. W. Deng, X. Ji, Q. Chen and C. E. Banks, *RSC Advances*, 2011, **1**, 1171-1178.

96. H. Jiang, J. Ma and C. Li, *Advanced Materials*, 2012, **24**, 4197-4202.

97. G. A. Snook, P. Kao and A. S. Best, *Journal of Power Sources*, 2011, **196**, 1-12.

98. U. S. A. B. Consortium, ed. L. E.-E. S. S. High Power, 2012.

99. U. S. A. B. Consortium, ed. FreedomCar, 2004.

100. , ed. E. E. R. E.-O. V. Technologies, 2014.

101. Y. Gogotsi, A. Nikitin, H. Ye, W. Zhou, J. E. Fischer, B. Yi, H. C. Foley and M. W. Barsoum, *Nature Materials*, 2003, **2**, 591-594.

102. M. Arulepp, J. Leis, M. Lätt, F. Miller, K. Rumma, E. Lust and A. F. Burke, *Journal of Power Sources*, 2006, **162**, 1460-1466.

103. R. Dash, J. Chmiola, G. Yushin, Y. Gogotsi, G. Laudisio, J. Singer, J. Fischer and S. Kucheyev, *Carbon*, 2006, **44**, 2489-2497.

104. V. Presser, L. Zhang, J. J. Niu, J. McDonough, C. Perez, H. Fong and Y. Gogotsi, *Advanced Energy Materials*, 2011, **1**, 423-430.

105. M. Molina-Sabio and F. Rodríguez-Reinoso, *Colloids and Surfaces A: Physicochemical and Engineering Aspects*, 2004, **241**, 15-25.

106. D.-W. Wang, F. Li, M. Liu, G. Q. Lu and H.-M. Cheng, *Angewandte Chemie International Edition*, 2008, **47**, 373-376.

107. P. Kurzweil, in *Encyclopedia of Electrochemical Power Sources*, ed. G. Editor-in-Chief: Jürgen, Elsevier, Amsterdam, 2009, pp. 634-648.

108. J. Chmiola, C. Largeot, P. L. Taberna, P. Simon and Y. Gogotsi, *Angewandte Chemie - International Edition*, 2008, **47**, 3392-3395.

109. J. Chmiola, P. L. T. Celine Largeot, P. Simon and Y. Gogotsi, *Science*, 2010, **328**, 480-483.

110. P. Simon and Y. Gogotsi, *Philosophical Transactions of the Royal Society A: Mathematical, Physical and Engineering Sciences*, 2010, **368**, 3457-3467.

111. D. Qu and H. Shi, *Journal of Power Sources*, 1998, **74**, 99-107.

112. R. Lin, P. Huang, J. Ségalini, C. Largeot, P. L. Taberna, J. Chmiola, Y. Gogotsi and P. Simon, *Electrochimica Acta*, 2009, **54**, 7025-7032.

113. P. Simon and Y. Gogotsi, *Accounts of Chemical Research*, 2012, **46**, 1094-1103.

114. J. Huang, B. G. Sumpter, V. Meunier, G. Yushin, C. Portet and Y. Gogotsi, *Journal of Materials Research*, 2010, **25**, 1525.

115. J. Huang, R. Qiao, B. G. Sumpter and V. Meunier, *Journal of Materials Research*, 2010, **25**, 1469-1475.

116. S. Kondrat and A. Kornyshev, *Journal of Physics: Condensed Matter*, 2011, **23**, 022201.

117. C. Largeot, C. Portet, J. Chmiola, P.-L. Taberna, Y. Gogotsi and P. Simon, *Journal of the American Chemical Society*, 2008, **130**, 2730-2731.

118. G. Salitra, A. Soffer, L. Eliad, Y. Cohen and D. Aurbach, *Journal of The Electrochemical Society*, 2000, **147**, 2486-2493.

119. J. Chmiola, G. Yushin, Y. Gogotsi, C. Portet, P. Simon and P. L. Taberna, *Science*, 2006, **313**, 1760-1763.

120. D. Roy and M. Maroncelli, *The Journal of Physical Chemistry B*, 2010, **114**, 12629-12631.

121. C. l. Merlet, M. Salanne, B. Rotenberg and P. A. Madden, *The Journal of Physical Chemistry C*, 2011, **115**, 16613-16618.

122. C. Merlet, B. Rotenberg, P. A. Madden, P.-L. Taberna, P. Simon, Y. Gogotsi and M. Salanne, *Nat Mater*, 2012, **11**, 306-310.

123. C. Merlet, C. Péan, B. Rotenberg, P. A. Madden, P. Simon and M. Salanne, *The Journal of Physical Chemistry Letters*, 2012, **4**, 264-268.

124. E. Frackowiak, K. Metenier, V. Bertagna and F. Beguin, *Applied Physics Letters*, 2000, **77**, 2421-2423.

125. D. N. Futaba, K. Hata, T. Yamada, T. Hiraoka, Y. Hayamizu, Y. Kakudate, O. Tanaike, H. Hatori, M. Yumura and S. Iijima, *Nature Materials*, 2006, **5**, 987-994.

126. P. W. Ruch, R. Kotz and A. Wokaun, *Electrochimica Acta*, 2009, **54**, 4451-4458.

127. S. Lee, M. S. Cho, J. D. Nam and Y. Lee, *Journal of Nanoscience and Nanotechnology*, 2008, **8**, 5036-5041.

128. S. W. Woo, K. Dokko and K. Kanamura, *Journal of Power Sources*, 2008, **185**, 1589-1593.

129. M. Hughes, M. S. P. Shaffer, A. C. Renouf, C. Singh, G. Z. Chen, D. J. Fray and A. H. Windle, *Advanced Materials*, 2002, **14**, 382-385.

130. M. Hughes, G. Z. Chen, M. S. P. Shaffer, D. J. Fray and A. H. Windle, *Chemistry of Materials*, 2002, **14**, 1610-1613.

131. O. Kimizuka, O. Tanaike, J. Yamashita, T. Hiraoka, D. N. Futaba, K. Hata, K. Machida, S. Suematsu, K. Tamamitsu, S. Saeki, Y. Yamada and H. Hatori, *Carbon*, 2008, **46**, 1999-2001.

132. L.-F. Chen, X.-D. Zhang, H.-W. Liang, M. Kong, Q.-F. Guan, P. Chen, Z.-Y. Wu and S.-H. Yu, *ACS Nano*, 2012, **6**, 7092-7102.

133. M. M. Shaijumon, F. S. Ou, L. J. Ci and P. M. Ajayan, *Chemical Communications*, 2008, 2373-2375.

134. W. Gao, N. Singh, L. Song, Z. Liu, A. L. M. Reddy, L. Ci, R. Vajtai, Q. Zhang, B. Wei and P. M. Ajayan, *Nat Nano*, 2011, **6**, 496-500.

135. M. D. Stoller, S. J. Park, Y. W. Zhu, J. H. An and R. S. Ruoff, *Nano Letters*, 2008, **8**, 3498-3502.

136. Y. W. Zhu, S. Murali, M. D. Stoller, A. Velamakanni, R. D. Piner and R. S. Ruoff, *Carbon*, 2010, **48**, 2118-2122.

137. S. Stankovich, D. A. Dikin, G. H. B. Dommett, K. M. Kohlhaas, E. J. Zimney, E. A. Stach, R. D. Piner, S. T. Nguyen and R. S. Ruoff, *Nature*, 2006, **442**, 282-286.

138. S. Stankovich, D. A. Dikin, R. D. Piner, K. A. Kohlhaas, A. Kleinhammes, Y. Jia, Y. Wu, S. T. Nguyen and R. S. Ruoff, *Carbon*, 2007, **45**, 1558-1565.

139. A. K. Geim and K. S. Novoselov, *Nature Materials*, 2007, **6**, 183-191.

140. K. S. Novoselov, A. K. Geim, S. V. Morozov, D. Jiang, Y. Zhang, S. V. Dubonos, I. V. Grigorieva and A. A. Firsov, *Science*, 2004, **306**, 666-669.

141. S. Murali, J. R. Potts, S. Stoller, J. Park, M. D. Stoller, L. L. Zhang, Y. Zhu and R. S. Ruoff, *Carbon*, 2012, **50**, 3482-3485.

142. Y. Wang, Z. Shi, Y. Huang, Y. Ma, C. Wang, M. Chen and Y. Chen, *Journal of Physical Chemistry C*, 2009, **113**, 13103-13107.

143. M. F. El-Kady, V. Strong, S. Dubin and R. B. Kaner, *Science*, 2012, **335**, 1326-1330.

144. V. Strong, S. Dubin, M. F. El-Kady, A. Lech, Y. Wang, B. H. Weiller and R. B. Kaner, *ACS Nano*, 2012, **6**, 1395-1403.

145. L. B. Hu, H. Wu and Y. Cui, *Applied Physics Letters*, 2010, **96**.

146. D.-W. Wang, F. Li, J. Zhao, W. Ren, Z.-G. Chen, J. Tan, Z.-S. Wu, I. Gentle, G. Q. Lu and H.-M. Cheng, *Acs Nano*, 2009, **3**, 1745-1752.

147. H. L. Wang, Q. L. Hao, X. J. Yang, L. D. Lu and X. Wang, *Electrochemistry Communications*, 2009, **11**, 1158-1161.

148. M. F. El-Kady and R. B. Kaner, *Nat Commun*, 2013, **4**, 1475.

149. K. Fic, M. Meller and E. Frackowiak, *Electrochimica Acta*, 2014, **128**, 210-217.

150. V. Presser, C. R. Dennison, J. Campos, K. W. Knehr, E. C. Kumbur and Y. Gogotsi, *Advanced Energy Materials*, 2012, **2**, 895-902.

151. J. W. Campos, M. Beidaghi, K. B. Hatzell, C. R. Dennison, B. Musci, V. Presser, E. C. Kumbur and Y. Gogotsi, *Electrochimica Acta*, 2013, **98**, 123-130.

152. C. R. Dennison, M. Beidaghi, K. B. Hatzell, J. W. Campos, Y. Gogotsi and E. C. Kumbur, *Journal of Power Sources*, 2014, **247**, 489-496.

153. K. B. Hatzell, M. Beidaghi, J. W. Campos, C. R. Dennison, E. C. Kumbur and Y. Gogotsi, *Electrochimica Acta*, 2013, **111**, 888-897.

154. X. Li, C. Han, X. Chen and C. Shi, *Microporous and Mesoporous Materials*, 2010, **131**, 303-309.

155. M. Biswal, A. Banerjee, M. Deo and S. Ogale, *Energy & Environmental Science*, 2013, **6**, 1249-1259.

156. K. B. Hatzell, E. Iwama, A. Ferris, B. Daffos, K. Urita, T. Tzedakis, F. Chauvet, P.-L. Taberna, Y. Gogotsi and P. Simon, *Electrochemistry Communications*, 2014, **43**, 18-21.

157. E. Avraham, Y. Bouhadana, A. Soffer and D. Aurbach, *Journal of The Electrochemical Society*, 2009, **156**, P95-P99.

158. J. M. Miller, B. Dunn, T. D. Tran and R. W. Pekala, *Journal of the Electrochemical Society*, 1997, **144**, L309-L311.

159. J. W. Long, K. E. Swider, C. I. Merzbacher and D. R. Rolison, *Langmuir*, 1999, **15**, 780-784.

160. D. A. McKeown, P. L. Hagans, L. P. L. Carette, A. E. Russell, K. E. Swider and D. R. Rolison, *Journal of Physical Chemistry B*, 1999, **103**, 4825-4832.

161. K. Naoi, S. Ishimoto, N. Ogihara, Y. Nakagawa and S. Hatta, *Journal of the Electrochemical Society*, 2009, **156**, A52-A59.

162. R. Liu, J. Duay, T. Lane and S. B. Lee, *Physical Chemistry Chemical Physics*, 2010, **12**, 4309-4316.

163. J. K. Chang, C. T. Lin and W. T. Tsai, *Electrochemistry Communications*, 2004, **6**, 666-671.

164. S. R. Sivakkumar, J. M. Ko, D. Y. Kim, B. C. Kim and G. G. Wallace, *Electrochimica Acta*, 2007, **52**, 7377-7385.

165. G. X. Wang, B. L. Zhang, Z. L. Yu and M. Z. Qu, *Solid State Ionics*, 2005, **176**, 1169-1174.

166. T. Brezesinski, J. Wang, J. Polleux, B. Dunn and S. H. Tolbert, *Journal of the American Chemical Society*, 2009, **131**, 1802-1809.

167. T. Brezesinski, J. Wang, S. H. Tolbert and B. Dunn, *Nature Materials*, 2010, **9**, 146-151.

168. T. Brezesinski, J. Wang, S. H. Tolbert and B. Dunn, *Nature Materials*, 2010, **9**, 146-151.

169. Z. Chen, Y. Qin, D. Weng, Q. Xiao, Y. Peng, X. Wang, H. Li, F. Wei and Y. Lu, *Advanced Functional Materials*, 2009, **19**, 3420-3426.

170. I. H. Kim, J. H. Kim, B. W. Cho, Y. H. Lee and K. B. Kim, *Journal of the Electrochemical Society*, 2006, **153**, A989-A996.

171. K.-W. Nam, K.-H. Kim, E.-S. Lee, W.-S. Yoon, X.-Q. Yang and K.-B. Ki, *Journal of Power Sources*, 2008, **182**, 642-652.

172. S. Suzuki, M. Hibino and M. Miyayama, *Journal of Power Sources*, 2003, **124**, 513-517.

173. S. D. Perera, B. Patel, J. Bonso, M. Grunewald, J. P. Ferraris and K. J. Balkus, *Acs Applied Materials & Interfaces*, 2011, **3**, 4512-4517.

174. S. Tepavcevic, H. Xiong, V. R. Stamenkovic, X. Zuo, M. Balasubramanian, V. B. Prakapenka, C. S. Johnson and T. Rajh, *ACS Nano*, 2011, **6**, 530-538.

175. P. H. Jampani, K. Kadakia, D. H. Hong, R. Epur, J. A. Poston, A. Manivannan and P. N. Kumta, *Journal of the Electrochemical Society*, 2013, **160**, A1118-A1127.

176. M. E. Spahr, P. Bitterli, R. Nesper, M. Muller, F. Krumeich and H. U. Nissen, *Angewandte Chemie-International Edition*, 1998, **37**, 1263-1265.

177. M. E. Spahr, P. Stoschitzki-Bitterli, R. Nesper, O. Haas and P. Novak, *Journal of the Electrochemical Society*, 1999, **146**, 2780-2783.

178. C. C. Hu, C. M. Huang and K. H. Chang, *Journal of Power Sources*, 2008, **185**, 1594-1597.

179. C. M. Huang, C. C. Hu, K. H. Chang, J. M. Li and Y. F. Li, *Journal of the Electrochemical Society*, 2009, **156**, A667-A671.

180. J. M. Li, K. H. Chang and C. C. Hu, *Electrochemistry Communications*, 2010, **12**, 1800-1803.

181. J. M. Li, K. H. Chang, T. H. Wu and C. C. Hu, *Journal of Power Sources*, 2013, **224**, 59-65.

182. D. Choi, G. E. Blomgren and P. N. Kumta, *Advanced Materials*, 2006, **18**, 1178-1182.

183. J. C. Badot and N. Baffier, *Journal of Materials Chemistry*, 1992, **2**, 1167-1174.

184. Y. Wang and G. Cao, *Chemistry of Materials*, 2006, **18**, 2787-2804.

185. F. Coustier, J. Hill, B. B. Owens, S. Passerini and W. H. Smyrl, *Journal of the Electrochemical Society*, 1999, **146**, 1355-1360.

186. T. Szorenyi, K. Bali and I. Hevesi, *Journal of Non-Crystalline Solids*, 1980, **35-6**, 1245-1248.

187. S. D. Perera, B. Patel, N. Nijem, K. Roodenko, O. Seitz, J. P. Ferraris, Y. J. Chabal and K. J. Balkus, *Advanced Energy Materials*, 2011, **1**, 936-945.

188. C. Y. Lee, H. M. Tsai, H. J. Chuang, S. Y. Li, P. Lin and T. Y. Tseng, *Journal of the Electrochemical Society*, 2005, **152**, A716-A720.

189. A. L. M. Reddy, M. M. Shaijumon, S. R. Gowda and P. M. Ajayan, *Nano Letters*, 2009, **9**, 1002-1006.

190. Z. Fan, J. Chen, K. Cui, F. Sun, Y. Xu and Y. Kuang, *Electrochimica Acta*, 2007, **52**, 2959-2965.

191. I. H. Kim, J. H. Kim and K. B. Kim, *Electrochemical and Solid State Letters*, 2005, **8**, A369-A372.

192. I. H. Kim, J. H. Kim, Y. H. Lee and K. B. Kim, *Journal of the Electrochemical Society*, 2005, **152**, A2170-A2178.

193. W. Wang and P. N. Kumta, *Journal of Power Sources*, 2007, **172**, 650-658.

194. S. D. Perera, B. Patel, N. Nijem, K. Roodenko, O. Seitz, J. P. Ferraris, Y. J. Chabal and K. J. Balkus, *Advanced Energy Materials*, 2011, **1**, 936-945.

195. M. Sathiya, A. S. Prakash, K. Ramesha, J. M. Tarascon and A. K. Shukla, *Journal of the American Chemical Society*, 2011, **133**, 16291-16299.

196. Z. Chen, Y. C. Qin, D. Weng, Q. F. Xiao, Y. T. Peng, X. L. Wang, H. X. Li, F. Wei and Y. F. Lu, *Advanced Functional Materials*, 2009, **19**, 3420-3426.

197. J. Benson, S. Boukhalfa, A. Magasinski, A. Kvit and G. Yushin, *ACS Nano*, 2011, **6**, 118-125.

198. S. Boukhalfa, K. Evanoff and G. Yushin, *Energy & Environmental Science*, 2012, **5**, 6872-6879.

199. Z. Chen, V. Augustyn, J. Wen, Y. Zhang, M. Shen, B. Dunn and Y. Lu, *Advanced Materials*, 2011, **23**, 791-795.

200. A. M. Engstrom and F. M. Doyle, *Journal of Power Sources*, 2013, **228**, 120-131.

201. S. D. Perera, A. D. Liyanage, N. Nijem, J. P. Ferraris, Y. J. Chabal and K. J. Balkus Jr, *Journal of Power Sources*, 2013, **230**, 130-137.

202. G. Wang, X. Lu, Y. Ling, T. Zhai, H. Wang, Y. Tong and Y. Li, *ACS Nano*, 2012, **6**, 10296-10302.

203. S. Chen, J. Zhu, X. Wu, Q. Han and X. Wang, *ACS Nano*, 2010, **4**, 2822-2830.

204. X. Lang, A. Hirata, T. Fujita and M. Chen, *Nat Nano*, 2011, **6**, 232-236.

205. M. Zhi, C. Xiang, J. Li, M. Li and N. Wu, *Nanoscale*, 2013, **5**, 72-88.

206. P.-C. Chen, G. Shen, Y. Shi, H. Chen and C. Zhou, *ACS Nano*, 2010, **4**, 4403-4411.

207. X. Lu, D. Zheng, T. Zhai, Z. Liu, Y. Huang, S. Xie and Y. Tong, *Energy & Environmental Science*, 2011, **4**, 2915-2921.

208. M. E. Franke, T. J. Koplin and U. Simon, *Small*, 2006, **2**, 36-50.

209. G. Korotcenkov, *Sensors and Actuators B: Chemical*, 2005, **107**, 209-232.

210. Y. Wei, C.-W. Ryu and K.-B. Kim, *Journal of Power Sources*, 2007, **165**, 386-392.

211. D. Hara, H. Ikuta, Y. Uchimoto and M. Wakihara, *Journal of Materials Chemistry*, 2002, **12**, 2507-2512.

212. H. K. Park, *Solid State Ionics*, 2005, **176**, 307-312.

213. L. Q. Mai, W. Chen, Q. Xu, J. F. Peng and Q. Y. Zhu, *Chem. Phys. Lett.*, 2003, **382**, 307-312.

214. K. Kadakia, M. K. Datta, P. H. Jampani, S. K. Park and P. N. Kumta, *Journal of Power Sources*, 2013, **222**, 313-317.

215. K. Kadakia, M. K. Datta, O. I. Velikokhatnyi, P. Jampani, S. K. Park, P. Saha, J. A. Poston, A. Manivannan and P. N. Kumta, *International Journal of Hydrogen Energy*, 2012, **37**, 3001-3013.

216. F. Coustier, S. Passerini and W. H. Smyrl, *Solid State Ionics*, 1997, **100**, 247-258.

217. Y. Takasu, S. Mizutani, M. Kumagai, S. Sawaguchi and Y. Murakami, *Electrochemical and Solid State Letters*, 1999, **2**, 1-2.

218. D. Yang, *Journal of Power Sources*, 2013, **228**, 89-96.

219. D. Yang, *Journal of Power Sources*, 2012, **198**, 416-422.

220. L.-Q. Mai, F. Yang, Y.-L. Zhao, X. Xu, L. Xu and Y.-Z. Luo, *Nat Commun*, 2011, **2**, 381.

221. H. Jiang, T. Zhao, C. Li and J. Ma, *Chemical Communications*, 2011, **47**, 8590-8592.

222. X. Xia, J. Tu, Y. Zhang, X. Wang, C. Gu, X.-b. Zhao and H. J. Fan, *ACS Nano*, 2012, **6**, 5531-5538.

223. Q. Qu, S. Yang and X. Feng, *Advanced Materials*, 2011, **23**, 5574-5580.

224. H. Wang, H. S. Casalongue, Y. Liang and H. Dai, *Journal of the American Chemical Society*, 2010, **132**, 7472-7477.

225. Y. Yang, D. Kim, M. Yang and P. Schmuki, *Chemical Communications*, 2011, **47**, 7746-7748.

226. D. Wei, M. R. J. Scherer, C. Bower, P. Andrew, T. Ryhänen and U. Steiner, *Nano Letters*, 2012, **12**, 1857-1862.

227. T.-H. Wu, Y.-H. Chu, C.-C. Hu and L. J. Hardwick, *Electrochemistry Communications*, 2013, **27**, 81-84.

228. Y. Gogotsi and P. Simon, *Science*, 2011, **334**, 917-918.

229. E. Iwama, P. L. Taberna, P. Azais, L. Brégeon and P. Simon, *Journal of Power Sources*, 2012, **219**, 235-239.

230. M. D. Stoller and R. S. Ruoff, *Energy & Environmental Science*, 2010, **3**, 1294-1301.

231. L. Hu, J. W. Choi, Y. Yang, S. Jeong, F. La Mantia, L.-F. Cui and Y. Cui, *Proceedings of the National Academy of Sciences*, 2009, **106**, 21490-21494.

232. A. Burke, *Journal of Power Sources*, 2000, **91**, 37-50.

233. F. Mazza and S. Trassatti, *Journal of The Electrochemical Society*, 1963, **110**, 847-849.

234. D. Choi and P. N. Kumta, *Journal of the American Ceramic Society*, 2011, **94**, 2371-2378.

235. D. Choi, Doctor of Philosophy, Carnegie Mellon University, 2005.

236. D. Choi and P. N. Kumta, *Journal of the Electrochemical Society*, 2006, **153**, A2298-A2303.

237. D. Choi and P. N. Kumta, *Journal of the American Ceramic Society*, 2007, **90**, 3113-3120.

238. D. W. Choi and P. N. Kumta, *Electrochemical and Solid State Letters*, 2005, **8**, A418-A422.

239. D. Choi and P. N. Kumta, *Journal of the American Ceramic Society*, 2007, **90**, 3113-3120.

240. C. L. Chen, D. L. Zhao, D. Xu and X. K. Wang, *Materials Chemistry and Physics*, 2006, **95**, 84-88.

241. T. C. Liu, W. G. Pell, B. E. Conway and S. L. Roberson, *Journal of the Electrochemical Society*, 1998, **145**, 1882-1888.

242. Y. G. Zhu, X. L. Li, H. L. Wang, J. B. He and D. R. Lu, *Journal of Inorganic Materials*, 2001, **16**, 1019-1023.

243. *United States Pat.*, 5680292, 1994.

244. D. J. T. M. R. Wixom, J. M. Parker, J. Q. Lee, P.-L. Chen, I. Song and L. T. Thompson, High Surface Area Metal Carbide and Metal Nitride Electrodes, 1997.

245. C. M. Ghimbeu, E. Raymundo-Pinero, P. Fioux, F. Beguin and C. Vix-Guterl, *Journal of Materials Chemistry*, 2011, **21**, 13268-13275.

246. P. J. Hanumantha, M. K. Datta, K. S. Kadakia, D. H. Hong, S. J. Chung, M. C. Tam, J. A. Poston, A. Manivannan and P. N. Kumta, *Journal of The Electrochemical Society*, 2013, **160**, A2195-A2206.

247. P. Pande, P. G. Rasmussen and L. T. Thompson, *Journal of Power Sources*, 2012, **207**, 212-215.

248. L. Zhang, C. M. B. Holt, E. J. Luber, B. C. Olsen, H. T. Wang, M. Danaie, X. W. Cui, X. H. Tan, V. W. Lui, W. P. Kalisvaart and D. Mitlin, *Journal of Physical Chemistry C*, 2011, **115**, 24381-24393.

249. X. Zhou, H. Chen, D. Shu, C. He and J. Nan, *Journal of Physics and Chemistry of Solids*, 2009, **70**, 495-500.

250. X. Zhou, C. Shang, L. Gu, S. Dong, X. Chen, P. Han, L. Li, J. Yao, Z. Liu, H. Xu, Y. Zhu and G. Cui, *Acs Applied Materials & Interfaces*, 2011, **3**, 3058-3063.

251. X. P. Zhou, H. Y. Chen, D. Shu, C. He and J. M. Nan, *Journal of Physics and Chemistry of Solids*, 2009, **70**, 495-500.

252. X. Lu, M. Yu, T. Zhai, G. Wang, S. Xie, T. Liu, C. Liang, Y. Tong and Y. Li, *Nano letters*, 2013, **13**, 2628-2633.

253. S.-J. Bao, C. M. Li, C.-X. Guo and Y. Qiao, *Journal of Power Sources*, 2008, **180**, 676-681.

254. F. Tao, Y.-Q. Zhao, G.-Q. Zhang and H.-L. Li, *Electrochemistry Communications*, 2007, **9**, 1282-1287.

255. H. Kwon, S. Choi and L. T. Thompson, *J. Catal.*, 1999, **184**, 236-246.

256. L. T. Thompson Jr, M. R. Wixom and J. M. Parker, Google Patents, 1997.

257. L. T. Thompson Jr and M. R. Wixom, Google Patents, 1999.

258. M. Wixom, D. Tarnowski, J. Parker, J. Lee, P. Chen, I. Song and L. Thompson, High surface area metal carbide and metal nitride electrodes, 1998.

259. L. Owens, L. T. Thompson Jr and M. R. Wixom, Google Patents, 1998.

260. A. M. Glushenkov, D. Hulicova-Jurcakova, D. Llewellyn, G. Q. Lu and Y. Chen, *Chem. Mat.*, 2010, **22**, 914-921.

261. F. Cheng, C. He, D. Shu, H. Chen, J. Zhang, S. Tang and D. E. Finlow, *Materials Chemistry and Physics*, 2011, **131**, 268-273.

262. R. L. Porto, R. Frappier, J. B. Ducros, C. Aucher, H. Mosqueda, S. Chenu, B. Chavillon, F. Tessier, F. Cheviré and T. Brousse, *Electrochimica Acta*, 2012, **82**, 257-262.

263. D. Choi, G. E. Blomgren and P. N. Kumta, *Advanced Materials*, 2006, **18**, n/a-n/a.

264. S. J. Bao, C. M. Li, C. X. Guo and Y. Qiao, *Journal of Power Sources*, 2008, **180**, 676-681.

265. Z. Stevic and M. Rajcic-Vujasinovic, *Journal of Power Sources*, 2006, **160**, 1511-1517.

266. F. Tao, Y. Q. Zhao, G. Q. Zhang and H. L. Li, *Electrochemistry Communications*, 2007, **9**, 1282-1287.

267. E. Eustache, R. Frappier, R. L. Porto, S. Bouhtiyya, J.-F. Pierson and T. Brousse, *Electrochem. Commun.*, 2013, **28**, 104-106.

268. O. Kartachova, A. M. Glushenkov, Y. Chen, H. Zhang, X. J. Dai and Y. Chen, *Journal of Power Sources*, 2012, **220**, 298-305.

269. M. Pourbaix, *Atlas of electrochemical equilibria in aqueous solutions*, Pergamon Press, Oxford, 1966.

270. Z. Chen, V. Augustyn, X. L. Jia, Q. F. Xiao, B. Dunn and Y. F. Lu, *ACS Nano*, 2012, **6**, 4319-4327.

271. C. Wu, F. Feng and Y. Xie, *Chemical Society Reviews*, 2013, **42**, 5157-5183.

272. J. Hojo, O. Iwamoto, Y. Maruyama and A. Kato, *Journal of the Less Common Metals*, 1977, **53**, 265-276.

273. H. O. Pierson, *Handbook of Refractory Carbides & Nitrides: Properties, Characteristics, Processing and Apps*, William Andrew, 1996.

274. B. Hu, X. Qin, A. M. Asiri, K. A. Alamry, A. O. Al-Youbi and X. Sun, *Electrochemistry Communications*, 2013, **28**, 75-78.

275. B. Hu, X. Qin, A. M. Asiri, K. A. Alamry, A. O. Al-Youbi and X. Sun, *Electrochimica Acta*, 2013, **100**, 24-28.

276. B. T. Zhu, Z. Wang, S. Ding, J. S. Chen and X. W. Lou, *RSC Advances*, 2011, **1**, 397-400.

277. Z. Jiang, W. Lu, Z. Li, X. Jiao, D. Chen, X. Li and K.-H. Ho, *Journal of Materials Chemistry A*, 2014.

278. Q. Wang, L. Jiao, H. Du, J. Yang, Q. Huan, W. Peng, Y. Si, Y. Wang and H. Yuan, *CrystEngComm*, 2011, **13**, 6960-6963.

279. Z. Yang, C.-Y. Chen and H.-T. Chang, *Journal of Power Sources*, 2011, **196**, 7874-7877.

280. P. Justin and G. Ranga Rao, *International Journal of Hydrogen Energy*, 2010, **35**, 9709-9715.

281. C.-Y. Chen, Z.-Y. Shih, Z. Yang and H.-T. Chang, *Journal of Power Sources*, 2012, **215**, 43-47.

282. T. Zhu, B. Xia, L. Zhou and X. Wen Lou, *Journal of Materials Chemistry*, 2012, **22**, 7851-7855.

283. Q. Xiao and X. Zhou, *Electrochimica Acta*, 2003, **48**, 575-580.

284. E. Frackowiak, V. Khomenko, K. Jurewicz, K. Lota and F. Béguin, *Journal of Power Sources*, 2006, **153**, 413-418.

285. C. Peng, S. Zhang, D. Jewell and G. Z. Chen, *Progress in Natural Science*, 2008, **18**, 777-788.

286. S. Ghosh and O. Inganäs, *Advanced Materials*, 1999, **11**, 1214-1218.

287. V. Khomenko, E. Frackowiak and F. Béguin, *Electrochimica Acta*, 2005, **50**, 2499-2506.

288. A. Balducci, R. Dugas, P. L. Taberna, P. Simon, D. Plee, M. Mastragostino and S. Passerini, *Journal of Power Sources*, 2007, **165**, 922-927.

289. E. Frackowiak, G. Lota and J. Pernak, *Applied Physics Letters*, 2005, **86**.

290. M. Lazzari, M. Mastragostino and F. Soavi, *Electrochemistry Communications*, 2007, **9**, 1567-1572.

291. G. G. Amatucci, F. Badway, A. Du Pasquier and T. Zheng, *Journal of the Electrochemical Society*, 2001, **148**, A930-A939.

292. J. P. Zheng, *Journal of the Electrochemical Society*, 2003, **150**, A484-A492.

293. J. L. Li and F. Gao, *Journal of Power Sources*, 2009, **194**, 1184-1193.

294. R. Inguanta, G. Ferrara, P. Livreri, S. Piazza and C. Sunseri, *Curr. Nanosci.*, 2011, **7**, 210-218.

295. C. J. Barnhart, M. Dale, A. R. Brandt and S. M. Benson, *Energy & Environmental Science*, 2013, **6**, 2804-2810.

296. J. Miller, BESTMag, 2011.

297. J. R. Miller and P. Simon, *Science Magazine*, 2008, **321**, 651-652.

298. J. Zhang and X. S. Zhao, *ChemSusChem*, 2012, **5**, 818-841.

299. H. D. Abruna, Y. Kiya and J. C. Henderson, *Physics Today*, 2008, **61**, 43-47.

300. J. B. Goodenough, H. Abruna and M. Buchanan, Basic research needs for electrical energy storage, 2007.

301. P. Krawiec, P. L. De Cola, R. Glaser, J. Weitkamp, C. Weidenthaler and S. Kaskel, *Advanced Materials*, 2006, **18**, 505-+.

302. R. Kapoor and S. T. Oyama, *Journal of Solid State Chemistry*, 1992, **99**, 303-312.

303. S. T. Oyama, R. Kapoor, H. T. Oyama, D. J. Hofmann and E. Matijevic, *Journal of Materials Research*, 1993, **8**, 1450-1454.

304. I. Galesic and B. O. Kolbesen, *Thin Solid Films*, 1999, **349**, 14-18.

305. O. Merdrignac-Conanec, K. El Badraoui and P. L'Haridon, *Journal of Solid State Chemistry*, 2005, **178**, 218-223.

306. P. Cai, Z. Yang, C. Wang, P. Xia and Y. Qian, *Materials Letters*, 2006, **60**, 410-413.

307. G. Hyett, M. A. Green and I. P. Parkin, *Chemical Vapor Deposition*, 2008, **14**, 309-312.

308. Y. X. Du, M. Lei and H. Yang, *Journal of Materials Science & Technology*, 2008, **24**, 737-741.

309. M. Lei, H. Z. Zhao, H. Yang, P. G. Li, H. L. Tang, B. Song and W. H. Tang, *Diamond and Related Materials*, 2007, **16**, 1974-1981.

310. M. Lei, H. Z. Zhao, H. Yang, B. Song, P. G. Li and W. H. Tang, *Materials Letters*, 2008, **62**, 1539-1542.

311. P. G. Li, M. Lei, H. Z. Zhao, H. L. Tang, H. Yang and W. H. Tang, *Materials Chemistry and Physics*, 2007, **105**, 234-239.

312. P. Krawiec and S. Kaskel, *Topics in Catalysis*, 2009, **52**, 1549-1558.

313. I. S. Kim, G. E. Blomgren and P. N. Kumta, *Journal of Power Sources*, 2004, **130**, 275-280.

314. I. Kim, P. N. Kumta and G. E. Blomgren, *Electrochemical and Solid State Letters*, 2000, **3**, 493-496.

315. N. Ozer, S. Sabuncu and J. Cronin, *Thin Solid Films*, 1999, **338**, 201-206.

316. W. Wang, R. Epur and P. N. Kumta, *Electrochemistry Communications*, 2011, **13**, 429-432.

317. W. Wang and P. N. Kumta, *ACS Nano*, 2010, **4**, 2233-2241.

318. D. Vernardou, P. Paterakis, H. Drosos, E. Spanakis, I. M. Povey, M. E. Pemble, E. Koudoumas and N. Katsarakis, *Solar Energy Materials and Solar Cells*, 2011, **95**, 2842-2847.

319. L. Michailovits, K. Bali, T. Szorenyi and I. Hevesi, *Acta Physica Academiae Scientiarum Hungaricae*, 1980, **49**, 217-221.

320. R. Binions, G. Hyett, C. Piccirillo and I. P. Parkin, *Journal of Materials Chemistry*, 2007, **17**, 4652-4660.

321. T. D. Manning and I. P. Parkin, *Polyhedron*, 2004, **23**, 3087-3095.

322. M. N. Field and I. P. Parkin, *Journal of Materials Chemistry*, 2000, **10**, 1863-1866.

323. T. D. Manning, I. P. Parkin, R. J. H. Clark, D. Sheel, M. E. Pemble and D. Vernadou, *Journal of Materials Chemistry*, 2002, **12**, 2936-2939.

324. I. P. Parkin and G. S. Elwin, *Journal of Materials Chemistry*, 2001, **11**, 3120-3124.

325. Z. Peng, W. Jiang and H. Liu, *The Journal of Physical Chemistry C*, 2006, **111**, 1119-1122.

326. O. Y. Berezina, A. A. Velichko, L. A. Lugovskaya, A. L. Pergament, G. B. Stefanovich, D. V. Artyukhin and A. N. Strelkov, *Tech. Phys. Lett.*, 2007, **33**, 552-555.

327. T. D. Manning and I. P. Parkin, *Journal of Materials Chemistry*, 2004, **14**, 2554-2559.

328. J. Shi, S. Zhou, B. You and L. Wu, *Solar Energy Materials and Solar Cells*, 2007, **91**, 1856-1862.

329. J. D. Butler, *Transactions of the Faraday Society*, 1960, **56**, 1842-1850.

330. S. K. Pal, S. Talapatra, S. Kar, L. Ci, R. Vajtai, T. Borca-Tasciuc, L. S. Schadler and P. M. Ajayan, *Nanotechnology*, 2008, **19**.

331. S. Talapatra, S. Kar, S. K. Pal, R. Vajtai, L. Ci, P. Victor, M. M. Shaijumon, S. Kaur, O. Nalamasu and P. M. Ajayan, *Nature Nanotechnology*, 2006, **1**, 112-116.

332. T. D. Manning, I. P. Parkin, M. E. Pemble, D. Sheel and D. Vernardou, *Chemistry of Materials*, 2004, **16**, 744-749.

333. C. S. Blackman, C. Piccirillo, R. Binions and I. P. Parkin, *Thin Solid Films*, 2009, **517**, 4565-4570.

334. D. Vernardou, M. E. Pemble and D. W. Sheel, *Chemical Vapor Deposition*, 2007, **13**, 158-162.

335. J. I. Langford, D. Louer and P. Scardi, *J. Appl. Crystallogr.*, 2000, **33**, 964-974.

336. H. Toraya, *J. Appl. Crystallogr.*, 1990, **23**, 485-491.

337. G. H. Kelsall, I. Thompson and P. A. Francis, *Journal of Applied Electrochemistry*, 1993, **23**, 417-426.

338. T. Suszko, W. Gulbinski and A. Urbanowicz, *Materials Letters*, 2011, **65**, 2146-2148.

339. M. A. Roldan, V. Lopez-Flores, M. D. Alcala, A. Ortega and C. Real, *J. Eur. Ceram. Soc.*, 2010, **30**, 2099-2107.

340. G. H. Kelsall, I. Thompson and P. A. Francis, *Journal of Applied Electrochemistry*, 1993, **23**, 417-426.

341. A. J. Bard, R. Parsons and J. Jordan, *Standard potentials in aqueous solution*, New York, 1985.

342. M. Pourbaix, *Atlas of electrochemical equilibria in aqueous solutions*, National Association of Corrosion Engineers, 1974.

343. M. Sathiya, A. S. Prakash, K. Ramesha, J. M. Tarascon and A. K. Shukla, *Journal of the American Chemical Society*, 2011, **133**, 16291-16299.

344. C.-C. Liu, D.-S. Tsai, D. Susanti, W.-C. Yeh, Y.-S. Huang and F.-J. Liu, *Electrochimica Acta*, 2010, **55**, 5768-5774.

345. K.-H. Chang and C.-C. Hu, *Applied Physics Letters*, 2006, **88**, 193102-193103.

346. C.-C. Hu, K.-H. Chang, M.-C. Lin and Y.-T. Wu, *Nano Letters*, 2006, **6**, 2690-2695.

347. A. V. Naumkin, A. Kraut-Vass, S. W. Gaarenstroom and C. J. Powell, in *NIST Standard Reference database 20*, National Institute of Standards & Technology, 2012, vol. Version 4.1.

348. C. D. Wagner and G. E. Muilenberg, *Handbook of x-ray photoelectron spectroscopy: a reference book of standard data for use in x-ray photoelectron spectroscopy*, Physical Electronics Division, Perkin-Elmer Corp., 1979.

349. D. Briggs and P. Seah, *Practical Surface Analysis: Auger and X-ray photoelectron spectroscopy*, Wiley, 1990.

350. E. Hryha, E. Rutqvist and L. Nyborg, *Surface and Interface Analysis*, 2012, **44**, 1022-1025.

351. C. W. Zou, X. D. Yan, J. Han, R. Q. Chen and W. Gao, *J. Phys. D-Appl. Phys.*, 2009, **42**.

352. D. L. Legrand, H. W. Nesbitt and G. M. Bancroft, *American Mineralogist*, 1998, **83**, 1256-1265.

353. I. P. Parkin and G. S. Elwin, *Journal of Materials Chemistry*, 2001, **11**, 3120-3124.

354. Rees W.S, Jr., *The chemistry of non metal CVD*, 1996.

355. H. Kim and B. N. Popov, *Journal of Power Sources*, 2002, **104**, 52-61.

356. I. P. Parkin and G. S. Elwin, *Journal of Materials Chemistry*, 2001, **11**, 3120-3124.

357. S. L. T. Andersson, *Journal of the Chemical Society, Faraday Transactions 1: Physical Chemistry in Condensed Phases*, 1979, **75**, 1356-1370.

358. L. Z. Zhao, S. H. Liu, D. H. Wang and C. H. Pan, *Journal of Electron Spectroscopy and Related Phenomena*, 1990, **52**, 571-580.

359. D. Choi and P. N. Kumta, *Electrochemical and Solid-State Letters*, 2005, **8**, A418-A422.

360. G. J. Brug, A. L. G. Vandeneeden, M. Sluytersrehbach and J. H. Sluyters, *Journal of Electroanalytical Chemistry*, 1984, **176**, 275-295.

361. C. Portet, G. Yushin and Y. Gogotsi, *Carbon*, 2007, **45**, 2511-2518.

362. M. D. Levi, H. Gizbar, E. Lancry, Y. Gofer, E. Levi and D. Aurbach, *Journal of Electroanalytical Chemistry*, 2004, **569**, 211-223.

363. M. D. Levi, Y. Gofer, D. Aurbach and A. Berlin, *Electrochimica Acta*, 2004, **49**, 433-444.

364. D. Aurbach, M. D. Levi and E. Levi, *Solid State Ionics*, 2008, **179**, 742-751.

365. M. Levi and D. Aurbach, *The Journal of Physical Chemistry B*, 1997, **101**, 4630-4640.

366. A. C. Ferrari and J. Robertson, *Physical Review B*, 2000, **61**, 14095-14107.

367. A. C. Ferrari and J. Robertson, *Physical Review B*, 2001, **64**.

368. E. Cazzanelli, G. Mariotto, S. Passerini, W. H. Smyrl and A. Gorenstein, *Solar Energy Materials and Solar Cells*, 1999, **56**, 249-258.

369. S. Santangelo, G. Messina, G. Faggio, M. G. Willinger, N. Pinna, A. Donato, A. Arena, N. Donato and G. Neri, *Diamond and Related Materials*, 2010, **19**, 590-594.

370. T. Belin and F. Epron, *Materials Science and Engineering: B*, 2005, **119**, 105-118.

371. C. H. Kiang, M. Endo, P. M. Ajayan, G. Dresselhaus and M. S. Dresselhaus, *Physical Review Letters*, 1998, **81**, 1869-1872.

372. J. Muster, G. T. Kim, V. Krstic, J. G. Park, Y. W. Park, S. Roth and M. Burghard, *Advanced Materials*, 2000, **12**, 420-+.

373. N. Takeno, *Atlas of Eh-pH diagrams*, National Institute of Advanced Industrial Science & Technology, 2005.

374. M.-G. Willinger, G. Neri, A. Bonavita, G. Micali, E. Rauwel, T. Herntrich and N. Pinna, *Physical Chemistry Chemical Physics*, 2009, **11**, 3615-3622.

375. L. Niinisto, M. Ritala and M. Leskela, *Mater. Sci. Eng. B-Solid State Mater. Adv. Technol.*, 1996, **41**, 23-29.

376. M. Zhang, M. Yudasaka, S. Bandow and S. Iijima, *Chem. Phys. Lett.*, 2003, **369**, 680-683.

377. M. Toupin, T. Brousse and D. Bélanger, *Chem. Mat.*, 2004, **16**, 3184-3190.

378. V. Subramanian, H. W. Zhu and B. Q. Wei, *Electrochemistry Communications*, 2006, **8**, 827-832.

379. C. Emmenegger, J. M. Bonard, P. Mauron, P. Sudan, A. Lepora, B. Grobety, A. Zuttel and L. Schlapbach, *Carbon*, 2003, **41**, 539-547.

380. G. Atthipalli, R. Epur, P. N. Kumta, M. Yang, J. K. Lee and J. L. Gray, *Journal of Physical Chemistry C*, 2011, **115**, 3534-3538.

381. V. L. Volkov, G. S. Zakharova, E. G. Volkova and M. V. Kuznetsov, *Russ. J. Inorg. Chem.*, 2006, **51**, 847-851.

382. A. Löfberg, T. Giornelli, S. Paul and E. Bordes-Richard, *Applied Catalysis A: General*, 2011, **391**, 43-51.

383. M. G. Nobbenhuis, A. Baiker, P. Barnickel and A. Wokaun, *Applied Catalysis A: General*, 1992, **85**, 157-172.

384. H. Liu, Y. Wu and J. Zhang, *Acs Applied Materials & Interfaces*, 2011, **3**, 1757-1764.

385. V. Stengl, D. Popelkova and P. Vlacil, *Journal of Physical Chemistry C*, 2011, **115**, 25209-25218.

386. G. T. Went, S. T. Oyama and A. T. Bell, *J. Phys. Chem.*, 1990, **94**, 4240-4246.

387. G. N. Kryukova, G. A. Zenkovets, G. Mestl and R. Schlogl, *Reaction Kinetics and Catalysis Letters*, 2003, **80**, 161-169.

388. N. Y. Topsoe, M. Anstrom and J. A. Dumesic, *Catal. Lett.*, 2001, **76**, 11-20.

389. J. B. MacChesney and H. J. Guggenheim, *Journal of Physics and Chemistry of Solids*, 1969, **30**, 225-234.

390. L. A. Balagurov, I. V. Kulemanov, A. F. Orlov and E. A. Petrova, *Russ Microelectron*, 2012, **41**, 503-507.

391. N. Serpone, D. Lawless, J. Disdier and J.-M. Herrmann, *Langmuir*, 1994, **10**, 643-652.

392. G. Zheng, L. Hu, H. Wu, X. Xie and Y. Cui, *Energy & Environmental Science*, 2011, **4**, 3368-3373.

393. A. Ponzoni, E. Comini, I. Concina, M. Ferroni, M. Falasconi, E. Gobbi, V. Sberveglieri and G. Sberveglieri, *Sensors*, 2012, **12**, 17023-17045.

394. J. M. Sieben, E. Morallón and D. Cazorla-Amorós, *Energy*, 2013, **58**, 519-526.

395. X. Liu and P. G. Pickup, *Journal of Power Sources*, 2008, **176**, 410-416.

396. N. Nagarajan, M. Cheong and I. Zhitomirsky, *Materials Chemistry and Physics*, 2007, **103**, 47-53.

397. Y. J. Kang, H. Chung and W. Kim, *Synthetic Metals*, 2013, **166**, 40-44.

398. N. Yamazoe, G. Sakai and K. Shimanoe, *Catalysis Surveys from Asia*, 2003, **7**, 63-75.

399. B. Hirschorn, M. E. Orazem, B. Tribollet, V. Vivier, I. Frateur and M. Musiani, *Electrochimica Acta*, 2010, **55**, 6218-6227.

400. A. M. Glushenkov, D. Hulicova-Jurcakova, D. Llewellyn, G. Q. Lu and Y. Chen, *Chemistry of Materials*, 2009, **22**, 914-921.

401. Z.-S. Wu, D.-W. Wang, W. Ren, J. Zhao, G. Zhou, F. Li and H.-M. Cheng, *Advanced Functional Materials*, 2010, **20**, 3595-3602.

402. G. Kresse and J. Furthmüller, *Physical Review B*, 1996, **54**, 11169-11186.

403. G. Kresse and J. Furthmüller, *Computational Materials Science*, 1996, **6**, 15-50.

404. G. Kresse and D. Joubert, *Physical Review B*, 1999, **59**, 1758-1775.

405. J. P. Perdew and W. Yue, *Physical Review B*, 1986, **33**, 8800-8802.

406. R. Enjalbert and J. Galy, *Acta Crystallographica Section C*, 1986, **42**, 1467-1469.

407. S. Laubach, P. C. Schmidt, Thi, F. J. Fernandez-Madrigal, Q.-H. Wu, W. Jaegermann, M. Klemm and S. Horn, *Physical Chemistry Chemical Physics*, 2007, **9**, 2564-2576.

408. V. Eyert and K. H. Höck, *Physical Review B*, 1998, **57**, 12727-12737.

409. A. Chakrabarti, K. Hermann, R. Druzinic, M. Witko, F. Wagner and M. Petersen, *Physical Review B*, 1999, **59**, 10583-10590.

410. D. R. Lide, *CRC Handbook of chemistry and physics, 86th edn, 2005–2006*, CRC Press, Boca Raton, 2005.

411. R. C. Weast, M. J. Astle and W. H. Beyer, *CRC handbook of chemistry and physics*, CRC press Boca Raton, FL, 1988.

412. J. M. Miller and B. Dunn, *Langmuir*, 1999, **15**, 799-806.

413. R. Liu and S. B. Lee, *Journal of the American Chemical Society*, 2008, **130**, 2942-2943.

414. A. L. M. Reddy, M. M. Shaijumon, S. R. Gowda and P. M. Ajayan, *Nano Lett.*, 2009, **9**, 1002-1006.

415. E. Raymundo-Pinero, V. Khomenko, E. Frackowiak and F. Beguin, *Journal of the Electrochemical Society*, 2005, **152**, A229-A235.

416. J. B. Claridge, A. P. E. York, A. J. Brungs and M. L. H. Green, *Chemistry of Materials*, 2000, **12**, 132-142.

417. G. S. Elwin and I. P. Parkin, *Chemical Vapor Deposition*, 2000, **6**, 59-+.

418. A. Newport, C. J. Carmalt, I. P. Parkin and S. A. O'Neill, *European Journal of Inorganic Chemistry*, 2004, 4286-4290.

419. A. C. Newport, J. E. Bleau, C. J. Carmalt, I. P. Parkin and S. A. O'Neill, *Journal of Materials Chemistry*, 2004, **14**, 3333-3336.

420. C. U. Bang, Y. C. Hong and H. S. Uhm, *Surface & Coatings Technology*, 2007, **201**, 5007-5011.

421. R. Fix, R. G. Gordon and D. M. Hoffman, *Chemistry of Materials*, 1993, **5**, 614-619.

422. C. Muratore, J. E. Bultman, S. M. Aouadi and A. A. Voevodin, *Wear*, 2011, **270**, 140-145.

423. R. A. Nyquist and R. O. Kagel, *Handbook of infrared and raman spectra of inorganic compounds and organic salts: infrared spectra of inorganic compounds*, Academic press, 1972.

424. M. Zhou and L. Andrews, *The Journal of Physical Chemistry A*, 1999, **103**, 478-484.

425. M. M. Thackeray, C. Wolverton and E. D. Isaacs, *Energy & Environmental Science*, 2012, **5**, 7854-7863.

426. P. G. Bruce, S. A. Freunberger, L. J. Hardwick and J.-M. Tarascon, *Nature Materials*, 2012, **11**, 19-29.

427. V. Etacheri, R. Marom, R. Elazari, G. Salitra and D. Aurbach, *Energy & Environmental Science*, 2011, **4**, 3243-3262.

428. M. K. Datta, J. Maranchi, S. J. Chung, R. Epur, K. Kadakia, P. Jampani and P. N. Kumta, *Electrochimica Acta*, 2011, **56**, 4717-4723.

429. R. Epur, M. K. Datta and P. N. Kumta, *Electrochimica Acta*, 2012, **85**, 680-684.

430. C. S. Johnson, N. Li, C. Lefief and M. M. Thackeray, *Electrochemistry Communications*, 2007, **9**, 787-795.

431. J. Cabana, L. Monconduit, D. Larcher and M. Rosa Palacin, *Advanced Materials*, 2010, **22**, E170-E192.

432. B. Scrosati and J. Garche, *Journal of Power Sources*, 2010, **195**, 2419-2430.

433. H. Wang, Y. Yang, Y. Liang, J. T. Robinson, Y. Li, A. Jackson, Y. Cui and H. Dai, *Nano Letters*, 2011, **11**, 2644-2647.

434. Z. Wei Seh, W. Li, J. J. Cha, G. Zheng, Y. Yang, M. T. McDowell, P.-C. Hsu and Y. Cui, *Nat Commun*, 2013, **4**, 1331.

435. X. Ji, K. T. Lee and L. F. Nazar, *Nature Materials*, 2009, **8**, 500-506.

436. J. Schuster, G. He, B. Mandlmeier, T. Yim, K. T. Lee, T. Bein and L. F. Nazar, *Angewandte Chemie International Edition*, 2012, **51**, 3591-3595.

437. X. Liang, Z. Wen, Y. Liu, H. Zhang, J. Jin, M. Wu and X. Wu, *Journal of Power Sources*, 2012, **206**, 409-413.

438. J. Wang, L. Lu, D. Shi, R. Tandiono, Z. Wang, K. Konstantinov and H. Liu, *ChemPlusChem*, 2013, **78**, 318-324.

439. C. Liang, N. J. Dudney and J. Y. Howe, *Chemistry of Materials*, 2009, **21**, 4724-4730.

440. G. Zheng, Q. Zhang, J. J. Cha, Y. Yang, W. Li, Z. W. Seh and Y. Cui, *Nano Letters*, 2013, **13**, 1265-1270.

441. Y.-S. Su and A. Manthiram, *Nat Commun*, 2012, **3**, 1166.

442. Z. Lin, Z. Liu, N. J. Dudney and C. Liang, *ACS Nano*, 2013, **7**, 2829-2833.

443. F. B. Dias, L. Plomp and J. B. J. Veldhuis, *Journal of Power Sources*, 2000, **88**, 169-191.

444. D. Marmorstein, T. H. Yu, K. A. Striebel, F. R. McLarnon, J. Hou and E. J. Cairns, *Journal of Power Sources*, 2000, **89**, 219-226.

445. J. Hassoun and B. Scrosati, *Advanced Materials*, 2010, **22**, 5198-5201.

446. Z. Liu, W. Fu, E. A. Payzant, X. Yu, Z. Wu, N. J. Dudney, J. Kiggans, K. Hong, A. J. Rondinone and C. Liang, *Journal of the American Chemical Society*, 2013, **135**, 975-978.

447. Z. Lin, Z. Liu, W. Fu, N. J. Dudney and C. Liang, *Angewandte Chemie International Edition*, 2013, **52**, 7460-7463.

448. N. Kamaya, K. Homma, Y. Yamakawa, M. Hirayama, R. Kanno, M. Yonemura, T. Kamiyama, Y. Kato, S. Hama, K. Kawamoto and A. Mitsui, *Nat Mater*, 2011, **10**, 682-686.

449. R. D. Shannon and B. E. Taylor, Google Patents, 1977.

450. M. Armand, C. Michot, N. Ravet, M. Simoneau and P. Hovington, Google Patents, 2000.

451. L. De Jonghe, S. J. Visco, Y. S. Nimon and A. M. Sukeshini, Google Patents, 2005.

452. I. A. Massalimov, A. R. Shainurova, A. N. Khusainov and A. G. Mustafin, *Russ J Appl Chem*, 2012, **85**, 1832-1837.

453. , ed. U. S. D. O. Energy, 2008.

454. Y. Gogotsi and P. Simon, *Science Magazine*, 2011, **334**, 917-918.

455. T. Xu, J. Song, M. L. Gordin, H. Sohn, Z. Yu, S. Chen and D. Wang, *ACS applied materials & interfaces*, 2013, **5**, 11355-11362.

456. J. Graetz, C. C. Ahn, R. Yazami and B. Fultz, *Electrochemical and Solid State Letters*, 2003, **6**, A194-A197.

457. M. D. Levi and D. Aurbach, *The Journal of Physical Chemistry B*, 1997, **101**, 4641-4647.

458. K. Zaghib, J. Shim, A. Guerfi, P. Charest and K. Striebel, *Electrochemical and Solid-State Letters*, 2005, **8**, A207-A210.

459. D. Tranqui, R. Shannon, H.-Y. Chen, S. Iijima and W. Baur, *Acta Crystallographica Section B: Structural Crystallography and Crystal Chemistry*, 1979, **35**, 2479-2487.

460. R. Shannon, *Acta Crystallographica Section A: Crystal Physics, Diffraction, Theoretical and General Crystallography*, 1976, **32**, 751-767.

461. S. Thieme, J. Brückner, I. Bauer, M. Oschatz, L. Borchardt, H. Althues and S. Kaskel, *Journal of Materials Chemistry A*, 2013, **1**, 9225-9234.

462. N. Brun, K. Sakaushi, L. Yu, L. Giebeler, J. Eckert and M. M. Titirici, *Physical Chemistry Chemical Physics*, 2013, **15**, 6080-6087.

463. J. Y. Song, H. H. Lee, Y. Y. Wang and C. C. Wan, *Journal of Power Sources*, 2002, **111**, 255-267.

464. S. S. Zhang, K. Xu and T. R. Jow, *Electrochimica Acta*, 2004, **49**, 1057-1061.

465. Daniel H. Doughty, Paul C. Butler, Abbas A. Akhil, Nancy H. Clark and J. D. Boyes, *The Electrochemical Society's Interface*, Fall 2010, **19**, 49-53.

466. D. Aurbach, G. Suresh, E. Levi, A. Mitelman, O. Mizrahi, O. Chusid and M. Brunelli, *Advanced Materials*, 2007, **19**, 4260-4267.

467. H. S. Kim, T. S. Arthur, G. D. Allred, J. Zajicek, J. G. Newman, A. E. Rodnyansky, A. G. Oliver, W. C. Boggess and J. Muldoon, *Nat Commun*, 2011, **2**, 427.

468. J. O. Besenhard and M. Winter, *ChemPhysChem*, 2002, **3**, 155-159.

469. B. Peng, J. Liang, Z. Tao and J. Chen, *Journal of Materials Chemistry*, 2009, **19**, 2877-2883.

470. Y. NuLi, Z. Guo, H. Liu and J. Yang, *Electrochemistry Communications*, 2007, **9**, 1913-1917.

471. W. Li, C. Li, C. Zhou, H. Ma and J. Chen, *Angewandte Chemie International Edition*, 2006, **45**, 6009-6012.

472. D. Aurbach, Y. Cohen and M. Moshkovich, *Electrochemical and Solid-State Letters*, 2001, **4**, A113-A116.

473. M. Matsui, *Journal of Power Sources*, 2011, **196**, 7048-7055.

474. O. R. Brown and R. McIntyre, *Electrochimica Acta*, 1985, **30**, 627-633.

475. Z. Lu, A. Schechter, M. Moshkovich and D. Aurbach, *Journal of Electroanalytical Chemistry*, 1999, **466**, 203-217.

476. L. P. Lossius and F. Emmenegger, *Electrochimica Acta*, 1996, **41**, 445-447.

477. C. Liebenow, *Journal of Applied Electrochemistry*, 1997, **27**, 221-225.

478. D. Aurbach, Z. Lu, A. Schechter, Y. Gofer, H. Gizbar, R. Turgeman, Y. Cohen, M. Moshkovich and E. Levi, *Nature*, 2000, **407**, 724-727.

479. O. Mizrahi, N. Amir, E. Pollak, O. Chusid, V. Marks, H. Gottlieb, L. Larush, E. Zinigrad and D. Aurbach, *Journal of The Electrochemical Society*, 2008, **155**, A103-A109.

480. J. Muldoon, C. B. Bucur, A. G. Oliver, T. Sugimoto, M. Matsui, H. S. Kim, G. D. Allred, J. Zajicek and Y. Kotani, *Energy & Environmental Science*, 2012, **5**, 5941-5950.

481. E. Lancry, E. Levi, A. Mitelman, S. Malovany and D. Aurbach, *Journal of Solid State Chemistry*, 2006, **179**, 1879-1882.

482. E. Levi, G. Gershinsky, D. Aurbach, O. Isnard and G. Ceder, *Chemistry of Materials*, 2009, **21**, 1390-1399.

483. P. Rabiller, M. Rabiller-Baudry, S. Even-Boudjada, L. Burel, R. Chevrel, M. Sergent, M. Decroux, J. Cors and J. L. Maufras, *Materials Research Bulletin*, 1994, **29**, 567-574.

484. E. Lancry, E. Levi, Y. Gofer, M. Levi, G. Salitra and D. Aurbach, *Chemistry of Materials*, 2004, **16**, 2832-2838.

485. G. Gershinsky, O. Haik, G. Salitra, J. Grinblat, E. Levi, G. Daniel Nessim, E. Zinigrad and D. Aurbach, *Journal of Solid State Chemistry*, 2012, **188**, 50-58.

486. R. E. Doe, R. Han, J. Hwang, A. J. Gmitter, I. Shterenberg, H. D. Yoo, N. Pour and D. Aurbach, *Chemical Communications*, 2014, **50**, 243-245.

487. K. S. Nanjundaswamy, N. Y. Vasanthacharya, J. Gopalakrishnan and C. N. R. Rao, *Inorganic Chemistry*, 1987, **26**, 4286-4288.

488. W. H. Pan, M. E. Leonowicz and E. I. Stiefel, *Inorganic Chemistry*, 1983, **22**, 672-678.

489. M. D. Levi, E. Lancry, H. Gizbar, Z. Lu, E. Levi, Y. Gofer and D. Aurbach, *Journal of the Electrochemical Society*, 2004, **151**, A1044-A1051.

490. M. D. Levi and D. Aurbach, *Journal of Power Sources*, 2005, **146**, 349-354.

491. E. Levi, E. Lancry, A. Mitelman, D. Aurbach, G. Ceder, D. Morgan and O. Isnard, *Chemistry of Materials*, 2006, **18**, 5492-5503.

492. E. Levi, M. Levi, O. Chasid and D. Aurbach, *J. Electroceram.*, 2009, **22**, 13-19.

493. E. Levi, Y. Gofer, Y. Vestfreed, E. Lancry and D. Aurbach, *Chemistry of Materials*, 2002, **14**, 2767-2773.

494. Z. Yang, J. Zhang, M. C. W. Kintner-Meyer, X. Lu, D. Choi, J. P. Lemmon and J. Liu, *Chemical Reviews*, 2011, **111**, 3577-3613.

495. M. S. Whittingham, *MRS Bull. MRS Bulletin*, 2008, **33**, 411-419.

496. *Linden's Handbook of Batteries (4th Edition)*, McGraw-Hill, 2010.

497. J. M. Tarascon and M. Armand, *Nature*, 2001, **414**, 359-367.

498. M. D. Slater, D. Kim, E. Lee and C. S. Johnson, *Advanced Functional Materials*, 2013, **23**, 947-958.

499. B. L. Ellis and L. F. Nazar, *Current Opinion in Solid State and Materials Science*, 2012, **16**, 168-177.

500. V. Palomares, P. Serras, I. Villaluenga, K. B. Hueso, J. Carretero-Gonzalez and T. Rojo, *Energy & Environmental Science*, 2012, **5**, 5884-5901.

501. N. Yabuuchi, M. Kajiyama, J. Iwatate, H. Nishikawa, S. Hitomi, R. Okuyama, R. Usui, Y. Yamada and S. Komaba, *Nat Mater*, 2012, **11**, 512-517.

502. L. Xiao, Y. Cao, J. Xiao, W. Wang, L. Kovarik, Z. Nie and J. Liu, *Chemical Communications*, 2012, **48**, 3321-3323.

503. S.-W. Kim, D.-H. Seo, X. Ma, G. Ceder and K. Kang, *Advanced Energy Materials*, 2012, **2**, 710-721.

504. D. Lide, *CRC Handbook of Chemistry and Physics, 88th Edition (CRC Handbook of Chemistry & Physics)*, CRC Press, 2007.

505. A. D. Tevar and J. F. Whitacre, *Journal of The Electrochemical Society*, 2010, **157**, A870-A875.

506. M. K. Datta, R. Epur, P. Saha, K. Kadakia, S. K. Park and P. N. Kumta, *Journal of Power Sources*, 2013, **225**, 316-322.

507. J. Qian, Y. Chen, L. Wu, Y. Cao, X. Ai and H. Yang, *Chemical Communications*, 2012, **48**, 7070-7072.

508. S. Komaba, W. Murata, T. Ishikawa, N. Yabuuchi, T. Ozeki, T. Nakayama, A. Ogata, K. Gotoh and K. Fujiwara, *Advanced Functional Materials*, 2011, **21**, 3859-3867.

509. A. Bhide and K. Hariharan, *Solid State Ionics*, 2011, **192**, 360-363.

510. Z. Lu and J. R. Dahn, *Journal of The Electrochemical Society*, 2001, **148**, A1225-A1229.

511. M. M. Doeff, T. J. Richardson and K.-T. Hwang, *Journal of Power Sources*, 2004, **135**, 240-248.

512. J. F. Whitacre, A. Tevar and S. Sharma, *Electrochem. Commun.*, 2010, **12**, 463-466.

513. F. Sauvage, L. Laffont, J. M. Tarascon and E. Baudrin, *Inorganic Chemistry*, 2007, **46**, 3289-3294.

514. D. Carlier, J. H. Cheng, R. Berthelot, M. Guignard, M. Yoncheva, R. Stoyanova, B. J. Hwang and C. Delmas, *Dalton Transactions*, 2011, **40**.

515. H. Pan, Y.-S. Hu and L. Chen, *Energy & Environmental Science*, 2013, **6**, 2338-2360.

516. Y. Cao, L. Xiao, W. Wang, D. Choi, Z. Nie, J. Yu, L. V. Saraf, Z. Yang and J. Liu, *Advanced Materials*, 2011, **23**, 3155-3160.

517. C. Delmas, C. Fouassier and P. Hagenmuller, *Physica B+C*, 1980, **99**, 81-85.

518. A. Yamada, M. Tanaka, K. Tanaka and K. Sekai, *Journal of Power Sources*, 1999, **81–82**, 73-78.

519. S. Komaba, N. Yabuuchi, T. Nakayama, A. Ogata, T. Ishikawa and I. Nakai, *Inorganic Chemistry*, 2012, **51**, 6211-6220.

520. H. Kim, D. J. Kim, D.-H. Seo, M. S. Yeom, K. Kang, D. K. Kim and Y. Jung, *Chem. Mat.*, 2012, **24**, 1205-1211.

521. E. Hosono, H. Matsuda, I. Honma, S. Fujihara, M. Ichihara and H. S. Zhou, *Journal of Power Sources*, 2008, **182**, 349-352.

522. P. Barpanda, G. Liu, C. D. Ling, M. Tamaru, M. Avdeev, S.-C. Chung, Y. Yamada and A. Yamada, *Chem. Mat.*, 2013.

523. J. Barker, M. Y. Saidi and J. L. Swoyer, *Electrochemical and Solid State Letters*, 2003, **6**, A1-A4.

524. W. Song, X. Ji, Z. Wu, Y. Yang, Z. Zhou, F. Li, Q. Chen and C. E. Banks, *Journal of Power Sources*, 2014, **256**, 258-263.

525. Y. Kawabe, N. Yabuuchi, M. Kajiyama, N. Fukuhara, T. Inamasu, R. Okuyama, I. Nakai and S. Komaba, *Electrochem. Commun.*, 2011, **13**, 1225-1228.

526. B. L. Ellis, W. R. M. Makahnouk, W. N. Rowan-Weetaluktuk, D. H. Ryan and L. F. Nazar, *Chem. Mat.*, 2009, **22**, 1059-1070.

527. Y. Lu, L. Wang, J. Cheng and J. B. Goodenough, *Chemical Communications*, 2012, **48**, 6544-6546.

528. X. Wu, W. Deng, J. Qian, Y. Cao, X. Ai and H. Yang, *Journal of Materials Chemistry A*, 2013.

529. C. D. Wessells, M. T. McDowell, S. V. Peddada, M. Pasta, R. A. Huggins and Y. Cui, *ACS Nano*, 2012, **6**, 1688-1694.

530. S. Komaba, T. Mikumo, N. Yabuuchi, A. Ogata, H. Yoshida and Y. Yamada, *Journal of The Electrochemical Society*, 2010, **157**, A60-A65.

531. J. Park, J.-S. Kim, J.-W. Park, T.-H. Nam, K.-W. Kim, J.-H. Ahn, G. Wang and H.-J. Ahn, *Electrochimica Acta*, 2013, **92**, 427-432.

532. C. Li, C. Yin, X. Mu and J. Maier, *Chem. Mat.*, 2013, **25**, 962-969.

533. E. Levi, G. Gershinsky, D. Aurbach and O. Isnard, *Inorganic Chemistry*, 2009, **48**, 8751-8758.

534. E. Gocke, W. Schramm, P. Dolscheid and R. Scho¨llhorn, *Journal of Solid State Chemistry*, 1987, **70**, 71-81.

535. J. M. Tarascon, G. W. Hull, P. Marsh and T. Haar, *Journal of Solid State Chemistry*, 1987, **66**, 204-224.

536. P. Saha, P. H. Jampani, M. K. Datta, C. U. Okoli, A. Manivannan and P. N. Kumta, *Journal of The Electrochemical Society*, 2014, **161**, A593-A598.

537. C. Suryanarayana, *Progress in Materials Science*, 2001, **46**, 1-184.

538. A. Le Bail, H. Duroy and J. L. Fourquet, *Materials Research Bulletin*, 1988, **23**, 447-452.

539. L. B. McCusker, R. B. Von Dreele, D. E. Cox, D. Louer and P. Scardi, *J. Appl. Crystallogr.*, 1999, **32**, 36-50.

540. Ø. Fischer, *Appl. Phys.*, 1978, **16**, 1-28.

541. E. Levi, A. Mitelman, D. Aurbach and O. Isnard, *Inorganic Chemistry*, 2007, **46**, 7528-7535.

542. M. Levi and D. Aurbach, *Journal of power sources*, 2005, **146**, 349-354.

543. J. Tarascon, G. Hull, P. Marsh and T. Haar, *Journal of Solid State Chemistry*, 1987, **66**, 204-224.

544. E. Gocke, R. Schoellhorn, G. Aselmann and W. Mueller-Warmuth, *Inorganic Chemistry*, 1987, **26**, 1805-1812.